

ADDRESS OF PUBLISHER  
& EDITOR'S OFFICE:

GDAŃSK UNIVERSITY  
OF TECHNOLOGY

Faculty of Ocean Engineering  
& Ship Technology  
G. Narutowicza 11/12  
80-233 Gdańsk, POLAND

EDITORIAL STAFF:

Wiesław Tarełko  
| Editor in Chief  
Janusz Kozak  
| Deputy Editors-in-Chief  
Wojciech Litwin  
| Deputy Editors-in-Chief

Price:  
single issue: 25 PLN

Prices for abroad  
single issue:  
- in Europe EURO 15  
- overseas USD 20

WEB:  
[pg.edu.pl/pmr](http://pg.edu.pl/pmr)

e-mail : [pmr@pg.edu.pl](mailto:pmr@pg.edu.pl)

ISSN 1233-2585

## CONTENS

4	<b>Yun Lu, Jinbo Wu, Weijia Li, Yaozhong Wu</b> <i>A NEW SIX-DOF PARALLEL MECHANISM FOR CAPTIVE MODEL TEST</i>
16	<b>Artur Karczewski, Łukasz Piątek</b> <i>THE INFLUENCE OF THE CUBOID FLOAT'S PARAMETERS ON THE STABILITY OF A FLOATING BUILDING</i>
22	<b>Fei Wang, Neng Chen</b> <i>DYNAMIC RESPONSE ANALYSIS OF DRILL PIPE CONSIDERING HORIZONTAL MOVEMENT OF PLATFORM DURING INSTALLATION OF SUBSEA PRODUCTION TREE</i>
31	<b>Piotr Iwicki, Jarosław Przewłócki</b> <i>SHORT REVIEW AND 3-D FEM ANALYSIS OF BASIC TYPES OF FOUNDATION FOR OFFSHORE WIND TURBINES</i>
40	<b>Wanchao Zhang, Yujie Zhou, Kai Wang, Xiaoguo Zhou</b> <i>FORCED MOTION CFD SIMULATION AND LOAD REFINEMENT EVALUATION OF FLOATING VERTICAL-AXIS TIDAL CURRENT TURBINES</i>
50	<b>Ozgur Ozguc</b> <i>ASSESSMENT OF BUCKLING BEHAVIOUR ON AN FPSO DECK PANEL</i>
59	<b>Tacjana Niksa-Rynkiewicz, Michał Landowski, Paweł Szalewski</b> <i>APPLICATION OF APRIORI ALGORITHM IN THE LAMINATION PROCESS IN YACHT PRODUCTION</i>
71	<b>Mariusz Deja, Mieczysław Stanisław Siemiątkowski, Dawid Zieliński</b> <i>MULTI-CRITERIA COMPARATIVE ANALYSIS OF THE USE OF SUBTRACTIVE AND ADDITIVE TECHNOLOGIES IN THE MANUFACTURING OF OFFSHORE MACHINERY COMPONENTS</i>
82	<b>Leszek Matuszewski</b> <i>APPLICATION OF SHAPE MEMORY ALLOYS IN PIPELINE COUPLINGS FOR SHIPBUILDING</i>
89	<b>Serhiy Serbin, Badri Diasamidze, Marek Dzida</b> <i>INVESTIGATIONS OF THE WORKING PROCESS IN A DUAL-FUEL LOW-EMISSION COMBUSTION CHAMBER FOR AN FPSO GAS TURBINE ENGINE</i>
100	<b>Pan Geng, Xiaoyan Xu, Tomasz Tarasiuk</b> <i>STATE OF CHARGE ESTIMATION METHOD FOR LITHIUM-ION BATTERIES IN ALL-ELECTRIC SHIPS BASED ON LSTM NEURAL NETWORK</i>

**ADDRESS OF PUBLISHER  
& EDITOR'S OFFICE:**

**GDAŃSK UNIVERSITY  
OF TECHNOLOGY**

**Faculty of Ocean Engineering  
& Ship Technology  
G. Narutowicza 11/12  
80-233 Gdańsk, POLAND**

- 109 Krzysztof Wołoszyk, Yordan Garbatov**  
*ANALYSIS OF ULTIMATE COMPRESSIVE STRENGTH OF CRACKED PLATES  
WITH THE USE OF DOE TECHNIQUES*
- 121 Yao Zilin, Wang Yu, Yang Xuefeng, Gao Anping, Zhang Rong, Jia Yanjie**  
*INVESTIGATIONS OF MECHANICAL PROPERTIES OF API P110 STEEL CASING  
TUBES OPERATED IN DEEP-SEA SOUR CONDENSATE WELL CONDITIONS*
- 130 Ewa Sobocka, Rafał Szlarczyński, Marcin Życzkowski**  
*EVOLUTIONARY MULTI-OBJECTIVE WEATHER ROUTING OF SAILBOATS*
- 140 Grzegorz Rutkowski**  
*DETERMINING THE BEST POSSIBLE SPEED OF THE SHIP IN SHALLOW WATERS  
ESTIMATED BASED ON THE ADOPTED MODEL FOR CALCULATION OF THE  
SHIP'S DOMAIN DEPTH*
- 149 Marcin Życzkowski**  
*SAILING ROUTE PLANNING METHOD CONSIDERING VARIOUS USER  
CATEGORIES*
- 159 Michał Szydłowski, Tomasz Kolerski**  
*HYDRODYNAMIC MODEL OF THE NEW WATERWAY THROUGH THE VISTULA  
SPIT*
- 168 Romana Antczak-Jarząbska, Maciej Niedostatkiwicz**  
*APPLICATION OF THE CHIMNEY CAP AS A METHOD OF IMPROVING THE  
EFFECTIVENESS OF NATURAL VENTILATION IN BUILDINGS*
- 176 Krystian Buszman**  
*ANALYSING THE IMPACT ON UNDERWATER NOISE OF CHANGES TO THE  
PARAMETERS OF A SHIP'S MACHINERY*
- 182 Andrzej Wróblewski, Aldona Skotnicka-Siepsiak**  
*EFFECT OF ROTATIONAL SPEED OF A SELF-ASPIRATING MIXER ON OXYGEN  
SATURATION IN WATER*

---

## Editorial

POLISH MARITIME RESEARCH is the scientific journal with a worldwide circulation. This journal is published quarterly (four times a year) by Gdansk University of Technology (GUT). On September, 1994, the first issue of POLISH MARITIME RESEARCH was published. The main objective of this journal is to present original research, innovative scientific ideas, and significant findings and application in the field of :

### Naval Architecture, Ocean Engineering and Underwater Technology,

The scope of the journal covers selected issues related to all phases of product lifecycle and corresponding technologies for offshore floating and fixed structures and their components.

All researchers are invited to submit their original papers for peer review and publications related to methods of the design; production and manufacturing; maintenance and operational processes of such technical items as:

- all types of vessels and their equipment,
- fixed and floating offshore units and their components,
- autonomous underwater vehicle (AUV) and remotely operated vehicle (ROV).

We welcome submissions from these fields in the following technical topics:

- ship hydrodynamics: buoyancy and stability; ship resistance and propulsion, etc.,
- structural integrity of ship and offshore unit structures: materials; welding; fatigue and fracture, etc.,
- marine equipment: ship and offshore unit power plants: overboarding equipment; etc.

---

### Scientific Board

**Chairman : Prof. JERZY GIRTLEK - Gdańsk University of Technology, Poland**

**Vice-chairman : Prof. CARLOS GUEDES SOARES, Universidade de Lisboa, Lisbon, Portugal**

**Vice-chairman : Prof. MIROSŁAW L. WYSZYŃSKI - University of Birmingham, United Kingdom**

<b>Prof. POUL ANDERSEN</b> Technical University of Denmark Kongens Lyngby Denmark	<b>Prof. STOJCE DIMOV ILCEV</b> Durban University of Technology Durban South Africa	<b>Prof. JERZY EDWARD MATUSIAK</b> Aalto University Espoo Finland
<b>Prof. JIAHN-HORNG CHEN</b> National Taiwan Ocean University Keelung Taiwan	<b>Prof. YORDAN GARBATOV</b> Universidade de Lisboa, Lisbon Portugal	<b>Prof. JERZY MERKISZ</b> Poznan University of Technology Poznan Poland
<b>Prof. VINCENZO CRUPI</b> University of Messina Messina Italy	<b>Prof. STANISŁAW GUCMA</b> Maritime University of Szczecin Szczecin Poland	<b>Prof. VALERI NIEKRASOV</b> Admiral Makarov National University of Shipbuilding Mikolaiv Ukraine
<b>Prof. MAREK DZIDA</b> Gdansk University of Technology Gdansk Poland	<b>Prof. ANTONI ISKRA</b> Poznan University of Technology Poznan Poland	<b>Prof. JOZEF SZALA</b> UTP University of Science and Technology Bydgoszcz Poland
<b>Prof. ODD MAGNUS FALTINSEN</b> Norwegian University of Science and Technology Trondheim Norway	<b>Prof. JAN KICINSKI</b> Institute of Fluid-Flow Machinery - Polish Academy of Sciences Gdansk Poland	<b>Prof. TADEUSZ SZELANGIEWICZ</b> Maritime University of Szczecin Szczecin Poland
<b>Prof. MASSIMO FIGARI</b> University of Genova Genova Italy	<b>Prof. ZBIGNIEW KORCZEWSKI</b> Gdansk University of Technology Gdansk Poland	<b>Prof. DRACOS VASSALOS</b> University of Strathclyde Glasgow United Kingdom
<b>Prof. HASSAN GHASSEMI</b> Amirkabir University of Technology Tehran Iran	<b>Prof. JOZEF LISOWSKI</b> Gdynia Maritime University Gdynia Poland	

## A NEW SIX-DOF PARALLEL MECHANISM FOR CAPTIVE MODEL TEST

Yun Lu  
Jinbo Wu  
Weijia Li  
Yaozhong Wu

School of Naval Architecture and Ocean Engineering,  
Huazhong University of Science and Technology, China

### ABSTRACT

*In order to obtain the hydrodynamic coefficients that can save cost and meet the accuracy requirements, a new hydrodynamic test platform based on a 6DoF (six degrees of freedom) parallel mechanism is proposed in this paper. The test platform can drive the ship to move in six degrees of freedom. By using this experimental platform, the corresponding hydrodynamic coefficients can be measured. Firstly, the structure of the new device is introduced. The working principle of the model is deduced based on the mathematical model. Then the hydrodynamic coefficients of a test ship model of a KELC tank ship with a scale of 1:150 are measured and 8 typical hydrodynamic coefficients are obtained. Finally, the measured data are compared with the value of a real ship. The deviation is less than 10% which meets the technical requirements of the practical project. The efficiency of measuring the hydrodynamic coefficients of physical models of ships and offshore structures is improved by the device. The method of measuring the hydrodynamic coefficients by using the proposed platform provides a certain reference for predicting the hydrodynamic performance of ships and offshore structures.*

**Keywords:** hydrodynamic coefficient, six DoF parallel mechanism, six component balance, captive model test

### INTRODUCTION

The hydrodynamic coefficients are the coefficients of the equations of motion of a ship or submersible. Therefore, the hydrodynamic coefficients must be determined first to simulate the manoeuvring motion and predict the manoeuvrability based on the ship manoeuvring motion equation [1-2]. At present, there are three main methods to obtain the hydrodynamic coefficients: the captive or free self-propelled model test, computer numerical simulation, and semi-theoretical and semi-empirical estimation [3-5].

Hydrodynamic model tests can be divided into captive model tests and free self-propelled ship model tests. There is a “scale effect” in the free self-propelled ship model test

and it is still difficult to solve this problem at present. So the main method used is captive ship model testing, which mainly includes the oblique running test (ORT) [6], which is also known as the straight-line towing test, rotating arm test (RAT) [7], and plane motion mechanism (PMM) test [8-9].

The position derivative and coupling hydrodynamic coefficients of the submersible in the state of drift angle and rudder angle can be determined by the oblique running test. The force or moment derivatives related to angular velocity can be determined by the rotating arm test. At present, many scholars have obtained the corresponding hydrodynamic coefficients through these two tests. In order to study the influence of the free surface on the resistance and lift coefficient of a submersible, Mansoorzadeh et al. [10] used

a 1:1 ship model to conduct a straight-line towing test in the towing pool and obtained the hydrodynamic coefficients of the submersible at different speeds and depths. Then they further studied the influence of the free surface on the resistance and lift coefficient. In order to research the hydrodynamic performance of small submersibles in the preliminary design, Gala et al. [11] obtained the hydrodynamic coefficients of small submersibles at different drift angles and attack angles using the ORT test and numerical simulation methods. They compared the results obtained by the two methods to verify the feasibility of the numerical method. For the same purpose, Li Gang et al. [12] took a certain submersible as a model to carry out the rotating arm test to obtain the rotating derivative, and used the data obtained to verify the accuracy of the numerical rotating arm pool model.

Avila et al. [13] conducted pure sway and pure yaw motion tests with a full-scale open frame submersible through a PMM to obtain the linear acceleration derivative and linear velocity derivative, thus providing sufficient hydrodynamic derivatives for manoeuvrability prediction. However, the simulation of pure sway and pure head roll can only obtain the inertial hydrodynamic coefficients of the horizontal plane, but not the vertical plane. Therefore, Xu et al. [14] conducted pure heave and pure pitch motion tests through a vertical plane motion mechanism and circulation tank, and obtained the inertial hydrodynamic coefficients of the vertical plane of the submersible. At present, more scholars are using the plane motion mechanism to test and study the hydrodynamic force of the submersible under the condition of the 6DoF coupling motion, and the research results are quite abundant. For example, Zhao et al. [15] took a small submersible with a pod as the research object to conduct hydrodynamic model tests, such as direct navigation, slant navigation, pure heave, pure pitch, pure heave and pure yaw, etc., to obtain the hydrodynamic coefficients needed for submersible manoeuvrability prediction and to compare and verify the calculated results with the numerical results. Pang et al. [16] used a VPMM (vertical PMM) in the circulation tank to conduct constraint model tests on submarine models without and with oars, and analysed the influence of the propeller on the hydrodynamic manoeuvrability of the submarine.

With the development of computers, the computational fluid dynamics (CFD) method is increasingly applied to the estimation of hydrodynamic derivatives. In 1990, Kijima and Nakiri [17] proposed a hydrodynamic derivative calculation method for manoeuvring motion, considering the stern shape based on the test data of 15 boats. In 1999, Maekawa et al. [18] proposed a CFD method to calculate the additional mass factor of the superstructure part of the ship. In 2000, Kijima et al. [19] used the constrained model test to measure a damaged ship in different trim states and obtained its hydrodynamic data. In 2000, Petersen and Lauridsen [20] proposed a new regression method with higher accuracy and adaptability based on the hydrodynamic derivatives of manoeuvring motion obtained from a PMM test. In 2006, through CFD calculation and verification analysis of a series of ship models, Yang [21] proved that the hydrodynamic CFD prediction

method for manoeuvrability of large ships had good accuracy and universality. In 2018, Gao et al. [22] proposed a space capture motion simulation method for determining the hydrodynamic model coefficients.

The Stewart platform originated from a six degrees of freedom flight simulation mechanism designed by Stewart [23], which simulates the flight state of an aircraft by generating 6DoF motion in space. The mechanism designed by Stewart is supported by a triangular platform. The spherical hinge is supported on three driving legs with adjustable lengths and angles, and connected to the ground through two axle joints. Yurt designed a Stewart platform with six degrees of freedom and a pneumatic actuator for a flight simulator by using the method of complex dynamic system modelling [24]. Landry designed and implemented a low-cost flight simulator using commercial components for the Royal Military Academy of Canada [25]. Phoemsapthawee studied a new autonomous underwater vehicle by combining a 6DoF motion simulator with an unsteady potential flow coupling model [26]. Kim developed a six axis force/moment sensor based on the Stewart platform [27].

There are different ship models and many appendages. At present, there is no systematic design data available for approximate calculation. Therefore, the empirical equations of surface ships, submarines, torpedoes, etc. are often used. The estimation of the hydrodynamic force has brought great errors. Generally speaking, the semi-empirical and semi-theoretical estimation method can save time and capital cost, but it cannot meet the precision required in engineering [28,29]. The hydrodynamic coefficients obtained by the computer simulation method have high accuracy and can meet the requirements of manoeuvrability design, motion prediction and simulation in the preliminary design stage. However, the hydrodynamic coefficients that can be accurately calculated are fewer, and the calculation of the ship coupling hydrodynamic coefficients is still not accurate enough. Moreover, with the computer simulation method it is difficult to select the optimal model, decouple and identify it, and it cannot be applied to all ships. In addition, the method has some errors in calculating the coefficient of viscosity.

The captive model test is the most mature method to determine the hydrodynamic coefficients and it is still the main method used to solve practical problems in engineering. The test results are often compared with the numerical simulation results. However, the model test usually needs a lot of manpower and material resources and the test period is long. It is the focus of scholars to find a method to obtain the hydrodynamic coefficients that can not only save costs but also meet the accuracy requirements. The 6DoF parallel motion mechanism studied in this paper has become a promising method to solve the above problems. The 6DoF mechanism can generate 6DoF independent or coordinated motion in a single device, which is of great significance for the effective measurement of the hydrodynamic coefficients of complex motion physical models.

## TEST MECHANISM AND THEORETICAL ANALYSIS

### STRUCTURE OF SIX DOF PARALLEL MECHANISM MODEL

The hydrodynamic test platform of the 6DoF parallel mechanism is composed of the 6DoF parallel mechanism, a six-dimensional force/torque sensor, a trailer, an ultrasonic rangefinder and a corresponding control system. The performance parameters of the test equipment are shown in Table 1. Because the electric driven 6DoF platform is quiet, clean and precise, this research adopts an electrically driven way to make the 6DoF platform generate motion. The basic motion of the platform is the linear reciprocating motion of six moving rods driven by the electric cylinder driven by the servo motor. For better installation and control, the upper and lower planes of the 6DoF platform are a motion plane and a fixed plane respectively. The fixed plane is connected with the lower half of the trailer frame, while the motion plane is connected with the test ship model, and the connected part is equipped with the six-dimensional force/moment sensor. Fig. 1 shows the structure of the hydrodynamic test platform.

Tab. 1. Types of experiment platform

Equipment	Type	Technical parameter
6DoF parallel mechanism	Motus TII	See Table 4
Ultrasonic rangefinder	UC2000-30GM-IUR2-V15	Sensing distance: 80–2000 mm
Six-dimensional force/torque sensor	K6D68 2kN/50N•m	See Table 5
Control system	Adv. Tech. S30861	–

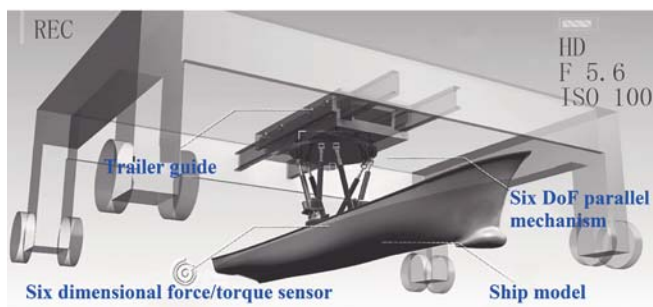


Fig. 1. Structure of the hydrodynamic test platform

The function of the 6DoF platform is embodied in the movement of six degrees of freedom. The motion is composed of the linear motion of six moving bars, including three displacements and three motions. The motion of these six degrees of freedom is essentially the same as that of the ship, i.e. roll, pitch, yaw, sway, surge and heave. In general, in order for the test device to drive the ship model to move according to the predetermined values of roll angle, pitch angle, yaw angle, sway displacement, surge displacement and heave

displacement, it is necessary to give motion instructions to all the moving rods of the 6DoF platform, i.e. to input six linear displacements, and output them to the ship's roll, pitch, yaw, sway, surge and heave after conversion. The working principle is elaborated in the second and third parts of this section.

### KINEMATICS ANALYSIS OF SIX-DOF PARALLEL MECHANISM

The terminal manoeuvring platform forces the experimental ship model to perform specific motions. Therefore, we need to calculate the motion relation between the input variables of the 6DoF parallel mechanism and the experimental ship model. The aim of kinematics analysis is mainly to establish the relationship between the pose of the manoeuvring platform and the input variables. Kinematics analysis is the basis of force analysis, workspace calculation, dynamics analysis, and robot motion planning and control.

For kinematics analysis, we define two right hand Cartesian coordinates which are shown in Fig. 2.  $\{B\}$  is the coordinate point vector of the upper control platform and its corresponding coordinate system  $O-X_B Y_B Z_B$  is a fixed coordinate system.  $\{b\}$  is the coordinate point vector of the bearing hinge point in the lower control platform and its corresponding coordinate system  $O-X_b Y_b Z_b$  is a moving coordinate system.

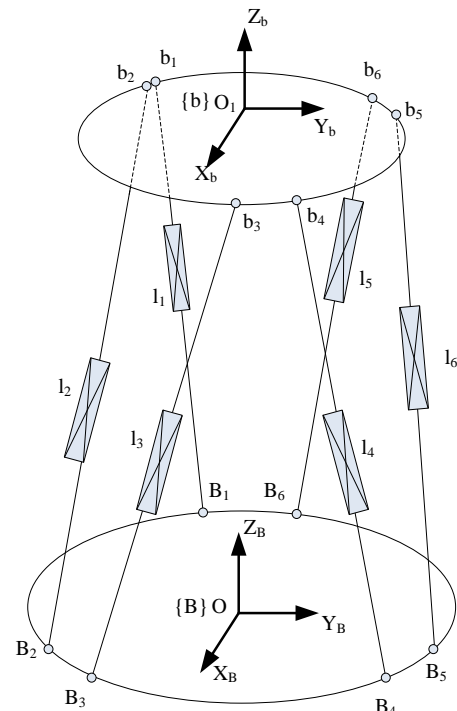


Fig. 2. Coordinate transformation of six-DoF parallel mechanism in two kinds of right-handed Cartesian coordinates

The rotation transformation of the platform occurs relative to axes X, Y and Z with the angles of  $\alpha$ ,  $\beta$  and  $\gamma$ , respectively, which is shown in the schematic diagram of the platform position (Fig. 3) and platform movement posture (Fig. 4). Using the rotation representation of the Euler angle,

Eqs. (1)-(3) can be obtained according to the homogeneous coordinate transformation method.

$$Rot(x, \alpha) = R_1 = \begin{bmatrix} 1 & 0 & 0 & 0 \\ 0 & \cos \alpha & -\sin \alpha & 0 \\ 0 & \sin \alpha & \cos \alpha & 0 \\ 0 & 0 & 0 & 1 \end{bmatrix} \quad (1)$$

$$Rot(y, \beta) = R_2 = \begin{bmatrix} \cos \beta & 0 & \sin \beta & 0 \\ 0 & 1 & 0 & 0 \\ -\sin \beta & 0 & \cos \beta & 0 \\ 0 & 0 & 0 & 1 \end{bmatrix} \quad (2)$$

$$Rot(z, \gamma) = R_3 = \begin{bmatrix} \cos \gamma & -\sin \gamma & 0 & 0 \\ \sin \gamma & \cos \gamma & 0 & 0 \\ 0 & 0 & 1 & 0 \\ 0 & 0 & 0 & 1 \end{bmatrix} \quad (3)$$

The translation transformation can be described as:

$$Trans(a, b, c) = \begin{bmatrix} 1 & 0 & 0 & a \\ 0 & 1 & 0 & b \\ 0 & 0 & 1 & c \\ 0 & 0 & 0 & 1 \end{bmatrix} \quad (4)$$

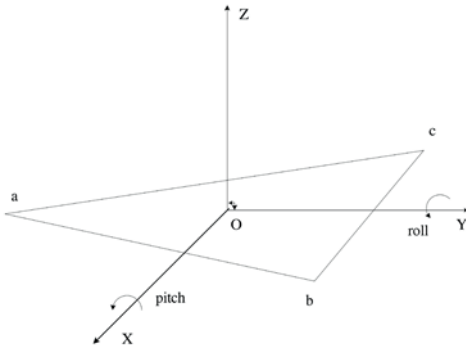


Fig. 3. Schematic diagram of platform position

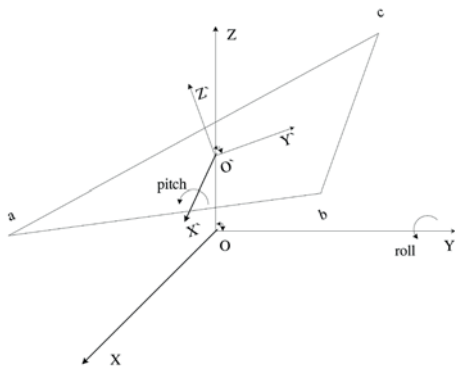


Fig. 4. Schematic diagram of platform movement posture

The coordinate transformation matrix  $T_{Bb}$  of coordinate point  $\{b\}$  in the moving coordinate system with respect to point  $\{B\}$  in the fixed coordinate system can be described as:

$$T_{Bb} = \begin{bmatrix} R_{Bb} & P_{Bb} \\ 0 & 1 \end{bmatrix} \quad (5)$$

In Eq. (5):

$R_{Bb}$  – rotation matrix of the spindle direction of the moving system  $\{b\}$  relative to the fixed system  $\{B\}$ ;

$P_{Bb}$  – position vector of the coordinate origin of the moving system  $\{b\}$  in the fixed system  $\{B\}$ ,

where:

$$R_{Bb}(\alpha, \beta, \gamma) = Rot(x, \alpha)Rot(y, \beta)Rot(z, \gamma)$$

$$P_{Bb} = [x, y, z]^T$$

$X = [x, y, z, \alpha, \beta, \gamma]^T$  is the spatial pose of a point in  $\{b\}$  relative to  $\{B\}$  which is described by six-dimensional column vectors. Here,  $b_{iM}$  is the pose vector while  $\alpha, \beta$  and  $\gamma$  are Euler angles of  $\{b\}$ . Any point  $b_{iM}$  on  $\{b\}$  can be expressed in the fixed coordinate system  $\{B\}$  as:

$$b_i = T_{Bb} b_{iM} \quad (6)$$

For the given parallel mechanism and the corresponding structure size, as well as the selected  $\{B\}$  and  $\{b\}$ , the coordinate values ( $b_i$  and  $B_i, i=1,2,\dots,6$ ) of each hinge point in the upper and lower platform in their respective coordinate systems can be calculated according to the geometric relations. For the given pose  $q=(P_{Bb}, R_{Bb})$  of the upper platform mechanism, the coordinate value of each hinge point of the upper platform in  $\{B\}$  can be calculated from Eq. (6) as follows:

$$b_i = R_{Bb} b_{iM} + P_{Bb}, \quad i = 1, 2, \dots, 6 \quad (7)$$

Thus, the length vector  $l_i, i=1,2,\dots,6$  of the six driving cylinder rods in the global coordinate system can be expressed as:

$$l_i = b_i - B_i = R_{Bb} b_{iM} + P_{Bb} - B_i \quad (8)$$

The length of a single leg can be expressed as the Eqs. (9):

$$l_i = |l_i| = f_i(x) = \sqrt{l_i^T l_i} = \sqrt{(R_{Bb} b_{iM} + P_{Bb} - B_i)^T (R_{Bb} b_{iM} + P_{Bb} - B_i)} \quad (9)$$

If the initial length of the leg is  $l_{i0}$ , the elongation of the leg can be expressed as:

$$\Delta l_i = l_i - l_{i0} \quad (10)$$

The Jacobian matrix represents the mapping from joint velocity to operational velocity, and  $J(x)$  can be noted as the Jacobian matrix in position  $x$ . By fully differentiating the vector Eq. (9), the Jacobian matrix  $H(x)$  of the parallel mechanism can be obtained.

$$dl = \begin{bmatrix} dl_1 \\ \dots \\ dl_6 \end{bmatrix} = \begin{bmatrix} df_1(x) \\ \dots \\ df_6(x) \end{bmatrix} = \begin{bmatrix} \frac{\partial f_1}{\partial x_1} & \dots & \frac{\partial f_1}{\partial x_6} \\ \dots & \dots & \dots \\ \frac{\partial f_6}{\partial x_1} & \dots & \frac{\partial f_6}{\partial x_6} \end{bmatrix} \begin{bmatrix} dx_1 \\ \dots \\ dx_6 \end{bmatrix} = H(x) dx \quad (11)$$

where  $H(x) = \begin{bmatrix} \frac{\partial f_1}{\partial x_1} & \dots & \frac{\partial f_1}{\partial x_6} \\ \dots & \dots & \dots \\ \frac{\partial f_6}{\partial x_1} & \dots & \frac{\partial f_6}{\partial x_6} \end{bmatrix}$ . Noted  $\mathbf{I}_{ni} = \frac{\mathbf{I}_i}{|\mathbf{I}_i|}$  and the auxiliary

matrix  $K = \begin{bmatrix} I_3 \\ 0 \end{bmatrix}_{4 \times 3}$ ,  $K_1 = \begin{bmatrix} 0 & 0 & 0 & 0 \\ 0 & 0 & -1 & 0 \\ 0 & 1 & 0 & 0 \\ 0 & 0 & 0 & 1 \end{bmatrix}$ ,  $K_2 = \begin{bmatrix} 0 & 0 & 1 & 0 \\ 0 & 0 & 0 & 0 \\ -1 & 0 & 0 & 0 \\ 0 & 0 & 0 & 1 \end{bmatrix}$ ,

$$K_3 = \begin{bmatrix} 0 & -1 & 0 & 0 \\ 1 & 0 & 0 & 0 \\ 0 & 0 & 0 & 0 \\ 0 & 0 & 0 & 1 \end{bmatrix}.$$

By taking the derivative with respect to time for Eq. (7), we can get Eq. (12):

$$\mathbf{V}_{b_i} = (\mathbf{v}_{iM} \mathbf{b}_{iM})_{4 \times 6} \dot{\mathbf{X}} \quad (12)$$

The velocity matrix of each driving leg can be written as Eq. (13) as follows:

$$\dot{\mathbf{l}}_i = \frac{\mathbf{I}_i}{|\mathbf{I}_i|} \mathbf{V}_{b_i} = \mathbf{I}_{ni} \mathbf{V}_{b_i} \quad (13)$$

The velocity vector of the six driving legs can be written as  $\dot{\mathbf{l}} = [\dot{l}_1 \ \dot{l}_2 \ \dot{l}_3 \ \dot{l}_4 \ \dot{l}_5 \ \dot{l}_6]$ , then we can get the Eqs. (14):

$$\dot{\mathbf{l}} = [\mathbf{I}_{n1} \mathbf{V}_{b_1} \ \mathbf{I}_{n2} \mathbf{V}_{b_2} \ \mathbf{I}_{n3} \mathbf{V}_{b_3} \ \mathbf{I}_{n4} \mathbf{V}_{b_4} \ \mathbf{I}_{n5} \mathbf{V}_{b_5} \ \mathbf{I}_{n6} \mathbf{V}_{b_6}] \quad (14)$$

Eq. (14) reflects the generalised velocity vectors between each drive leg and the upper manoeuvring platform. By taking the derivative with respect to time for Eq. (14), we can get Eq. (15), which reflects the generalised acceleration vectors between each drive leg and the upper manoeuvring platform.

$$\ddot{\mathbf{l}} = [\dot{\mathbf{I}}_{n1} \mathbf{V}_{b_1} + \mathbf{I}_{n1} \dot{\mathbf{V}}_{b_1} \ \dot{\mathbf{I}}_{n2} \mathbf{V}_{b_2} + \mathbf{I}_{n2} \dot{\mathbf{V}}_{b_2} \ \dots \ \dot{\mathbf{I}}_{n6} \mathbf{V}_{b_6} + \mathbf{I}_{n6} \dot{\mathbf{V}}_{b_6}] \quad (15)$$

The upper manoeuvring platform is connected with the experimental ship model through a rigid two-force bar, so the motion of the upper manoeuvring platform can be regarded as the motion of the experimental ship model. From Eqs. (9)–(10) and (14)–(15), the displacement, velocity and acceleration relations between the six driving legs and the ship model are established. Once the theoretical motion of the ship model is given, the corresponding elongation of the driving legs can be calculated to drive the ship model to achieve the specified motion.

## THEORETICAL ANALYSIS OF MANOEUVRING HYDRODYNAMIC COEFFICIENT

It is necessary to make some assumptions before establishing the manipulation motion equation, which can make it more convenient and rigorous for us to study the problem. Previous studies have shown that these assumptions have little influence on the hydrodynamic characteristics and manipulation performance. These assumptions include the following:

- 1) The ship is a rigid body with constant mass and its geometric shape does not change. The actual situation is that due to the movement of the internal structure and movement of persons, the mass and centroid of the ship are changing, such as the change of mass and centroid caused by ballast abandonment or ballast tank drainage. The influence of these changes on the hydrodynamic force is no longer within the scope of this paper.
- 2) The reference frame (definite frame) is the Earth, and its rotational motion effect is ignored.
- 3) The only forces acting on the manned deep submersible are gravity, buoyancy, hydrodynamic force and control force, and the other forces under special circumstances are not included in the scope of consideration, such as water entering the damaged cabin, being attacked, and the internal reaction of the working object, etc.
- 4) It is assumed that the dimensionless hydrodynamic coefficients are all constant in the study of hydrodynamic problems by means of an analytical method or Taylor expansion. This assumption is based on the “small disturbance”, which has achieved great success for submarines. The dimensionless hydrodynamic changes are not considered in this paper.
- 5) In the analysis of hydrodynamic coefficients, the flow field around the manned submersible is assumed to be infinite and unaffected by the seabed and free surface.

A rectangular coordinate system is usually used to study ship motion. The basic coordinate system is a fixed coordinate system and a moving coordinate system. According to convention, the right hand system is adopted. The system of parameters and symbols used in the study of ship motion is generally recommended by the International Water Pool Conference and by the Shipbuilding and Marine Engineering Society. This system is also used in this study. The fixed

coordinate system E- $\xi\eta\zeta$  and moving coordinate system O-XYZ are shown in Fig. 5.

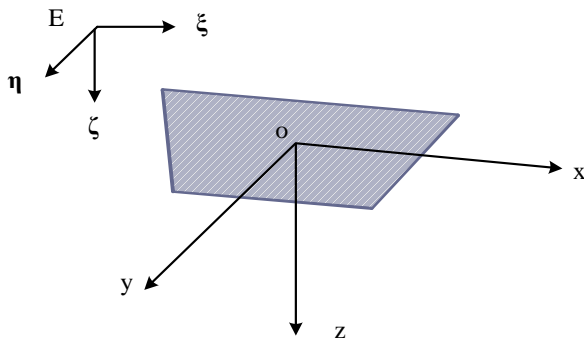


Fig. 5. The coordinate system

The description of the main symbols in the fixed coordinate system is given in Table 2, and in the moving coordinate system, it is shown in Table 3. Assuming that the environmental condition is infinite water depth, according to Newton's motion theorem and the definition of the MMG model, the ship's 6DoF operating motion equation can be expressed as follows:

$$\begin{cases} m(u - vr + wq) = X \\ m(v - pw + ur) = Y \\ m(w - uq + vp) = Z \\ I_{xx}p - K \\ I_{yy}q + (I_{xx} - I_{zz})pr = M \\ I_{zz}r + (I_{yy} - I_{xx})pq = N \end{cases} \quad (16)$$

In Eq. (16):

$m$  – mass of the ship;

$I_{xx}, I_{yy}, I_{zz}$  – moment of inertia about the X, Y and Z axes.

Tab. 2. Main symbols in the fixed coordinate system

Points or vectors	$\xi$ axis	$\eta$ axis	$\zeta$ axis
Centre of gravity, -G	$\xi_G$	$\eta_G$	$\zeta_G$
Origin, o	$\xi_o$	$\eta_o$	$\zeta_o$
Velocity, U	$U_\xi$	$U_\eta$	$U_\zeta$
Angular velocity, $\Omega$	$\Omega_\xi$	$\Omega_\eta$	$\Omega_\zeta$
Force, F	$F_\xi$	$F_\eta$	$F_\zeta$
Torque, T	$T_\xi$	$T_\eta$	$T_\zeta$

Tab. 3. Main symbols in the moving coordinate system

Vectors	X axis	Y axis	Z axis
Velocity, U	u	v	w
Angular velocity, $\Omega$	p	q	r
Force, F	X	Y	Z
Torque, T	K	M	N

The hydrodynamic force of a ship can be expressed as a function of four major factors, namely, the flow field characteristics, the hull characteristics, the ship's motion state

and the ship's manoeuvring factors. Before Taylor expansion of the hydrodynamics, the following points should be made clear: the flow field characteristics are variable elements, the ship motion state and control elements must change at any time and, on the contrary, the ship body keeps its inherent state unchanged. The hypothesis is shown as follows:

- 1) The flow field characteristics remain relatively unchanged for a period of time.
- 2) Only three degrees of freedom motion including direct flight, transversal drift and turning head are considered in the horizontal plane, and the motion parameters include (angular) velocity and (angular) acceleration.
- 3) The initial motion of the ship is assumed to be straight sailing at a constant speed.
- 4) The higher derivative is considered to be infinitesimal and the influence of parameter  $a$  is minimal.
- 5) The hull moves in a small linear range. In practical application, the second-order increment of motion parameters can be ignored and the amplitude of motion parameters can be changed slightly according to specific requirements.
- 6) The linear proportional relationship between flow force and (angular) acceleration is established. The expansion does not include the higher-order term and the resultant term of (angular) acceleration.
- 7) The coupling in all directions is ignored.
- 8) The ship is symmetrical left and right.

In conclusion, the hydrodynamic force  $G$  can be expressed as follows:

$$G = G(u, v, r, \dot{u}, \dot{v}, \dot{r}, \delta_r) \quad (17)$$

where  $\delta_r$  is the rudder angle. According to the above hypothesis, after Taylor expansion, the following results can be obtained:

$$G = G_0 + G_u \dot{u} + G_v \dot{v} + G_r \dot{r} + G_u(u - u_0) + G_v v + G_r r + G_{\delta_r} \delta_r \quad (18)$$

where  $G_0, G_u, G_v, G_r, G_u, G_v, G_r, G_{\delta_r}$  are the hydrodynamic coefficients. Taking  $G_u$  as an example, its specific form is as follows:

$$G_u = \left. \frac{\partial G}{\partial u} \right|_{u_0=v_0=r_0=\dot{u}_0=\dot{v}_0=\dot{r}_0=\delta_{r,0}=0}$$

These hydrodynamic coefficients have practical physical meaning. They respectively represent the force in the direction in which the velocity or acceleration is generated. In Eq. (18), the zero-order term represents the inherent hydrodynamic force of a ship in a straight voyage of uniform speed, while the first-order term is all the hydrodynamic force caused by speed or acceleration and exists in the form of increments. Therefore, the first-order term can be regarded as the modification of the zero-order hydrodynamic force.

In this paper, the horizontal plane motion model is established. By taking X, Y and N into different motion directions, the hydrodynamic expression of the model is derived:

$$\begin{cases} X = X_0 + X_u \dot{u} + X_v \dot{v} + X_r \dot{r} + X_u(u - u_0) + X_v v + X_r r + X_{\delta} \delta_r \\ Y = Y_0 + Y_u \dot{u} + Y_v \dot{v} + Y_r \dot{r} + Y_u(u - u_0) + Y_v v + Y_r r + Y_{\delta} \delta_r \\ N = N_0 + N_u \dot{u} + N_v \dot{v} + N_r \dot{r} + N_u(u - u_0) + N_v v + N_r r + N_{\delta} \delta_r \end{cases} \quad (19)$$

In the above equation, the velocity term is the fluid inertial force, and the inertial force term is only related to the acceleration primary term. The viscous force of fluid is related to the properties of velocity and flow field. The lower-order velocity term may contain both the inertial force term and the viscous force term. However, in the higher-order model, the third and higher degree terms of velocity only represent the viscous force.

## HYDRODYNAMIC TEST PLATFORM

The main equipment of the 6DoF parallel mechanism test platform includes the 6DoF parallel mechanism, six-dimensional force/torque sensor and ultrasonic distance meter. The 6DoF parallel mechanism is shown in Fig. 6, and its kinematic performance index is shown in Table 4. The six-dimensional force/torque sensor is FC-K6D68 from Germany, and its performance parameters are shown in Table 5. According to the theoretical calculation, the model of the six-component balance should be K6D68 2 kN/50 Nm.

Tab. 4. Kinematic performance index of 6DoF parallel mechanism

Posture	Displacement	(Angular) Velocity	(Angular) Acceleration	Oscillation frequency (Hz)
Roll	$\pm 20$	10–32 /s	5–51 /s <sup>2</sup>	0.5–1.6
Pitch	$\pm 5$	2.5–8 /s	1.3–13 /s <sup>2</sup>	0.5–1.6
Yaw	$\pm 15$	7.5–24 /s	3.8–38 /s <sup>2</sup>	0.5–1.6
Surge	$\pm 150$ mm	75–240 mm/s	38–384 mm/s <sup>2</sup>	0.5–1.6
Sway	$\pm 150$ mm	75–240 mm/s	38–384 mm/s <sup>2</sup>	0.5–1.6
Heave	$\pm 100$ mm	50–160 mm/s	26–256 mm/s <sup>2</sup>	0.5–1.6

Tab. 5. Performance parameters of the sensors

Type	F <sub>x</sub> /kN	F <sub>y</sub> /kN	F <sub>z</sub> /kN	M <sub>x</sub> /N•m	M <sub>y</sub> /N•m	M <sub>z</sub> /N•m
K6D68 1 kN/20 N•m	1	1	2	20	20	20
K6D68 2 kN/50 N•m	2	2	4	50	50	50
K6D68 5 kN/50 N•m	5	5	10	50	50	50
K6D68 10 kN/100N•m	10	10	20	100	100	100
K6D68 10 kN/500N•m	10	10	20	500	500	500

In order to ensure the stability of the box structure and full contact between the towing frame and the 6DoF platform during assembly, a stiffener structure is set on the right side of the lower half of the towing frame. Finally, limited by

space, the 6DoF platform can only be connected with the lower half of the trailer frame by hoisting from the side near the pool of the trailer frame platform. In order to facilitate the installation, a deep inverted trapezoid key-way is cut horizontally on the bottom steel plate of the lower half. Considering the positioning accuracy during the installation, the length of the key-way is less than the width of the steel plate. As the trailer frame is closely connected with the cross-beam on the trailer platform, the cross-section of the cross-beam is shown in Figure 7.



Fig. 6. The 6DoF parallel mechanism.

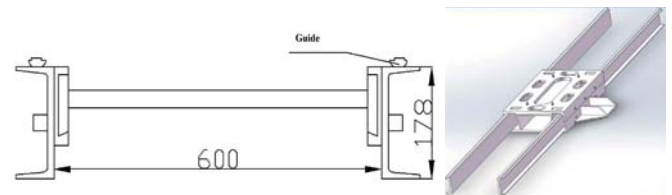


Fig. 7. The cross-beam and trailer rack.

The test ship model of the KELC tank ship designed by China Ship Scientific Research Centre (CSSRC) with a scale of 1:150 is used in the experiment. The basic parameters of the ship model on the liquid surface used in the test are shown in Table 6.

Tab. 6. Main parameters of the ship model

Main parameter	Value
Length (m)	1.347
Moulded breadth (m)	0.30
Moulded depth (m)	0.29
Design draft (m)	0.04
Drainage quality (kg)	13.75
Maximum cross-sectional area (S <sub>M</sub> /m <sub>2</sub> )	0.11
Focus	(0.02,0,0)
Moment of inertia I <sub>x</sub> , I <sub>y</sub> , I <sub>z</sub> (kg · m <sup>2</sup> )	3.52, 128.36, 135.1

## EXPERIMENT RESULTS AND ANALYSIS

In order to measure the hydrodynamic coefficients of the test ship model, captive model tests were carried out on the test ship model by using the 6DoF parallel mechanism test

device. The steady-state test of the captive model includes an oblique running test and rudder angle test. The simple harmonic motion test of the captive model includes a sway test and yaw test. The hydrodynamic coefficients of the ship model were collected and analysed. The experiment was carried out in the Ship Model Towing Tank Laboratory (SMTTL) of SNAOE in Huazhong University of Science and Technology. The tank, which is a member of the International Towing Tank Conference (ITTC), is 175 m long, 6 m wide and 4 m deep. The influence of the free surface is not taken into account in this paper.

### OBLIQUE RUNNING TEST

The oblique running test is a drift angle test. In this test, the equation of ship motion is shown as follows:

$$\begin{cases} u = u_0 \cos \beta \\ v = -u_0 \sin \beta \\ r = 0 \text{ rad / s} \\ \delta = 0 \text{ rad} \end{cases}$$

where  $u_0$  denotes the dragging velocity, which is set according to the "Similarity Principle";  $\beta$  denotes the drift angle. It can be seen from the above equation that when the drift angle  $\beta$  changes, the transverse and longitudinal velocities will change correspondingly. By changing the drift angle  $\beta$ , a series of longitudinal force, transverse force and yaw moment under different drift angles can be measured. The curves of longitudinal force, transverse force and yaw moment with transverse velocity can be obtained. Then the corresponding hydrodynamic coefficients are calculated after data fitting.

By adjusting the angle in the horizontal plane of the six-DoF motion mechanism, the drift angle  $\beta$  can be tested, where  $\beta \in [-10^\circ, 10^\circ]$ ,  $\Delta\beta = 1^\circ$ . The six component forces are measured by the six-dimensional force/torque sensor. Considering the non-linear effect of the horizontal force and torque, non-linear fitting is adopted to obtain the linear velocity coefficients  $Y'_v$ ,  $N'_v$ . The water density  $\rho = 1 \times 10^3 \text{ kg/m}^3$  and dragging velocity  $u_0 = 1.2 \text{ m/s}$ . The results for the hydrodynamic coefficients are summarised in Table 7. The diagram of transverse force and yaw moment changes with speed is shown in Fig. 8.

Tab. 7. Hydrodynamic coefficients of the ship model in oblique running test

Hydrodynamic coefficient	Test value $\times 10^{-2}$	Value from real ship $\times 10^{-2}$ [30]	Percentage of difference/%
$N'_v$	-1.592	-1.609	1.06%
$Y'_v$	-6.201	-6.394	3.02%

### RUDDER ANGLE TEST

The rudder angle test is carried out by changing the rudder angle of the steering gear when the drift angle is zero, where  $\delta_r \in [-30^\circ, 30^\circ]$ ,  $\Delta\delta_r = 2.5^\circ$ . The corresponding hydrodynamic force acting on the hull is measured through the test, and the rudder angle coefficients  $Y'_{\delta_r}$ ,  $N'_{\delta_r}$  are obtained by linear fitting within the stall angle range and dimensionless. The results are summarised in Table 8. The test results of the rudder are shown in Fig. 9.

Tab. 8. Hydrodynamic coefficients of the ship model in rudder angle test

Hydrodynamic coefficient	Test value $\times 10^{-2}$	Value from real ship $\times 10^{-2}$ [30]	Percentage of difference/%
$Y'_{\delta_r}$	-0.694	-0.712	2.53%
$N'_{\delta_r}$	0.371	0.381	2.62%

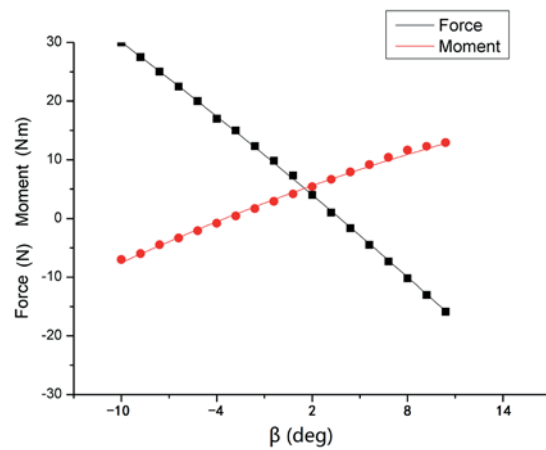


Fig. 8. The force and moment changes with speed

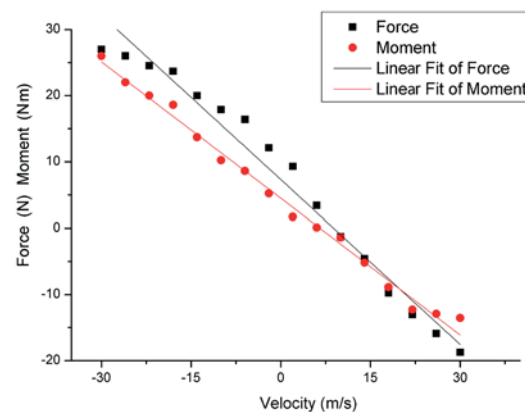


Fig. 9. The force and moment changes with rudder angle

### SWAY TEST

The measured constraint force (moment) can be written in the form shown in Eq. (20) by means of motion decomposition,

the inertial force (in-phase component) is represented by the subscript *in*, the damping force (orthogonal component) is represented by the subscript *out*, and the rest is constant.

$$\begin{cases} F_x(t) = X_{in} \sin(\omega t) + X_{out} \cos(\omega t) - Z_0 \\ M_y(t) = M_{in} \sin(\omega t) + M_{out} \cos(\omega t) - M_0 \end{cases} \quad (20)$$

When the ship model makes the transverse motion in the horizontal plane, the drift angle is always 0. The motion parameters of the ship model are set as follows:

$$\begin{cases} y = a \sin(\omega t) \\ \psi = \dot{\psi} = 0 \\ v = \dot{y} = a\omega \cos(\omega t) \\ \dot{v} = -a\omega^2 \sin(\omega t) \end{cases} \quad (21)$$

In Eq. (21):

$y$  – transversal displacement of ship model;

$a$  – amplitude of the motion;

$\omega$  – frequency of the motion;

$\psi, \dot{\psi}$  – the tilt angle and angular velocity of the ship model around a vertical axis;

$v, \dot{v}$  – transverse velocity and acceleration of the ship model.

Suppose that the force exerted on the object along the transverse direction is  $Y$  and the torque around the vertical axis is  $N$ , then these two terms can be decomposed as follows according to the physical meaning of hydrodynamic force:

$$\begin{aligned} Y &= Y_v v + Y_{\dot{v}} \dot{v} + Y_0 \\ &= -a\omega^2 Y_{\dot{v}} \sin \omega t + a\omega Y_v \cos \omega t + Y_0 \end{aligned} \quad (22)$$

$$\begin{aligned} N &= N_v v + N_{\dot{v}} \dot{v} + N_0 \\ &= -a\omega^2 N_{\dot{v}} \sin \omega t + a\omega N_v \cos \omega t + N_0 \end{aligned} \quad (23)$$

Obviously, the amplitude of the mass force (moment)  $F_\lambda, M_\lambda$  and viscous force (moment)  $F_\mu, M_\mu$  can be obtained by monitoring the change of force along the direction of motion with time. Then the hydrodynamic coefficient can be calculated as follows:

$$\begin{cases} Y_{\dot{v}} = -\frac{F_\lambda}{a\omega^2}, Y_v = \frac{F_\mu}{a\omega} \\ N_{\dot{v}} = -\frac{M_\lambda}{a\omega^2}, N_v = \frac{M_\mu}{a\omega} \end{cases} \quad (24)$$

Fig. 10 shows the sway motion of the test ship model. The change trend of the corresponding damping force and inertia force with the speed and acceleration is obtained through the

test. The corresponding hydrodynamic coefficients can be obtained by linear fitting and combining the hydrodynamic model parameters in Table 6 into Eq. (24). The hydrodynamic coefficients obtained by the dimensionless treatment are summarised in Table 9. The test results are shown in Fig. 11.

Tab. 9. Hydrodynamic coefficients of the ship model in sway test

Hydrodynamic coefficient	Test value $\times 10^{-2}$	Value from real ship $\times 10^{-2}$ [30]	Percentage of difference/%
$Y'_{\dot{v}}$	-1.651	-1.636	0.92%
$Y'_v$	-6.108	-6.394	4.68%
$N'_{\dot{v}}$	-0.058	-0.061	4.92%
$N'_v$	-1.581	-1.609	1.74%

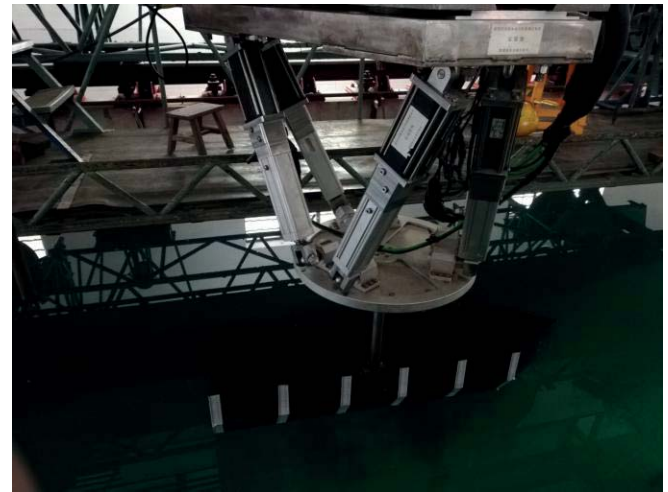


Fig. 10. The sway motion of the test ship model

## YAW TEST

When the ship model makes a yaw motion in the horizontal plane, the incidence angle is always 0. The motion parameters of the ship model are set as follows:

$$\begin{cases} \psi = \theta_0 \cos(\omega t) \\ v = \dot{v} = 0 \\ r = \dot{\psi} = -\theta_0 \omega \sin(\omega t) \\ \dot{r} = -\theta_0 \omega^2 \cos(\omega t) \end{cases} \quad (25)$$

In Eq. (25):

$\theta_0$  – amplitude of yaw motion;

$\omega$  – frequency of yaw motion;

$r, \dot{r}$  – the tilt angle and angular velocity of yaw motion.

It needs to be noted that, in order to ensure that the centre line of the model is consistent with the direction of resultant velocity at all times,  $\theta_0 = -\frac{a\omega^2}{u}$ , where  $a$  is the amplitude of heave motion of the ship model;  $\omega$  is the frequency of heave motion and  $u$  denotes the inflow velocity.

Supposing that the force exerted on the object along the transverse direction is  $Y$  and the torque around the rotation axis is  $N$ , we can get:

$$\begin{aligned} Y &= Y_r r + Y_{\dot{r}} \dot{r} + Y_0 \\ &= -\theta_0 \omega^2 Y_{\dot{r}} \cos \omega t - \theta_0 \omega Y_r \sin \omega t + Y_0 \end{aligned} \quad (26)$$

$$\begin{aligned} N &= N_r r + N_{\dot{r}} \dot{r} + N_0 \\ &= -\theta_0 \omega^2 N_{\dot{r}} \cos \omega t - \theta_0 \omega N_r \sin \omega t + N_0 \end{aligned} \quad (27)$$

Using the same data processing method as for the sway motion, the hydrodynamic coefficients can be calculated as follows:

$$\begin{cases} Y_{\dot{r}} = -\frac{F_{\lambda}}{\theta_0 \omega^2}, Y_r = -\frac{F_{\mu}}{\theta_0 \omega} \\ N_{\dot{r}} = -\frac{M_{\lambda}}{\theta_0 \omega^2}, N_r = -\frac{M_{\mu}}{\theta_0 \omega} \end{cases} \quad (28)$$

Similarly, the corresponding hydrodynamic coefficients can be obtained by substituting the test results into Eq. (28) through linear fitting. The hydrodynamic coefficients obtained by the dimensionless treatment are summarised in Table 10. The test results are shown in Fig. 12.

Tab. 10. Hydrodynamic coefficients of the ship model in yaw test

Hydrodynamic coefficient	Test value $\times 10^{-2}$	Value from real ship $\times 10^{-2}$ [30]	Percentage of difference/%
$Y'_r$	1.201	1.242	3.30%
$N'_r$	-0.721	-0.703	2.56%
$Y'_{\dot{r}}$	-0.156	-0.159	1.89%
$N'_{\dot{r}}$	-0.172	-0.158	8.86%

It can be seen from the test results that, compared with the empirical equation and the test results of the circulation tank, the maximum deviation of the test device proposed in this paper is 8.86%. The deviation result is less than 10%, and the deviation range meets the technical requirements of general practical engineering. The results show that the 6DoF parallel mechanism test platform proposed in this paper can accurately measure 8 typical hydrodynamic coefficients in the horizontal plane of the ship.

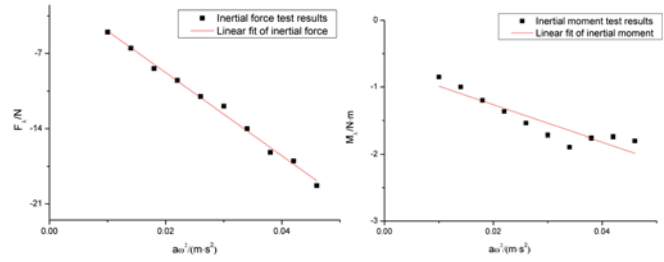


Fig. 11. The test results of sway test

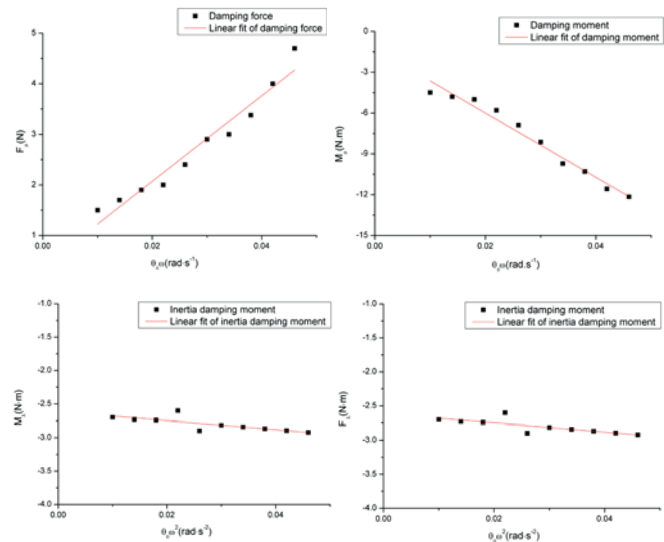


Fig. 12. The test results of yaw test

## CONCLUSIONS

In this paper, a 6DoF parallel mechanism test platform is presented which can be used in the hydrodynamic testing of ships. With this new device, a ship model can be forced to generate 6DoF motions independently or harmoniously, which cannot be accomplished by traditional plane motion mechanisms (PMM) or circulating flume tests alone. Firstly, this paper designed the test platform of the 6DoF parallel mechanism and selected the type of 6DoF force/torque sensor. Secondly, the principle of measuring the hydrodynamic coefficients by using a mathematical model was described. Finally, eight typical hydrodynamic coefficients of a ship model were measured by means of experimental research. The test results show that the new hydrodynamic coefficient test platform can accurately measure the 10 typical hydrodynamic coefficients of the ship's horizontal motion, and the deviation is less than 10%, which can meet the needs of practical engineering.

The advantage of this model is that only one test platform can drive the ship model to move with six degrees of freedom, and some coupling hydrodynamic coefficients that are difficult to measure can also be measured. In future work, we will use this model to measure the hydrodynamic coefficients of

coupled hydrodynamic coefficients and the hydrodynamic coefficients of an underwater vehicle model.

## ACKNOWLEDGEMENTS

This project is partially supported by the National Natural Science Foundation of China (No. 51679101, No. 51979117, No. 51405117) and Fundamental Research Funds for the Central Universities (No. 0118140031, No. 0118140032).

## REFERENCES

1. Muscari R., Dubbioso G., Viviani M., Mascio A. D. (2017): *Analysis of the asymmetric behavior of propeller-rudder system of twin screw ships by CFD*. Ocean Engineering, 143, 269–281.
2. Lidtke A. D., Turnock S. R., Downes J. (2017): *Hydrodynamic design of underwater gliders using k-kL- $\omega$  RANS transition model*. IEEE Journal of Oceanic Engineering, 43(2), 356–368.
3. Chen J., Wei J., Yang L. (2018): *Hydrodynamic optimization of appendages on ROPAX by using CFD and model tests*. Ship Building of China, 59(2), 33–41.
4. Jianglong S., Haiwen T., Yongnian C., De X., Jiajian Z. (2016): *A study on trim optimization for a container ship based on effects due to resistance*. Journal of Ship Research, 60(1), 30–47.
5. Haiwen T., Yunfei Y. et al. (2018): *A modified admiralty coefficient for estimating power curves in EEDI calculations*. Ocean Engineering, 150, 309–317.
6. Chuang Z., Steen S. (2013): *Speed loss of a vessel sailing in oblique waves*. Ocean Engineering, 64, 88–99.
7. Lee P.-M., Jun B.-H., Kim K.-H., Lee J.-H., Aoki T., Hyakudome T. (2007): *Simulation of an inertial acoustic navigation system with range aiding for an autonomous underwater vehicle*. IEEE Journal of Oceanic Engineering, 32(2), 327–345.
8. Li B., Su T.-C. (2016): *Nonlinear heading control of an autonomous underwater vehicle with internal actuators*. Ocean Engineering, 125, 103–112.
9. Kim J.-Y., Kim K.-H., Choi H.-S., Seong W.-J., Lee K.-Y. (2002): *Estimation of hydrodynamic coefficients for an AUV using nonlinear observers*. IEEE Journal of Oceanic Engineering, 27(4), 830–840.
10. Mansoorzadeh S., Javanmard E. (2014): *An investigation of free surface effects on drag and lift coefficients of an autonomous underwater vehicle (AUV) using computational and experimental fluid dynamics methods*. Journal of Fluids & Structures, 51(1), 161–171.
11. Gala F. L., Dubbioso G., Ortolani F., et al. (2012): *Preliminary evaluation of control and manoeuvring qualities for the AUTODROP-UUV vehicle*. IFAC Proceedings Volumes, 45(27), 132–137.
12. Li G. (2011): *Numerical and experimental research on hydrodynamic characters of shuttle submersible*. Harbin Engineering University, Harbin, 2011.
13. Avila J. P. J., Adamowski J. C. (2011): *Experimental evaluation of the hydrodynamic coefficients of a ROV through Morison's equation*. Ocean Engineering, 38(17), 2162–2170.
14. Xu F., Zou Z. J., Yin J. C., et al. (2013): *Identification modeling of underwater vehicles' nonlinear dynamics based on support vector machines*. Ocean Engineering, 67, 68–76.
15. Zhao J.-X. (2011): *The hydrodynamic performance calculation and motion simulation of an AUV with appendages*. Harbin Engineering University, Harbin.
16. Pang Y.-J., Wang Q.-Y., Li W.-P. (2017): *Model test study of influence of propeller and its rotation on hydrodynamics of submarine maneuverability*. Journal of Harbin Engineering University, 38(1), 109–114.
17. Kijima K., Nakiri Y. (1990): *On a numerical simulation for predicting of ship manoeuvring performance*. 19th International Towing Tank Conference, Madrid, Spain, Vol. 2, 559–568.
18. Maekawa K., Shuto C., Karasuno K., Nonaka K. (1999): *Estimation of added mass coefficients  $m_x', m_y'$  by using CFD through oblique towing test with constant acceleration*. Journal of Kansai Society of Naval Architects Japan, 232, 55–61.
19. Kijima K., Nakari Y., Furukawa Y. (2000): *On a prediction method for ship manoeuvrability*. International Workshop on Ship Manoeuvrability at the Hamburg Ship Model Basin, Hamburg, Germany, pp. 536–543.
20. Petersen, J. B., Lauridsen, B. (2000): *Prediction of hydrodynamic forces from a database of manoeuvring derivatives*. MARSIM 2000, Orlando, FL, USA, pp. 401–420.
21. Yang C.-F., Wu B.-S., Shen H.-C. (2006): *Analysis of experiment validation for full-ship maneuverability hydrodynamic forces prediction*. Journal of Ship Mechanics, 10(4), 559–568.
22. Gao T., Wang Y.-X., Pang Y.-J., Chen Q.-L., Tang Y.-G. (2018): *A time-efficient CFD approach for hydrodynamic*

*coefficient determination and model simplification of submarine.* Ocean Engineering, 154, 16–26.

23. Stewart D. (1966): *A platform with six degrees of freedom.* Aircraft Engineering and Aerospace Technology, 38(4), 30–35.
24. Yurt S. N., Ozkol I., Hajiyeve C. (2004): *Error analysis and motion determination of a flight simulator.* Aircraft Engineering and Aerospace Technology, 76(2), 185–192.
25. Landry S. J., Jacko J. (2012): *Pilot Procedure-Following Behavior during Closely Spaced Parallel Approaches.* International Journal of Human-Computer Interaction, 28(2), 131–139.
26. Phoemsaphawee S., Le Boulluec M. (2013): *A potential flow based flight simulator for an underwater glider.* Journal of Marine Science and Application, 12(1), 112–121.
27. Kim G. S. (2007): *Design of a six-axis wrist force/moment sensor using FEM and its fabrication for an intelligent robot.* Sensors and Actuators A Physical, 133(1), 27–34.
28. Nekrasov V. (2019): *Mean-Square Non-Local Stability of Ship in Storm Conditions of Operation.* Polish Maritime Research, 26(4), 6-15.
29. Kun D., Yunbo L. (2019): *Manoeuvring Prediction of KVLCC2 with Hydrodynamic Derivatives Generated by a Virtual Captive Model Test.* Polish Maritime Research, 26(4), 16-26.
30. CSSRC (2018): *Ship test report for KELC tank ship.* Report (Wuhan China), pp. 17–24.

## CONTACT WITH THE AUTHORS

**Yun Lu**

*e-mail:* hustluyun@hust.edu.cn

**Jinbo Wu**

*e-mail:* 2373751844@qq.com

**Weijia Li**

*e-mail:* 61525963@qq.com

**Yaozhong Wu**

*e-mail:* no2kenk98@sina.com

School of Naval Architecture and Ocean Engineering  
Huazhong University of Science and Technology

Luoyu Road 1037#  
Hongshan District  
430074 Wuhan

**CHINA**

## THE INFLUENCE OF THE CUBOID FLOAT'S PARAMETERS ON THE STABILITY OF A FLOATING BUILDING

Artur Karczewski<sup>1</sup>

Łukasz Piątek<sup>2</sup>

<sup>1</sup> Gdańsk University of Technology, Poland

<sup>2</sup> Warsaw University of Technology Department of Architectural and Urban Design, Poland

### ABSTRACT

*Usually, the concept of sufficient stability of a floating structure is connected with the capacity to keep a small heel angle despite the moment of heeling. The variable responsible for these characteristics is the initial metacentric height, which is the relation between the hydrostatic features of the pontoon and the mass properties of the entire object. This article answers the questions of how heavy the floating system should be, what the minimum acceptable draft is, and whether it is beneficial to use internal fixed ballast. To cover various technologies, a theoretical model of a cuboid float with average density representing different construction materials was analysed. The results indicate that the common practice of using heavy and deep floating systems is not always reasonable. In the case of floating buildings, which, unlike ships, can be exploited only under small heel angles, the shape and width of the submerged part of the object may influence the stability more than the weight or draft.*

**Keywords:** floating buildings, floating houses, houseboats, stability, floating body

### INTRODUCTION

The tradition of building at the interface between land and water using various kinds of floating objects that derive from water vessels goes back to antiquity [22]. In the twentieth century in Western Europe and North America, new construction technology allowed traditional rafts and ship hulls to be replaced with floating systems built of waterproof concrete and extruded polystyrene [5]. Modern floating buildings were born and started to grow in number.

Nowadays, there are around 40–50 thousand stationary floating structures of various kinds around the world, excluding those that incorporate any kind of watercraft, like houseboats [6]. Contemporary floating buildings using various materials and technologies developed for floating platforms such as wood, steel, aluminium, reinforced concrete, fibreglass, and plastics [21] have already proven to be safe and reliable building constructions. They are gaining attention as a potential solution to the problem of sea-level rise [10]

and due to their sustainability [13], [9]. This growth trend is very strong in countries where floating development became popular only in the twenty-first century [16]. However, not much effort has been made toward the scientific exploration of the stability analysis of floating buildings.

Once in the water, the floating object has to sustain different environmental conditions: wind and water pressure, snow weight, ice, and waves. A separate group of loads to be considered is shock loads due to vibration, impacts, accelerations, or inertia. Depending on the properties of the construction materials, the problems of thermal expansion, water-absorbability, and corrosion must be considered in the long term. Finally, the variable live loads must be included. Thus, it is of utmost importance for such an object occupied by people – such as a ship, floating offshore structure, or floating house – to remain safe and afloat in all conditions. Especially in the case of water-based facilities for users who do not have special training, the stability of floating objects is one of the most important factors that influence the safety and comfort onboard.

Tab. 1 Freeboard and heel angle requirements according to different guidelines

Title	Region	Min. freeboard, Fb	Max. heel angle	Min. residual freeboard
		[m]	[°]	[m]
Building Code for Float Homes [2]	Alaska, USA	0.36 (14")	4	1/2 Fb
Regulation of the Construction and Maintenance of Floating Homes [7]	California, USA	0.38 (15")	4	1/3 Fb
British Columbia Float Home Standard [1]	British Columbia, Canada	0.40	5	1/2 Fb
Technical Regulation on the Stability, Buoyancy, etc. of Houseboats and Floating Structures [3]	Denmark	0.50	4	1/3 Fb
Queensland Development Code. MP 3.1 Floating Buildings [4]	Queensland, Australia	0.40	–	0.25
NTA 8111 Drijvende bouwwerken [Floating constructions] [11]	Netherlands	0.00 or 0.30	4	0.00 or 0.30
AS 3962-2001 The Australian Standard: Guidelines for Design of Marinas [20]	Australia	–	15	0.05
PN-EN 14504: 2010 Inland navigation vessels – Floating landing stages and floating bridges on inland waters - Requirements, tests [17–	EC	0.03	10	–
Guidelines for Floating Platforms for Yacht Marinas [8]	Poland	0.05	6	–

In terms of engineering, stability analysis evaluates a floating object when heeled from equilibrium by external forces and determines its capability to sustain them by finding a new position of balance. An object can be considered safe if it retains its ability to return to its original position after cessation of the heeling forces. Insufficient stability can lead to flooding of the object, destruction of its elements, or even sinking.

Generally, there is a consensus in academia and industry about the assessment of the ship's stability. This problem can be divided into two issues: the initial stability at so-called 'small heel angles' (smaller than the deck immersion angle) and stability at large heel angles (over 25 degrees) [15] when the ship's safety after the deck immersion is being checked. Heel angles of less than 6 degrees are not taken into consideration, as they overlap with the period of ship's own sway. Stability criteria for ships are strongly connected with the ships' geometry (high freeboard and a large reserve of hull volume) based on their function.

Floating buildings have different operational conditions and geometric characteristics. Unlike ships, they are located on calm or sheltered waters, allowing them to have relatively low freeboards, which are very convenient for marina or swimming facilities. On the other hand, they are used and equipped like buildings (e.g., they have movable furniture inside). For these reasons, a heel angle of over 10 degrees or immersion of the deck would pose a danger to the people onboard. Therefore, the stability criteria introduced for ships cannot be directly applied to floating buildings. This difference is visible in various local guidelines and regulations on the stability of stationary floating objects (Table 1), requiring a smaller heel angle and larger residual freeboard than the criteria for ships. However, in terms of stability, floating buildings are often confused with ships. A common habit of associating a heavy and deep floating system with improving stability is an example of this problem.

For these reasons, this article focuses on the problem of the impact of the flotation type on the stability, which

has to be examined for 'very small angles of heel', meaning angles smaller than 10 degrees. This issue was not previously considered, probably due to its apparent triviality or lack of usefulness for the shipping industry. But for floating buildings, it is an essential safety consideration.

According to theory [18], [19], the stability characteristics at small angles of heel are correlated with the initial metacentric height  $GM$  defined by the equation<sup>1</sup>:

$$GM = \frac{T}{2} + \frac{B^2}{12 \cdot T} - VCG \quad (1)$$

where  $T$  is the draft [m],  $B$  is the breadth [m], and  $VCG$  is the vertical height of the object's centre of gravity [m].

It is clear that the  $GM$  and initial stability will be increased by enlarging the breadth and lowering the centre of gravity. The latter may suggest the advantage of heavy floating systems. But the relation of  $VCG$  to  $T$  is complex because these factors are indirectly connected with many other parameters not visible in Eq. (1). For example, adding ballast to the existing building would lower its centre of gravity and increase the draft at the same time. Therefore, formulating simple guidelines based on the interpretation of the simplified  $GM$  formula is difficult.

## METHODS – STABILITY EVALUATION

The initial research question is whether heavy and deep floating systems can increase the stability of floating buildings at heel angles of up to 10 degrees. To examine this issue in an exploratory way, three scenarios of changes in the basic parameters of the floating system were determined:

- (1) increasing the weight (density);
- (2) increasing the depth;
- (3) increasing both the weight and depth in such relation that the freeboard does not change.

<sup>1</sup> Provided that the heeling of the object free-floating on the calm water is due to the effect of the static force of wind and the shape of the submerged part of the floating body is cuboid.

To assess the relative influence of the weight and draft on stability, all research scenarios were conducted for two numerical models of theoretical floating structures having different breadths. Both objects consisted of a cuboid floating system (flotation device, float) and an open superstructure. In simplification, the upper part inflicts loads (gravity and wind pressure), while the lower part generates the reaction (buoyancy and righting moment) in the system. The selected parameters of the floating system were subject to change, whereas the parameters of the superstructure were constant (Table 2).

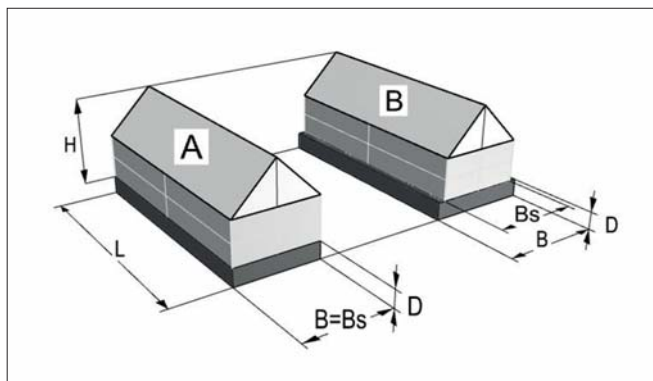


Fig. 1 Main dimensions of examined objects

Table 2 General constant characteristics of examined models

Model		A	B
Characteristic	Symbol		
Float and superstructure length	$L$ [m]	16.0	
Float breadth	$B$ [m]	6.0	7.0
Superstructure height	$H$ [m]	6.0	
Superstructure breadth	$B_s$ [m]	6.0	
Superstructure density	$q_s$ [kg/m <sup>3</sup> ]	75	

In the numerical simulation, the stability of two models was computed according to simplified formulas for angles in which the side of the floating system was not entirely submerged:

$$\varphi = \frac{M_H}{m \cdot g \cdot GM} \quad (2)$$

where  $\varphi$  is the heel angle [°],  $M_H$  is the heeling moment [Nm],  $m$  is the mass of the object [kg],  $g$  is 9.81 [m/s<sup>2</sup>], and

$$Fb_\varphi = \cos\varphi(D - T - tg\varphi \cdot 0.5 \cdot B) \quad (3)$$

where  $Fb_\varphi$  is the residual freeboard [m],  $D$  is the depth of the floating system [m], and:

$$M_H = q \cdot A_w \cdot (D + 0.5 \cdot (H - T)) \quad (4)$$

where  $q$  is wind pressure [Pa], and  $A_w$  is the area of side surface exposed to wind [m<sup>2</sup>].

To simplify the problem, no live loads were taken into consideration in the simulations. Reducing the problem of stability to the response to the high wind pressure acting perpendicular to the longer wall can be justified by the relatively higher impact of this factor on the stability as well as its independence from the breadth of the float. Therefore it was assumed to be acceptable in the theoretical study investigating the relationship between the characteristics of the floating system and stability. To achieve a significant change in the observed parameters, a relatively high wind pressure (600 Pa) was introduced. This configuration corresponds to the requirements for the assessment of floating scaffoldings set in [18].

## RESULTS

The results of the above simulations are presented in Figs. 2–4. In each figure, there is a chart showing the heel angle (dashed line) and residual freeboard (solid line) for both model A (red lines) and model B (green lines). Under the charts, the change of the metacentric height is presented on the model A sections (where  $M$  is the metacentre,  $G$  is the centre of gravity, and  $F$  is the centre of buoyancy).<sup>2</sup>

### INCREASING THE WEIGHT OF THE FLOAT (FIG. 2)

In this case, the density of the floating system  $q$  was increased from 50 kg/m<sup>3</sup> (value representative for steel pontoon) to 550 kg/m<sup>3</sup> (heavy-duty reinforced concrete float). To a certain extent, this scenario represents placing fixed ballast inside the floating system as well.

As a result:

- (1) The heel angle decreased. This has to do with the fact that as the mass of the object increases, the righting moment also increases because it is the product of the mass and righting arm. The advantage of adding the mass is not as large as one would have expected (less than 2 degrees improvement in heel angle for model A). This is because there is a decrease in metacentric height at the same time due to the increase in the draft. For a wider model B, the difference between a light and a heavy float is particularly small.
- (2) The residual freeboard decreased rapidly. As the weight increases, the freeboard is reduced in favour of the draft. This seems obvious, as the float has a limited reserve of volume. For this reason, it is easy to predict that there is always a limit of mass for a given size of the floating system, and, after exceeding it, the criterion of residual freeboard will not be met.
- (3) The metacentric height decreased. A heavier floating system shifts the centre of gravity downwards. However, neither the increase in the height of the buoyancy centre nor the decrease in the centre of gravity prevents a decrease in the metacentric height. Therefore, the object with a heavier float has lower initial stability.

<sup>2</sup> The tendency of the change in the metacentre is the same for model A and model B.

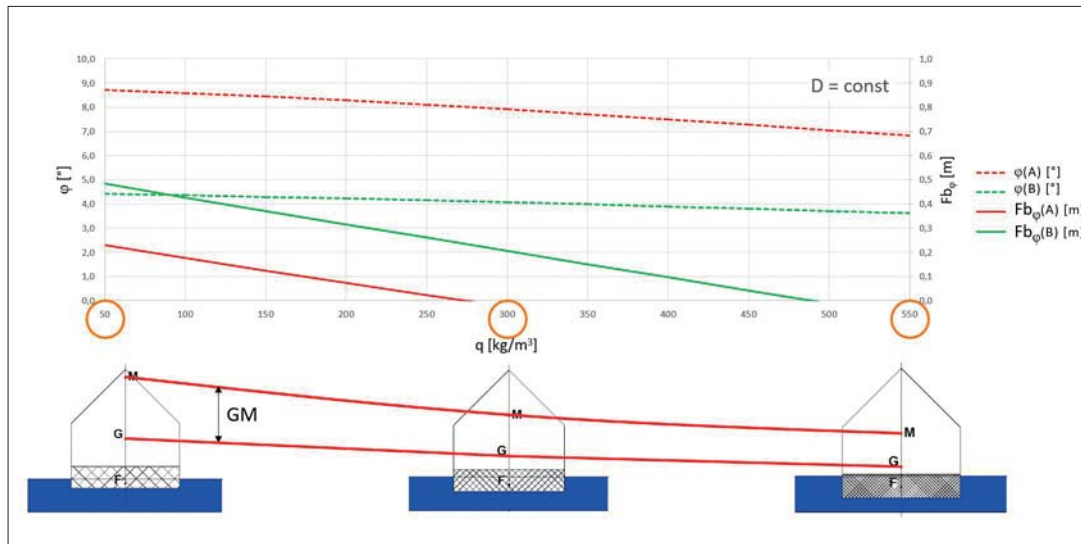


Fig. 2 Increasing the density of the floating system

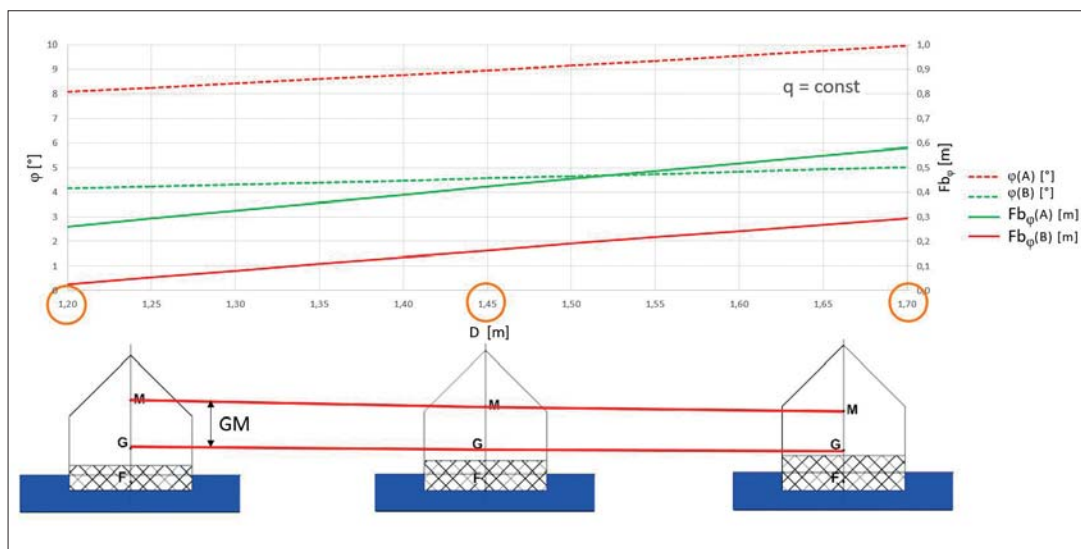


Fig. 3 Increasing the depth of the floating system

### INCREASING THE DEPTH OF THE FLOAT (FIG. 3)

In the second scenario, the depth of the floating system  $D$  was increased from 1.2 to 1.7 m, while its density  $q$  was constantly equal to  $275 \text{ kg/m}^3$  (average value for different materials).

As a result:

- (1) The heel angle increased. The density of the floating system is four times smaller than the density of water, so the volume reserve is larger for the higher floats. The float emerges from the water, which increases the wind profile and the heeling moment. As a result, the heel angle increased by about 2 degrees for model A and 1 degree for model B.
- (2) The residual freeboard increased. As the deck moves away from the water, the deck flooding angle increases. However, the design solution can be unacceptable, as in an upright position the deck may be too high above

the water surface, which is contradictory to architects' ideas and users' expectations [12].

- (3) The metacentric height did not change significantly. The influences of mass properties, such as the height of the centre of gravity, and hydrostatic characteristics, such as draft, balanced each other out.

### INCREASING THE DENSITY AND THE DEPTH OF THE FLOAT WITHOUT AFFECTING THE FREEBOARD (FIG. 4)

In the last scenario, both parameters were increased (the density from  $50$  to  $550 \text{ kg/m}^3$  and the depth from  $1.06$  to  $2.11 \text{ m}$ ) in such proportion that the freeboard in the upright position remained unaffected. It required an additional calculation of the float height corresponding with a linear increase in the weight of the floating system. This scenario is highly probable in floating-building designs, where a fixed

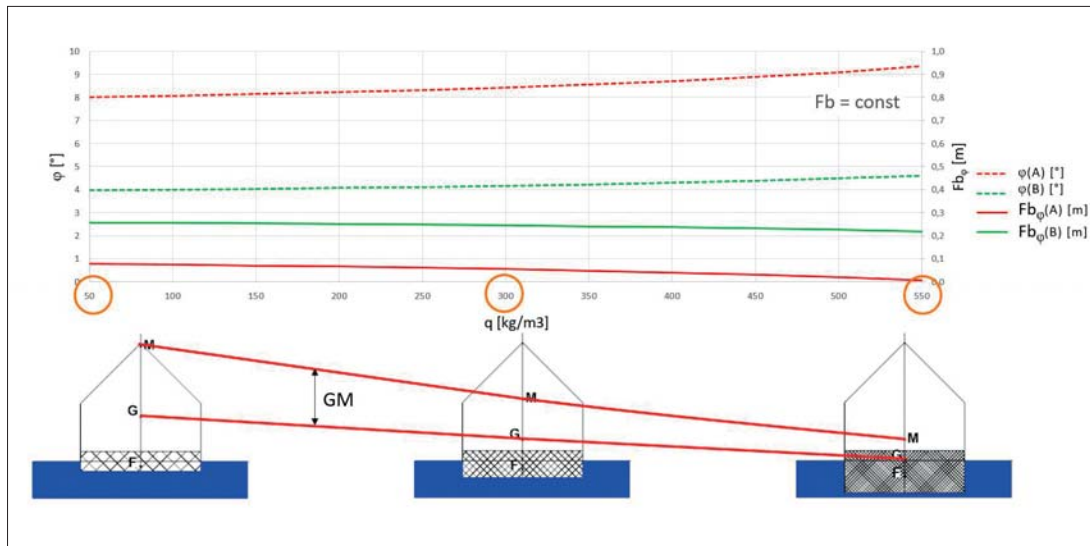


Fig. 4 Increase of weight and depth of floating system without affecting the freeboard

freeboard height is one of the main initial assumptions resulting from specific land access conditions.

As a result:

- (1) The heel angle increased. Similarly to the second scenario, the changes are in the range of 1–2 degrees. The wider model B is less susceptible to change. In Eq. (2), the breadth is in the square, so for the assumed dimensions of floats, it gives about a 36% reserve in this parameter for all changes.
- (2) The residual freeboard decreased. Although in both cases the decrease in the whole examined spectrum was only a few centimetres, it may become crucial for meeting the stability criteria.
- (3) The metacentric height decreased. The submerged part of the structure increases in volume while maintaining a constant shape and area of waterplane. Therefore, the metacentric height decreases very fast. The increase in float depth plays a major role. Theoretically, even though the increase of heel angle and decrease of residual freeboard are small, the final stability properties are worse for the heavy and deep floating system than for a lightweight and shallow one.

## DISCUSSION

This article discusses the stability of a floating building that has a relatively low draft, intended for very shallow waters or suitable for one-story structures. This problem has not been investigated before, probably due to its seeming triviality or the relatively low popularity of low-draft floating buildings. Despite that, lightweight floating buildings are gaining more and more attention [14].

There are many reasons why the introduction of different, heavy, and deep floating systems may be required, such as a large weight of the multi-story superstructure, high live load, or the demand for underwater usable space in the hull.

It has to be said that the dynamics of the movement may be more important for the structure's safety and comfort than the maximum heel angle. Therefore, heavier floats having higher inertia may be suitable for places with higher waves or gusty winds, as long as they meet the stability criteria.

Another issue is the problem of the additional reserve of stability that may be required for a floating building in extreme wind conditions. Even in such cases, after evacuating people ashore, the structure should remain stable at larger heel angles than 10 degrees and must not capsize. This may require a float that is deep (to maintain the deck over the water and the bilge under the water) and heavy (to balance a higher heeling moment in extreme winds).

In all cases, it is beneficial to design a lightweight superstructure, as it lowers the centre of gravity and increases the freeboard at the same time.

## CONCLUSIONS

Intuitive solutions are not always suitable. Research shows that increasing the weight of a floating system (including adding fixed ballast) does not improve stability in a significant way but does have a large influence on the residual freeboard. On the other hand, increasing the depth of the floating system improves safety because it is safe from flooding. However, the utility of the building decreases as the freeboard is too high in the upright position. In all examined scenarios, enlarging the breadth of the floating system resulted in a far better improvement of the stability. Increasing the beam decreases the heel angle, which in turn increases the residual freeboard.

An additional important conclusion is that there is no simple way in which the stability can be improved after the construction phase starts because, usually, maintaining the freeboard in an upright position is the utility constraint and there is no reserve there. Design errors revealed at this stage may become very difficult or even impossible to correct, unless some additional buoyancy is added to the floating system

or the superstructure is redesigned to be lighter. Therefore, a precise design, including weight and stability calculations that will be carefully followed, is crucial. It is particularly important in the case of narrow or high floating structures.

## REFERENCES

1. B.C. Building Code (2003): *British Columbia Float Home Standard*.
2. City and Borough of Sitka, Alaska. (2019): *Home Rule Charter of the City and Borough of Sitka. Chapter 19.15 Building Code for Float Homes*.
3. Danish Maritime Authority. (2007): *Technical Regulation on the Stability, Buoyancy, etc. of Houseboats and Floating Structures*. Retrieved from <https://www.dma.dk/Vaekst/Rammevilkaar/Legislation/Pages/Technical-regulations.aspx>.
4. Department of Housing and Public Works. (2007): *Queensland Development Code. MP 3.1 Floating Buildings*. Retrieved from <http://www.hpw.qld.gov.au/construction/BuildingPlumbing/Building/BuildingLawsCodes/QueenslandDevelopmentCode/Pages/QueenslandDevelopmentCodeCurrentParts.aspx>.
5. Flanagan B. (2003): *The Houseboat Book*. Universe, New York.
6. Holcombe S. (2017): *Applications and Huge Potential Demand for Amphibious Structures*. Proceedings of the First International Conference on Amphibious Architecture, Design & Engineering, 138.
7. Marin County, California. (2016): *California Municipal Code. Chapter 19.18. Regulation of the Construction and Maintenance of Floating Homes*.
8. Mazurkiewicz B. (2010): *Yacht Harbors and Marinas. Designing*. Foundation for the Promotion of Industry Shipbuilding and Maritime Economy, Gdańsk.
9. Moon C. (2014): *Three Dimensions of Sustainability and Floating Architecture*. International Journal of Sustainable Building Technology and Urban Development, Vol. 2, 123–127.
10. Nakajima T., Umeyama M. (2015): *A New Concept for the Safety of Low-lying Land Areas from Natural Disasters*. Journal of Ocean Engineering and Marine Energy, Vol. 1, 19–29.
11. Nederlands Normalisatie-Instituut (2011): *NTA 8111 Drijvende Bouwwerken [Floating Constructions]*. NEN, Delft.
12. Nillesen A. L., Singelenberg J. (2011): *Amphibious Housing in the Netherlands. Architecture and Urbanism on The Water*. NAI, Rotterdam.
13. Olthuis K., Keuning D. (2011): *Float! Building on Water to Combat Urban Congestion and Climate Change*. Frame, Amsterdam, 204–231
14. Ostrowska-Wawryniuk K., Piątek Ł. (2020): *Lightweight Prefabricated Floating Buildings for Shallow Inland Waters. Design and Construction of The Floating Hotel Apartment in Poland*. Journal of Water and Land Development, Vol. 44 (I–III), 118–125.
15. Papanikolaou, A. (2014): *Ship Design, Methodologies of Preliminary Design*. Springer; London.
16. Piątek Ł. (2018): *Architecture of Floating Buildings: Conditions and Directions of Development in Poland after 2000*. PhD Thesis, Warsaw University of Technology.
17. Polish Committee for Standardization (2019): *PN-EN 14504: 2010 Inland navigation vessels – Floating landing stages and floating bridges on inland waters – Requirements, tests*. Warsaw.
18. Polish Register of Shipping (2019): *Rules for Classification and Construction of Inland Waterways Vessels, Part IV, Stability and Freeboard*. Gdańsk.
19. Rawson, K. J., Tupper, E. C. (2001): *Basic Ship Theory, v. 1, Hydrostatics and Strength*. 5th Edition, Butterworth Heinemann. Oxford.
20. Standards Australia (2001): *AS 3962-2001 The Australian Standard: Guidelines for Design of Marinas*. Sydney.
21. Szymczak-Graczyk A. (2018): *Floating platforms made of monolithic closed rectangular tanks*. Bulletin of the Polish Academy of Sciences: Technical Sciences, 2, Vol. 66, 209–219.
22. Wang C. M., Wang B. T. (2014): *Great Ideas Float on the Top. Large Floating Structures: Technological Advances*. Springer, 1–36.

## CONTACT WITH THE AUTHORS

**Artur Karczewski**

*e-mail: artkarcz@pg.gda.pl*

Gdańsk University of Technology

11/12 Gabriela Narutowicza Street, 80-233 Gdańsk

**POLAND**

**Łukasz Piątek**

*e-mail: lukasz.piatek@pw.edu.pl*

Warsaw University of Technology

Department of Architectural and Urban Design

Pl. Politechniki 1, 00-661 Warszawa

**POLAND**

# DYNAMIC RESPONSE ANALYSIS OF DRILL PIPE CONSIDERING HORIZONTAL MOVEMENT OF PLATFORM DURING INSTALLATION OF SUBSEA PRODUCTION TREE

Fei Wang

Neng Chen

School of Mechatronic Engineering, Southwest Petroleum University, Chengdu, China

## ABSTRACT

*In order to study the dynamic response of a drill pipe under the motion of the float platform, current and waves during the installation of a subsea production tree (SPT), a numerical model was established to analyse the mechanical properties of the drill pipe. The effects of the float platform motion on the mechanical behaviours of the drill pipe are carried out as well as the operation depth, submerged weight of the SPT, current velocity and drill pipe specification. At the same time, the evolution mechanism of the dynamic response of the drill pipe was also explored. The results show that the bending stress of the drill pipe approaches the maximum value when the platform moves to about one fourth of its period. Based on the research, the deeper the operation depth, the smaller the range of motion of the bottom of the drill pipe; the current velocity and the size of drill pipe have the greatest influence on the lateral displacement and bending stress.*

**Keywords:** SPT installation, drill pipe, dynamic response, vibration range, bending stress.

## INTRODUCTION

Because the installation of a subsea production tree (SPT) directly affects the success of deep water oil production and the economic efficiency of the whole project, an accurate grasp of the deformation and stress distribution where the SPT is attached at the bottom end has a positive effect on the ocean engineering. With the rapid development and utilisation of oil and gas resources from shallow sea to deep water, study of the dynamic response of the drill pipe underwater, which is related to the cost and risk of installing the SPT, has become a difficult and hot point in drill operation.

The literature offers many research studies on the drill pipe's dynamic response. Chakrabarti and Frampton [1] reported on the progress of riser analysis and gave a detailed derivation of the horizontal motion equation of the riser. Safai Hachemi [2] wrote a computer program based on theory and a numerical method to calculate the nonlinear dynamic response of deep water risers. Ahmad and Datta [3-4] used the time integration method and the frequency domain iteration method to

analyse the effects of the relative velocity square drag term, drift oscillation, instantaneous ship motion and the velocity of the current on the bending stress of marine risers under random waves. Wang [5] introduced the dynamic equation of horizontal motion of the riser and put forward the finite element method to solve the displacement of the riser under the action of waves and current. Based on the study of Ahmad and Datta, Khan et al. [6] obtained the response time history of bending stress and the influence of various harmonics on the bending stress with ABAQUS/Aqua software when the SCR was subjected to random wave loads. Qi et al. [7] studied the structural force and strength check of the whole drilling riser, and at the same time carried out a weakness analysis and parameter sensitivity analysis of the drilling riser. Zhou et al. [8] discovered the "one third effect" of a deep water drilling riser under the condition of the shear flow through independent research and developed a mechanical property test system of a deep water drilling riser. Guo et al. [9] studied the dynamic response of the internal solitary wave, the surface wave and the platform motion and found that the internal

solitary wave has a great influence on the displacement and stress of the drill pipe. Wang et al. [10] established a transverse vibration model during the installation of a riser by means of a variation method and minimum energy principle to analyse the influence of the harmonic motion of the platform on the transverse vibration of the riser. Fan et al. [11] analysed the influence of internal solitary waves on the mechanical properties of the riser in the process of expansion on the basis of solving the governing equation of the hang off mode of the drilling riser with Wilson's  $\theta$  method and a generalised minimal residual method. Hu et al. [12] established a model varying the drill pipe length to analyse the dynamic effect of environmental loads on the stress and displacement and the model was solved by the Keller box method. Olszewski et al. [13] analysed the effect of the clamping force on the stress distribution of a riser with finite element software and verified it on a specially designed experimental platform. Wodtke et al. [14] analysed risers using the finite element method under the conditions of ocean load and connecting to different mining platforms to evaluate their operation conditions. Wang et al. [15] deduced the axial vibration differential equation by establishing a mechanical model of a pipe installation and analysed some factors that affect the natural frequency of axial vibration and the axial vibration load. Chen et al. [16] studied the influence of complex pre-stress on the natural frequency and modal shape of the riser's dynamic characteristics. Liu et al. [17] established a dynamic behaviour model of a riser system of a deep water drilling platform under the condition of emergency evacuation, which was solved by Newmark's method, and then its effectiveness was verified by ANSYS software.

Although there are many studies on the dynamic response of SPT installation, most of them are about different types of waves acting on the drill pipe, and there is little research on the impact of platform motion on the installation of the SPT. The purpose of this paper is to investigate the dynamic influence

of the low frequency motion and the wave frequency motion of the platform on the drill pipe during the installation of the SPT. Based on the analysis of the axial and lateral loads of the drill pipe, mathematical models of the deformation and stress of the drill pipe under the action of waves, platform motion and current are established. The governing equation of the analysis model has been deduced and solved, and the parameters that may affect the dynamic response of the drill pipe have been considered. The research results can help personnel better understand the mechanical state of the drill pipe in the process of installing the SPT, and at the same time ensure the installation accuracy of the SPT and reduce the risk during installation.

## MECHANICAL MODEL

### MODEL ANALYSIS

Fig. 1 shows the schematic diagram of the installation by a drill pipe to lower the SPT. After the conductor is installed, the bottom end of the drill pipe with the SPT is lowered from the float platform to the bottom of the sea and connected to the subsea wellhead. In this process, the drill pipe is subjected to lateral current force, wave force, float platform movement and the axial gravity of the SPT. The global coordinate system is established with the SPT's downward point as the origin  $O(0, 0)$ . The  $x$  axis is perpendicular to the sea surface and the positive direction is directed to the subsea wellhead; the  $y$  axis is parallel to the sea surface and the positive direction is in the opposite direction to the current.

It is assumed that the drill pipe experiences a small deformation under its own gravity and environmental load, and that the deformation only occurs in the  $xoy$  plane. A microelement segment of the drill pipe with length  $ds$  is selected from Fig. 1 to analyse the dynamic response of the drill pipe during installation of the SPT. The force of

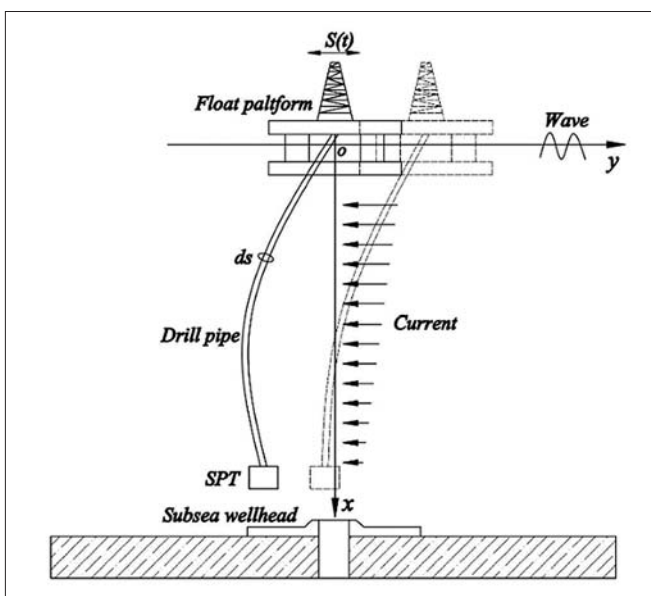


Fig. 1. Installation schematic diagram of SPT

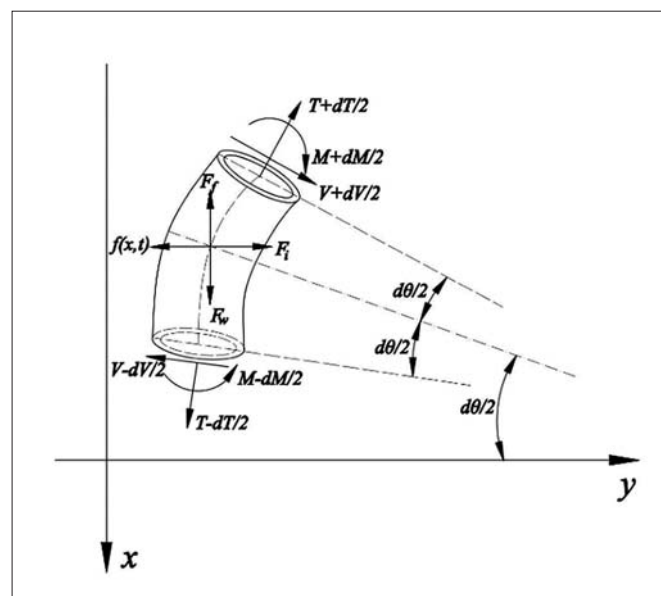


Fig. 2. Analysis model of drill pipe micro-element section

the microelement segment is shown in Fig. 2, where  $M$ ,  $V$ ,  $FW$ ,  $F_p$ ,  $F_b$  and  $f(x, t)$  are the bending moment, shear force, gravity, buoyancy, inertia force and environmental force, respectively.

According to the force of the microelement segment, the equilibrium equations of the  $x$  axis,  $y$  axis and bending moment are as follows:

$$\begin{cases} \Sigma x=0: -\left(V-\frac{dV}{2}\right)\sin\left(\theta-\frac{d\theta}{2}\right)+\left(V+\frac{dV}{2}\right)\sin\left(\theta+\frac{d\theta}{2}\right) \\ +\left(T-\frac{dT}{2}\right)\cos\left(\theta-\frac{d\theta}{2}\right)-\left(T+\frac{dT}{2}\right)\cos\left(\theta+\frac{d\theta}{2}\right)+F_w-F_f=0 \\ \Sigma y=0: \left(V+\frac{dV}{2}\right)\cos\left(\theta+\frac{d\theta}{2}\right)-\left(V-\frac{dV}{2}\right)\cos\left(\theta-\frac{d\theta}{2}\right) \\ -\left(T-\frac{dT}{2}\right)\sin\left(\theta-\frac{d\theta}{2}\right)+\left(T+\frac{dT}{2}\right)\sin\left(\theta+\frac{d\theta}{2}\right)-f(x, t)+mads=0 \\ \Sigma M=0: dT\left(1-\cos\frac{d\theta}{2}\right)+\frac{1}{R_p}dM+2V\sin\frac{d\theta}{2}=0 \end{cases} \quad (1)$$

where  $m$  is the unit length mass of the drill pipe, kg;  $a$  is the acceleration of the pipe in the negative direction of the  $x$  axis,  $m/s^2$ ;  $R_p$  is the radius of curvature of the microelement segment, m.

The microelement section is considered a small amount, Hence, it can be obtained from Eq. (1) that  $\cos d\theta = 1$ ,  $\sin d\theta = d\theta$ . For the whole of the drill pipe, the transverse deformation of the drill pipe is small, so  $ds = x$ ,  $\cos\theta = 1$ ,  $\sin\theta = \theta = dy/dx$ ,  $d\theta/dx = d^2y/dx^2$  can be obtained by the small deformation theory of the beam. The geometric relations obtained above are substituted into Eq. (1), and then simplified and sorted out. The governing equation of the drill pipe can be obtained by substituting the vertical balance equation and moment balance equation of the drill pipe into the horizontal balance equation:

$$EI \frac{d^4y}{dx^4} - T(x) \frac{d^2y}{dx^2} + m \frac{d^2y}{dt^2} = f(x, t) \quad (2)$$

where  $E$  is the Young's modulus of the drill pipe, MPa;  $I$  is the rotational inertia moment,  $m^4$ ;  $T(y)$  is the axial tension, N;  $m$  is the mass per unit length of drill pipe, kg.

## BOUNDARY AND INITIAL CONDITIONS

Because of the fixed connection with the float platform at the upper end of the drill pipe, the top of the drill pipe moves synchronously with the platform and the bending moment is related to the connection stiffness and the rotation angle. Hence, the upper boundary conditions are as follows:

$$\begin{cases} y|_{x=0} = S(t) \\ M|_{x=0} = EI \frac{\partial^2 y}{\partial x^2} \Big|_{x=0} = k_b \frac{\partial y}{\partial x} \Big|_{x=0} \end{cases} \quad (3)$$

where  $S(t)$  represents the lateral response of the platform motion;  $k_b$  is the connection stiffness when  $x = 0$ , N/rad;  $M$  is the bending moment, MPa.

Because the bottom end of the drill pipe is free, there is no slope and shear force. Therefore, the lower boundary conditions are as follows:

$$\begin{cases} \theta|_{x=N} = \frac{\partial y}{\partial x} \Big|_{z=N} = 0 \\ Q|_{x=N} = \frac{\partial^2 y}{\partial x^2} \Big|_{z=N} = 0 \end{cases} \quad (4)$$

where  $\theta$  is the angle of roll, rad;  $Q$  is the shear force, N;  $N$  is the operation depth, m.

Because the drill pipe has no displacement and velocity at the beginning, the initial conditions of the governing equation are as follows:

$$\begin{cases} y|_{t=0} = 0 \\ y'|_{t=0} = 0 \end{cases} \quad (5)$$

## LOAD DETERMINATION

Because the SPT is connected directly to the bottom of the drill pipe, it can be simplified to a mass point. The axial tension is as follows:

$$T(x) = G_{SPT} + 0.25\pi(\rho_s - \rho_w)(D_o^2 - D_i^2)(N - x) \quad (6)$$

where  $x$  is the height of the node on the drill pipe to the sea surface, m;  $G_{SPT}$  is the submerged weight of the SPT, N;  $\rho_s$  is the density of the drill pipe,  $kg/m^3$ ;  $\rho_w$  is the density of the sea water,  $kg/m^3$ ;  $D_o$  and  $D_i$  are the outer diameter and inner diameter of the drill pipe respectively, m.

The environmental load on the drill pipe is mainly caused by waves and currents. According to Morrison's equation [18], the environmental load can be expressed as follows:

$$f(x, t) = 0.5C_D\rho_w D_o [u_w(x) + u_c(x)]|u_w(x) + u_c(x)| + 0.25\pi C_M \rho_w D_o^2 \alpha_w(x)$$

$$\begin{cases} u_w(x_i) = \frac{\pi H_w}{T_w} \exp(-k_n \cdot x_i) \cdot \cos(k_n y - \omega_w t) \\ a_w(x_i) = \frac{2\pi^2 H_w}{T_w^2} \exp(-k_n \cdot x_i) \cdot \sin(k_n y - \omega_w t) \end{cases} \quad (7)$$

where  $C_D$  is the drag force coefficient, a dimensionless quantity;  $C_M$  is the inertia force coefficient, a dimensionless quantity;  $u_w$  is the horizontal velocity of a water particle at the seawater depth  $x$ , m/s;  $u_c$  is the velocity of the current at the sea surface, m/s;  $a_w$  is the acceleration of the water particle at water depth  $x$ ,  $m/s^2$ ;  $H_w$  is the wave height, m;  $T_w$  is the wave period, s;  $k_n$  is the wave number;  $\omega_w$  is the wave circular frequency.

In addition to the environmental load, the motion of the platform has a great effect on the mechanical behaviour of the drill pipe. From the study by Sexton and Agbezuge [19], the platform motion is as follows:

$$S(t) = S_0 + S_L \sin\left(\frac{2\pi t}{T_L} - \alpha_L\right) + \sum_{i=1}^N S_n \cos(k_n S(t) - \omega_n t + \phi_n + \alpha_n) \quad (8)$$

where  $S_0$  is the mean offset,  $m$ ;  $S_L$  is the amplitude of the low frequency motion of the platform,  $m$ ;  $T_L$  is the low frequency response period of the platform,  $s$ ;  $\alpha_L$  is the phase angle between the wave and platform;  $S_n$  is the amplitude response of the platform to the period and amplitude of the wave,  $s$ ;  $k_n$  is the number of the wave;  $\varphi_n$  is the wave phase angle;  $\alpha_n$  is the phase angle between the platform motion and the wave of the period.

Because the platform motion caused by all the wave frequencies is too complicated, this paper only focuses on the low frequency motion of the platform and the surge response of the platform with a 180° wave.

### MODEL SOLUTION

The finite difference method is used to find the numerical solution of the definite solution of partial (or ordinary) differential equations and systems of equations. In this paper, the difference quotient is used instead of the derivative to discretise and solve the differential governing equation. In order to facilitate the calculation, one and three nodes are respectively added to the top and bottom of the drill pipe to carry out the auxiliary calculation. The solution region is divided into  $M$  rows and  $N+5$  columns, as shown in Fig. 3.  $T$  represents the total time,  $\Delta t$  is the time step,  $N+5$  represents the total length of the drill pipe (including the virtual nodes),  $h$  is the step length.

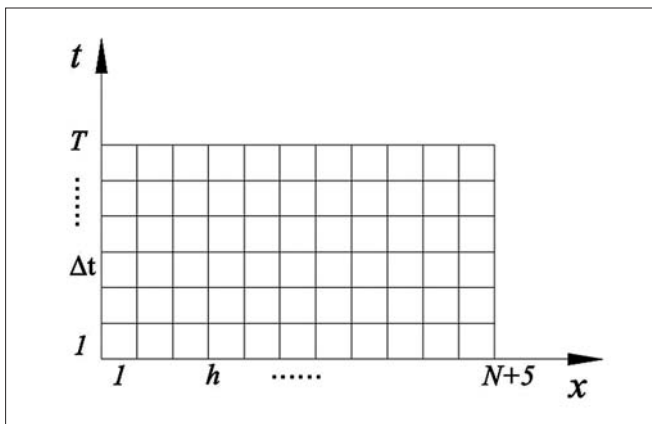


Fig. 3. Differential grid diagram

The finite difference method is used to discretise the governing differential equations (Eq. (2)) into:

$$EI \frac{y_{i+2}^m - 4y_{i+1}^m + 6y_i^m - 4y_{i-1}^m + y_{i-2}^m}{h^4} - T(x) \frac{y_{i+1}^m - 2y_i^m + y_{i-1}^m}{h^2} + m \frac{y_{i+1}^m - 2y_i^m + y_{i-1}^m}{\Delta t^2} = f(x, t) \quad (9)$$

The differential format of the drill pipe's top boundary condition, Eq. (3), is as follows:

$$\begin{cases} y_2^m = S_2^m \\ EI \frac{y_3^m - 2y_2^m + y_1^m}{h^2} = k_b \frac{y_2^m - y_1^m}{2h} \end{cases} \quad (10)$$

The differential format of the drill pipe's bottom boundary condition, Eq. (4), is as follows:

$$\begin{cases} \frac{y_{N+4}^m - y_{N+2}^m}{2h} = 0 \\ \frac{y_{N+5}^m - 2y_{N+4}^m + 2y_{N+2}^m - y_{N+1}^m}{h^3} = 0 \end{cases} \quad (11)$$

Sort out Eq. (9) to Eq. (11) as follows:

$$\begin{cases} y_i^{m+1} = ay_{i-2}^m + by_{i-1}^m + cy_i^m + by_{i+1}^m + ay_{i+2}^m + d - y_i^{m-1} \\ y_2^m = S_2^m \\ y_1^m = ey_2^m + fy_3^m \\ y_{N+4}^m = y_{N+2}^m \\ y_{N+5}^m = 2y_{N+4}^m - 2y_{N+2}^m + y_{N+1}^m \end{cases} \quad (12)$$

where

$$a = \frac{EI\Delta t^2}{mh^3}, b = \frac{4EI\Delta t^2}{mh^3} + \frac{T(x)\Delta t^2}{mh^2}, c = -\frac{6EI\Delta t^2}{mh^3} - \frac{2T(x)\Delta t^2}{mh^2} + 2$$

$$d = \frac{\Delta t^2 f(x, t)}{m}, e = \frac{4EI}{2EI + k_b h}, f = \frac{k_b h - 2EI}{k_b h + 2EI}$$

The differential format of the initial condition is as follows:

$$y_i^1 = y_i^2 = 0 \quad (13)$$

By discretisation, the governing differential equations and boundary conditions are transformed into a series of linear equations, so that the higher order differential equations can be solved in a reduced order. The lateral displacement of each section of the drill pipe which changes with time can be obtained by solving Eq. (12), and other mechanical properties of the drill pipe can also be solved by the same method. The specific process of solving the lateral displacement of the drill pipe is shown in Fig. 4.

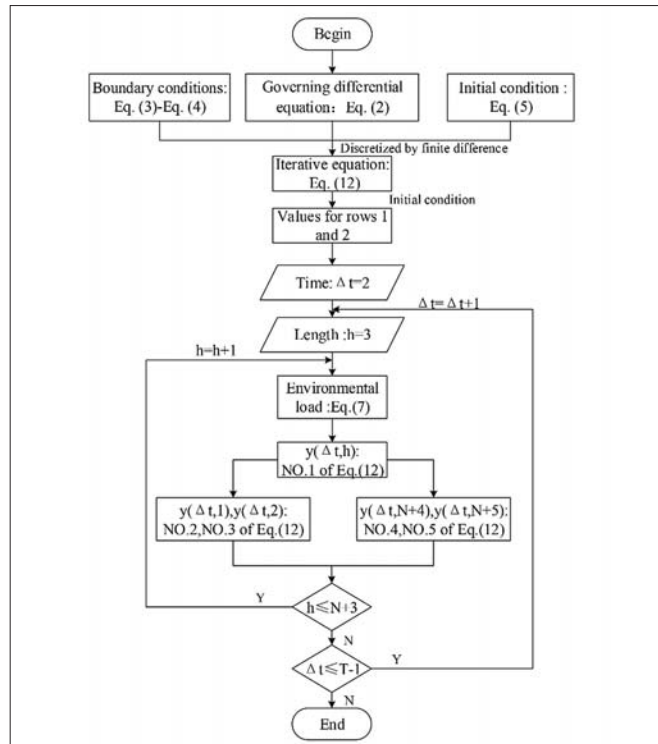


Fig. 4. Computational flow chart

## EXAMPLE ANALYSIS

A drilling operation in a certain sea area needs to install an SPT, where the operation parameters are as shown in Table 1.

Tab. 1. Operation parameters of SPT installation

Parameters	Value	Parameters	Value
Operation water depth $N$ (m)	600	Density of seawater $\rho_w$ ( $kg.m^{-3}$ )	1030
Wave height $H_w$ (m)	7	Wave period $T_w$ (s)	10
Surface velocity of current (m/s)	1.5	Drag force coefficient $C_D$	1
Inertia force coefficient $C_M$	2	Outer diameter of the pipe $D_o$ (mm)	127
Inner diameter of the pipe $D_i$ (mm)	101.6	Density of pipe $\rho_s$ ( $kg.m^{-3}$ )	7850
Young's modulus of the pipe $E$ (GPa)	210	Submerged weight SPT GSPT ( $kN$ )	300
Platform response period TL (s)	200	Platform response amplitude $S_L$ (m)	8
Connection stiffness $k_b$ (N/rad)	0		

In the process of calculation, the response of the platform is the composite motion of low frequency motion and the surge response of the platform, and its specific response is shown in Fig. 5. The maximum and minimum amplitudes of the platform response are 9.63 m, and  $-9.72$  m, respectively, and are not on the special time node.

Under the influence of horizontal force (generated by waves and current), axial force (generated by its own gravity and the gravity of the SPT) and platform motion, the maximum

value and minimum value of lateral displacement of each node in the whole installation process are shown in Fig. 6.

It is worth noting that the maximum and minimum values (the absolute value of the extreme value and the following text is the same) in Fig. 6 are the vibration extremum of each node in the whole installation process, not the overall lateral displacement of the drill pipe at a certain time. It can be seen from Fig. 6 that, with the increase of operation depth, the extreme value of the drill pipe vibration increases gradually while the rate of increase decreases gradually. The extreme values of lateral displacement at the top end of the drill pipe are  $-9.72$  m and 9.63 m, respectively, and the maximum and minimum lateral displacements at the bottom of the drill pipe are  $-16.18$  m and  $-8.92$  m, respectively. During the whole installation process, the whole drill pipe vibrates within the range of the maximum and minimum values.

The historical movement of the lateral displacement of the bottom of the drill pipe is shown in Fig. 7. It can be seen that the extreme value of the lateral displacement in Fig. 6 includes the unstable vibration portion of the drill pipe due to the fact that the effect of the platform movement is not transmitted to the bottom of the drill pipe along the drill pipe in the early stages of the installation of the SPT. Hence, under the ideal conditions of this paper, the whole installation process is divided into two parts: one is the unstable period when the movement of the SPT has not yet been transferred to the bottom end; the other is the stable period when the movement is transmitted to the bottom end, and the bottom end of the drill pipe is subjected to regular motion. When the drill pipe is lowered and vibrated smoothly, the lateral vibration area is as shown in Fig. 8.

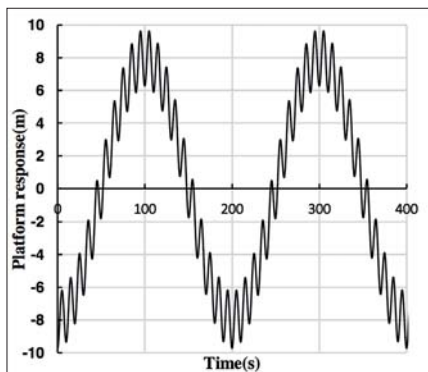


Fig. 5. Platform horizontal response motion

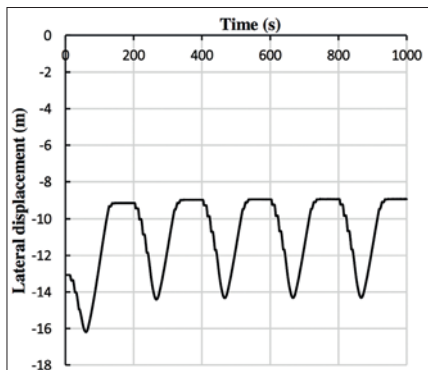


Fig. 7. History of movement of the bottom end of the drill pipe

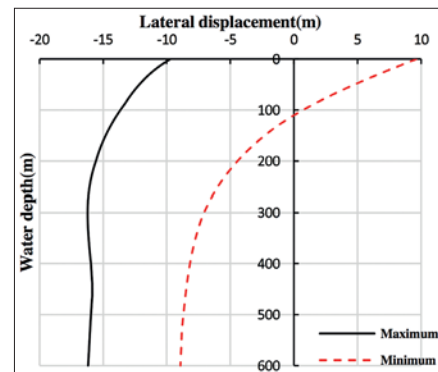


Fig. 6. Lateral displacement response of the drill pipe

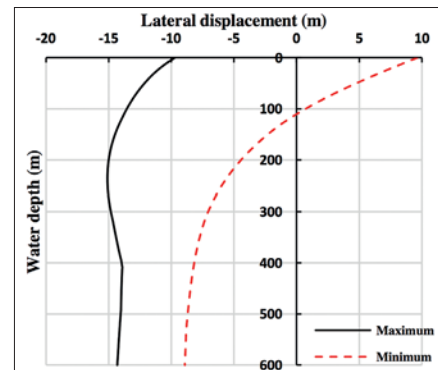


Fig. 8. Lateral displacement boundary of the drill pipe with stable vibration

As can be seen from Fig. 7, when the response motion of the platform at the top end of the drill pipe is transferred to the bottom end, the bottom end of the drill pipe does not run according to the original trajectory at the top end of the drill pipe. The reason for this phenomenon is the attenuation caused by the resistance of the sea water, and the degree of attenuation is related to the operation depth. The intersection of the curve and the ordinate shows that the lateral displacement of the drill pipe under the current action is only  $-13.06$  m, and then the bottom end of the drill pipe starts to experience distortion vibration when the stress wave is transmitted to the bottom due to the movement of the platform.

The trend in Fig. 8 is roughly similar to that in Fig. 6, but slightly different in value. The maximum and minimum values of the lateral displacement of the bottom end of the drill pipe in Fig. 8 are  $-14.31$  m and  $-8.92$  m, respectively. The difference between the extreme value of the unstable stage and the extreme value of the stable stage is 25%, so the lateral displacement of the bottom of the drill pipe in the unstable stage is also very important.

In order to more intuitively reflect the influence of the platform motion on the lateral displacement of the drill pipe during the stable period, the influence of the platform motion on the lateral displacement is measured by the standard deviation, and the standard deviation is shown in Fig. 9.

As can be seen from Fig. 9, the standard deviation is nearly linearly reduced in the first 500 m; in other words, the influence of the platform motion on the lateral displacement decreases gradually with the increase of water depth. In the latter 100 m, the standard deviation tends to increase, which may be caused by the inertia force of the SPT connected at the end of the drill pipe.

## EVOLUTIONARY MECHANISM OF DRILL PIPE DYNAMIC RESPONSE

In the process of SPT installation, the distribution of the lateral displacement and bending stress of the drill pipe is particularly important for the success of SPT installation, so it is necessary to study these two parameters. In order to explore the influence of the platform motion on the process of these two parameters, five time nodes ( $t = 0, T_L/4, T_L/2, 3T_L/4, T_L$ ) of the platform response period are taken, and the dynamic influence of the platform movement on the lateral displacement and bending stress are shown in Fig. 10 and Fig. 11.

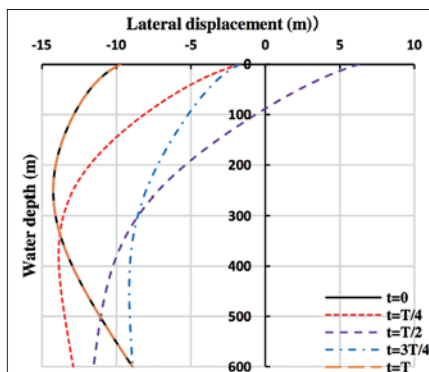


Fig. 10. Dynamic response of lateral displacement

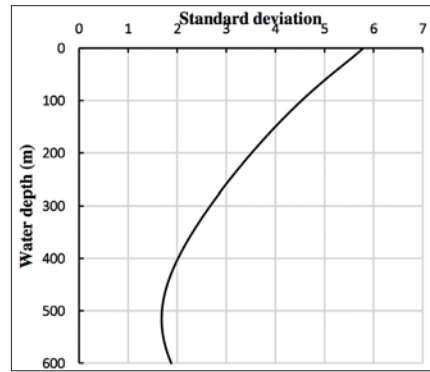


Fig. 9. Standard deviation of displacement during stability

It can be seen from Fig. 10 that when the upper end of the drill pipe reaches the extreme value, the lower end of the drill pipe does not reach the corresponding extreme value, but has a certain delay. When  $t = T_L/4$ , there is a maximum lateral displacement of 12.9 m in each time node at the bottom end of the drill pipe; when  $t = 0, 3T_L/4$ , and  $T_L$ , there is a minimum displacement of 8.9 m in each time node at the bottom end of the drill pipe. This differs from the extreme value of the bottom of the drill pipe in Fig. 2 by 1.2% and 0.2%, respectively. Because the motion state of the drill pipe is different at each time node, the lateral displacement of the drill pipe is not symmetrical.

Fig. 11 shows that the bending stress of the drill pipe reaches the maximum near the top, and then gradually decreases to zero with the increase of the operation depth (because there is only a large difference in the first few tens of metres, only the stress distribution of the first 50 m is shown, as is the same below). When  $t = T_L/4$ , the maximum bending stress in each time node is 25.2 MPa; when  $t = 3T_L/4$ , the minimum bending stress in each time node is 18.9 MPa. This corresponds exactly to the maximum and minimum lateral displacement at the bottom end of the drill pipe in Fig. 10. Therefore, the drill pipe is in the “dangerous” stage when  $t = T_L/4$ .

## EFFECT OF OPERATION WATER DEPTH ON LATERAL DISPLACEMENT AND BENDING STRESS

With the development of oil and gas exploitation to the deep sea, the depth of operation is the parameter that has to be considered. Five different ocean depths varying from 600 m

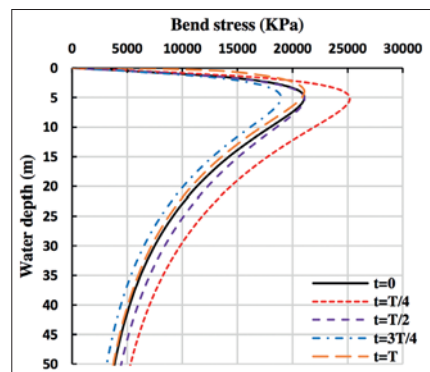


Fig. 11. Dynamic response of bending stress

to 1400 m are selected to analyse the mechanical behaviour of the drill pipe, and the other working parameters are the same. The lateral displacement and bending stress of the drill pipe are shown in Fig. 12 and Fig. 13.

It can be seen from Fig. 12 that, with increase of the operation water depth, the maximum boundary and minimum boundary of the lateral displacement of the drill pipe are also gradually increased. The differences between the maximum value and the minimum value of the bottom end of the drill pipe in different water depths are 7.26 m, 6.9 m, 6.45 m, 5.12 m and 4.1 m respectively. If the platform rotates, the active range of the SPT is a circle whose diameter is the difference between the maximum and minimum lateral displacement at the bottom of the drill pipe. Hence, the deeper the water, the smaller the SPT range at the bottom of the drill pipe, and the higher the installation accuracy.

It can be seen from Fig. 13 that the bending stress increases rapidly to the maximum value in the first few metres, and then decreases gradually. The maximum bending stresses of different water depths are 30.8 MPa, 27.9 MPa, 25.6 MPa, 23.6 MPa, and 21.9 MPa, respectively. Therefore, with increase of the operation depth, the bending stress decreases gradually, and the amplitude of the decrease is not large.

#### EFFECT OF SUBMERGED WEIGHT OF THE SPT ON LATERAL DISPLACEMENT AND BENDING STRESS

Since the submerged weight of most SPTs used under water ranges from 200 kN to 400 kN, five data are selected to analyse its impact on the drill pipe, while the other operation parameters remain unchanged. The lateral displacement

and bending stress of the drill pipe are shown in Fig. 14 and Fig. 15.

As can be seen from Fig. 14, with increase of the submerged weight of the SPT, the maximum boundary and minimum boundary of the lateral displacement of the drill pipe decrease gradually. The differences between the maximum and minimum lateral displacement of the bottom end of the drill pipe under the different submerged weights of the SPT are 5.46 m, 6 m, 6.45 m, 5.88 m and 5.29 m, respectively. It can be seen that, with increase of the submerged weight of the SPT, the vibration area of the drill pipe first increases and then decreases. Therefore, in order to ensure high installation accuracy, it is necessary to select the appropriate submerged weight of the SPT.

Fig. 15 shows that, with increase of the submerged weight of the SPT, the bending stress distribution curve of the drill pipe moves in the direction of a smaller value. The maximum bending stresses are 30 MPa, 27.5 MPa, 25.4 MPa, 23.8 MPa and 22.2 MPa, respectively. This phenomenon is caused by increase of the axial force and decrease of the lateral displacement.

#### EFFECT OF CURRENT VELOCITY ON LATERAL DISPLACEMENT AND BENDING STRESS

In order to explore the mechanical influence of the tidal current velocity of the sea surface on the drill pipe, five different current speeds ranging from 1.3 m/s to 1.7 m/s are selected for comparison, while the other working conditions remain the same. The distribution of the lateral displacement vibration boundary and maximum bending stress is shown in Fig. 16 and Fig. 17.

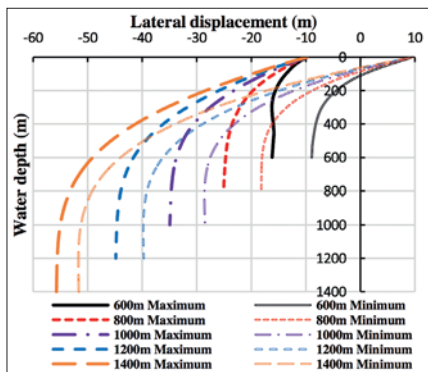


Fig. 12. Lateral displacement boundary with different operation depth

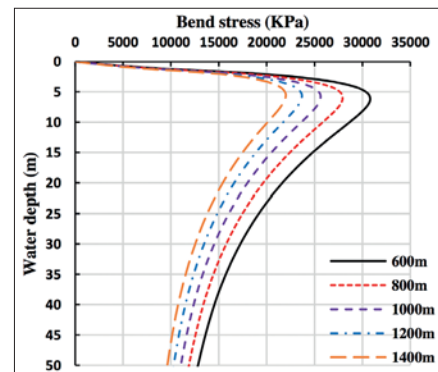


Fig. 13. Bending stress with different operation depth

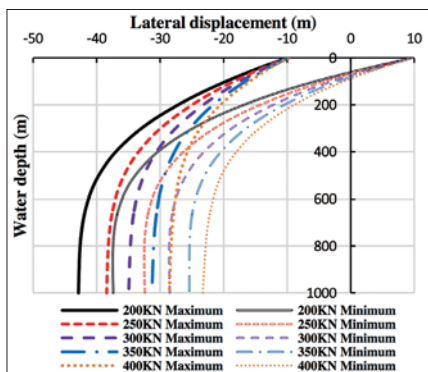


Fig. 14. Lateral displacement boundary with different submerge weight of SPT

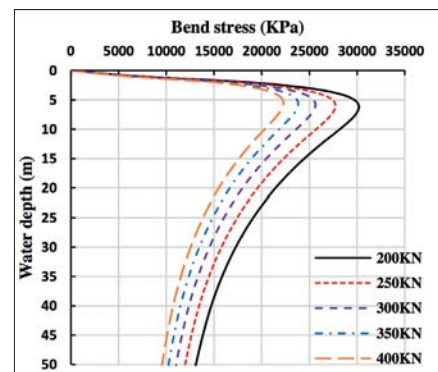


Fig. 15. Bending stress with different submerge weight of SPT

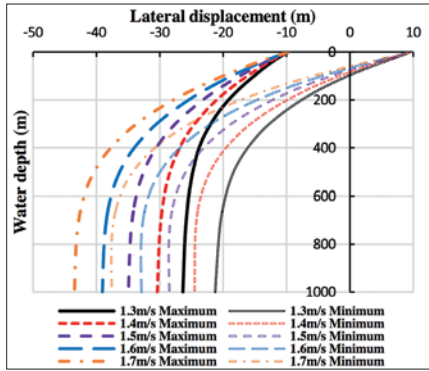


Fig. 16. Lateral displacement boundary with different current velocity

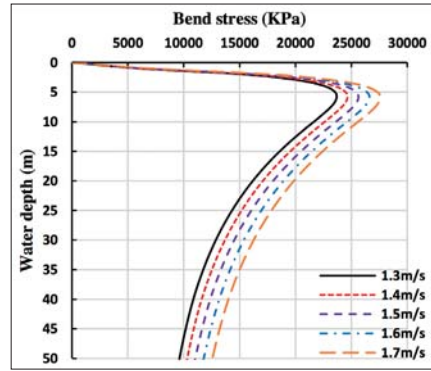


Fig. 17. Bending stress with different current velocity

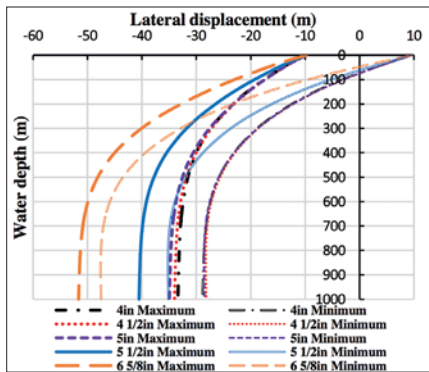


Fig. 18. Lateral displacement boundary with different drill pipe specifications

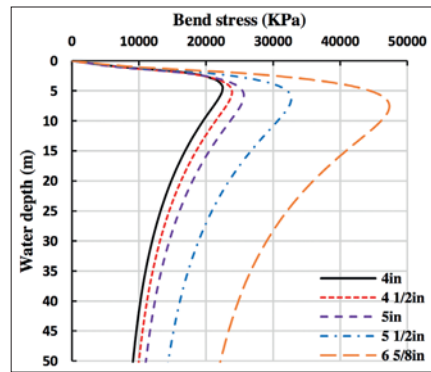


Fig. 19. Bending stress with different drill pipe specifications

As shown in Fig. 16, the current velocity of the sea surface is only changed by 0.1 m/s, and the lateral vibration boundary of the drill pipe is very different. Under different current velocities, the ranges of activity at the bottom end of the drill pipe are 5.1 m, 5.87 m, 6.45 m, 6.17 m and 5.89 m, respectively. It can be seen that the range of activity at the bottom of the drill pipe does not always increase as the velocity of the current increases. Therefore, in order to ensure accurate installation of the SPT, it is necessary to accurately measure and select the suitable sea surface current velocity.

It can be seen from Fig. 17 that the bending stress increases with increase of the current velocity; and the maximum bending stresses at different current velocities are 23.7 MPa, 24.6 MPa, 25.6 MPa, 26.6 MPa and 27.58 MPa, respectively. The maximum bending stress increases by 1 MPa for every 0.1 m/s increase of the current velocity.

#### EFFECT OF DRILL PIPE SPECIFICATION ON LATERAL DISPLACEMENT AND BENDING STRESS

Five kinds of drill pipes of different specifications (ranging from 4 in to 6 5/8 in) are used to analyse the dynamic influence, while the other operation parameters remain unchanged. The lateral displacement boundary and bending stress are shown in Fig. 18 and Fig. 19.

Fig. 18 clearly shows that when the drill pipe specification increases from 4 in to 5 in, the vibration boundaries of transverse displacement of the drill pipe change only slightly. However, when the drill pipe specification increases from 5 in to 6 5/8 in, the maximum and minimum values of the

lateral displacement of the drill pipe increase greatly. Although the extreme value of the lateral displacement increases with increase of the drill pipe specification, the range of movement of the lower end of the drill pipe first reduces and then increases.

It can be seen from Fig. 19 that the bending stress distribution curve moves to the right as the drill pipe specification increases. The maximum bending stress increases slightly from 4 in to 5 in, and in particular the maximum bending stress increases significantly from 5 in to 6 5/8 in. The maximum bending stresses of the drill pipe with different specifications are 22.42 MPa, 23.85 MPa, 25.62 MPa, 32.66 MPa, and 47.27 MPa, respectively.

### CONCLUSION

Based on the research reported above, the following conclusions and results can be obtained:

(1) The maximum displacement of the pipe at the bottom decreased by about 1.7 m when the variable environment load was considered.

(2) The bend stress of the pipe reaches its maximum value of 25.2 MPa at 5 m and the displacement at bottom reaches its maximum value of 12.9 m when  $t = T_L/4$  ( $t$  reflects the variable time of the drill pipe,  $T_L$  reflects the response period of the platform).

(3) The displacement of each joint of the pipe increases with the water depth, current velocity and specification of the pipe, and the distance between the SPT and the wellhead was approximately linear with the water depth.

(4) The movement of the SPT increases with the specification of the pipe, weight of the SPT and current velocity at the first stage only, but then decreases gradually.

(5) The current velocity and the weight of the pipe significantly affect the bend stress of the pipe during the installation of the SPT and more attention should be paid to this during the design stage of the project.

#### ACKNOWLEDGEMENT

The authors would like to acknowledge the support of the Scientific Research Starting Project of SWPU (No.2017QHZ010), China.

#### REFERENCES

1. Chakrabarti S. K., Frampton R. E. (1982): *Review of riser analysis techniques*. Applied Ocean Research, 4(2), 73-90.
2. Safai Hachemi V. (1983): *Nonlinear dynamic analysis of deep water risers*. Applied Ocean Research, 5(4), 215-225.
3. Ahmad S., Datta T. K. (1989): *Dynamic analysis response of marine risers*. Engineering Structures, 11, 179-188.
4. Ahmad S., Datta T. K. (1992): *Nonlinear response analysis of marine risers*. Composite Structures, 43(2), 281-295.
5. Wang D. D. (2006): *Computational analysis on loads and motion of underwater risers*. Master's Thesis, Dalian University of Technology.
6. Khan R. A., et al. (2011): *Nonlinear dynamic analysis of marine risers under random loads for deep water fields in Indian offshore*. Procedia Engineering, 14, 1334-1342.
7. Qi B. (2012): *Global strength analysis of ultra deepwater drilling riser*. Master's Thesis, Harbin Engineering University.
8. Zhou S. W., Liu Q. Y., et al. (2013): *The discovery of "One Third Effect" for deep water drilling riser: Based on the theoretical and experimental study of deformation characteristics of deep water drilling riser by ocean currents*. China Offshore Oil and Gas, 25(06), 1-7.
9. Guo H. Y., Zhang L., et al. (2013): *Dynamic responses of top tensioned riser under combined excitation of internal solitary wave, surface wave and vessel motion*. Journal of Ocean University of China, 12(1), 6-12.
10. Wang Y. B., et al. (2015): *Study on lateral nonlinear dynamic response of deepwater drilling riser with consideration of the vessel motions in its installation*. Computers, Materials and Continua, 48(1), 57-75.
11. Fan H. H., et al. (2017): *Dynamic analysis of a hang off drilling riser considering internal solitary wave and vessel motion*. Journal of Natural Gas Science and Engineering, 37, 512-522.
12. Hu Y. L., et al. (2018): *Dynamic behaviors of a marine riser with variable length during the installation of a subsea production tree*. Journal of Marine Science and Technology (Japan), 23(2), 378-388.
13. Olszewski A., et al. (2018): *FEM analysis and experimental tests of rigid riser hanging system*. Polish Maritime Research, 25(2), 108-115.
14. Wodtke M., et al. (2018): *FEM calculations in analysis of steel subsea water injection flowlines designing process*. Polish Maritime Research, 25(3), 84-93.
15. Wang C., et al. (2019): *Simulation of axial vibration characteristics of marine riser under suspension mode*. Journal of System Simulation, 31(10), 2122-2130.
16. Chen L. Y., et al. (2019): *Dynamic characteristic study of riser with complex pre-stress distribution*. Polish Maritime Research, 26(3), 87-97.
17. Liu J., et al. (2018): *Dynamic behavior of a deepwater hard suspension riser under emergency evacuation conditions*. Ocean Engineering, 150, 138-151.
18. Wilson J. F. (Ed). (1991): *Dynamics of offshore structures*. Beijing Petroleum Industry Press.
19. Sexton R. M., Agbezuge L. K. (1976): *Random wave and vessel motion effects on drilling riser dynamics*. In 8th Annual Offshore Technology Conference.

#### CONTACT WITH THE AUTHORS

**Fei Wang**

*e-mail: wangfei\_swpu@126.com*  
Southwest Petroleum University  
Xindu, 610500 Chendu  
**CHINA**

**Neng Chen**

*e-mail: 2812087241@qq.com*  
Southwest Petroleum University  
Xindu, 610500 Chendu  
**CHINA**

## SHORT REVIEW AND 3-D FEM ANALYSIS OF BASIC TYPES OF FOUNDATION FOR OFFSHORE WIND TURBINES

Piotr Iwicki  
Jarosław Przewłócki  
Gdańsk University of Technology, Poland

### ABSTRACT

*Some problems of the foundations of offshore wind turbines are considered in this paper. A short review is presented on the two basic types of foundations, i.e. monopiles and gravity foundations, including their basic features and applications as well as general design considerations. Also, some issues regarding analysis are discussed, including geotechnical problems and modelling techniques. A numerical model of offshore turbine and some preliminary computations are presented. Finite element analysis was carried out for wind turbines supported on both gravity and monopile foundations. The wind turbine tower, blades (simplified model), gravity foundation and part of the surrounding soil are included in the model. The turbine was loaded by wind and loads induced by waves, inertia and gravity. Both non-linear static and dynamic analysis of the wind turbine was performed. The displacements and stresses under the tower foundations were calculated and a comparison analysis carried out.*

**Keywords:** offshore wind turbine, monopile, gravity foundation, FEM analysis

Table 1. Properties of turbines for a water depth of 30 m

### INTRODUCTION

Wind energy is one of the most widely used types of renewable energy. Recently, there has been a significant development of offshore wind farms. Their construction was an important element of the European government strategy aiming to achieve the target of 20% of energy from renewable sources by 2020. Offshore wind turbines (OWTs) are generally larger than those installed on land, and a nominal capacity of 3 to 5 MW is now the norm. Usually, rotor diameters are larger than 100 m and nacelle locations are more than 80 m above mean sea level. Currently, modern 6–10 MW turbines are being introduced. However, turbines of up to 10 MW and with rotor diameters as large as 150 m are coming soon. The potential of offshore wind energy in Europe is expected to steadily increase up to 25 MW in 2026 [21]. Outline properties of present day and forthcoming turbines are shown in Table 1 [5]. The basic components of a wind turbine system supported on a monopile foundation, including their estimated dimensions, are presented in Fig. 1.

Parameter	Unit	Turbine rated power			
		3.6 MW	5.0 MW	6–7 MW	8.0 MW
Rotor diameter	m	120	126	153	164
Rated wind speed	m/s	13	11.4	13	14
Hub height	m	80	85	100	110
Max thrust at hub	MN	1.20	1.20	2.00	2.30
Max mudline moment $M_{max}$	MNm	136	137	265	323
Maximum wave height	m	12	12	12	12
Typical monopile diameter	m	6	6.5	7	7.5
Horizontal wave force	MN	4.2	4.81	5.43	6.09
Mudline moment from waves	MNm	120	137	155	175
Unfactored design moment	MNm	256	274	420	498

The main advantages of offshore wind farms are that the wind is more stable, giving more efficient use of turbines; there is lack of technological constraints – a turbine installed at sea may be far higher and thus more effective; wind force at sea is higher at a lower altitude, which enables the use of lower towers. Besides that, wind strength increases with distance from the shore and the sea provides more space for the location of wind turbines. The main disadvantages are greater difficulty in accessing the facility during repair or maintenance, and much more expensive maintenance and service facility power.

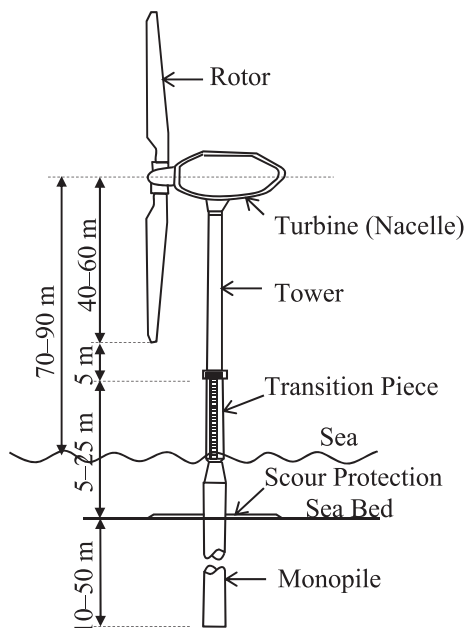


Fig. 1. Offshore wind turbine system components

Foundations of OWTs are considerably more costly than for the equivalent onshore ones. The cost of the support structure varies from 25% to 35% of the overall cost [6] and it can even reach 50% [10]. Such costs mainly depend on the sea depth and distance from shore. Their influence can be introduced by a correction factor, given in Table 2 [9]. It can be assumed that in the next dozen or so years, most OWTs will be located at sites in water depth greater than 30–40 m.

Table 2. Cost factor dependency on distance and depth

Depth (m)	Distance from shore (km)							
	> 0	> 10	> 20	> 30	> 40	> 50	> 100	> 200
10–20	1.00	1.02	1.04	1.07	1.09	1.18	1.41	1.60
20–30	1.07	1.09	1.11	1.14	1.16	1.26	1.50	1.71
30–40	1.24	1.26	1.29	1.32	1.34	1.46	1.74	1.98
40–50	1.40	1.43	1.46	1.49	1.52	1.65	1.97	2.23

The cost of the foundation includes, besides the cost of the structure itself, transport, installation and scour protection. Scour protection consists of a filter layer and an armour layer. In the case of monopiles, depending on the hydrodynamic environment, the horizontal extent of the armour layer can be between 10 and 15 m, having a thickness of between 1 and 1.5 m. Filter layers are usually 0.8 m thick and reach up to 2.5

m further than the armour layer. The total diameter of the scour protection is assumed to be five times the pile diameter. There are many different standards and recommendations for calculating the extent and thickness of scour protection. Interesting design guidelines to determine these parameters in relation to the pile diameter are provided in [24].

In the case of a gravity foundation, it should also include seabed preparation.

OWTs are subjected to higher environmental loading than those situated on land. It is necessary to provide the right connection with the subsoil. The foundation of the turbine transfers the forces from the structure to the ground. Thus, the foundation is a critical part in designing the OWT and a thorough analysis is essential. Recently, the finite element method (FEM) has found wide application in soil–structure interaction problems. In this paper, 3-D FEM computations were carried out for wind turbines supported on monopile and gravity foundations. Non-linear static and dynamic analysis of the wind turbine was performed. Both stresses and displacements beneath the foundation were computed. Comparison analysis was performed. A short review of the basic supporting structures of OWTs, i.e. gravity foundations and monopiles, is also presented. The most important characteristics for both cases are discussed as well as some problems of their analysis or design.

## TYPES OF FOUNDATION

It is characteristic for an OWT that the wind and wave loadings lead to greater forces on the structure than those that would occur onshore. In the case of a 3.5 MW turbine, the vertical load is of the order of ca. 6 MN, the maximum horizontal load applied on the foundation may be ca. 4 MN and the overturning moment ca. 120 MNm (or equivalent to the horizontal load being applied 30 m above the base), see [6]. The ratio between the horizontal and vertical loads (H/V) for an OWT is between 1.4 and 2.6 [14]. Axial and lateral loads act at a point at the interface level between the monopile and the turbine shaft that is located ca. 20 m above sea level. Thus, it is necessary to ensure that sufficient connection with the ground is provided, otherwise the structure will move irreversibly.

Foundations for wind turbines can be classified into two main types: bottom-fixed (Fig. 2a–d) and floating (Fig. 2e).

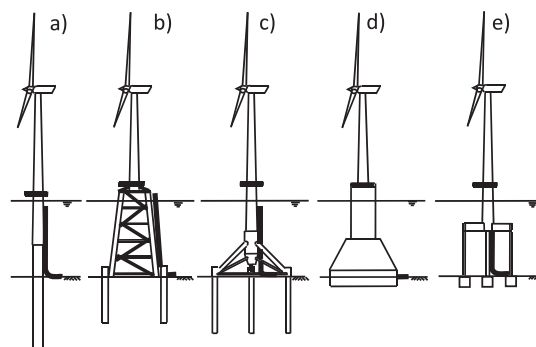


Fig. 2. Foundation types: a) monopile foundation, b) jacket foundation, c) tripod foundation, d) gravity foundation, e) floating structure

Foundations are also classified into three categories according to the depth of the seabed. Gravity-based or monopile foundations are feasible for shallow waters (0–30 m), tripod or jacket foundations for transitional waters (30–50 m) and the floating concept is the best for deep waters (50–200 m). It is worth noting that, presently, steel monopiles can be installed in water depths of 40 to 45 m. Approximately 20% of currently installed OWTs are supported by gravity foundations and 75% by monopile structures [8, 10]. Most small OWTs are located at relatively small depths (up to 20 m) and close to the mainland (up to 20 km). However, it is anticipated that by 2030, the location of wind farms will be standard in 60 m seas and up to 60 km from the mainland [21].

Tables 3 and 4 give very preliminary estimated dimensions for a few different sizes of turbines and the two types of foundation considered in this paper, i.e. gravity and monopile [16].

Table 3. Basic dimensions of gravity foundations for turbines of different power

Gravity	3.0 MW	3.6 MW	4.0 MW	8.0 MW
Shaft diameter	3.5–5.0 m	3.5–5.0 m	4.0–5.0 m	5.0–6.0 m
Width of base	18–23 m	20–25 m	22–28 m	25–35 m
Ballast	Infill sand	Infill sand	Infill sand	Infill sand

Table 4. Basic dimensions of monopile foundations for turbines of different power

Monopile	3.0 MW	3.6 MW	4.0 MW	8.0 MW
Outer diameter at seabed level	4.5–6.0 m	4.5–6.0 m	5.0–7.0 m	6.0–8.0 m
Pile length	50–60 m	50–60 m	50–60 m	50–70 m
Ground penetration (below mud line)	25–32 m	25–32 m	26–33 m	28–35 m
Transition piece				
Length	10–20 m	10–20 m	10–20 m	15–25 m
Outer diameter (based on a conical monopile)	3.5–5.0 m	3.5–5.0 m	4.0–5.5 m	5.0–6.5 m

## GRAVITY FOUNDATIONS

A gravity foundation is a shallow foundation resting on the upper sediment layer, where the soil lying directly under the seabed has adequate bearing capacity. It transfers the loading by a large base to the seabed and resists overturning

loads solely by means of its own gravity. Such a foundation must also provide sufficient resistance against sliding and vertical bearing capacity. It is made from concrete, with or without small amount of steel, and its weight is in a range from 1400 to over 3000 tons. Reinforced gravity foundations are built onshore and floated out to sea where they are filled with gravel and sand. They are used on suitable soil sites in shallow waters or where installation of piles in the underlying seabed is difficult. Gravity foundations are uneconomical in deeper waters due to the very high moment loads applied by the wind turbines. The increase in mass of such foundations with water depth follows an approximately quadratic relation. Also, a disadvantage is the necessity of proper preparation of the seabed to ensure the structure's stability. The benefit of installing gravity foundations is that they can be floated out to their location, although heavy lifting vessels are needed for those of great weights. Installation requires little time and favourable weather conditions.

Gravity foundations for OWTs are usually used at water depths of up to 25 m. A reasonable concept for a gravitational-type foundation intended for waters with a depth of up to 40 m, including numerical analysis, has been proposed by Niklas [22].

## MONOPILE FOUNDATIONS

Monopiles consist of a foundation pile and a transition part, on top of which the turbine tower is placed (Fig. 1). The weight of each element usually does not exceed 250 tons. A monopile support structure is exposed to both vertical and horizontal loads. The former are carried by the pile wall friction and tip resistance and the latter are transferred to the soil by mobilizing the lateral resistance of the soil through bending.

The foundation pile is made from steel plate which is rolled and welded together to form a cylindrical section. The length of the monopile in general depends on the overturning capacity under extreme conditions, or the maximum allowable tilt of the OWT due to accumulated rotations from cyclic loading [17]. Its diameter is usually governed by requirements for the frequency of the turbine that is closely related to the stiffness response of the soil. The wall thickness is usually determined by employing either fatigue loads or shell buckling during the installation phase. Monopiles for OWTs are usually 30–40 m long. The diameters of steel piles are in the range 3.5–6 m and wall thicknesses are as much as 150 mm. They can be classified as rigid monopiles for which the length to diameter ratio (L/D) is generally less than 12. Depending on subsoil conditions, piles are driven using hammers or vibrators, using drilling or excavation of seabed material until the final depth, typically 20–40 m, is reached. An embedment length of 30 m (5–6 times the diameter) is usually considered sufficient to meet design criteria, including vertical stability and horizontal deflection requirements.

For larger wind turbines of higher power, the monopile diameter would have to be as large as 7.5 m [3]. Scharff and Siems [28], in a study based on a new-generation 6 MW turbine situated at a water depth of 35 m, found that the diameter of the monopile should be over 8 m. According to Saleem [27],

an increase in the diameter of the monopile by 1 m generally means that the pile can be installed in water 10 m deeper. The diameter limit these days is around 6 m, so a 7 m diameter monopile might be installable in water depths of around 40 m. However, it should not be presumed that this statement, i.e. a linear relation, is true for greater depths.

Although monopile foundations can reduce material costs while maintaining performance, they require heavy equipment for installation that may cause considerable vibration, noise and suspended sediment. So, some environmental issues should be considered for this technology. Advantages include minimal seabed preparation requirements and resistance to seabed movement, scour or ice flow damage. Also, there are relatively small production costs due to the simplicity of the structure, storage and installation although there is the high price of steel and fabrication of the pile itself. At greater depths, the disadvantages are flexibility of the monopile, decreased stiffness or the cost of installation due to the time the grout needs to set. Monopiles are not suitable for locations with many large boulders in the seabed. Also, at sites where drilling is necessary, installation is very slow and expensive. Some difficulties are relevant during production and installation of large-diameter piles because of limitations on available steel plate sizes and pile driving capacity.

## FOUNDATION SELECTION

In order to choose the best foundation type, first of all water depth and geotechnical site conditions should be considered. Scour and erosion potential and environmental loading conditions must also be taken into account. In addition, the economic issue should be considered as well.

Comparison analysis considering multiple engineering, economic and environmental attributes for three foundation types (monopile, tripod and jacket) for a 5.5 MW wind turbine and water depth of 40 m has been performed by Lozano-Minguez et al. [18]. They concluded that the tripod is the best option overall although the monopile is the most economical and less harmful to the environment, because the former suffers less from wave-resonance.

Monopiles are commonly used where the water depth is less than 35 m and the near-surface soil conditions are poor. Compared to monopiles, gravity foundations are more onerous considering their transport, installation, scouring protection, dependency on subsoil conditions or removal after the design life. Besides that, they have a minimal and localized environmental impact.

In shallow waters, monopile foundations are the best solution for OWTs up to 3.6 MW, whereas gravity foundations are most suitable for big OWTs [20]. Some considerations aiming to find the optimal foundations of the OWT with a size greater than 10 MW were carried out in [26].

## GENERAL ANALYSIS AND DESIGN CONSIDERATION

Foundations for OWTs are generally more complex than for onshore turbines. Proper analysis should include such additional factors as the harsh marine environment as well as the short- and long-term impacts under wave loading. The offshore environment loadings from wind and waves are characterized by a large number of load cycles that affect the seabed and can significantly change soil properties. In turn, they influence the foundation's response to the loads. It is of great importance to investigate the effects of cyclic loading on the structures supporting OWTs. It is essential to perform both short- and long-term analyses, which are neither incompatible nor mutually exclusive. The former in saturated soils leads to a build-up of water pressure and eventually liquefaction phenomena that cause foundation failure. In the latter case, soil densification and hardening are in general observed. It is also important to distinguish fully drained, partially drained and undrained conditions. For example, the accumulating displacements in drained sands can lead to foundation failure. The most remarkable effect of cyclic lateral loading, in comparison to its static behaviour in the case of monopiles, is an increase of deflection and rotation.

An appropriate technical design for the foundations of OWTs is crucial for the safe, efficient and economic development of offshore wind farms. The main objective of the support structure design is to determine the dimensions of its components, taking into account operability, load resistance and economics. The design procedure for OWT foundations is typically based on design standards. The detailed specification of foundation design procedures is referred to in [7].

The most commonly used method for OWT foundation analysis is the limit states design method. There are four types of limit state: the ultimate limit state (ULS), fatigue limit state (FLS), accidental limit state (ALS) and serviceability limit state (SLS). ULS verifies the strength and stability of the foundation while SLS checks its maximum displacement. FLS verifies that the structure is able to withstand accumulated damage throughout its design life, which is critical for large modern OWTs. For offshore foundation design, only ULS uses non-degraded soil parameters. Other limit states use cyclically degraded soil properties for design calculations.

For design purposes of gravity-based foundations, the following factors should be accounted for: 1) total stability failure, 2) rupture in soil-carrying capacity, 3) sliding ruptures, 4) combined ruptures in soil and structure, 5) ruptures due to foundation movements, 6) unacceptable movements and oscillations, 7) eigenfrequency analysis, 8) liquefaction risk analysis (when set upon sandy soils), 9) zones of local strong soil or rock and 10) design of the gravel bed (differential settlement analysis, requirement for grading curve, levelling of gravel base, base minimum thickness) [29, 30].

Piled foundations should be examined in the following contexts: 1) elastic ULS, where only one pile per foundation is allowed to reach the yield point as a maximum, 2) plastic ULS (accounting for cyclic load strength degradation), where piles

are allowed to yield if still absorbing design loads, 3) fatigue in terms of both actual fatigue load on structure and the damaging effects of pile driving, 4) pile driving analysis, 5) eigenfrequency analysis (i.e. characteristic representation of the dynamic response of the pile) and 6) a soil damping estimate [4, 30].

When designing monopile foundations, it is rare that the ultimate lateral bearing capacity is a decisive factor. More important is the monopile's stiffness due to possible fatigue failure. Thus, the pile–soil interaction problem must be analysed. Design recommendations for monopiles [7] adopt the soil pressure–pile deflection (*p-y*) method. However, there are other methods of analysing laterally loaded piles like the limit state method, subgrade reaction method, elasticity method and FEM. The last one is an important research tool for soil–structure interactions and optimizing the support design.

A review of modelling of soil–OWT structure interaction, including modelling of soil and foundations, is given in [23]. Presently, FEM is commonly used in studies on modelling of OWT foundations [2, 11, 12, 13, 15, 19]. Many computer programs using FEM have been developed for offshore settings (e.g. ABAQUS, PLAXIS and ROSAP).

## NUMERICAL ANALYSIS

### DESCRIPTION OF THE WIND TURBINE TOWER

Finite element calculations were carried out for a steel wind turbine tower with a height of about 80 m and rotor blade of about 80 m. The tower of the wind turbine was tubular with diameter of 4 m at the bottom and 2.3 m at the top, with a varying cross-section thickness ( $t = 14\text{--}36$  mm) along the column height. Two types of turbine foundation were considered.

In the first variant, a gravity foundation was analysed (Fig. 3a). The wind turbine tower was set on a concrete column, 8 m high and diameter  $D = 5$  m, that was supported by a gravity base with a circular fundament slab of diameter 18 m and

thickness 2 m. Two soil blocks in the shape of a cylinder were included in the numerical model. The bottom block height was 32 m and the upper block height was 6 m. The block diameter was 32 m. In the upper part of the soil, a cut was made for the concrete foundation block.

In the second variant, a turbine resting on a monopile was considered (Fig. 3b). The monopile was 32 m long while it penetrated 24 m into the seabed. The diameter of the steel pile was 4 m and wall thickness was 70 mm. Two cylinder soil blocks were modelled. The bottom block height was 10 m and the upper block height was 24 m. The block diameter was 32 m. The soil block inside the monopile was also modelled. The Mohr–Coulomb model was used for the soil. The following soil parameters were assumed: density 2.1 t/m<sup>3</sup>, Young modulus 20 MPa, Poisson's ratio 0.25, friction angle 15°, cohesion 27 kPa and dilation angle 0.1°.

The wind turbine tower was loaded by inertia and gravity loads, wind and wave loads (Fig. 3c). In the present analysis, the wind load was taken according to the Polish code [25] for a characteristic wind speed of 30 m/s and air density of 1.23 kg/m<sup>3</sup>, resulting in a characteristic wind speed pressure of 550 Pa. Wave load predictions should account for the size, shape and type of the proposed structure. In this paper, the wave forces on a slender wind turbine tower cylinder submerged in water were predicted by Morison's equation. In this model, wave load  $F$  per unit length is given in [26]:

$$dF = dF_M + dF_D = C_M \rho \pi \frac{D^2}{4} \ddot{x} dz + C_D \rho \frac{D}{2} |\dot{x}| \dot{x} dz, \quad (1)$$

where the inertia coefficient  $C_M$  was set at 2, drag coefficient  $C_D$  was equal to 1, and  $\rho$ , the density of water, is 1000 kg/m<sup>3</sup>. Water depths and wave data for an example case were taken according to [26]. The wave height was assumed to be 3.5 m and its length 45 m. The wave force is a function of time and reaches a maximal value described by following formula:

$$F_{\max} = C_M \rho \pi \frac{D^2}{4} U \frac{\sinh(kd)}{k}, \quad k = \frac{2\pi}{\lambda}, \quad (2)$$

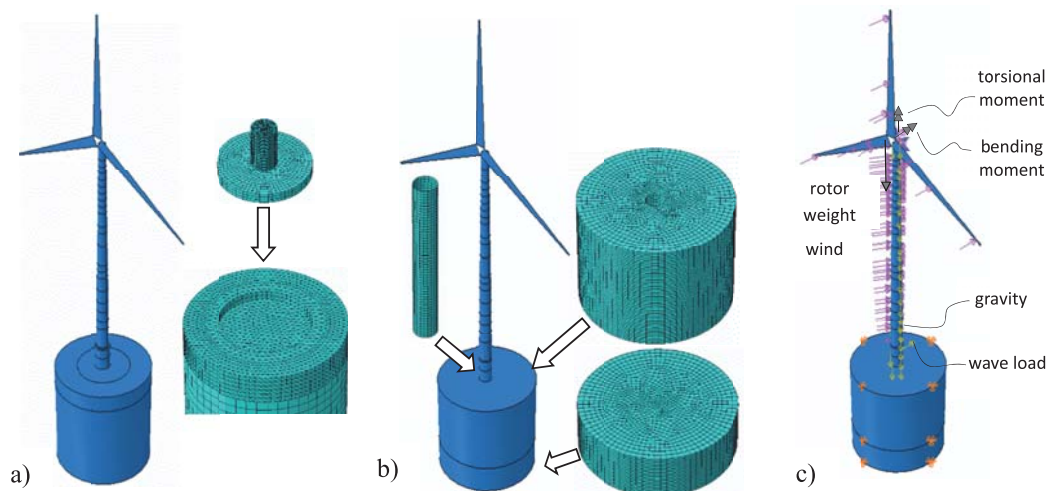


Fig. 3. Wind turbine tower resting on: a) gravity foundation, b) monopile foundation; c) loads applied on the OWT

where the constant  $U$  represents the maximal velocity at the bottom and  $\lambda$  is wavelength. The concrete column supporting the wind turbine tower was subjected to waves with a ratio between inertia and drag force amplitude of 9.8, causing a maximum horizontal wave force of 2793 kN whose vertical arm measured from the sea floor was 4.37 m. The forces caused by the blades and rotor were taken according to [31]: concentrated vertical force 1200 kN, torsional moment 215 kNm and bending moment 2733 kNm at the top of wind turbine tower.

Numerical static analysis was performed by means of a commercial program [1]. Both non-linear static (the arc-length method by Riks) and implicit dynamic (quasi-static) analysis was used.

In the numerical model of a tower set on a gravity foundation, 21756 four-node doubly curved thin or thick S4R shell elements with reduced integration were used to simulate the wind turbine tower, and 21492 eight-node hexahedral finite C3D8R elements with reduced integration were used for the fundament slab, concrete column and soil. The upper part of the soil was modelled with 37195 ten-node quadratic tetrahedral C3D10 elements. For the tower set on the monopile, 22428 S4R shell elements were used to simulate the wind turbine tower, and 59276 eight-node hexahedral C3D8R elements for the soil. The soil parameters were the same in the two models and the ground layers. The soil was divided into different zones in order to save the number of finite elements. The wind turbine rotor blades were modelled by an approximate method using shell S4R elements as a flat plate. The blades were included in the model to calculate the wind load only. The gravity of the blades was taken into account in the form of the concentrated force at the top of the tower. The rotor blades were eccentrically connected to the wind turbine tower by a rigid connection. The contact between the fundament or monopile and the soil was modelled with possible separation between the slab and the soil. The contact conditions between the fundament slab or monopile and the soil were controlled in the normal and tangential directions. The friction coefficient was 0.2. The current load and ice loading were omitted in the analysis performed.

## RESULTS OF NUMERICAL SIMULATIONS

### Wind turbine tower on a gravity foundation

In the case of the tower on a gravity foundation, the load was applied in two steps: in the first, the tower dead weight was applied; in the second, the remaining load as for example wind or wave loads. The results of the numerical analysis of the wind turbine tower are presented in Figs. 4–6. The static solution lost convergence in the second step at load level 0.817 that corresponded to a tower top displacement of 1.09 m. In this case, dynamic analysis was used. In the quasi-static implicit dynamic analysis, the dead weight was applied in 1 s and the wind, sea and turbine loads in 5 s. The displacement of the tower top increased to 1.39 m (Fig. 4b); the vertical displacement of the foundation slab was 5.4 cm for static and 7 cm for dynamic analysis (Fig. 5). The zone of separation of the foundation slab from the ground increased significantly. It expanded to the

reinforced concrete column (Fig. 5). The displacement of the top of the tower for different soil conditions was 0.96 m [26], while the vertical displacement of the fundament slab was 0.027 m. Geodetic monitoring of a similar wind turbine tower situated on the land on a square fundament slab (16 m × 16 m × 2 m) [31] showed maximum displacement of about 0.40 m for a measured wind speed of 10 m/s and predicted displacement of about 0.9 m for a wind speed of 24 m/s.

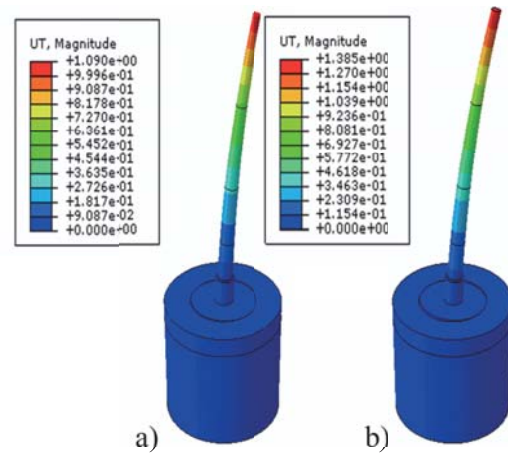


Fig. 4. Displacement of wind turbine tower on gravity foundation: a) non-linear static analysis for load factor 0.817, b) implicit dynamic analysis for load factor 1.0 (scale by factor 10 in m)

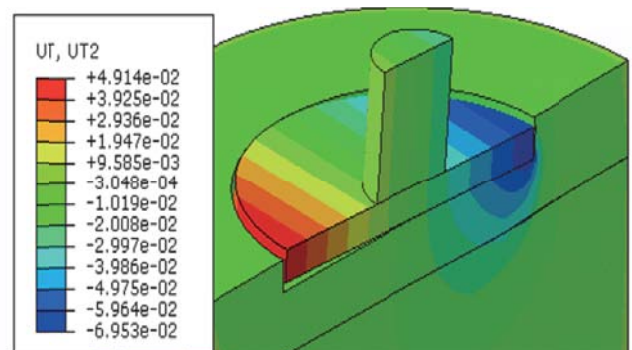


Fig. 5. Vertical displacement of wind turbine tower gravity foundation: implicit dynamic analysis for load factor 1.0 in m

Forces acting on the foundation, including loads exerted by wind and waves, caused maximal compression stress in the soil equal to 170–200 kPa (Fig. 6a). This effect caused a non-linear relation between the load and the displacement of the tower, resulting in less rotational stiffness of the foundation. The maximal von Mises stress in the steel tower equal to 125 MPa was calculated at the bottom of the steel tower (Fig. 6b).

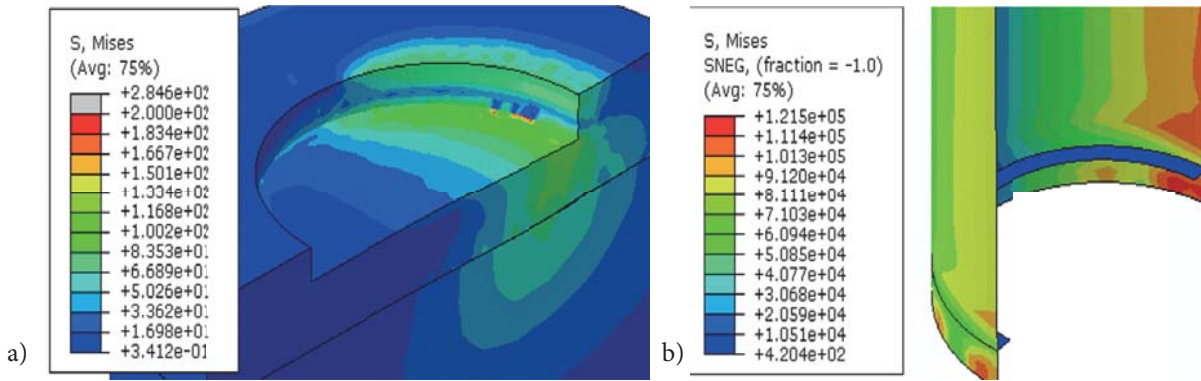


Fig. 6. Von Mises stress for wind turbine tower resting on gravity foundation in: a) soil, b) steel tower in kPa

### Wind turbine tower resting on a monopile

In the case of the tower resting on a monopile, the load was applied in one step. The computed results of the wind turbine tower numerical analysis are presented in Figs. 7 and 8. The static solution lost convergence at a load level of 0.387 that corresponded to tower top displacement of 0.60 m. In this case, dynamic analysis was used. In the quasi-static implicit dynamic analysis, all of the load was applied in 5 s. The displacement of the tower top increased to 2.49 m (Fig. 7a), while the displacement of the foundation slab was 0.21 m. A zone of separation of the monopile from the ground was observed. The displacements of the top of the tower were 1.8 times higher than for a gravity foundation.

Forces acting on the foundation, including loads exerted by wind and waves, caused maximal compression stress in the soil equal to 150 kPa (Fig. 8a). The maximal von Mises stress in the steel tower equal to 235 MPa was calculated at the bottom of the tower (Fig. 8b). Displacements of the top of a similar tower grounded on a monopile with different soil conditions for short-term cyclic loading in SLS were 0.764 m and for ULS were 1.608 m [19].

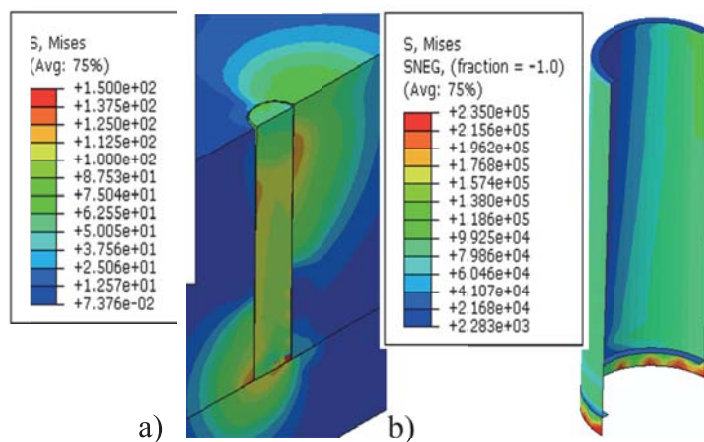


Fig. 8. Von Mises stress for wind turbine tower resting on monopile in: a) soil, b) steel tower in kPa

### CONCLUSIONS

Construction of OWTs seems to be one of the best ways of producing renewable energy. However, besides some technical problems or more expensive maintenance and service facilities, their main disadvantages are the costs of building. Thus, an optimization procedure for both the structure and foundation should be performed. Considering that the dimensions of turbines are still increasing, their proper analysis is particularly important. Foundations of OWTs are one of the most important and expensive parts of turbines; therefore, they require special treatment. The short review presented in this paper should provide some knowledge about the two basic types and direct further research.

Numerical analysis of wind turbine towers requires advanced and costly computational programs. The performed analysis leads to the conclusion that an approximate approach for wind towers may be carried out by FEM with Abaqus software [1]. The soil–structure interaction is a non-linear problem, thus obtaining a solution by static analysis could be difficult or even impossible due to the lack of convergence. In such a case, dynamic analysis

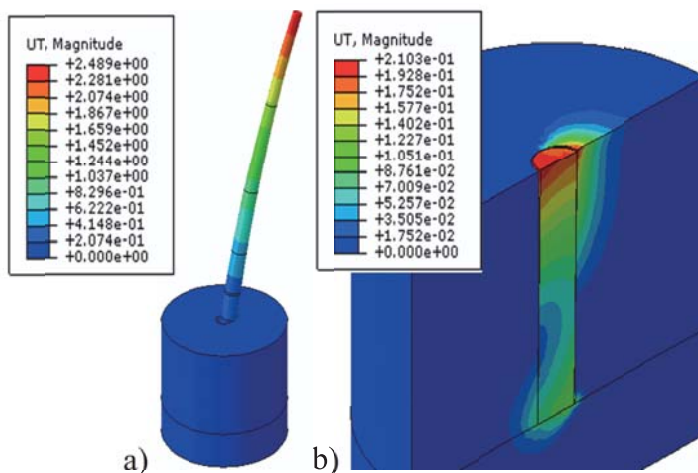


Fig. 7. Displacement of wind turbine tower resting on monopile for load factor 1.0: a) whole tower, b) anchorage in the ground in m

should be applied. In order to choose the best foundation type, first of all water depth and geotechnical site conditions should be considered. The detachment of a gravity foundation results in a reduction of foundation stiffness. In the case of a wind tower resting on a monopile, deformation of the soil at the top and bottom of the monopile also causes a decrease in foundation stiffness.

## REFERENCES

- Dassault Systèmes. (2008): *ABAQUS Theory Manual, Version 6.8*, Hibbit, Karlsson & Sorensen Inc.
- Achmus M., Abdel-Rahman K. (2005): *Finite element modelling of horizontally loaded monopile foundations for offshore wind energy converters in Germany*. In: Proceedings of the First International Symposium on Frontiers in Offshore Geotechnics (ISFOG), 391–396, doi: 10.1201/NOE0415390637.ch38
- Achmus M., Kuo Y., Abdel-Rahman K. (2009): *Behaviour of monopile foundations under cyclic lateral load*. Computers and Geotechnics, Vol. 36(5), 725–735.
- Arany L., Bhattacharya S., Macdonald J., Hogan S. J. (2017): *Design of monopiles for offshore wind turbines in 10 steps*. Soil Dynamics and Earthquake Engineering, Vol. 92, 126–152.
- Bhattacharya, S., Nikitas, G., Arany, L., Nikitas, N. (2017): *Soil-structure interactions for offshore wind turbines*. Engineering and Technology Reference, Vol. 1(1), 1–16. <http://digital-library.theiet.org>
- Byrne B. W., Houlsby G. T. (2003): *Foundations for offshore wind turbines*. Philosophical Transactions of the Royal Society of London Series A: Mathematical, Physical and Engineering Sciences, Vol. 361, 2909–2930.
- DNV (2010): *DNV-OS-J101 Design of Offshore Wind Turbine Structures*.
- EWEA (2013): *Deep Water—the Next Step for Offshore Wind Energy*. July 2013.
- EWEA (2009): *Pure Power: Wind Energy Targets for 2020 and 2030*. Technical Report of the European Wind Energy Association. URL <http://www.ewea.org/>.
- Gavin K. G., Igoe D. I., Doherty P. (2011): *Piles for offshore wind turbines: A state of the art review*. Proceedings of ICE Journal, Geotechnical Engineering, Vol. 164(4), 245–256.
- Haiderali A., Cilingir U., Madabhushi G. (2013): *Lateral and axial capacity of monopiles for offshore wind turbines*. Indian Geotechnical Journal, Vol. 43(3), 181–194, doi: 10.1007/s40098-013-0056-4
- Hansen N. M. (2012): *Interaction Between Seabed Soil and Offshore Wind Turbine Foundations*, PhD thesis, Department of Mechanical Engineering, Technical University of Denmark.
- Hearn E. E., Edgers L. (2010): *Finite element analysis of an offshore wind turbine monopile*. In: GeoFlorida 2010: Advances in Analysis, Modeling & Design (GPS 199), 1857–1865.
- Houlsby G., Ibsen L., Byrne B. (2005). *Suction caissons for wind turbines*. In: G. A. Cassidy (Ed.), Frontiers in Offshore Geotechnics: ISFOG 2005, pp. 75–93, Taylor and Francis Group, London.
- Jung S., Kim S.-R., Patil A., Hung L. C. (2015): *Effect of monopile foundation modeling on the structural response of a 5-MW offshore wind turbine tower*. Ocean Engineering, Vol. 109, 479–488.
- Kriegers Flak (2013): *Technical Project Description for the Large-Scale Offshore Wind Farm (600 MW) at Kriegers Flak*. Technical project description.
- LeBlanc C., Houlsby G. T., Byrne B. W. (2009): *Response of stiff piles in sand to long-term cyclic lateral loading*. Geotechnique, Vol. 60, 79–90.
- Lozano-Minguez E., Kolios A. J., Brennan F. P. (2011): *Multi-criteria assessment of offshore wind turbine support structures*. Renewable Energy, Vol. 36(11), 2831–2837.
- Maa H., Yanga J., Chen L. (2017): *Numerical analysis of the long-term performance of offshore wind turbines supported by monopiles*, Ocean Engineering, Vol. 136, 94–105.
- Madariaga A., Martinez de Alegria I., Martin J. L., Eguia P., Ceballos S. (2012): *Current facts about offshore wind farms*. Renewable and Sustainable Energy Reviews, Vol. 16(5), 3105–3116.
- Myszkowska A. (2014): *Fundamentowanie morskich farm wiatrowych. Doświadczenia z województwa zachodniopomorskiego*. Inżynieria Morska i Geotechnika, Vol. 3, 238–244.
- Niklas K. (2017): *Strength analysis of a large-size supporting structure for an offshore wind turbine*. Polish Maritime Research, Special Issue S1 (93), Vol. 24, 156–165.
- Oh K. Y., Namb W., Ryuc M. S., Kimc J. Y., Epureanu B. I. (2018): *A review of foundations of offshore wind energy convertors: Current status and future perspectives*. Renewable and Sustainable Energy Reviews, Vol. 88, 16–36.
- Petersen T. U. (2014): *Scour Around Offshore Wind Turbine Foundations*, PhD thesis, Department of Mechanical Engineering, Technical University of Denmark.

25. PN-77/B-02011. (1990): *Obciążenia w Obliczeniach Statycznych. Obciążenie Wiatrem*, PKN, Warszawa.
26. Przewłócki J., Iwicki P. (2016): *Some problems of supporting offshore wind turbines*. In: L. Małyszko, R. Tarczewski (eds.), XXII Lightweight Structures in Civil Engineering, pp. 71–76, Wydawnictwo UWM, Olsztyn.
27. Saleem Z. (2011): *Alternatives and modifications of monopile foundation or its installation technique for noise mitigation*. Report by Delft University of Technology for Stichting De Noordzee (the North Sea Foundation).
28. Scharff, R., Siems, M. (2013): *Monopile foundations for offshore wind turbines – solutions for greater water depths*. Steel Construction, Vol. 6(1), 47–53.
29. Tempel J., Diepeveen N. F. B., Salzmänn D. J., Vries W. E. (2010): *Design of support structures for offshore wind turbines*. WIT Transactions on State of the Art in Science and Engineering, Vol. 44, 559–591. [www.witpress.com](http://www.witpress.com)
30. Westgate, Z. J., DeJong J. T. (2005): *Geotechnical Considerations for Offshore Wind Turbines*, MTC-OWC.
31. Widerski T. (2013): *Pomiary i Prognozowanie Przemieszczeń Elektrowni Wiatrowych Metodami Geodezyjnymi*, PhD thesis, Department of Geodesy, Faculty of Civil and Environmental Engineering, Gdańsk University of Technology.

## CONTACT WITH THE AUTHORS

**Piotr Iwicki**

*e-mail: piwicki@pg.edu.pl*

Gdańsk University of Technology  
Narutowicza 11/12, 80-233 Gdańsk

**POLAND**

**Jarosław Przewłócki**

*e-mail: jprzew@pg.edu.pl*

Gdańsk University of Technology  
Narutowicza 11/12, 80-233 Gdańsk

**POLAND**

# FORCED MOTION CFD SIMULATION AND LOAD REFINEMENT EVALUATION OF FLOATING VERTICAL-AXIS TIDAL CURRENT TURBINES

**Wanchao Zhang**

Jiangsu University of Science and Technology, China

**Yujie Zhou**

Jiangsu University of Science and Technology, China

**Kai Wang**

Wuhan Second Ship Design & Research Institute, China

**Xiaoguo Zhou**

Jiangsu University of Science and Technology, China

## ABSTRACT

*Simulation of the hydrodynamic performance of a floating current turbine in a combined wave and flow environment is important. In this paper, ANSYS-CFX software is used to analyse the hydrodynamic performance of a vertical-axis turbine with various influence factors such as tip speed ratio, pitching frequency and amplitude. Time-varying curves for thrust and lateral forces are fitted with the least squares method; the added mass and damping coefficients are refined to analyse the influence of the former factors. The simulation results demonstrate that, compared with non-pitching and rotating turbines under constant inflow, the time-varying load of rotating turbines with pitching exhibits an additional fluctuation. The pitching motion of the turbine has a positive effect on the power output. The fluctuation amplitudes of thrust and lateral force envelope curves have a positive correlation with the frequency and amplitude of the pitching motion and tip speed ratio, which is harmful to the turbine's structural strength. The mean values of the forces are slightly affected by pitching frequencies and amplitudes, but positively proportional to the tip speed ratio of the turbine. Based upon the least squares method, the thrust and lateral force coefficients can be divided into three components, uniform load coefficient, added mass and damping coefficients, the middle one being significantly smaller than the other two. Damping force plays a more important role in the fluctuation of loads induced by pitching motion. These results can facilitate study of the motion response of floating vertical-axis tidal current turbine systems in waves.*

**Keywords:** vertical-axis tidal current turbine, hydrodynamic loads, pitching motion, added mass, damping coefficients

## INTRODUCTION

Traditional fossil fuels account for a major part of the world's energy consumption, but we will no longer use fossil fuels in the next few years, according to the current mining rates [17]. Therefore, more and more countries in the world have begun to develop clean and renewable energy sources, and as a kind of marine renewable energy, tidal current energy is gradually entering people's vision.

As the main development device of tidal current energy, tidal current turbines can be divided into vertical- and horizontal-axis turbines according to the relative location of the main shaft and flow direction [2]. Compared to a horizontal-axis turbine, a vertical-axis turbine has the

following characteristics: 1. the rotating direction is not affected by flow direction, and there is no yaw mechanism; 2. easy processing and low cost because of simple blade structure; 3. the power generation system and speed-increasing mechanism can be installed above the surface to reduce the difficulty of underwater sealing.

At present, the main theories used to study the hydrodynamics of vertical-axis turbines are flow tube theory, vortex theory, experimental and CFD (computational fluid dynamics) methods. Compared with the former two theories, the ability of CFD to capture more instantaneous flow field information is the biggest advantage. Experiments are not massively used because of their high expenditure. Furthermore, a full-scale model can be simulated by

using CFD. Taking these advantages into consideration, currently CFD is extensively employed in research concerning vertical-axis tidal current turbines [13, 17].

Over the past several decades, vertical-axis tidal current turbines rotating with a fixed upright axis have been the main research subjects, and a mass of research achievements has been captured. Li and Calisal [8, 9] examined the influence of the incoming flow angle, relative distance and rotating direction on the power output and torque fluctuation by modelling twin-turbine systems in 2009–2010. The results showed that the total power output of a twin-turbine system with optimal layout can be about 25% higher than two times that of a stand-alone turbine, and when the co-rotating system is optimally configured, the downstream turbine should be partially in the wake of the upstream turbine. In 2011, Li [10] conducted a series of experiments with vertical-axis turbines to research the hydrodynamic influence of density, leaf number, pitch angle and chord length, and then compared the results with those from a numerical simulation to validate the reliability of CFD. It showed that the SST turbulence model can provide higher computational accuracy, and the grid has little influence when  $Y^+ \leq 2$ . His research also proved that fixed pitch angle turbines are poor at self-starting, but free variable pitch angle turbines can self-start quickly and have higher energy utilization. In 2014, Li et al. [4] developed a hybrid approach that combines a discrete vortex method with a finite element method that can simulate the integrated hydrodynamic and structural response of a vertical-axis turbine. They discovered that the optimization of a three-blade vertical-axis turbine design using the hybrid method yielded a turbine H/R ratio of about 3.0 for reliable maximum power output.

In summary, these researches mentioned above are on vertical-axis turbines revolving around a fixed upright axis. In fact, the floating platform of the floating tidal current power station will undergo six degrees of freedom motion induced by waves, and the axis of turbines will be skewed to the incoming flow. Recently, little research on wave-induced motions about vertical-axis tidal current turbines has been done. However, horizontal-axis tidal turbines can offer us a series of predeterminations and experiences. In 2010, Galloway et al. [3] conducted experimental research on three-blade horizontal-axis tidal turbines in regular waves and deep water (wave height = 0.08 m, inflow velocity = 1.5 m/s); the results showed that the mean parameters (thrust and torque) are the same with or without waves, but the transient values were highly influenced by waves: the fluctuation of thrust increased by 37% and torque reached up to 35%. The analogy analysis method can also be used to predict the change regulation of vertical-axis turbine parameters in waves. In fact, vertical-axis turbines will move with the platform, and then the velocity distribution around the turbine also alters with different distributions of wave height and frequency. Therefore, as with a horizontal-axis tidal turbine, the load and torque of the turbine must also fluctuate greatly.

Study of vertical-axis wind turbine rotated in oblique flow or tilted conditions can provide some creative proposals for

the study of vertical-axis tidal current turbines. In 2016, Chowdhury et al. [1] carried out a numerical validation of an existing experimental work on vertical axis wind turbines (VAWT) in upright and tilted conditions. The numerical validation was accomplished by means of CFD analysis; mesh dependency analysis and optimum time step were also conducted. The results showed that the result obtained from SST k- $\omega$  was closest to the experimental one and a VAWT in the tilted condition produces greater torque downwind in comparison to an upright one. The wake of a tilted-axis turbine would proceed downstream in a tilted manner. As a result, the wake of a tilted turbine would be shifted downward. In 2011, the vorticity transport model was used to simulate aerodynamic performance and wake dynamics by Scheurich and Brown [14]. The results partly confirmed previous experimental measurements and suggested that a straight-bladed vertical-axis wind turbine operated in oblique flow might produce a higher power coefficient than when it is operated in normal flow. This is because oblique flow skews the convection of the wake, which allows a significant portion of the blade to operate. In such a case, over its entire azimuth in a flow region, the influence of the wake is significantly reduced compared to the situation in normal flow. VAWT and tidal current turbines have almost the same operating principles. Therefore, studying VAWT in tilted flow conditions can provide constructive comments on the research on tidal current turbines rotating around a skewed axis. Later in 2017, Zhang et al. [20] established a 3-D calculation model in the CFD software and evaluated the effect of extension length on the hydrodynamic loads and the wake field. In 2018, Li et al. [6] further explored a vertical-axis tidal turbine array with a single blade and studied the phenomenon of hydrodynamic interference of the tidal turbine array based upon their former proposed unsteady boundary element model [5]. Later they further explored the effect of the configuration parameters on the vertical-axis tidal turbine and obtained the hydrodynamic loads characteristics [7]. Tomporowski [16] designed a floating and innovative water turbine to convert the mechanical energy to electrical energy and analyzed the effect of geometrical and dynamic features on the pressures, forces and torques.

However, most of the current research on turbines focuses on the conversion efficiency of the turbine under environmental conditions such as different velocity or deflection angle, and there are few reports on load refinement evaluation of turbines in additional wave environments. Especially when the coupling model of the turbine and the floating platform is placed in a wave and current environment, research on its complex motion and hydrodynamic characteristics is worthy of attention. In fact, a tidal power station in practical application is often accompanied by the action of waves. Therefore, it is very important for the design, construction and application of tidal power stations to simulate the motion of a tidal power station in a complex marine environment based on current software functions. This paper studied the hydrodynamic performance of a vertical-axis turbine with compulsorily

pitching motion under the steady inflow condition using ANSYS-CFX. The axis of a vertical-axis tidal current turbine is assumed to stay in the tilted condition during pitching motion in waves. A series of simulated working conditions with several tip speed ratios, frequencies and amplitudes was conducted. The time-varying hydrodynamics curves for thrust and lateral forces were measured, and fitted to get the added mass and damping coefficients by using the least squares fitting method. This research can provide vital data for research on wave-induced responses of floating support structures for tidal current turbines.

## NUMERICAL SIMULATIONS

### BASIC THEORIES

The incoming flow velocity of the turbines is represented as  $V$ , the diameter of the turbine as  $D$ , the number of blades as  $Z$  and the rotational speed of the turbine as  $\omega$ ; the positive direction of the X-axis is the inflow direction. The relative parameters which will be employed in the following text are given in Table 1.  $C_{FX}$ ,  $C_{FY}$  and  $C_p$  are essential indices for assessing the hydrodynamic performance of a turbine.

Tab. 1. Nomenclature for turbines

Symbol	Explanation	Symbol	Explanation
$V$	Incoming flowing velocity	$F_x$	Thrust of turbine
$D$	Diameter of turbine	$F_y$	Lateral force of turbine
$Z$	Number of blades	$\lambda$	Tip speed ratio
$\omega$	Angular velocity of turbine	$Q$	Torque of turbine
$\theta$	Blade azimuth angle	$H$	Blade length
$\omega'$	Pitching angular velocity	$\xi$	Pitching angle
$A$	Pitching amplitude	$R'$	Length of pitching arm
$C$	Chord length	$\omega_z$	Pitching frequencies

The following dimensionless parameters are defined by

Tip speed ratio:

$$\lambda = R\omega/V \quad (1)$$

Thrust coefficient:

$$C_{FX} = F_x / (0.5\rho V^2 DH) \quad (2)$$

Lateral force coefficient:

$$C_{FY} = F_y / (0.5\rho V^2 DH) \quad (3)$$

Power coefficient:

$$C_p = Q\omega / (0.5\rho V^3 DH) \quad (4)$$

Dimensionless angular velocity of pitching motion:

$$\bar{\omega}' = \omega'R'/V \quad (5)$$

Dimensionless angular acceleration of pitching motion:

$$\bar{a}' = (\partial_t \omega)' R'^2 / V^2 \quad (6)$$

Pitching angle:

$$\xi = A \sin(\omega_z t) \quad (7)$$

According to the motion response of the floating structure and the symbolic characterization of physical quantities such as displacement, velocity and acceleration in waves, the coefficients of thrust and lateral forces can be divided into three components: the homogeneous hydrodynamic term, the damping term and the added mass term, respectively.

$$C_{FX} = C_x^0 + n_{xx} \bar{\omega}' + m_{xx} \bar{a}' \quad (8)$$

$$C_{FY} = C_y^0 + n_{yy} \bar{\omega}' + m_{yy} \bar{a}'$$

$$\bar{\omega}' = \frac{\omega'R'}{V} = \frac{\partial_t \xi R'}{V} = \frac{A\omega_z \cos(\omega_z t) R'}{V} \quad (9)$$

$$\bar{a}' = \frac{(\partial_t \omega)' R'^2}{V^2} = \frac{\partial_t^2 \xi R'^2}{V^2} = \frac{-A\omega_z^2 \sin(\omega_z t) R'^2}{V^2}$$

The damping and added mass terms are functions of  $\theta$  (blade azimuth angle), which can be developed into triangular series functions as follows:

$$\begin{aligned} n_{xx} &= \frac{\delta C_{FX}}{\delta \bar{\omega}'} = n_{xx}^0 + \sum_{k=1}^{\infty} n_{xx}^k \sin(kz\theta(t) + \psi_{\omega'_x}^k) \\ n_{yy} &= \frac{\delta C_{FY}}{\delta \bar{\omega}'} = n_{yy}^0 + \sum_{k=1}^{\infty} n_{yy}^k \sin(kz\theta(t) + \psi_{\omega'_y}^k) \\ m_{xx} &= \frac{\delta C_{FX}}{\delta \bar{a}'} = m_{xx}^0 + \sum_{k=1}^{\infty} m_{xx}^k \sin(kz\theta(t) + \psi_{a'_x}^k) \\ m_{yy} &= \frac{\delta C_{FY}}{\delta \bar{a}'} = m_{yy}^0 + \sum_{k=1}^{\infty} m_{yy}^k \sin(kz\theta(t) + \psi_{a'_y}^k) \end{aligned} \quad (10)$$

Finally, the thrust and lateral force coefficients are expressed as follows:

$$\begin{aligned} C_{FX} &= C_x^0 + n_{xx} \bar{\omega}' + m_{xx} \bar{a}' \\ &= C_x^0 + \sum_{k=1}^{\infty} C_{xx}^k \sin(kz\theta(t) + \psi_{\omega'_x}^k) + \left\{ n_{xx}^0 + \sum_{k=1}^{\infty} [n_{xx}^k \sin(kz\theta(t) + \psi_{\omega'_x}^k)] \right\} \bar{\omega}' + \left\{ m_{xx}^0 + \sum_{k=1}^{\infty} [m_{xx}^k \sin(kz\theta(t) + \psi_{a'_x}^k)] \right\} \bar{a}' \\ C_{FY} &= C_y^0 + n_{yy} \bar{\omega}' + m_{yy} \bar{a}' \\ &= C_y^0 + \sum_{k=1}^{\infty} C_{yy}^k \sin(kz\theta(t) + \psi_{\omega'_y}^k) + \left\{ n_{yy}^0 + \sum_{k=1}^{\infty} [n_{yy}^k \sin(kz\theta(t) + \psi_{\omega'_y}^k)] \right\} \bar{\omega}' + \left\{ m_{yy}^0 + \sum_{k=1}^{\infty} [m_{yy}^k \sin(kz\theta(t) + \psi_{a'_y}^k)] \right\} \bar{a}' \end{aligned} \quad (11)$$

The time-varying curves for thrust and lateral force coefficients can be obtained by CFD. And then, by using the least squares method, the load coefficients for the homogeneous hydrodynamic, damping and added mass terms can also be obtained. ANSYS-CFX software can simulate small scale turbines and obtain relatively accurate calculation results. Because this paper mainly through the calculation of forced motion of the turbine load, and on this basis, combined with the theory of floating body in waves, the load of the turbine is decomposed and the hydrodynamic coefficients of different orders can be obtained, which can be

coupled with the floating platform analysis. In such a case, the fittings according to different geometrical and environmental parameters, as well as the accuracy of the decomposition, have a great effect on the reliability of the obtained hydrodynamic coefficients. However, the least squares method is widely applied in curve fitting and is accurate enough. Therefore, the methodology adopted in this paper included the least squares method and CFD simulation for better robustness, and is applicable to turbines of different sizes.

## CFD SIMULATION

The two-bladed vertical-axis turbine used in this simulation model was developed by Harbin Engineering University (HEU). Table 2 shows the detailed particulars of the HEU turbine model. A series of experiments was conducted in the circulating water tunnel laboratory of HEU. The two-bladed turbine is installed on a test platform, which is installed in the circulating water tunnel working segment (8 m × 1.7 m × 1.5 m). By changing the velocity, the hydrodynamic performance of the turbine can be studied under different work conditions, which can be tested for a long time (see. Fig. 1).

Tab. 2. Particulars of turbine model

Item	Symbol	Data	Unit
Diameter of turbine	D	0.8	m
Velocity	V	1.0	m/s
Blade length	H	0.6	m
Chord	C	0.12	m
Blade airfoil	NACA0018		
Number of blades	Z	2	

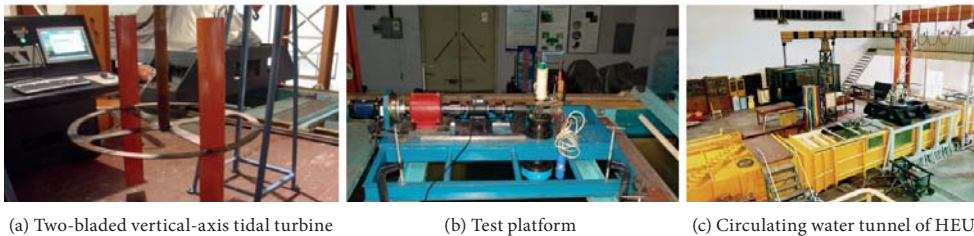


Fig. 1. Experimental facilities and test site

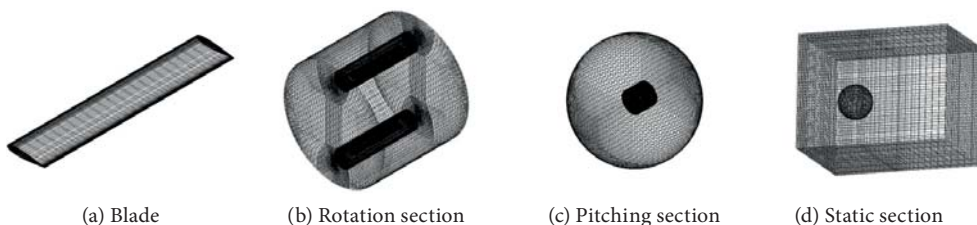


Fig. 2. Grid model

Before using the CFD method to simulate the hydrodynamic performance of a turbine, the most significant work is to discretize the simulated area, namely by grid partitioning. For

all CFD numerical simulations, the storage of structured grids can be recorded by a computer multidimensional array, and the simulation's precision and speed are significantly superior to those of unstructured grids. Therefore, structured grids are employed to divide the calculation domain of the turbine.

Fig. 2 shows the mesh grid models of the vertical-axis turbine. In order to fully simulate the vertical-axis turbine field characteristics, a sufficiently large computational domain needs to be established. The entire fluid domain employed in this paper is rectangular, with length  $25D$  and width  $40D$ . The calculation domain is divided into three sections, namely rotation, pitching and static sections. They are connected by sliding mesh interfaces. In such a case, grid deformation does not exist during the simulation, which can ensure grid quality and improve the calculation precision. Quadrilateral structured O grids are used in three sections because of their high quality in dividing grids around cambered models. A pitching motion ( $\xi = A \sin(\omega_z t)$ ) is applied to the rotation and pitching sections. Furthermore, rotary motion occurs concurrently around the centre of the rotation section, and the grids of the static section remain motionless.

The first layer of the turbine's surface meshes are defined as 0.00003m especially, which ensures  $Y^+ < 2$ . The total number of grids is 1200000, and the SST model is chosen to simulate the vertical-axis turbine. The SST model proposed by Menter [11] in 1994 combines the advantages of  $k - \epsilon$  and  $k - \omega$  models. It can also capture extreme pressures and velocity gradients in the vicinity of the turbine blades more accurately. It has been proven by many researchers, including Wang et al., Ponta and Dutt, and Shiono et al., that the SST model is more suitable for calculations of vertical-axis wind or water turbines [13, 15, 18]. Based on CFX software, the CEL code

is programmed. According to previous research experience, the boundary conditions are set as follows. The reference atmospheric pressure is established, and the inlet boundary is set as entry speed with  $V = 1.0$  m/s. The turbulence parameters and speeds are set simultaneously, and the outlet uses a pressure outlet boundary with a relative pressure of zero. The period during which the blade rotates  $1^\circ$  is adopted as the time step of the entire simulation, and the blades rotate around the Z axis.

## CFD SIMULATION VERIFICATION

The power coefficient of the turbine in constant inflow is illustrated in Fig. 3. The simulated and experimental values of power coefficients are in good accordance. The error between

the results may come from the influence of free surface and wall on the hydrodynamic characteristics of the turbine, which are not considered in the calculation. This comparison result demonstrates that the CFD simulation method for tidal current turbines has satisfactory accuracy.

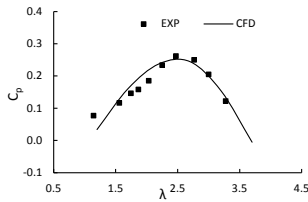


Fig. 3. Comparison of experimental and CFD simulation results

## SIMULATION RESULTS ANALYSIS

The time-varying curves for thrust and lateral forces under non-pitching motion with an incoming flow velocity  $V = 1$  m/s and optimal turbine speed ratio  $\lambda = 2.5$  are shown in Fig. 4(a) and (b), respectively. Fig. 4(c) and (d) illustrate the time-varying curves for thrust and lateral forces under pitching motion ( $A = 10^\circ$ ,  $W_z = 1.2$  rad/s) with the same velocity and turbine speed ratio. In the second condition, the turbine revolves around the fixed main axis in uniform flow. The upper and lower envelopes of Fig. 4(a) and (b) are approximately straight lines.

However, the envelopes under pitching motion in Fig. 4(c) and (d) exhibit obvious cyclical fluctuations because of an added pitching motion. The main axis of the turbine undergoes a pitching movement when the turbine revolves around the main axis. Therefore, an additional fluctuation to that induced by turbine rotation itself is observed in the thrust and lateral forces of the turbine. In this paper, we study the hydrodynamic performance of vertical-axis tidal current turbines under pitching motion with different speed ratios, pitching frequencies and amplitudes.

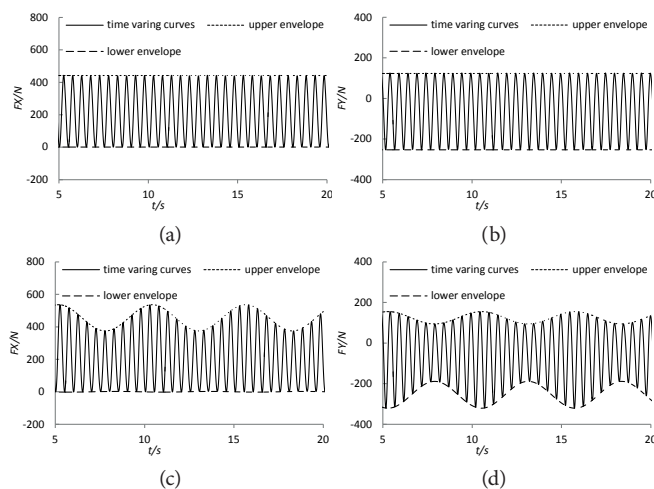


Fig. 4. Time-varying curves for thrust and lateral forces under pitching and non-pitching motion

## TIP SPEED RATIOS

The power coefficient is the most significant factor for the initial design of a turbine. Therefore, the power coefficients of turbines were first compared under pitching and non-pitching motion. Fig. 5(a) presents the differences in power coefficients for the two motions with different tip speed ratios. The power coefficients in the former motion are obviously higher than those in the latter one, especially at middle and high tip speed ratios. Compared with turbines under non-pitching motion, the fluid speed distribution around the turbine of pitching motion changed because the additional pitching motion changes the transient force and torque of the turbine. Therefore, the transient values of the power coefficient under pitching motion will be higher. Then we compared the blade tangential force between non-pitching and pitching motion. The transient values of blade tangential force reflect the power coefficient of turbines directly.

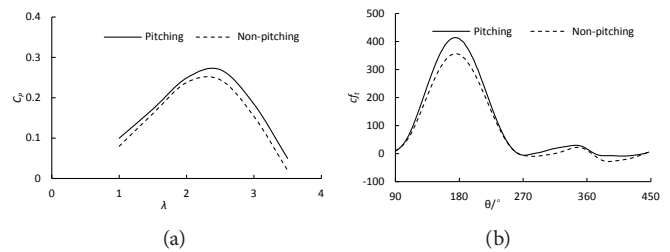


Fig. 5. Comparison of power coefficients and tangential force between non-pitching and pitching motion

As shown in Fig. 5(b), the power coefficient  $cf_t$  of pitching motion is obviously higher than that of non-pitching motion at a blade azimuth angle approximately from  $120^\circ$  to  $200^\circ$ . The upstream disk is the main work area for the turbine because the downstream values are almost zero. In consequence, the power coefficient under pitching motion is higher than that under non-pitching motion.

The thrust and lateral force envelope curves under pitching motion with five different tip speed ratios ( $\lambda = 1.5, 2.0, 2.5, 3.0, 3.5$ ) are also considered in this study. The envelope curves for thrust and lateral forces on the turbine should be stable if the pitching motion is not taken into consideration. The pitching frequency is set as 1.2 rad/s, and the amplitude is  $10^\circ$ . Fig. 6 shows the upper and lower envelope thrust curves in panels (a) and (b) and the lateral force in panels (c) and (d). The envelope curves for thrust and lateral forces under pitching motion fluctuate obviously. As the tip speed ratio increases, the upper envelope curves for thrust and lateral forces increase obviously. On the contrary, the lower envelope curves decrease with a rising tip speed ratio. The oscillation of thrust and lateral force of turbines under pitching motion impedes the stability of the output electricity and the security of the structure.

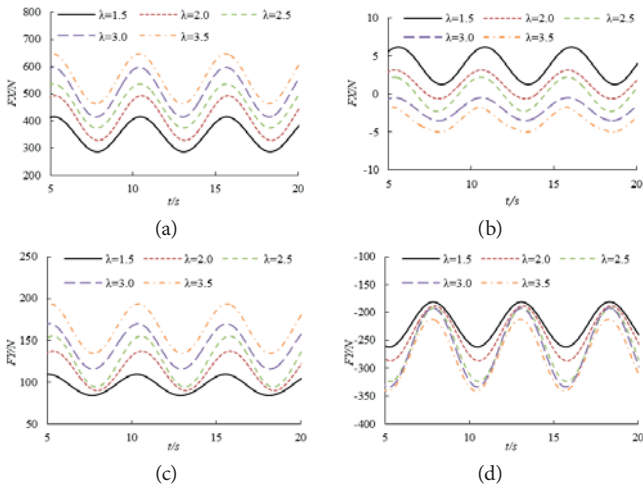


Fig. 6. Envelope curves for thrust and lateral forces of pitching motion under different tip speed ratios

The fluctuation amplitudes are defined by  $\widehat{FX} = FX_{\max} - FX_{\min}$  and  $\widehat{FY} = FY_{\max} - FY_{\min}$ . Fig. 7 shows the fluctuation amplitudes of thrust and lateral forces with different tip speed ratios. It is shown that the fluctuation amplitudes increase gradually with increasing tip speed ratios. The fluctuation amplitude under pitching motion is obviously higher than that under non-pitching motion with the same tip speed ratio. When the tip speed ratio is 2.5, the thrust fluctuation amplitude under pitching motion can be up to 29% larger than that under non-pitching motion, with a 28% increase for lateral force. Therefore, when the turbine works in waves and current, the structure should be strengthened because there will be pitching motion.

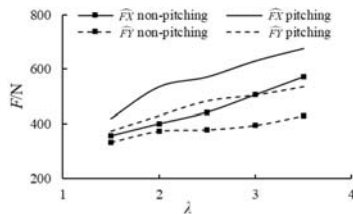


Fig. 7. Comparison of fluctuation amplitude under different tip speed ratios

## PITCHING FREQUENCIES

The pitching frequencies of the turbine are related to wave frequencies. Therefore, the pitching frequencies were selected as 0.4, 0.8, 1.2, 1.6, and 2.0 rad/s, respectively. The tip speed ratio of the turbine was set as 2.5 and the pitching amplitude is  $10^\circ$ .

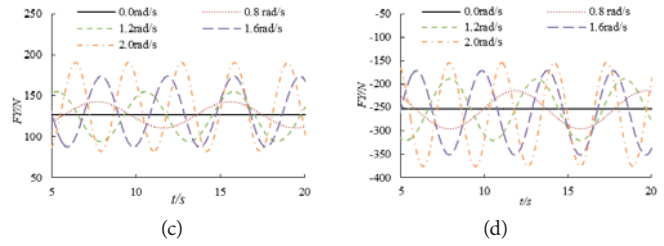
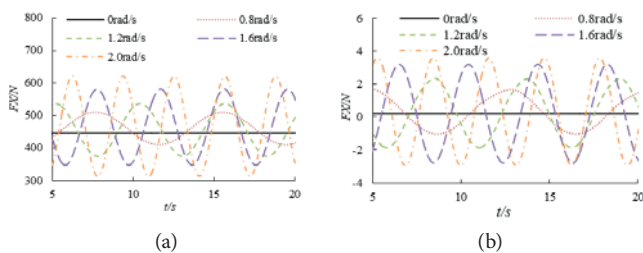


Fig. 8. Envelope curves for thrust and lateral forces of pitching motion with different frequencies

Fig. 8 shows how the envelope curves for thrust and lateral forces under different pitching frequencies change with time. In the following figures, the graphic legends represent the pitching frequencies and 0 rad/s means non-pitching. The upper and lower envelope curves for thrust are shown in subgraphs (a) and (b) and those for lateral force in subgraphs (c) and (d), respectively.

When the turbine works in waves, the load envelope curves fluctuate, with the envelope curves for a non-pitching load as the baseline. The upper envelope curves' fluctuation amplitude of thrust is obviously higher than that of the lower envelope curves, and the lateral force of the envelope curves fluctuates with almost same the order of magnitude. According to the graphs, as the pitch frequency increases, their fluctuation amplitudes rise while their periods decrease. For example, when the pitching frequency is 2.0, the fluctuation amplitude of the lateral force's upper envelope curve can be as large as 85.1% of the non-pitching value and 87.6% for the lower envelope curve. The pitching motion changes the fluid speed distribution around the turbine, which links to the transient force and torque of the turbine. Therefore, the loads on the turbine oscillate with high frequency and large amplitude when high-frequency waves occur, and the turbine structure should be strengthened in high-frequency waves.

The mean values and fluctuation amplitudes are defined by

$$\overline{FX} = \int_{t_1}^{t_2} FX dt / (t_2 - t_1), \widehat{FX} = FX_{\max} - FX_{\min}, \overline{FY} = \int_{t_1}^{t_2} FY dt / (t_2 - t_1)$$

and  $\widehat{FY} = FY_{\max} - FY_{\min}$ . The mean values and fluctuation amplitudes of thrust and lateral forces under the designed working conditions (incoming speed 1.0 m/s, tip speed ratio 2.5 and amplitude  $10^\circ$ ) are shown in Table 3. We can conclude that the mean values have minimal influence with increasing pitching frequencies and that the fluctuation amplitudes increase gradually. For example, when the pitching frequency is 2.0 rad/s, the fluctuation amplitude of thrust force can be up to 41.3% higher than that in non-pitching motion, with a 71.3% increase for lateral force.

Tab. 3. Comparison of average values and fluctuation amplitudes

$\omega_z$	$\overline{FX}$	$\widehat{FX}$	$\overline{FY}$	$\widehat{FY}$
0	218.37	442.19	-51.90	378.43
0.4	221.69	510.97	-48.57	400.87
0.8	220.64	522.97	-49.78	447.93
1.2	218.35	572.20	-51.03	508.98
1.6	222.82	614.55	-51.36	585.89
2.0	223.08	624.81	-51.04	648.46

## PITCHING AMPLITUDES

The calculation results with a tip speed ratio of 2.5 and pitching frequency of 1.2 rad/s considering different pitching amplitudes ( $0^\circ$ ,  $5^\circ$ ,  $10^\circ$  and  $15^\circ$ ) are shown in Fig. 9. Here,  $0^\circ$  means no pitching motion occurs. Similarly, the envelope curves for hydrodynamic loads fluctuate with the baseline defined by the envelope curves for non-pitching loads, when the turbine pitches in waves. When the pitching amplitude increases, the amplitudes of envelope curves increase, while their mean values remain stable. Increasing pitching amplitude has a negative impact on structural security. It also adds difficulty to the control of electricity output because of the fluctuation induced by the pitching motion.

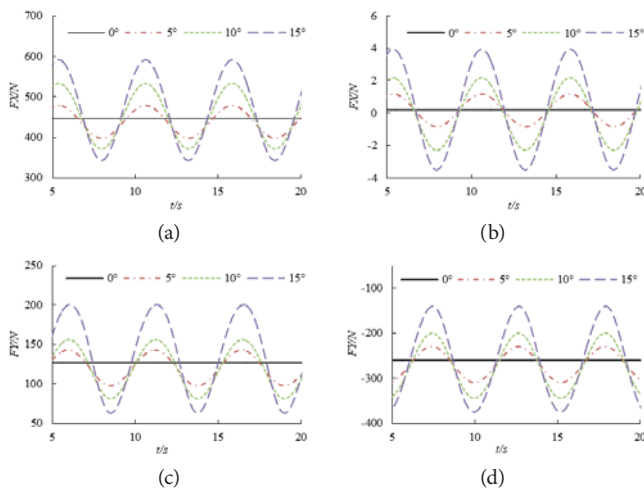


Fig. 9. Envelope curves for thrust and lateral force for pitching motion under different amplitudes

## FITTING RESULTS ANALYSIS

Time-varying curves with different tip speed ratios, pitching frequencies and amplitudes were obtained by CFD simulation. Based on the former simulation results, using the least squares method, the added mass and damping coefficients can be obtained. The fitting and CFD simulation results for a given condition ( $V_A = 1.0 \text{ m/s}$ ,  $\lambda = 2.5$ ,  $\omega_Z = 1.2 \text{ rad/s}$ ,  $A = 10^\circ$ ) are shown in Fig. 10. Obviously, the CFD simulation results can be perfectly fitted by using the least squares method.

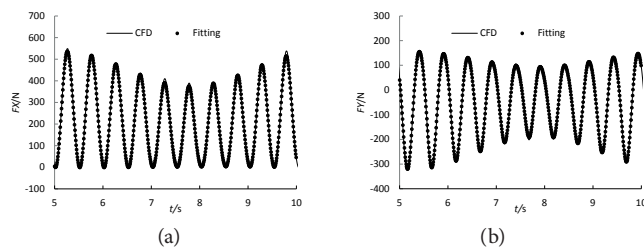


Fig. 10 Comparison between fitting and CFD results

## TIP SPEED RATIO

Coefficients of  $C_{FX}$  and  $C_{FY}$  series were obtained by fitting the time-varying curves for thrust and lateral forces with different tip speed ratios. Table 4 shows the coefficients for the constant terms and first-order terms of  $C_{FX}$  and  $C_{FY}$ .

Tab. 4(a).  $C_{FX}$  expansion coefficients under different tip speed ratios

$\lambda$	$C_{xx}^0$	$C_{xx}^1$	$\psi_{xx}^1$	$n_{xx}^0$	$n_{xx}^1$	$\psi_{\omega'x}^1$	$m_{xx}^0$	$m_{xx}^1$	$\psi_{a'x}^1$
1.5	0.688	0.711	-80.235	0.905	0.930	-78.198	-0.011	0.074	-130.239
2.0	0.839	0.858	-80.783	1.296	1.357	-86.297	-0.017	0.090	120.862
2.5	0.915	0.946	-82.431	1.485	1.366	-76.936	-0.024	0.122	-122.325
3.0	0.980	1.050	-85.127	1.679	1.481	-83.093	-0.064	0.150	-75.114
3.5	1.033	1.157	-86.128	1.696	1.520	-89.522	-0.073	0.178	-60.948

Tab. 4(b).  $C_{FY}$  expansion coefficients under different tip speed ratios

$\lambda$	$C_{yy}^0$	$C_{yy}^1$	$\psi_{yy}^1$	$n_{yy}^0$	$n_{yy}^1$	$\psi_{\omega'y}^1$	$m_{yy}^0$	$m_{yy}^1$	$\psi_{a'y}^1$
1.5	-0.196	0.69	177.91	-0.44	1.57	-150.11	0.01	0.16	102.94
2.0	-0.198	0.75	171.67	-0.45	1.61	164.48	-0.01	0.19	-27.09
2.5	-0.204	0.79	173.98	-0.47	1.62	169.51	-0.02	0.20	-35.23
3.0	-0.207	0.81	175.37	-0.49	1.65	164.07	-0.04	0.24	-121.85
3.5	-0.209	0.83	178.62	-0.51	1.67	166.57	-0.07	0.25	-151.98

It is concluded from Table 4(a) that with an increase of tip speed ratio, the absolute values of constant terms and first-order terms for homogeneous hydrodynamic, damping and added mass coefficients increase obviously. However, compared with the values for damping coefficients, added mass coefficients are significantly lower. Table 4(b) shows similar changing trends for the constant terms and first-order terms for the coefficients. Therefore, the time-varying oscillations of  $C_{FX}$  and  $C_{FY}$  induced by pitching motion are mainly attributed to the damping terms, and their fluctuation amplitude increases with an increase in tip speed ratio.

## PITCHING FREQUENCIES

Series coefficients of  $C_{FX}$  and  $C_{FY}$  are obtained by fitting the time-varying curves for thrust and lateral forces with different pitching frequencies; their constant and first-order terms are shown in Table 5.

Tab. 5(a).  $C_{FX}$  expansion coefficients under different frequencies

$\omega_Z$	$C_{xx}^0$	$C_{xx}^1$	$\psi_{xx}^1$	$n_{xx}^0$	$n_{xx}^1$	$\psi_{\omega'x}^1$	$m_{xx}^0$	$m_{xx}^1$	$\psi_{a'x}^1$
0.40	0.914	0.951	-83.544	1.348	1.207	-83.125	-0.039	0.125	91.337
0.80	0.913	0.954	-83.027	1.356	1.272	-74.697	-0.090	0.152	-117.685
1.20	0.915	0.946	-82.431	1.485	1.366	-76.936	-0.024	0.122	-122.325
1.60	0.913	0.946	-82.296	1.530	1.460	-76.942	-0.063	0.223	-102.953
2.00	0.911	0.952	-82.163	1.543	1.539	-76.812	-0.010	0.122	-98.097

Tab. 5(b).  $C_{FY}$  expansion coefficients under different frequencies

$\omega_Z$	$C_{yy}^0$	$C_{yy}^1$	$\psi_{yy}^1$	$n_{yy}^0$	$n_{yy}^1$	$\psi_{\omega'y}^1$	$m_{yy}^0$	$m_{yy}^1$	$\psi_{a'y}^1$
0.40	-0.203	0.79	174.29	-0.57	1.93	-175.39	-0.07	0.23	23.75
0.80	-0.209	0.79	173.77	-0.51	1.72	170.65	-0.06	0.11	-102.94
1.20	-0.204	0.79	173.98	-0.47	1.62	169.51	-0.02	0.20	-35.23
1.60	-0.204	0.81	174.01	-0.43	1.58	168.36	-0.02	0.19	-58.02
2.00	-0.202	0.80	173.72	-0.40	1.56	168.10	-0.06	0.23	-54.01

## CONCLUSIONS

Table 5(a) and (b) show that the fitting homogeneous hydrodynamic expansion coefficients ( $C_{xx}^0$ ,  $C_{xx}^1$ ,  $C_{yy}^0$  and  $C_{yy}^1$ ) of the turbine's thrust and lateral forces are not related to the acceleration and velocity of the pitching motion. The constant and first-order terms of the homogeneous hydrodynamic coefficient will remain stable with the growth of pitching frequencies. When the frequencies increase, the constant and first-order terms of damping coefficients in Table 5(a) will increase obviously and the corresponding terms (absolute values) of damping coefficients in Table 5(b) oppositely decrease. The tables also show that the added mass coefficient is one order of magnitude lower than the homogeneous hydrodynamic and damping coefficients. Therefore, the main factors that induce the time-varying fluctuation of  $C_{FX}$  and  $C_{FY}$  under pitching motion are the damping terms.

### PITCHING AMPLITUDES

Similarly, by fitting the time-varying curves for the thrust and lateral forces with different pitching amplitudes, the series coefficients of  $C_{FX}$  and  $C_{FY}$  are obtained. Their constant and first-order terms are shown in Table 6.

Tab. 6(a). CFX expansion coefficients under different amplitudes

A	$C_{xx}^0$	$C_{xx}^1$	$\psi_{xx}^1$	$n_{xx}^0$	$n_{xx}^1$	$\psi_{a'x}^1$	$m_{xx}^0$	$m_{xx}^1$	$\psi_{a'x}^1$
5	0.917	0.949	-82.628	1.478	1.347	-78.487	-0.028	0.121	123.312
10	0.915	0.946	-82.431	1.485	1.366	-76.936	-0.024	0.122	-122.325
15	0.919	0.945	-82.052	1.498	1.403	-76.768	-0.029	0.125	122.225

Tab. 6(b). CFY expansion coefficients under different amplitudes

A	$C_{yy}^0$	$C_{yy}^1$	$\psi_{yy}^1$	$n_{yy}^0$	$n_{yy}^1$	$\psi_{a'y}^1$	$m_{yy}^0$	$m_{yy}^1$	$\psi_{a'y}^1$
5	-0.205	0.788	172.691	-0.480	1.632	169.267	0.01	0.21	45.761
10	-0.204	0.791	173.98	-0.470	1.621	169.51	-0.02	0.20	-35.23
15	-0.201	0.801	174.838	-0.434	1.617	166.230	-0.01	0.23	42.092

As seen from Table 6, the main conclusions for different amplitudes are similar to the conclusions given in the section 'CFD SIMULATION'. As the pitching amplitude increases, the constant and first-order terms of the homogeneous hydrodynamic coefficients remain stable. The absolute values of constant and first-order terms for damping coefficients in Table 6(a) increase with the growth of amplitudes, but the absolute values of the corresponding terms for damping coefficients in Table 6(b) decrease significantly. What is more, the constant and first-order terms for added mass in the two tables are lower by an order of magnitude. Therefore, the fluctuation induced by pitching motion under different amplitudes is mainly concerned with the damping coefficient.

Floating vertical-axis tidal current turbines undergo motion in six degrees of freedom induced by waves and currents. Pitching motion only belongs to one of the six degrees of freedom. The methodology of this paper including the least squares method and CFD simulation can also be used to calculate the hydrodynamic performance for other freedoms of motion, such as sway and surge. This will be the key points of our study in the future. The main content of this paper is to calculate the added mass and damping coefficients for a turbine caused by waves. In such a case, by introducing these results, it is possible to conduct coupled dynamic analysis between the floating platform, mooring system and tidal current turbines in time and frequency domains.

The pitching motions of vertical-axis tidal current turbines under different tip speed ratios, frequencies and amplitudes were simulated by CFX software, and then the least squares fitting method was used to fit time-varying curves and obtain added mass and damping coefficients. The study demonstrates that:

(1) The fluctuation of a vertical-axis turbine induced by waves and currents cannot be neglected during the design stage, because it can cause the fluctuation of thrust and lateral forces. The fluctuation amplitudes of thrust and lateral forces have a positive correlation with pitching tip speed ratios, frequencies and amplitudes. At a high pitching frequency such as 2.0 rad/s, the fluctuation amplitude of the thrust force can be up to 41.3% higher than that under non-pitching motion, with a 71.3% increase for lateral force. Therefore, the fluctuation induced by waves and currents will have obvious negative impacts on the turbine's structural security, and turbines under pitching motion require a greater structural strength to extend the turbine's fatigue life.

(2) Compared with turbines under non-pitching motion, the pitching motion induced by waves and currents has a positive effect on the power output of turbines, which will increase the tangential force of blades during the upstream disk.

(3) The mean values of thrust and lateral forces are marginally affected by pitching frequencies and pitching amplitudes. However, increasing tip speed ratio has a positive effect on the average (absolute values) thrust and lateral forces.

(4) The thrust and lateral forces of the turbine are analysed with the least squares method. The damping coefficient plays a more important role than added mass in the fluctuation of loads induced by pitching motion. The constant and first-order terms of damping coefficients have a positive correlation with tip speed ratios, frequencies and amplitudes. These can provide some useful references for the motion response analysis (in time or frequency domain) of floating tidal current power stations.

## ACKNOWLEDGEMENTS

This paper is financially supported by the National Natural Science Foundation of China (No. 51909111) and the Natural Science Foundation of Jiangsu Province (No. BK20180980).

## REFERENCES

1. Chowdhury A. M., Akimoto H., Hara Y. (2016): *Comparative CFD analysis of vertical axis wind turbine in upright and tilted configuration*. *Renewable Energy*, Vol. 85(1), 327–337.
2. Dai J., Shan Z. D., Wang X. F. (2010): *Current research progress of water turbine*. *Renewable Energy*, Vol. 28(4), 130–133.
3. Galloway P. W., Myers L. E., Bahaj A. S. (2010): *Studies of a scale tidal turbine in close proximity to waves*. In: Third International Conference and Exhibition on Ocean Energy, Bilbao, Spain, 6–8 Oct, 2010.
4. Li B. Y., Karri N., Wang Q. (2014): *Three-dimensional numerical analysis on blade response of a vertical-axis tidal current turbine under operational conditions*. *Journal of Renewable and Sustainable Energy*, Vol. 6(4), 043123.
5. Li G. N., Chen Q. R., Gu H. B. (2018): *An unsteady boundary element model for hydrodynamic performance of a multi-blade vertical-axis tidal turbine*. *Water*, Vol. 10, 1413.
6. Li G. N., Chen Q. R., Gu H. B. (2018): *Study of hydrodynamic interference of vertical-axis tidal turbine array*. *Water*, Vol. 10, 1228.
7. Li G. N., Chen Q. R., et al. (2020): *Study on hydrodynamic configuration parameters of vertical-axis tidal turbine*. *Polish Maritime Research*, Vol. 27(1): 8–15.
8. Li Y., Calisal S. M. (2011): *Modeling of twin-turbine systems with vertical axis tidal current turbines: Part I—Power output*. *Ocean Engineering*, Vol. 37(7), 627–637.
9. Li Y., Calisal S. M. (2011): *Modeling of twin-turbine systems with vertical axis tidal current turbines: Part II—Torque fluctuation*. *Ocean Engineering*, Vol. 38(4), 550–558.
10. Li Z. C. (2011): *Numerical Simulation and Experimental Study on Hydrodynamic Characteristic of Vertical Axis Tidal Turbine*. Doctoral thesis, Harbin Engineering University, (in Chinese).
11. Menter F. R. (1994): *Two-equation eddy-viscosity turbulence models for engineering applications*. *AIAA Journal*, Vol. 32(8), 1598–1605.
12. Ponta F., Dutt G. S. (2000): *An improved vertical axis water current turbine incorporating a channeling device*. *Renewable Energy*, Vol. 20(2), 223–241.
13. Ponta F. L., Jacovkis P. M. (2011): *A vortex model for Darrieus turbine using finite element techniques*. *Renewable Energy*, Vol. 24(1), 1–18.
14. Scheurich, F., Brown, R. E. (2011): *Vertical-axis wind turbines in oblique flow: sensitivity to rotor geometry*. In: European Wind Energy Conference and Exhibition Brussels, Belgium, 14–17 Mar, 2011.
15. Shiono M., Suzuki K., Kiho S. (2002): *Output characteristics of Darrieus water turbine with helical blades for tidal current generations*. In: Proceedings of 12th International Offshore and Polar Engineering Conference, Kitakyushu, Japan, 26–31 May, 2002.
16. Tomporowski A., Al-Zubiedy A., et al. (2019): *Analysis of the project of innovative floating turbine*. *Polish Maritime Research*, Vol. 26(4): 124–133.
17. Wang S., Yuan P., Li D., Jiao Y. (2011): *An overview of ocean renewable energy in China*. *Renewable and Sustainable Energy Reviews*, Vol. 15(1), 91–111.
18. Wang S. Y., Derek B. I., Ma L., Pourkashanian M., Tao Z. (2012): *Turbulence modeling of deep dynamic stall at relatively low Reynolds number*. *Journal of Fluids and Structures*, Vol. 33(8), 191–209.
19. Yang B., Lawn C. (2011): *Fluid dynamic performance of a vertical axis turbine for tidal currents*. *Renewable Energy*, Vol. 36(12), 3355–3366.
20. Zhang Z. Y., Ma Y., et al. (2017): *3-D simulation of vertical-axial tidal current turbine*. *Polish Maritime Research*, Vol. 23(4): 73–83.

## DATA AVAILABILITY STATEMENT

The CFD simulation raw data used to support the findings of this study are available from the corresponding author upon request.

## CONTACT WITH THE AUTHORS

**Wanchao Zhang**

*e-mail: zhangwanchao@just.edu.cn*

Jiangsu University of Science and Technology,  
No.2 Mengxi Road, 212000 Zhenjaing,

**CHINA**

**Yujie Zhou**

*e-mail: zhouyujie@just.edu.cn*

Jiangsu University of Science and Technology,  
Mengxi Road, 212000 Zhenjiang

**CHINA**

**Kai Wang**

*e-mail: wangkai198949@qq.com*

Wuhan Second Ship Design & Research Institute,  
450 Zhongshan Road, 430064 Wuhan, China

**CHINA**

**Xiaoguo Zhou**

*e-mail: zhouxiaoguo@just.edu.cn*

Jiangsu University of Science and Technology,  
Mengxi Road, 212000 Zhenjiang, China

**CHINA**

## ASSESSMENT OF BUCKLING BEHAVIOUR ON AN FPSO DECK PANEL

**Ozgur Ozguc**

Istanbul Technical University

Department of Naval Architecture and Ocean Engineering, TURKEY

### ABSTRACT

*Stiffened plates are the main structural building block in ship and offshore hulls and their structural response subject to loads is a topic of significant practical interest in ship and offshore structural design. To investigate the structural capacity for design and evaluation purposes, it is becoming an efficient and reliable practice to carry out non-linear finite element (FE) analysis. The present study is to assess the buckling strength of a stiffened deck panel on an FPSO vessel using the nonlinear finite element code ADVANCE ABAQUS, where imperfection sensitivity work is also accounted for. The cases studied correspond to in-plane bi-axial compression in the two orthogonal directions. The findings are compared with the DNVGL PULS (Panel Ultimate Limit State) buckling code for the stiffened panels. It is found that the strength values from the ADVANCE ABAQUS and DNVGL PULS code are very close. The results and insights developed from the present work are discussed in detail.*

**Keywords:** buckling strength,imperfection sensitivity,nonlinear finite element analysis,FPSO unit,deck panel

### INTRODUCTION

A typical ship and an offshore structure can be considered as an assemblage of continuous stiffened plates with equally spaced longitudinal stiffeners of approximately the same size. In order to analyse the ship's ultimate strength, the ultimate strength of the stiffened panels must be taken into account.

Since the overall failure of a ship or offshore hull is normally governed by buckling and plastic collapse of the deck, the bottom and the side shell stiffened plates, it is important to accurately calculate the ultimate strength of the stiffened panels in the deck, bottom and side shell in order to achieve a more advanced structural design of the ship.

Buckling is caused by in-plane stresses exceeding the buckling stability of the structure, causing local yield and permanent deformation of the structure. The buckling capacity is a property of the plate, depending on the stiffener spacing and the thickness.

Ship and offshore structures have been investigated by nonlinear finite element analysis in a large number of research works concerning ultimate strength and ultimate limit state (ULS) aspects. These studies have been utilised for plates, stiffened plates and three cargo holds in mid-ship areas [1]. Estimates of the ultimate strength of continuous plates were studied and developed by a simplified method that proposes formulae with more accurate predictions of the

ultimate strength compared to NFEM results [7]. Assessment of the ultimate strength for unstiffened plates surrounded by supporting members under combined uniaxial/biaxial compressive loads and lateral pressures has been performed based on a series of benchmark studies on the methods [19]. For rectangular plates under biaxial loadings the elasto-plastic buckling behaviour has also been studied [25]. The one-bay plate models from a  $1/2 + 1 + 1/2$  bay continuous plate were investigated by Paik and Seo [20, 21] to reveal the fact that the ultimate strength of unstiffened plate under biaxial compressive loads was significantly influenced by rotational restraint under lateral pressure actions. A new method to analyse the geometric nonlinear behaviour of plates was developed, in which large elastic deflection or post-buckling of plates with partially restrained rotation and the torsional rigidity condition was applied [18].

Regarding the stiffened panel assessment, results were obtained in order to continuously develop improved methods for accurate and efficient prediction of the ultimate strength. To estimate the ultimate strength, some direct methods were proposed by Caldwell [2] and Mansour et al. [12] and a simplified method (Smith's method and the idealised structural unit method, ISUM) was later widely applied for analysis of hull girders under longitudinal bending loads only. By applying the mentioned methods to the analysis, results were rapidly obtained, but the accuracy depends on the average stress-strain relationship of individual structural members. The simplified method was developed [28] for evaluation of the collapse strength for hatch covers with a folding type and a side-sliding type of bulk carrier [16, 17]. The ALPS/ULSAP method was used to determine the ultimate limit state of a stiffened panel under uniaxial or biaxial compression and lateral pressures, and the results were compared to the ANSYS nonlinear finite element analysis. Related to the parameter effects on the collapse behaviour of stiffened panels, a shaped model with two (1 + 1) full bays was studied by FEM. In addition to the ultimate strength of the plates, nonlinear FE software was used to analyse a two half bays plus one full bay ( $1/2 + 1 + 1/2$  bay) model in the longitudinal direction by Zhang and Khan [30] and Fujikubo et al. [8]. The influence of the stiffener's geometry and boundary conditions on the ultimate strength of stiffened panels under a combined thrust acting load including 3 bays,  $1/2 + 1 + 1/2$  bays, 1 + 1 bays and 1 bay, were analysed by Xu and Guedes Soares [27].

Ozguc et al. [14] developed new simple design equations for predicting the ultimate compressive strength of stiffened plates with initial imperfections in the form of welding-induced residual stresses, and geometric deflections were developed in the study. To perform ANSYS elastic-plastic buckling analyses, a non-linear finite element method was employed, where a wide range of typical ship panel geometries from 60 different models was accounted for. The reduction factors of the ultimate strength were produced from the results of the 60 ANSYS inelastic finite element analyses. The accuracy of the proposed equations was validated by the experimental results. Comparisons indicated that the adopted

method had sufficient accuracy for practical applications in ship design.

Xu et al. [26] investigated the influence of the lateral pressure and stiffener type on the collapse behaviours of steel stiffened panels using FE (finite element) analysis. Based on the numerical results, the empirical expressions were derived for the ultimate strength assessment of stiffened panels under combined in-plane axial compression and different levels of lateral pressure. The regression formulae only included the plate slenderness ratio and column (stiffener) slenderness ratio. Hence, to consider the influence of the stiffener type, the databases of sample points were separately grouped for various cross-sections in the regression process.

Kim et al. [10] carried out a comprehensive technical review on existing empirical formulations that predicted the ultimate limit state (ULS) of a stiffened panel under longitudinal compression. A detailed investigation on the lower range value of  $\lambda$  was conducted using an ANSYS nonlinear finite element method (NLFEM)-based numerical simulation. A total of 10,500 cases were modelled using ANSYS numerical simulation by considering relevant size changes in the plate thickness, web thickness, flange thickness, height of web, and breadth of flange. In the case of an initial imperfection, only the average level of initial deflection to the plate and initial distortion to the stiffener elements were considered, while the residual stress due to welding was not considered. A detailed procedure including the selection of reliable scenarios, finite element (FE) modelling, FE analysis, and sensitivity analysis results, was also documented. The outcome obtained could be useful for understanding the ultimate compressive strength behaviour of a stiffened panel. Moreover, the applicability of the existing empirical formulations could also be assessed from the statistical analysis results.

Lee et al. [11] applied the ultimate limit states as the structural design criteria of a box girder crane. For this purpose, a reference box girder crane structure which was originally designed and constructed based on the allowable working stress criteria and still in operation was selected. The structure was then redesigned applying the ultimate limit state criteria, where other types of limit states such as serviceability limit states and fatigue limit states were also considered. A nonlinear finite element method was applied to analyse the progressive collapse behaviour of the structure until and after the ultimate limit state was reached. While the ultimate strength or maximum load-carrying capacity of the structure has never been realised as far as the allowable working stress based design method was applied, this study started by identifying it by the nonlinear finite element method.

Tekgoz et al. [24] analysed the effect of different finite element models on the ultimate strength assessment of stiffened plates, where the effect of the element size, and type, boundary conditions, shape of initial imperfection, thickness and net sectional configurations were accounted for. Four different finite element models and different structural configurations were compared to the solution described by the Common Structural Rules (CSR). Zhang and Jiang [29]

developed a simple method for the ultimate strength analysis of square plates under combined longitudinal and transverse compressive stresses. The method was fully validated with the results of a systematic non-linear FE analysis. They also compared the methods from the industry standards BS5400 and DIN18800. Analysis examples were also provided in the paper for reference and discussion.

Oksina et al. [13] applied the idealised structural unit method (ISUM) for collapse analysis of large structures. The evaluation of the maximum load-carrying capacity of structures is an essential issue in determining their safety. Only if the prediction of the ultimate strength is ensured can their probability of survival in extreme load conditions be estimated. Particularly for safe dimensioning of ship structures, the determination of the structural strength against buckling and yielding is required by Common Structural Rules (CSR).

Shi et al. [22] evaluated the ultimate strength of stiffened panels under compressive loads by numerical simulations, for comparison with tests done to investigate the influence on the ultimate strength of varying the pit location, pit diameter and pit depth. The validated model was used for a numerical study on the influence of pitting on the residual ultimate strength of stiffened panels by a series of non-linear finite element analyses. The parameters of the pit position, diameter, number, depth, and corroded volume loss were investigated for the stiffened panels subjected to axial compressive load with initial deformations. It was found that the pits would induce the buckling failure of stiffened panels. All parameters were discussed to understand the significant influence on the residual ultimate strength of the pitting-corroded stiffened panel. Further, a formula was derived by introducing the reduction of plate slenderness and column slenderness.

Do et al. [6] applied the finite element method (FEM) and developed it to solve a complicated problem accurately. In particular, with the help of aid tool and software, as well as the nonlinear finite element method (NFEM), the ultimate strength of their large model was improved significantly and accurately. They investigated the ultimate stiffened panel strength in the cargo hold areas for a very larger ore carrier built in China.

The buckling strength assessment of a deck of a double-hull oil tanker was performed by Ozguc [15] using the non-linear finite element code ADVANCE ABAQUS [9, 31]. Comparisons were carried out with the Det Norske Veritas (DNVGL) PULS (Panel Ultimate Limit State) buckling code [23] for the stiffened panels, DNVGL Classification Notes (CN) No. 30.1 [3] and the DNVGL Ship Rules [4]. The case studied corresponds to axial compression. Two levels of imperfection tolerances were analysed, in accordance with the specifications in the DNVGL Instruction to Surveyors (IS) [5] and the DNVGL Classification Notes No. 30.1 [3]. Both “as built” and DNVGL Rule [4] “net” dimensions were calculated.

The present work is to perform the buckling strength assessment of a stiffened deck panel on an FPSO vessel using the nonlinear finite element code ADVANCE ABAQUS, where an imperfection sensitivity work is also accounted for. The

cases studied correspond to in-plane bi-axial compression in the two orthogonal directions. The findings are compared with the DNVGL PULS (Panel Ultimate Limit State) buckling code for the stiffened panels. It is found that the strength values from ADVANCE ABAQUS and DNVGL PULS code are very close.

This study determines that the quality and accuracy of the non-linear FE analysis results are highly dependent on the user’s skills and the analysis procedures used for ship-shaped offshore FPSO vessels, where the deck structure is exposed to mostly buckling failure, which can be a good reference for the safety estimation.

Further, the buckling resistance of a deck depends on the plate thickness and the size and spacing of the supporting stringers. The results produced from the present work can inform the safe design of FPSO facilities.

## THE FINITE ELEMENT MODEL FOR ANALYSIS

Typical stiffened panels are used in offshore structures through a comparison with non-linear finite element analyses. The main particulars of the panel are taken from the deck structure of an FPSO platform, and it has the dimensions (measured between girders) given in Table 1.

Tab. 1 Main scantling for analysed deck panel

Stiffener length	2500 mm
Stiffener spacing	500 mm
Number of stiffeners	24
Plate thickness	9 mm
Stiffener height (including flange thickness)	160 mm
Web thickness	12 mm
Flange width	100 mm
Flange thickness	12 mm
Profile type	Angle

The number of stiffeners has been reduced to eight in the finite element model to keep its size down and enhance its manageability. This should have only minor implications for the analysis results, since the number of stiffeners is still high. The latter is confirmed by the PULS elastic buckling calculation, which shows that the elastic buckling shape has a half-wave length in the order of the stiffener spacing in the transverse direction. To reduce the uncertainties introduced through boundary conditions, the finite element model has been extended by a half-frame spacing at each end, resulting in a model length of twice the stiffener length.

The strain hardening effect together with a bi-linear stress-strain curve is shown in Fig. 1. The Cowper-Symonds rate enhancement formula is used to consider the effect of the strain rate on the material properties as given in Eqs. (1)–(3), which are shown in Fig. 1 and Fig. 2. The material parameters are shown in Table 2.

Tab. 2 The material properties

Young's modulus, E [N/mm <sup>2</sup> ]	206 000
Poisson ratio, ν	0.30
Material yield stress [N/mm <sup>2</sup> ]	235
Strain hardening parameter, ET [N/mm <sup>2</sup> ]	1000
Strain rate (C)	40.4
Strain rate (P)	5.0

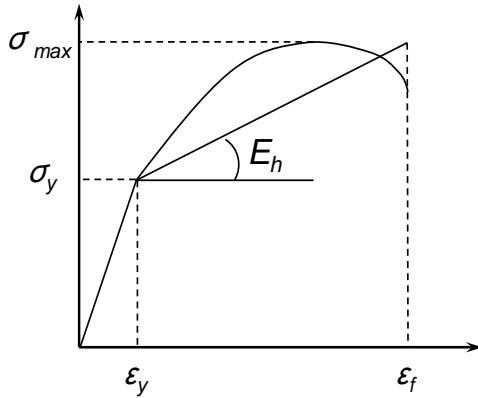


Fig. 1. Stress-strain curve for bi-linear material

$$\sigma_p = \sigma_y + \frac{EE_h}{E - E_h} \varepsilon_p \quad (1)$$

$$E_h = \frac{\sigma_{max} - \sigma_y}{\varepsilon_f - \varepsilon_y} \quad (2)$$

σ<sub>y</sub> = Yield stress

E<sub>h</sub> = Hardening modulus

σ<sub>p</sub>, ε<sub>p</sub> = Plastic stress & plastic strain

E = Young's modulus

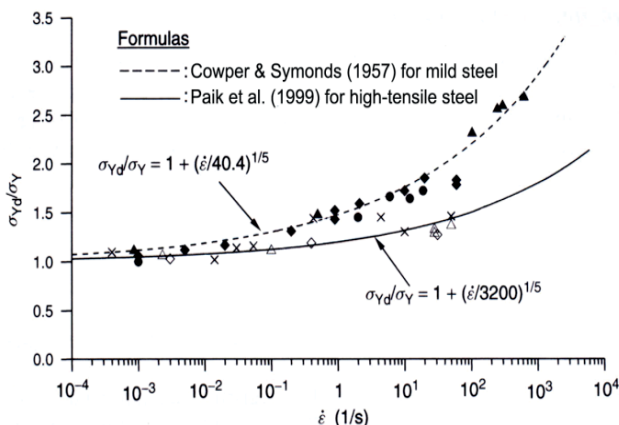


Fig. 2. Strain rate effect

$$\frac{\sigma_{yd}}{\sigma_y} = 1 + \left\{ \frac{\varepsilon}{D} \right\}^{1/q} \quad (3)$$

It is noted that for mild steel grade D = 40.4 and q = 5 are used.

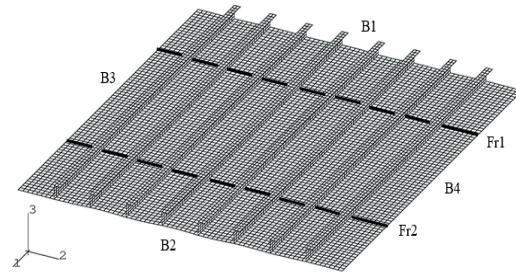


Fig. 3. The finite element model with labelled boundaries

Boundary conditions are imposed on the edges and lines indicated in Fig. 3. Symmetry conditions are given on edges B1 and B2. This might represent a constraint on the deformation of the plate and on the web and flange of the stiffener, but experience from other similar analyses indicates that this has little impact on the results. Edge B2 is fixed in the 1-direction.

Edges B3 and B4 are fixed in the lateral direction and in the rotation about the 1-axis. The latter is to keep the panel from collapsing in one of the outermost plate fields. Edge B4 is fixed in the 2-direction, while edge B3 is free to move in this direction but with the edge constrained to remain straight.

Lines labelled Fr1 and Fr2 correspond to the positions of transverse frames or girders. At these locations the panel is fixed in the lateral direction. Furthermore, the stiffeners are constrained to remain vertical in order to simulate the presence of frames/girders.

## GEOMETRIC IMPERFECTIONS

Steel structures are typically fabricated by flame cutting and welding, and thus initial imperfections in the form of initial distortions and residual stresses may develop and will reduce the collapse capacity. These initial imperfections should therefore be included in the structural design as parameters of influence.

When local heating is applied to structural steels, the heated part will expand, but because of adjacent cold parts it will be subjected to compressive stress and distortion. When the heated part is cooled down, it will be locally shrunk rather than revert to its initial shape and thus now be subjected to tensile stress. Approximate methods based on the insights from measurements are usually adopted for design purposes because of the complexity of the phenomena involved, while some efforts have been made to estimate the initial imperfections theoretically or numerically. In this study, the tolerances level on the plate out-of-flatness and stiffener

out-of-straightness are taken from the DNVGL Classification Notes No. 30.1 [3] as follows in Fig. 4.

$$\begin{aligned} \delta_{P0} &= 0.01s \\ \delta_{S0} &= 0.0015L \\ \delta_{T0} &= 0.0015L \end{aligned}$$

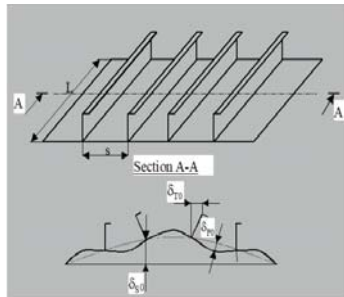


Fig. 4. The imperfection parameters used in this study

In addition to the base tolerance level, six other tolerance levels have been analysed as shown in Table 3, in order to study the imperfection sensitivity of the panel strength.

Tab. 3. Imperfection tolerance levels

Identification	$\delta_{p0}$	$\delta_{s0}$	$\delta_{t0}$
Level 1	0.005s	0	0.0015L
Level 2	0.01s	0	0.0015L
Level 3 (base level)	0.01s	0.0015L	0.0015L
Level 4	0.01s	0.003L	0.003L
Level 5	0.02s	0	0.0015L
Level 6	0.02s	0.0015L	0.0015L
Level 7	0.02s	0.003L	0.003L

The shape of the imperfections is generally composed of a local component (plate out-of-flatness and stiffener flange out-of-straightness) and a global component (stiffener out-of-straightness). The local component is itself composed from a subset of the elastic buckling modes for the panel for the specific load combination at hand. Ten of these buckling modes are shown in Fig. 5 below. Strictly, this procedure requires that the deformation pattern in the buckling modes excludes lateral deflection of the stiffeners, a requirement that is not entirely met in this case. However, to distribute out-of-plane deformations in the shape of the lowest eigenmodes, also involving some minor lateral deflections of stiffeners, is always conservative. Analyses are performed for three different local imperfection shapes defined in Table 4.

Tab. 4. Composition of the three local imperfection shapes used in the analyses

Mode	Weight factors for the ten lowest buckling modes in the local imperfections									
	1	2	3	4	5	6	7	8	9	10
Local 1	10	1	1	1	1	1	1	1	1	1
Local 2	1	1	1	1	1	1	1	1	1	1
Local 3	1	0	0	0	0	0	0	0	0	0

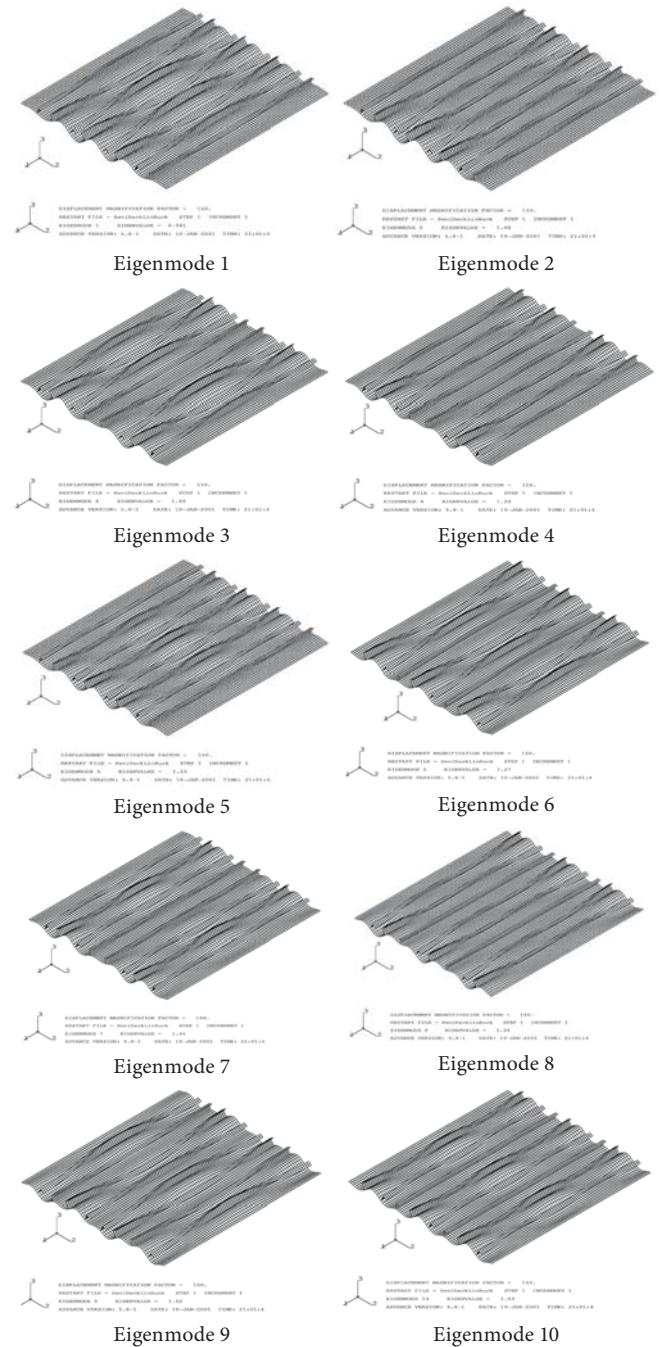


Fig. 5. The ten lowest buckling modes for the deck panel

## GLOBAL IMPERFECTION PATTERN

Global stiffener imperfections are specified in a half sine wave pattern along the stiffener length, and two different patterns in the transverse direction: an alternating short wave pattern with linearly varying displacements between each stiffener as illustrated in Fig. 6 (Global 1), and a half sine wave variation as illustrated in Fig. 7 (Global 2). These half-wave patterns span the total panel width of eight stiffeners, and the three-stiffener model is only used for illustration purposes.

The first of these transverse patterns is expected to yield the most conservative results in cases where large transverse compressive loads are present, since it closely resembles the lowest global eigenmodes in PULS.

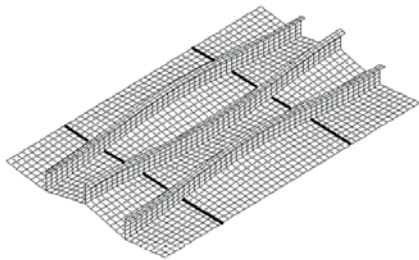


Fig. 6. Linearly varying alternating stiffener imperfection mode (Global 1)

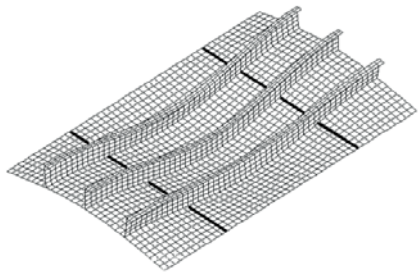


Fig. 7. Sine varying stiffener imperfection mode (Global 2)

Tab. 5. Definition of the analysed imperfection combinations

Identification	Local shape	Global shape	Tolerance level
Case 1	Local 1	-	Level 2
Case 2	Local 1	Global 1	Level 3 (base level)
Case 3	Local 1	Global 1	Level 4
Case 4	Local 1	Global 2	Level 2
Case 5	Local 3	-	Level 1
Case 6	Local 3	-	Level 2
Case 7	Local 3	-	Level 5
Case 8	Local 2	-	Level 2
Case 9	Local 1	-	Level 5
Case 10	Local 1	Global 1	Level 6
Case 11	Local 1	Global 1	Level 7
Case 12	Local 3	Global 1	Level 2

Twelve different combinations of global imperfection shapes, local imperfection shapes and tolerance levels have been analysed, and are defined in Table 5. A comparison of the results from Case 1 – Case 3 and Case 9 – Case 11 will give information about the sensitivity to global stiffener imperfections for the given geometry and load combination. However, the behaviour observed here may be restricted to the selected imperfection shape.

Furthermore, a pairwise comparison of Case 1 – Case 9, Case 2 – Case 10 and Case 3 – Case 11 will give information about the sensitivity to plate / torsional imperfections. The same will be the case by comparing Case 5 to Case 7, but then with another imperfection shape as a basis.

Case 2 and Case 4 differ only in the shape of the global stiffener imperfection, and differences in results must be related to this difference. The imperfection shape is also the

only thing separating Case 2 from Case 12 and Case 1 from Case 6 and Case 8, but for these the difference is in the shape of the local imperfection.

## LOAD APPLICATION

All analyses are performed in load control, i.e. the non-linear solution is found by incrementing the magnitude of the applied forces proportionally. All edges are constrained to remain straight, and the model is loaded by applying a resultant nodal force consistent with the design stresses to one node on each of the two loaded edges. This is illustrated in Fig. 8.

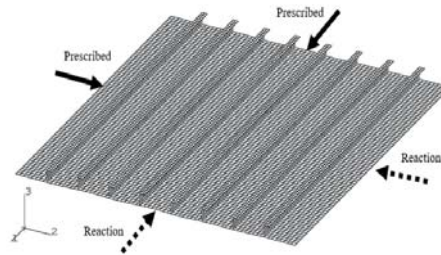


Fig. 8. Illustration of how loads are applied to the FE model

The design loads for the panel are as follows:

$\sigma_1 = 100$  MPa (axial stress),

$\sigma_2 = 60$  MPa (transverse stress),

$\tau_{12} = 5$  MPa (in-plane shear stress)

For simplicity, the shear loads have been disregarded in the finite element analyses, since the load component is small and is expected to have little impact on the results.

## FINITE ELEMENT RESULTS

All results will be given as a load proportionality factor (LPF) with the design loads as the reference state. A summary of the results from the ADVANCE ABAQUS analyses is given in Table 6. They show that the effects of the global stiffener imperfections are small, and reduce the capacity by the order of 2.5 % for the variations in magnitude analysed here. The sensitivity to plate imperfections is larger, but still the difference introduced by quadrupling its magnitude is below 15 %. A doubling of the plate imperfection magnitude reduces the capacity by the order of 8–10 %. Note that the local imperfection scaling also includes some marginal stiffener imperfections. Comparing Case 1 with Case 8, the effect of the different imperfection shape appears to be of the same magnitude as the variations in the size of the imperfections. For this panel and load combination, a local imperfection in the shape of the first elastic buckling mode appears to produce the most conservative capacity estimate. Case 12 thus represents a lower capacity bound for the given tolerance level. However, the difference between Case 12 and the other

cases representing the same tolerance level (Case 1, Case 2, Case 4, Case 6 and Case 12) is very small.

Tab. 6. Calculated load proportionality factors associated with collapse of the panel for Case 1 to Case 12

Identification	LPF ADVANCE	Case 1 / Case 12
Case 1	1.341	1.033
Case 2 (Basis case)	1.324	1.019
Case 3	1.305	1.005
Case 4	1.339	1.033
Case 5	1.379	1.063
Case 6	1.315	1.014
Case 7	1.199	0.927
Case 8	1.414	1.089
Case 9	1.242	0.959
Case 10	1.233	0.951
Case 11	1.216	0.938
Case 12	1.299	1.000

Based on the results in Table 6, it can be concluded that an LPF in the area of 1.3 is a good representation of the strength of the panel for imperfection tolerances on and around the requirements in DNVGL CN30.1 [3]. The calculated failure mode is collapse of a plate field between two stiffeners, and is identical for all the analysed cases. This failure mode is characteristic of panels loaded with a large transverse stress. Figs. 9 to 11 show contour plots of the stresses and plastic strains at the ultimate load level, which illustrates the failure mode.

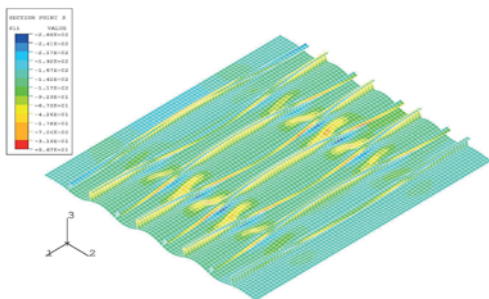


Fig. 9. Axial membrane stress in the panel at the ultimate load level

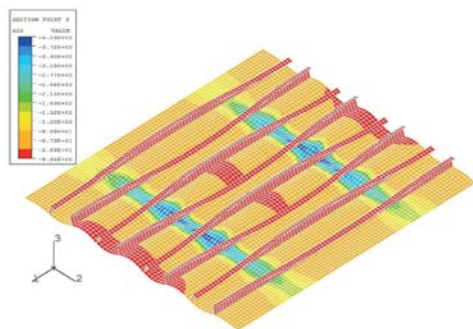


Fig. 10. Transverse membrane stress in the panel at the ultimate load level

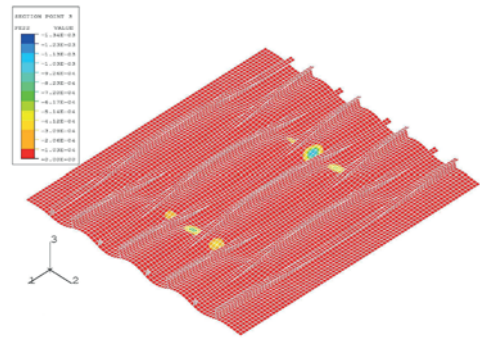


Fig. 11. Membrane yield zones in the panel at the ultimate load level

## COMPARISON WITH PULS CODE

The findings show that the DNVGL PULS code produces capacity estimates in very good agreement with the ABAQUS finite element analysis results based on the initial imperfection levels and shapes described in the paper, where the results from DNVGL PULS are well on the conservative side. The strength predictions are considered valid for imperfection levels relevant for ship and offshore structures in the “as-built” condition. For the example geometry and load combination, DNVGL PULS estimates an ultimate strength load proportionality factor of 1.33, whereas the ADVANCE ABAQUS results are in the range of 1.32–1.35 for the DNVGL CN30.1 tolerance level.

Clearly, this result accords very well with the finite element results. The DNVGL PULS code predicted nearly the same strength for the original design load combination with an additional shear stress of  $\tau_{12} = 5$  MPa.

## CONCLUDING REMARKS

The finite element code ADVANCE ABAQUS has been used in a nonlinear buckling analysis of a stiffened deck panel on an FPSO platform. The PULS code computerised buckling code is employed to compare the capacity estimates obtained from nonlinear finite element analysis by ABAQUS. A single bi-axial load combination has been investigated. The imperfection tolerances given in DNVGL CN30.1 have been used as the basis for the analyses, but several other combinations with both larger and smaller tolerances have been analysed. In total, twelve different shapes and magnitudes of geometric imperfections have been analysed. The results show that the PULS code produces capacity estimates which are in very good agreement with the nonlinear finite element results. Given in terms of the load proportionality factor on the design loads, the DNVGL PULS code estimates a capacity of 1.33, whereas the ADVANCE ABAQUS results are in the range of 1.32–1.35 for the CN30.1 tolerance level, depending on the shape of the imperfections. For this specific example, the results also indicate that the DNVGL PULS code results are valid for tolerance levels exceeding the DNVGL CN30.1

tolerance. Direct application of geometrical non-linear plate theory is the main concept in the new Panel Ultimate Limit State (PULS) stiffened panel models recently recognised by DNVGL as part of the new rules and standards for ships and offshore constructions. The focus is on assessment of the ultimate capacity limit, rather than the more traditional elastic buckling limit. The method is streamlined for rules based on modern ultimate limit state design principles. The models are validated against non-linear FE analyses.

## REFERENCES

1. Amlashi H., Moan T. (2009): *Ultimate strength analysis of a bulk carrier hull girder under alternate hold loading condition, Part 2: Stress distribution in the double bottom and simplified approaches*. Marine Structures, 22 (3), 522-544.
2. Caldwell J. B. (1965): *Ultimate longitudinal strength*. Trans. Royal Inst. Nav. Arch., 107, 411-430.
3. DNV GL Classification Notes (2017): *Buckling strength analyses*, CN 30.1.
4. DNV GL Rules for Classification (2018): *Hull structural design ships with length 100 meters and above*, Part 3 Chapter 1.
5. DNV GL Rules (2015): *Hull survey – workmanship standard*, DNV Instructions to Surveyors No. I-B3.3.
6. Do H. C., Jiang W., Jin J., Chen X. (2013): *An investigation of ultimate strength for VLOC stiffened panel structure*. Modern Transportation, 2(2), 23-38.
7. Fujikubo M., Harada M., Yao T., Khedmati M. R., Yanagihara D. (2005): *Estimation of ultimate strength of continuous stiffened panel under combined transverse thrust and lateral pressure, Part 2: Continuous stiffened panel*. Marine Structures, 18, 411-427.
8. Fujikubo M., Yao T., Khedmati M. R., Harada M., Yanagihara D. (2005): *Estimation of ultimate strength of continuous stiffened panel under combined transverse thrust and lateral pressure, Part 1: Continuous plate*. Marine Structures, 18, 383-410.
9. Karlson H., Sorensen I. (2012): ABAQUS/Standard User's Manual.
10. Kim D. K., Lim H. L., Yu S. Y. (2018): *A technical review on ultimate strength prediction of stiffened panels in axial compression*. Ocean Engineering, 170(15), 392-406.
11. Lee D. H., Kim S. J., Lee M. S., Paik J. K. (2019): *Ultimate limit state based design versus allowable working stress based design for box girder crane structures*. Thin-Walled Structures, 134, 491-507.
12. Mansour A. E., Liu D., Paulling J. R. (2008): *Strength of ships and ocean structures*. Principles of Naval Architecture Series (Society of Naval Architects and Marine Engineers (US). Jersey City, N.J.: Society of Naval Architects and Marine Engineers.
13. Oksina A., Lindemann T., Kaeding P., Fujikubo M. (2016): *Idealized structural unit method: A review of the current formulation*. International Conference on Offshore Mechanics and Arctic Engineering, Volume 9: Prof. Norman Jones Honoring Symposium on Impact Engineering; Prof. Yukio Ueda Honoring Symposium on Idealized Nonlinear Mechanics for Welding and Strength of Structures.
14. Ozguc O., Das P. K., Barltrop N. (2007): *The new simple design equations for the ultimate compressive strength of imperfect stiffened plates*. Ocean Engineering, 34(7), 970-986.
15. Ozguc O. (2018): *Estimation of buckling response of the deck panel in axial compression*. Polish Maritime Research, 25, No. 100, 98-105.
16. Paik J., Kim B., Seo J. (2008a): *Methods for ultimate limit state assessment of ships and ship-shaped offshore structures: Part I—Unstiffened plates*. Ocean Engineering, 35(2), 261-270.
17. Paik J., Kim B., Seo J. (2008b): *Methods for ultimate limit state assessment of ships and ship-shaped offshore structures: Part II—Stiffened plates*. Ocean Engineering, 35(2), 261-270.
18. Paik J., Kim B., Seo J. (2008c): *Methods for ultimate limit state assessment of ships and ship-shaped offshore structures: Part III—Hull girders*. Ocean Engineering, 35 (2), 281-286.
19. Paik J. K., Kim D. K., Lee H., Shim Y. L. (2012): *A method for analyzing elastic large deflection behavior of perfect and imperfect plates with partially rotation-restrained edges*. Journal of Offshore Mechanics and Arctic Engineering, 134.
20. Paik J. K., Seo J. K. (2009a): *Nonlinear finite element method models for ultimate strength analysis of steel stiffened-plate structures under combined biaxial compression and lateral pressure actions—Part I: Plate elements*. Thin-Walled Structures, 47(8-9), 1008-1017.
21. Paik J. K., Seo J. K. (2009b): *Nonlinear finite element method models for ultimate strength analysis of steel stiffened-plate structures under combined biaxial compression and lateral pressure actions—Part II: Stiffened panels*. Thin-Walled Structures, 47(8-9), 998-1007.

22. Shi X. H., Zhang J., Soares C. G. (2018): *Numerical assessment of experiments on the ultimate strength of stiffened panels with pitting corrosion under compression*. Thin-Walled Structures, 133, 52-70.
23. Steen E., Byklum E., Vilming K. G. (2010): *PULS verification manual - PULS Version 2.0*.
24. Tekgoz M., Garbatov Y., Soares C. G. (2012): *Ultimate strength assessment accounting for the effect of finite element modelling*. Maritime Engineering and Technology, 59-74.
25. Wang G., Sun H., Peng H., Uemori R. (2009): *Buckling and ultimate strength of plates with openings*. Ships and Offshore Structures, 4(1), 43-53.
26. Xu M. C., Song Z. J., Zhang B. W., Pan J. (2018): *Empirical formula for predicting ultimate strength of stiffened panel of ship structure under combined longitudinal compression and lateral loads*. Ocean Engineering, 162, 161-175.
27. Xu C. M., Guedes Soares C. (2012): *Numerical assessment of experiments on the ultimate strength of stiffened panels*. Engineering Structures, 45, 460-471.
28. Yao T. (2003): *Hull girder strength*. Marine Structures, 16(1), 1-13.
29. Zhang S., Jiang L. A. (2015): *Method for ultimate strength assessment of plates in combined stresses*. International Conference on Offshore Mechanics and Arctic Engineering, 3, 145-167.
30. Zhang S., Khan I. (2009): *Buckling and ultimate capability of plates and stiffened panels in axial compression*. Marine Structures, 22(4), 791-808.
31. ABAQUS Analysis User's Guide (2017): *Unstable Collapse and Post-buckling Analysis*.

## CONTACT WITH THE AUTHOR

**Ozgur Ozguc**

*e-mail: ozguco@yahoo.com.sg*

Istanbul Technical University,  
 Dept. of Naval Architecture and Ocean Eng.,  
 Maslak, 34469 Istanbul,  
**TURKEY**

## APPLICATION OF APRIORI ALGORITHM IN THE LAMINATION PROCESS IN YACHT PRODUCTION

Tacjana Niksa-Rynkiewicz

Michał Landowski

Paweł Szalewski

Gdańsk University of Technology, Poland

### ABSTRACT

*The article specifies the dependence of defects occurring in the lamination process in the production of yachts. Despite great knowledge about their genesis, they cannot be completely eliminated. Authentic data obtained through cooperation with one of the Polish yacht shipyards during the years 2013–2017 were used for the analysis. To perform a simulation, the sample size was observed in 1450 samples, consisting of 6 models of yachts with closed and open deck. Finding the dependence of the occurrence of specific defects will allow for faster procedures and more effective quality control, which will contribute to lower costs. The use of new methods based on artificial intelligence related to Big Data allows for easier observation of dependencies in the complex structure of data from yacht production. The association rules were defined using the algorithm Apriori and define interdependent defects. A number of dependencies were found for the occurrence of production defects not obvious to technologists, but occurring with a high probability of coexistence. The presented research results may allow the planning process of production tasks to be improved.*

**Keywords:** Apriori algorithm, quality control, laminate defects

### INTRODUCTION

Today, fibrous polymer composites are used in all fields of technology, replacing traditional materials and giving new possibilities for design solutions, especially in relation to means of transport [1]. The most important group of these materials are layered composites – laminates. Polymer laminates are commonly used in the construction of small vessels such as yachts and pleasure boats, patrol boats for the police and army, fishing boats [40]. The length of these units is usually from a few to about 30 meters. Larger units are built for the needs of the navy and here their length is gradually increasing and the Swedish navy plays a leading role. The amagnetic corvettes built by it are even 90 m (and more) long [27]. However, this requires the use of modern materials and technologies. In addition to the reinforcement made of traditional glass fibers, carbon fibers with a high Young's modulus (stiffness) and high-strength aramid fibers are used [11, 39]. Also, traditional

polyester matrices in shipbuilding are replaced with vinyl ester or epoxy. Effective use of new materials in the construction of laminate elements requires the use of more advanced manufacturing techniques that guarantee better structural quality of the material associated with a smaller number of technological defects and the possibility of reducing the proportion of resin in the structure, which leads to an increase in strength, resistance to cracking and service life [12, 22, 29]

Currently, Poland is one of the European leaders in the market of producers of yachts and boats made of polymer laminates. However, most of our shipyards use the hand lay-up method of laminating process, some are working on implementing the infusion or Resin Transfer Moulding RTM method. However, this requires the employment of a professional workforce, which must be well paid, and this industry bases its profitability on the cheap labour that can be found in Poland, which ensures its competitiveness in relation to numerous manufacturers of this type of units in the West Europe.

Attempts to introduce infusion technology are also associated with a certain risk of failure to obtain the appropriate quality of the material, when the process parameters (especially negative pressure and the density of the arrangement of vacuum tubes) are not properly selected by an inexperienced manufacturer [3, 45].

The number of defects arising during the lamination process is very large. It depends on many factors, such as the conditions in the production hall, the storage of materials, the method of reducing the laminate or even the level of personnel qualification. Vacuum methods allow to obtain a laminate with fewer technological defects, but sometimes they cause new defects not found in manual lamination – e.g. overdrying of the reinforcement [22, 43].

The lamination process in a shipyard should fulfil a number of requirements set out by the classification society Det Norske Veritas Germanischer Lloyd (DNV GL) Polish Register of Shipping (PRS). Good quality control is very important in the boat manufacturing process [31]. Therefore, tools supporting the assessment of defects play an important role. In the quality assessment process, most tests are visual tests, so it is important to clearly define what defects should be classified. Some particularly dangerous defects may be difficult to detect by visual testing, therefore other NDT methods are used [5, 16]. For example, delamination can be detected by UT and RT. Due to expensive equipment and high qualifications of the person performing (interpreting) tests, they are usually not used in quality control in production in small shipyards. In such cases, old methods such as Tap Test work well [5, 34]. The area of their occurrence is also important, which allows you to estimate the time needed to repair given defects or determine the lack of profitability of repair in the case of small boats. Therefore, quality control charts are kept in production facility.

Data from quality control cards may also allow finding defects in production processes if they are combined with delivery schedules, personnel work or the results of measurements of humidity and temperature conditions in the production facility.

The main concern of this article is issues related to the hand lay-up lamination process of yachts hulls. Podsiadlo and Tarelko in their works [36, 49] emphasized that the yacht production process can be separated into areas by the specifics of the activities: Planning, Project-Production-Delivery and Risk Reduction. The lamination process consists of a sequence of steps. There is a possibility of making mistakes at every stage of the lamination process – from storage and preparation of materials through the lamination process to the process of removing the cured hull from the mold. Some defects may arise due to the wrong process of designing a laminate structure, it is necessary to remember to adapt the design to the technological resources in the production company. There can be many reasons for these mistakes. The conducted research allowed to describe the relationships between the existing defects. They were written in the form of association rules. For this purpose, the A-priori algorithm was used. Observations made in one of the Polish small shipyards made it possible to pinpoint specific operations which contain lamination processes.

Computer aided mechanical and materials engineering has been facilitating the boat design process for many years.

It allows you to simulate many variants of shapes in order to obtain the best conditions for the flow of the yacht [13, 44], but also the selection of materials to obtain the optimal ratio of strength properties to weight and price [18, 46]. The problems of determining the main factors needed for qualitative or quantitative analysis can be solved by means of classical statistical methods [32] as well as techniques based on the basic nearest neighbour algorithm [33] or fuzzy logic theory, by designing fuzzy systems [9].

For quality control and production management, the analysis of quality factors is very important. In the study [24], it was recognized that the Apriori algorithm and the analysis of association rules is one of the most frequently used techniques for quality analysis. The authors proposed the use of the Apriori algorithm with approximate sets to evaluate the mechanical properties of steel products. The analysis was carried out using data on the chemical composition and mechanical properties of the products. A similar approach brought many benefits described in the work [26].

## METHODS PRESENTED IN THE LITERATURE

Depending on the model of yacht (its size) and the form in use, three main methods of lamination are used in the studied shipyard [41, 48]: Hand Lay-Up, Spray Lay-Up and Resin Transfer Moulding (RTM).

Currently, in the production of small boats, manual work with the use of simple tools – Hand Lay-Up, Spray Lay-Up. Vacuum methods such as RTM, Vacuum Bagging and Infusion are increasingly used in the production of advanced units and in larger shipyards [10, 30]. Vacuum techniques allow for higher strength properties due to a higher volume fraction of reinforcement in the laminate [20]. Production with vacuum techniques requires higher qualifications of the personnel – a big role in whether optimal properties will be obtained during the lamination process is played by the arrangement of the resin supply and outlet pipes (in-let and out-let), selection of the appropriate resin parameters (viscosity, gel time [35]). As a result, a large part of the industry still relies on manual techniques in the production process of small vessels [7]. Also, the staff is often unqualified, which reduces production costs, but does not allow the use of techniques that require compliance with the technological regime.

From a scientific point of view, it is interesting to develop new materials [21, 22], newer methods [28] or modify older ones to improve the quality and strength of the laminates obtained [14, 19]. This type of research is used by the industry in the production of more advanced units, e.g. racing boats [25]. Carbon or aramid fibers [42] and epoxy resins are often used there – these materials allow for higher strength parameters, but are much more expensive – hence the need to produce laminates with few defects and a large share of reinforcement [15, 17]. Practices of this type make it possible to obtain boats of much lower weight – that is, increase in speed and range. Therefore, the boatbuilding industry is divided into two branches – low-cost production (oversized laminates with a lot of technological defects) and hi-tech production (advanced vacuum techniques to obtain thin laminates with

few technological defects). Although science and industry are still moving forward [8, 47], there is a part of the industry that conservatively uses the simplest and cheapest production methods (hand lay-up and spray lay-up lamination).

Depending on the model of yacht (its size) and the form in use, three main methods of lamination are used in the studied shipyard: Hand Lay-Up, Spray Lay-Up and Resin Transfer Moulding (RTM).

From the methods that can be implemented for research, the method that is the best from the point of view of our research was selected due to:

- it must allow the observation of the largest number of defects – the observations from hand lay-up were used for the study, due to the possibility of a large number of defects (large number of defects) during the technological process compared to other more advanced methods (RTM).
- it must make it possible to observe the relationship between defects with the cheapest possible technology
- the method should be widely used in small shipyards.

The results of the quality inspection of yachts manufactured by hand laminating were selected for the research.

## NOVELTY ELEMENTS

So far, no cross-relationships of material defects formation during the use of the manual laminating method have been described in the literature. Observation of these dependencies makes it possible to eliminate them, and thus the working time can be reduced. The method makes it easier to locate the most sensitive stages of production. Thanks to the prior identification of coexisting defects that disqualify the product for further processing, it will be possible to develop a “quick elimination path” in quality control. The research carried out on the lamination method causing the highest number of defects will allow to check the possibility of using quality control support in the production of laminates also with other more advanced production methods. At the same time, these are preliminary studies to introduce a time-cost analysis of the profitability of repairs and to create tools to reduce inspection time while maintaining a similar level of quality control.

## DESCRIPTION OF THE PROBLEM

The yacht production process, regardless of the method of their production, is associated with the occurrence of defects in the laminate. Defects should be eliminated at individual stages of production through appropriate process control or by repairing the finished product. But even the best-controlled process cannot protect itself from defects.

Defects should be detected by means of quality control and the possibility of repairing them should be assessed (due to the economy and repair techniques) or the hull scrapped when the time and cost of repairing the defects exceed the assumed acceptable level.

## MONITORING OF THE LAMINATION PROCESS

The manufacturing process strongly depends on the environmental conditions of the production. In the analysed production process, humidity and temperature are continuously monitored with the use of thermos-hygrometers both in the production hall and in the material warehouse. Factory premises are well ventilated in accordance with the recommendations of protecting workers' health. The rooms are heated by a boiler room with individual temperature control. The temperature of the storage and processing environment was selected on the basis of the technological cards of the components.

## POSSIBLE DEFECTS IN THE LAMINATION PROCESS

The lamination process is burdened with the risk of occurrence of many defects that may affect the quality of the end product. A properly executed monitoring process described in the chapter “Lamination Process Monitoring” allows the number of mistakes to be reduced. The elements of the yacht hull are assessed during quality control. The list of observed defects during this stage is presented in Table 1.

Tab. 1. Summary information on the repair activities assessed and their weighting factors in the yacht lamination process (defect on production)

Defect symbol	Short name of defect	Name / description of defect
A	Air Bubbles	Air bubbles of up to 15 cm long or area similar to A5*
B	Burnt surfaces	Burnt surfaces (area similar to A4*)
C	Surpluses to grind	Surpluses or loss of material - repair by grinding
D	Wrinkling	Wrinkling or “alligatoring”
E	Scratches	Small scratches (area similar to A4*) and scratches to be repaired
F	Cracks	Cracks (up to 25 cm long or area similar to A4*)
G	Inprint	Fibre Pattern (inprint)
H	Deformation	Deformation
I	Demould defects	Demould defects (up to 25 cm long or area similar to A4*)
J	Delaminations	Delaminations and other construction laminate defects
K	Porosity	Porosity
L	Dimplings	Accelerator spots / Dimplings
M	Dry reinforcement	Dry glass reinforcements
N	Spots	Spots
O	Anti-sliding defects	defects of Anti-sliding surface (3 cm <sup>2</sup> )
P	Matte finish	Matte finish
Q	Other defects	Other defects

\* A4 and A5 are the size of the surface that corresponds to the size of the sheet of paper in the appropriate size

The defects of the structural laminate and delamination (J), areas of dry reinforcement (M) and large air bubbles (A) are the most serious defects occurring in the lamination process – their presence significantly reduces the strength of the structure. The remaining technological defects assessed during the quality control are cosmetic defects that reduce the value of the final product or contribute indirectly to the reduction of the service life of laminates [38].

Dry reinforcement (M) is caused by the resin's gelling time being too short, which may be caused by failure to meet temperature and humidity conditions or incorrect proportions of resin and hardener. It also happens that dry reinforcement (M) occurs by underestimating the amount of resin needed to laminate the laminate layer. Damage to the anti-skid surface (O) on the deck can be caused by improper preparation of the mold (I), inaccurate application of the separating layer or not preparing it (polishing and dust removal). This defect (O) can also be due to the use of an inappropriate lamination technology or laminate demoulding process. Repairing such damage (O) often involves removing a significant area and replacing it with a new anti-skid element. Scratches on the hull (E) usually occur during rough handling of the final product, but they can also appear at the beginning of the process by improper grinding and polishing of the mold, not cleaning the mold surface before applying the first layer of gelcoat.

The smoothness and general condition of the yacht's outer surface largely depends on the quality of the mold preparation, because any imperfections in the preparation will be transferred into the form of defects (e.g. scratches (E), matt surface (P), stains (N) and porosity (K)) on the surface of the gelcoat. In some cases, poor preparation of the mold – failure to cover the mold with molding gelcoat causes the reinforcement texture to reflect on the gelcoat surface (G). This is an defect that needs to be caught at an early stage of production so that subsequent boats produced in this form do not have to be repaired. The so-called INPRINT (G), i.e. the mapping of the reinforcement texture on the surface of the gelcoat, occurs when the gelcoat layer is too thin [37].

Repairing this type of damage (G) involves grinding a part of the material (gelcoat and part of construction laminate) and applying a layer of gelcoat from the outside, and then grinding and polishing to obtain a smooth surface. Elimination of this type of defects is possible already at the laminate design stage by using the so-called SkinCoat layers consisting of a resin layer with a thin mat laid on a gelcoat before applying the structural laminate [10]. Air bubbles (A) may be caused by irregular application of the resin, lack of the resin degassing process (partially, when the resin is mechanically mixed with the hardener, we introduce air bubbles into it), incorrect temperature (outside the range required by the technological card) in the working room. Such defects may occur in both the gelcoat and the structural laminate. A small amount of small air bubbles in the structural laminate is natural and does not significantly reduce the strength properties of the laminate, but large bubbles act as dry reinforcement and weaken the strength of the element [4]. Air bubbles (A) in the gelcoat layer can cause faster degradation of the protective

layer, which is the gelcoat, and allow water to penetrate the structural laminate [23].

Wrinkling, also known as “alligatoring” (D), is a defect of a gelcoat caused by too quick deformation of the laminate, too thin a layer or insufficient cure of the gelcoat. The gelcoat layer plays an aesthetic role, but you should not forget about its protective effect. Structural laminate is much less resistant to water, therefore appropriate protective layers (gelcoat or complex systems consisting of gelcoat, skincoat and barriercoat) must be applied on its surface [23].

When performing repairs using complex protection systems, we are not able to recreate the correct layout and thickness of these layers. Therefore, when using advanced materials, a high technological regime should be maintained in order to avoid defects. Most gelcoats are prepared by the manufacturer in the appropriate colour, but the pigment contained in them may be subject to slow sedimentation or agglomeration. Poor mixing of the gel coat prior to application may result in stains (N) and colour irregularities. If pigments or dyes are used to change the colour of the gelcoat, failure to care for the proportions and thorough mixing may also cause stains and colour irregularities (N). Such defects can also be caused by the action of UV rays on the uncured product [6].

A matt finish (P) or rough surface can be the result of poor hardening, often caused by poor mixing of the resin with the hardener. It may also be the result of poor laminate deformation due to mistakes made during the application and preparation of the release layer. There are also defects resulting from the degradation of materials during storage – incorrect temperature and humidity conditions, contamination with grinding products, dust, expiry date (for resins).

Some of the defects result from incorrect proportions of resin and hardener, others from too thick or too thin gel coat. The influence of the ambient temperature is also significant. From this information it can be concluded that some of the material defects depend on common factors. Such conclusions contributed to the issue of creating association rules for defects occurring in the lamination process.

## PROBLEM FORMULATION

The current research work and the results presented in the literature concern the influence of production methods on the mechanical properties or service life of laminates. Science focuses on the development of new materials and manufacturing techniques, and not on the analysis of the causes of defects in old but still widely used methods. This work is aimed at combining modern data processing techniques with the analysis of technological defects in the basic manufacturing technique.

It is easy to indicate works which describe the causes of defects even in guides and manufacturers' manuals [50, 51], but there are no works on dependencies and rules between coexisting defects.

The goal of this research is to determine association rules to improve the monitoring stage. A system of knowledge that considers issues concerning dependencies of the defects

occurring can allow prediction of the possible consequences of the occurrence of similar defects, allowing repair processes and additional costs to be minimized.

## APRIORI ALGORITHM AND FORMULATION OF ASSOCIATION RULES

The algorithms *Apriori* and *Apriori TID* for discovering strong binary association rules were described in 1994 [2]. Let  $L = \{l_1, l_2, \dots, l_m\}$  describe the set of elements. A transaction of elements or transaction is any nonempty subset  $T$  of  $L$ ,  $T \subseteq L$  i  $T \neq \emptyset$ .

$T$  supports an element  $x \in L$  if  $x$  is  $T$ ,  $x \in T$ .  $T$  supports set  $X \subseteq L$  if  $T$  supports every element in  $X$ ,  $X \subseteq T$ . The size of transaction  $T$ ,  $size(T)$ , is the number of elements in  $T$ . The set of input data  $D$  is called the set of  $T$ ,  $D = (T_1, T_2, \dots, T_n)$  where  $T_i \subseteq L$ ,  $i = 1, 2, \dots, n$ .

The binary association rule is the relation  $X \rightarrow Y$ , where  $X \subseteq L$ ,  $Y \subseteq L$  i  $X \cap Y \neq \emptyset$ .  $X$  is called the antecedent of the rule, and  $Y$  is the consequent of the rule. The binary association rule  $X \rightarrow Y$  has  $supp(X \rightarrow Y)$  in the data set  $D$ ,  $0 \leq supp \leq 1$ .

$$supp(X \rightarrow Y) = \frac{|\{T_i \in D \mid T_i \text{ wspiera } X \cup Y\}|}{|D|}, \quad (1)$$

confidence  $conf(X \rightarrow Y)$  in the database  $D$ ,  $0 \leq conf \leq 1$ :

$$conf(X \rightarrow Y) = \frac{|\{T_i \in D \mid T_i \text{ wspiera } X \cup Y\}|}{|\{T_j \in D \mid T_j \text{ wspiera } X\}|}, \quad (2)$$

and  $lift(X \rightarrow Y)$  in the database  $D$

$$lift(X \rightarrow Y) = \frac{conf(X \rightarrow Y)}{supp(Y)}. \quad (3)$$

Support is a value measure of the association rule, because it defines the number of transactions in set  $D$  which confirm said rule.

Apriori pseudocode

INPUT: Database

OUT: Large item set

//  $L = \{l_1, l_2, \dots, l_m\}$

$L_1 = \{\text{large one-item sets}\}$ ;

for ( $k = 2$ ;  $L_{k-1} \neq \emptyset$ ;  $k++$ )

//New candidates

$C_k = \text{apriori\_gen}(L_{k-1})$ ;

for all transactions  $t \in D$

//Candidates in  $t$

$C_t = \text{subset}(C_k, t)$ ;

for all candidates  $c \in C_t$

$c.\text{count}++$

end

$F_k = \{c \in C_k \mid c.\text{count} \geq \text{minsup}\}$ ;

end

end

Answer =  $\bigcup_k L_k$

## SIMULATIONS

The lamination process was observed in 2013–2017. The data used in the research were collected during observation of the production of 6 yachts models with the following parameters: length 6–9 m. and width 2.5–3 m, immersion 0.4–0.75 m and total mass 1000–3000 kg (Tab. 2).

Tab. 2. Information about model observed in 2013–2017

No.	Name	Length [m]	Width [m]	Immersion [m]	Total mass [kg]	Set sample size [u]
1	CC6LA	6.4	2.48	0.43	1036	542
2	CW6L	6.59	2.48	0.66	1050	365
3	CW8K	8.42	2.98	0.75	2540	99
4	CW8P					102
5	MF8K	8.90	2.99	0.63	3060	168
6	MF8P					

Each unit produced is controlled. The number of faults and mistakes is described quantitatively on a special card. An example of a quality control card is shown in Fig. 1.

UNIT	TID	Upside part (shiny)			Downside part (mat)		
		PREPA	Quantity	Unit time	PREPA	Quantity	Unit time
A	Pęcherze powietrzne (do 15cm lub A5)	1	10	15	1	10	15
B	Przypalenia (A4)	1	5	10	1	5	10
C	Ubyteki żelazotu	1	1	1	1	1	1
D	Raki	1	4	8	1	4	8
E1	Rysy do zeszlifowania (A4)	1	2	4	1	2	4
E2	Rysy do naprawy	1	1	1	1	1	1
F	Pęknięcia (do 25cm lub A4)	1	1	1	1	1	1
G	Odbicia włókien	1	17	34	1	17	34
H	Deformacje	1	1	1	1	1	1
I	Wady z formy (do 25cm lub A4)	1	15	30	1	15	30
J	Wady laminatu (niekierunkowe, wady w kierunku)	1	1	1	1	1	1
K	Porowatość	1	1	1	1	1	1
L	Plamy i kropki utwardzacza	1	1	1	1	1	1
M	Niedosygnięcie szkła	1	1	1	1	1	1
N	Plamy	1	1	1	1	1	1
O	Uszkodzenia przeciwsłoneczne (3cm <sup>2</sup> )	1	1	1	1	1	1
P	Matowa powierzchnia	1	7	14	1	7	14
Q	Inne wady	0.5	1	0.5	1	0.5	0.5
QUOTATION shiny		337			QUOTATION mat		0
TOTAL QUOTATION OF REPAIR :							337 h

Fig. 1. Example of a quality control card

Based on the information thus compiled, a set was created  $T_i$ . It contains a list of all mistakes that were made in the production of each yacht. An example data set (TID),  $T_i$  for  $i = 1..n$ , is presented in Table 3.

Tab. 3. Set of sample transactions  $T_i$ ,  $n = 5$

Transaction ID	Item Defects
$T_1$	{A, B, C, D, F, H, I, O, P}
$T_2$	{A, C, F, H, I, O, P}
$T_3$	{A, B, C, G, I, J, O, P}
$T_4$	{A, B, F, H, I, K, O, P}
$T_5$	{A, B, C, D, E, H, I, J, O, P}

First, the elements of the  $k$ -set, for  $k = 1$ , were determined. An example of samples occurring in this form is described in Tables 3 and 4. Information about the occurrence of the specified defect during the production of the  $i$ -th yacht ( $T_i$ ). The number of all transactions is  $n = 542$ . Binary representation was used in the Apriori algorithm as shown in the pseudocode.

Tab. 4. An example binary table  $T_i$ ,  $n = 5$

Defect symbol	$T_1$	$T_2$	$T_3$	$T_4$	$T_5$
A	1	1	1	1	1
B	1	0	1	1	1
C	1	1	1	0	1
D	1	0	0	0	1
E	0	0	0	0	1
F	1	1	0	1	0
G	0	0	1	0	0
H	1	1	0	1	1
I	1	1	1	1	1
J	0	0	1	0	1
K	0	0	0	1	0
L	0	0	0	0	0
M	0	0	0	0	0
N	0	0	0	0	0
O	1	1	1	1	1
P	1	1	1	1	1
Q	0	0	0	0	0

Following the algorithm described in Chapter 3, the full set of samples for all yachts was analysed. The procedure is presented in detail only for the (CC6LA) case (Tab. 5), where  $n = 542$ .

Tab. 5. Set of values for all defects and  $(C_1)$ ,  $conf(C_1)$ , and item set  $C_1, F_1$

Defect symbol	$count(C_1)$	$conf(C_1)$ (%)	$F_1$
A	542	100	Yes
B	505	93.2	Yes
C	366	67.5	No
D	192	35.4	No
E	180	33.2	No
F	207	38.2	No
G	426	78.6	No
H	103	19	No
I	534	98.5	Yes
J	7	1.3	No
K	65	12	No
L	58	10.7	No
M	9	1.7	No
N	6	1.1	No
O	343	63.3	No
P	526	97	Yes
Q	3	0.6	No

The best results for the Apriori algorithm were acquired for values of  $sup = 0.9$  and  $conf = 0.8$ . Using the full data set  $n = 542$ . For the purpose of building the frequent sets,  $k = 2$  elements of were used. Information on the elements is listed in Tables 5 and 6.

The most common defects are: A, B, I and P, less frequent defects: G, C. Other defects do not occur more often than 40% of the yachts produced. A and B are rather independent of each other. The defect I is generated by causes other than the A and B defects, while the P defect may depend on the B and / or I defects. The next step is to determine frequent 2-element sets (Table 6).

Tab. 6. Set of values for all defects,  $count(C_2)$ ,  $conf(C_2)$ , and item set  $C_2, F_2$

$X$	$count(C_2)$	$conf(X)$	$X_2$
{A,B}	505	93.2	Yes
{A,G}	426	78.6	No
{A,I}	534	98.5	Yes
{A,P}	526	97	Yes
{B,G}	402	74.2	No
{B,I}	502	92.6	Yes
{B,P}	495	91.3	No
{G,I}	423	78.3	No
{G,P}	419	77.3	No
{I,P}	521	96.1	Yes

To create three-element frequent sets  $k = 3$ , the sets {A, B}, {A, I}, {B, I}, {I, P} were selected (Table 7).

Tab. 7. Set of values for all defects,  $count(C_3)$ ,  $conf(C_3)$ , and item set  $C_3, F_3$

$X$	$count(C_3)$	$conf(X)$	$F_3$
{A,B,I}	502	92.6	Yes
{A,B,P}	495	91.3	No
{A,I,P}	521	96.1	Yes

In the process of building association rules, only {A, B, I} and {A, I, P} were taken into account. The algorithm allowed 32 association rules to be defined (Fig. 7).

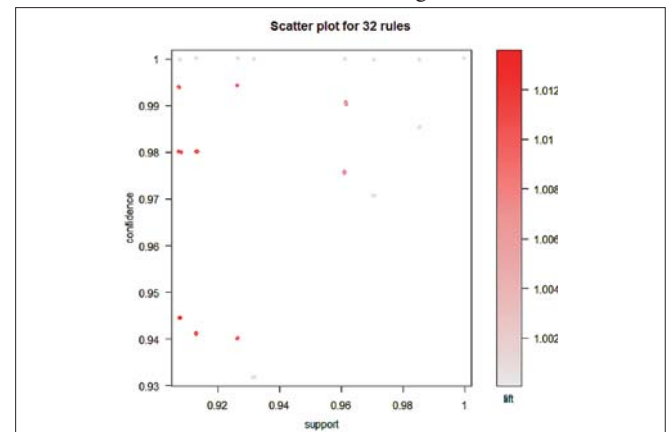


Fig. 7. Scatter plot of 32 association rules for model J1CC6LA; results for Apriori algorithm were acquired for values of  $supp = 0.9$  and  $conf = 0.8$

The value lift = 1 indicates defects occurring independently of each other. A value of lift > 1 indicates a positive correlation while lift < 1 indicates a negative correlation. After analysing the results obtained, the most important rules were selected (Fig. 8).

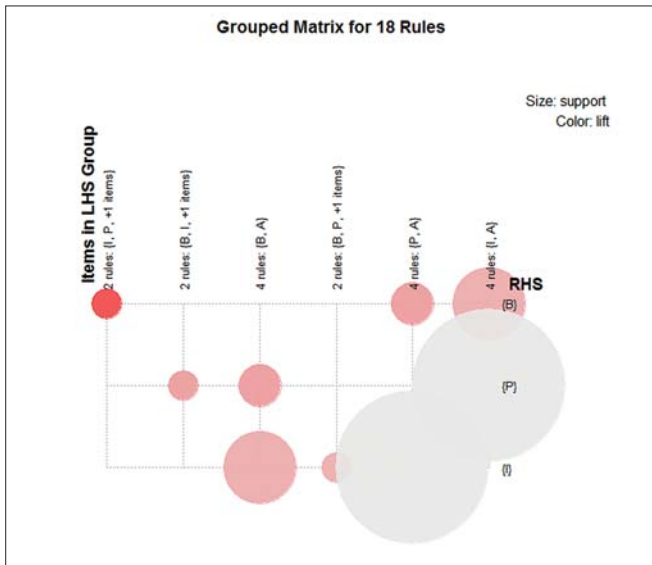


Fig. 8. Grouped matrix for 18 rules, where lift > 1 (Model: J1CC6LA, supp = 0.9, conf = 0.8)

After elimination of unnecessary rules, 18 rules were left in the set. The lift value indicates high associations between {P}, {B}, and {I}, respectively, and “matte finish”, “burnt surfaces” (A4), and “moulds defects”.

The lamination process of other yacht models, namely: CC6LA, CW6L, CW8K, CW8P, MF8K and MF8P, was analysed analogically. Correlations between defects that are rare in the laminating process are particularly interesting. Therefore, the value of the parameter was taken from the range < 0.1 to 0.9 > (Tables 8–13).

Tab. 8. Set of information about association rules with values: supp (X → Y) ≥ 0.9; conf (X → Y) ≥ 0.9; lift (X → Y) > 1; model: J2(C6LA)

X → Y	supp (*)	conf (*)	lift (*)
{P} ⇒ {B}	0.9132841	0.9801980	1.010014
{B} ⇒ {P}	0.9132841	0.9410646	1.010014
{I,P} ⇒ {B}	0.9077491	0.9443378	1.013527
{B,I} ⇒ {P}	0.9077491	0.9800797	1.009892
{B} ⇒ {I}	0.9261993	0.9940594	1.008952
{I} ⇒ {B}	0.9261993	0.9400749	1.008952
{B,P} ⇒ {I}	0.9077491	0.9939394	1.008830
{P} ⇒ {I}	0.9612546	0.9904943	1.005333
{I} ⇒ {P}	0.9612546	0.9756554	1.005333

Tab. 9. Set of information about association rules with values: supp (X → Y) ≥ 0.8; conf (X → Y) ≥ 0.9; lift (X → Y) ≥ 1; model: J2(CC6L)

X → Y	supp (*)	conf (*)	lift (*)
{I,P} ⇒ {B}	0.9041096	0.9510086	1.030024
{B,I} ⇒ {P}	0.9041096	0.9880240	1.027432
{B} ⇒ {P}	0.9095890	0.9851632	1.024457
{P} ⇒ {B}	0.9095890	0.9458689	1.024457
{B,P} ⇒ {I}	0.9041096	0.9939759	1.021975
{B} ⇒ {I}	0.9150685	0.9910979	1.019016
{I} ⇒ {B}	0.9150685	0.9408451	1.019016
{P} ⇒ {I}	0.9506849	0.9886040	1.016452
{I} ⇒ {P}	0.9506849	0.9774648	1.016452

Tab. 10. Set of information about association rules with parameters of supp (X → Y) ≥ 0.4; conf (X → Y) ≥ 0.6; lift (X → Y) ≥ 0.8; model: J3(CW8K)

X → Y	supp (*)	conf (*)	lift (*)
{H} ⇒ {C}	0.4040404	0.7547170	1.1151788
{I} ⇒ {G}	0.4141414	0.7068966	1.0291582
{I} ⇒ {C}	0.4040404	0.6896552	1.0190427
{C} ⇒ {G}	0.4343434	0.6417910	0.9343723

Tab. 11. Set of information about association rules with parameters: supp (X → Y) ≥ 0.4; conf (X → Y) ≥ 0.8; lift (X → Y) > 0.8; J4(CW8P)

X → Y	supp (*)	conf (*)	lift (*)
{I,O} ⇒ {B}	0.4411765	0.9375000	1.8389423
{O} ⇒ {B}	0.4509804	0.8518519	1.6709402
{B} ⇒ {O}	0.4509804	0.8846154	1.6709402
{B,I} ⇒ {O}	0.4411765	0.8823529	1.6666667
{B} ⇒ {I}	0.5000000	0.9807692	1.3518711
{B,O} ⇒ {I}	0.4411765	0.9782609	1.3484136
{O} ⇒ {I}	0.4705882	0.8888889	1.2252252
{G} ⇒ {I}	0.4901961	0.7142857	0.9845560
{C} ⇒ {I}	0.4019608	0.7068966	0.9743709

Tab. 12. Set of information about association rules with parameters:  $supp(X \rightarrow Y) \geq 0.1$ ;  $conf(X \rightarrow Y) \geq 0.9$ ;  $lift(X \rightarrow Y) > 1.5$ ; J5(MF8K)

$X \rightarrow Y$	$supp(*)$	$conf(*)$	$lift(*)$
{F,K} => {H}	0.1011905	1.0000000	1.768421
{I,K} => {H}	0.1428571	1.0000000	1.768421
{F,I,K} => {H}	0.1011905	1.0000000	1.768421
{B,I,K} => {H}	0.1369048	1.0000000	1.768421
{K} => {H}	0.1428571	0.9600000	1.697684
{B,K} => {H}	0.1369048	0.9583333	1.694737
{E,F,H} => {B}	0.1607143	0.9642857	1.572816
{K} => {B}	0.1428571	0.9600000	1.565825
{H,K} => {B}	0.1369048	0.9583333	1.563107

Tab. 13. Set of information about association rules with parameters:  $supp(X \rightarrow Y) \geq 0.1$ ;  $conf(X \rightarrow Y) \geq 0.8$ ;  $lift(X \rightarrow Y) > 1.5$ ; J6(MF8P)

$X \rightarrow Y$	$supp(*)$	$conf(*)$	$lift(*)$
{O} => {G}	0.1379310	0.9230769	1.889593
{L} => {B}	0.1264368	1.0000000	1.380952
{I,K} => {B}	0.3678161	0.9696970	1.339105
{E} => {B}	0.1666667	0.9666667	1.334921
{K,P} => {B}	0.1379310	0.9600000	1.325714
{F,C,I,K} => {B}	0.2471264	0.9555556	1.319577
{C,E} => {B}	0.1091954	0.9500000	1.311905
{H,K} => {B}	0.1091954	0.9500000	1.311905
{K} => {B}	0.3735632	0.9285714	1.282313
{F,H} => {C}	0.1321839	0.8846154	1.241315
{F,G} => {C}	0.1896552	0.8250000	1.157661
{H} => {C}	0.1839080	0.8000000	1.122581

Due to the lack of information about situations in which there is no "A" defect, it was assumed that it is independent and the rules in which it participates were not considered. First, sets of rules were defined to define the relationship between defects during the production of individual models. The next stage of the dependency analysis focused on defects that rarely appear (Fig. 9).

Table 14 Set of information about association rules with parameters: model: CC6LA, CW6L, CW8K, CW8P, MF8K, MF8P, n = 1450, The obtained rules were saved in Table 12. Symbols indicate high (•), medium (■), and low (◦) trust in the rule for the selected model.

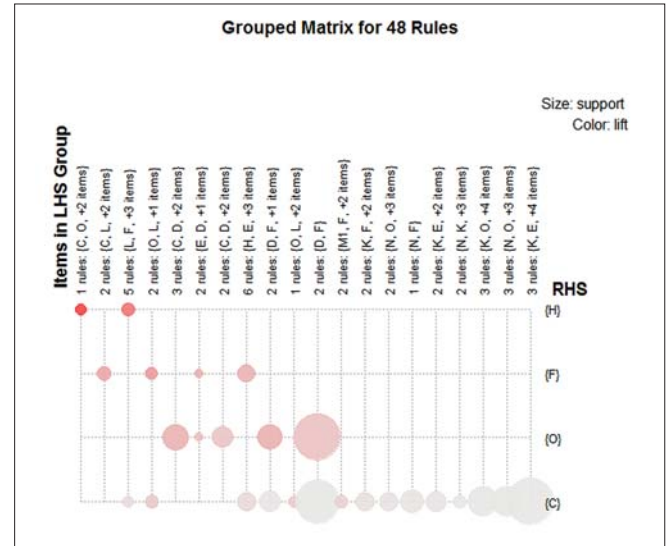


Fig. 9. Grouped matrix for 48 rules, where  $lift > 1$  (Model: J1CC6LA, J2CC6LA, J3CW8K, J4CW8P, J5MF8K, J6MF8P,  $supp = 0.1$ ,  $conf = 0.8$ ,  $n = 1450$ )

Tab. 14. Set of information about association rules with parameters: model: J1(CC6LA), J2(CC6L), J3(CW8K), J4(CW8P), J5(MF8K), J6(MF8P), n = 1450

$X \rightarrow Y$	J1	J2	J3	J4	J5	J6
{ } => {A}	•	•	•	•	•	•
{E} => {B}	◦	◦	◦	◦	◦	•
{I} => {B}	•	•	◦	◦	◦	◦
{K} => {B}	◦	◦	◦	◦	•	•
{L} => {B}	◦	◦	◦	◦	◦	•
{O} => {B}	◦	◦	■	•	◦	◦
{P} => {B}	•	•	◦	◦	◦	◦
{C,E} => {B}	◦	◦	◦	◦	◦	•
{H,K} => {B}	◦	◦	◦	◦	•	•
{I,K} => {B}	◦	◦	◦	◦	◦	•
{I,P} => {B}	•	•	◦	◦	◦	◦
{K,P} => {B}	◦	◦	◦	◦	◦	•
{E,F,H} => {B}	◦	◦	◦	◦	•	◦
{F,C,I,K} => {B}	◦	◦	◦	◦	◦	•
{D} => {C}	■	■	■	■	■	■
{H} => {C}	◦	◦	■	◦	◦	•
{I} => {C}	◦	◦	■	◦	◦	◦
{E,F,H,L} => {C}	■	■	■	■	■	■
{F,G} => {C}	◦	◦	◦	◦	◦	•
{F,H} => {C}	◦	◦	◦	◦	◦	•
{F,H,L} => {C}	■	■	■	■	■	■
{F,H,L,O} => {C}	■	■	■	■	■	■
{E,M} => {C}	■	■	■	■	■	■
{H,L} => {C}	■	■	■	■	■	■
{H,L,O} => {C} or {F}	■	■	■	■	■	■
{C,H,L,O} => {F}	■	■	■	■	■	■
{C} => {G}	◦	◦	■	◦	◦	◦
{I} => {G}	◦	◦	■	◦	◦	◦

Tab. 14. Set of information about association rules with parameters: model: J1(C6LA), J2(CC6L), J3(CW8K), J4(CW8P), J5(MF8K), J6(MF8P), n = 1450

$X \rightarrow Y$	J1	J2	J3	J4	J5	J6
{O} => {G}	o	o	o	o	o	•
{B,K} => {H}	o	o	o	o	•	o
{B,I,K} => {H}	o	o	o	o	•	o
{C,F,L,O} => {H}	■	■	■	■	■	■
{F,K} => {H}	o	o	o	o	•	o
{F,I,K} => {H}	o	o	o	o	•	o
{F,L,O} => {H}	■	■	■	■	■	■
{I,K} => {H}	o	o	o	o	•	o
{K} => {H}	o	o	o	o	•	o
{B} => {I}	•	•	o	•	o	o
{B,O} => {I}	o	o	o	•	o	o
{B,P} => {I}	•	•	o	o	o	o
{O} => {I} or {B}	o	o	o	•	o	o
{~C} => {I}	o	o	o	■	•	o
{~G} => {I}	o	o	o	■	o	o
{P} => {I}	•	•	o	o	o	o
{B} => {O}	o	o	o	•	o	o
{C,D,H} => {O}	■	■	■	■	■	■
{C,D,F,H} => {O}	■	■	■	■	■	■
{D} => {O}	■	■	■	■	■	■
{D,H} => {O}	■	■	■	■	■	■
{D,F,H} => {O}	■	■	■	■	■	■
{B} => {P}	•	•	o	o	o	o
{B,I} => {P}	•	•	o	o	o	o
{I} => {P}	•	•	o	o	o	o

In manual production it is very easy to get air bubbles in the laminate, therefore the defect (A) occurs with such a high probability coefficient. The rules obtained can be logically justified, because the deformed gelcoat is repaired by grinding and rebuilding the correct gelcoat layer. Grinding is necessary in case of defects: scratches to be sanded, cracks, deformations, hardener stains and drops, and glass under-saturation. The occurrence of anti-skid damage is repaired by grinding and removing a fairly large surface and supplementing with new elements. Wearing defects, cracks, anti-skid damage and hardener stains often contribute to the deformation defect. The anti-skid failure defect most often coexists with the following defects: surpluses to grind, gel coat deformations as well as cracks and deformations.

Not all the observed relationships can be easily justified. They could have had a more complex basis. The possible reasons for their existence should be considered more deeply and analysed, for example, if there is an defect of “mold defects” and “matt surface”, then there is also a “burn” defect. The relationship between defects: “burns” and “mold defects”, which can be observed during the production of selected models, requires

more consideration. Additionally, the relationship between defects: “porosity” and “deformation”; “Anti-skid damage” and “rebound fibers”;

The low probability of defects resulting from “deformation” and “defects to be ground” is puzzling – these defects should have a high confidence factor.

An interesting rule was generated for the CW8K model. For 64% of the units the following relationship was confirmed: defect: “fiber reflections” occurs if there was no “surpluses to grind” defect. The observation may result if there are allowances for grinding, it is most often because the layer of gelcoat was too thick, and the defect of “fiber reflection” occurs when the gelcoat is too thin. Rules whose successor contains a “burn” defect are quite common in the resulting set. This can be justified by a fairly large number of occurrences of this defect, as they may not have practical justification.

## SUMMARY

The article reveals the dependencies of the occurrences of specific defects, which were shown by association and formulation of the association rules. Grouping of defects and their dependencies can allow for better monitoring, control, and implementation of prevention activities, which can allow minimization of repair costs and avoidance of additional costs.

This work used the Apriori algorithm and association methods. The research was conducted on data acquired from the lamination process of one chosen yacht. To perform the simulation, a sample size of 1450 samples observed in 2013–2017 was used. Execution of the algorithm allowed the formulation of a set of association rules which can be used to specify the certainty of occurrence of a given defect. Finding dependencies can reduce uncertainty in the occurrence of specific defects and lead to improvement of quality and reduction of costs. The use of new methods and tools backed by artificial intelligence relating to Big Data allows better management of uncertainty and complexity.

## REFERENCES

1. Amran, Y. M., Alyousef, R., Rashid, R. S., Alabduljabbar, H., & Hung, C. C.: *Properties and applications of FRP in strengthening RC structures: A review*. In Structures, Vol. 16, pp. 208–238, Elsevier 2018.
2. Agrawal, R., R. Srikant: *Fast Algorithms for Mining Association Rules in Large Databases*, Journal of Computer Science and Technology, 15, 1994, 487–499.
3. Alizadeh, F., Sutherland, L. S., & Soares, C. G.: *Effect of vacuum bag pressure on the flexural properties of GFRP composite laminates*. Maritime technology and engineering, 3, 2016, 429–434.

4. Bolf, D., Zamarin, A., & Basan, R.: *Composite Material Damage Processes*. Pomorski zbornik, (3), 2020, 307–323.
5. Bossi, R. H., & Giurgiutiu, V.: *Nondestructive testing of damage in aerospace composites*. In *Polymer Composites in the Aerospace Industry*, Woodhead Publishing 2015, 413–448.
6. Bugg, D.: *New D-Iso/NPG gelcoat offers exceptional UV colour stability: Feature Marine*. JEC composites, (67), 2011, 42–46.
7. Calabrese, L., Di Bella, G., & Fiore, V.: *Manufacture of marine composite sandwich structures*. In *Marine Applications of Advanced Fibre-Reinforced Composites*, Woodhead Publishing 2016, 57–78.
8. Castegnaro, S., Gomiero, C., Battisti, C., Poli, M., Basile, M., Barucco, P., ... & Lazzaretto, A.: *A bio-composite racing sailboat: Materials selection, design, manufacturing and sailing*. *Ocean Engineering*, 133, 2017, 142–150.
9. Cpalka, K., K. Łapa, A. Przybył: *A New Approach to Design of Control Systems Using Genetic Programming, Information Technology and Control*. 44, 2015, 433–442.
10. Cucinotta, F., Guglielmino, E., & Sfravara, F.: *Life cycle assessment in yacht industry: A case study of comparison between hand lay-up and vacuum infusion*. *Journal of cleaner production*, 142, 2017, 3822–3833.
11. Fragassa C.: *Marine Applications of Natural Fibre-Reinforced Composites: A Manufacturing Case Study*. In: Pellicer E. et al. (eds) *Advances in Applications of Industrial Biomaterials*. Springer, Cham. 2017, [https://doi.org/10.1007/978-3-319-62767-0\\_2](https://doi.org/10.1007/978-3-319-62767-0_2).
12. Gaiotti, M., & Rizzo, C. M.: *Buckling behavior of FRP sandwich panels made by hand layup and vacuum bag infusion procedure*. Rizzuto & Guedes Soares (eds), *Sustainable Maritime Transportation and Exploitation of Sea Resources*, 2011, 385–392.
13. Gelesz, P., Karczewski, A., Kozak, J., Litwin, W., & Piątek, Ł.: *Design methodology for small passenger ships on the example of the ferryboat Motława 2 driven by hybrid propulsion system*. *Polish Maritime Research*, 24(s1), 2017, 67–73.
14. Gombos, Z. J., & Summerscales, J.: *In-mould gel-coating for polymer composites*. *Composites Part A: Applied Science and Manufacturing*, 91, 2016, 203–210.
15. Hashin, Z.: *Failure Criteria for Unidirectional Fiber Composites 1*, 1980.
16. Hassen, A. A., Taheri, H., & Vaidya, U. K.: *Non-destructive investigation of thermoplastic reinforced composites*. *Composites Part B: Engineering*, 97. 2016, 244–254.
17. Hoge, J., & Leach, C., *Epoxy resin infused boat hulls*. *Reinforced Plastics*, 60(4), 2016, 221–223.
18. Jang, J. W., Jeong, S., Oh, D., Cho, J. H., & Noh, J.: *Test and Evaluation Procedure of Foam Core Materials for Composite Ships*. *Journal of the Korean Society of Marine Environment & Safety*, 26(3), 2020, 286–296.
19. Koziół, M., Wieczorek, J., & Hekner, B.: *Surface quality and mechanical properties of epoxy-glass fibre laminates manufactured by RTM method with use of gelcoat*. *Composites Theory and Practice (Kompozyty)*, 16(3), 2016, 189–195.
20. Landowski, M., Budzik, M., & Imielińska, K. (2011). *On degradation of glass / polyester laminate immersed in water*. *Advances in Materials Science*, 11 (1), 35–39.
21. Landowski, M., & Imielińska, K.: *Degradation of GFRP Marine Laminates with Nano Particle Modified Coatings*, *Advances in Materials Science*, 13(2), 2013, 19–22., doi: <https://doi.org/10.2478/adms-2013-0006>.
22. Landowski, M., Budzik, M., & Imielińska, K., *Water sorption and blistering of GFRP laminates with varying structures*. *Advances in materials science*, 12(4), 2013 23–29.
23. Landowski, M., Budzik, M., & Imielińska, K. *Water absorption and blistering of glass fibre-reinforced polymer marine laminates with nanoparticle-modified coatings*. *Journal of Composite Materials*, 48(23), 2014, 2805–2813.
24. Liu Cai-yan Youfa Sun Youfa Sun, *Application of Data Mining in Production Quality Management*, Conference: Intelligent Information Technology Application, 2009. IITA 2009. Third International Symposium on Volume: 2, DOI: 10.1109/IITA.2009.81.
25. Mathijssen, D. *Designing boats for the Volvo Ocean Race: An ongoing process of optimization and finding the right compromise*. *Reinforced Plastics*, 62(4), 2018, 203–207.
26. Mehmed Kantardzic. *Data Mining: Concepts, Models, Methods, and Algorithms*. Wiley-IEEE Press.2002.10
27. Mouritz, A. P., Gellert, E., Burchill, P., & Challis, K. *Review of advanced composite structures for naval ships and submarines*. *Composite structures*, 53(1), 2001 21–42.
28. Musio-Sale, M., Nazzaro, P. L., & Peterson, E. *Visions, Concepts, and Applications in Additive Manufacturing for Yacht Design*. In *International Conference on Applied Human Factors and Ergonomics* (pp. 401–410). Springer, Cham. 2019, July.
29. Naik, N. K., Sirisha, M., & Inani, A. *Permeability characterization of polymer matrix composites by RTM/VARTM*. *Progress in aerospace sciences*, 65, 2014, 22–40.

30. Neşer, G. *Polymer based composites in marine use: history and future trends*. Procedia engineering, 194, 2017, 19–24.
31. Nikbakt, S., Kamarian, S., & Shakeri, M. *A review on optimization of composite structures Part I: Laminated composites*. Composite Structures, 195, 2018, 158–185.
32. Niksa-Rynkiewicz, T., & Witkowska, A. *Analysis of Impact of Ship Model Parameters on Changes of Control Quality Index in Ship Dynamic Positioning System*, Polish Maritime Research, 26(1), 2019, 6-14. doi: <https://doi.org/10.2478/pomr-2019-0001>.
33. Nowak, B.A., R.K. Nowicki, M. Woźniak, C. Napoli: *Multi-class Nearest Neighbour Classifier for Incomplete Data Handling*, in: Springer, Cham, 2015, 469–480.
34. Oral, I.: *Characterization of damages in materials by computer-aided tap testing*. In IOP Conference Series: Materials Science and Engineering, Vol. 707, No. 1, p. 012019, IOP Publishing, 2019.
35. Osborne, T., *An introduction to resin infusion*. Reinforced Plastics, 58(1), 2014, 25–29.
36. Podsiadlo, A., W. Tarelko: *Modelling and Developing a Decision-Making Process of Hazard Zone Identification in Ship Power Plants*. International Journal of Pressure Vessels and Piping, 83, 2006, 287–298. doi.org/10.1016/j.ijpvp.2006.02.017.
37. Pomázi, Á., & Toldy, A. *Multifunctional gelcoats for fiber reinforced composites*. Coatings, 9(3), 2019, 173.
38. Quattrocchi, A., Freni, F., & Montanini, R., *Air-coupled ultrasonic testing to estimate internal defects in composite panels used for boats and luxury yachts*. International Journal on Interactive Design and Manufacturing (IJIDeM), 14(1), 2020, 35–41.
39. Ray, B. C., & Rathore, D., *Environmental damage and degradation of FRP composites: A review report*. Polymer Composites, 36(3), 2015, 410–423.
40. Rubino, F., Nisticò, A., Tucci, F., & Carlone, P., *Marine application of fiber reinforced composites: a review*. Journal of Marine Science and Engineering, 8(1), 2020, 26.
41. Scott, R.J.: *Fiberglass Boat Design and Construction*, Society of Naval Architects and Marine Engineers, 1996.
42. Singha, M., & Singha, K., *Applications of textiles in marine products*. Marine Science, 2(6), 2012, 110–119.
43. Smoleń, J., Cyganek, A., & Kozioł, M., *Manufacture of transmission housing by contact layer technique using vacuum bag*. Compos. Theory Pract, 19, 2019, 18–22.
44. Sørensen, S. N., & Lund, E., *Topology and thickness optimization of laminated composites including manufacturing constraints*. Structural and Multidisciplinary Optimization, 48(2), 2013, 249–265.
45. Stewart, R., *Better boat building—trend to closed-mould processing continues*. Reinforced plastics, 55(6), 2011, 30–36.
46. Such M., Ward C., Hutabarat W., Tiwari A., *Intelligent Composite Layup by the Application of Low Cost Tracking and Projection Technologies*, Procedia CIRP, 25, 2014, 122–131, <https://doi.org/10.1016/j.procir.2014.10.020>.
47. Summerscales, J., Hoppins, C., Anstice, P., Brooks, N., Wiggers, J., Yahathugoda, D., ... & Cooper, M., *In-mould gel coating for resin transfer moulding*. In The 10 th International Conference on Flow Processes in Composite Materials (FPCM10), Monte Verità, Ascona, CH–July, 2010, 11–15.
48. Taggart, R.: *Ship Design and Construction*, 10048th ed., The Society of Naval Architects and Marine Engineers, One World Trade Center, New York, 1980.
49. Tarelko, W., T. Kowalewski: *Modeling of Decision-Making Process Relating to Design of Ship Power Plants Safe for Operators*, in: 2013 12th Mexican International Conference on Artificial Intelligence, IEEE, 2013, 17–23. DOI: 10.1109/MICAL.2013.8.
50. [www.jp.scottbader.com/uploads/files/5527\\_gelcoat-quality-guide-english.pdf](http://www.jp.scottbader.com/uploads/files/5527_gelcoat-quality-guide-english.pdf).
51. [www.westsystem.com/wp-content/uploads/Fiberglass-Manual-2015.pdf](http://www.westsystem.com/wp-content/uploads/Fiberglass-Manual-2015.pdf).

## CONTACT WITH THE AUTHORS

**Tacjana Niksa-Rynkiewicz**  
*e-mail: tacniksa@pg.edu.pl*

Gdańsk University of Technology  
11/12 Gabriela Narutowicza Street, 80-233 Gdańsk  
**POLAND**

**Michał Landowski**  
*e-mail: miclando@pg.edu.pl*

Gdańsk University of Technology  
11/12 Gabriela Narutowicza Street, 80-233 Gdańsk  
**POLAND**

**Paweł Szalewski**  
*e-mail: pawel.szalewski@pg.edu.pl*

Gdańsk University of Technology  
11/12 Gabriela Narutowicza Street, 80-233 Gdańsk  
**POLAND**

# MULTI-CRITERIA COMPARATIVE ANALYSIS OF THE USE OF SUBTRACTIVE AND ADDITIVE TECHNOLOGIES IN THE MANUFACTURING OF OFFSHORE MACHINERY COMPONENTS

Mariusz Deja

Mieczysław Stanisław Siemiątkowski

Dawid Zieliński

Gdańsk University of Technology

Faculty of Mechanical Engineering, Department of Manufacturing and Production Engineering, Poland

## ABSTRACT

*The dynamic development of additive manufacturing technologies, especially over the last few years, has increased the range of possible industrial applications of 3D printed elements. This is a consequence of the distinct advantages of additive techniques, which include the possibility of improving the mechanical strength of products and shortening lead times. Offshore industry is one of these promising areas for the application of additive manufacturing. This paper presents a decision support method for the manufacturing of offshore equipment components, and compares a standard subtractive method with an additive manufacturing approach. An analytic hierarchy process was applied to select the most effective and efficient production method, considering CNC milling and direct metal laser sintering. A final set of decision criteria that take into account the specifics of the offshore industry sector are provided.*

**Keywords:** offshore industry, additive technologies, maritime and offshore equipment components, decision support systems, analytic hierarchy process (AHP)

## INTRODUCTION

Additive technologies, commonly referred to as 3D printing, are a set of methods enabling the layered construction of objects based on 3D computer models, and without using part-dependent tools [1, 15]. The strong increase in interest in additive technologies that has been particularly noticeable in recent years is related to developments in the methods and systems of 3D printing [33]. Advanced materials, including those with reinforcement phases, can be used to create products [26, 29, 32]. The current range of components that can be made by additive technologies extends beyond the original applications of rapid prototyping. In particular, 3D printing with metal powder allows for the production of fully functional spare parts for mechanical devices. The term additive manufacturing (AM) refers to the fabrication of components with specific mechanical and functional properties.

Nowadays, high-quality, reliable components for offshore industry are manufactured by material removal processes,

including five-axis milling. Additive technologies are characterised by their competitive features compared to traditional machining methods. The main advantages of AM include the design and manufacture of components with complex geometry. The manufacture of these types of objects can be difficult and sometimes impossible to achieve with the use of traditional cutting and casting methods. Other advantages are the relatively short processing time and the lack of a need for production tools. These factors may also reduce the overall production costs.

The wide variety of manufacturing techniques that are currently available, such as material removal processes and 3D printing powder technology, must be taken into account during the selection of the most efficient fabrication method. This must involve consideration of the relevant criteria related to the capabilities of the specific manufacturing techniques. This paper presents the results obtained from a multi-criteria decision making (MCDM) method called an analytic hierarchy process (AHP) for the selection of the

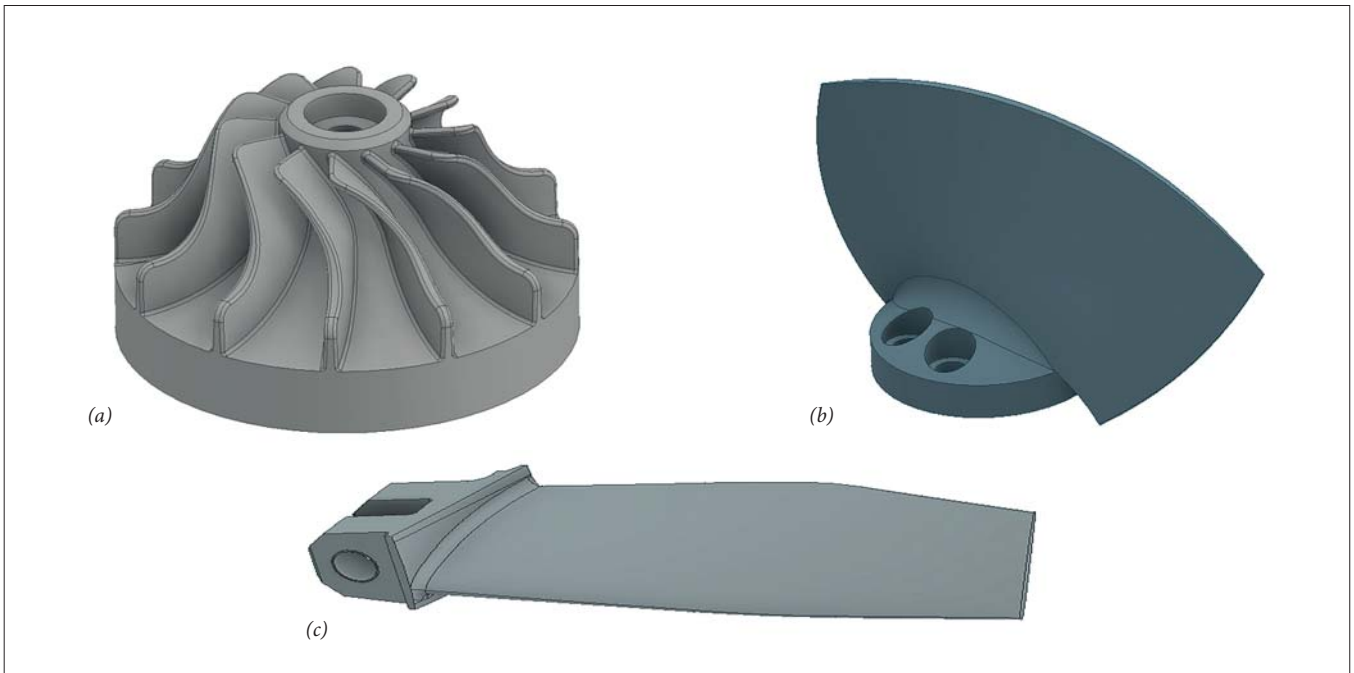


Fig. 1. Examples of mechanical components with free-form surfaces that can be produced by additive manufacturing: (a) impeller; (b) short propeller blade; (c) long propeller blade

most suitable technology for manufacturing components for offshore machinery, using the example of an impeller. The type and form of the material, its mechanical and physical properties, and the production time and cost were analysed and compared in the process of selecting the most suitable fabrication method using a multi-criteria analysis.

## ADDITIVE MANUFACTURING IN OFFSHORE INDUSTRY

The maritime industry is one of the leading areas for the potential application of additive technologies. The mechanical components of marine constructions are affected by environmental factors such as sea water and variability in the loads that affect these structures. Demanding and difficult working conditions cause frequent damage to the components of technical equipment used in the coastal zone and at sea. The efficiency of machines can therefore be maintained and process continuity improved through the rapid manufacture of spare parts. 3D printing technologies can offer an alternative to the traditional material removal processes generally used in the offshore industry. Nowadays, the most common and advanced additive technologies

include direct metal laser sintering (DMLS) and electron beam melting (EBM). These allow for the production of elements with complex geometries (Fig. 1) consistently high-level mechanical properties, and homogeneous internal structures. The process of 3D printing is based on the direct conversion of 3D data into physical objects by applying successive layers of material in the form of powder, which can be either melted or sintered. Among the benefits of this technology is that it allows for flexible production of various items at no extra cost in terms of manufacturing, without the need for additional tools or moulds [19]. Table 1 presents the characteristics of the 3D metal powder technologies currently used in this industry.

3D printing powder technologies can be used to produce a wide range of complex machine elements for different sectors of industry with similar characteristics, including the maritime and shipping industry. According to [19], this industry can be characterised as conservative with respect to change, although DMLS and selective laser melting (SLM) technologies are currently being successfully used to manufacture high-pressure blades for gas and Tesla turbines [7, 14, 18, 20, 23, 30]. These kinds of parts have complex geometries, including inner features in the form of miniature holes [10] and channels for delivering cooling

Tab. 1. Characteristics of 3D metal powder technologies currently used in different sectors of industry

Additive technology	Method used to create an object	Energy source	Areas of possible application
Direct metal laser sintering	Joining particles of metallic powder by sintering	Laser beam	Aircraft and aerospace, automotive, tool making, maritime, medical, military
Selective laser melting	Joining particles of metallic powder by full melting		
Electron beam melting	Joining particles of metallic powder by full melting	Electron beam	Aircraft, maritime, aerospace, automotive

Tab. 2. Scale of relative importance, adapted from Saaty [25]

Intensity of importance	Description	Explanation
1	Equally important	Two factors contribute equally to the objective
3	Slightly more important	Experience and judgement slightly favour one factor over the other
5	Much more important	Experience and judgement strongly favour one factor over the other
7	Significantly important	Experience and judgement very strongly favour one factor over the other to show its dominance in practice
9	Extremely important	The evidence favouring one factor over the other is of the highest possible validity
2, 4, 6, 8	Intermediate values	Always used where a compromise is required
Reciprocals of the above	If a criterion $i$ has one of the above non-zero members assigned to it when compared with criterion $j$ , then $j$ has the reciprocal value when compared with $i$	

fluid. The creation of complex inner features by conventional machining methods can be difficult, and in some cases even impossible. Industrial impellers are another group of parts commonly used in the marine industry, and these can be made by 3D powder technologies [28]. In addition to their complex geometries, elements of this type have thin walls, which are difficult to make by material removal processes.

Hybrid manufacturing is a promising approach for widening the scope of AM applications. DMLS can be used in association with more traditional processes, such as electro-discharge machining (EDM) or high-speed machining (HSM) to give a hybrid rapid tooling process [22] that can reduce the time needed to create tools and dies.

The use of AM can therefore be a beneficial solution for the rapid production of spare parts on ships and major systems on platforms or offshore industrial installations, which operate in remote locations and are in continuous movement. Spare parts must often be delivered in a timely manner to the next port of call of the ship. AM can shorten the supply chain for spare parts in the maritime industry, since the part can be made near to or even in the place where it will be needed [19]. Although AM can be used to create a wide variety of products in a controlled and static environment, the use of such techniques while afloat creates questions about the feasibility of the incremental processes [27].

AM technology can radically change supply chains, product designs and production in several sectors of industry, thanks to advantages such as on-demand, localised production and the ease of creating complex shapes. However, cost-effectiveness considerations, gaps in knowledge, process variability and a lack of full standardisation have tended to limit the adaptation of AM within the maritime construction sector [2]. The standardisation and normalisation of AM processes currently under way will certainly help in identifying and widening the possibilities for implementation in offshore industry [11, 21].

The selection of an appropriate manufacturing method is one of the most crucial decisions in the product development cycle [8, 9]. We therefore propose a decision support method for manufacturing offshore equipment components. AHP is applied to the selection of the most effective and efficient production method, including CNC milling and DMLS, and

a set of decision criteria that take into account the specifics of the offshore industry sector are developed. The resultant ranking list of analysed alternatives is generated.

### MULTI-CRITERIA DECISION MAKING USING THE AHP METHOD

MCDM is one of the most well-known approaches to making decisions in the presence of multiple, often opposing objectives. Characteristic features considered in MCDM include alternatives, attributes, criteria and sub-criteria, weights representing their importance, and decision matrices. The AHP method, introduced by Saaty [25], is one of the most commonly applied methods in this area. It enables the determination of the priorities of a set of alternatives and the relative importance of individual factors in a multi-criteria evaluation task [24, 31]. In this approach, relatively simple pairwise comparison judgements are carried out, which are then utilised to develop overall priorities that are used to rank the alternatives. The quantification of priorities is typically carried out using integers in the range one to nine and their reciprocals (Table 2) [6, 25]. AHP involves applying consecutive steps in the frame of an iterative procedure, as listed below:

**Step 1.** Definition of the problem and decomposition into a systematic hierarchical structure, including the definition of the main criteria/sub-criteria used with a comparative analysis of process alternatives.

**Step 2.** Creation of matrices for pairwise comparisons of the selected main criteria, using an established rating scale as shown in Table 2.

**Step 3.** Calculation of the importance weights for individual criteria and determination of an appropriate ranking list to identify preferences for the criteria based on which alternatives are evaluated. This activity is equivalent to computing the vectors of normalised weights for criteria or sub-criteria. This step is followed by validation of the previous calculations.

**Step 4.** Checks on the consistency of the relevant matrix formed at specified levels of the hierarchy, corresponding to definite sets of criteria or sub-criteria. This validation-related activity entails calculations of the principal eigenvalues of

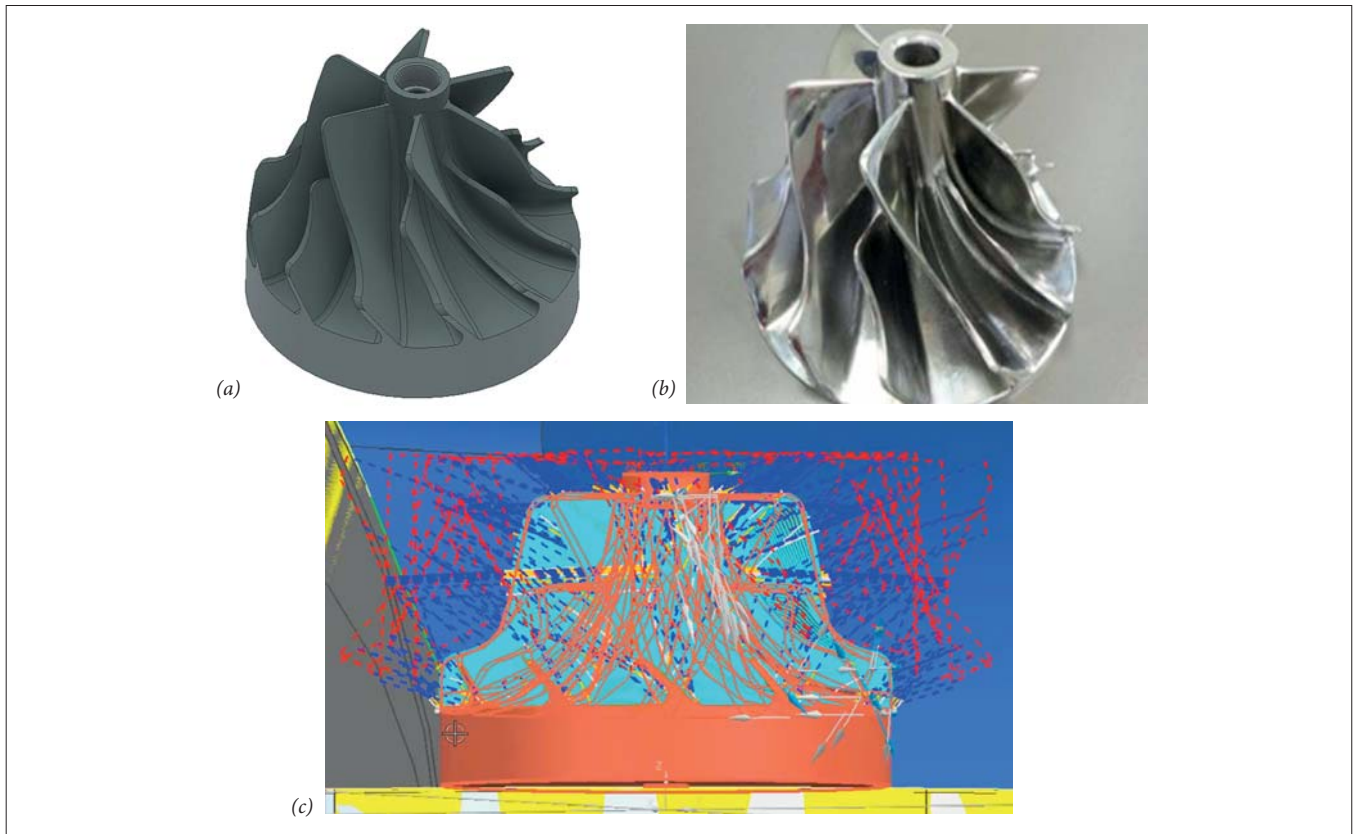


Fig. 2. Example of a part used in an illustrative case study: (a) 3D model of an impeller type part; (b) real part; (c) tool paths used in the estimation of machining time

the relevant matrices, and the values of the consistency index (*CI*) and consistency ratio (*CR*). Consistency of the matrices generated in the decision process requires that, in any instance, inequality constraints (1) and (2) are met:

$$CI = \frac{\lambda_{max} - n}{n - 1} \leq 0,1 \quad (1)$$

$$CR = \frac{CI}{RI} \leq 0,1 \quad (2)$$

where:  $\lambda_{max}$  is the maximum eigenvalue of the relevant matrix, *n* is the order of the matrix, and *RI* is a random index that depends on the value of *n* [20].

It should be noted that the value of  $\lambda_{max}$  can be computed as a sum of the products of each weight of the criteria (alternatives) and the calculated sums of columns derived from the matrix of pairwise comparisons of criteria (alternatives).

In the decision scheme, the calculations carried out in steps 2–4 need to be repeated with respect to the lower level of the hierarchy, i.e. with regard to all related subordinate criteria. Consequently, the preferences for the sub-criteria are computed both locally and globally. The local weights (reflecting the importance) of both criteria and sub-criteria are determined as arithmetic averages. The global importance (weight) of each subordinate criterion is in turn computed as the product of its relative (local) weight and the weight(s) of the criterion at the respective level(s) of the hierarchy.

**Step 5.** Creation of matrices for pairwise comparisons of the process alternatives in terms of individual decision

criteria, using the established rating scale given in Table 2. This procedure is continued after checking of the validation conditions given in Step 4.

**Step 6.** Computation of the matrix  $S = [S_{ij}]_{m \times n}$  of normalised performance metrics (scores) for the alternatives for each criterion, where  $i = 1, \dots, m$ , and  $m$  is the total number of alternatives, and where  $j = 1, \dots, n$ , and  $n$  is the total number of assumed criteria (design/process attributes).

As a result, a list of preferences of the alternatives being compared (i.e. a ranked list of alternatives) is produced on a global scale, based on the sum of the partial values of the normalised performance metrics calculated with reference to individual criteria, as recorded in the *S* matrix.

## METHODS OF MANUFACTURING AN IMPELLER COMPONENT

Impellers and turbine blades are widely used in equipment for the maritime industry. These types of parts are characterised by a complex geometry with thin walls. The selection of the most efficient manufacturing method requires consideration of numerous factors related to the material, mechanical and functional properties of the product, as well as the speed and cost of delivering the final components. CNC machining with a five-axis milling machine was used to manufacture an impeller component (Fig. 2). The DMLS method, as the most suitable 3D printing technology, was also used.

Tab. 3. Parameters of the methods for manufacturing an impeller

Parameter	Manufacturing method	
	CNC milling	DMLS
Machine	Pinnacle AX320*	EOSINT M280**
Material	Steel 34 HNM/1.6582 (34CrNiMo6)	EOS nickel alloy IN718 EOS maraging steel MS1
Material form	Rod bar	Powder; thickness of a single layer of material: 40 µm

Note:  
 \* The Pinnacle AX320 with Heidenhain TNC640 is a five-axis milling machine tool. The applied material (steel 34 HNM) is used to build highly loaded parts, exposed to impacts, twisting, and vibrations like turbine blades and impellers.  
 \*\* EOSINT M280 3D printer is a market-leading industrial system working in DMLS/SLM technology. EOS Nickel Alloy IN718 is characterised by high strength, resistance to high temperatures and very high corrosion resistance. EOS MaragingSteel MS1 is also characterised by high strength and hardness, and is therefore commonly used to build elements for injection moulds.

Tab. 4. A set of decision criteria for selecting the method of manufacturing an impeller

Criteria	Manufacturing method		
	CNC-milling	DMLS IN718	DMLS MS1
<b>Mechanical and physical properties</b>			
Tensile strength (MPa)	1400	1060 – x,y direction 1400 – z direction	2050 – x,y direction 2050 – z direction
Material density (g/cm <sup>3</sup> )	8	8.15	8.0 – 8.1
Hardness (HRC)	60	47	50 – 56
<b>Process-related factors</b>			
Processing time [min]*	596	2520	2520
Roughness [µm]	Ra = 0.4 – 0.6	Ra = 2.5 – 3.5	Ra = 2.5 – 3.5
Accuracy of manufacture [mm]	+/- 0.02	+/- 0.05	+/- 0.05
<b>Costs of manufacturing</b>			
Material cost [€]	60	270	257
Total processing cost [€]	955	1540	1540
Post-processing cost [€]	0	80	80

Note:  
 \* Includes the machining and setup times. With regard to DMLS technology, the machining time is related to the printing of the impeller model and the support structure with a height of 10 mm, and the setup time is related to the preparation of the machine for processing. In the case of 3D printing powder technology, the time component includes heating of the working chamber and cooling down after the manufacturing process.

Important parameters related to these manufacturing processes, such as the machine, type and the form of the material, are listed in Table 3.

In order to solve a decision problem concerning the selection of the most efficient method for manufacturing an impeller, three main criteria and nine sub-criteria were defined (Table 4). These sets of main and sub-criteria were determined in view of the possible heavy-duty operating conditions of the impeller in a maritime equipment.

The anisotropic mechanical properties of the 3D metal printed components shown in Table 4, are examples of the basic disadvantages of additive technology, and may affect the functionality of an impeller working under variable loading conditions. In view of this, a strength analysis must be carried out at the design stage that takes into account the mechanical properties arising from the orientation of the component in the working chamber of the 3D printer. It was assumed in this study that selected materials meet established design requirements, in accordance with material data sheets [12, 13].

Data on the mechanical and physical properties and the accuracy of manufacture were determined considering the heat treatment in additive [12, 13] and subtractive processes [34, 35].

Output process parameters concerning the times required for printing (2220 minutes) and related setup (300 minutes) were calculated using dedicated EOSINT M280 software. The machining time for the subtractive method was derived using a CNC Heidenhain TNC640 controller and amounted to 553 minutes, and the setup time was 43 minutes.

The 3D printing of the impeller involves the cost of the utilised material, depending on the model volume. The operating costs of the 3D printer were also included, following manufacturing practices recommended by the Institute of Fundamental Technological Research, Polish Academy of Sciences. The cost of using the 3D printer was assumed to be 70€ per hour, taking into account factors such as the cost of acquisition and installation, a five-year amortisation period (i.e. 20% per year), maintenance costs, and the costs of energy and ancillary materials. In the case of DMLS technology, the required post-processing costs, such as cleaning the model of

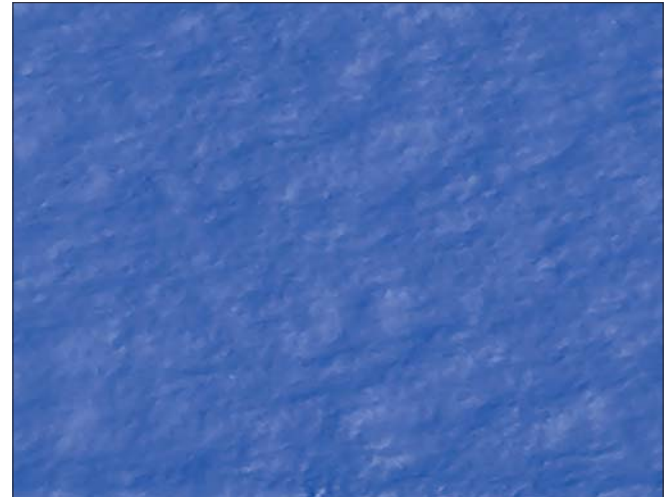


Fig. 3. Part of the surface of a workpiece made of MS1 material by DMLS: (a) a microscopic image of a real surface using OLYMPUS BX51; (b) digital model of the surface obtained with computer tomography

the remaining unmelted powder, shot-peening and additional heat treatment, were also taken into account.

The total operation cost of CNC milling,  $C_o$ , comprised two components: machine costs and tool utilisation costs. It was calculated using the following cost model for a multi-cut operation [3]:

$$C_o = c_o \sum_i \frac{t_{mi} + t_{smi}}{60} + \sum_i c_{Ti} \frac{t_{mi}}{T_{li}}, \quad (3)$$

where  $t_{mi}$  [min] is the machining time for the tool path of the  $i$ -th tool,  $t_{smi}$  [min] is the supplementary machine time for the  $i$ -th tool,  $T_{li}$  [min] is the tool life under cut for the  $i$ -th tool,  $c_o$  is the hourly machine operating cost, and  $c_{Ti}$  [€ tool life under cut of the  $i$ -th tool] is the cost of the  $i$ -th tool, calculated as the sum of the costs of amortisation and tool exchange in the magazine.

The costs of using the machine tool during the cutting process were assumed to be 45€ per hour, based on the same factors as for the 3D printer. In this case, a seven-year amortisation period was assumed (i.e. 14.3% per year), due to the relatively slow technological development of CNC machine tools compared to 3D printing equipment.

Nineteen tools of various types were utilised in the milling of the impeller, including an end mill, a spherical mill, chamfer mill cutters and drillers. In the calculations, the costs of the individual tools were assumed to be in the range 27–36€, while the values for the life under cut for the individual tools were between 15 and 30 minutes.

The surface quality (roughness) is another important factor which has a fundamental importance in the functional properties of the impellers, such as their wear and corrosion resistance, strength properties and flow resistance [16]. In industrial practice, to ensure the optimal functioning of parts such as impellers that are subjected to variable loads, a surface roughness in the range  $Ra = 0.2 - 0.6 \mu m$  is required [17]. This value can be obtained by CNC milling, and has been confirmed by reports in the literature [4, 5], as given in Table 4.

For DMLS, a microscopic analysis was carried out. Fig. 3 shows part of the surface of a workpiece created using this technology.

The images in Figure 3 show that an irregular surface structure, characteristic of DMLS printed elements, was obtained. The results of surface roughness measurements obtained with a Hommel Tester T500 (Fig. 4) were significantly higher than the required surface roughness of  $Ra = 0.2 - 0.6 \mu m$ . To obtain the required surface roughness, which is essential for elements such as impellers, there is therefore a need to perform additional finishing operations to smooth the surface. In the calculations below, the values of achievable  $Ra$  parameter were assumed based on the results of the authors' research and literature reports (Table 4).

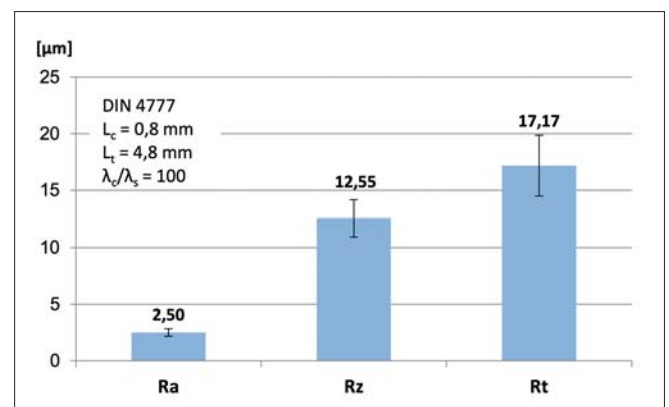


Fig. 4. Parameters of the surface roughness of a workpiece made of MS1 by DMLS

## AHP-BASED SELECTION OF IMPELLER MANUFACTURING TECHNOLOGY

The application of the AHP method as an efficient decision support framework, has been demonstrated as a case study of manufacturing impeller-type components. The first step in the process of selecting a manufacturing technology for an impeller using AHP is to develop a hierarchical structure for

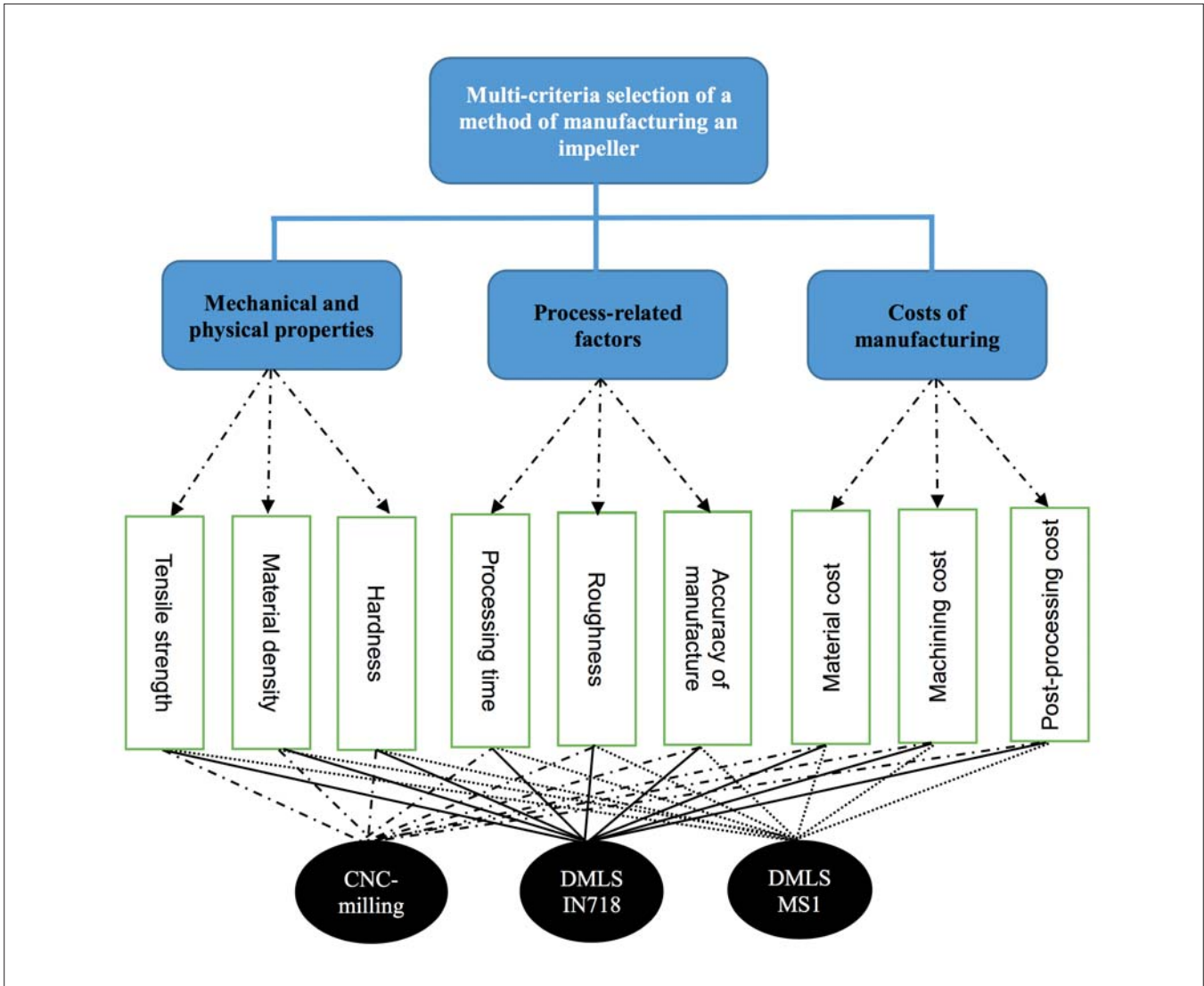


Fig. 5. Hierarchical structure of the decision problem related to selecting the impeller manufacturing technology with the AHP method

the decision problem (see Step 1 above). In the present study, the hierarchical diagram consists of four levels: the goal of the decision problem, the main criteria level, the sub-criteria level, and the scheme level, which is related to the overall rankings and the selection of the best process alternatives (Fig. 4).

At the next level, the main criteria were quantitatively assessed using pairwise comparisons. The results of these calculations are shown in Tables 5 and 6.

Pairwise comparisons of the main criteria were used to compute the importance weights of the individual main criteria (Steps 2 and 3 above), and based on these weights, a ranking list of the main criteria was created. Following the AHP methodology, the principal eigenvalue of  $\lambda_{max}$  was calculated and the validation conditions were checked using the consistency index (CI) and consistency ratio (CR).

Tab. 5. Pairwise comparisons of the main criteria

	Mechanical and physical properties	Process related factors	Costs of manufacturing	Sum
Mechanical and physical properties	1	4	6	11
Process-related factors	0.25	1	3	4.25
Costs of manufacturing	0.17	0.33	1	1.50
Sum	1.42	5.33	10	

Tab. 6. Importance of the main criteria

	Mechanical and physical properties	Process related factors	Costs of manufacturing	Weight	Rank
Mechanical and physical properties	0.71	0.75	0.60	0.685	1
Process-related factors	0.18	0.19	0.30	0.221	2
Costs of manufacturing	0.12	0.06	0.10	0.093	3
Sum	1	1	1		

The values at this level of the analysis are as follows (for  $\lambda_{max} = 3.085$ ):

$$CI = \frac{3.085 - 3}{3 - 1} = 0.043 \leq 0.1,$$

and

$$CR = \frac{0.043}{0.52} = 0.082 \leq 0.1.$$

The relevant calculations at the level of the subordinate criteria (Step 4) were performed in the same way as for the main criteria. All of the weight values at this level (i.e. at the global scale) were obtained by multiplying the local weights by the weight of the corresponding criteria. The results for the sub-criteria for the mechanical and physical properties of impeller material are given in Tables 7 and 8, respectively.

Tab. 7. Pairwise comparisons of the sub-criteria for the mechanical and physical properties of the impeller material

	Tensile strength	Material density	Hardness	Sum
Tensile strength	1	4	5	10
Material density	0.25	1	3	4.25
Hardness	0.17	0.33	1	1.50
Sum	1.42	5.33	9	

Tab. 8. Importance of the sub-criteria for the mechanical and physical properties of the impeller material

	Tensile strength	Material density	Hardness	Local weight	Global weight	Ranking
Tensile strength	0.71	0.75	0.56	0.670	0.459	1
Material density	0.18	0.19	0.33	0.232	0.159	2
Hardness	0.12	0.06	0.11	0.097	0.067	3
Sum	1	1	1	1	0.69	

The results of the consistency test at this level showed that the required conditions (see Eqs. 1 and 2) were met. The values obtained for  $CI$  and  $CR$  coefficients are given below for  $\lambda_{max} = 3.063$ :

$$CI = \frac{3.063 - 3}{3 - 1} = 0.032 \leq 0.1,$$

and

$$CR = \frac{0.032}{0.52} = 0.061 \leq 0.1.$$

Tables 9 and 10 present comparisons of the results for the alternative processes (Steps 5 and 6 above) from the viewpoint of the tensile strength, which turned out to be the most important factor in the mechanical and physical properties of the material. These results were obtained in a similar way to the corresponding calculations at the sub-criteria level.

Tab. 9. Pairwise comparison of the alternatives in terms of the criterion tensile strength for applied material

	CNC milling	DMLS-IN718	DMLS-MS1	Sum
Tensile strength	1400	1060	2050	
CNC milling	1	2	0.25	3.25
DMLS-IN718	0.50	1	0.20	1.70
DMLS-MS1	4	5	1	10
Sum	1.63	3.13	18	

Tab. 10. The importance of the tensile strength sub-criterion

	CNC milling	DMLS-IN718	DMLS-MS1	Local weight	Global weight	Ranking
CNC milling	0.18	0.25	0.17	0.201	0.063	2
DMLS-IN718	0.09	0.13	0.14	0.118	0.037	3
DMLS-MS1	0.73	0.63	0.69	0.681	0.214	1
Sum	1	1	1	1	0.31	

The validation conditions were also checked (Step 4) and were shown to be fulfilled, as shown below, for an eigenvalue of  $\lambda_{max} = 3.038$ :

$$CI = \frac{3.038 - 3}{3 - 1} = 0.019 \leq 0.1,$$

and

$$CR = \frac{0.019}{0.52} = 0.037 \leq 0.1.$$

Finally, the partial values of the normalised performance metrics, calculated for each of the process alternatives and for all nine decision criteria, are shown in Table 11. This table also includes the cumulative values of the performance metrics for each alternative, and its ranking. Cutting technology, with a value of 0.744, was the best alternative. It can be observed that for CNC machining, factors related to the manufacturing process accounted for around 84% of the cumulative value of the normalised performance. The accuracy of manufacture is the largest component, amounting to around 81%. These criteria also have high levels of importance for DMLS technology, and in particular for Nickel Alloy IN718 yield altogether 79% for process related factors, but with the lowest cumulative value (0.259). For Maraging Steel MS1, however, the mechanical and physical properties have the largest impact on the cumulative value of normalised performance, at around 54%. The results of a quantitative evaluation of the alternatives, based on the above calculations, are also presented in the form of a bar chart (Fig. 6). CNC milling proved to be the most appropriate method for fabricating this type of offshore machinery component, and is used in current industrial practice. However, in the near future, following the intensive development of additive technologies, 3D printing may gain an advantage over subtractive technologies.

Tab. 11. Results of the multi-criteria selection of alternative processes with corresponding ranking

	Mechanical and physical properties			Process related factors			Costs of manufacturing			Cumulative value of normalised performance	Ranking
	Tensile strength	Material density	Hardness	Processing time	Roughness	Accuracy of manufacture	Material cost	Machining cost	Post-processing cost		
CNC milling	0.063	0.025	0.025	0.003	0.022	0.600	0.002	0.004	0.0005	0.744	1
DMLS-IN718	0.037	0.007	0.007	0.0006	0.0045	0.200	0.0002	0.001	0.0001	0.259	3
DMLS-MS1	0.214	0.014	0.014	0.0006	0.0045	0.200	0.0004	0.001	0.0001	0.448	2

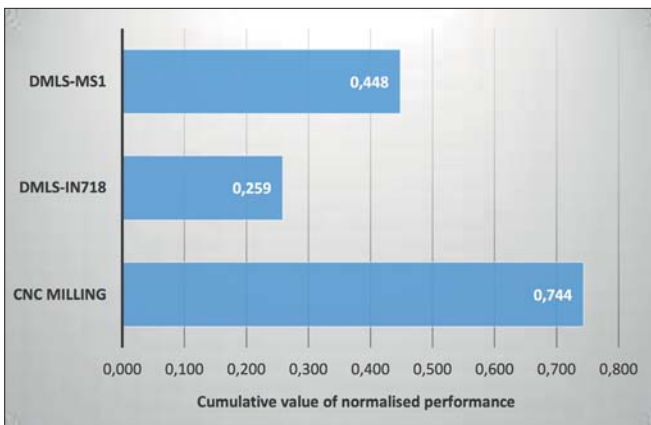


Fig. 6. Comparison of process alternatives based on a multi-criteria evaluation using the AHP method

## CONCLUSIONS

The selection of an appropriate manufacturing method is one of the most crucial decisions in the product development cycle. AM technologies, and especially 3D printing metal powder methods, can radically change supply chains, product designs and production in certain sectors of industry, since a part with complex geometry can be made near or even in the exact place it is needed. However, processing costs and high design requirements might limit the adaptation of AM processes within these industrial sectors. In this study, we propose a decision support method for selecting a suitable manufacturing technology for offshore equipment components, which can help in the wider implementation of DMLS technology in the maritime construction sector.

AHP, as an efficient decision support framework, was applied to the selection of the most suitable manufacturing method for fabrication of complex mechanical components, and an impeller part was used as an illustrative case study. CNC machining and the DMLS method were considered as alternative processes for producing the final part. A final set of decision criteria that focused on the specifics issues of the offshore industry sector were provided, and a ranking list of the analysed alternatives was generated to show that for the specified technical requirements and production resources,

CNC milling was the highest-ranked position. Taking into account the intensive developments in DMLS technology, including the dynamic development of contemporary engineering materials, it can be expected that the importance of the main criteria will change. In consequence, the ranking positions of process alternatives may differ from those presented here.

Further research work will focus on the continuous development of the DMLS process and the standardisation measures that are periodically introduced in the offshore sector for critical components in maritime constructions. In particular, the use of DMLS systems while afloat should be also examined before making the decision to build products or spare parts that are normally produced in a controlled, static environment.

## ACKNOWLEDGEMENTS

The authors would like to thank Dr. Piotr Pawłowski from the Department of Intelligent Technologies, Institute of Fundamental Technological Research Polish Academy of Sciences (<https://www.ippt.pan.pl/>) and Mr. Piotr Sender from RADMOR S.A. (<http://www.radmor.com.pl/eng>) for providing the data used in this research.

Computations were carried out using software and computers from Academic Computer Centre in Gdansk - TASK (<http://www.task.gda.pl>).

## REFERENCES

1. ASTM, ISO. ASTM52900-15 (2015): *Standard Terminology for Additive Manufacturing—General Principles—Terminology*, ASTM International, West Conshohocken, PA.
2. Bergsma J.M., Van der Zalm M., Pruyn J.F.J. (2016): *3D-Printing and the Maritime Construction Sector*. In: 10th Symposium on High-Performance Marine Vehicles, HIPER 16, Cortona, 17–19 oktober 2016; Part of collection Maritime Archive, p. 428–442.

3. Bocheński T., Deja M., Siemiątkowski M.S. (2016): *Planning Strategies for Complex Shape Pocket Milling in Mechanical Parts* (in Polish). *Mechanik*, 89(10), 1496–1497.
4. Burek J., Żurek P., Żurawski K. (2016): *The Influence of Inclination Angle on Surface Roughness with Milling Using a Ball Mill* (in Polish). *Mechanik*, 10, 1478–1479.
5. Chen X., Zhao J., Dong Y., Han S., Li A., Wang D. (2013): *Effects of Inclination Angles on Geometrical Features of Machined Surface in Five-Axis Milling*. *Intl. Journal of Advanced Manufacturing Technology*, 65, 1721–1733.
6. Çimren E., Çatay B., Budak E. (2007): *Development of a Machine Tool Selection System Using AHP*. *The International Journal of Advanced Manufacturing Technology*, 35(3-4), 363–376.
7. Deja M., Dobrzyński M., Flaszynski P., Haras J., Zieliński D. (2018): *Application of Rapid Prototyping Technology in the Manufacturing of Turbine Blade with Small Diameter Holes*. *Polish Maritime Research*, 25(s1), 119–123.
8. Deja M., Siemiątkowski M.S. (2018): *Machining Process Sequencing and Machine Assignment in Generative Feature-Based CAPP for Mill-Turn Parts*. *Journal of Manufacturing Systems*, 48, 49–62.
9. Deja M., Siemiątkowski M.S., Sender P. (2017): *Comparative Study of Machining Technology Selection to Manufacture Large-Size Components of Offshore Constructions*. *Polish Maritime Research*, 24(s1), 38–45.
10. Deja M., Zieliński D. (2020): *A Pilot Study to Assess an In-Process Inspection Method for Small Diameter Holes Produced by Direct Metal Laser Sintering*. *Rapid Prototyping Journal*, 26(2), 418–436.
11. DNVGL-CG-0197, Class Guideline, *Additive Manufacturing - Qualification and Certification Process for Materials and Components*, available at: <http://www.dnvgl.com> (accessed 28 March 2019).
12. EOS GmbH - Electro Optical Systems, *EOS NickelAlloy IN718*, available at: <https://drukarki3d.pl/wp-content/uploads/2015/09/karta-materia%C5%82owa-EOS-NickelAlloy-IN718-ENG.pdf> (accessed 9 April 2019).
13. EOS GmbH - Electro Optical Systems, *EOS MaragingSteel MS1*, available at: <https://drukarki3d.pl/wp-content/uploads/2015/09/karta-materia%C5%82owa-EOS-MaragingSteel-MS1-ENG.pdf> (accessed 10 May 2019).
14. Flaszynski P., Doerffer P., Piotrowicz M. (2017): *Effect of Jet Vortex Generators on Shock Wave Induced Separation on Gas Turbine Profile*. In: *Proceedings of the 13th International Symposium on Experimental Computational Aerothermodynamics of Internal Flows*, 7–11 May 2017, Okinawa, Japan.
15. Gebhardt A. (2011): *Understanding Additive Manufacturing*. Carl Hanser Verlag, Munich 2012, p. 2.
16. Grzesik W. (2015): *Effect of Surface Topography Features of Machine Parts on Machine Service* (in Polish). *Mechanik*, 8(9), 587–593.
17. Grzesik W. (2019): *Influence of Surface Roughness on the Fatigue Life of Machine Elements - Experimental Investigations and Simulations* (in Polish). *Mechanik*, 5(6), 307–313.
18. Iftikhar A., Khan M., Alam K., Imran Jaffery S.H., Ali L., Ayaz Y., Khan A. (2013): *Turbine Blade Manufacturing Through Rapid Tooling (RT) Process and its Quality Inspection*. *Materials and Manufacturing Processes*, 28(5), 534–538.
19. Kostidi E., Nikitakos N. (2018): *Is It Time for the Maritime Industry to Embrace 3D Printed Spare Parts?* *TransNav: International Journal on Marine Navigation and Safety of Sea Transportation*, 12, 3, p. 557–564.
20. Lampart P., Kosowski K., Piwowarski M., Jędrzejewski Ł. (2009): *Design Analysis of Tesla Micro-Turbine Operating on a Low-Boiling Medium*. *Polish Maritime Research*, Special issue S1, pp. 28–33.
21. Lloyd's Register Group Limited and TWI Ltd (2017): *Guidance Notes for the Certification of Metallic Parts made by Additive Manufacturing*. Published by Lloyd's Register Group Limited. Registered office (Reg. no. 08126909), 71 Fenchurch Street, London, EC3M 4BS, United Kingdom, p. 1–9.
22. Mognol P., Rivette M., Jégou L., Lesprier T. (2007): *A First Approach to Choose Between HSM, EDM and DMLS Processes in Hybrid Rapid Tooling*. *Rapid Prototyping Journal*, 13(1), 7–16.
23. Navrotsky V., Graichen A., Brodin H. (2015): *Industrialisation of 3D Printing (Additive Manufacturing) for Gas Turbine Components Repair and Manufacturing*. *VGB PowerTech*, 12, 48–52.
24. Piotrowski N., Barylski A. (2016): *Multi-Criteria Robot Selection Problem for an Automated Single-Sided Lapping System*. In *Mechatronics: Ideas, Challenges, Solutions and Applications*. Springer, Cham, p. 1–13.
25. Saaty, T.L. (1990): *Decision Making For Leaders: The Analytic Hierarchy Process for Decisions in a Complex World*, RWS Publications, 1990.

26. Sercombe T.B., Li X. (2016): *Selective Laser Melting of Aluminium and Aluminium Metal Matrix Composites*. *Materials Technology*, 31(2), 77–85.
27. Strickland J.D. (2016): *Applications of Additive Manufacturing in the Marine Industry*. In: *Proceedings of PRADS2016*, 4th – 8th September, 2016 Copenhagen, Denmark, p. 1–5.
28. Tan X., Kok Y., Tor S.B., Chua C.K. (2014): *Application of Electron Beam Melting (EBM) in Additive Manufacturing of an Impeller*. In: *Proceedings of the 1st International Conference on Progress in Additive Manufacturing (Pro-AM 2014)*, Singapore: Research Publishing Services, p. 327–332.
29. Tekinalp H.L., Kunc V., Valez-Garcia G.M., Duty C.E., Love L.J., Naskar A.K., Blue C.A., Ozcan S. (2014): *Highly Oriented Carbon Fiber–Polymer Composites Via Additive Manufacturing*. *Composites Science and Technology*, 105, 144–150.
30. Vaezi M., Safaeian D., Chua C.K. (2011): *Gas Turbine Blade Manufacturing by Use of Epoxy Resin Tooling and Silicone Rubber Molding Techniques*. *Rapid Prototyping Journal*, 17(2), 107–115.
31. Velasquez M., Hester P.T. (2013): *An Analysis of Multi-Criteria Decision Making Methods*. *International Journal of Operations Research*, 10(2), 56–66.
32. Zhao X., Song B., Fan W., Zhang Y., Shi Y. (2016): *Selective Laser Melting of Carbon/AlSi10Mg Composites: Microstructure, Mechanical and Electronical Properties*. *Journal of Alloys and Compounds*, 665, 271–281.
33. Zieliński D. (2020): *3D Printing of Polymers on an Industrial Scale in SLS Technology* (in Polish). *Tworzywa Sztuczne w Przemysle*, 55(1), 71–72.
34. <http://akrostal.pl/stale/1-658234crnimo6/?print=pdf> (accessed 3 September 2019).
35. <https://www.dostal.com.pl/stal-do-ulepszenia-cieplnego.html> (accessed 3 September 2019).

## CONTACT WITH THE AUTHORS

### **Mariusz Deja**

*e-mail: mdeja@pg.edu.pl*

Gdańsk University of Technology  
 Faculty of Mechanical Engineering  
 Department of Manufacturing and Production Engineering  
 11/12 Gabriela Narutowicza Street, 80-233 Gdańsk  
**POLAND**

### **Mieczysław Stanisław Siemiątkowski**

*e-mail: mieczyslaw.siemiatkowski@pg.edu.pl*

Gdańsk University of Technology  
 Faculty of Mechanical Engineering  
 Department of Manufacturing and Production Engineering  
 11/12 Gabriela Narutowicza Street, 80-233 Gdańsk  
**POLAND**

### **Dawid Zieliński**

*e-mail: dawid.zielinski@pg.edu.pl*

Gdańsk University of Technology  
 11/12 Gabriela Narutowicza Street, 80-233 Gdańsk  
**POLAND**

## APPLICATION OF SHAPE MEMORY ALLOYS IN PIPELINE COUPLINGS FOR SHIPBUILDING

Leszek Matuszewski

Gdańsk University of Technology, Poland

### ABSTRACT

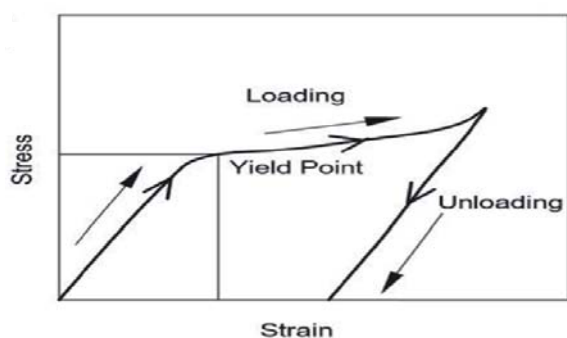
*The aim of the study is to analyse shape memory alloy (SMA) pipeline joints in limited space applications for all kinds of ships. Generally, the space available in various areas on ships is strictly limited and service works usually meet many obstacles. If we consider a pipeline, the flange joints always require a larger free space around the pipe than the pipe alone. A simultaneous problem can occur with the propeller shaft line coupling between bearings. SMA couplings require less space around the pipe and service should be easier, e.g., insulation fixing, painting and so on. SMA couplings last for a lifetime and there is no need for periodical seal replacement. Herein, some proposals among other unpublished data are discussed. There is a significant technological interest in the use of SMAs for applications not widely used yet. A wide variety of alloys present the shape memory effect and many generate an expressive restitution force considerable for commercial interests.*

**Keywords:** pipelines, couplings, shape memory alloys, shipbuilding, coupling durability

### INTRODUCTION

Shape memory alloys (SMA) constitute a group of metallic materials with the ability to recover a previously defined length or shape when subjected to an appropriate thermomechanical load. SMAs exhibit vastly different stress-strain behaviour in comparison to ordinary metals, as shown in Fig. 1.

a)



b)

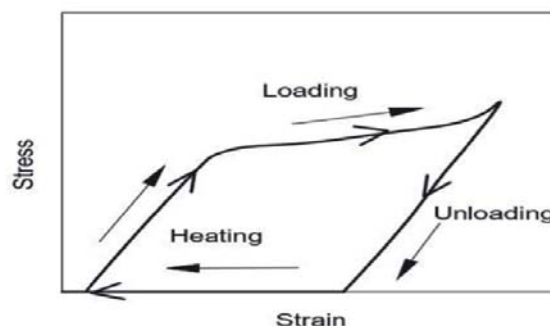


Fig. 1. Comparison of stress-strain behaviour of an ordinary metal (a) with permanent plastic deformation remaining after unloading and of a shaped memory alloy (b) with its original shape recoverable on heating [1]

When there is a limitation of shape recovery, these alloys promote high restitution forces. Because of these properties, there is significant technological interest in the use of SMAs for different applications. Although a relatively wide variety

of alloys present the shape memory effect, only those that can recover from a large amount of strain or generate an expressive restitution force are of commercial interest. In particular, alloys based on Ni-Ti and Cu, such as Cu-Zn-Al and Cu-Al-Ni, are especially important. SMAs based on Ni-Ti are most frequently used in commercial applications because they combine good mechanical properties with shape memory [1–5].

SMAs have found many technical applications, including in fluid sealing technology. They are ideally suited for stationary sealing conditions, for instance in static flange pipe joints, high-pressure hydraulic fittings, pipe and tube coupling systems, fasteners, connectors and clamps in a variety of applications. These materials are also utilised in dynamic sealing conditions, such as in lip radial oil seals, mechanical face seals, soft gland packing and magnetic fluid seals [5].

This article presents some constructional solutions of pipe couplings that make use of SMAs. These couplings are used, in addition, in hydraulic systems in aviation and shipbuilding, as well in oil and gas transportation pipelines. Applying metal alloys with the shape memory effect for sealing pipe couplings provides an opportunity for the significant simplification of their structure and ensures extremely durable and leak proof coupling.

## MECHANISM OF SHAPE MEMORY EFFECT IN SMAs

SMAs can return to a predetermined shape when heated. The shape memory effect is caused by the temperature dependent crystal structure. SMAs can exist in two different crystal structures (phases) known as martensite and austenite. Martensite has a monoclinic structure and is a relatively soft and easily deformed phase that exists at lower temperatures. Austenite has a high-temperature cubic structure and is the stronger phase of a SMA. When martensite is heated, it begins to change into austenite. The temperature at which this phenomenon starts is known as the austenite start temperature  $A_s$ . The temperature at which this phenomenon is completed is the austenite finish temperature  $A_f$ . When austenite is cooled, it begins to change into martensite. The temperature at which this phenomenon starts is the martensite start temperature  $M_s$ . The temperature at which martensite is again completely reverted is known as the martensite finish temperature  $M_f$ . When the SMA is below its phase transformation temperature, the material can be deformed into another shape with relatively little force. The new shape is retained provided that the material is kept

below its transformation temperature. When heated above this temperature, the material reverts to its parent structure, causing it to return to its original shape (Fig. 2). The shape memory effect is repeatable and can typically result in up to

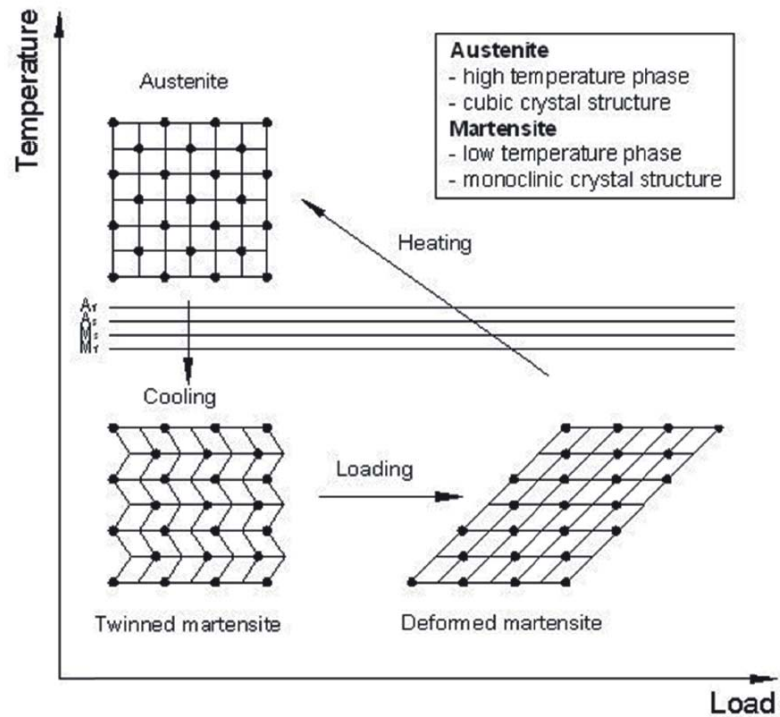


Fig. 2. Transformation from the austenite to martensite phase and shape memory effect [1]:  $A_f$  – austenite finish temperature;  $A_s$  – austenite start temperature;  $M_s$  – martensite start temperature;  $M_f$  – martensite finish temperature

8% strain recovery [1, 2].

The transformation temperature is a function of the alloy type and composition, as well as the thermomechanical treatments applied. The transformation from austenite to martensite (cooling) and the reverse cycle from martensite to austenite (heating) do not occur at the same temperature, due to a thermal hysteresis curve for every alloy that defines the complete transformation cycle (Fig. 3). The magnitude of the thermal hysteresis varies with the alloy type and is typically in the range of 10–50 °C.

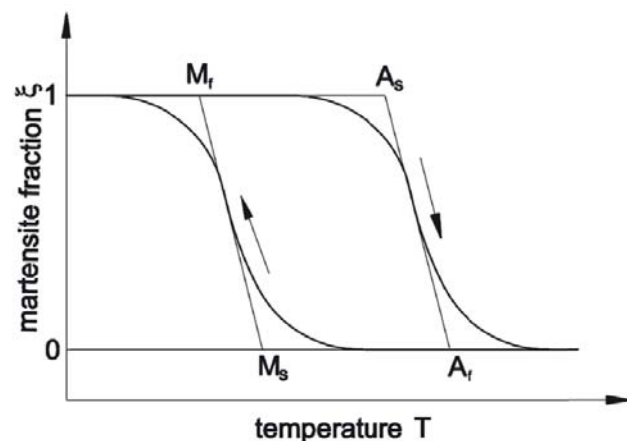


Fig. 3. Hysteresis curve for a thermoelastic martensitic transformation of a SMA, where  $\xi$  denotes the fraction of martensite in the material [1]

Despite a growing list of alloys with the shape memory effect, only two alloy systems have achieved some level of commercial exploitation. These are Ni-Ti (nitinol) and copper-based alloys (Cu-Zn-Al and Cu-Al-Ni). The properties of both systems are quite different. Ni-Ti alloys have greater shape memory strain (up to 7–8% versus 4–6% for copper-based alloys), tend to be much more thermally stable and have excellent corrosion resistance and much higher ductility. The composition of Ni-Ti alloys, which can change from 48% to 52% Ni, has a significant impact on the temperature of the high-temperature phase transformation into martensite (this temperature can vary from –40 to 100 °C). Ni-Ti alloys are frequently doped with other chemical elements to decrease or increase their transformation temperature. The main three-component alloys are Ni-Ti-Cu and Ni-Ti-Nb. Copper-based alloys are much lower in cost and exhibit higher actuation temperatures (approximately from –200 to 200 °C) than Ni-Ti alloys, and are sometimes the only choice for high-temperature applications above 100 °C. Unfortunately, these copper-based alloys tend to suffer from low mechanical strength and poor corrosion resistance.

### PIPE COUPLING DESIGNS BASED ON SMAs

Skilled pipe welders and brazers are in short supply. Expensive training efforts have failed to supply an adequate number of qualified personnel for shipbuilding programs. Field welded and/or brazed piping and tubing pose numerous installation problems. The recent introduction of heat recoverable pipe couplings into shipyard production methods provides a means to help alleviate some of these problems. Nitinol, a SMA, is usually selected for evaluation of its applicability to shipboard piping systems. Nitinol couplings are cryogenically cooled, expanded, installed on a pipe joint and allowed to warm, where they contract over the pipe to form a high-pressure sealed joint. The evaluation indicated potential labour savings warranting incorporation in ongoing contracts [6].

Figure 4 shows successive phases of making of a SMA-based high-pressure hydraulic tube coupling [7]. The coupling is machined at normal temperature to have an inner diameter

smaller by 4% than the outer diameter of the tubes to be joined (Fig. 4a). After cooling the coupling (in liquid nitrogen) at  $M_p$ , its inner diameter is expanded to become slightly greater than the outer tube diameter (Fig. 4b). Then, when the coupling is warmed to the austenite phase, it shrinks in diameter and strongly holds the tube ends together (Fig. 4c). The tubes prevent the coupling to recover its original shape. This generates stresses strong enough to create a more powerful joint than a weld.

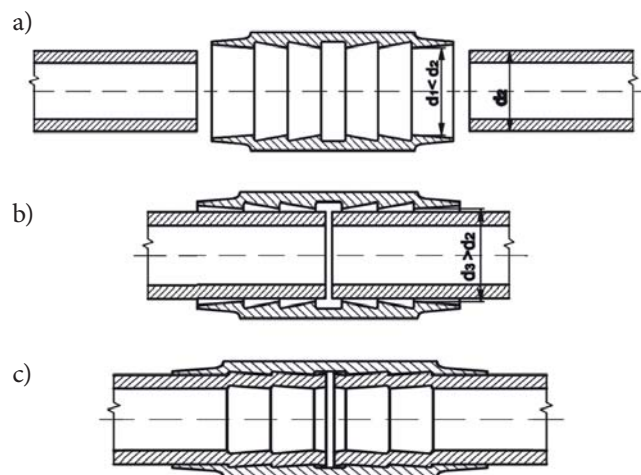


Fig. 4. Phases of joining for hydraulic SMA tube coupling: a) coupling is machined with an inside diameter slightly smaller than the tube outside diameter; b) expanded coupling have an inside diameter slightly larger than the tube outside diameter; c) tube is swaged by the warming coupling, but prevents complete recovery of the coupling

Figure 5 shows a high-pressure pipe coupling device comprising heat shrinkable sleeve 3 made from a memory shape metal and metallic insert 4 with a configuration that facilitates the formation of a secure coupling [8]. In the design shown in Fig. 5a, insert 4 is equipped with several rectangular teeth 4a placed on its interior surface, while in Fig. 5b, the rectangular teeth 4a are placed on the exterior surface of insert 4. Upon heat recovery of compression sleeve 3, insert 4 is compressed about the ends of pipes 1 and 2, as shown in Figs. 5a' and 5b', thus providing a tight pipe connection.

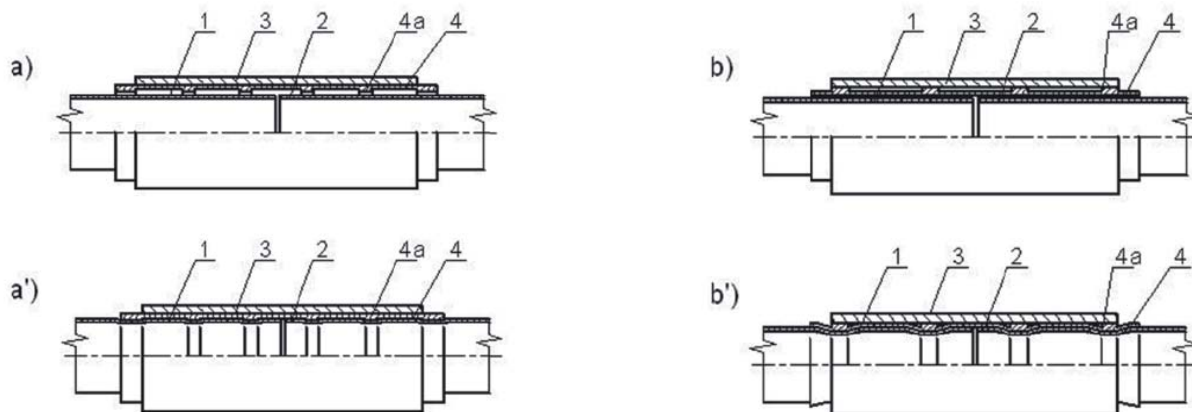


Fig. 5. High-pressure pipe coupling device: a), b) coupling before sleeve deformation; a'), b') coupling after sleeve deformation. 1 and 2 – ends of the pipes, 3 – heat recoverable sleeve made of SMA, 4 – metallic insert and 4a – circumferential tooth

Figure 6 shows a pipe coupling device with a flexible steel insert and clamping rings [9]. In this case, flexible insert 3 is mounted on the ends of pipes 1 and 2, and then the clamping rings 4, made from the SMA, are fixed around the insert. The inner cylindrical surface of insert 3 has projections 3a, with a triangular cross section, and longitudinal cuts 3b at both ends of the insert to facilitate its deformation.

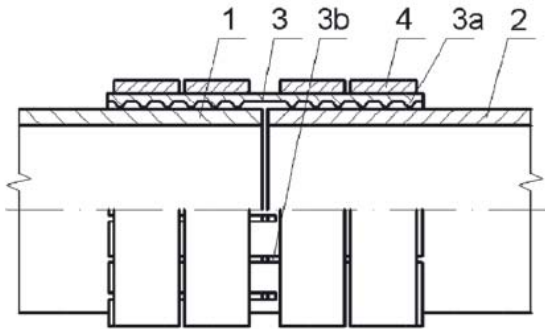


Fig. 6. Pipe coupling device with flexible steel insert and clamping rings made of SMA. 1 and 2 - ends of pipes, 3 - flexible steel insert, 3a - projection, 3b - longitudinal cut and 4 - clamping ring made of SMA

Figure 7 shows a tubular joint sealing system for use in high-temperature conditions, e.g., in equipment applied in the oil and gas industries [10]. The coupled connection consists of upper tubular member 1, lower tubular member 2, cylindrical sleeve 3, back-up ring 4 made from the SMA (e.g. nitinol) and elastomeric O-ring seals 5. Tubular members 1 and 2 are retained within sleeve 3 by threads formed on both the sleeve and tubular members. O-ring seals 5 are located in grooves formed at both end faces of the back-up ring 4 (Fig. 7a). After the connection has been mechanically completed, back-up ring 4 is heated, which makes it expand to its original axial dimensions (Fig. 7b) and fill the previously unoccupied spacing gaps between two tubular members 1 and 2. The back-up ring 5 prevents the compliant sealing rings 5 from extruding out of the grooves when subjected to high-temperature and pressure conditions.

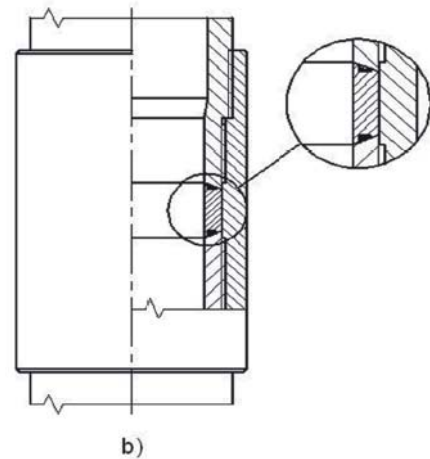
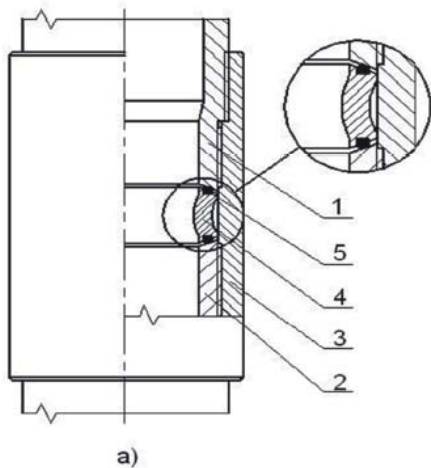


Fig. 7. Tubular joint sealing system with use of an element with shape memory effect: a) joint seal after assembly; b) joint seal in operating conditions after thermal deformation of SMA back up ring. 1 and 2 - tubular members to be joined, 3 - cylindrical sleeve, 4 - back up ring made from SMA and 5 - elastomeric O-ring seal

Figure 8 shows the sealing of a flange pipe joint by means of a SMA ring [5]. The SMA sealing ring 5 is fitted into grooves 4 of pipe flanges 1 and 2, and then fastening bolts 3 are preliminarily tightened to such an extent to bring flanges 1 and 2 into close contact with each other under no load. When the assembly is heated to or above the atmospheric temperature, sealing ring 5 resumes the originally memorised shape, and simultaneously, a reverse transformational stress works so that the faces of ring 5 are pressed, respectively, against face surfaces 4a and 4b of groove 4 in the flanges 1 and 2 to constitute sealing surfaces. Accordingly, it is unnecessary to provide any high fastening force by bolts 3, and it is sufficient to only preliminarily bring flanges 1 and 2 into contact with each other by bolts 3 under no load. In addition, the distribution of stresses in the circumferential direction is made to be relatively uniform. In the case shown in Fig. 8c, sealing ring 5 is made of a SMA and has a large diameter section of a cylindrical annular body, the diametral outer portion of which is opened. Sealing ring 6, also made of SMA and with a small diameter section of a similar cylindrical annular body, with the diametral inner portion opened, is fitted in the inner peripheral face of sealing ring 5. The sealing performance that is set can be achieved without causing abnormal deformation [11].

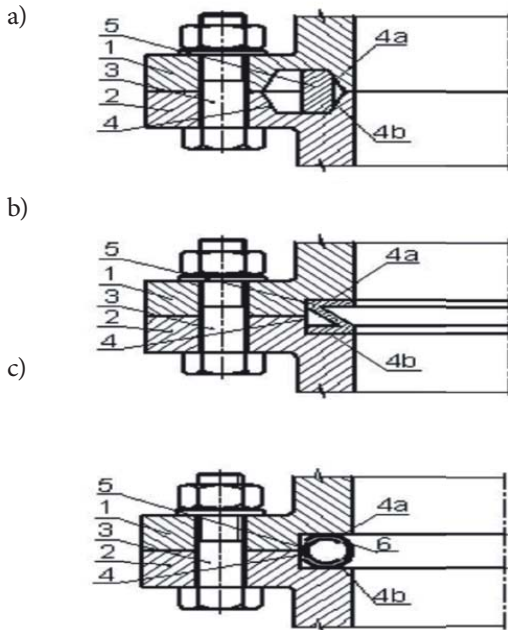


Fig. 8. Sealing of flange pipe joint by means of SMA rings with a-c) variants of design. 1 and 2 – flanges, 3 – bolt, 4 – groove, 4a and 4b – contact surfaces and 5 and 6 – sealing rings made of SMA

Figure 9 shows a method to seal a threaded pipe coupling with sealing rings made of the SMA [12]. These sealing rings are arranged between the butts of the interconnected tubing pipes. Earlier, the sealing rings are pre-cooled in a cryostat to low temperature, e.g., that of liquid nitrogen, to be stained therein, changing in shape and height. Thereafter, they are quickly fitted in place inside the coupling between the pipe butts. When the coupling is heated to or above the atmospheric temperature, the sealing rings resume the originally memorised shape, causing elastic and elasto-plastic deformation of the thread joint elements and thus providing a tight pipe connection.

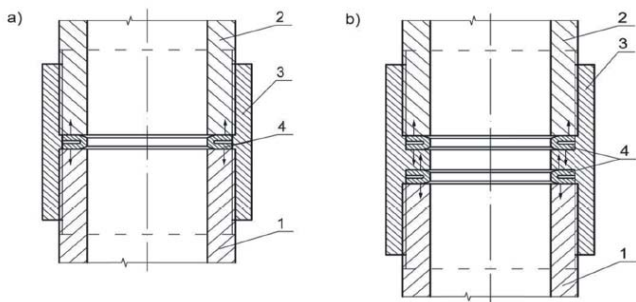


Fig. 9. Threaded pipe coupling with sealing rings made of SMA: a) coupling with one sealing ring; b) coupling with two sealing rings. 1 and 2 – ends of pipes, 3 – threaded coupler and 4 – sealing ring made of SMA

Figure 10 presents a device for detachably joining pipes [13]. The connection comprises sleeve 4 and split ring 3, which has a small axially extending gap formed on its interior surface with a shallow channel between two radially-inwardly extending

edge flanges 3a. The channel receives and locates two flanges 1a and 2a formed on pipes 1 and 2, respectively. Sleeve 4, positioned outwards of split ring 3, is made from the SMA, which can be used to compress the compressible split ring by closing the gap; hence, connecting pipes 1 and 2.

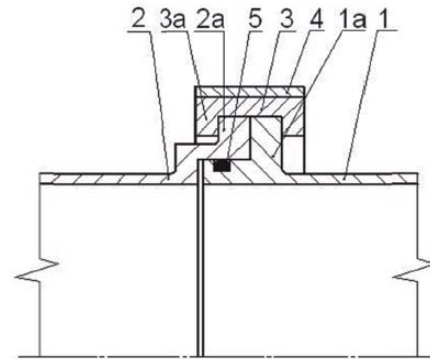


Fig. 10. Connecting device for detachable joining of pipes. 1 and 2 – ends of pipes, 1a and 2a – flanges of pipes, 3 – split ring, 3a – edge flange, 4 – sleeve made of SMA and 5 – elastomeric O-ring seal

Figure 11 shows a diameter-reducing member joint made of a heat-shrinkable type of the SMA [14]. The large diameter connection portion of diameter-reducing pipe joint 3 and large-diameter pipe end 1 are tightened to each other by the shape recovery force when heat-shrinkable sleeve 6 is thermally shrunk and the small-diameter connection portion at the other end of diameter-reducing pipe joint 3 is connected to the small-diameter pipe end 2 in a similar manner, thus providing simple and reliable pipe connection.

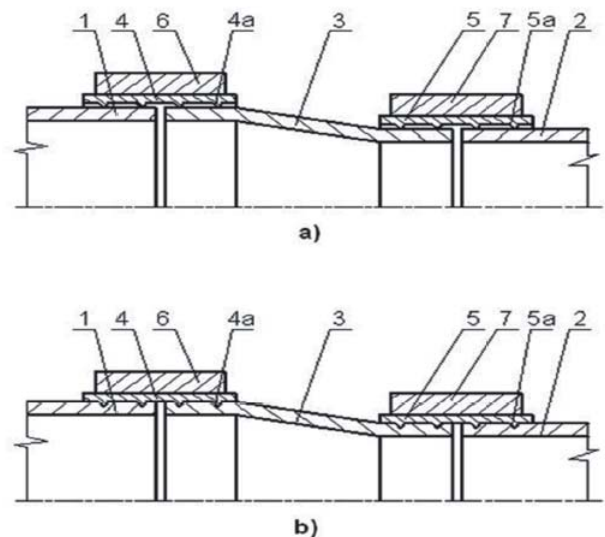


Fig. 11. Diameter-reducing member joint using heat-shrinkable sleeves made of the SMA: a) pipe joint before thermal deformation; b) pipe joint after thermal deformation. 1 and 2 – ends of pipes, 3 – diameter-reducing pipe joint, 4 – large-diameter liner, 5 – small-diameter liner, 4a and 5a – projections and 6 and 7 – heat-shrinkable sleeves made of SMA heating element

Figure 12 shows an SMA pipe coupling for underwater pipes [15]. The pipe coupling comprises tube 3 made of the

SMA and a cover, made of stainless steel 4 having high corrosion resistance, by which high-temperature water can be prevented from making the SMA brittle and from its corroding and damaging, particularly through galvanic corrosion, even in the case where such water exists inside or outside of the pipes.

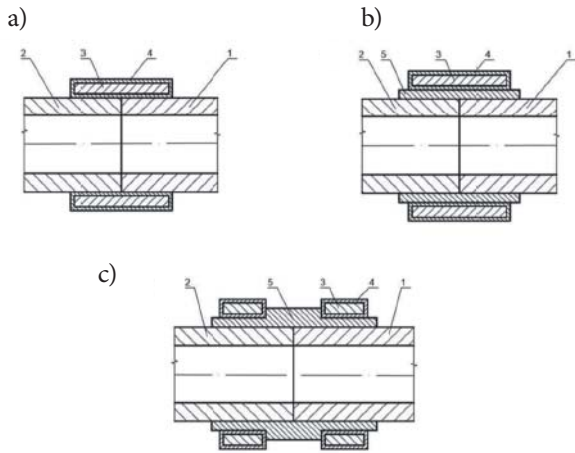


Fig. 12. SMA pipe coupling used for underwater pipe with a-c) variants of design. 1 and 2 - ends of pipes, 3 - tube of SMA, 4 - coating made of stainless steel and 5 - supporting tube

Figure 13 shows a high-pressure pipe coupling device, which is mainly applied in large-diameter undersea oil and gas transportation pipelines [16] or shafts [17]. In the design shown in Fig. 13a, the ends of coupled pipes 1 and 2 are placed inside a composite connector consisting of corrosion resistant liner 4, a number of clamping rings 5 made of SMA, two tensile rings 6, also made of SMA, a thin-walled metallic sleeve 3 and two external support rings 7. The liner 4, with projections on its inner cylindrical surface, is pulled over the ends of coupled pipes 1 and 2. Then, clamping rings 5 are mounted around liner 4. The entire assembly of liner 4 with clamping rings 5 and tensile rings 6 is placed inside the thin-walled metallic sleeve 3, closed with external support rings 7 at both ends. In the solution shown in Fig. 13b, a supplementary heating element 8 is arranged between clamping rings 5 and sleeve 3. The heat delivered by this element accelerates the transformation process and causes deformation of clamping rings 5.

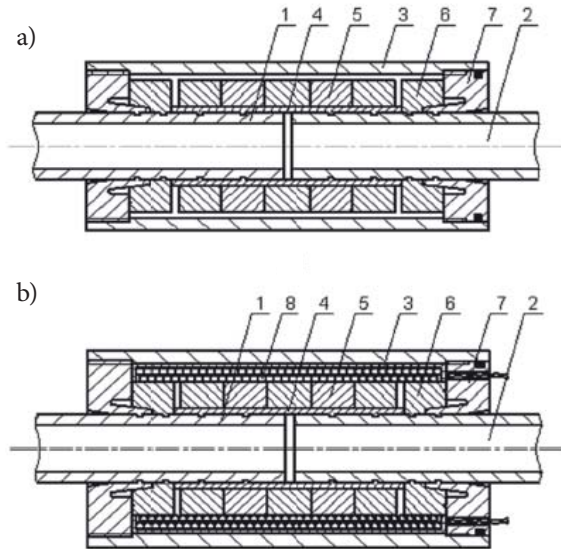


Fig. 13. High-pressure pipe coupling device, especially for large diameter pipe utilised in undersea gas and oil transport: a) design of coupling; b) design of coupling with supplemental heaters. 1 and 2 - ends of pipes, 3 - thin-walled metallic sleeve, 4 - corrosion resistant liner, 5 - clamping ring made of SMA, 6 - tensile ring made of SMA, 7 - external support ring and 8 - electric heating element

## CONCLUDING REMARKS

Metal alloys with shape memory (SMA) belong to a group of intelligent materials that have an ability to memorise the initial shape and, after permanent deformations, resume this shape in certain circumstances. The physical phenomenon which makes shape resuming possible is reversible martensitic transformation, which reveals large deformation and the shape memory effect when heated.

SMA fitting systems are an excellent example of a product that helps significantly reduce process costs in comparison with traditional assembly methods, such as welding, brazing or swaging, and offers as many advantages, such as:

- no expansive tooling;
- leak-proof and permanent connection;
- light-weight design;
- quick and easy installation;
- lower space required around the pipes or shafts.

The presented examples of constructional solutions of SMA-based pipe couplings provide opportunities for significant simplification of their structure, simultaneously ensuring extremely durable and leak proof coupling. They are used in hydraulic systems in aviation and shipbuilding, as well in oil and gas transportation pipelines, among other areas.

## REFERENCES

1. Humbeeck J. V. (2001): Shape Memory Alloys: A Material and a Technology. *Advanced Engineering Materials*, vol. 3, no. 11, pp. 837-850.

2. Duerig T. W., Melton K. N., Stöckel D.: Engineering Aspects of Shape Memory Alloys, Butterworth-Heinemann Publishing, London, 1990, pp. 3-20.
3. Borden T. (1991): Shape Memory Alloys Forming a Tight Fit, Mechanical Engineering, vol. 113, October, pp. 66-70.
4. M. C. Lugg, "Shape Memory Metal Fittings: Enhance the Reliability, maintainability and supportability of Aircraft Hydraulic Systems", Aircraft Engineering and Aerospace Technology, Vol. 62, (1990) No. 5, pp. 10-11.
5. Ochoński W. (2010): Application of shape memory materials in fluid sealing technology, Industrial Lubrication and Tribology, vol.60, no 2.
6. (1979): Use of Heat Recoverable Coupling Technology in Shipyard Production, NAVAL ENGINEERS JOURNAL, Maurice R. Caskey, Gerald D. Embry, Vol. 91, 2, 45-59
7. Patent US, Int.Cl. F16L25/00, no 4035007, Heat recoverable metallic coupling.
8. Patent US, Int.Cl. F16L25/00, no 4469357, Composite coupling.
9. Company Aerofit Inc. (USA): Catalog of products.
10. Patent US, Int.Cl. no 4537406, Hostile environment joint seal and method for installation.
11. Patent JP, Int.Cl. F16J15/08, no 1153871, Gasket.
12. Patent RU, Int.Cl.E21B17/08, no 2517344, Method of sealing casing by gasket with memory.
13. Patent EP, Int.Cl. F16B1/00, no 0302618, Connecting device.
14. Patent US, Int.Cl. F16L55/17, no 5338070, Diameter-reducing member joint device.
15. Patent US, Int.Cl.F16L35/00, no 5687995, Shape memory alloy pipe coupling for underwater pipe.
16. Patent US, Int.Cl. F16L13/04, no 4314718, Tensile ring composite pipe coupling.
17. Marine propeller shaft bearings under low-speed conditions: water vs. oil lubrication, W. Litwin – TRIBOLOGY TRANSACTIONS – 2019 TRIBOLOGY TRANSACTIONS pp 1 - 11, ISSN: 1040-2004

## CONTACT WITH THE AUTHOR

**Leszek Matuszewski**

*e-mail: leszekma@pg.edu.pl*

Gdańsk University of Technology  
Narutowicza 11/12, 80-233 Gdańsk  
**POLAND**

# INVESTIGATIONS OF THE WORKING PROCESS IN A DUAL-FUEL LOW-EMISSION COMBUSTION CHAMBER FOR AN FPSO GAS TURBINE ENGINE

Serhiy Serbin <sup>1</sup>

Badri Diasamidze <sup>1</sup>

Marek Dzida <sup>2</sup>

<sup>1</sup> Admiral Makarov National University of Shipbuilding, Ukraine

<sup>2</sup> Gdańsk University of Technology, Poland

## ABSTRACT

*This investigation is devoted to an analysis of the working process in a dual-fuel low-emission combustion chamber for a floating vessel's gas turbine. The low-emission gas turbine combustion chamber with partial pre-mixing of fuel and air inside the outer and inner radial-axial swirlers was chosen as the object of research. When modelling processes in a dual-flow low-emission gas turbine combustion chamber, a generalized method is used, based on the numerical solution of the system of conservation and transport equations for a multi-component chemically reactive turbulent system, taking into consideration nitrogen oxides formation. The Eddy-Dissipation-Concept model, which incorporates Arrhenius chemical kinetics in a turbulent flame, and the Discrete Phase Model describing the interfacial interaction are used in the investigation. The obtained results confirmed the possibility of organizing efficient combustion of distillate liquid fuel in a low-emission gas turbine combustion chamber operating on the principle of partial preliminary formation of a fuel-air mixture. Comparison of four methods of liquid fuel supply to the channels of radial-axial swirlers (centrifugal, axial, combined, and radial) revealed the advantages of the radial supply method, which are manifested in a decrease in the overall temperature field non-uniformity at the outlet and a decrease in nitrogen oxides emissions. The calculated concentrations of nitrogen oxides and carbon monoxide at the flame tube outlet for the radial method of fuel supply are 32 and 9.1 ppm, respectively. The results can be useful for further modification and improvement of the characteristics of dual-fuel gas turbine combustion chambers operating with both gaseous and liquid fuels.*

**Keywords:** gas turbine engine; dual-fuel combustion; combustion chamber; liquid fuel

## INTRODUCTION

Increased production in deep-sea and remote terrestrial areas has led to an increase in the number of Floating Production, Storage, and Offloading (FPSO) vessels. By the end of 2018, there were 183 FPSO vessels operating in the offshore fleet, with 55 more expected to be built by 2022 [1]. One of the main factors that ensure the efficient operation of the first link in the logistics chain of production (transportation – supply of offshore oil and gas) is indicators of power plant's energy efficiency. The composition and characteristics of the installations of such offshore infrastructure vary widely. The main drive engines for power generators and process

compressors are gas turbine engines and medium-speed diesel engines.

FPSO power plants that are commonly used are gas turbines and combined plants. So, on board the FPSO Global Producer III, the power plant consists of two gas turbine units with a total capacity of 32 MW and a utilization facility that provides heat to all consumers associated with the technological cycle [2]. The main power plant of the FPSO Armada Olombendo has three gas turbine engines of 21 MW each [3]. The combined power plant of the FPSO Dhirubhai-1 has three gas turbogenerators with a capacity of 4 MW and two main boilers for the operation of steam turbogenerators with a total capacity of 17 MW [4]. Several

works are devoted to the improvement of power plants that can be used on FPSOs [5–7].

One of the possible ways to increase the manoeuvrability, flexibility, and efficiency of gas turbine power modules for a FPSO unit is the use of dual-fuel combustion in the combustion chamber. The main problem in developing dual-fuel combustion chambers is to ensure the minimal emission of nitrogen oxides when working on liquid fuel. Compared to gaseous fuels, the emission of nitrogen oxides can significantly increase due to deterioration of the fuel-air mixture conditions, an increase in the flame emissivity, and increases in combustion length and the working fluid's residence time in high-temperature zones. Very often, steam or water is supplied to the primary combustion chamber's zone to suppress the formation of nitrogen oxides; however, this reduces the reliability of the power plant due to the presence of additional systems and raises the cost of maintenance. Therefore, the development of gas turbine dual-fuel combustion chambers that provide the necessary emissions of nitrogen oxides without steam or water injection is an urgent task.

The problem of improving the emission performance in combustion devices of gas turbine engines was considered in [8–10]. It should be noted that many researchers [11, 12] indicate that improving the quality of mixture formation, turbulent interaction under conditions of strongly swirling flows, and increasing the quality of liquid fuel atomization lead to the homogenization of mixtures, more active burning of fuels with different phase compositions, and, as a result, a reduction in nitrogen oxide emissions.

Despite a large amount of scientific research in the field of low-emission combustion chambers, the methodological and technical aspects of solving the problem of development of dual-fuel combustion chambers for an FPSO power system have not been sufficiently developed to date. It should be noted that most investigations of dual-fuel combustion chambers have been done exclusively by experimental methods, while only a small number of researchers [13–15] have used methods of computational fluid dynamics (CFD). In our opinion, research in this area will be relevant and will be able to significantly increase the efficiency of dual-fuel chamber workflow as well as expand the limits of flame propagation in flame tubes and the range of sustainable and ecologically clean operation.

To increase the efficiency of a dual-fuel gas turbine combustion chamber for an FPSO, the idea of preliminary partial evaporation and mixing of liquid fuel with air in radial-axial swirlers is proposed. This will ensure the necessary emission characteristics of gas turbine engines when operating on light distillate liquid fuels without additional injection of steam or water.

## MATHEMATICAL MODELLING

The modelling of physical and chemical processes in a dual-fuel low-emission combustion chamber for an FPSO

is based on the solution of the differential equations of mass, impulse, and energy conservation for the multi-component, turbulent, chemically reacting system [16–18]. A detailed description of the equations and methods of solving them in the case of using gaseous fuel is given in [19–22].

The main equations of the gaseous phase model are as follows [21, 22]:

– the continuity equation

$$\frac{\partial \rho}{\partial t} + \frac{\partial}{\partial x_i} (\rho u_i) = \dot{\rho}^S, \quad (1)$$

– the equation of momentum conservation

$$\begin{aligned} \frac{\partial}{\partial t} (\rho u_j) + \frac{\partial}{\partial x_i} (\rho u_i u_j) = \frac{\partial}{\partial x_i} \left[ \mu \left( \frac{\partial u_j}{\partial x_i} + \frac{\partial u_i}{\partial x_j} \right) \right] - \frac{\partial p}{\partial x_j} + \\ + \rho g_j + \dot{F}^S + \frac{\partial}{\partial x_i} (\overline{\rho u_i' u_j'}), \end{aligned} \quad (2)$$

– the transfer equations for the kinetic energy of turbulence  $k$  and the dissipation rate of turbulent energy  $\varepsilon$  for the RNG turbulence model [23]:

$$\begin{aligned} \frac{\partial}{\partial t} (\rho k) + \frac{\partial}{\partial x_i} (\rho k u_i) = \frac{\partial}{\partial x_j} \left[ \left( \alpha_k \mu_{eff} \right) \frac{\partial k}{\partial x_j} \right] + \\ + G_k + G_b - \rho \varepsilon - Y_M + S_k, \end{aligned} \quad (3)$$

$$\begin{aligned} \frac{\partial}{\partial t} (\rho \varepsilon) + \frac{\partial}{\partial x_i} (\rho \varepsilon u_i) = \frac{\partial}{\partial x_j} \left[ \left( \alpha_\varepsilon \mu_{eff} \right) \frac{\partial \varepsilon}{\partial x_j} \right] + \\ + C_{1\varepsilon} \frac{\varepsilon}{k} (G_k + C_{3\varepsilon} G_b) - C_{2\varepsilon} \rho \frac{\varepsilon^2}{k} - R_\varepsilon + S_\varepsilon. \end{aligned} \quad (4)$$

– the energy conservation equation

$$\begin{aligned} \frac{\partial}{\partial t} (\rho h_0) + \frac{\partial}{\partial x_i} (\rho u_i h_0) = \frac{\partial}{\partial x_i} \frac{k_m + k_t}{c_p} \left[ \frac{\partial (h_0 - u^2/2)}{\partial x_i} - \sum_j h_j \frac{\partial X_j}{\partial x_i} \right] - \\ - \frac{\partial}{\partial x_i} \sum_j h_j J_{ji} + \frac{\partial p}{\partial t} - \frac{\partial}{\partial x_i} (\tau_{ik} u_k) + S_h + \dot{Q}^S, \end{aligned} \quad (5)$$

– the equation for the conservation of chemical components

$$\frac{\partial}{\partial t} (\rho Y_i) + \frac{\partial}{\partial x_i} (\rho u_i Y_i) = \frac{\partial}{\partial x_i} J_i + R_i + \dot{\rho}^S \delta_i. \quad (6)$$

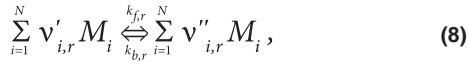
In Eqs. (1)–(6),  $t$  is the time;  $x_i$  and  $x_j$  are the coordinates;  $\rho$ ,  $u$ ,  $\mu$ ,  $p$ , and  $g$  are the density, velocity, viscosity, pressure, and gravity acceleration;  $\mu_{eff}$  is the efficient viscosity coefficient;  $\alpha_k$  and  $\alpha_\varepsilon$  are the reverse values of the efficient Prandtl number for  $k$  and  $\varepsilon$ , respectively;  $\dot{\rho}^S$ ,  $\dot{F}^S$ ,  $\dot{W}^S$ , and  $\dot{Q}^S$  are the sources for interaction of the gas and liquid phases;  $G_k$  is the source describing the generation of turbulent energy;  $C_1$ ,  $C_2$  and  $C_3$  are the empirical constants;  $h_0$  is the stagnation enthalpy;  $h_j$  is the component's enthalpy;  $k_m$  and  $k_t$  are the coefficients of molecular and effective thermal conductivity;  $c_p$  is the specific heat of the mixture at constant pressure;  $\tau_{ik}$  is the shear stress tensor;  $J_{ji}$  is the component  $j$  flow in the direction  $i$ ;  $S_h$  is the source term from the chemical reaction;  $Y_i$  is the mass fraction of component  $i$ ;  $R_i$  is the rate of the component's formation or destruction;  $J_i$  is the diffusion component's flow; and  $\delta_i$  is the Dirac delta function.

The net source of chemical species  $i$  due to the reaction is computed as the sum of the Arrhenius reaction sources over the  $N_R$  reactions in which the species participate:

$$R_i = M_{w,i} \sum_{r=1}^{N_R} R_{i,r}, \quad (7)$$

where  $M_{w,i}$  is the molecular weight of species  $i$  and  $R_{i,r}$  is the Arrhenius molar rate of creation/destruction of species  $i$  in reaction  $r$ .

Consider the  $r$ -th reaction written in general form:



where  $N$  is the number of chemical species in the system;  $v'_{i,r}$  is the stoichiometric coefficient for reactant  $i$  in reaction  $r$ ;  $v''_{i,r}$  is the stoichiometric coefficient for product  $i$  in reaction  $r$ ;  $M_i$  is the symbol denoting species  $i$ ;  $k_{f,r}$  is the forward rate constant for reaction  $r$ ; and  $k_{b,r}$  is the backward rate constant for reaction  $r$ .

For a non-reversible reaction, the molar rate of creation/destruction of species  $i$  in reaction  $r$  is given by

$$R_{i,r} = \Gamma(v''_{i,r} - v'_{i,r}) \cdot \left( k_{f,r} \prod_{j=1}^N [C_{j,r}]^{\eta'_{j,r}} \right), \quad (9)$$

where  $C_{j,r}$  is the molar concentration of species  $j$  in reaction  $r$ ;  $\eta'_{j,r}$  is the rate exponent for reactant species  $j$  in reaction  $r$ ;  $\eta''_{j,r}$  is the rate exponent for product species  $j$  in reaction  $r$ ; and  $\Gamma$  presents the net effect of third bodies on the reaction rate:

$$\Gamma = \sum_j^{N_r} \gamma_{j,r} C_j, \quad (10)$$

where  $\gamma_{j,r}$  is the third-body efficiency of the  $j$ -th species in the reaction  $r$ .

The Eddy Dissipation Concept (EDC) combustion model [24] includes detailed chemical mechanisms in turbulent flows and is applied in the present investigation. It assumes that the reaction occurs in small turbulent structures, called fine scales. The length fraction of the fine scales is modelled as

$$\xi^* = C_\xi (v\varepsilon/k^2)^{0.75}, \quad (11)$$

where  $C_\xi$  is the volume fraction constant and  $\nu$  is the kinematic viscosity.

Species are assumed to react in the fine structures over a time scale

$$\tau^* = C_\tau (v/\varepsilon)^{0.5}, \quad (12)$$

where  $C_\tau = 0.4082$  is the time-scale constant.

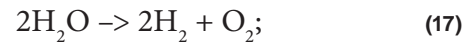
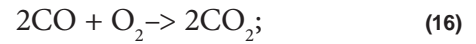
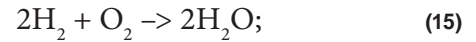
Reactions proceed over the time scale  $\tau^*$ , governed by the Arrhenius rates, and are integrated numerically using the ISAT algorithm [25]. The validity of the EDC approach for modelling physicochemical processes is demonstrated for two-phase turbulent swirl liquid spray combustion in a complex gas turbine combustion chamber [26] and for a model gas turbine combustor [27].

Modelling of nitrogen oxides emissions was carried out using transfer equations which include convection, diffusion, formation, and decomposition of NO and related compounds. The influence of the reaction volume's residence time on the mechanism of nitrogen oxide formation is considered in the convection terms of the defining equations written in the Euler reference system. For thermal and prompt nitrogen oxides, it is necessary to solve the NO transfer equation [18, 21]:

$$\frac{\partial}{\partial t}(\rho Y_{\text{NO}}) + \nabla \cdot (\rho \vec{v} Y_{\text{NO}}) = \nabla \cdot (\rho D \nabla Y_{\text{NO}}) + S_{\text{NO}}, \quad (13)$$

where  $\rho$  is the nitrogen oxide density;  $Y_{\text{NO}}$  is the NO mass fraction;  $D$  is the diffusion coefficient;  $\vec{v}$  is the velocity vector; and  $S_{\text{NO}}$  is the source term depending on the NO formation mechanism.

To simulate the formation of carbon monoxide and molecular hydrogen in the combustion chamber, it is proposed to use a five-step combustion model: Eqs. (14)–(18). The kinetic mechanism of hydrocarbon  $C_{16}H_{29}$  (equivalent to light distillate fuel) combustion is as follows:



Validation of similar global chemical mechanisms for the conditions of a gas turbine combustion chamber was carried out in a number of works [18, 28, 29].

For calculations of liquid fuel combustion in a low-emission combustion chamber, the Discrete Phase Model (DPM), which calculates the trajectories of motion for individual particles, was selected [18, 30].

The model predicts the particle trajectories of the discrete phase by integrating their motion equations written in the Lagrange form [18, 30, 31] (given only for the  $x$ -direction):

$$\frac{du_p}{dt} = F_D (u - u_p) + \frac{g_x(\rho_p - \rho)}{\rho_p} + F_x, \quad (19)$$

where  $F_x$  is the additional term that takes into consideration the gas flow acceleration;  $F_D(u - u_p)$  is the drag force, which is per unit mass of the particle:

$$F_D = \frac{18\mu}{\rho_p d_p^2} \frac{C_D \text{Re}}{24}. \quad (20)$$

In the above expressions,  $u$  is the gas phase velocity;  $u_p$  is the particle velocity;  $\mu$  is the coefficient of the gas phase molecular viscosity;  $\rho$  is the gas phase density;  $\rho_p$  is the particle density;  $d_p$  is the current particle diameter;  $\text{Re}$  is the Reynolds number; and  $C_D$  is the particle drag coefficient.

The turbulent dispersion of the particles over their averaged trajectory is calculated using statistical methods. The particle distribution over the averaged trajectory is represented as the Gaussian probability density function, whose change is determined by the degree of particle dispersion due to the action of turbulent pulsations. Turbulent dispersion is calculated by integrating the equations of motion of individual particles using instantaneous values of the gas phase velocities in their vicinity.

The inert heating model is used when the droplet temperature is less than the evaporation temperature. To calculate the change in particle temperature over time  $T_p(t)$ , the heat balance equation is used, which takes into consideration convective and radiative heat transfer:

$$m_p c_p \frac{dT_p}{dt} = h A_p (T_\infty - T_p) + \varepsilon_p A_p \sigma (\theta_R^4 - T_p^4), \quad (21)$$

where  $m_p$  is the mass of the particle;  $c_p$  is the specific heat of the particle at constant pressure;  $A_p$  is the particle surface;  $T_\infty$  is the local gas phase temperature;  $h$  is the heat transfer coefficient;  $\varepsilon_p$  is the particle radiation coefficient;  $\sigma$  is the Stefan-Boltzmann constant; and  $\theta_R$  is the radiation temperature.

The heat transfer coefficient  $h$  is calculated using the Ranz and Marshall correlation:

$$\text{Nu} = \frac{h d_p}{k_\infty} = 2.0 + 0.6 \text{Re}_d^{1/2} \text{Pr}^{1/3}, \quad (22)$$

where  $k_\infty$  is the coefficient of thermal conductivity of the gas phase;  $\text{Re}_d$  is the Reynolds number, which is determined by the droplet diameter and its relative velocity; and  $\text{Pr}$  is the Prandtl number for the gaseous phase.

The radiation temperature and the incident radiation  $G$  are:

$$\theta_R = (G/4\sigma)^{1/4} \quad (23)$$

$$G = \int_{\Omega=4\pi} I d\Omega, \quad (24)$$

where  $I$  is the radiation intensity;  $\Omega$  is the solid angle.

The above equations are integrated over time using an approximately linear form, which implies that the temperature of the particles changes rather slowly.

The evaporation pattern is initiated when the particle temperature reaches the evaporation temperature  $T_{evap}$  and is used as long as the temperature does not exceed the boiling point  $T_{bp}$  or until the volatile particle components are completely consumed (in the case of residual fuel combustion).

The equation of particle heat transfer with gas phase during their evaporation takes into consideration the convective and radiative heat flows as well as the process of vaporization:

$$m_p c_p \frac{dT_p}{dt} = h A_p (T_\infty - T_p) + \varepsilon_p A_p \sigma (\theta_R^4 - T_p^4) + \frac{dm_p}{dt} h_{fg}, \quad (25)$$

where  $h_{fg}$  is the latent heat of evaporation.

The mass of the particle during evaporation decreases in accordance with the balance equation:

$$m_p(t + \Delta t) = m_p(t) - N_i A_p M_{w,i} \Delta t, \quad (26)$$

where  $M_{w,i}$  is the molecular weight of the particle  $i$ .

The degree of evaporation is determined by the diffusion flow of fuel vapour into the gas phase and is proportional to the gradient of vapour concentrations on the particle surface and in the gas environment:

$$N_i = k_c (C_{i,S} - C_{i,\infty}), \quad (27)$$

where  $N_i$  is the molar flow of evaporated substance;  $k_c$  is the mass transfer coefficient;  $C_{i,S}$  is the vapour concentration on the droplet surface; and  $C_{i,\infty}$  is the vapour concentration in the gas environment.

When the particle temperature reaches the boiling point, the following equation is used to change its diameter:

$$-\frac{d(d_p)}{dt} = \frac{2}{\rho_p h_{fg}} \left[ \frac{2k_\infty [1 + 0.23\sqrt{\text{Re}_d}]}{d_p} (T_\infty - T_p) + \varepsilon_p \sigma (\theta_R^4 - T_p^4) \right]. \quad (28)$$

For simplicity, it is assumed that the temperature of the droplet does not change when boiling. The energy required for evaporation is taken into consideration as a source term in the equation for the energy conservation of the gas phase. Liquid evaporation is also a source of chemical component for the gas phase.

## EXPERIMENTAL SETUP AND VERIFICATION OF THE MATHEMATICAL MODEL

A low-emission combustion chamber with partial preliminary mixing of fuel and air for a 25-MW UGT25000 gas turbine engine produced by Zorya-Mashroekt [21, 32] operating on gaseous fuel was chosen as the object of investigation. The combustion chamber has a cannular counterflow structure (Fig. 1), which implements the principle of dry combustion of a partially mixed lean mixture [21]. The main element of such a chamber is a burner device consisting of two radial-axial swirlers of the first and second channels, behind which the annular mixing chambers are located. The proportion of air flowing through the first and second swirlers' channels is approximately 12 and 61%, respectively, of the total air flow through the flame tube. The fuel gas is fed through a series of holes made in the blades of the radial-axial swirlers of the first and second channels.

To verify the results of a three-dimensional mathematical model, experimental measurements of the temperature field at 25 points of the outlet section of the single burner compartment of a gas turbine combustion chamber for seven operating modes were performed (Table 1). The operating modes differed in the inlet parameters of air and fuel and in the distribution of gaseous fuel flow rates between the outer and inner swirlers' channels [21]. Due to the features of the used test bench, the operating pressure in the compartment did not exceed 0.15 MPa in all operating modes.

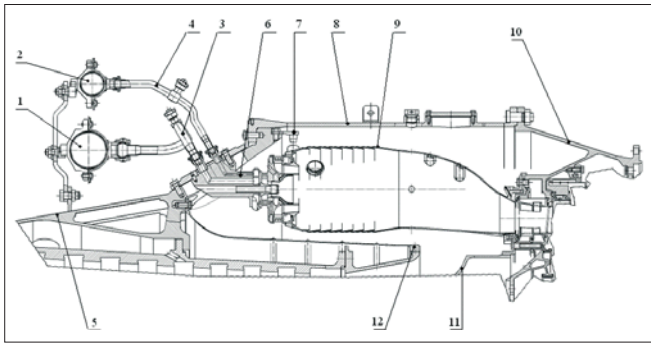


Fig. 1. Low-emission gas turbine combustion chamber: 1, 2 – collectors of the first and second channels; 3, 4 – delivery pipes of the first and second channels; 5 – compressor casing; 6 – burner; 7 – holder; 8 – combustor casing; 9 – flame tube; 10 – load-carrying body; 11 – diffuser; 12 – inner casing

Note that operating modes 3 and 6 approximately correspond to the nominal mode of the gas turbine engine according to the gas temperature at the turbine inlet.

Tab. 1. Operating modes of bench experiment

Mode number	Air flow through the compartment, kg/s	Inlet air temperature, K	Total fuel mass flow rate $G_f$ , kg/h	Fuel temperature, K
1	0.395	389	4.8	286.0
2	0.313	624	18.8	287.2
3	0.318	626	22.6	287.5
4	0.315	628	25.6	287.6
5	0.315	627	25.0	287.5
6	0.316	605	20.9	287.5
7	0.327	667	27.9	288.0

Figure= 2 shows a comparison of the measured and calculated gas temperatures at the outlet of the low-emission combustion chamber [21], from which it can be concluded that that using three-dimensional methodology it is possible to reliably predict the exhaust gas temperature distribution for a wide range of operating modes.

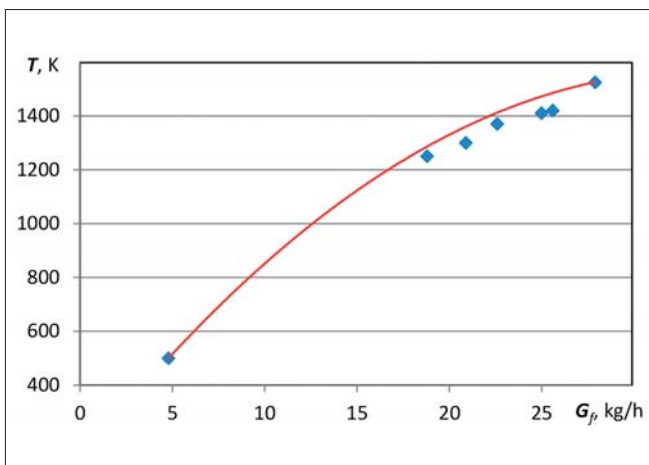


Fig. 2. The distribution of the average temperature at the combustion chamber's outlet: ◆ - experiment; — - calculation

The measured and calculated values of the nitrogen oxide emission for the seven test modes are presented in Fig. 3. A good correlation of the data indicates adequacy of the mathematical model of the formation/decomposition of nitrogen oxides.

Note that the investigation of the aerodynamic flow structure in a low-emission gas turbine combustion chamber under isothermal and non-isothermal conditions confirms the reliability of the proposed mathematical model, its adequacy for physical processes, and the qualitative and quantitative agreement of the experimental and calculated data, which makes it possible to use it for predicting the parameters of a dual-fuel gas turbine combustion chamber for an FPSO.

## INVESTIGATION OF CHARACTERISTICS OF WORKING PROCESSES IN A DUAL-FUEL LOW-EMISSION COMBUSTION CHAMBER

For a 1/16 part of a low-emission combustion chamber of a 25-MW gas turbine engine, the finite-difference mesh consists of 2.7 million tetrahedrons. The following initial conditions are accepted: an air temperature at the diffuser inlet of 770 K, a pressure of 20.523 MPa, an air flow rate of 4.355 kg/s, and a total liquid fuel consumption through the fuel supply pipes of 359.64 kg/h. These parameters correspond to the nominal operating mode of a 25-MW gas turbine engine. To simplify the calculations, the flame tube walls were taken as adiabatic. Typical root mean square (RSM) residuals to establish the solution convergence are about  $1e-4$ .

Four methods of supplying liquid fuel to the flame tube's burner are considered:

- 1) a centrifugal method, in which 100% of the fuel is fed through a central centrifugal nozzle (Fig. 4a);
- 2) an axial method, in which 95% of the fuel (0.09495 kg/s) is fed axially through 15 tubes located in the outer swirler and 5% of the fuel (0.00495 kg/s) is fed axially through 15 tubes located in the inner swirler (Fig. 4b);

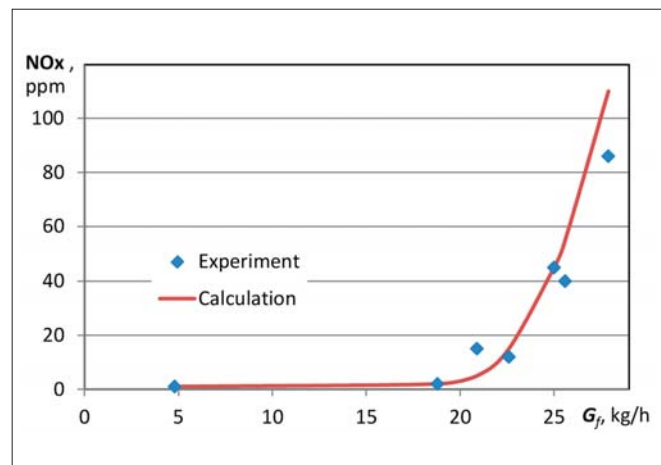


Fig. 3. Emission of nitrogen oxides depending on gaseous fuel mass flow rate

- 3) a combined method (radial-centrifugal), in which 92% of the fuel (0.09193545 kg/s) is fed through the outer swirler radially, 4.8% of the fuel (0.0048375 kg/s) is fed through the inner swirler radially, and 3.2% of the fuel (0.003225 kg/s) is fed through the central centrifugal nozzle (Fig. 4c); and
- 4) a radial method, in which 95% of the fuel is fed radially through the outer swirler and 5% of the fuel is fed radially through the inner swirler (Fig. 4d).

In most cases, the modelling uses a “single” fuel injection method: a fuel stream flows through a series of small-diameter single tubes that are fed into the radial-axial swirlers. The initial diameters of the fuel droplets for the cases with the central centrifugal nozzle are based on the Rosin-Rammler distribution (from 5 to 75  $\mu\text{m}$ ); for all other cases (axial and radial supply of liquid fuel) the starting average diameter is taken as 50  $\mu\text{m}$ . The accepted parameters of distillate fuel spraying are an initial droplet flow velocity of 50 m/s and a fuel spray angle of 70°. The computer program ANSYS Fluent is used for calculations.

Figure 4 shows liquid particle traces in the longitudinal section of the flame tube, depending on the supply method,

taking into consideration the features of mixing the fuel with the oxidizer in the channels of the radial-axial swirlers. Centrifugal and axial methods of liquid fuel supply (1 and 2) are characterized by the longest track lines, and the process of droplet evaporation is completed only in the area of the third shell of the flame tube. This indicates the unsatisfactory quality of the processes of droplet heating, evaporation, and mixing of the fuel vapour with the oxidizer.

This is confirmed by the data in Fig. 5, which shows the temperature contours in the longitudinal section of the flame tube, depending on the method of fuel supply. When the centrifugal supply method (1) is used, the fuel torch extends almost to the flame tube’s outlet; the liquid fuel does not completely burn out, causing extremely high temperature-field non-uniformity at the outlet (Table 1). When the axial fuel supply method (2) is used, the droplets are concentrated in the area of the flame tube walls and burn down in these regions, which leads to a sharp increase in the temperature of the flame tube’s shells and their possible burnout. Methods 3 and 4 lack the aforementioned disadvantages, which results in significantly more efficient liquid fuel combustion.

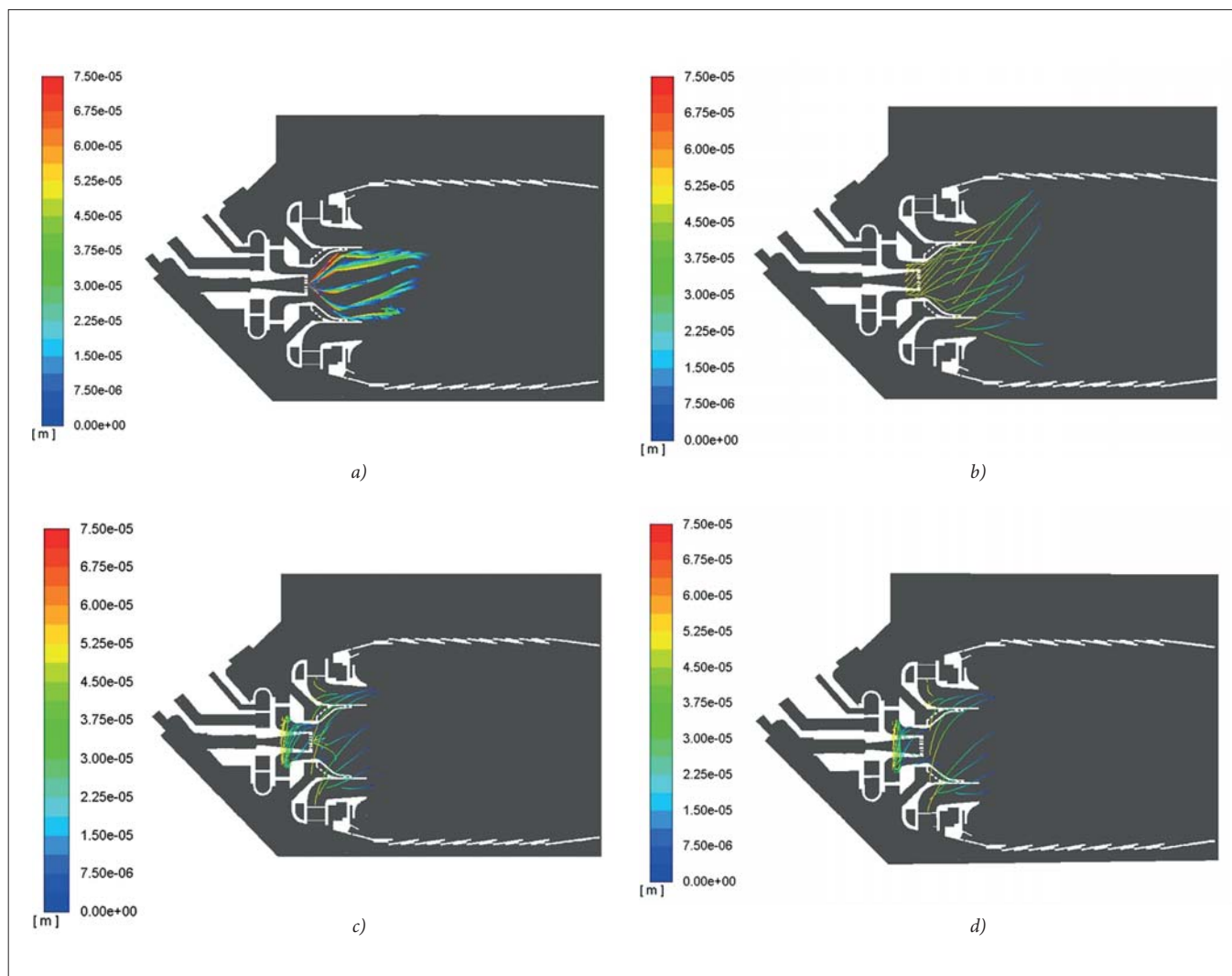


Fig. 4. Liquid particle traces coloured by particle diameter (m) with different supply methods: (a) 1; (b) 2; (c) 3; (d) 4

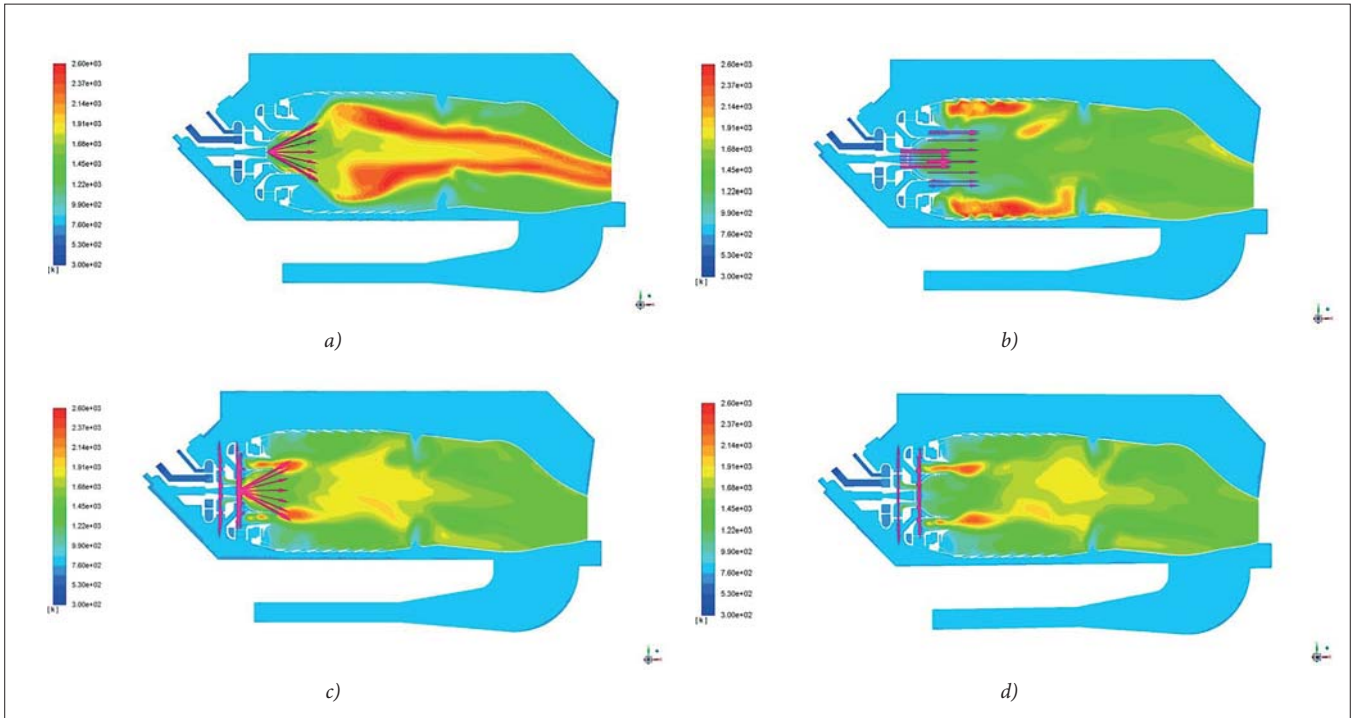


Fig. 5. Distribution of gas temperatures along the flame tube with different fuel supply methods: (a) 1; (b) 2; (c) 3; (d) 4

It should be noted that the liquid fuel supply into the primary zone of the low-emission combustion chamber with a high air-excess coefficient can lead to a deterioration of the conditions of flame stabilization, pulsations, and even the possible extinction of the torch. To increase the stability of liquid fuel combustion under dual-fuel combustion chamber conditions, it is advisable to use plasma-chemical combustion intensifiers [33, 34], which,

as shown in [16, 18], significantly extend the flame propagation limits and stability under conditions of very lean fuel-air mixtures.

Figure 6 shows the contours of volume concentrations of nitrogen oxides in the flame tube's longitudinal section, which are determined by the appropriate temperature distribution since the main factor is the thermal mechanism of nitrogen oxides formation.

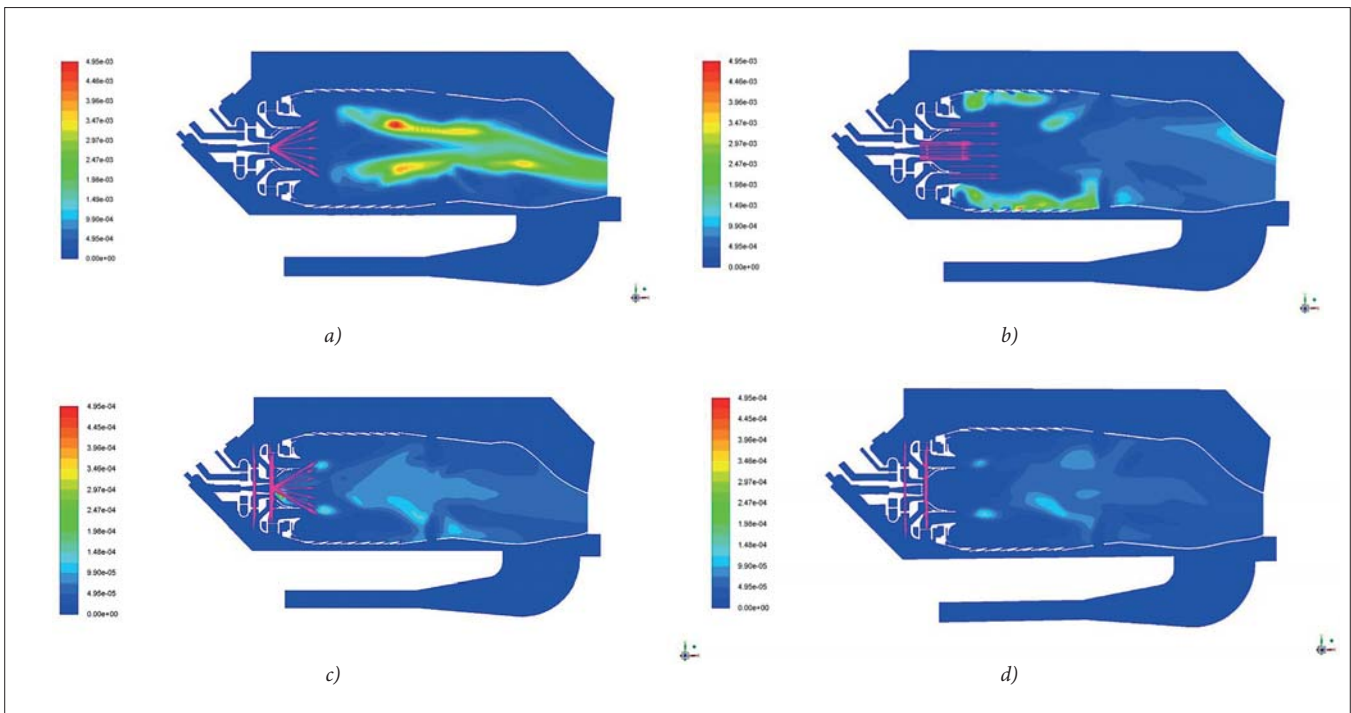


Fig. 6. Distribution of NO mole fractions with different fuel supply methods: (a) 1; (b) 2; (c) 3; (d) 4

Liquid fuel supply methods 3 and 4 with a lower maximum combustion temperature are also determined by lower levels of nitrogen oxide emissions.

Figure 7 shows the calculated dependencies of NO and CO emissions (at 15% O<sub>2</sub>, dry basis) and the overall temperature-field non-uniformity  $\delta$  at the exit combustion chamber section on the fuel supply methods.

It should be noted that the coefficient of the overall temperature-field non-uniformity is determined by the formula

$$\delta = \frac{T_{max} - T_{min}}{T_{av}}, \quad (29)$$

where  $T_{max}$ ,  $T_{min}$ , and  $T_{av}$  are the maximum, minimum, and average gas temperature in the outlet flame tube's section.

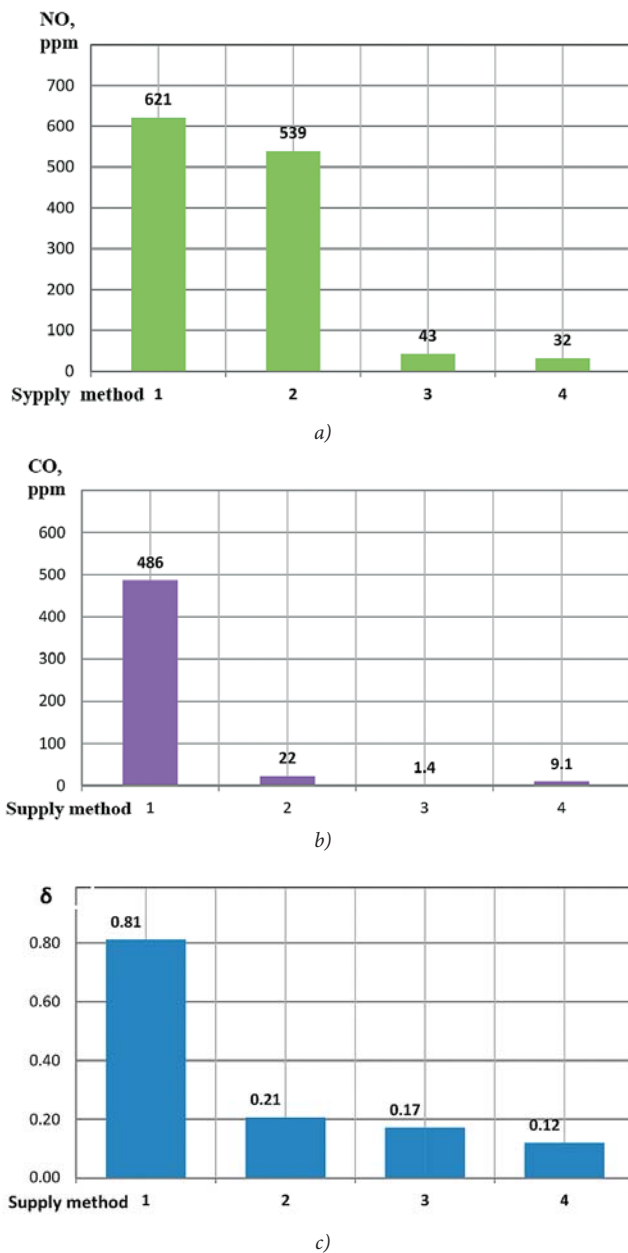


Fig. 7. Combustion chamber's outlet parameters with different fuel supply methods: (a), (b) NO and CO emission at 15% O<sub>2</sub>, dry basis; (c) temperature-field non-uniformity

For the most effective radial fuel supply method, the effect of the liquid fuel outflow velocities on the characteristics of a dual-fuel combustion chamber was also analysed. There is a close connection between temperature distribution (Fig. 8), nitrogen oxides concentrations (Fig. 9), turbulence, and flow patterns.

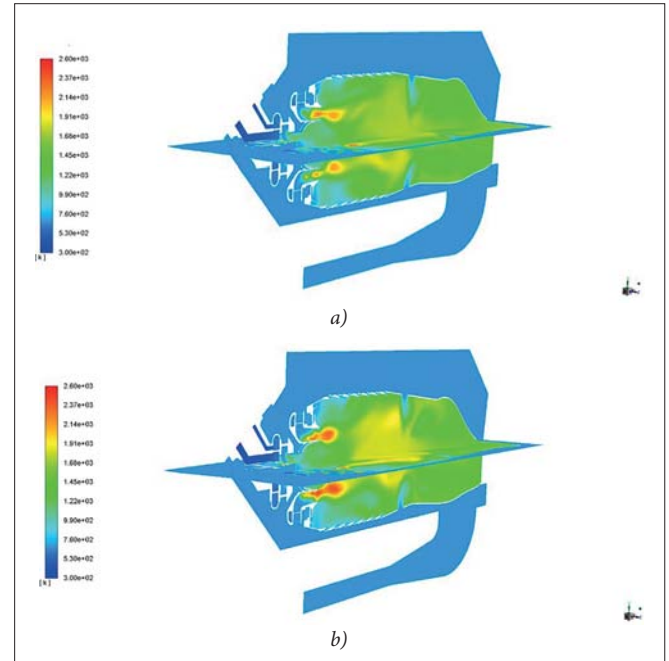


Fig. 8. Temperature contours (K) at different fuel outflow velocities: (a) 5 m/s; (b) 50 m/s

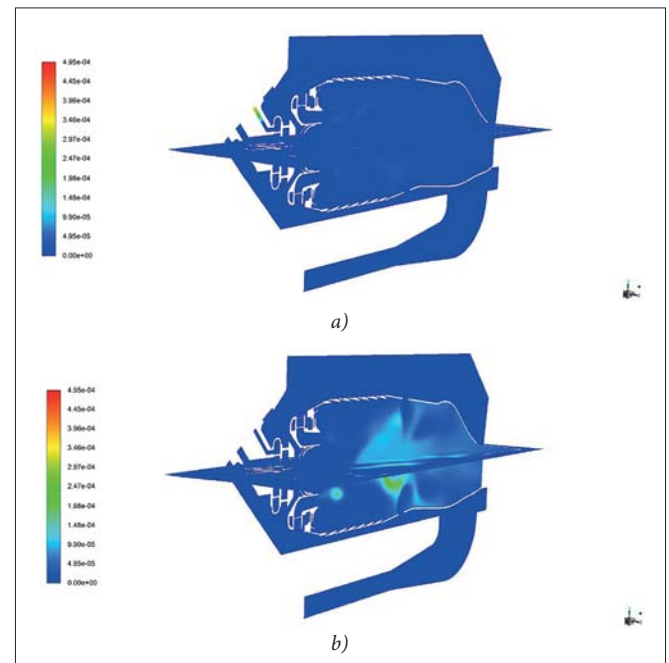


Fig. 9. Contours of NO mole fractions at different fuel outflow velocities: (a) 5 m/s; (b) 50 m/s

The dependence of nitrogen oxides emissions on the fuel outflow velocity  $V_{out}$  is presented in Fig. 10. Improvement in the conditions of mixing and better homogenization of the mixture of evaporated fuel and air in the outer and inner

swirlers' channels with a decrease in the fuel outflow velocities lead to a decrease in the rate of nitrogen oxides formation. In addition, growth in the fuel outflow velocities shifts the high-temperature zone to the secondary air supply holes (Fig. 9) and causes higher concentrations of nitrogen oxides in these areas, which are closer to the exit section of the flame tube.

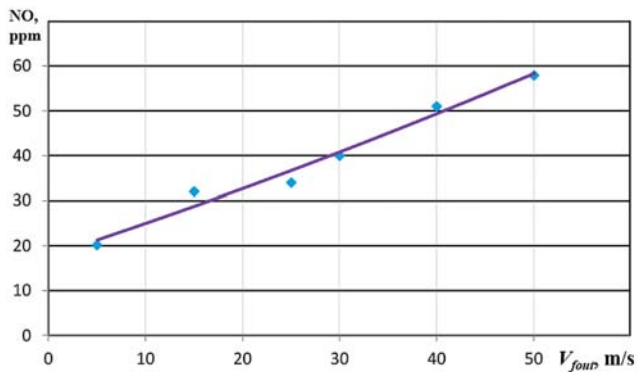


Fig. 10. Influence of nitrogen oxides emission (at 15% O<sub>2</sub>, dry basis) on the fuel outflow velocities

Note that with the radial liquid fuel supply, the processes of droplet evaporation and mixing of vapours with air occur quite quickly. The combustion process even begins inside the swirlers' channels, which can lead to increases in the temperature of the metal surfaces and carbon deposition and decrease the reliability of the flame tube operation in general. To solve this problem, in the next investigations, it is planned to redistribute the amount of air entering the swirlers' channels and the flame tube mixer and to partially change the design of the front device.

It is known that gas turbine engines (including combined cycle gas turbines) using light and middle distillates as liquid fuels in the European Union should be subject to emission limit values of 90 mg/nm<sup>3</sup> (~44 ppm) for NO<sub>x</sub> and 100 mg/nm<sup>3</sup> (~80 ppm) for CO, and those using natural gas as fuel should be subject to emission limit values of 50 mg/nm<sub>3</sub> (~25 ppm) for NO<sub>x</sub> and 100 mg/nm<sup>3</sup> (~81 ppm) for CO [35].

The radial method of liquid fuel supply to a dual-fuel gas turbine combustion chamber for an FPSO energy module, in which 95% of the fuel is fed radially through the outer swirler and 5% of the fuel is fed radially through the inner swirler, provides calculated NO<sub>x</sub> and CO emissions (32 and 9.1 ppm) that satisfy international environmental requirements.

## FINAL CONCLUSIONS

To implement the principle of low-emission combustion of liquid distillate fuel in a dual-fuel gas turbine combustion chamber without additional injection of water or steam, the idea of preliminary mixing of the evaporated fuel in the outer and inner channels of radial-axial swirlers is proposed. The performed three-dimensional calculations of the aerodynamic and emission parameters of the cannular counterflow combustion chamber allow us to draw the following conclusions.

1. To increase the efficiency of the working processes in a dual-fuel gas turbine chamber for an FPSO it is proposed to use the idea of pre-mixing of liquid fuel with air in radial-axial swirlers.
2. The developed three-dimensional mathematical model of liquid fuel burning in a dual-fuel low emission combustion chamber contains the following equations: continuity, impulse, energy conservation, and transfer of chemical components, taking into consideration dissipation of vortices, formation, and decomposition of nitrogen oxides in interaction with the discrete phase.
3. The results of three-dimensional mathematical modelling confirmed the feasibility of the radial liquid fuel method of supply into the swirlers' channels in a low-emission gas turbine combustion chamber for an FPSO and its advantages over the traditional centrifugal fuel supply method.
4. For the radial supply method, the calculated indexes of nitrogen oxide NO and carbon monoxide CO emissions in the outlet section of the flame tube are 32 and 9.1 ppm respectively (at 15% O<sub>2</sub>, dry basis), which satisfy the current emission requirements for gas turbine engines. The radial liquid fuel supply method has the minimum coefficient of the overall temperature-field non-uniformity in the outlet section (0.12).
5. Increasing the fuel outflow velocities when feeding liquid fuel into the channels of the inner and outer flame tube's swirlers from 5 to 50 m/s increases the estimated nitrogen oxides emissions from 20 to 58 ppm.

## REFERENCES

1. Offshore Technology (2018): *Report: 55 FPSOs to start operations by 2022*. Retrieved from <https://www.offshore-technology.com/news/report-55-fpsos-start-operations-2022/>.
2. Offshore Magazine (2002): *Leadon FPSO delivered on time, complete, within budget*. Retrieved from <https://www.offshore-mag.com/production/article/16759844/leadon-fpso-delivered-on-time-complete-within-budget>.
3. ENI (2016): *Block 15-06 East Hub Development Project*. Retrieved from [https://www.eni.com/docs/en\\_IT/enicom/publications-archive/publications/brochures-booklets/countries/brochure\\_eni\\_angola\\_ese\\_web.pdf](https://www.eni.com/docs/en_IT/enicom/publications-archive/publications/brochures-booklets/countries/brochure_eni_angola_ese_web.pdf).
4. Aker Floating Production (2009): *FPSO Dhirubhai-1*. Retrieved from <http://www.akerfloatingproduction.com/s.cfm/3-12/FPSO-Dhirubhai-1-Operation>.
5. Cherednichenko O., Serbin S., Dzida M. (2019): *Application of Thermo-Chemical Technologies for Conversion of Associated Gas in Diesel-Gas Turbine Installations for Oil and Gas Floating Units*. Polish Maritime Research, 3(103), Vol. 26, 181–187.

6. Cherednichenko O., Serbin S., Dzida M. (2019): *Investigation of the Combustion Process in the Gas Turbine Module of an FPSO Operating on Associated Gas Conversion Products*. Polish Maritime Research, 4(104), Vol. 26, 149–156.
7. Domachowski Z., Dzida M. (2019): *Applicability of Inlet Air Fogging to Marine Gas Turbine*. Polish Maritime Research, 1(101), Vol. 26, 15–19.
8. Burunsuz K.S., Kuklinovsky V.V., Serbin S.I. (2019): *Investigations of the Emission Characteristics of a Gas Turbine Combustor with Water Steam Injection*. Refrigeration Engineering and Technology, Vol. 55(2), 77–83.
9. Lindman O., Andersson M., Persson M., Munktel E. (2014): *Development of a Liquid Fuel Combustion System for SGT-750*. In ASME Turbo Expo 2014: Turbine Technical Conference and Exposition. American Society of Mechanical Engineers Digital Collection.
10. Malte P.C., Pratt D.T. (1975): *Measurement of Atomic Oxygen and Nitrogen Oxides in Jet-Stirred Combustion*. In Symposium (International) on Combustion, Vol. 15(1), 1061–1070.
11. Stöhr M., Boxx I., Carter C.D., Meier W. (2012): *Experimental Study of Vortex-flame Interaction in a Gas Turbine Model Combustor*. Combustion and Flame, Vol. 159, 2636–2649.
12. Aleiferis P.G., Serras-Pereira J., Romunde Z., Caine J., Wirth M. (2010): *Mechanisms of Spray Formation and Combustion from a Multi-Hole Injector with E85 and Gasoline*. Combustion and Flame, Vol. 157(4), 735–756.
13. Hertel M., Tartsch D., Sattelmayer S. (2019): *Ignition of Diesel Pilot Fuel in Dual-Fuel Engines*. Journal of Engineering for Gas Turbines and Power, doi: 141.10.1115/1.4043485.
14. Ibrahim I.A., Shabaan M.M., Shehata M.A., Farag T.M. (2014): *Investigation of Dual-Fuel Combustion Characteristics inside a Gas Turbine*. Combustor International Conference on Machine Learning, Electrical and Mechanical Engineering (ICMLEME'2014). Dubai (UAE). Retrieved from: [http://iieng.org/images/proceedings\\_pdf/2853E0114035.pdf](http://iieng.org/images/proceedings_pdf/2853E0114035.pdf).
15. Kurji H. (2017): *Fuel Flexibility with Low Emissions for Gas Turbine Engines*, PhD thesis, Cardiff University.
16. Matveev I., Serbin S., Mostipanen A. (2007): *Numerical Optimization of the "Tornado" Combustor Aerodynamic Parameters*. Collection of Technical Papers – 45th AIAA Aerospace Sciences Meeting, Reno, Nevada, AIAA 2007-391, Vol. 7, 4744–4755.
17. Matveev I.B., Serbin S.I., Vilkul V.V., Goncharova N.A. (2015): *Synthesis Gas Afterburner Based on an Injector Type Plasma-Assisted Combustion System*. IEEE Transactions on Plasma Science, Vol. 43(12), 3974–3978.
18. Serbin S.I. (1998): *Modeling and Experimental Study of Operation Process in a Gas Turbine Combustor with a Plasma-Chemical Element*. Combustion Science and Technology, Vol. 139, 137–158.
19. Matveev I., Matveeva S., Serbin S. (2007): *Design and Preliminary Result of the Plasma Assisted Tornado Combustor*. 43rd AIAA/ASME/SAE/ASEE Joint Propulsion Conference, Collection of Technical Papers, Cincinnati, OH, AIAA 2007-5628, Vol. 6, 6091–6098.
20. Matveev I., Serbin S. (2006): *Experimental and Numerical Definition of the Reverse Vortex Combustor Parameters*. 44th AIAA Aerospace Sciences Meeting and Exhibit, Reno, Nevada, AIAA-2006-0551, 1–12.
21. Serbin, S.I., Matveev, I.B., Mostipanen, G.B. (2011): *Investigations of the Working Process in a "Lean-Burn" Gas Turbine Combustor with Plasma Assistance*. IEEE Trans. Plasma Sci., Vol. 39(12), 3331–3335.
22. Launder B.E., Spalding D.B. (1972): *Lectures in Mathematical Models of Turbulence*. London: Academic Press, 327.
23. Choudhury D. (1993): *Introduction to the Renormalization Group Method and Turbulence Modeling*. Fluent Inc. Technical Memorandum TM-107.
24. Magnussen B.F. (1981): *On the Structure of Turbulence and a Generalized Eddy Dissipation Concept for Chemical Reaction in Turbulent Flow*. Nineteenth AIAA Meeting, St. Louis, 1–7.
25. Pope S.B. (1997): *Computationally efficient implementation of combustion chemistry using in-situ adaptive tabulation*. Combustion Theory and Modeling, Vol. 1, 41–63.
26. Wang F., Huang Y., Deng T. (2009): *Gas Turbine Combustor Simulation with Various Turbulent Combustion Models*. Proceedings of ASME Turbo Expo 2009: Power for Land, Sea and Air GT2009, 1–11.
27. Benim A.C., Iqbal S., Meier W., Joos F., Wiedermann A. (2017): *Numerical Investigation of Turbulent Swirling Flames with Validation in a Gas Turbine Model Combustor*. Applied Thermal Engineering, Vol. 110(2), 202–212.
28. Abou-Taouk A., Sigfrid I.R., Whiddon R., Eriksson L.E. (2012): *A Four-Step Global Reaction Mechanism for CFD Simulations of Flexi-Fuel Burner for Gas Turbines*. Proceedings of the 17th International Symposium on Turbulence, Heat and Mass Transfer Palermo, Italy, 1–12.
29. Novoselov I.V., Malte P.C. (2007): *Development and Application of an Eight-Step Global Mechanism for CFD and CRN Simulations of Lean-Premixed Combustors*. Proceedings of GT2007 ASME Turbo Expo 2007: Power for Land, Sea and Air, 1–11.

30. Faeth G.M. (1979): *Spray Combustion Models: A Review*, AIAA Paper (293), 1–18.
31. James S., Anand M., Pope S. (2002): *The Lagrangian PDF Transport Method for Simulations of Gas Turbine Combustor Flows*. In 38th AIAA/ASME/SAE/ASEE Joint Propulsion Conference & Exhibit, 4017.
32. Romanovsky G.F., Serbin S.I., Patlaychuk V.M. (2005): *Modern Gas Turbine Units of Russia and Ukraine*. Vol. 1, Mikolayiv: NUK, 344 (in Ukrainian).
33. Gatsenko N.A., Serbin S.I. (1995): *Arc Plasmatrons for Burning Fuel in Industrial Installations*. Glass and Ceramics, Vol. 51(11/12), 383–386.
34. Serbin S.I., Matveev I.B., Goncharova N.A. (2014): *Plasma Assisted Reforming of Natural Gas for GTL. Part I*. IEEE Transactions on Plasma Science, Vol. 42(12), 3896–3900.
35. *Directive 2010/75/EU of the European Parliament and of the Council of 24 November on Industrial Emissions (Integrated Pollution Prevention and Control)* (2010): Official Journal of the European Union. Retrieved from <https://eur-lex.europa.eu/legal-content/EN/TXT/?uri=CELEX%3A32010L0075>.

## CONTACT WITH THE AUTHORS

### Serhiy Serbin

*e-mail: serbin1958@gmail.com*

Admiral Makarov National University of Shipbuilding  
Geroes of Ukraine Ave., 9, 54025 Mikolayiv

**UKRAINE**

### Badri Diasamidze

*e-mail: badri.diasamidze@nuos.edu.ua*

Admiral Makarov National University of Shipbuilding  
Geroes of Ukraine Ave., 9, 54025 Mikolayiv

**UKRAINE**

### Marek Dzida

*e-mail: dzida@pg.edu.pl*

Gdańsk University of Technology  
11/12 Gabriela Narutowicza Street, 80-233 Gdańsk

**POLAND**

# STATE OF CHARGE ESTIMATION METHOD FOR LITHIUM-ION BATTERIES IN ALL-ELECTRIC SHIPS BASED ON LSTM NEURAL NETWORK

**Pan Geng**

Shanghai Maritime University, China

**Xiaoyan Xu**

Shanghai Maritime University, China

**Tomasz Tarasiuk**

Gdynia Maritime University, Poland

## ABSTRACT

*All-electric ships (AES) are considered an effective solution for reducing greenhouse gas emissions as they are a platform to use clean energy sources such as lithium-ion batteries, fuel cells and solar cells instead of fossil fuel. Even though these batteries are a promising alternative, the accuracy of the battery state of charge (SOC) estimation is a critical factor for their safe and reliable operation. The SOC is a key indicator of battery residual capacity. Its estimation can effectively prevent battery over-discharge and over-charge. Next, this enables reliable estimation of the operation time of fully electric ferries, where little time is spent at the harbour, with limited time available for charging. Thus, battery management systems are essential. This paper presents a neural network model of battery SOC estimation, using a long short-term memory (LSTM) recurrent neural network (RNN) as a method for accurate estimation of the SOC in lithium-ion batteries. The current, voltage and surface temperature of the batteries are used as the inputs of the neural network. The influence of different numbers of neurons in the neural network's hidden layer on the estimation error is analysed, and the estimation error of the neural network under different training times is compared. In addition, the hidden layer is varied from 1 to 3 layers of the LSTM nucleus and the SOC estimation error is analysed. The results show that the maximum absolute SOC estimation error of the LSTM RNN is 1.96% and the root mean square error is 0.986%, which validates the feasibility of the method.*

**Keywords:** All-electric ships, Lithium-ion battery, state of charge, neural network

## INTRODUCTION

Shipping is generally the most energy-effective mode of global mass cargo transportation. Nevertheless, the air pollution from shipping is still growing, while land-based emission is gradually declining. This is becoming a driving factor for the development of innovative and ecofriendly technologies for shipping [1]. One of the solutions is the large-scale introduction of energy storage technologies, particularly using Li-ion batteries with high energy storage capacity [2]. The use of batteries onboard vessels is growing rapidly, leading to the development of ships with hybrid power systems or fully all-electric ships (AES), which are charged when in harbour, or back zero-emission sources like fuel-cells, solar

panels, thermo-electric generators, wind energy conversion systems etc. [3–5]. In the former, due to the limited time spent in dock, high-power wireless charging technologies are being developed [2,6]. The number of AES is increasing rapidly and they are becoming a promising tool for reducing greenhouse gas emissions and the dependency on fossil fuels [3,4]. An example of a scheme for future zero emission AES, incorporating a lithium-ion battery pack, fuel-cell stack, super-capacitor bank and a photovoltaic (PV) power system, is shown in Fig. 1 [7].

With the advantages of high energy density, long service life and low self-discharge rate, lithium-ion batteries are becoming an important part of the energy source capacity in the AES. There are two main factors, when dealing with

such energy storage systems: optimal sizing [8] and SOC assessment. The SOC of lithium-ion batteries is the main basis for power management and control strategies. It plays a very important role in battery protection, working efficiency and service life extension as well as quality of service assessment, leading to an increase in the safety of the entire AES. Therefore, accurate estimation of the SOC of the batteries is essential for their efficient use and energy management throughout all ship services.

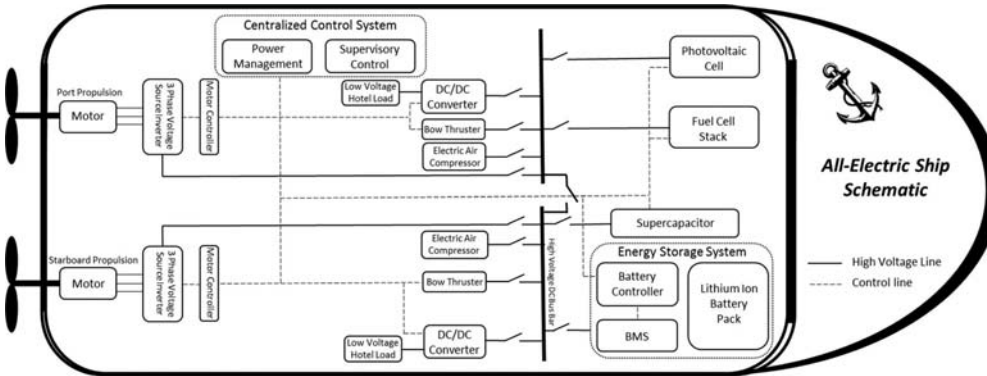


Fig. 1. Schematic diagram of a future zero-emission all-electric ship

Currently, methods of SOC estimation are divided into three categories. The first category directly predicts the SOC based on the voltage, current or internal resistance of the batteries. The main methods of this category include the ampere-time integration method, the open circuit voltage method and the estimation method based on the internal resistance of the batteries [9-11]. The second category is based on an algorithmic estimation of equivalent battery models, such as the sliding mode observer [12] and the Luenberger observer [13]. The third category is the machine learning-based prediction method developed nearly five years ago, mainly including the support vector machine [14,15], extreme learning machine [16], RBF kernel function neural network [17], recurrent neural network RNN [18], and other less popular solutions.

The ampere-time integration method achieves SOC estimation by measuring and integrating the current, but it cannot solve the cumulative error and the inaccurate SOC initial value problem [19]. The disadvantage of the open circuit voltage method is that SOC estimation requires the battery to stand for a long time and is not suitable for online measurement [20]. The internal resistance method is rarely used because of the difference in the number and consistency of battery types [21].

The equivalent battery models generally use the equivalent resistance and capacitance to simulate the dynamic response of the battery, but ignore the physical and chemical reactions inside the battery unit. When the battery is over-charged or over-discharged causing severe physical and chemical reactions, the equivalent model cannot then be used to represent the real battery model [20]. This method is computationally intensive, and requires additional parameters

or different battery models to estimate the SOC in different environments in practical applications. In [21], the adaptive sigma-point Kalman filter for optimising the battery model is used to estimate the SOC, but it only partly reduces the disadvantages of the complexity of the battery model and requires computational effort. In addition, improved algorithms such as the Gray extended Kalman filter [22] and a square root unscented Kalman filter [23] have been proposed. Such Kalman filtering algorithms rely on high-precision

battery models and result in increased computational complexity [24].

Researchers have also used a machine learning-based prediction method to perform SOC estimation, which relies on traditional machine learning techniques. In [25], SVM technology is used for SOC estimation. In [26], researchers use the extreme learning machine algorithm

for SOC estimation. Traditional machine learning techniques have common defects, and the training speed is slow and easily falls into the local minimum point. In view of the shortcomings of the above three types of methods, this paper uses the long short-term memory (LSTM) cell based recurrent neural network (RNN) to reduce the absolute error of SOC estimation to less than 2% [27]. In an extension of [27], the paper investigates the impact of the LSTM RNN properties on the estimation accuracy. It uses more experiments and additional factors for performance evaluation.

In recent years, with the continuous development of deep learning technology, some deep learning models have been gradually applied to the study of time series data. The deep learning model is a deep learning neural network model with multiple non-linear implicit levels. It can abstract the input signal layer by layer and extract features to dig deeper potential laws [28]. In real life, deep learning is used in content filtering of search engines, social media personal preference analysis and natural language processing on various portable smart devices. The prediction methods used in these successful deep learning application cases can be attributed to a branch of the artificial neural network, which is called the recurrent neural network with long short-term memory (LSTM) cells.

This paper will use the recurrent neural network with LSTM cells as a new machine learning technology, which can estimate the battery's SOC by learning the parameters such as network weight and offset. The SOC cannot be directly measured but there is non-linear correlation between the SOC and easily measurable signals like the voltage, current and surface temperature. The three parameters have no correlation in terms of the battery's physical characteristic. This technology can accurately map various items of information measured from the battery, such as the voltage, current and battery surface temperature, to the state of charge of the battery [27]. It avoids the cumbersome parameter estimation

process such as the Kalman filter during the training process. Only information about the number of hidden layer neurons, the batch size, the number of iterations, and the number of LSTM nuclei during training is required to obtain the optimal model. An LSTM recurrent neural network can derive different network parameter models under different operating conditions, different input parameter variables and even different battery types. This process only needs to sample a different type of battery to obtain a certain amount of training data.

## LSTM RECURRENT NEURAL NETWORKS MODEL

Recurrent neural networks are different from BP neural networks or other conventional machine learning neural networks, where the current input parameter to the neural network is to calculate the output of the current time. Recurrent neural networks can transmit a series of information from the previous time to the current time. The RNN standard model and expansion model are shown in Fig. 2. When the input enters a sequence  $x=(x_1, x_2 \dots x_t)$ , a hidden layer sequence  $h=(h_1, h_2 \dots h_t)$  can be calculated by Eq. (1). The input sequence and hidden layer sequence can calculate an output sequence  $y=(y_1, y_2 \dots y_t)$  using Eq. (2). Eq. (1) and Eq. (2) have been described in [27,29]:

$$h_t = f(W_{xh}x_t + W_{hh}h_{t-1} + b_h) \quad (1)$$

$$y_t = W_{hy}h_t + b_y \quad (2)$$

where  $f(\cdot)$  represents the activation function, subscript  $t$  denotes the time,  $W$  is the network weight coefficient and  $b$  is the offset vector [29].

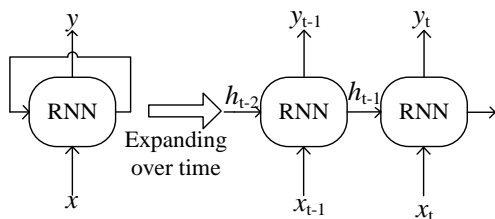


Fig. 2. RNN standard model and expansion model

Although the RNN can effectively deal with non-linear time series over time, recurrent neural networks will generate a series of problems, such as gradient descent or gradient explosion, which will lead to the loss of effective information in the early stage or cause an error in the estimate by invalid information. Therefore, the LSTM recurrent neural networks are applied, and the RNN cell nuclei of the traditional recurrent neural networks are replaced with LSTM cell nuclei, which have long-term memory ability. This solves

the problem of predicting and estimating long-term data with better success. The LSTM cell nuclei are shown in Fig. 3 [29].

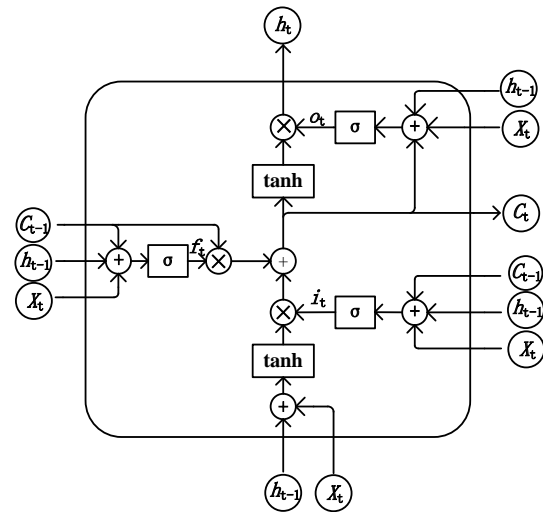


Fig. 3. LSTM cell nuclei structure

In the LSTM cell nuclei,  $C_t$  is the state unit of the LSTM, which runs through the entire cell. The LSTM cell is able to fill the state unit with effective information or remove invalid information. The structure used in the process is called the threshold. The threshold consists of a sigmoid function and matrix point multiplication. The sigmoid function outputs a number between 0 and 1, describing the extent to which each item of information passes the threshold, where 0 means that all information is prohibited and 1 means that all information passes. There are three thresholds in the entire LSTM cell, namely the forgetting gate  $f$ , the input gate  $i$  and the output  $o$ . The forward propagation of the LSTM neural networks can be expressed by the following formula [27,29]:

$$\begin{cases} i_t = \sigma(W_{xi}X_t + W_{hi}h_{t-1} + b_i) \\ f_t = \sigma(W_{xf}X_t + W_{hf}h_{t-1} + b_f) \\ c_t = f_t * c_{t-1} + \tanh(W_{xc}X_t + W_{hc}h_{t-1} + b_c) \\ o_t = \sigma(W_{xo}X_t + W_{ho}h_{t-1} + b_o) \\ h_t = o_t \tanh(c_t) \end{cases} \quad (3)$$

where the initial state matrix of the hidden layer is set to an all-zero matrix,  $\sigma$  and  $\tanh$  represent the sigmoid activation function and the double-tangent activation function,  $i_t$  represents input at time  $t$ ,  $f_t$  represents forget at time  $t$ ,  $o_t$  represents output at time  $t$  and  $c_t$  represents the state of the cell.  $W$  represents a matrix of weight coefficients between different layers (for example,  $W_{xi}$  represents the weighting matrix of the input layer to the input threshold  $i$ ),  $b$  represents the bias term of the different layers (for example,  $b_i$  represents the bias term of the input threshold  $i$ ). The training framework is based on an LSTM battery. The SOC model includes input layers, hidden layers and output layers, where the input layer characterises the input variables, the hidden layer can be one or more LSTM cell nuclei, and the output characterises

the output variables. The fully connected layer realises the hidden layer's linear output  $h_t$  according to the combination of the weight  $W$  and the offset  $b$ , and then the output value at time  $t$  can be obtained through the output layer.

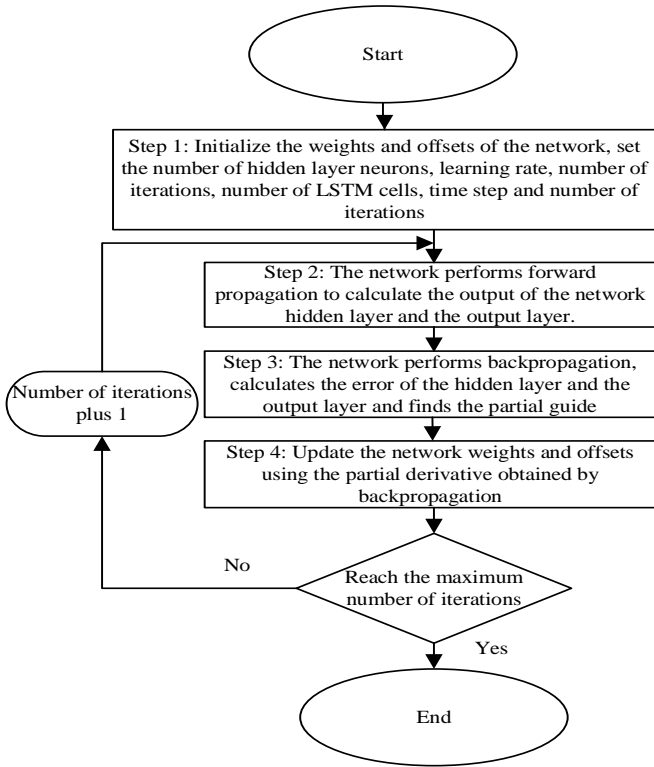


Fig. 4. Model training framework flow chart

As shown in Fig. 4, after the LSTM recurrent neural network performs forward propagation, the error function is used to calculate the error between the network output value and the true value by Eq. (4):

$$L = \frac{1}{T} \sum_{t=0}^T (SOC_t - SOC_t^*)^2 \quad (4)$$

where  $T$  represents the entire sequence length selected by the SOC estimation, and  $SOC_t$  and  $SOC_t^*$  represent the estimated and true values of the battery SOC at time  $t$  respectively. In each training iteration, the LSTM recurrent neural network performs backpropagation, using the Adam [30] optimisation method to update the weights and offsets of the network as presented in Eq. (5):

$$\begin{cases} m_\epsilon = \beta_1 m_{\epsilon-1} + \nabla L(W_{\epsilon-1}) \\ \gamma_\epsilon = \beta_2 \gamma_{\epsilon-1} + \nabla L(W_{\epsilon-1})^2 \\ \tilde{m}_\epsilon = \frac{m_\epsilon}{1-\beta_1^\epsilon} \\ \tilde{\gamma}_\epsilon = \frac{\gamma_\epsilon}{1-\beta_2^\epsilon} \\ W_\epsilon = W_{\epsilon-1} - \alpha \frac{\tilde{m}_\epsilon}{\tilde{\gamma}_\epsilon - \theta} \end{cases} \quad (5)$$

where  $L$  represents the error function, the attenuation coefficients  $\beta_1$  and  $\beta_2$  are usually set between 0.9 and 0.999, the learning rate  $\alpha$  is generally set to 0.0001, the constant number  $\theta$  is  $10^{-8}$ , and  $W_\epsilon$  is the weight matrix. Finally, the number of training iterations reaches the preset maximum number, signifying the end of the trained model. This trained model, which now meets the performance requirements, is saved and later selected for future prediction.

## EXPERIMENTAL TESTING AND DATA PREPROCESSING

### EXPERIMENTAL TESTING

In this paper, the battery unit used is similar to that of the Tesla Electric Vehicle. The NCR18650PF lithium-ion battery produced by Panasonic Corporation is investigated as the experimental object. The rated capacity of the battery is 2.9 A·h and the rated internal resistance is 35 mΩ. See Table 1 for further battery specifications.

Tab. 1. Panasonic NCR18650PF battery unit parameters

Rated voltage	3.6 V
Rated battery capacity	2.9 A·h
Maximum charging voltage / discharge cut-off voltage	4.2 V/2.5 V
Internal resistance	35 mΩ
Weight	47.5 g
Discharge temperature	-20~+60°C

The established single-cell battery test bench is shown in Fig. 5. It consists mainly of a single-section Panasonic 18650 lithium-ion battery, a Chroma charger, a WT1600 power meter, and a temperature acquisition unit. The Chroma charger can charge the lithium-ion battery according to the set voltage and current. The WT1600 power meter can realise the battery voltage and current collection function. All experiments were performed at room temperature.

In order to obtain battery discharge data for training and verification of the LSTM recurrent neural network, the battery is charged using the 4.2 V/2.9 A charging mode. When the battery voltage reaches 4.2 V, the charging current reduces to 50 mA, indicating that the battery is fully charged. After the charging process is completed, the battery is allowed to stand at room temperature for 1 hour, and a constant value 0.5 Ω resistor is used to discharge the battery. The discharge of the battery is recorded. When the battery voltage drops to 2.5 V, the battery power is completely discharged. The battery is allowed to stand for another hour again, the charge and discharge test is repeated, and the data are recorded. The voltage, current and the surface temperature change of the battery in a single discharge phase are as shown in Fig. 6.

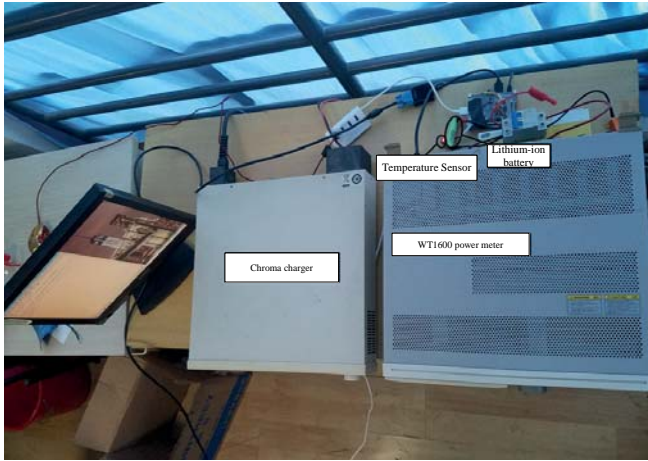
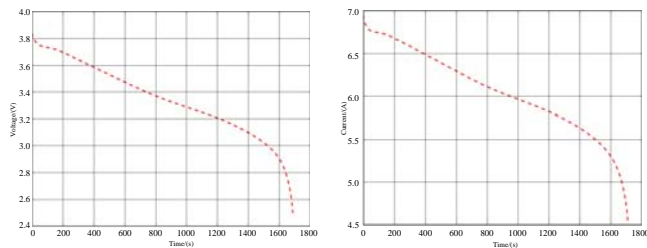
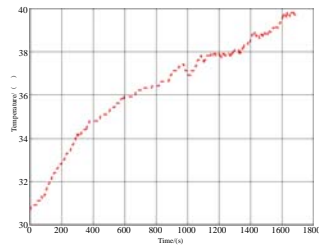


Fig. 5. Battery charge and discharge test bench



a) 18650 lithium-ion battery discharge voltage curve

b) 18650 lithium-ion battery discharge current curve



c) 18650 lithium-ion battery discharge temperature curve

Fig. 6. Battery real-time discharge data curve

At room temperature, the battery has been charged and discharged five times. Four sets of data are used to train the LSTM neural network. The remaining group is used as the test set of the LSTM neural network to test the trained neural network's accuracy. The SOC estimation result based on the LSTM recurrent neural network model is compared with the real value. The following formulae are used to evaluate the performance of the SOC prediction model based on the LSTM recurrent neural network: the root mean square error RMSE, the mean absolute error MAE, and the maximum absolute error MAX.

$$\text{RMSE} = \sqrt{\frac{1}{N} \sum_{i=1}^N (I_{esi} - I_{ai})^2} \quad (6)$$

$$\text{MAE} = \frac{1}{N} \sum_{i=1}^N |I_{esi} - I_{ai}| \quad (7)$$

$$\text{MAX} = \max\left\{\left|\frac{I_{ai} - I_{esi}}{I_{ai}}\right|, i = 1 \dots N\right\} \quad (8)$$

$I_{esi}$  represents the estimated value,  $I_{ai}$  is the actual value, and  $N$  is the number of observations.

## DATA PREPROCESSING

LSTM neural network training selects three important factors, including the voltage, current, and battery surface temperature. Through proper data preprocessing, the training data of the network will be more effective and robust. The arithmetic average filtering algorithm is used to smooth out each set of raw data, and then all the data are normalised to improve the convergence speed of the network model training. The input and output are normalised to a range between 0 and 1 using the following formula:

$$x = \frac{x - x_{min}}{x_{max} - x_{min}} \quad (9)$$

where  $x_{max}$  and  $x_{min}$  are the maximum and minimum values of the LSTM neural network input vector.

## RESULT AND ANALYSIS

As described in the previous chapter, the LSTM neural network input is  $X_t$  and the output is  $\text{SOC}_t$ . The  $\text{SOC}_t$  is the measured value of the battery state of charge at time  $t$ , and  $X_t$  represents the input of the neural network at time  $t$ , which is a vector  $X_t = [V_t, I_t, T_t]$ , including the battery voltage  $V_t$ , battery current  $I_t$ , and battery surface temperature  $T_t$ . After the training process, the neural network can self-learn the entire network parameters for later actual estimation, as illustrated in Fig. 7. In this paper, 5 sets of battery discharge data were collected at room temperature, 4 groups were used as the training set to train the neural network, and 1 group was used as a verification set to verify the accuracy of the saved model. This means that 20% of the 5 groups of data is proposed as testing data. So, 20% of all the input data, measured by the unit of batch size, serves as a predictor of reliability, which seems sufficient for the purpose.

The LSTM neural network is set to a single-layer LSTM cell. After debugging, the number of hidden layer neurons is set to 320, the batch size is 200, and the maximum number of iterations is 200, which produced the best result in the practical project of lithium-ion battery SOC prediction. The neural network is trained with four sets of data for a total time of 117s. The obtained model is used for the verification set. The maximum absolute error, MAX, in the final prediction result is 1.96%, while the mean absolute error, MAE, and the root mean square error, RMSE, are 0.455% and 0.986%, respectively. It is noted that the predicted value deviates from the true value to a small extent. The performance of

the SOC estimation model based on the LSTM neural network is shown in Fig. 8.

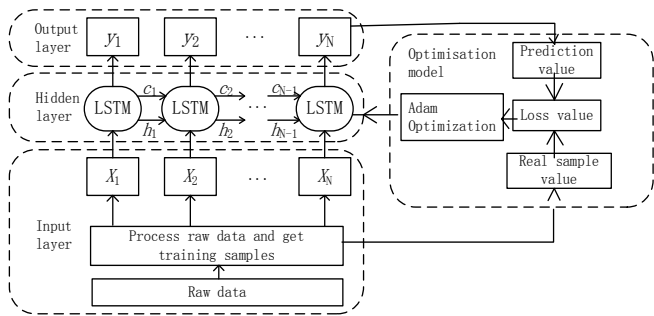


Fig. 7. LSTM-based battery SOC estimation model training framework

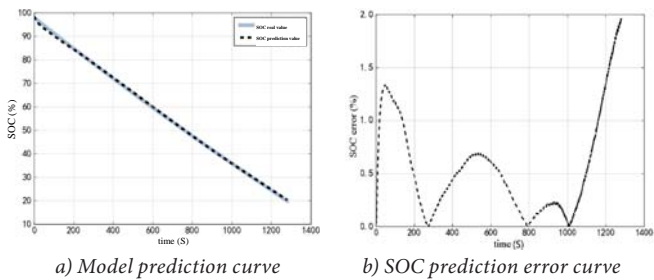


Fig. 8. Performance graph of SOC estimation model based on LSTM neural network

### INFLUENCE OF HYPER-PARAMETERS OF LSTM NEURAL NETWORK ON SOC PREDICTION RESULTS

The number of hidden layer neurons  $n$  and batch size  $B_s$  are important hyper-parameters of the LSTM neural network, in which batch size  $B_s$  is divided into several small batch data to be input into the neural network. These are the two main hyper-parameters, whose adjustments have an important influence on the accuracy of the LSTM neural network SOC prediction.

Firstly, the hidden layer is set to single-layer LSTM cell cores, the batch size is set to 512, the maximum number of iterations is set to 200, and the numbers of hidden layer neurons are set to 80, 260, and 440, respectively. Next, the total training time of the neural network, the maximum absolute error MAX, the mean absolute error MAE, and the root mean square error RMSE are selected to evaluate the prediction results, as shown in Fig. 9.

As the number of neurons  $n$  increases, the training time of the entire SOC prediction network model increases. The MAE and the RMSE show a moderately downward trend. Nevertheless, the increase in the number of neurons as a whole reduces the two errors. Fortunately, the MAX error drops significantly. When  $n=80$ , the MAX is greater than 6%. When  $n=440$ , the MAX is less than 4%. In order to achieve good accuracy and reliability of the SOC prediction model while also considering the model training time, the number of neurons in the hidden layer LSTM nuclear unit should be appropriately increased.

To further verify the effect of the batch size on the SOC prediction results, the hidden layer is set to a single-layer LSTM cells nucleus. The number of hidden layer neurons is set to 200, the maximum number of training iterations is set to 200, and the batch size is set to 200, 356, and 512, respectively. The results from the LSTM neural network prediction and the prediction errors trained for the different batch sizes are shown in Fig. 10.

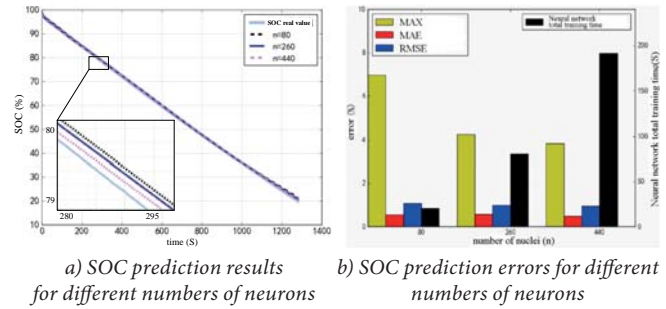


Fig. 9. Performance of SOC estimation model for different numbers of neurons

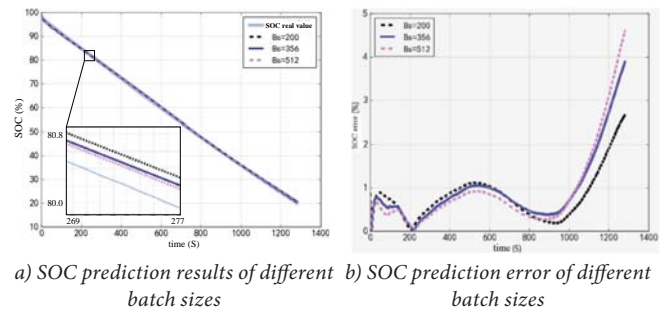


Fig. 10. SOC prediction for different batch sizes

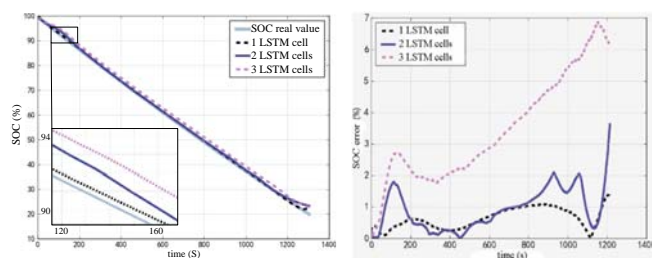
Table 2 shows that, as the batch size increases, the total training time of the neural network decreases. At the same time, the increase of the batch size will increase the maximum absolute error, but the overall root mean square error and the average mean error will be reduced, which improves the overall accuracy of the model prediction. In order to reduce the model training time, the batch size should be increased, taking into account the maximum absolute error limit of SOC prediction. However, the batch size cannot be increased too much, or else the maximum absolute error of SOC prediction will exceed 5%, resulting in inaccurate SOC prediction.

Tab. 2 Network performance indicators when different batch sizes are taken

Batch size	Root mean square error RMSE (%)	Mean absolute error MAE (%)	Maximum absolute error MAX (%)	Neural network total training time (s)
200	1.028	0.612	2.667	50
356	1.009	0.633	3.887	42
512	1.003	0.591	4.620	40

## INFLUENCE OF THE NUMBER OF LSTM NUCLEI ON SOC PREDICTION RESULTS

The LSTM neural network can be designed for multiple LSTM nuclei in the hidden layer. In order to reflect the influence of multiple LSTM nuclei on the SOC prediction results, the number of neurons in the hidden layer of a single LSTM cell is set to 320, the batch size is set to 400, and the maximum number of training iterations is set to 200, while the hidden layer is changed from 1, 2, and 3 LSTM nuclei, and the SOC prediction error is obtained for different numbers of LSTM nuclei in the hidden layer. The SOC prediction results are obtained for the hidden layers with different numbers of LSTM nuclei. The performance of the model is shown in Fig. 11.



a) SOC prediction results for different numbers of LSTM nuclei  
b) SOC prediction errors of the different numbers of LSTM cell nuclei  
Fig. 11. SOC prediction results of the different numbers of LSTM nuclei

When the LSTM hidden layer is designed as one or two LSTM nuclei, the SOC prediction error can be guaranteed to be less than 4%. When the hidden layer is selected as three LSTM nuclei, the error of the trained SOC prediction model is large. After the SOC reaches 40%, the prediction error is larger than 5%, and accurate prediction of the SOC cannot be achieved. Therefore, the designed number of hidden layer LSTM nuclei should be less than 3, or else the trained prediction model will be over-fitted and a good prediction result cannot be attained.

## CONCLUSION

The SOC prediction error of a lithium-ion battery and an SOC prediction method based on an LSTM neural network for the same has been investigated. This paper aims to solve three problems. Firstly, it solves the problem of the battery physics modelling used for SOC prediction in the past and uses the LSTM neural network to directly map battery-related measured values (such as voltage, current and temperature) to the SOC. Secondly, the solution can free researchers from manual calculation of the battery model parameters or estimation algorithms such as those in the Kalman filter algorithm. The LSTM neural network can use the data collected from the original training to train the neural network to self-learn all network parameters. The third contribution lies in the accuracy of the battery SOC prediction. Through experimental verification, the maximum absolute error of the established prediction model is less than

2%, which is lower than the actual application requirement of 5%, thus meeting the practical application requirements. In summary, the LSTM neural network has been experimentally validated and has achieved good performance. It has proven to be a powerful tool for estimation of the SOC of lithium-ion batteries and may be another diagnostic strategy for batteries for consideration in future work. Considering the amount of data generated by the energy storage system, it is natural to consider machine learning algorithms to perform state and parameter estimation. This paper shows how these algorithms self-learn the parameters of the prediction model, even if exposed to scarce data sets, in order to achieve competitive evaluation performance. As a result, the proposal can be a powerful tool supporting the management of power systems onboard the ever-increasing number of ships with energy storage facilities containing lithium-ion batteries. This is relevant to ships with hybrid power systems and fully electric ships, especially those utilising various charging technologies in dock. The necessary docking time can be optimised by improving ferry fleet management.

## ACKNOWLEDGEMENT

This work was partially supported by Shanghai S&T Commission under Grant 19040501700 and the Sino-Polish S&T Cooperation Project 37-11.

## REFERENCES

- Alnes O., Eriksen S., Vartdal B. (2017): *Battery-Powered Ships: A Class Society Perspective*. IEEE Electrification Mag., 5(3), 10–21.
- Guidi G., Suul J., Jensen F., Sorfonn I. (2017): *Wireless Charging for Ships: High-Power Inductive Charging for Battery Electric and Plug-In Hybrid Vessels*. IEEE Electrification. Mag., 5(3), 22–32.
- McCoy T. (2015): *Electric ships past, present, and future [technology leaders]*. IEEE Electrification Mag., 3(2), 4–11.
- Skjong E., Volden R., Rødskar E., Molinas M., Johansen T., Cunningham J. (2016): *Past, Present, and Future Challenges of the Marine Vessel's Electrical Power System*. IEEE Transactions on Transportation Electrification, 2(4), 522–537.
- Mofor L., Nuttall P., Newell A. (2015): *Renewable energy options for shipping*. Int. Renewable Energy Agency, Abu Dhabi, UAE, Tech. Rep.
- Wartsila. *Wireless Charging* (<https://www.wartsila.com/marine/build/power-systems/shore-connections/wireless-charging>), last accessed 11.07.2019.
- Abkenar A., Nazari A., Jayasinghe S., Kapoor A., Negnevitsky M. (2017): *Fuel Cell Power Management Using*

- Genetic Expression Programming in All-Electric Ships*. IEEE Transactions on Energy Conversion, 3(2), 779–787.
8. Boveri A., Silvestro F., Molinas M., Skjong E. (2019): *Optimal Sizing of Energy Storage Systems for Shipboard Applications*. IEEE Transactions on Energy Conversion, 34 (2), 801–811.
  9. Fei Y., Xie C., Tang Z., Zeng C., Quan S. (2017): *State-of-Charge Estimation Based on Square Root Unscented Kalman Filter Algorithm for Li-ion Batteries*. Proceedings of the CSEE, 37(15), 4514–4520.
  10. Yu H., Lu R., Zhu C., Ma R. (2012): *State of Charge Estimation Calibration for Ni-MH Battery Based on Ampere-Hour Method*. Transactions of China Electrotechnical Society, 27(6), 12–18.
  11. Weng C., Sun J., Peng H. (2014): *A unified open-circuit-voltage model of lithium-ion batteries for state-of-charge estimation and state-of-health monitoring*. Journal of Power Sources, 258(14), 228–237.
  12. Sun D., Chen X. (2015): *Charge State Estimation of Li-ion Batteries Based on Discrete-time Sliding Mode Observers*. Proceedings of the CSEE, 35(1), 185–191.
  13. Waag W., Fleischer C., Viejo B., et al. (2014): *Critical review of the methods for monitoring of lithium-ion battery in electric and hybrid vehicles*. Journal of Power Sources, 258, 321–339.
  14. Meng J., Luo G., Gao G. (2016): *Lithium Polymer Battery State-of-Charge Estimation Based on Adaptive Unscented Kalman Filter and Support Vector Machine*. IEEE Transactions on Power Electronics, 31(3), 2226–2238.
  15. Álvarez Antón J., García Nieto P., de Cos Juez, F., et al. (2013): *Battery state-of-charge estimator using the SVM technique*. Applied Mathematical Modeling, 37(9), 6244–6253.
  16. Du J., Liu Z., Wang Y. (2014): *State of charge estimation for Li-ion battery based on model from extreme learning machine*. Control Engineering Practice, 26, 11–19.
  17. Chang W. (2013): *Estimation of the state of charge for a LFP battery using a hybrid method that combines a RBF neural network, an OLS algorithm and AGA*. International Journal of Electrical Power and Energy Systems, 53, 603–611.
  18. Chaoui H., Ibe-Ekeocha C. C. (2016): *State of Charge and State of Health Estimation for Lithium Batteries Using Recurrent Neural Networks*. IEEE Transactions on Vehicular Technology, 66(10), 8773–8783.
  19. El Mejdoubi A., Oukaour A., Chaoui H., et al. (2016): *State-of-Charge and State-of-Health Lithium-Ion Batteries' Diagnosis According to Surface Temperature Variation*. IEEE Transactions on Industrial Electronics, 63(4), 2391–2402.
  20. Chen L., Wang Z., Lü Z., et al. (2018): *A Novel State-of-charge Estimation Method of Lithium-ion Batteries Combining the Grey Model and Genetic Algorithms*. IEEE Transactions on Power Electronics, 33(10), 8797–8807.
  21. Liu Y., Tan G., He X. (2017): *Optimized Battery Model Based Adaptive Sigma Kalman Filter for State of Charge Estimation*. Transactions of China Electrotechnical Society, 32(2), 108–118.
  22. Pan H., Lu Z., Li J., Chen L. (2017): *Estimation of Lithium-Ion Battery State of Charge Based on Grey Prediction Model-Extended Kalman Filter*. Transactions of China Electrotechnical Society, 32(21), 1–8.
  23. Aung H., Soon Low K., Ting Goh S. (2015): *State-of-charge Estimation of Lithium-Ion Battery Using Square Root Spherical Unscented Kalman Filter (Sqrt-UKFST) in Nanosatellite*. IEEE Transactions on Power Electronics, 30(9), 4774–4783.
  24. Sheng H., Xiao J., Wang P. (2017): *Lithium Iron Phosphate Battery Electric Vehicle State-of-Charge Estimation Based on Evolutionary Gaussian Mixture Regression*. IEEE Transactions on Industrial Electronics, 64(1), 544–551.
  25. Anton J., Nieto P., Viejo C., et al. (2013): *Support vector machines used to estimate the battery state of charge*. IEEE Transactions on Power Electronics, 28(12), 5919–5926.
  26. Wang Q., Sun Y., Ni F., Luo Y. (2016): *A New Method of Battery State of Charge Prediction in the Hybrid Electric Vehicle*. Transactions of China Electrotechnical Society, 31(9), 189–196.
  27. Yang F., Song X., Xu F., Tsui K. (2019): *State-of-Charge Estimation of Lithium-Ion Batteries via Long Short-Term Memory Network*. IEEE Access, 7, 53792–53799.
  28. Han L., Yu C., Xiao K., Zhao X. (2019): *A New Method of Mixed Gas Identification Based on a Convolutional Neural Network for Time Series Classification*. Sensors, 19(9), 1–23.
  29. Shrestha A., Mahmood A. (2019): *Review of Deep Learning Algorithms and Architectures*. IEEE Access, 7, 53040–53065.
  30. Kingma D., Ba J. (2015): *Adam: A method for stochastic optimization*. International Conference on Learning Representations, May 7–9, 2015, San Diego, 1–13.

## CONTACT WITH THE AUTHORS

**Pan Geng**

*e-mail: pangeng@shmtu.edu.cn*

Shanghai Maritime University,  
1550 Hai Gang Da Dao, 201306 Shanghai,  
**CHINA**

**Xiaoyan Xu**

*e-mail: xuxy@shmtu.edu.cn*

Shanghai Maritime University,  
1550 Hai Gang Da Dao, 201306 Shanghai,  
**CHINA**

**Tomasz Tarasiuk**

*e-mail: t.tarasiuk@we.umg.edu.pl*

Gdynia Maritime University,  
Morska, 81-225 Gdynia,  
**POLAND**

# ANALYSIS OF ULTIMATE COMPRESSIVE STRENGTH OF CRACKED PLATES WITH THE USE OF DOE TECHNIQUES

Krzysztof Wołoszyk<sup>1</sup>

Yordan Garbatov<sup>2</sup>

<sup>1</sup> Gdańsk University of Technology, Faculty of Ocean Engineering and Ship Technology, Poland

<sup>2</sup> Universidade de Lisboa, Centre for Marine Technology and Ocean Engineering (CENTEC), Portugal

## ABSTRACT

*The objective of this work is to investigate the structural compressive response of plates with locked cracks accounting for all relevant factors and correlation between them. The nonlinear FE model considering both geometric and material nonlinearities is employed herein, and the FE model of the structural response of intact plates is validated with the available experimental data. In the common studies, based on One Factor at a Time analysis, some of the parameters and interactions between them are excluded. In the present study, the numerical investigations are conducted with the use of the Design of Experiments techniques, where all essential parameters and their interactions are adequately considered. With a total of 32 numerical analyses, the most influential factors and their interactions are identified. As a study outcome, empirical formulations, which allow for a fast estimation of the ultimate compressive strength of intact plates, plates with locked cracks, and repaired cracked plates, are derived. The developed formulations represent a fast and practical tool for estimating the ultimate compressive strength of intact, cracked, and repaired plates, which can be easily employed in the reliability analysis. results followed by their discussion.*

**Keywords:** cracks, Design of Experiments, plate, ultimate strength, FEM

## INTRODUCTION

Ships and offshore structures are subjected to different degradation effects, such as corrosion and cracks and deformations [1, 2]. The latter could be the result of fatigue damage or impact loads. The fatigue cracks are often undetected, and they can have an impact on the strength reduction of structural components.

The effect of locked cracks and their influence on the load-carrying capacity has been investigated experimentally and numerically for some years now. Some of the first attempts to assess the importance of a transverse crack to the buckling capacity of plates were made in [3–6], showing the importance of this problem. In all cases, the buckling strength was significantly lower compared to non-cracked plates. Further studies were performed analysing the elastoplastic collapse, considering the geometry, and material nonlinearities. One

of the more advanced studies was conducted by Paik et al. [7], where both numerical and experimental analyses were carried out. They found that the presence of cracks can significantly reduce the ultimate strength of plates (by up to 50%).

Additionally, the conservative estimation of strength reduction is related to the cross-sectional area reduction with the presence of a crack. However, due to the cycling load, which may change from tensile to compressive, in some cases the cracks may close, and then their behaviour is somehow similar to a non-cracked plate. Additionally, nonlinear FE analysis was found to be a useful tool in predicting the behaviour of cracked plates subjected to compressive load.

A quite comprehensive review related to the ultimate strength of cracked ship structural elements was presented in [8]. A limited number of experimental studies were conducted with regard to cracked plates [7, 9] and cracked stiffened plates [10]. However, only a limited number of

cases were investigated. The joint effect of locked cracks and openings was experimentally investigated in [11], showing that the presence of these two phenomena could result in a significant loss of plate capacity. Additionally, it is hard to model the boundary conditions in the experimental domain, and these may differ from the joining conditions of real ship structural components. Recently, more attention has been paid to the numerical analysis. The ultimate strength of different structural elements subjected to cracks was investigated, including plates [12–16], stiffened plates [15, 17], stiffened panels [18], box girders [19] and ageing ship hulls [20]. Based on these studies, the governing factors that have the most influence on the structural capacity reduction can be identified. The governing parameters that may be identified with regard to the impact of the crack are the crack length, crack location, crack orientation, and the shape of the crack tip. In all studies, for transverse cracks, the reduction is higher with increase of the crack length. In the case of the longitudinal orientation of locked cracks, no significant effect is observed in most of the studied cases. However, some studies recognise that this parameter is a relevant one. In the case of the crack tip shape, in [21] and [22] it was shown that it will not influence the ultimate strength in general. However, the stress concentration around the crack tip will be influenced by the FE mesh density and tip shape.

Nevertheless, the factors that typically influence the ultimate strength of plates will potentially interact with the crack parameters, such as the plate slenderness ratio, plate aspect ratio, and welding-induced imperfections and residual stresses. The combined effects of cracking and initial imperfections were studied in [16]. It was concluded that for small cracks, the ultimate strength is additionally reduced for the higher levels of initial distortions. However, in the case of long cracks, the crack damage effect plays a dominant role.

Based on the different studies, empirical formulations were developed too. Babazadeh and Khedmati [21] derived empirical formulations for the ultimate strength reduction of transversely cracked plates as a function of the crack length, plate slenderness ratio, and plate aspect ratio. In contrast, Paik et al. [7] derived the formula as a function of the plate slenderness ratio and crack length.

Although in previous studies the importance of different individual factors was investigated, investigations that take into account all relevant factors and their joint effect seem to be lacking. Additionally, the studies usually used the OFAT (One Factor At a Time) [23] technique during the sensitivity analysis, i.e. they changed only one parameter, leaving the rest of them unchanged. This technique is very good for initial studies to examine the relevant parameters. However, the possible interaction between factors is lacking. To investigate that, the DoE (design of experiments) [24] methodology seems to be suitable. Another benefit of the DoE is the significantly reduced number of observations compared to OFAT analysis. Based on the DoE analysis, the response surface takes into consideration the relevant factors, and the interactions between them can be established with a significantly lower number of observations compared to classical regression analysis.

Depending on the considered experimental plan, the response surface may be linear or nonlinear.

The objective of the present study is to assess the ultimate strength of cracked plates subjected to compressive loads with the use of the nonlinear FE method and DoE techniques. At the beginning, all relevant parameters related to the locked crack, as well as the plate, are taken into consideration. However, based on the OFAT analysis some of them are not considered further due to their lower impact. The present study also investigates the importance of the variables related to the drilling holes, which are commonly used to stop crack propagation in emerging cases. Furthermore, once the most important governing parameters are identified, the ultimate strength assessment with the predefined DoE plan is conducted. As a result, the most influential factors and interactions are found. Additionally, the response surfaces, allowing for fast estimation of the ultimate strength of cracked plates as well as intact and repaired plates, are established, and the results are compared with other existing empirical formulations and experimental data from the literature.

## FE MODELLING

The compressive structural behaviour of a cracked plate is modelled with the use of the nonlinear finite element method (FEM), considering both geometrical and material nonlinearities. The implicit static solver (Newton–Raphson iterative procedure) is used, employing the commercial software ANSYS [25]. The material is modelled as bilinear with hardening, and in the following the material properties of normal strength steel are considered, such as a yield strength ( $R_y$ ) of 235 MPa, Young’s modulus ( $E$ ) of 206 GPa and hardening stiffness ( $E_h$ ) of 430 MPa. This type of steel is commonly used in shipbuilding, and the material properties are considered as required by Classification Societies Rules, such as Common Structural Rules for Bulk Carriers and Oil Tankers [26]. The plate was modelled with the use of SHELL181 elements, and the contact between the edges was modelled with the use of CONTAC52 elements.

The initial imperfections are modelled considering one half-sine wave as suggested by Smith [27] with an average level of  $0.1\beta^2t$ , where  $\beta$  is the plate slenderness ratio, defined as:

$$\beta = \frac{w}{t} \sqrt{\frac{Re}{E}} \quad (1)$$

where  $w$  is the plate width, and  $t$  is the plate thickness.

At the beginning of the analysis, the optimum mesh density needs to be established. In this order, the element size convergence studies are performed considering the initial parameters of the analysis, as presented in Table 1. At this stage, the drilling holes are not considered, and the central transverse crack is taken into account. The gap between cracked edges is 2 mm, and the cracked tips are modelled as circular ones.

Tab. 1. Initial parameters of the analysis

Parameter	Symbol	Value	Unit
Plate length	$l$	1.5	m
Plate width	$w$	0.6	m
Plate thickness	$t$	10.5	mm
Crack length	$CL$	0.15	m
Crack orientation	$\alpha$	0	degrees

A typical plate being a part of the ship hull structure is spanned between longitudinal stiffeners and transverse girders. Based on that, the unloaded edges can be considered as simply supported. However, in the case of the transverse edges of the plate, since these are supported by very rigid girders, their behaviour can be assumed as something between simply supported and clamped conditions. In this study, the clamped boundary conditions are considered on the loaded edges.

To simulate the strain distribution appropriately around crack tips, the element size of 0.5 mm was found to be the right solution. The additional transition area around the crack is distinguished to provide the proper mesh distribution. The element size along the cracked edges is considered as 3 mm to avoid an excessive aspect ratio of the elements in that region. An example of an element mesh distribution around the crack tip is presented in Fig. 1.

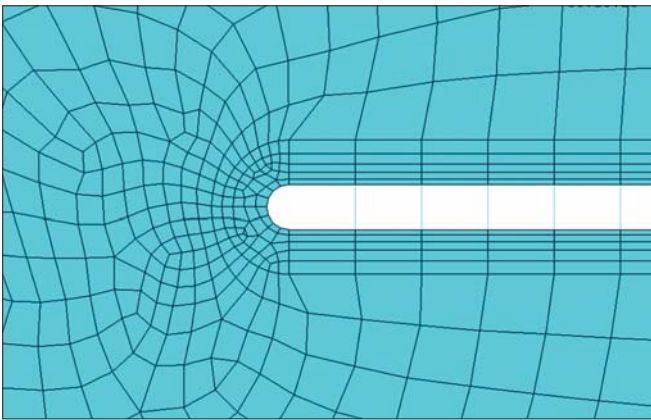


Fig. 1. The mesh distribution around crack region

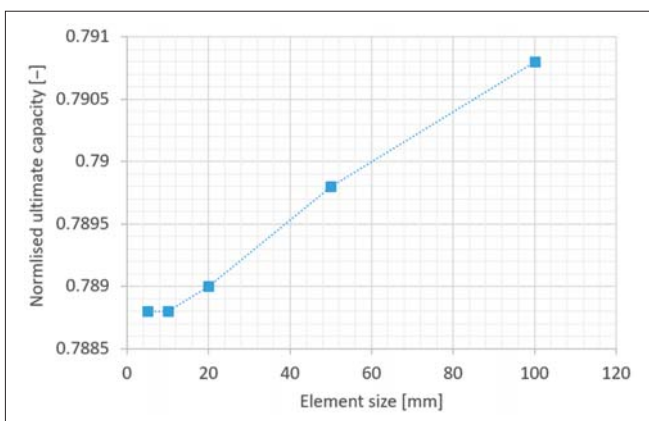


Fig. 2. Mesh convergence

The results of the mesh convergence studies are presented in Fig. 2. The normalised ultimate capacity of the plate is shown in the vertical axis, which is the ratio between the ultimate stress in the plate and the yield stress of the considered material. It can be seen that, with the mesh refinement, the ultimate strength tends to arrive at the actual value. Based on these results, the 20 mm element size is chosen for further analyses, as it provides both accurate results and quite low computation times.

The plate FE model of the considered element size of 20 mm and initial analysis parameters from Table 1 are presented in Fig. 3, where the mesh distribution around the crack edge is also visible. In Fig. 4, the von Mises stress distribution together with the deflection shape of the considered model are presented. As can be seen, the stress concentration around crack tips is significant. Additionally, in the crack position, the deflections are very high, leading to different shapes of plate and levels of deflections compared to the intact plate.

Welding-induced residual stresses may also reduce the plate strength, and are often taken into account [28]. However, based on different studies, it is evident that after multiple cycles of loading the residual stresses are significantly reduced, which is called a shakedown effect [29]. Thus, when the crack initiates and starts to propagate, the influence of residual stresses is already released. For that reason, the residual stresses are not considered in this study, which may lead to an overestimation of the plate strength.

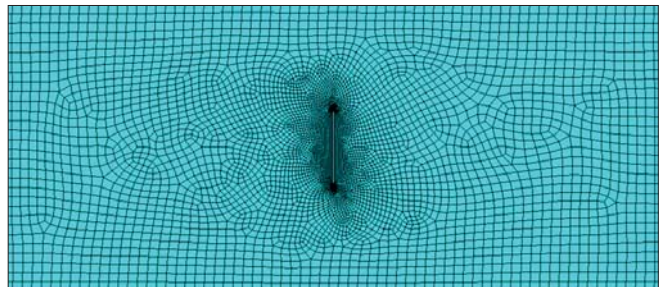


Fig. 3. FE model of the cracked plate

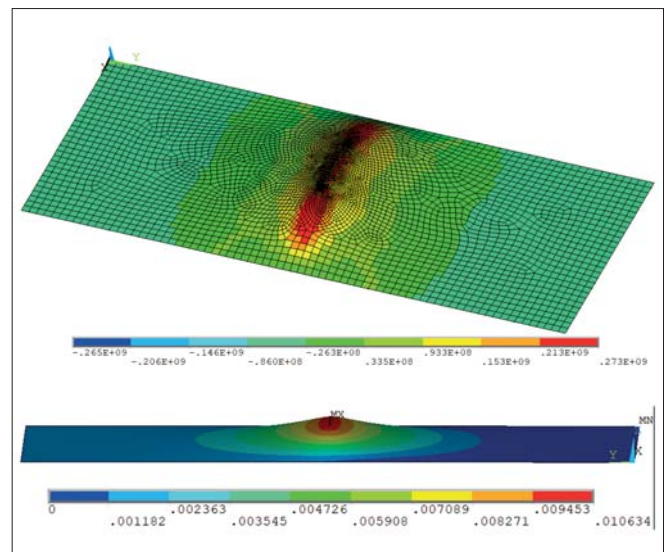


Fig. 4. Von Mises stress distribution [Pa] (top) and total deflections [m] (bottom) of plate

## VALIDATION OF INTACT PLATE MODEL

To validate the FE model, the results of intact plate calculations are compared with the experimental investigations of [30], where plates with different aspect ratios and slenderness ratios were investigated. The material properties considered in that experiment were based on tested coupons, and are equal to  $E = 206 \text{ GPa}$ ,  $Re = 290 \text{ MPa}$ . For the boundary conditions, all edges were simply supported. The level of initial imperfections was not studied, so in the FE model, the mean initial imperfections are considered, as mentioned in the previous section. The plate dimensions and results for both numerical and experimental results are presented in Table 2. A total of 9 specimens were considered, with the same plate width of 400 mm. Additionally, the results were compared with the formula of Faulkner [31], where the classical formulation for the critical buckling stress of an infinitely long thin elastic plate was extended in terms of the ultimate strength and considering the mean level of the initial imperfections. The ultimate strength, in that case, is a function of the plate slenderness ratio and yield strength:

$$\sigma_U = Re \left( \frac{1}{\beta} - \frac{2}{\beta^2} \right)$$

Tab. 2. Results of intact plate validation

No	Length [mm]	t [mm]	Ultimate stress [MPa]			Difference between FEM and Exp. [%]
			Exp. [30]	FEM	Faulkner formula [31]	
1	800	4	194	187	134	3.6
2	1200	4	186	173	134	7.0
3	1600	4	165	157	134	4.8
4	800	6	259	227	186	12.4
5	1200	6	216	225	186	4.2
6	1600	6	216	222	186	2.8
7	800	8	276	265	227	4.0
8	1200	8	258	266	227	3.1
9	1600	8	260	266	227	2.3

As can be seen, the deviations between the numerical and experimental results are minimal, and this can be the result of the non-ideal behaviour of the boundary conditions during the experiment and unknown values of initial imperfections. Additionally, the mechanical properties considered in the FE model are the mean value, whereas, in real conditions, they are subject to uncertainties. However, it can be seen that Faulkner's simplified formulation underestimates the ultimate strength.

Based on that study, one can conclude that the FE model can predict the behaviour of a real plate accurately.

## INITIAL SENSITIVITY ANALYSIS

Based on the literature review, it is evident that the plate aspect ratio, plate slenderness, crack length, initial imperfections level and crack orientation are undoubtedly the most important

governing factors on the ultimate strength. However, in the case of the crack position, the conclusions are divergent. Additionally, the influence of the presence of drilling holes has not been studied previously. Considering these three parameters related to the longitudinal and transverse position of the crack and the drilling holes diameter, an OFAT analysis is performed to determine their importance. The rest of the parameters considered here are presented in Table 1, and the variable ranges are given in Table 3.

Tab. 3. Parameters for sensitivity analysis

Parameter	Symbol	Min	Mean	Max	Unit
Longitudinal crack position	$b/l$	0.15	0.33	0.5	-
Transverse crack position	$a/w$	0.15	0.33	0.5	-
Drilling hole diameter	$d$	2	11	20	mm

The plate with 20 mm drilling holes is presented in Fig. 5. The holes are modelled in such a way that they are not extending the length of the crack. The considered crack positions are presented in Fig. 6.

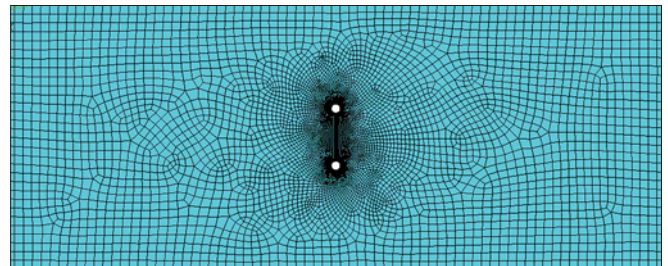


Fig. 5. FE model of the cracked plate with drilling holes

The results of the sensitivity analysis are presented in Fig. 7. As can be seen, the drilling holes have almost no influence on the ultimate strength. Nevertheless, a bigger drilling hole presents a lower stress concentration level. This will have a significant influence in the case of fatigue strength. In the case of the crack position, some influence is visible. In the case of the transverse position, the ultimate strength is higher for the middle crack location compared to the side crack position. In the case of the longitudinal position, the capacity is higher for a crack located near the loaded edge. It may be observed that the relations are not linear, and for the mean positions of the crack, the results do not deviate much from the results of the middle crack position. The differences between the maximum and minimum values are around 6%.

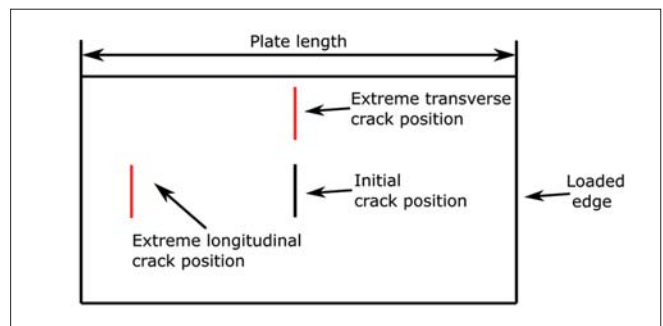


Fig. 6. Considered crack positions

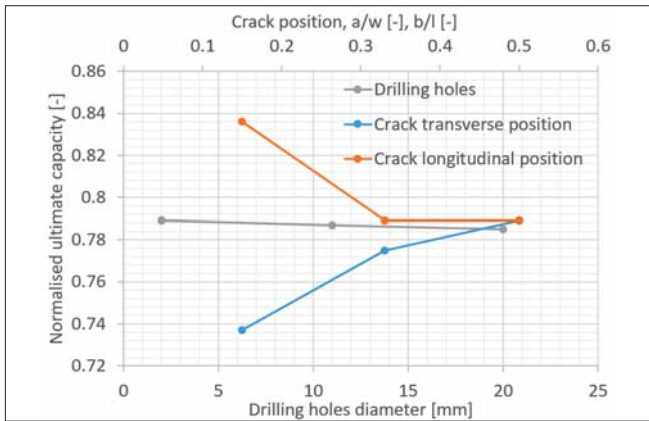


Fig. 7. Sensitivity analysis results

Apart from some significance of the crack position, this effect will not be analysed further. The influence seems to be much less compared to other governing variables, which can be concluded also from the previously mentioned studies.

## DOE MODEL

Having established that five variables are the most influential ones, the proper engineering design experimental plan needs to be chosen. A full factorial analysis ( $2^k$ ) seems to be an excellent option to analyse the design space and provide information about the interaction between effects [32]. In DoE, the factors considered are referred to with letters from the alphabet. The factors with the minimum and maximum values are presented in Table 4.

Tab. 4. Factors considered in DoE

Factor	Symbol	Min	Max	Unit
Plate aspect ratio ( $l/w$ )	A	1	4	-
Plate slenderness ratio ( $\beta$ )	B	1.351	2.533	-
Crack length/ width ( $CL/w$ )	C	0.1	0.4	-
Crack orientation ( $\alpha$ )	D	0	90	°
Level of initial imperfections ( $w_0$ )	E	0.05	0.3	-

The plate aspect ratio is considered between 1 to 4. In the case of the slenderness ratio, the range is based on the statistical data [33]. The typical values of that parameter in the case of ship structures are between 1.4 and 2.5. The corresponding thickness values for the slenderness ratios from Table 3 are 15 mm and 8 mm, respectively. In the case of the crack length, the maximum length corresponds to 40% of the plate width. The crack length cannot be too long because it will not be possible to stop its propagation [7]. Thus, 40% of the plate width is considered as a critical crack length. In the case of the crack orientation, 0 degrees corresponds to a transverse crack, while 90 degrees corresponds to a longitudinal crack. The level of the initial imperfections is estimated by  $w = w_0 \beta^2 t$  where the range of  $w_0$  is based on the statistical analysis that may be found in [27].

The output of the analysis is the normalised ultimate stress. Each combination of factors considering either their minimum or maximum values is considered in the full factorial analysis. This leads to a  $2^k$  number of cases, where  $k$  is the number of factors. In this case, five factors are taken into account, so  $2^5 = 32$  cases are computed. The analysed points are only those at the extreme values of the variable range, so linear behaviour is assumed in the region between the observations. The upper limit of the variable is considered as +1, whereas the lower limit of the variable has the value of -1. Having designed a test matrix, the FE simulations are carried out, and the values of output normalised ultimate stress are presented in Table 5.

Tab. 5. Full factorial test matrix with normalised ultimate stress

Observation number	A	B	C	D	E	Normalised ultimate stress [-]
1	-1	-1	-1	-1	-1	0.978
2	-1	-1	-1	-1	1	0.809
3	-1	-1	-1	1	-1	1.022
4	-1	-1	-1	1	1	0.832
5	-1	-1	1	-1	-1	0.740
6	-1	-1	1	-1	1	0.652
7	-1	-1	1	1	-1	0.996
8	-1	-1	1	1	1	0.814
9	-1	1	-1	-1	-1	0.700
10	-1	1	-1	-1	1	0.617
11	-1	1	-1	1	-1	0.720
12	-1	1	-1	1	1	0.624
13	-1	1	1	-1	-1	0.588
14	-1	1	1	-1	1	0.538
15	-1	1	1	1	-1	0.687
16	-1	1	1	1	1	0.588
17	1	-1	-1	-1	-1	0.996
18	1	-1	-1	-1	1	0.952
19	1	-1	-1	1	-1	1.068
20	1	-1	-1	1	1	1.007
21	1	-1	1	-1	-1	0.708
22	1	-1	1	-1	1	0.693
23	1	-1	1	1	-1	1.017
24	1	-1	1	1	1	0.985
25	1	1	-1	-1	-1	0.776
26	1	1	-1	-1	1	0.894
27	1	1	-1	1	-1	0.783
28	1	1	-1	1	1	0.888
29	1	1	1	-1	-1	0.612
30	1	1	1	-1	1	0.674
31	1	1	1	1	-1	0.716
32	1	1	1	1	1	0.887

Based on the results from Table 4, further statistical analysis is carried out. First, the effect of each factor and interaction is evaluated to analyse whether it is significant or not by calculating the average responses:

$$Eff = \frac{\sum Response_+}{n_+} - \frac{\sum Response_-}{n_-} \quad (2)$$

where  $Response_+$  is the response where either the factor or the multiplication of factors is positive, and  $Response_-$  is the response to the negative value of the factor or their multiplication. Accordingly,  $n_+$  is the number of cases for positive responses and  $n_-$  is the number of cases for negative responses. In the presented study,  $n_+ = n_- = 16$ .

In this way, all the effect identification factors can be established. There are five main effects (A, B, C, D, E) and 26 interaction effects (AB, AC, AD, AE, BC, BD, BE, CD, CE, DE, ABC, ABD, ABE, ACD, ACE, ADE, BCD, BCE, BDE, CDE, ABCD, ABCE, ABDE, ACDE, BCDE, ABCDE), so the total number of effects is 31. The higher the effect identification factor, the more influential the response.

To evaluate the significant effects, several methodologies may be used. The first of them is based on the statistics that are commonly used in the DoE methodology. The cumulative probability value is calculated for the sorted effects and plotted at a half-normal plot [34], as presented in Fig. 8. The significant effects are those that diverge from the dashed line, which represents the probability of observation noise. That means that all effects that are lying on that line are stochastically originated. The effects that deviate from the dashed line are B, C, A, D, CD, AE, BE, DE, E, and AB.

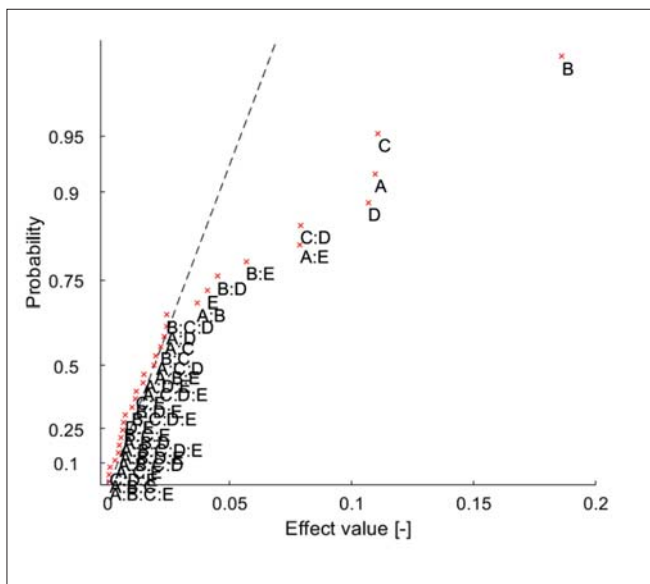


Fig. 8. Half-normal probability plot for effects

Another possible way is to perform the t-test for each effect (to find whether the difference between the population means is significant or not). In this way, the t-values are used to measure the size of the difference between means concerning variation in the data. The t-value for each effect is calculated as follows:

$$t\text{-value}_i = \frac{|Eff_i|}{\sqrt{MS_{Res} \cdot \left(\frac{1}{n_+} + \frac{1}{n_-}\right)}} \quad (3)$$

where  $MS_{Res}$  is the mean of the sum of squares of the residuals (insignificant) effects, equal to:

$$MS_{Res} = \frac{SS_{Res}}{DOF} \quad (4)$$

$$SS_{Res} = \sum_{i=1}^{DOF} \frac{Eff_i^2}{N} \quad (5)$$

where  $DOF$  is the number of degrees of freedom, and is equal to the number of insignificant effects, and  $N$  is the total number of observations (equal to 32 in this case). The  $DOF$  in the present study is 21.  $MS_{Res}$  is calculated, and it is 0.0316.

Based on that, the t-values for the analysed effects are shown in Table 5. To quantify whether the effect is significant or not, the critical t-value is calculated, which is equal to a two-tailed t-value for a 0.05-probability and the given value of the degrees of freedom. In this case, the critical t-value is 2.074. All effects with t-values higher than the critical one can be considered as important. To distinguish that, the Pareto chart is plotted, as shown in Fig. 9. The results of this analysis are in line with the half-normal plot shown in Fig. 8.

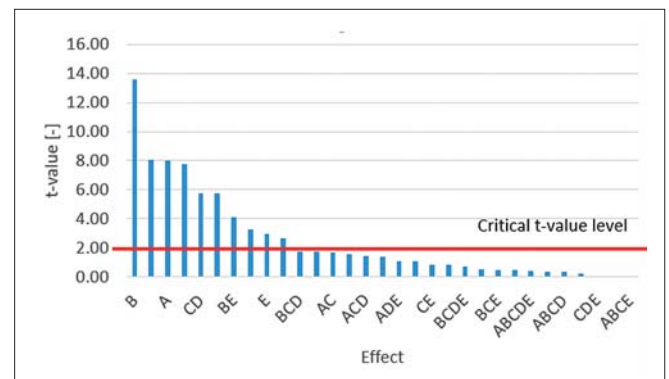


Fig. 9. Pareto chart as a function of the importance of effects

Based on the importance analysis, the significant and insignificant effects are distinguished, and the significant effects are shown in Table 6. The effects are ranked from the most important one to the least important.

Tab. 6. Effect ranking

Rank	Effects	Impact [-]	t-value [-]
1	B (plate slenderness ratio)	0.1861	13.56
2	C (crack length)	0.1107	8.07
3	A (plate aspect ratio)	0.1094	7.97
4	D (crack orientation)	0.1067	7.77
5	CD	0.0789	5.75
6	AE	0.0788	5.74
7	BE	0.0568	4.14
8	BD	0.0449	3.27
9	E	0.0408	2.97
10	AB	0.0366	2.66

As can be seen, ten effects from the overall number of 31 were found to be significant. The essential factor is the plate slenderness ratio, which is known as a parameter that has the most impact on the ultimate strength in general. The three next factors (crack length, crack orientation, and plate aspect ratio) have a similar impact on the ultimate stress. In general, five main effects and five interaction effects are found to be influential. Additionally, in the case of the interaction effects, only interactions consisting of two factors are considered.

From all the interaction factors, the most important one is the interaction between the crack length and crack orientation. This is obvious because, for a long crack, the structural capacity is severely reduced where it is a transversely oriented crack and slightly reduced when it is a longitudinally oriented crack. Similar observations can be found in [8, 22]. What is interesting is that the impact of the initial imperfections level is smaller itself in comparison to its interaction with other factors. The two interaction effects concerning the initial imperfections are influential, with the plate aspect ratio and plate slenderness ratio due to their mutual magnification effect. The interaction between the plate slenderness ratio and crack orientation is also essential. In the case of slender plates, for transversely oriented cracks, the reduction of the structural capacity is not very severe in comparison to stockier plates.

Based on the analysis of the effects, the Response Surface [35] can be established. Since the preliminary plan was based on the Full Factorial Design and considering the main effects and interactions of two factors, the function will take a general form of:

$$\bar{y} = B_0 + \sum_{i=1}^k B_i x_i + \sum_{i < j=2}^k \sum B_{ij} x_i x_j \quad (6)$$

where  $x_i$  corresponds to the model variables and the parameters  $B_i$  and  $B_{ij}$  correspond to linear coefficients, and are equal to half of the considered effect values. It needs to be noted that, in this case, the coefficients may be positive or negative, depending on the effect sign. In the importance analysis, the absolute values of the effects were taken into account.  $B_0$  is calculated as a mean value from all observations.

One can see that, in the DoE analysis, the variables  $x_i$  were in the range between -1 and 1. However, as can be seen in Table 3, the range of the real variables is different. For that reason, the variables need to be normalised, and their values are estimated to:

$$x_1 = \frac{\left(\frac{l}{w}\right) - 2.5}{1.5} \quad (7)$$

$$x_2 = \frac{\beta - 1.942}{0.591} \quad (8)$$

$$x_3 = \frac{\left(\frac{c_l}{w}\right) - 0.25}{0.15} \quad (9)$$

$$x_4 = \frac{\alpha - 45}{45} \quad (10)$$

$$x_5 = \frac{w_0 - 0.175}{0.125} \quad (11)$$

The parameters of the response surface are  $B_0 = 0.7988$ ,  $B_1 = 0.05472$ ,  $B_2 = -0.09303$ ,  $B_3 = -0.05534$ ,  $B_4 = 0.05334$ ,  $B_5 = -0.02041$ ,  $B_{12} = 0.01828$ ,  $B_{15} = 0.03941$ ,  $B_{24} = -0.02247$ ,  $B_{25} = 0.02841$ ,  $B_{34} = 0.03947$ .

The final response surface takes the following form:

$$\begin{aligned} \bar{y} = & 0.7988 + 0.05472x_1 - 0.09303x_2 - \\ & - 0.05534x_3 + 0.05334x_4 - 0.02041x_5 + \\ & + 0.01828x_1x_2 + 0.03941x_1x_5 - 0.02247x_2x_4 + \\ & + 0.02841x_2x_5 + 0.03947x_3x_4 \quad (12) \end{aligned}$$

The response surface gives the estimation of the normalised ultimate strength. As mentioned previously, a linear relationship in the factors range is assumed here, which can be different, considering the FE analysis. To get a higher level of estimation, a Central Composite Design can be considered. In this type of design, additional central and axial points are considered, and the total number of observations is equal to  $2^k + 2k + 1$ . Based on the results of this analysis, one can obtain the polynomial response surface, which is more advanced compared to the linear one. To avoid the more complex polynomial response surface, the formula from Eq. (12) is verified for the central and axial design points.

To expand the Full Factorial Design into a Central Composite Design, additionally  $2k + 1$  axial and central points need to be calculated. In the presented study, the number of additional points is 11. For these points, both exact FE results and estimations from Eq. (12) are presented in Table 7.

Tab. 7. Factorial matrix for additional design points

Observation number	A	B	C	D	E	Normalised ultimate stress [-]	
						FEM	Eq. (12)
33	0	0	0	0	0	0.830	0.801
34	-1	0	0	0	0	0.714	0.746
35	1	0	0	0	0	0.860	0.855
36	0	-1	0	0	0	0.875	0.892
37	0	1	0	0	0	0.823	0.706
38	0	0	-1	0	0	0.917	0.856
39	0	0	1	0	0	0.747	0.745
40	0	0	0	-1	0	0.789	0.747
41	0	0	0	1	0	0.934	0.854
42	0	0	0	0	-1	0.830	0.822
43	0	0	0	0	1	0.830	0.780

The difference between the exact FE solution and the estimation from Eq. (12) is presented in Fig. 10. One can see that for both the FFD points and the central and axial points, the differences are not very significant. The mean error of the estimation for the FFD points is about 3.6%, whereas for the central and axial points it is about 4.8%. The correlation

factor of the linear regression is equal to 0.956. This leads to the conclusion that the response surface from Eq. (12) also predicts the ultimate strength very well for axial and central points. Nevertheless, the derivation of the polynomial response surface can reduce the estimation error slightly.

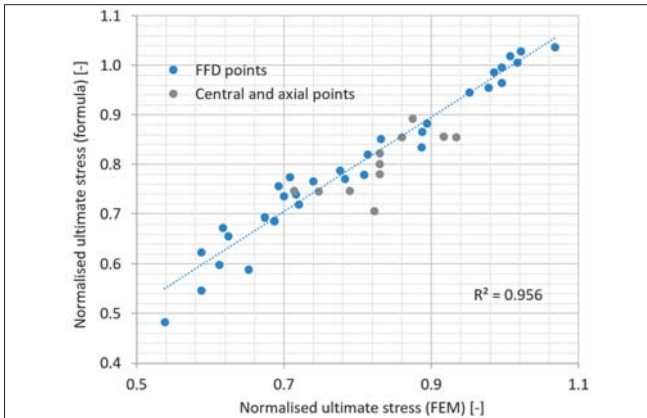


Fig. 10. Comparison between response surface estimation and exact solution

Based on the presented results, the simple empirical formulation in predicting the ultimate strength of cracked plates considering five variables is established. Additionally, the impact of different factors and their interactions is established. It seems that 32 observations are sufficient even in the case of a physical experiment.

## COMPARISON WITH OTHER EMPIRICAL FORMULATIONS

A comparative analysis is carried out to investigate the differences between the proposed formulation and other existing formulations as proposed by Paik et al. [7] and Babazadeh and Khedmati [21].

The formula presented in [7] seems to be the most conservative one, which means that all estimates based on it are higher than expected. Firstly, the ultimate strength of the intact plate is calculated based on the formula of Paik et al. as a function of the plate slenderness ratio [36]:

$$\left(\frac{\sigma_U}{Re}\right)_{intact} = \begin{cases} -0.032\beta^4 + 0.002\beta^2 + 1.0, & \beta \leq 1.5 \\ \frac{1.274}{\beta}, & 1.5 < \beta \leq 3.0 \\ \frac{1.248}{\beta^2} + 0.283, & \beta > 3.0 \end{cases} \quad (13)$$

Then, based on the formula from [7], the capacity of a cracked plate is estimated as:

$$\left(\frac{\sigma_U}{Re}\right)_{cracked} = \frac{A_c}{A_0} \left(\frac{\sigma_U}{Re}\right)_{intact} \quad (14)$$

where  $A_c$  is a reduced plate cross-sectional area due to the presence of a crack and  $A_0$  is the cross-sectional area of the intact plate.

The second formula as proposed in [21] takes into account the plate slenderness ratio, plate aspect ratio, and crack length. The formula was derived for transversely oriented cracks only. For that reason, in the case of longitudinally oriented cracks, the crack length is taken as equal to 0. In the case of inclined cracks, the crack length is calculated as a projection of the crack in the transverse direction. The formula considers the medium level of the initial imperfections. The ultimate strength of the intact plate is calculated as:

$$\left(\frac{\sigma_U}{Re}\right)_{intact} = \begin{cases} 1.176e^{-0.25\beta}, & \frac{l}{w} = 1 \\ 1.82e^{-0.447\beta}, & \frac{l}{w} = 2, 3, 4 \end{cases} \quad (15)$$

Then, the ultimate strength of a cracked plate is calculated based on:

$$\left(\frac{\sigma_U}{Re}\right)_{cracked} = \left(\frac{\sigma_U}{Re}\right)_{intact} - 0.00075e^{-0.45\beta} CL \quad (16)$$

where  $CL$  is the crack length.

Comparisons between the proposed formula in [7] and other empirical formulas are presented in Figs. 11 and 12. The straight line shows the situation when the estimations from both formulations are equal to each other, whereas particular points are the values of the ultimate strength for the specified values of the design variables. When the selected point is above that line, it means that the estimation from the proposed formula is less conservative compared to the other formulation. In the case of Fig. 11, it is visible that the estimation is very conservative. For almost all cases, the ultimate strength is higher based on the formulation developed in the current study. The mean difference between the two formulations is about 27%.

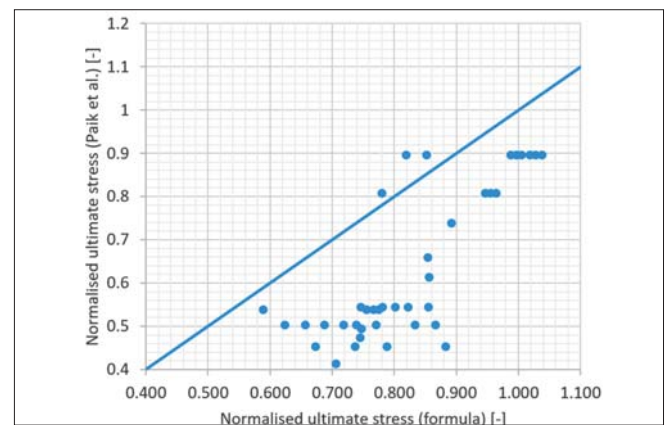


Fig. 11. Formula developed from the current study vs one proposed in [7]

In the case of the comparison presented in Fig. 12, it can be seen that the deviations are significantly less between the formula developed in the current study and the one proposed in [21]. In general, the formulation from Eq. (12) seems to be slightly less conservative compared to Babazadeh and Khedmati's [21] formula. The mean difference between the two formulations is about 12%. The differences may originate from various sources, such as differences in the

boundary conditions. Additionally, in the case of the second formulation, only the mean level of the initial imperfections is considered.

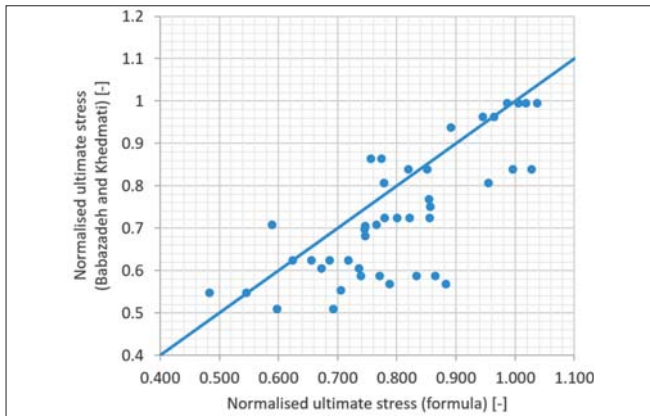


Fig. 12. Formula developed from the current study vs one proposed in [21]

### SIMPLE FORMULATIONS FOR INTACT AND REPAIRED PLATE

The objective of this work was to perform a structural reliability assessment based on the experimentally and numerically estimated ultimate strength.

To determine the difference in capacity reduction during the entire life-cycle of the plate, two additional experiments were carried out, following the same methodology as presented in the section on the DoE model above. The first experiment is related to the intact plate, and the second is related to the plate after repair. In both cases, the FFD analysis is carried out.

#### INTACT PLATE

In the case of the intact plate, only three variables need to be considered, which are the plate aspect ratio, plate slenderness ratio, and level of initial imperfections. This led to  $2^3 = 8$  cases which need to be calculated. The ranges of the variables are the same as presented in Table 4. The results of the calculations with the DoE matrix are presented in Table 8.

Tab. 8. Full factorial test matrix for intact plate case

Observation number	A	B	C	Normalised ultimate stress [-]
1	-1	-1	-1	1.034
2	-1	-1	1	0.839
3	-1	1	-1	0.728
4	-1	1	1	0.628
5	1	-1	-1	1.093
6	1	-1	1	1.016
7	1	1	-1	0.773
8	1	1	1	0.888

Further, the importance analysis is performed, and the following factors and interactions are found to be influential: A, B, E, AE, BE. It can be seen that the same effects were found in the case of a cracked plate. Based on the analysis results, a simple formulation is derived. The variables  $x_1$ ,  $x_2$  and  $x_5$  will be the same as presented in Eqs. (7), (8), and (11), respectively. The estimated ultimate capacity for the intact plate is equal to:

$$\bar{y}_{intact} = 0.875 + 0.06765x_1 - 0.1206x_2 - 0.03202x_5 + 0.04163x_1x_5 + 0.03598x_2x_5 \quad (17)$$

Compared to the exact FE results, the mean value of the estimation concerning Eq. (17) is equal to 1.5%.

#### REPAIRED PLATE

The repair of crack damage is usually done by butt welding of the cracked edges. Sometimes an additional doubler plate is considered. The welding could cause additional residual stresses in the region around the crack, which may have an impact on the plate capacity reduction.

In the presented study, the simplified distribution of residual stresses acting in the longitudinal direction of the crack is considered. As presented in [37], in the weld zone, there are existing tensile stresses with a value equal to the yield stress. The total width of the heat-affected zone is taken as three times the plate thickness. In the region outside the welding zone, there are existing compressive stresses of about 20% of the yield stress. The width of that region is calculated to satisfy the internal force equilibrium in the plate and is equal to 7.5 times the plate thickness on one side of the crack. The resulting typical zones for the inclined crack are presented in Fig. 13. The residual stresses are applied as the initially induced stresses in the FE model.

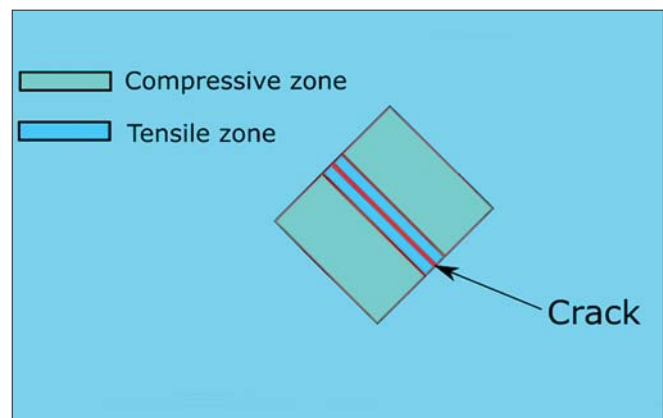


Fig. 13. Welding-induced stress zones after crack welding

Similarly to the cracked plate, the five variables with their ranges, as presented in Table 4, are considered in the experiment. The analysis results, together with the factorial test matrix, are presented in Table 9.

Tab. 9. Full factorial test matrix with normalised ultimate stress

Observation number	A	B	C	D	E	Normalised ultimate stress [-]
1	-1	-1	-1	-1	-1	1.024
2	-1	-1	-1	-1	1	0.833
3	-1	-1	-1	1	-1	1.009
4	-1	-1	-1	1	1	0.824
5	-1	-1	1	-1	-1	1.015
6	-1	-1	1	-1	1	0.817
7	-1	-1	1	1	-1	1.012
8	-1	-1	1	1	1	0.826
9	-1	1	-1	-1	-1	0.724
10	-1	1	-1	-1	1	0.627
11	-1	1	-1	1	-1	0.723
12	-1	1	-1	1	1	0.625
13	-1	1	1	-1	-1	0.715
14	-1	1	1	-1	1	0.619
15	-1	1	1	1	-1	0.723
16	-1	1	1	1	1	0.624
17	1	-1	-1	-1	-1	1.070
18	1	-1	-1	-1	1	1.001
19	1	-1	-1	1	-1	1.051
20	1	-1	-1	1	1	0.995
21	1	-1	1	-1	-1	1.054
22	1	-1	1	-1	1	0.993
23	1	-1	1	1	-1	1.041
24	1	-1	1	1	1	0.987
25	1	1	-1	-1	-1	0.785
26	1	1	-1	-1	1	0.888
27	1	1	-1	1	-1	0.786
28	1	1	-1	1	1	0.888
29	1	1	1	-1	-1	0.775
30	1	1	1	-1	1	0.887
31	1	1	1	1	-1	0.783
32	1	1	1	1	1	0.886

As a result of the importance analysis, the factors A, B, E, AE, BE are found to be the most significant. This leads to the conclusion that the crack parameters and associated residual stresses do not have a significant impact on the structural capacity of the plate compared to the intact one. And only a slight reduction of 1–2% is observed in the case of a 90-degree crack orientation concerning the direction of the applied compressive load. The estimated ultimate strength for the repaired plate is defined as:

$$\bar{y}_{repaired} = 0.8628 + 0.06648x_1 - 0.1093x_2 - 0.03032x_5 + 0.04153x_1x_5 + 0.03214x_2x_5 \quad (18)$$

## CONCLUSIONS

The presented study analysed the ultimate strength of cracked plates subjected to compressive loads considering five governing parameters related to the plate aspect ratio, plate slenderness ratio, crack length and orientation, and the level of initial imperfections. Based on the initial sensitivity analysis, it was found that the existence of drilling holes and the crack position do not influence the plate capacity significantly, and they were not considered in the present analysis. The DoE techniques were used considering the Full Factorial Design. When incorporating the DoE techniques into the FE analysis, one can perform the sensitivity analysis in a quite straightforward way. Compared to the OFAT analysis, which was used in previous studies, the interaction between factors is established, and the number of observations needed in the analysis is significantly reduced. Additionally, this allows more variables to be considered with a similar computational effort.

In terms of the ultimate strength of cracked plates, the plate slenderness ratio was found to be the most influential factor. The plate aspect ratio, crack length, and orientation have a similar impact. Four interaction effects were also found.

As a result of the analysis, a linear response surface was found, which allows for a fast estimation of the ultimate strength of cracked plates. The simplified formulation was found to deviate slightly from the exact results. The developed formulation is a fast and practical tool for estimating the ultimate strength of cracked plates and can be successfully used in the reliability analysis. Additionally, the simplified formulations for estimation of the ultimate strength of intact and repaired plates subjected to compressive loads were developed. These three formulations cover the entire life-cycle of the plate element in terms of possible crack damage.

The comparison between the intact and cracked plates reveals that, for the most critical case of a transverse crack, the reduction of the ultimate strength reaches the level of 35%. In the case of repaired plates, their ultimate strength is only slightly reduced compared to intact plates.

## ACKNOWLEDGEMENTS

This work has been supported by the National Science Centre, Poland (grant No. 2018/31/N/ST8/02380). The ANSYS software used in the simulations presented in this paper was available as a part of the partnership cooperation agreement between ANSYS Inc., MESco sp. z o.o., and the Gdansk University of Technology.

## REFERENCES

1. Woloszyk K., Kahsin M., Garbatov Y. (2018): *Numerical assessment of ultimate strength of severe corroded stiffened plates*. Engineering Structures, 168, 346–54.
2. Saad-Eldeen S., Garbatov Y., Guedes Soares C. (2016): *Ultimate strength analysis of highly damaged plates*. Marine Structures, 45, 63–85.
3. Roy Y. A., Shastry B. P., Rao G. V. (1990): *Stability of square plates with through transverse cracks*. Computers and Structures, 36, 387–8.
4. Shaw D., Huang Y. H. (1990): *Buckling behaviour of a central cracked thin plate under tension*. Engineering Fracture Mechanics, 35, 1019–27.
5. Riks E., Rankin C. C., Brogan F. A. (1992): *The buckling behaviour of a central crack in a plate under tension*. Engineering Fracture Mechanics, 43, 529–48.
6. Kumar Y. V. S., Paik J. K. (2004): *Buckling analysis of cracked plates using hierarchical trigonometric functions*. Thin-Walled Structures, 42, 687–700.
7. Paik J. K., Satish Kumar Y. V., Lee J. M. (2005): *Ultimate strength of cracked plate elements under axial compression or tension*. Thin-Walled Structures, 43, 237–72.
8. Babazadeh A., Khedmati M. R. (2018): *Ultimate strength of cracked ship structural elements and systems: A review*. Engineering Failure Analysis, 89, 242–57.
9. Seifi R., Khoda-Yari N. (2011): *Experimental and numerical studies on buckling of cracked thin-plates under full and partial compression edge loading*. Thin-Walled Structures, 49(12), 1504–1516.
10. Shi X. H., Zhang J., Guedes Soares C. (2017): *Experimental study on collapse of cracked stiffened plate with initial imperfections under compression*. Thin-Walled Structures, 114, 39–51.
11. Saad-Eldeen S., Garbatov Y., Guedes Soares C. (2016): *Experimental investigation on the residual strength of thin steel plates with a central elliptic opening and locked cracks*. Ocean Engineering, 115, 19–29.
12. Brighenti R. (2005): *Numerical buckling analysis of compressed or tensioned cracked thin plates*. Engineering Structures, 27, 265–76.
13. Rahbar-Ranji A., Zarookian A. (2015): *Ultimate strength of stiffened plates with a transverse crack under uniaxial compression*. Ships and Offshore Structures, 10, 416–25.
14. Cui C., Yang P., Xia T., Du J. (2016): *Assessment of residual ultimate strength of cracked steel plates under longitudinal compression*. Ocean Engineering, 121, 174–83.
15. Bayatfar A., Khedmati M. R., Rigo P. (2014): *Residual ultimate strength of cracked steel unstiffened and stiffened plates under longitudinal compression*. Thin-Walled Structures, 84, 378–392.
16. Xia T., Yang P., Hu K., Cui C. (2018): *Combined effect of imperfections on ultimate strength of cracked plates under uniaxial compression*. Ocean Engineering, 150, 113–23.
17. Cui C., Yang P., Li C., Xia T. (2017): *Ultimate strength characteristics of cracked stiffened plates subjected to uniaxial compression*. Thin-Walled Structures, 113, 27–38.
18. Yu C. L., Chen Y. T., Yang S., Liu Y., Lu G. C. (2018): *Ultimate strength characteristic and assessment of cracked stiffened panel under uniaxial compression*. Ocean Engineering, 152, 6–16.
19. Saad-Eldeen S., Garbatov Y., Soares C. (2015): *Ultimate strength of a corroded box girder subjected to pure bending and a non-propagating crack*. In: Soares C., Dejhalla R., Pavletic D. (eds.), *Towards Green Maritime Technology and Transport*, CRC Press, pp. 373–80.
20. Saad-Eldeen S., Garbatov Y., Soares C. (2016): *Emergency repair of a single hull structure with locked cracks*. In: Soares C., Santos T. (eds.), *Maritime Technology and Engineering III*, CRC Press, pp. 521–9.
21. Babazadeh A., Khedmati M. R. (2019): *Empirical formulations for estimation of ultimate strength of cracked continuous unstiffened plates used in ship structure under in-plane longitudinal compression*. Engineering Failure Analysis, 100, 470–84.
22. Xu M. C., Garbatov Y., Guedes Soares C. (2014): *Residual ultimate strength assessment of stiffened panels with locked cracks*. Thin-Walled Structures, 85, 398–410.
23. Daniel C. (1973): *One-at-a-Time Plans*. Journal of the American Statistical Association, 68, 353–60.
24. Wu C.-F., Hamada M. (2009): *Experiments: planning, analysis, and optimisation*, Wiley.
25. ANSYS (2019): *Online Manuals, Release 19*.
26. International Association of Classification Societies (2018): *Common Structural Rules (BC & OT)*.
27. Smith S. (1977): *Influence of local compressive failure on ultimate longitudinal strength of a ship's hull*. Proceedings of International Symposium on Practical Design in Shipbuilding, 73–9.

28. Tekgoz M., Garbatov Y., Guedes Soares C. (2013): *Finite element modelling of the ultimate strength of stiffened plates with residual stresses*. In: Guedes Soares C., Romanoff J. (eds.), *Analysis and Design of Marine Structures*, CRC Press, pp. 309–17.
29. Tekgoz M., Garbatov Y. (2013): *Ultimate strength of a plate accounting for shakedown effect and corrosion degradation*. In: Guedes Soares C., López Peña F. (eds.), *Developments in Maritime Transport and Exploitation of Sea Resources*, CRC Press, pp. 395–403.
30. Kim U.-N., Choe I.-H., Paik J. K. (2009): *Buckling and ultimate strength of perforated plate panels subject to axial compression: experimental and numerical investigations with design formulations*. *Ships and Offshore Structures*, 4, 337–61.
31. Faulkner D. (1975): *A review of effective plating for use in the analysis of stiffened plating in bending and compression*. *Journal of Ship Research*, 19, 1–17.
32. Montgomery D. C. (2006): *Design and Analysis of Experiments*, John Wiley & Sons Ltd, USA.
33. Zhang S. (2016): *A review and study on ultimate strength of steel plates and stiffened panels in axial compression*. *Ships and Offshore Structures*, 11(1), 81-91.
34. Daniel C. (1959): *Use of half-normal plots in interpreting factorial two-level experiments*. *Technometrics*, 1, 311–41.
35. Gunst R. F., Myers R. H., Montgomery D. C. (1996): *Response surface methodology: Process and product optimisation using designed experiments*. *Technometrics*, 38, 285.
36. Paik J. K., Thayamballi A. K., Lee J. M. (2004): *Effect of initial deflection shape on the ultimate strength behavior of welded steel plates under biaxial compressive loads*. *Journal of Ship Research*, 48, 45–60.
37. Tall L., Rao N. (1961): *Residual stresses in welded plates*. *Welding Journal, Research Supplement*, 40(1), 468–480.

## CONTACT WITH THE AUTHORS

**Krzysztof Woloszyk**

*e-mail: krzwolos@pg.edu.pl*

Gdańsk University of Technology  
 Faculty of Ocean Engineering and Ship Technology  
 11/12 Gabriela Narutowicza Street, 80-233 Gdańsk  
**POLAND**

**Yordan Garbatov**

*e-mail: yordan.garbatov@tecnico.ulisboa.pt*

Centre for Marine Technology and Ocean Engineering  
 (CENTEC), Instituto Superior Técnico  
 Universidade de Lisboa, Avenida Rovisco Pais  
 1049-001 Lisboa  
**PORTUGAL**

# INVESTIGATIONS OF MECHANICAL PROPERTIES OF API P110 STEEL CASING TUBES OPERATED IN DEEP-SEA SOUR CONDENSATE WELL CONDITIONS

Yao Zilin<sup>1</sup>

Wang Yu<sup>2</sup>

Yang Xuefeng<sup>3</sup>

Gao Anping<sup>4</sup>

Zhang Rong<sup>5</sup>

Jia Yanjie<sup>6</sup>

<sup>1</sup> College of Chemistry and Chemical Engineering, Southwest Petroleum University, China

<sup>2</sup> Robotics Research Center, School of Mechanical Engineering, China

<sup>3</sup> Heavy Oil Development Company of PetroChina Xinjiang Oilfield Company, China

<sup>4</sup> Wuxi China Resources Gas Co., Ltd, China

<sup>5</sup> Petroleum Engineering School, Southwest Petroleum University, China

<sup>6</sup> Petrochina Southwest Pipeline Company, China

## ABSTRACT

*Due to the complexity of the marine environment, in deep-sea drilling, all kinds of strings are corroded by different deep-sea conditions for a long time, accompanied by high temperature and high pressure, which lead to the continuous change of mechanical properties of materials. In order to solve the problem that the material mechanical parameters cannot be accurately described in the performance analysis of the casing, deep-sea simulated corrosion and material damage experiments of P110 material were carried out in this paper. Mass loss and tensile experiments on corrosion-damaged test pieces were conducted under different corrosion experimental periods. The changes in mechanical properties of the material were analyzed. Equations of the variation of the equivalent yield strength and the equivalent tensile strength were obtained. The results show that the equivalent yield strength and the equivalent tensile strength decrease with the increase of the weight loss rate. Based on the experimental results and finite element analysis, a method for establishing the material corrosion model was proposed in this paper. The deep-sea drilling corrosion performance model of P110 material was established, which greatly reduced the error caused by the material uniformity assumption in finite element analysis. This paper provides a theoretical basis for the analysis of reliability and life of P110 materials in wells.*

**Keywords:** deep-sea drilling environment, mechanical properties, yield strength, tensile strength, corrosion modeling

## INTRODUCTION

With the gradual expansion of global offshore oil and gas field development, the damage of downhole strings becomes more and more serious with the increase of the service cycle. Especially in the process of deep-sea drilling, because the deep-sea corrosion environment is too complex, the corrosion damage accumulates with the time, resulting in continuous change of the mechanical properties of the casing, resulting in casing damage accidents, resulting in huge economic losses, which brings great difficulties to the oil well exploitation [1, 2, 3].

In recent years, a large number of studies on casing corrosion of oil and gas wells has been carried out. Regularized treatment of casing corrosion defects with different shapes according to the latest safety assessment standards for pressure vessels with defects is carried out by Zhu et al. [4, 5, 6, 7]. The crushing strength of a casing containing corrosion defects was analyzed by the ANSYS finite element simulation method. Mack et al. studied the indoor evaluation method of casing material selection and analyzed the change in performance of downhole tools due to the corrosive environment during the service period [8]. Chen et al. investigated the effect of alternate

injection frequency of empty foam liquid on the corrosion of casing steel during high-pressure oil and gas foam flooding [9, 10]. The aforementioned studies have focused on the effect of the corrosion rate of the casing and the corrosion defects on the residual strength. However, there were few studies on the properties of casing materials after corrosion.

Most research assumes that the material is isotropic, and the material is uniform when using the finite element method for mechanical analysis. This assumption is more reasonable for new materials because the basic requirements for qualified new materials are isotropic, uniform material, and the error can be negligible [11, 12, 13]. However, under complex corrosive conditions, the degree of corrosion is affected by the direction and location of corrosion. Thus, the above assumptions are unreasonable for complex corrosion conditions. Moreover, at present, most of the studies on the performance of casing clothing are focused on land drilling, and there are few studies on deep-sea drilling corrosion.

In this paper, based on deep-sea oil and gas wells, the degree of casing corrosion is directly expressed by the P110 weight loss rate obtained by corrosion damage experiment. A slow strain tensile experiment was performed in the case of casing damage. According to the API value rule, the influence of weight loss rate on the plasticity of the casing is obtained. A dynamic model of the performance of the material under the influence of corrosion is obtained. This paper provides a new idea for the selection of engineering casings and provides a theoretical basis for the life analysis and reliability analysis of casing.

## MATERIAL CORROSION EXPERIMENT

The material and mechanical properties of casings commonly used in oil and gas drilling are shown in Table 1. Due to the high requirements for mechanical properties of materials in deep-sea drilling, P110 material casings are most commonly used in deep-sea drilling. Therefore, P110 material was selected as the research object in this paper, in which carbon accounts for about 3% and iron accounts for about 50%.

Tab. 1. Mechanical properties of several common casings in API

Material	Yield strength (MPa)	Tensile strength (MPa)	Maximum elongation (%)
J55	379-552	≥517	24
K55	379-552	≥689	20
N80	552-758	≥689	19
P110	758-965	≥862	15

The corrosive fluid used in this experiment was the drilling fluid used in deep-sea drilling. Due to the particularity of offshore drilling, it was mixed with sea water according to the proportion in actual production during the experiment.

The main device used in the deep-sea temperature and pressure environment experiment was a self-developed high-temperature autoclave, as shown in Fig. 1. The high-temperature autoclave was used in this experiment. The maximum

experimental pressure of the equipment is 70 MPa, the maximum experimental temperature is 200°C, the volume is 5 L, the inner diameter is 150 mm, and the depth is 300 mm.



Fig. 1. High-temperature autoclave

The material of this experiment was the casing of ocean oil and gas wells, as shown in Fig. 2. Samples of the casing and tensile test pieces are shown in Figs. 2 and 3. Corrosive liquids were mixed in laboratory tests.



Fig. 2. Before casing sampling



Fig. 3. Tensile test pieces

Three tensile test pieces were taken for each experiment and polished step-by-step with 240#, 400#, 600#, 800#, and 1200# sandpaper, in order to eliminate machined knife marks. The test pieces were cleaned by degreasing with petroleum ether and removing water with alcohol. After drying the test pieces in cold air, they were measured for specific size and weight. Finally, the test pieces were placed in a dry box for use.

At the beginning of the corrosion experiment, the tensile test pieces were hung on a bracket placed in a high-temperature autoclave, and a corrosive liquid was added. Then, a nitrogen gas pressure test was applied to the high-temperature autoclave to ensure the tightness of the autoclave. The oxygen was removed by introducing nitrogen for 2 hours, and the temperature was raised to the design temperature. CO<sub>2</sub> and nitrogen were introduced to pressurize to the design pressure. After the experimental time was reached, the operation of the test pieces was finished, and the tensile test pieces were taken out after the pressure was released. The corrosive medium on the surface of the test pieces was removed by liquid for removing the membrane. The method of removing corrosion products was to place the test pieces in a cleaning solution and clean them in an ultrasonic cleaner. The samples were immersed in a saturated sodium bicarbonate solution for about 2 to 3 minutes for neutralization. The samples were rinsed with tap water, blotted with filter paper, and soaked in anhydrous alcohol or acetone for 3 to 5 minutes. The test pieces were dried for a certain period of time to prepare for material damage experiments.

In the first experiment, three of the threaded and unthreaded tensile test pieces were placed in a high-temperature autoclave, the experimental pressure was 10 MPa, the experimental temperature was 100°C, and the experimental period was one week (168 h). After the end of the experiment, the pressure was released, and the test pieces were taken out until the temperature was lowered to about 60 °C. The tensile test pieces were compared before and after corrosion as shown in Fig. 4.

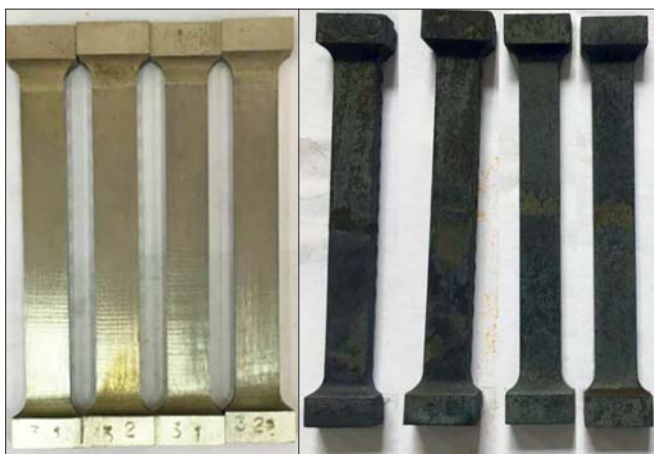


Fig. 4. Comparison of tensile test pieces before and after the experiment

The taken tensile test pieces were washed, air-dried, and weighed, and the weight was compared between before and after the experiment, as shown in Table 2. The three groups

of samples were weighed three times respectively, and their values were indicated by serial numbers 1, 2 and 3.

Tab. 2. Weight before and after the first experiment

Pre-experiment weight /g			Post-experiment weight /g		
1	2	3	1	2	3
53.871	53.739	53.815	50.089	50.071	50.081
53.874	53.743	53.815	50.090	50.066	50.081
53.675	53.740	53.815	50.090	50.073	50.081

The results of the first experiment were analyzed. The weights of the three parallel test pieces before the experiment were 53.807, 53.741, and 53.815 g, respectively. The weights after the experiment were 50.090, 50.070, and 50.081 g, respectively. The weight loss rates of the three parallel test pieces were 7.0%, 6.8%, and 6.9%, respectively.

The second experimental temperature and pressure were the same as the first experiment, and the experimental period was 15 d (360 h). The tensile test pieces after corrosion were cleaned and air-dried. The three groups of samples were weighed three times respectively, and their values were indicated by serial numbers 4, 5 and 6, as shown in Table 3.

Tab. 3. Weight before and after the second experiment

Pre-experiment weight /g			Post-experiment weight /g		
4	5	6	4	5	6
34.254	34.662	34.558	29.729	30.145	30.084
34.254	34.662	34.558	29.728	30.144	30.084
34.255	34.663	34.558	29.728	30.145	30.084

In the analysis of the results of the second experiment, the average weights of the three unthreaded tensile test pieces before the experiment were 34.254, 34.662, and 34.558 g, respectively. The average weights after the experiment were 29.728, 30.145, and 30.0845 g, respectively. The weight loss rates of the three parallel test pieces were 13.2%, 13.0%, and 12.9%, respectively.

The third experimental temperature and pressure were the same as the first experiment, and the experimental period was 12 d (288 h). The tensile test pieces after corrosion were cleaned, air-dried, and weighed, using the same method. The results are shown in Table 4.

Tab. 4. Weight before and after the third experiment

Pre-experiment weight /g			Post-experiment weight /g		
7	8	9	7	8	9
34.095	34.867	34.547	30.644	31.188	30.893
34.095	34.867	34.547	30.645	31.188	30.893
34.095	34.867	34.547	30.645	31.188	30.893

In the analysis of the results of the third experiment, the average weights of the three unthreaded tensile test pieces before the experiment were 34.0954, 34.8676, and 34.5472 g, respectively. The average weights after the experiment were

30.6451, 31.1886, and 30.8933 g, respectively. The weight loss rates of the three parallel test pieces were 10.1%, 10.5%, and 10.6%, respectively.

The experiment was continued in the same way. The experimental pressure was set to 10 MPa, and the experimental temperature was 100°C. Ten groups of samples were taken to change the experimental corrosion time. After the corrosion experiment, the weight data before and after the experiment were measured according to the experimental method described by the above three groups of samples.

A test piece having a severe corrosion pit as shown in Fig. 5 was removed. The test piece, shown in Fig. 6, was taken for washing and weighing, and the results are shown in Table 5.



Fig. 5. Severely corroded test piece



Fig. 6. Selected test pieces

In the corrosion experiments, the degree of corrosion is expressed as the corrosion rate. The corrosion rate is the weight loss in years after the corrosion experiment of the standard test pieces were carried out. In this paper, the degree of corrosion of the material is expressed by the weight loss rate. After the corrosion experiments were completed, the corrosion test pieces were stretched to study the effect of corrosion on the mechanical properties of the material, and the influence law was analyzed.

## MATERIAL TENSILE EXPERIMENT

The material tensile experiment used an MTS hydraulic universal experimenting machine. The servo motor drives the high-precision screw pair to drive the beam up and down to realize the tensile, compression and bending experiments of the test pieces.

Tab. 5. Weight and weight loss rate before and after the experiments

Experiment number	Time	Pre-experiment weight	Post-experiment weight	Weight loss rate
10	300 h	34.2148 g	30.4956 g	10.9%
11	300 h	34.1689 g	30.3945 g	11.0%
12	400 h	34.8127 g	29.8720 g	14.2%
13	450 h	33.9654 g	28.6941 g	15.5%
14	450 h	34.5334 g	29.1472 g	15.6%
15	500 h	34.7038 g	29.0512 g	16.3%
16	550 h	33.8899 g	27.8835 g	17.7%
17	550 h	33.7530 g	27.7130 g	17.9%
18	600 h	33.8523 g	27.0480 g	20.1%
19	700 h	34.0259 g	25.1792 g	26%

Before the experiment, the parallel test pieces were numbered with a steel stamp, the parallel test piece size was measured, and then a tensile experiment was performed. According to the size of the tensile test pieces, two fixtures were fabricated for assisting stretching in this experiment.

Three sets of parallel test pieces were taken in the experiment. The results are shown in Fig. 7. According to the API rule, the average value of the three groups of data was calculated. The yield strength of the new material with no thread was 960 MPa, and the tensile strength was 1039 MPa. The results satisfy the strength requirements of P110 steel casing with yield strength range of 758–965 MPa and tensile strength  $\geq 862$  MPa.

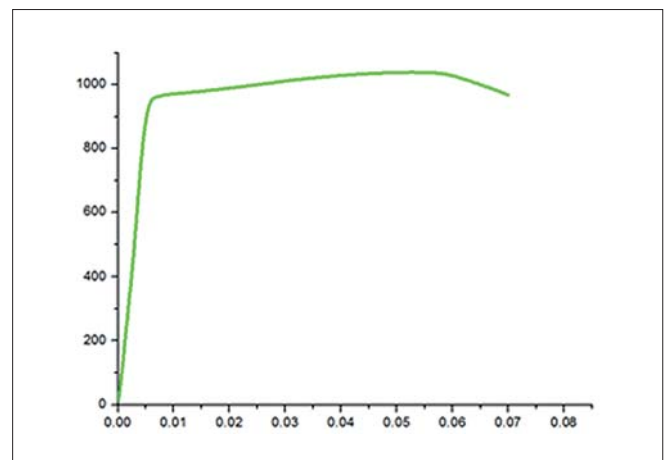


Fig. 7. Stress (X axis)–strain (Y axis) curve of new material without thread

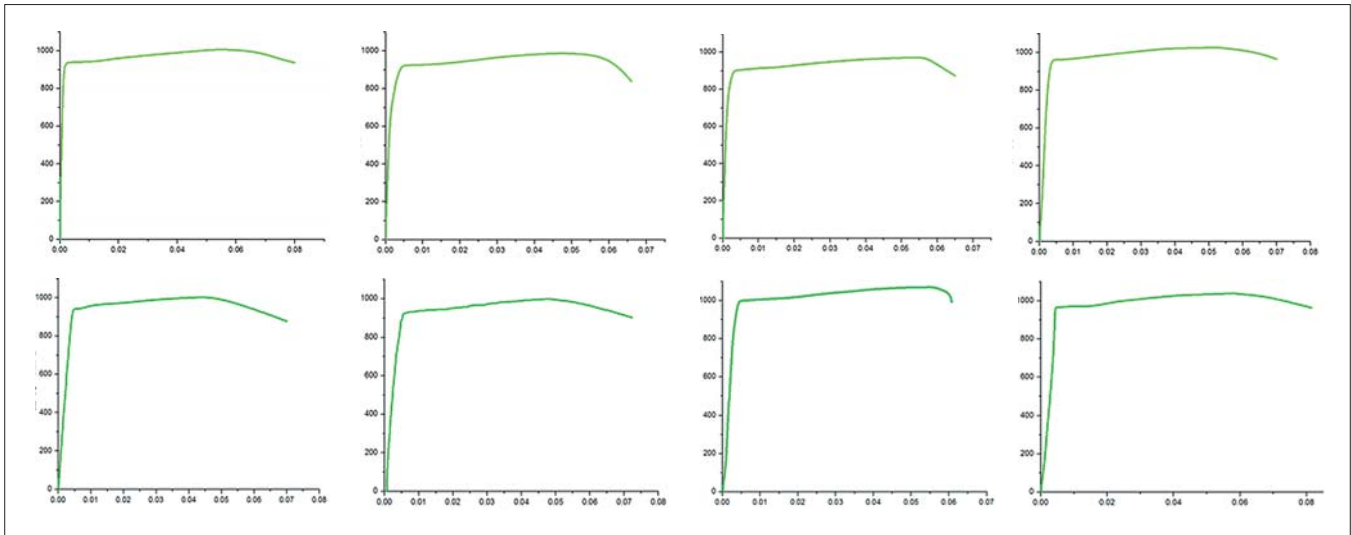


Fig. 8. Stress (X axis)–strain (Y axis) curve after corrosion

After the tensile experiments, the fracture was observed and the tensile data were analyzed. There were at least two normal parallel test pieces for each tensile test piece group. The normal fractured test piece group was selected, as shown in Fig. 8.

### DISCUSSION OF EXPERIMENTAL RESULTS

According to the test results, without considering the influence of corrosion on the area of the test piece, the equivalent yield strength and the equivalent tensile strength of the material after corrosion were calculated by the tensile test data. The mechanical property ratio of the material before and after corrosion was also calculated in Table 6. It can be seen from Table 6 that when the weight loss rate was less than 15%, the equivalent yield strength and the equivalent tensile strength decrease with the increase of the weight loss rate. When the weight loss rate was greater than 15%, the decrease rate of the equivalent yield strength was significantly accelerated, and the equivalent tensile strength was basically unchanged. When the weight loss rate was greater than 20%, the equivalent yield strength of the material was less than 758 MPa, which does not meet the requirements for use of the P110 material. According to the data summarized in the table, the equivalent yield strength of all test pieces with weight loss rate less than 20% in this experiment was calculated, and the curve was fitted to Fig. 9 (left). The equivalent tensile strength of all test pieces with a weight loss rate of less than 15% in this experiment was calculated, and the curve was fitted to Fig. 9 (right).

In Fig. 9, the green line is the experimental data, the red line is the fitting curve, which are for the change of the equivalent yield strength when the weight loss rate was less than 20% and the change of the equivalent tensile strength when the weight loss rate was less than 15%, respectively.

Tab. 6. Relationship between weight loss rate and performance parameter changes

Weight loss rate $G_s$	Equivalent yield strength	Yield strength ratio	Equivalent tensile strength	Tensile strength ratio
6.6%	959	99.9%	1020	98.1%
6.8%	956	99.6%	1010	97.1%
7.0%	951	99.1%	1008	96.9%
10.1%	940	97.9%	998	96.0%
10.5%	938	97.7%	999	96.1%
10.9%	930	96.7%	991	95.3%
11.0%	924	96.3%	988	95.0%
11.3%	915	95.3%	978	94.1%
13.1%	887	92.4%	962	92.5%
13.3%	889	92.6%	965	92.8%
14.2%	881	91.8%	950	91.3%
15.5%	879	91.6%	952	91.5%
16.3%	807	84.1%	957	92.0%
17.9%	785	81.8%	943	90.7%
20.1%	751	78.3%	947	91.1%
20.6%	705	73.4%	953	91.6%

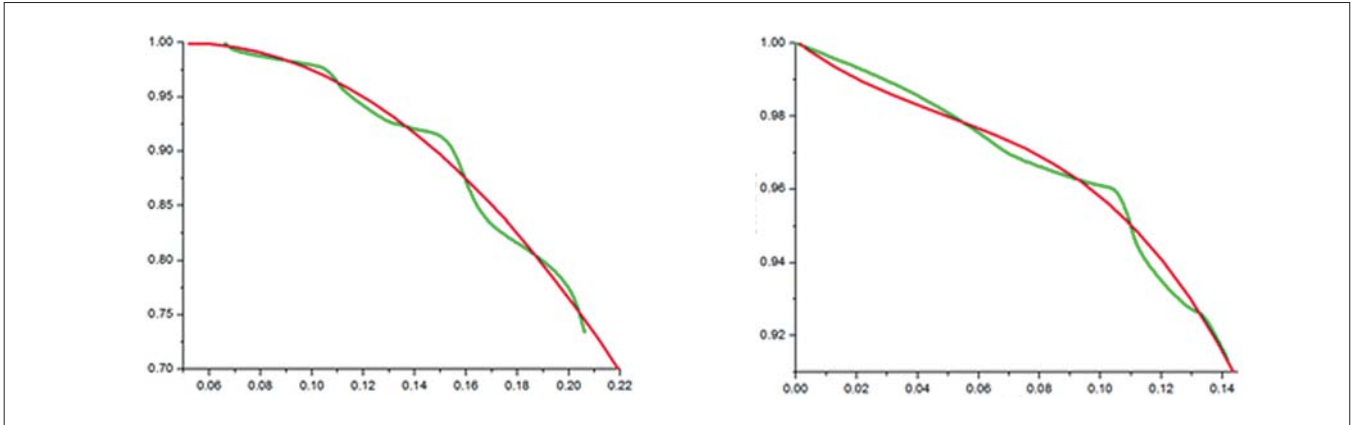


Fig. 9. Relationship between material performance parameters (Y axis) and weight loss rate (Y axis)

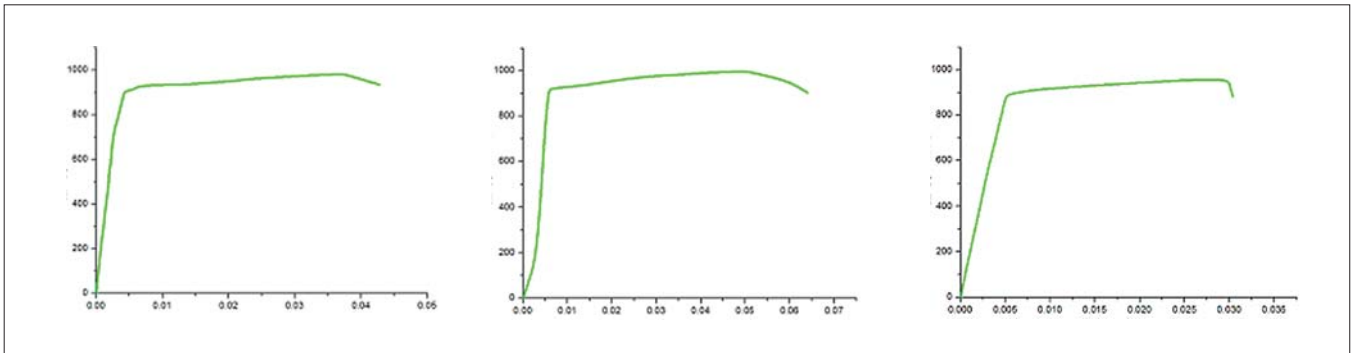


Fig. 10. Stress (X axis)–strain (Y axis) curve of the casing materials

## THE CORROSIVE MATERIAL PERFORMANCE MODEL

Due to the degree of corrosion, the mechanical properties of the inner and outer walls of the casing may differ. Samples from the inner, the outer, and the whole casing were taken. Then, tensile experiments were performed. The outer, whole, and inner stress–strain curves are described in turn in Fig. 10, and the morphology of the specimen after fracture is shown in Fig. 11.



Fig. 11. Fracture of the tensile test pieces

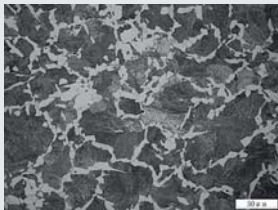
As shown in Fig. 11, the whole, the inner and outer layered tensile test pieces were observed. It can be found from the fracture that the fracture of the intermediate tensile test piece was flattened, while the tensile test pieces layered on the left and right of Fig. 11 were close to flush.

Metallographic inspection was carried out for inner side and outer side, and the results are shown in Tables 7 and 8.

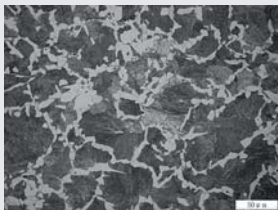
It was very difficult to sample the corroded test pieces, so the number of test pieces in this paper does not meet the standards of the tensile experiment, and the results can only be used as a reference for modeling. Although the inner wall was more corroded than the outer wall, there were many cases

where the outer wall was corroded more seriously than the inner wall or the two were almost the same. Therefore, the modeling calculations in this paper were based on sampling, but the method of establishing the model can be used in any case, that is, different corrosive material models can be used to reflect different corrosion characteristics.

Tab. 7. Casing inner side metallographic analysis

Metallographic microstructure	 <p>Pearlite + Reticular ferrite, Grain size 6</p>
-------------------------------	---

Tab. 8. Casing outer side metallographic analysis

Metallographic microstructure	 <p>Pearlite + Reticular ferrite, Grain size 5.5</p>
-------------------------------	---

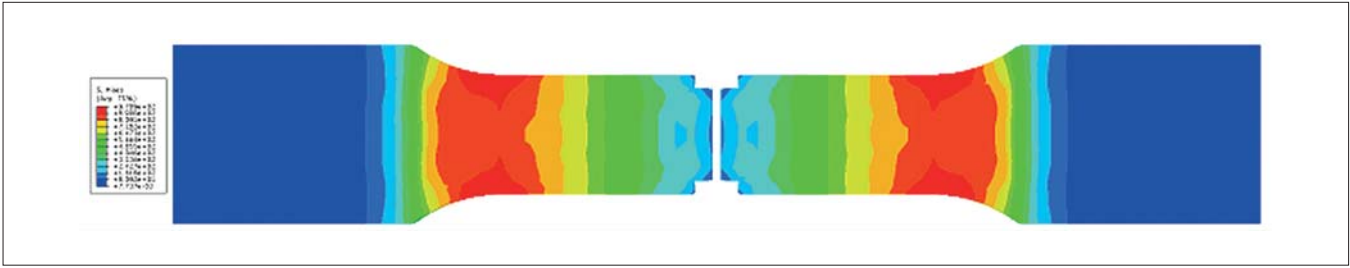


Fig. 12. Tensile experiment simulation

Tensile fractures were simulated using ABAQUS on the above three tensile test pieces prior to the modeling of the casing. In the model, the test piece was divided into two layers, one layer imparting material properties to the inner wall and the other layer imparting material properties to the outer wall [14, 15]. The parameters are shown in Fig. 12, and the results of the simulation are shown in Fig. 12.

The simulation results show that the stress at break of the test piece was between the tensile strength of the inner wall and the outer wall in the tensile experiment, which was close to the tensile strength of the material when the whole test piece was stretched. It can be seen that for the corrosive material model, the hierarchical setting method proposed in this paper was feasible. Taking the casing analyzed in this paper as an example, a model that gradually weakens the mechanical properties from the outside to the inside was established. The model establishment scheme is shown in Fig. 13.

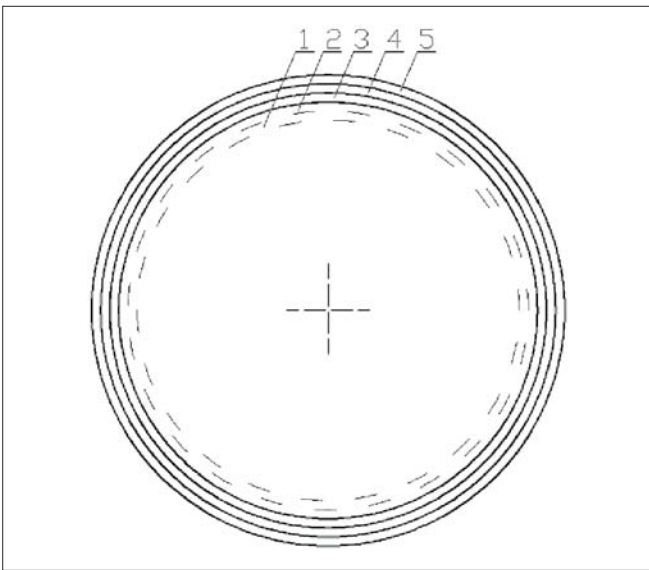


Fig. 13. Establishing scheme for linear weakening model of casing

In the model shown in Fig. 13, the first layer and the second layer indicated by broken lines were portions which have been etched; the third, fourth and fifth layers indicated by solid lines were etched casing. The general principle of material parameter setting is layer 3 < layer 4 < layer 5. The properties of the fourth layer are consistent with that of the second layer, and the properties of the fifth layer are consistent with that of the first layer. The inner wall was defined as the first layer, and its specific expression is:

$$A_{i+j} = \begin{cases} A_{i-j} & i \geq j \\ A_1 & i < j \end{cases} \quad (1)$$

where  $A$  is the material parameters,  $A_1$  is the first layer of the casing inner wall before corrosion,  $i$  is the first layer of the casing inner wall after corrosion, and  $j$  is the number of layers.

In Eq. (1), the following relationship needs to be satisfied

$$i \geq \frac{h}{\delta} \quad (2)$$

where  $h$  is the original wall thickness of the casing, and  $\delta$  is the maximum wall thickness of each layer.

The model in Fig. 17 was refined according to Eqs. (1) and (2). The tensile test piece model was divided into three layers by using the obtained experimental data. The calculation results are shown in Fig. 14.

It was found that the maximum stress was closer to the tensile strength of the tensile test piece than that of Fig. 14 when the test piece was broken, which further proves the validity of the corrosive material model proposed in this paper.

## CONCLUSION

In this paper, the casing of ocean oil and gas wells was taken as the object, the corrosive fluid in the complex environment of deep-sea drilling was proportioned, and the temperature

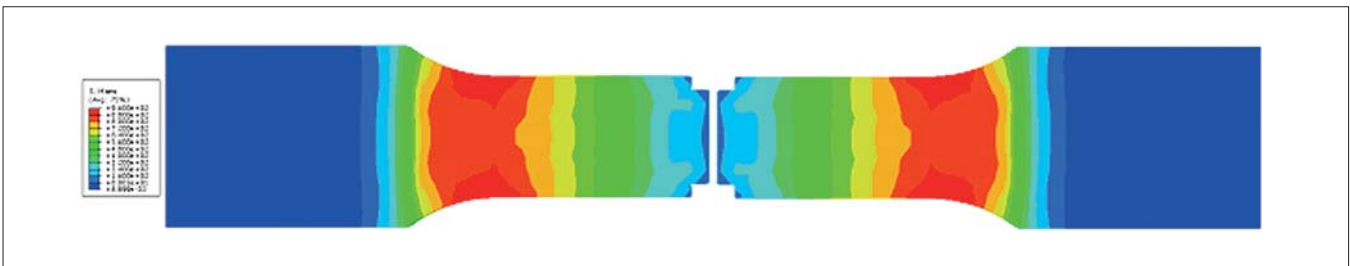


Fig. 14. Model verification

and pressure were set according to the deep-sea drilling environment. The corrosion experiment, tensile experiment and finite element analysis were carried out on P110 material, and the following conclusions were obtained:

- (1) When the weight loss rate of P110 material was less than 15% after corrosion, the equivalent yield strength and the equivalent tensile strength decrease with the increase of the weight loss rate. When the weight loss rate of P110 material was greater than 15%, the reduction rate of equivalent yield strength increases, while the reduction rate of equivalent tensile strength tends to be flat.
- (2) When the weight loss rate of P110 material was greater than 20%, the equivalent yield strength of the material was less than 758 MPa, which does not meet the requirements for the use of the P110 material.
- (3) Equations for the yield strength and tensile strength of the P110 material during corrosion are obtained.
- (4) A method of establishing a performance model of corrosive material was proposed. The performance model of P110 corrosive material was established according to this method.

#### ACKNOWLEDGMENTS

This work reported in this paper was supported by the Sichuan Science and Technology Program (2017TD0023); Project of Sichuan Provincial Department of Education, Robot and Intelligent Equipment Research and Innovation Team of Sichuan Universities (15TD0016).

#### REFERENCES

1. Zhao Y., Ding W., Zhang Z., Xu, Y. (2015): *Research on the tubing string integrity under complex well conditions and product development*. Baosteel Technology, 33(1), 66–71.
2. Shi, X., Chen P., Xu J., Jiang, Z., Nie, R., Qing, X., Zhao, D., Wang, D. (2006): *Analysis on residual strength of CO<sub>2</sub> tubercular corrosion for casings of oil/gas wells*. Natural Gas Industry, 26(2), 95–97.
3. Xu, Z., Yan, X., Yang, X. (2014): *Strength time varying analysis of casing with CO<sub>2</sub> corrosion defects*. Journal of Mechanical Engineering, 50(1), 169–177.
4. Zhu, X.-H., Gao, Y., Jia, Y.-J. (2012): *The parameter sensitivity analysis of buttress casing connecting thread under action of bending loading*. Engineering Mechanics, 29(10), 301–307.
5. Zhu, X.-H., Dong, L., Tong, H., Gao, Y., Pang, R. (2013): *Mechanical behaviors of short-round thread of the API casing under combined load of stretching and bending moment*. Acta Petrolei Sinica, 34(1), 157–163.
6. Zhu, X.-H., Zhang, Z., Chang, X, Li, L. (2015): *Three-dimensional mechanical behavior of worn casing connecting thread in complex structural well*. Acta Petrolei Sinica, 36(6), 748–753.
7. Wu, L., Chen, P., Zhu, X.-H., Zhang, W., Jia, Y., Li, J. (2012) *Contrast of fatigue failure cycles of drill string during gas drilling*. Petroleum Drilling Techniques, 40(1), 42–46.
8. Filippov, A., Mack, R., Cook, L., York, P., Ring, L., McCoy, T. (1999): *Expandable Tubular Solutions*. Society of Petroleum Engineers, SPE-56500-MS.
9. Chen, S.-J., An, Q., Zhang, Y., Gao, L.-X., Li, Q. (2010): *Loading analysis on the thread teeth in cylindrical pipe thread connection*. Journal of Pressure Vessel Technology, 132(3), 031202.
10. Chen S.-J., An, Q., Zhang, Y., Li, Q. (2011): *Research on the calculation method of tightening torque on P-110S threaded connections*. Journal of Pressure Vessel Technology, 133(5), 051207.
11. Cong, Y. (2015): *Finite element analysis of casing strength with crack defects*. Journal of Shengli College China University of Petroleum, 29(2), 25–27.
12. Li, Y., Deng, J., Wei, B., Tan, Q., Yan, W., Dong, G. (2012): *Research on the stress concentration effect of global corrosion cavity of casing inner wall*. China Petroleum Machinery, 40(9), 79–77.
13. Wang, C., Wang, S., Xu, S. (2017): *Effect of forming temperature on strength of monohole expandable tubular with thread connection*. Journal of Plasticity Engineering, 24(3), 50–56.
14. Wang, Y., Ai, Z., Shi, C., Ai, Y. (2017): *Study on contact between double metal composite and pipe power slip for offshore well*. Polish Maritime Research, 24, 66–73.
15. Zhu, X.-H., Wang, Y., Tong, H. (2013): *The parameter sensibility analysis for fishing box tap based on the overall process of elastoplasticity in oil and gas wells*. Mathematical and Computer Modelling, 58(7–8), 1540–1547.

## CONTACT WITH THE AUTHORS

**Yao Zilin**

*e-mail: 23578993@qq.com*

College of Chemistry and Chemical Engineering  
Southwest Petroleum University  
8 Xindu Avenue, Xindu District  
610000 Chengdu City, Sichuan Province  
**CHINA**

**Wang Yu**

*e-mail: xhwangyu@yeah.net*

Robotics Research Center  
School of Mechanical Engineering, Xihua University  
9999 Hongguang Avenue, Pidu District,  
611730 Chengdu City, Sichuan Province  
**CHINA**

**Yang Xuefeng**

*e-mail: 2781493209@qq.com*

Heavy oil development company  
of PetroChina Xinjiang Oilfield Company  
40 Xinyue Road, 834000 Kelamayi City  
Xinjiang Province  
**CHINA**

**Gao Anping**

*e-mail: 250815479@qq.com*

Wuxi China Resources Gas Co., Ltd,  
393 Jinshidong Road, 214000 Wuxi City  
Jiangsu Province  
**CHINA**

**Zhang Rong**

*e-mail: 253297549@qq.com*

Petroleum Engineering School  
Southwest Petroleum University  
8 Xindu Avenue, Xindu District  
610000 Chengdu City, Sichuan Province  
**CHINA**

**Jia Yanjie**

*e-mail: jiayj007@163.com*

Petrochina Southwest Pipeline Company  
6 Yingbin Road, 610000 Chengdu City  
Sichuan Province  
**CHINA**

# EVOLUTIONARY MULTI-OBJECTIVE WEATHER ROUTING OF SAILBOATS

Ewa Sobecka

Rafał Szłapczyński

Marcin Życzkowski

Gdańsk University of Technology, Poland

## ABSTRACT

*The paper presents a multi-objective method, which optimises the route of a sailboat. The presented method makes use of an evolutionary multi-objective (EMO) algorithm, which performs the optimisation according to three objective functions: total passage time, a sum of all course alterations made during the voyage and the average angle of heel. The last two of the objective functions reflect the navigator's and passenger's comfort, which may decrease with multiple turns or when experiencing an excessive heel angle for a long time. The optimisation process takes into account static bathymetry-related constraints as well as dynamic constraints related to the sailboat's safety in changing wind and wave conditions. The method makes use of all of the above and finally returns an approximated Pareto set containing non-dominated solutions to the optimisation problem. The developed method has been implemented as a simulation application. The paper includes selected simulation results followed by their discussion.*

**Keywords:** sailing vessels, weather routing, evolutionary multi-objective optimization, weather forecasts, navigation

## INTRODUCTION

Weather routing is planning a ship's route including weather conditions, which are essential to the navigability of the sailing vessel. Choosing the right route affects not only the travel time, but also its safety, as well as the comfort of passengers and crew. The weather's impact is particularly large in the case of sailboats. Adverse wind conditions may greatly increase the passage time. They may also result in excessive heel angles, thus causing major discomfort for people on board or even compromising the sailboat's safety. The paper addresses this problem by proposing a multi-objective sailboat weather routing optimisation method. The method applies an improved Strength Pareto Evolutionary Algorithm (SPEA 2) [1], which performs the optimisation according to three objective functions: total passage time, the sum of all course alterations made during the voyage and the average angle of heel. Instead of aggregating these objectives into one, the algorithm searches for a Pareto-optimal set containing

all non-dominated solutions. The number of non-dominated solutions may vary depending on the circumstances and in some cases it may be too large, making it hard for the navigator to choose one route to follow. Therefore a preference-based approach called r-dominance [2] is additionally applied here. The navigator can specify a reference solution as a point in the 3-dimensional objective space. The specified point represents desired or acceptable values of all objectives. Owing to this, the optimisation method is able to focus on solutions reflecting the navigator's preferences, which results in a shorter processing time, better approximation of the true Pareto set and a limited set of final solutions to choose from. The method has been implemented as a software tool. Following this, a series of computer simulations have been carried out. Their results confirm the method's effectiveness (given by the quality of the recommended routes) and efficiency (acceptable computational time for all scenarios). The rest of the paper is organised as follows. Section 2 presents current research in the field of weather routing and points out limitations of

the various approaches applied. Section 3 describes weather routing as an optimisation problem. Section 4 describes the proposed weather routing optimisation method, which solves this problem. Following this, Section 5 contains the results of the simulations carried out using the proposed method. Finally, the summary and conclusions are presented in Section 6.

## RELATED WORKS

Published works on weather routing of sailboats are relatively few; however, the discussed problem is closely related to weather routing of merchant ships, which has been widely researched. Nowadays, in maritime shipping, a travel plan is required by the International Convention for the Safety of Life at Sea (SOLAS) and requires planning of the route before starting a sea journey [3]. Route planning applies to all vessels, including sailing ones. Route planning depends on the user's requirements, including the need to perform the tasks and taking into account the restrictions arising from the existing conditions in the area of navigation. There are different approaches to developing route planning methods for vessels, and the methods that are being used can be divided into two groups: deterministic and non-deterministic. The first are methods that repeatedly return the same solution for the same input data. Updating the input data or changing the method itself can lead to returning a different solution. The second group are non-deterministic methods, which are usually applied in situations when deterministic solutions would be too time-consuming.

In deterministic methods we can distinguish isochron methods [4, 5], dynamic methods [6–9] as well as those rooted in a graph theory. The isochron method is based on the analysis of meteorological forecasts, and knowing the speed characteristics of the ship it is possible to manually determine the minimum time path. In dynamic methods, the next  $P_i$  position, with the  $S_i$  state, depends directly on the  $S_{i+1}$  state. As for graph-oriented methods, when all possible waypoints are defined and the possible flows between them are known, one can implement routing as determining the optimal path in the graph. Examples include methods using the modified Dijkstra algorithm [10–15] or the A\* algorithm [16, 17].

Non-deterministic methods may include genetic and evolutionary methods, methods based on distributed intelligence, and others. Both genetic and evolutionary methods [18–21] are based on the heuristic algorithm for finding solutions according to natural selection. As this group is based on distributed intelligence [22–24] their idea is derived from imitating the behaviour of living beings (e.g. ants, bees or wolves). Other examples of non-deterministic routing methods include rapid walking [25].

Routing methods differ greatly in their range of use and include transoceanic routing based on long-term weather forecasts as well as relatively short-distance planning, which may take into account local weather data [26, 27] downloaded on route by means of a wireless network [28]. The common

feature of most of the above methods is that they rely on single-objective optimisation. Exceptions are few and concern solely the routing of merchant vessels [22, 23, 29]. As for methods dedicated to sailboats, up till now they have applied multiple objectives by means of a single aggregated goal function [13, 14]. Such an approach is seriously limiting because it excludes many potential solutions, which cannot be obtained this way. The current paper aims to fill this gap by offering a truly multi-objective method of weather routing for sailboats.

## SAILBOAT WEATHER ROUTING AS A MULTI-OBJECTIVE OPTIMISATION PROBLEM

In the considered problem, a vector of three objective functions  $F(x)$  (1) is subject to optimisation. The vector consists of the total passage time,  $f_{time}$  (2), the sum of direction changes  $f_{chdir}$  (3) within a route and the weighted average of heel angles  $f_{heel}$  (4) computed over all route segments.

$$F(x) = [f_{time}, f_{chdir}, f_{heel}] \quad (1)$$

$$f_{time} = \sum_{i=1}^n \frac{s_i}{V_i} \rightarrow \min \quad (2)$$

$$f_{chdir} = \sum_{k=1}^{n-1} \Delta \alpha_{k,k+1} \rightarrow \min \quad (3)$$

$$f_{heel} = \frac{\sum_{i=1}^n \varphi_i \cdot t_i}{t} \rightarrow \min \quad (4)$$

where:

$s_i$  – distance covered by the sailboat on the  $i$ -th segment of a route,

$$s_i = \sqrt{(x_i - x_{i+1})^2 + (y_i - y_{i+1})^2}$$

$V_i$  – sailboat's speed on the  $i$ -th segment of a route (between points  $k$  and  $k+1$ )

$$V(P_k, P_{k+1}) = \gamma(\vec{w}_k, \alpha_{i,i+1}) = \gamma(w_k, \beta_{i,i+1})$$

where:

$\alpha_{i,i+1}$  – direction from point  $P_k$  to  $P_{k+1}$   
 $\beta_{i,i+1}$  – angle between the sailboat's course and true wind direction

$w_k$  – wind speed

$\gamma(w_k, \beta_{i,i+1})$  – sailboat's speed calculated on the basis of the polar diagram for a given wind speed  $w_k$  and direction  $\beta_{i,i+1}$

$\varphi_i$  – tilt on the  $i$ -th segment of a route [rhumb]

$t_i$  – time to complete the  $i$ -th segment of a route [h]

$t$  – time to cover the entire route,  $t = \sum_{i=1}^n t_i$  [h].

The control variables of each route are geographical coordinates of route waypoints – a sequence of latitude and longitude values.

The goal is to minimise simultaneously all three objective functions, while making sure that the solutions are acceptable in terms of meeting the constraints. The choice of objective functions is supposed to reflect the practical needs of various potential decision makers. As for the heel angle, it reflects both the passenger's safety and comfort, though other objectives are possible here, namely roll velocity or roll acceleration, as mentioned in [30]. In general, the three objective functions may be contradictory; for example, smooth routes usually take more time. Therefore in practice the result of the optimisation process is not one route but a set of Pareto-optimal routes, where each route within the set is defined by a sequence of waypoints – pairs of latitude and longitude geographical coordinates.

A solution is acceptable if the following constraints are met throughout the route:

- the ship's safety isobath is not violated,
- the heel angle does not exceed a maximum acceptable value (defined by the user),
- the wind's speed does not exceed a maximum acceptable value (defined by the user).

The optimisation problem given above can be approached in a number of ways, applying both deterministic and indeterministic methods mentioned in the section on related works. Deterministic approaches include the multi-objective Dijkstra algorithm, multi-objective dynamic programming and multi-objective linear convolution of the functional. Their huge advantage is that, given enough time, they always converge to the optimal solution set. However, considering the complexity of map-derived constraints, deterministic approaches are not always acceptable in terms of time-efficiency, as their computational time rises with the size of the map and number of waypoints, as observed in [31]. Therefore, an indeterministic approach has been chosen here, namely, one of evolutionary multi-objective optimisation algorithms (EMO). Details are provided in the following section.

## THE PROPOSED METHOD OF WEATHER ROUTING

In this section the proposed method is described in detail, covering the applied multi-objective evolutionary algorithm SPEA2 (The Applied Algorithm section),

### THE APPLIED ALGORITHM

The proposed method uses an evolutionary multi-objective (EMO) algorithm to solve the problem. EMO algorithms belong to multi-objective metaheuristics (MOMH), whose common feature is that they search for a Pareto-optimal set containing all non-dominated solutions to a problem. For minimisation of all objectives, a solution  $y$  is non-dominated if there is no other solution  $x$  in the set, for which the following dominance relation would hold true:

$\exists_i(f_i(x) < f_i(y))$  and  $\forall_i(f_i(x) \leq f_i(y))$ , where  $f_i(x), f_i(y)$  are the values of the  $i$ -th objective for solutions  $x$  and  $y$ .

It is worth mentioning that an acceptable solution (one that meets the constraints) always dominates an unacceptable one, even if the latter has better (here – lower) values of all objectives.

What distinguishes EMO algorithms from other MOMH approaches is that they implement mechanisms similar to those observed during evolution in nature. Randomly generated individuals are subject to mutation and crossbreeding processes, creating a new population of individuals in which units with a higher adaptation rate have greater chances of survival and extension, according to pre-set criteria. In general, the operation of each evolutionary algorithm is based on a loop, which is formed successively by reproduction, genetic operations, evaluation and succession. It is visualised in Fig. 1.

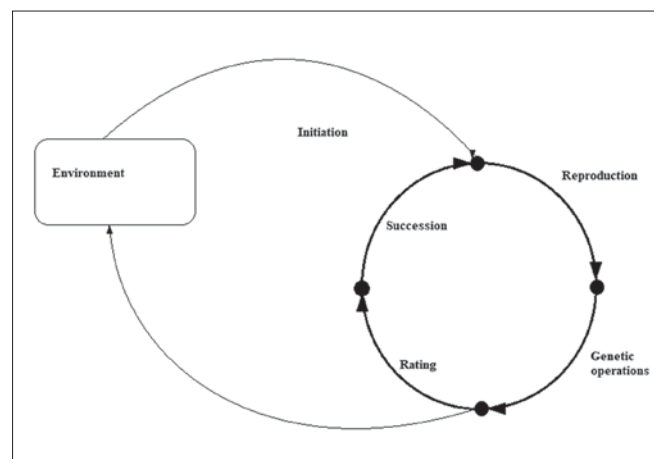


Fig. 1. The loop of operations in an evolutionary algorithm framework

From among many algorithms of evolutionary multi-objective optimisation, the improved Strength Pareto Evolutionary Algorithm (SPEA2) was selected to solve the problem specified in Section 3. SPEA2 extends the classic evolutionary approach from Fig. 1; here the main algorithm loop consists of the following elements:

- Initialisation – the initial base population and empty archive are generated at this stage.
- Fitness assignment – fitness values are calculated for all individuals.
- Environmental selection – all non-dominated individuals are copied to the next population.
- Termination – if any of the end conditions are met at this stage, the loop should be stopped.
- Mating selection – followed by a binary tournament selection of parents, who will reproduce.
- Variation – recombination and mutation takes place, a new generation follows, the future population becomes present, go to Fitness assignment.

As for initialisation, the base population includes: orthodrome and loxodrome routes (including their random variations) as well as purely random routes. There is no guarantee that any route from the initial population is acceptable; however, they are systematically improved by the process in the course of subsequent generations, which is given in Fig. 2.

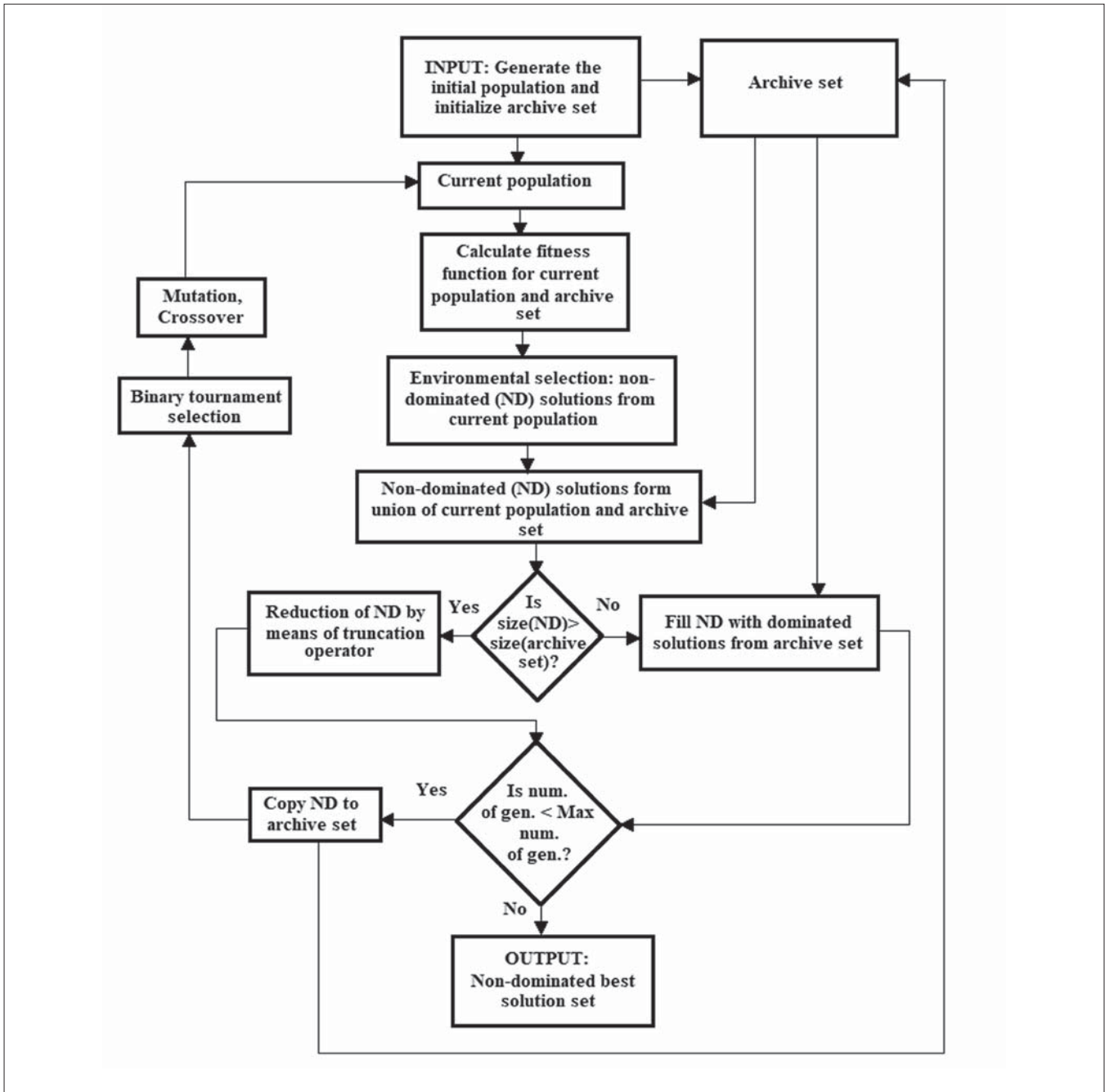


Fig. 2. SPEA2 algorithm framework

## SELECTED PREFERENCE-BASED APPROACH

A popular approach in Multi-Objective Meta-Heuristics (MOMH) is to take into account user preferences, whereby the algorithm may focus on the part of the objective space that is most interesting to the user. Among others, limiting the objective space results in reduction of the Pareto front and thus in a faster convergence of the algorithm. Making use of the preferences can be done in a number of ways [32]. A common one is that of a reference point (RP) – a point in the objective space, which represents a solution that is desired and seems possible to reach by the method [33–35]. An RP may be directly used for dominance relation [2, 36], thus extending

strict Pareto dominance. Of various RP-based methods, r-dominance [2] is particularly successful and flexible and has therefore been chosen to be applied here.

The r-dominance mechanism works as follows. First a user specifies a reference point (RP) – the desired values of all objective functions. The task of the algorithm is then to strive to reach final values as close to the set values as possible while maintaining dominance in the Pareto sense.

This means that non-dominated solutions that have a smaller distance from the RP in the space of optimal solutions will be rated better than non-dominated solutions at a larger distance from the RP. This distance is expressed by the following formula (5):

$$Dist(x, g) = \sqrt{\sum_{i=1}^M w_i \left( \frac{f_i(x) - f_i(g)}{f_i^{max} - f_i^{min}} \right)^2}$$

$$w_i \in ] 0,1 [ \quad [\sum_{i=1}^M w_i = 1 \quad (5)$$

where:

$Dist(x, g)$  – weighted Euclidean distance between point  $x$  and  $g$ ,

$x$  – a solution that is considered,

$g$  – reference point with  $i$  coordinates,

$f_i^{max}$  – upper limit of the value of the  $i$ -th goal function,

$f_i^{min}$  – lower limit of the value of the  $i$ -th goal function,

$w_i$  – weight assigned to the  $i$ -th goal function.

### APPLYING THE ALGORITHM TO SOLVE THE OPTIMISATION PROBLEM

In order to apply the algorithms, apart from algorithm implementation, two kinds of mechanisms have to be prepared first:

- checking if all constraints are met (including safe distance from landmasses, acceptable heel angle and acceptable wind speed),
- determining objective functions values.

Of all the constraints, checking the geographical ones is most time-consuming. First, an electronic navigational chart has been converted to a bitmap to make use of the bathymetric data [37]. Following this, information on whether a map cell is passable or not can be read directly from a bitmap. Consequently, it is possible to check if a route segment does not cross any landmass or safety isobaths. It is assumed that the route must be at least one bitmap cell away from the safety isobath. As for the other constraints, wind speed is read directly from a saved weather forecast file, while the heel angle is read from the sailboat's polar diagram provided for a particular

combination of wind speed and relative angle between the sailboat's course and the true wind direction.

The detailed values of constraint thresholds assumed for simulations are as follows:

- maximal acceptable angle of heel – 30 degrees,
- minimal acceptable distance from safety isobath – the size of a bitmap cell: 0.17 NM (315 m).

The sailboat's speed can be read directly from the provided diagram of velocity polar prediction (VPP) [14]. Knowing the sailboat's speed and heel angle for all the sampled combinations of wind conditions and sailboat courses, all the objective function values can be computed for each segment of the route. Having done this, each objective value is aggregated over all route segments and the final objective values are obtained.

### SIMULATION RESULTS

In this section examples of simulation results are provided and discussed. Brief descriptions of all scenarios, followed by their detailed results, are given in the next four subsections. This is followed by a discussion of the results.

Throughout all the scenarios the same sailboat was used, whose parameters are presented in Table 1, with the polar diagram given in Fig. 3.

Tab. 1. CONRAD 1200 RT – sailing vessel details

Parameter	Value	[]
Volume (displaced)	8.450	m <sup>3</sup>
Draft amidships	2.0	m
WL length	12.00	m
Beam max extents on WL	3.1	m
Sail area	80	m <sup>2</sup>

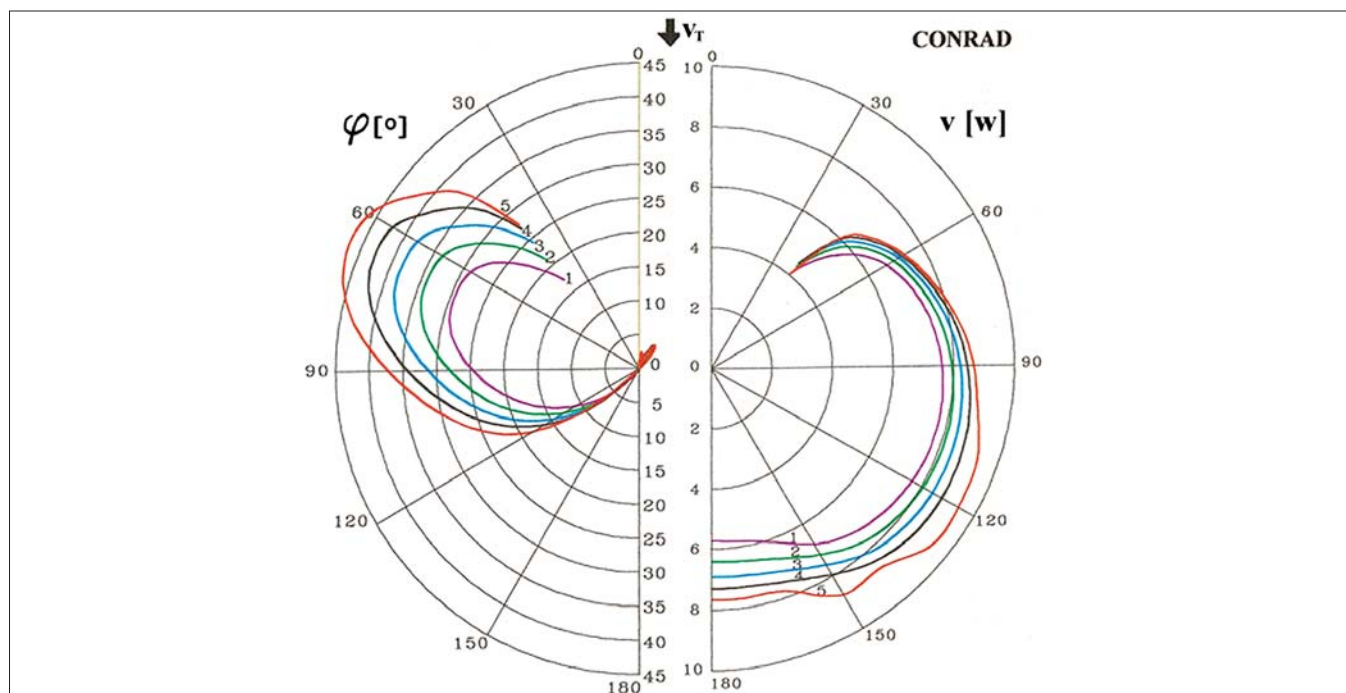


Fig. 3. A polar diagram of VPP and angle of heel, source [34]. True wind speed: 1 – 12 kt, 2 – 14 kt, 3 – 16 kt, 4 – 18 kt, 5 – 20 kt

Tab. 2. Input data for all four scenarios

Scenario	From	To	Number of objectives	Wind directions and speeds for subsequent periods of travel [m/s] / [kt]		
				1	3	3
1	Gulf of Gdańsk	Świnoujście	2	5.12 / 10 NE	6.6 / 12.8 NE	5.9 / 11.5 NE
2	Gulf of Gdańsk	Świnoujście	3	5.12 / 10 NE	6.6 / 12.8 NE	5.9 / 11.5 NE
3	Świnoujście	Gulf of Gdańsk	3	5.12 / 10 NE	6.6 / 12.8 NE	5.9 / 11.5 NE
4	Świnoujście	Gulf of Gdańsk	3	13 / 25.3 NE	13.78 / 26.8 NE	13.4 / 26 NE

The following parameter values are used there: true wind speed  $V_r$ : 1 – 12 knots, 2 –

14 knots, 3 – 16 knots, 4 – 18 knots, 5 – 20 knots.  $\rightarrow$  – true wind direction with velocity  $v_r$  [w],  $\gamma$  – heading angle of vessel [°],  $v$  – speed forecast of vessel:  $v = v(v_r, \gamma)$ .

Additional data for all four scenarios is presented in Table 2, where the travel direction, wind conditions (direction and speed) and applied objective functions are given. Finally, the SPEA2 and r-dominance settings are given in Table 3.

Tab. 3. SPEA2 and r-dominance settings

Parameter	Time [hours]	Total direction changes	Angle of heel [degrees]
Reference point coordinates	30	20	15
Weights for 2- objective case (Scenario 1)	0,7	–	0,3
Weights for 3- objective cases (Scenarios 2, 3 and 4)	0,6	0,2	0,2

### SCENARIO 1

Scenario 1 involves finding a route from the Gulf of Gdańsk to Świnoujście in mild weather conditions for two optimisation objectives: total passage time and average angle of heel. The resulting set of solutions approximating true Pareto-optimal routes is shown in Fig. 4. Objective values of all selected routes are visualised in the 2-dimensional objective space in Fig. 5.

### SCENARIO 2

Scenario 2 involves finding a route from the Gulf of Gdańsk to Świnoujście in the same weather conditions as scenario 1, but this time for three optimisation objectives: total passage time, average angle of heel and the sum of all direction changes. The resulting set of solutions approximating true Pareto-optimal routes is shown in Fig. 6. Objective values of all selected routes are visualised in a 3-dimensional objective space in Fig. 7.

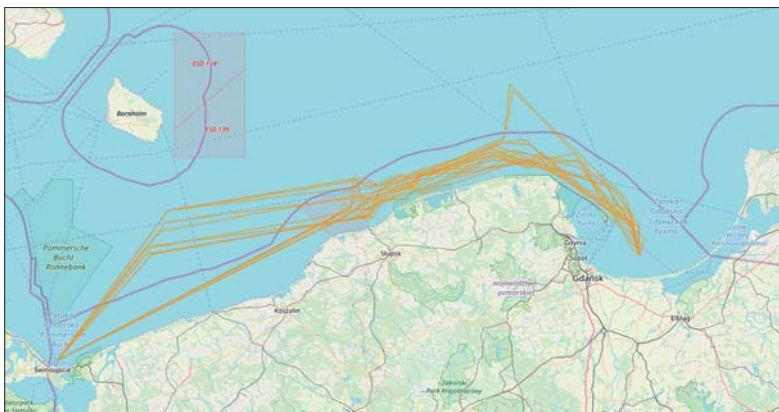


Fig. 4. Routes found in Scenario 1

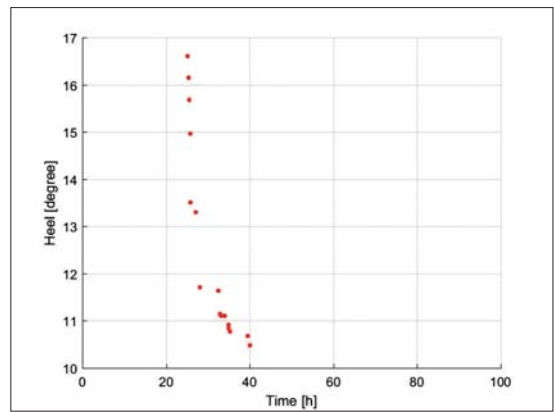


Fig. 5. Objective values of routes found in Scenario 1

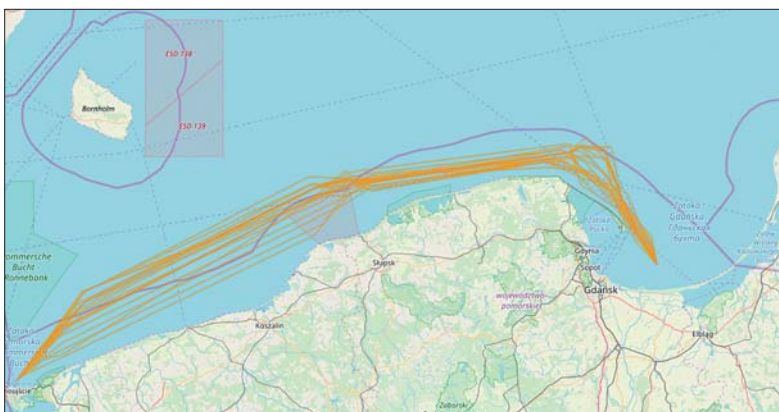


Fig. 6. Routes found in Scenario 2.

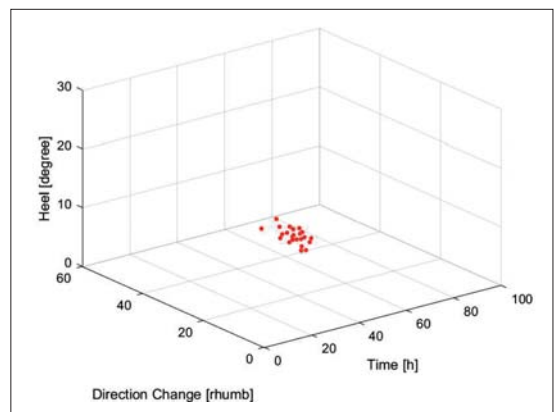


Fig. 7. Objective values of routes found in Scenario 2

As can be seen, the addition of a third goal function, the one minimising the sum of course changes, has smoothed the route shape. Previously, when only voyage times and average angle of heel were minimised, frequent multiple turns were visible (Fig. 4). Their purpose was to increase the sailboat's speed on a given segment of a route by making the best use of the wind. Such policy made the total time shorter but the routes would be harder to follow, especially for a less experienced sailor. Now, after incorporating the third objective, the routes are now less diverse, much closer to each other and easier to follow, as they do not include so many turns. However, the smoothness of the routes is obtained at the cost of a much longer voyage time – it grows from 30-40 hours (Scenario 1) to over 60 (Scenario 2). Smoother routes also result in a much smaller average angle of heel. The latter can be attributed to very sharp heel angle curves in the left part of Fig. 3. Namely, a small change in the relative angle to the wind may cause a significant difference in the heel angle.

### SCENARIO 3

Scenario 3 involves finding a route back from Świnoujście to the Gulf of Gdańsk for all three optimisation objectives. The resulting set of solutions approximating true Pareto-optimal routes is shown in Fig. 8. Objective values of all selected routes are visualised in a 3-dimensional objective space in Fig. 9. As can be seen, the routes have different shapes from those in Scenario 2. Because of sailing in the opposite direction,

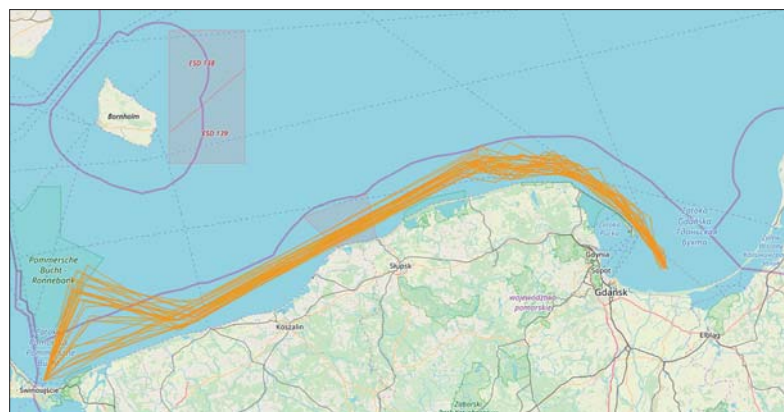


Fig. 8. Routes found in Scenario 3.

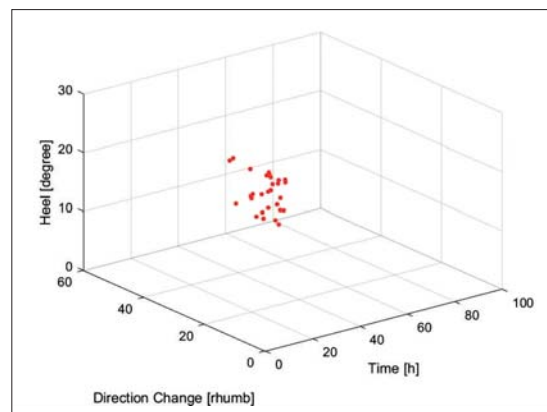


Fig. 9. Objective values of routes found in Scenario 3



Fig. 10. Routes found in Scenario 4

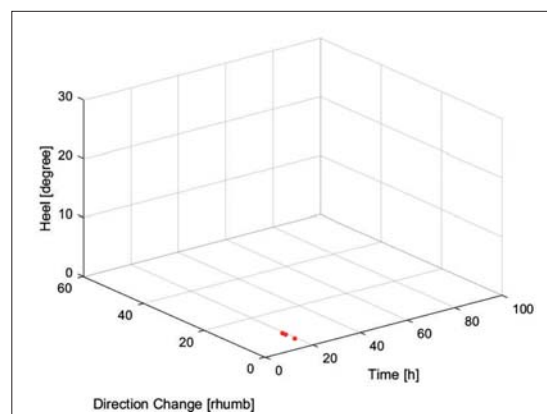


Fig. 11. Objective values of routes found in Scenario 4

the sailboat faces different wind conditions, which results in different turns made to minimise the objective values.

### SCENARIO 4

Scenario 4 again involves finding a route from Świnoujście to the Gulf of Gdańsk for all three optimisation objectives. This time, however, the sailing conditions are much harder due to a very strong wind. The resulting set of solutions approximating true Pareto-optimal routes is shown in Fig. 10. Objective values of all selected routes are visualised in a 3-dimensional objective space in Fig. 11. The strong wind seriously limits the manoeuvring possibilities of the sailboat – not all courses are taken into account, as some of them would result in excessive heel angles (larger than the assumed limit of 30 degrees). This limitation translates to a much smaller choice of acceptable solutions, which in turn limits the final set of Pareto-optimal routes, with fewer optimal routes. However, all of the returned Pareto-optimal routes are very good in terms of objective values. Strong wind makes it possible to achieve a greater speed and thus reduces the travel time. The shapes of the routes are smoother, with a smaller number of turns. Multiple turns are avoided because they could lead to a much larger sum of direction changes, lower average speed and larger angle of heel for some of the route segments. In contrast, smooth routes make it possible to avoid the latter, thus achieving a successful minimisation of all objectives simultaneously.

## SUMMARY AND CONCLUSIONS

The article presents the multi-objective evolutionary method, which searches for the optimal routes of a sailboat navigating in changing wind conditions. The method uses an improved Strength Pareto Evolutionary Algorithm (SPEA 2), additionally enhanced by a preference-based r-dominance method, which is applied to improve the algorithm's performance and to focus on solutions which are compliant with the navigator's preferences. For this reason, the method is able to return the routes faster while making sure they are customised for a particular user. The routes obtained bypass obstacles in the form of land and choose the course with the most favourable position to the wind. The aim is to complete the route as quickly as possible while maintaining reasonable safety and comfort throughout the voyage. The method was tested in a series of computer simulations, whose examples are provided in the text. The simulation results vary, depending on the chosen scenario. First, the results differ for two and three optimisation objectives. By adding the third objective, namely, a sum of course changes, one can limit the number and size of turns, thus simplifying the task of following a route. The influence of weather conditions on the shape of the route is also visible. When encountering strong wind, the method returns a reduced set of solutions, because there are fewer acceptable ones to choose from. The resulting routes are then smoother because such shape translates to greater safety, comfort and efficiency of travel, and the smallest possible inclination. In general, the experiments confirmed that the chosen method can be an interesting alternative to the already existing ones and that the multi-objective approach can offer flexibility of the navigator's modelling within an acceptable computational time.

For now, the presented method suffers from some simplifications in the modelled environment. Among others, passenger comfort is modelled by the average angle of heel, whereas roll velocity and acceleration are often more uncomfortable in practice. Also, the method does not take into account such factors as the influence of waves or sea currents on the sailboat's speed. It is planned, however, to include these elements in upcoming research that will focus on utilising more advanced modelling to bring the method closer to marine reality. Once this is done, experiments with a real sailboat are envisaged. Other plans include handling the uncertainty of weather predictions by means of ensemble forecasts and refining the optimisation algorithm.

## REFERENCES

1. Zitzler E, Laumanns M, Thiele L. *SPEA2: Improving the Strength Pareto Evolutionary Algorithm*. *Evol Methods Des Optim Control with Appl to Ind Probl* 2001;95–100. <https://doi.org/10.1.1.28.7571>.
2. Ben Said L, Bechikh S, Ghedira K. *The r-Dominance: A new dominance relation for interactive evolutionary multicriteria decision making*. *IEEE Trans Evol Comput* 2010;14:801–18. <https://doi.org/10.1109/TEVC.2010.2041060>.
3. Jurdziński M. *Podstawy Nawigacji Morskiej*. Wydawnictwo Akademii Morskiej w Gdyni; 2003.
4. Brooks RL, Jasper NH, James RW. *Statistics on wave heights and periods for the North Atlantic Ocean*. *Trans Am Geophys Union* 1958;39:1064. <https://doi.org/10.1029/TR039i006p01064>.
5. Wiśniewski B, Medyna P. *Prognozowany zasięg pola sztormowego cyklonu tropikalnego jako domena rozmyta cyklonu*. *Zesz Nauk Akad Morskiej w Szczecinie* 2004;nr 2:419–30.
6. Lisowski J. *The Sensitivity of State Differential Game Vessel Traffic Model*. *Polish Marit Res* 2016;23:14–8. <https://doi.org/10.1515/pomr-2016-0015>.
7. Spaans J. *Windship Technology: Proceedings of the International Symposium on Windship Technology*, Southampton, U.K., April 24-25, 1985., Elsevier Science; 1985, p. 385.
8. Motte R. *On The Selection of Discrete Grid Systems for On-Board Microbased Weather Routeing*. *J Navig* 1990;43:104–17.
9. Wiśniewski B. *Programowanie tras statków na oceanach*. *Zesz Nauk / Akad Morska w Szczecinie* 2012;29:164–73.
10. Singh Y, Sharma S, Sutton R, Hatton D. *Optimal Path Planning of an Unmanned Surface Vehicle in a Real-Time Marine Environment using a Dijkstra Algorithm*. *Proc. 12th Int. Conf. Mar. Navig. Saf. Sea Transp.*, Gdynia: 2017, p. 399–402.
11. Neumann T. *Method of Path Selection in the Graph – Case Study*. *TransNav, Int J Mar Navig Saf Sea Transp* 2014;8:557–62. <https://doi.org/10.12716/1001.08.04.10>.
12. Mannarini G, Coppini G, Oddo P, Pinardi N. *A Prototype of Ship Routing Decision Support System for an Operational Oceanographic Service*. *TransNav, Int J Mar Navig Saf Sea Transp* 2013;7:53–9. <https://doi.org/10.12716/1001.07.01.06>.
13. Zyczkowski M, Krata P, Szłapczyński R. *Multi-objective weather routing of sailboats considering wave resistance*. *Polish Marit Res* 2018;25. <https://doi.org/10.2478/pomr-2018-0001>.
14. Zyczkowski M, Szłapczyński R. *Multi-Objective Weather Routing of Sailing Vessels*. *Polish Marit Res* 2017;24. <https://doi.org/10.1515/pomr-2017-0130>.
15. Życzkowski M. *Sailing Vessel Routing Considering Safety Zone and Penalty Time for Altering Course*. *TransNav, Int J Mar Navig Saf Sea Transp* 2017;11:49–54. <https://doi.org/10.12716/1001.11.02.04>.

16. Naus K, Wąż M. *The idea of using the A\* algorithm for route planning an unmanned vehicle "Edredon."* Zesz Nauk / Akad Morska w Szczecinie 2013;143--147.
17. Goldberg A V. *Point-to-Point Shortest Path Algorithms with Preprocessing.* LNCS 4362 - SOFSEM 2007 Theory Pract. Comput. Sci., 2007.
18. Mostefa M-S. *ScienceDirect The branch-and-bound method, genetic algorithm, and dynamic programming to determine a safe ship trajectory in fuzzy environment.* Procedia Comput Sci 2014;35:348–57. <https://doi.org/10.1016/j.procs.2014.08.115>.
19. Walther L, Shetty S, Rizvanolli A, Jahn C. *Comparing Two Optimization Approaches for Ship Weather Routing, Springer, Cham; 2018, p. 337–42.* [https://doi.org/10.1007/978-3-319-55702-1\\_45](https://doi.org/10.1007/978-3-319-55702-1_45).
20. Vettor R, Szlapczynska J, Szlapczynski R, Tycholiz W, Soares CG. *Towards improving optimised ship weather routing.* Polish Marit Res 2020;27:60–9. <https://doi.org/10.2478/pomr-2020-0007>.
21. Ni S, Liu Z, Cai Y, Wang X. *Modelling of Ship's Trajectory Planning in Collision Situations by Hybrid Genetic Algorithm.* Polish Marit Res 2018;25:14–25. <https://doi.org/https://doi.org/10.2478/pomr-2018-0092>.
22. Lazarowska A. *Multi-criteria ACO-based Algorithm for Ship's Trajectory Planning.* TransNav, Int J Mar Navig Saf Sea Transp 2017;11:31–6. <https://doi.org/10.12716/1001.11.01.02>.
23. Lisowski J. *Optimization Methods in Maritime Transport and Logistics.* Polish Marit Res 2018;25:30–8. <https://doi.org/10.2478/pomr-2018-0129>.
24. Tsou M-C, Cheng H-C. *An Ant Colony Algorithm for efficient ship routing.* Polish Marit Res 2013;20:28–38. <https://doi.org/10.2478/pomr-2013-0032>.
25. Liu Y, Bucknall R. *Path planning algorithm for unmanned surface vehicle formations in a practical maritime environment.* Ocean Eng 2015;97:126–44. <https://doi.org/10.1016/j.oceaneng.2015.01.008>.
26. Szlapczynski R, Krata P. *Determining and visualizing safe motion parameters of a ship navigating in severe weather conditions.* Ocean Eng 2018;158. <https://doi.org/10.1016/j.oceaneng.2018.03.092>.
27. Życzkowski M, Szlapczyńska J, Szlapczyński R. *Review of Weather Forecast Services for Ship Routing Purposes.* Polish Marit Res 2019;26:80–9. <https://doi.org/https://doi.org/10.2478/pomr-2019-0069>.
28. Zhao J, Fan J. *A Ship Network Dynamic Routing Algorithm Based on Vector Network.* Polish Marit Res 2018;25:62–8. <https://doi.org/https://doi.org/10.2478/pomr-2018-0075>.
29. Krata P, Szlapczynska J. *Ship weather routing optimization with dynamic constraints based on reliable synchronous roll prediction.* Ocean Eng 2018;150:124–37. <https://doi.org/10.1016/j.oceaneng.2017.12.049>.
30. Pérez Arribas FL, López Piñeiro A. *Seasickness prediction in passenger ships at the design stage.* Ocean Eng 2007;34:2086–92. <https://doi.org/10.1016/j.oceaneng.2007.02.009>.
31. Wang HB, Li XG, Li PF, Veremey EI, Sotnikova M V. *Application of Real-Coded Genetic Algorithm in Ship Weather Routing.* J Navig 2018;71:989–1010. <https://doi.org/10.1017/S0373463318000048>.
32. Bechikh S, Kessentini M, Said L Ben, Ghédira K. *Preference Incorporation in Evolutionary Multiobjective Optimization: A Survey of the State-of-the-Art.* Adv Comput 2015;98:141–207. <https://doi.org/10.1016/bs.adcom.2015.03.001>.
33. Sindhya K, Miettinen K, Deb K. *A hybrid framework for evolutionary multi-objective optimization.* IEEE Trans Evol Comput 2013;17:495–511. <https://doi.org/10.1109/TEVC.2012.2204403>.
34. Deb K, Jain H. *An evolutionary many-objective optimization algorithm using reference-point-based nondominated sorting approach, Part I: Solving problems with box constraints.* IEEE Trans Evol Comput 2014;18:577–601. <https://doi.org/10.1109/TEVC.2013.2281535>.
35. Ishibuchi H, Imada R, Setoguchi Y, Nojima Y. *Reference Point Specification in Inverted Generational Distance for Triangular Linear Pareto Front.* IEEE Trans Evol Comput 2018;22:961–75. <https://doi.org/10.1109/TEVC.2017.2776226>.
36. Jaimes AL, Montaña AA, Coello CAC. *Preference incorporation to solve many-objective airfoil design problems.* 2011 IEEE Congr Evol Comput CEC 2011 2011:1605–12. <https://doi.org/10.1109/CEC.2011.5949807>.
37. Sielicka MW, Stateczny A. *Clustering Bathymetric Data for Electronic Navigational Charts.* J Navig 2016;69:1143–53. <https://doi.org/10.1017/S0373463316000035>.

## CONTACT WITH THE AUTHORS

**Ewa Sobecka**

*e-mail: ewa.warsinska@pg.edu.pl*

**Rafał Szłapczyński**

*e-mail: rafal.szlapczynski@pg.edu.pl*

**Marcin Życzkowski**

*e-mail: marzyczk@pg.edu.pl*

Gdańsk University of Technology

11/12 Gabriela Narutowicza Street

80-233 Gdańsk

**POLAND**

# DETERMINING THE BEST POSSIBLE SPEED OF THE SHIP IN SHALLOW WATERS ESTIMATED BASED ON THE ADOPTED MODEL FOR CALCULATION OF THE SHIP'S DOMAIN DEPTH

Grzegorz Rutkowski

Gdynia Maritime University, Poland

Master Mariners Association, Poland

## ABSTRACT

*The purpose and scope of this article is to present the best marine practices used to determine the ship's domain depth (compared to the safety depth parameter in ECDIS) and the safest and best possible speed (also known as optimal speed) of the ship in restricted sea areas limited by the depth of navigation waters. The author also presents a method that can be used to estimate the safe speed of a ship in shallow waters and the so-called navigational risk factor (specified in the range from 0 to 1), using the safety depth parameter specified in ECDIS based on the analysis of a three-dimensional model of the ship's domain. The essence of the method proposed in this paper is a systematic approach to the operation of a seagoing ship in the aspect of assessing its navigation safety (navigational risk factor) when manoeuvring in restricted sea areas, in particular in shallow waters including navigable canals and fairways.*

**Keywords:** safe speed, best possible speed, optimal speed, ship's domain, safety depth, under keel clearance (UKC), navigational risk factor, ship squat

## INTRODUCTION

Among the most important problems arising when studying the literature on the selection of the ship's speed in restricted sea areas limited by the depth of navigation waters [1, 3, 5, 8, 9, 10, 11, 15, 16, 18, 20, 21, 25], the following conclusions can be drawn:

Specific values of the speed at which the ship should operate in restricted waters and in particular in shallow waters are not provided. When defining the ship's speed in restricted sea areas (confined waters), verbal (descriptive) speed indicators (e.g. critical, boundary, achievable, recommended, optimal, best possible etc.) are used that are not always correct and clearly defined.

According to voyage instructions and charter party requirements, every vessel shall undertake her passage at

sea at the 'best possible speed', weather and safe navigation permitting, unless otherwise required.

According to the COLREG (*International Rules and Regulations for Prevention of Collisions at Sea*) guidelines of the Land Control Services and Movement Organizations (including pilot services and vessel traffic systems VTS), the recommendations of local maritime administrations, ship owners' guidelines and the rules of so-called good sea practice, the ship should always move at a 'safe speed'.

However, a safe speed understood according to the provisions of COLREG is not the same as the safe speed set according to the rules of so-called good maritime practice [11, 18, 19].

In fact, safe speed in the understanding of COLREG applies only to the speed that allows collision-free operation of the ship with respect to objects located on the water surface, and

not objects located under water. In addition, these regulations do not specify what should be understood by the term 'safe speed', and what should be considered as the value of that safe speed and what is a dangerous speed.

The selection of the appropriate value of the ship's speed and the trajectory of the ship's movement in restricted sea areas, and especially in shallow waters, navigational channels or sharp bends of the fairway, is left in the hands of the person conning the ship (usually the captain) and the rules of so-called 'good seamanship' or 'maritime practice', while the very concept of 'good seamanship', although it is widely used and used in the provisions of the COLREG regulation, is still not clearly defined.

Another point is term 'ship's domain'. The ship's domain in maritime terminology [4, 6, 7, 12, 13, 14, 22, 23, 24] is defined as the area around a vessel which is indispensable for maintaining the safety of navigation. According to the definition of the ship's domain, every ship will be safe (in the navigational sense) as long as she is the exclusive object that can generate danger within her domain [18, 19]. This means that the appearance of any navigational obstacle (intruder) within the ship's domain (its 'exclusivity' area) will dramatically increase the navigational risk and may result in an inevitable collision. The ship's domain will therefore determine a certain area (two-dimensional domain) or some part of space (three-dimensional domain) around the ship, in which to graphically assess the navigational safety of the ship and determine its navigational risk.

The ship's domain as a measurement of a ship's safety has been well studied since it was proposed. Although there are many ship's domains with different shapes [4, 6, 12, 19, 24] and sizes obtained by the method of statistical analysis [4, 6, 7] and artificial intelligence [13, 22, 23, 24], most of these are not objective domains that can ensure the ship's safety by avoiding collisions because most of the models take into account the navigator's subjective psychological factors.

Domains are mainly specific to open [6, 14] or restricted waters [12, 22, 23] and cannot be used for ships in different waters. Domains for restricted sea areas used in open waters are too conservative, while the domains for open waters applied to restricted waters will also not be suitable for the conditions of restricted waters. Meanwhile, the ship's domain even in the same kind of water can differ with differences in the water environment, and an individual ship's domain on a certain kind of water cannot represent the ship's domain for this entire class of ship.

As a result of these analyses, the author suggests the use of a simplified three-dimensional model of the ship's domain [18, 19], in which the selection of the optimal speed of the ship should be considered depending on the potential threats detected in relation to its three axes of shading (X, Y, Z), where:

$V_x=$  is the safe speed due to the braking distance (stopping the ship at the appropriate time) to avoid collision, taking into account the need to retain the manoeuvrability of the ship, and in particular its turning ability.  $V_x$  depends on the length of the vessel's domain  $SD_L$ ,

$V_y=$  is the safe speed due to external disturbances and restrictions on the water lane (fairway), taking into account the need to maintain the manoeuvrability of the ship and in particular its course stability.  $V_y$  depends on the width of the vessel's domain  $SD_w$ ,

$V_z=$  is the safe speed due to the limited value of the under-keel clearance (UKC) and/or over-head clearance (OHC), considering the maximum value of the ship's squat effect, the ship's draft and air draft, UKC and OHC.  $V_z$  depends on the depth  $SD_D$  and height  $SD_H$  of the ship's domain.

From a practical point of view, determining the optimal speed of the ship is required in particular due to the settlement of the ship (ship's squat) when manoeuvring on shallow water ( $V_z$ ) and in addition also when manoeuvring on restricted waters where navigational obstacles are arranged in the directions ahead of the ship's bow ( $V_{XF}$ ) on the ship's port ( $V_{Yp}$ ) and starboard side ( $V_{Ys}$ ).

In this paper, the study will focus on determining the ship's optimal safe speed  $V_{ZD}$  in shallow waters based on the analysis of a 3-D model of the ship's domain parameters in the OZ plane, and in particular the ship's domain depth parameter  $SD_D$ .

## METHODOLOGY FOR DETERMINING SHIP'S OPTIMAL SAFE SPEED $V_{ZD}$ BY MEANS OF SHIP'S DOMAIN DEPTH $SD_D$

For selection of the ship's domain depth  $SD_D$  we will use the author's simplified 3-D model of the ship's domain presented in his monograph [19].

Determining the ship's domain depth ( $SD_D$ ) in practice amounts to determining the safety depth (SD) parameter required in ECDIS for the ship's safe passage through shallow waters [17].

The safety depth (SD) is a value that serves to detect the depths that are a danger to navigation. A depth equal to or less than the safety depth is highlighted on the ENC chart in bold type when the display of the spot sounding is turned on. This alerts the user to know the depths that are insufficient for the vessel to safely pass over. Additionally, if any extra allowance of depth is required due to the local port or berth requirements, the same should be included in the calculation of the safety depth (SD), ship's domain depth ( $SD_D$ ), safety contour (SC) and under-keel clearance (UKC).

The safety contour (SC) value is calculated considering the safety depth and allowing for the category zone of confidence (CATZOC) displayed on an electronic navigational chart (ENC); (safety contour = safety depth + CATZOC). ECDIS selects and highlights the default safety contour, which is equal to or deeper than the safety contour value selected by the user [17, 19]. The safety contour on the ENC display will default to the next deeper contour if the depth contour of the set value is not available in the displayed ENC source data. The safety contour marks the division between navigable (safe) and non-navigable (unsafe) water. During route planning, an

indication will be made if the route is planned to cross the ship's safety contour. At the time of route monitoring, ECDIS should give an alarm if, within a specified time set by the navigator, the ship is likely to cross the safety contour [17].

One of the main factors needed to estimate the ship's domain depth ( $SD_D$ ) equated to the safety depth ( $SC$ ) is the ship's vertical reserve for squat ( $R_{squat}$ ). The ship's squat is an increase of body sinkage and a change of trim due to the ship's movement through water [1, 2, 3, 5, 11, 25]. Squat depends mainly on the water speed on the side and under the keel clearance (UKC).

The under-keel clearance (UKC) means the minimum clearance available between the deepest point on the vessel and the bottom in still water.

$$UKC = (h_{CD} + Tide) - T_{max} \quad [m] \quad (1)$$

where:

$UKC$  = Under-keel clearance [m],

$h_{CD}$  = Charted water depth [m],

$Tide$  = Height of tide [m],

$T_{max}$  = Static deep ship's draft.

For squat and UKC calculation, the user should always use the form designated for his vessel and accepted by the company [19], otherwise the estimated risk indicator ( $R_{ND}$ ) may not be adequate for the ship.

In US waters, we should also be guided by US Coast Guard Publication 33 CFR 157.455. When calculating the dynamic UKC, one must use the latest depth information from the port agent. It is vital to remember that at many dry-bulk cargo berths, due to the falling ore or coal, the depth along the dock wall may be considerably smaller than the one denoted on the official charts. In addition, one must also comply with the local UKC requirements or more stringent charterers' instructions. Generally, as a rule of thumb and good seamanship [11, 19], one must ensure that the following UKC requirements are fulfilled:

In port, a UKC not less than 0.60 m is required. This rule applies when navigating within a port (including the fairways, channels, canals), secured to a berth or any other installation such as SPM (single-point mooring) or CBM (conventional buoy mooring) systems, except under special circumstances.

When navigating at sea (except in very special circumstances), the UKC must never be less than:

- In confined (restricted) waters and port approaches, a minimum dynamic UKC of 10% of the deepest static draft,
- In open coastal waters, a minimum dynamic UKC of 20% of the deepest static draft,
- On an ocean passage, one must keep clear of localised shallow areas and as far as possible in depths over 50 m.
- When transiting the Malacca and Singapore Straits when the draft is more than 15 m or on a tanker greater than 150 000 MT DWT, a minimum UKC of 3.5 m must be ensured.

Special circumstances: If the voyage orders specify a draft or cargo nomination that, after the Master's best efforts, will result in a UKC less than the ship's operator limits, the Master must notify the operator's technical and commercial operations departments. A UKC limit less than the limits mentioned above may be permitted if in compliance with the local regulations, rules or recommendations by the relevant authorities and if it has been confirmed that other vessels of similar build, size, draft and speed have already established the safety of such a transit under prevailing environmental conditions [19].

Depending on the circumstances of the case, the following conditions may need to be checked with the relevant authorities, agents or terminal:

- Will the vessel be in calm sheltered waters under a controlled speed?
- Will it be possible to verify the ship's draft accurately?
- Are there locks or dock sills to cross?
- Can the latest sounding chart and information for the berth, including the nature of the sea bottom, be obtained directly from the local authorities or terminals well before arrival or lightering?
- Can berthing at discharge ports and unberthing at load ports be carried out during high water only? At discharge ports, plan to start cargo operations well before the low water.

If the conditions set by the shipowner and/or charterer of the ship cannot be met and the vessel is required to breach the UKC limits, the Master must generate temporary deviations from the company procedures. If in doubt, he/she must abort the passage or vacate the berth, keep all parties informed and maintain suitable records. In addition, if it is ever suspected that the vessel has touched the bottom, it is important to notify the pilot and make the appropriate logbook entries, including the date, time and position, and the company management team must be notified and the incident investigated to check for damage.

The squat effect occurs at all times when a vessel is making headway through the water, or secured alongside a berth with a flow of water passing around the hull, but the amplified effects experienced in confined and shallow waters have a profound effect on the safety of the vessel.

The squat effect is caused when buoyancy or the hull pressure is reduced and the vessel is forced deeper into the water to support its weight [11]. Generally, as a rule of thumb the squat increases where a channel width is less than 8.25 times the beam, combined with a static UKC of less than 20% of the draft [19, 25].

The squat of the vessel is an approximation of additional immersion based on the following: the vessel's draft, speed and block coefficient; the width and shape of the channel and the available depth.

Squat should be calculated using the speed through the water rather than the speed over the ground [19]. Reducing the speed is the best means to reduce a vessel's dynamic draft and is an essential consideration for passage planning. Also, on full form ships (such as tankers), the squat effect leads to

an increase of the forward draft and tends to trim a vessel by the head.

The tidal stream and current need only be considered in calculating squat when a vessel is secured alongside a berth. Since the main factor in calculating squat is speed through the water, the tidal stream and current will not affect the amount of squat a vessel experiences when underway and making way. It must also be noted that any calculation made for squat is approximate and for guidance only. Due to the inherent inaccuracy of the information affecting it, extreme caution and judgment should be exercised in calculating and applying squat, keeping potential error on the safe side [2, 11, 15, 19, 25].

The squat effect equals the total parallel body sink plus any subsequent trimming of the vessel [19, 25]. The water flow will follow different patterns in relation to the different shapes of the forward and aft hull. The aft hull is shaped to give a stable inflow to the propeller, while the forward hull is designed for other objectives. Differences in the flow pattern influence the hull pressure or buoyancy. Fluctuations in the buoyancy on the forward and aft hulls lead to trimming of the vessel. In general, the following applies [11, 19, 25]:

- Block coefficient  $C_B > 0.7$  – vessel trims forward;
- Block coefficient  $C_B = 0.7$  – no apparent trim;
- Block coefficient  $C_B < 0.7$  – vessel trims aft.

For vessels with a block coefficient  $C_B > 0.7$ , the application of squat is based on the following: 75% of the squat is an increase in body sinkage and 25% is a change in trim by the head [19, 25].

While navigating in confined (restricted) waters, other conditions that should be considered along with squat include turning, which causes listing and increased drafts, depending on the beam of the vessel. Also, the steering characteristics and course-keeping ability can be affected when the UKC diminishes (that is, the turning circle radius may increase).

In such case the required speed  $V_{ZD}$  can be defined as the ship's safe and/or optimal speed due to the limited value of the under-keel clearance, taking into account the maximum value of the ship's squat, ship's draft and UKC.  $V_{ZD}$  depends on the ship's domain depth  $SD_D$ .

When studying the professional publications, there are many methods for estimating the ship's squat (e.g. [1–3, 9–11, 15, 20, 25]) when proceeding in a restricted sea area across shallow water. In practice, for ship's domain depth ( $SD_D$ ) calculations purposes, the different criteria and formulae should be considered where no computer-based program is available.

Similarly, the final formulae for the ship's bordered optimal safe speed  $V_{ZD}$  due to the limited value of the required under-keel clearance ( $V_{ZD}$  dependent on  $SD_D$ ), obtained after transforming the formulae presented below for the ship's domain depth  $SD_D$  relative to the unknown speed value  $V$ , with the limitation: depth of the basin  $h > T_{max}$  aligned to desired ship's domain depth  $h = SD_D$ ,  $SD_D \geq n \cdot T_{max} + k \cdot h_f$  will then take a form depending on the calculation method used.

- Using precisely the method by C.B. Barrass [1, 11] for estimating the ship's squat, with the limitation  $0.5 \leq C_B \leq 0.9$ ;  $0 \leq t/L \leq 0.005$ ;  $1.1 \leq h/T \leq 1.4$ :

$$SD_D = n \cdot T_{max} + \frac{m \cdot C_B}{30} \cdot \left( \frac{B \cdot T}{b \cdot h - B \cdot T} \right)^{\frac{2}{3}} \cdot V^{2.08} + k \cdot h_f \quad [m] \quad (2)$$

$$V_{ZD} = \left( \frac{30 \cdot (SD_D - n \cdot T_{max} - k \cdot h_f)}{m \cdot C_B \cdot \left( \frac{B \cdot T}{b \cdot h - B \cdot T} \right)^{\frac{2}{3}}} \right)^{\frac{25}{52}} \quad [kn] \quad (3)$$

- Using the simplified Barrass [1] method for estimating the ship's squat in shallow water, with the limitation:  $1.1 \leq h/T \leq 1.2$ :

$$SD_D = n \cdot T_{max} + m \cdot (0.01 \cdot C_B \cdot V^2) + k \cdot h_f \quad [m] \quad (4)$$

$$V_{ZD} = \sqrt{\frac{SD_D - n \cdot T_{max} - k \cdot h_f}{0.01 \cdot m \cdot C_B}} \quad [kn] \quad (5)$$

- Using the simplified Barrass [1] method for estimating the ship's squat in a narrow channel, with the limitation:  $0.06 \leq \frac{B \cdot T}{b \cdot h} \leq 0.3$ :

$$SD_D = n \cdot T_{max} + m \cdot (0.02 \cdot C_B \cdot V^2) + k \cdot h_f \quad [m] \quad (6)$$

$$V_{ZD} = \sqrt{\frac{SD_D - n \cdot T_{max} - k \cdot h_f}{0.02 \cdot m \cdot C_B}} \quad [kn] \quad (7)$$

- Using the Eryuzlu & Hausser method (based on [11]) for estimating the ship's squat in a sea area, with the limitation:  $C_B \geq 0.7$ ;  $1.08 \leq \frac{h}{T} \leq 2.78$ :

$$SD_D = n \cdot T_{max} + m \cdot \left( 0.113 \cdot B \cdot \left( \frac{h}{T} \right)^{-0.27} \cdot \left( \frac{0.514 \cdot V}{\sqrt{g \cdot h}} \right)^{1.8} \right) + k \cdot h_f \quad [m] \quad (8)$$

$$V_{ZD} = 6.533 \sqrt{g \cdot h} \cdot \left( \frac{h}{T} \right)^{0.15} \cdot \left( \frac{SD_D - n \cdot T_{max} - k \cdot h_f}{m \cdot B} \right)^{\frac{5}{9}} \quad [kn] \quad (9)$$

- Using the Soukhomel & Zass method (based on [11]) for estimating the ship's squat in shallow unrestricted water, with the limitation:  $3.5 \leq \frac{L}{B} \leq 9$ :

$$SD_D = n \cdot T_{max} + m \cdot l \cdot 0.049047542 \cdot V^2 \cdot \sqrt{\frac{T}{h}} \cdot \left(\frac{L}{B}\right)^{-1.11} + k \cdot h_f \quad [\text{m}] \quad (10)$$

$$V_{ZD} = 4.5154 \cdot \sqrt{\frac{SD_D - n \cdot T_{max} - k \cdot h_f}{m \cdot l \cdot \sqrt{\frac{T}{h}} \cdot \left(\frac{L}{B}\right)^{-1.11}}} \quad [\text{kn}] \quad (11)$$

where:

- $SD_D$  = Ship's domain depth, [m],
- $V$  = Ship's speed through the water, [kn],
- $V_{ZD}$  = Ship's safe speed  $V_Z$  due to the limited value of the required under-keel clearance and ship's domain depth  $SD_D$ , [kn],
- $R_{squat}$  = Vertical reserve for ship's squat effect, [m],
- $B$  = Ship's width, [m],
- $L$  = Ship's length, [m],
- $T=T_{max}$  = Ship's maximum draught (static),  $T=T_{max}$ , [m],
- $C_B$  = Ship's block coefficient,
- $h$  = The depth of sea area, [m],
- $b$  = The width of sea area, [m],
- $h_f$  = Wave height (swell), [m],
- $g$  = The standard gravity of the Earth, the net acceleration that is imparted to objects due to the combined effect of gravitation and the centrifugal force from the Earth's rotation,  $g = 9.81 \frac{m}{s^2}$ .
- $n$  = Numeric coefficient (factor) dependent on type of sea areas and sea bottoms based on author's own research (2000) regarding determining ship's static vertical navigational reserve.
- $m$  = Numeric factor ( $1.0 \leq m \leq 2.0$ ) correcting the function values  $R_{squat} = f(m, V, B, L, T, C_B, h, b)$  depending on the navigational situation in which the ship finds itself (e.g. overtaking, passing, navigating over inequalities, navigation in ice, silt) and discrepancies in the ship's parameters and parameters of the basin from the parameters adopted in the method of calculating the ship's squat
- $k$  = Numeric coefficient (factor  $k$ ) dependent on ship's particulars (speed= $V$ , width= $B$ , length= $L$ , block coefficient= $C_B$ ) and waves characteristics (length= $\lambda$ , height= $h_f$  and wave attack angle= $q$ ), which determines the ship's dynamic vertical navigational reserve  $R_d$  on sea waves.
- $l$  = Numeric coefficient (factor):  $1.1 \leq l \leq 1.5$ , dependent on ship's length  $L$  and ship's width  $B$ .

Tab. 1. Relation between numeral coefficient (factor)  $l$  and ship's length  $L$  and width  $B$ .

Source: Based on author's own research. [19]

$L$ to $B$ ratio	$7 \leq \frac{L}{B} \leq 9$	$5 \leq \frac{L}{B} \leq 7$	$3.5 \leq \frac{L}{B} \leq 5$
Factor $l$ value	1.10	1.25	1.50

Tab. 2. Numeral coefficient (factor  $n$ ) dependent on type of sea areas and sea bottoms, which determines ship's static vertical navigational reserve for required UKC based on author's own research

$n$	Type of sea area	Type of sea bottom
1.1	Port area, internal and inshore channels	Mud
1.15	Road, approaching channels to the port, inshore area	Sand
>1.2	Open sea	Rock, stone

Tab. 3. The value of  $m$  numeric factor ( $1.0 \leq m \leq 2.0$ ) correcting the function values  $R_{squat} = f(m, V, B, L, T, C_B, h, b)$  depending on the navigational situation in which the ship finds itself (e.g. overtaking, passing, navigating over inequalities, navigation in ice, silt) and discrepancies in the ship's parameters and parameters of the basin from the parameters adopted in the method of calculating the ship's squat. Source: Author's own research

$m$	Parameters of the ship	Parameters of the channel or other navigable waters
1.0	Compliant with the accepted method of calculation, or incompatible but less stringent, for example, slender ships and slower ships accepted in the calculation method	Compliant with the accepted method of calculation or incompatible but less stringent, e.g. sea area parameters with navigation waters higher than those recommended in the method ( $b, h$ )
1.5	Not compatible with the calculation method used, e.g. ships more full-featured than those recommended in the method	Compliant with the accepted method of calculation or incompatible but less stringent e.g. sea area parameters higher than those recommended in the method ( $b, h$ )
1.5	Compliant with the accepted method of calculation, or incompatible but less stringent, for example, slender ships and slower ships accepted in the calculation method	Not compliant with the calculation method (sea area parameters with navigation water lower than recommended), off-axis navigation, overtaking or passing in the channel
2.0	Not compatible with the calculation method used, e.g. ships more full-featured than those recommended in the method	Not compliant with the calculation method (sea area parameters with navigation water lower than recommended), off-axis navigation, overtaking or passing in the channel

Tab. 4. Numeric coefficient (factor  $k$ ) dependent on ship's particulars:  $V, B, L, C_B$  and waves characteristics:  $\lambda, h_f$  and  $q$ , which determines ship's dynamic vertical navigational reserve  $R_d$  on sea waves based on author's own research

$k$	Sea wave direction equal to ship's heading line (waves from ahead or astern of the vessel $q \approx 000^\circ$ or $180^\circ$ )	Sea wave direction perpendicular to ship's heading (waves from the port or starboard beam of the vessel, $q \approx 090^\circ$ )
0.33	When: $V = 0$ and $L > \lambda$	When: $V = 0$ & $B > 0.5 \cdot \lambda$
0.66	When: $V \geq 10$ kn and $L > \lambda$	When: $V \geq 10$ kn & $B > 0.5 \cdot \lambda$
0.75	When: $V < 10$ kn and $L < 0.5 \cdot \lambda$	When: $V < 10$ kn & $B < 0.5 \cdot \lambda$
1.00	When: $V \geq 10$ kn and $L < 0.5 \cdot \lambda$	When: $V \geq 10$ kn & $B < 0.5 \cdot \lambda$

## RESULTS FOR DETERMINING THE SHIP'S OPTIMAL SAFE SPEED $V_{ZD}$ ON SHALLOW WATERS AND NAVIGATIONAL CHANNELS

Tables 5 and 6 depict examples of the bordered (optimal) ship's safe speed  $V_{ZD}$  calculated according to the above formulas, for VLCC Warta and ULCC Blue Lady manoeuvring in a navigational channel inside a port limit area with the following parameters: width  $b=150$  m, assumed depth of the basin  $h > T_{max}$  aligned to the desired ship's domain depth  $h=SD_D$  (with the limitation  $SD_D \geq n \cdot T_{max} + k \cdot h_f$ ), measured at calm sea with wave height  $h_f=0$  m.

For comparison, see also Tables 7 and 8 with the results of calculations made for the aforementioned ships moving in shallow waters with the following parameters: width  $b=350$  m, assumed depth of the basin  $h > T_{max}$  aligned to the desired ship's domain depth  $h=SD_D$  (with the limitation  $SD_D \geq n \cdot T_{max} + k \cdot h_f$ ), measured at moderate sea with wave height  $h_f=1.5$  m and wave length  $\lambda \approx 200$  m (factor  $k=0.66$ ).

Tab. 5. Sample values of the bordered safe speed  $V_{ZD}$  calculated for VLCC Warta manoeuvring in navigational channel inside port area with the following parameters: width  $b=150$  m, assumed depth of the basin  $h > T_{max}$  aligned to desired ship's domain depth  $h=SD_D$ , navigational risk  $R_{ND}=0$ , with limitation with the limitation  $SD_D > n \cdot T_{max} + k \cdot h_f$ , measured at calm sea with wave height  $h_f=0$  m. Source: Author's own research Apr. 2019

Accepted method for $V_{ZD}$ (Equation No.)		VLCC WARTA $D=176967$ t, $L=293$ m, $B=48.0$ m $T=15.5$ m, $C_B=0.844$ , $V_{max}=15$ kn, $P=29000$ HP, 122 rpm, $H_{HP}=55$ m, $n=1.1$ , $m=1.0$ , $k=0.33$ , $l=1.25$				
Desirable $SD_D=h$		17.1 [m]	17.5 [m]	18.0 [m]	18.5 [m]	19.0 [m]
Bordered safe speed $V_{ZD}$ [knots]	(3)	1.76	5.10	7.40	9.18	10.71
	(5)	2.43	7.30	10.61	13.11	15.20
	(7)	1.72	5.16	7.50	9.27	10.75
	(9)	1.89	6.51	10.04	12.93	15.51
	(11)	2.53	7.62	11.15	13.87	16.20

Tab. 6. Sample values of the bordered safe speed  $V_{ZD}$  calculated for ULCC Blue Lady manoeuvring in navigational channel inside port area with the following parameters: width  $b=150$  m, assumed depth of the basin  $h > T_{max}$  aligned to desired ship's domain depth  $h=SD_D$ , navigational risk  $R_{ND}=0$ , with limitation with the limitation  $SD_D > n \cdot T_{max} + k \cdot h_f$ , measured at calm sea with wave height  $h_f=0$  m. Source: Author's own research Apr. 2019

Accepted method for $V_{ZD}$ (Equation No.)		ULCC BLUE LADY $D=323660$ t, $L=331$ m, $B=57.0$ m, $T=20.6$ m, $C_B=0.790$ ; $V_{max}=15$ kn, $P=27000$ HP, 85 rpm, $H_{HP}=75$ m, $n=1.1$ , $m=1.0$ , $k=0.33$ , $l=1.25$				
Desirable $SD_D=h$		22.7 [m]	23.0 [m]	23.5 [m]	24.0 [m]	24.5 [m]
Bordered safe speed $V_{ZD}$ [knots]	(3)	1.50	4.23	6.60	8.35	9.82
	(5)	2.25	6.56	10.31	13.02	15.26
	(7)	1.59	4.64	7.29	9.21	10.79
	(9)	1.75	5.80	9.72	12.77	15.43
	(11)	2.20	6.43	10.15	12.89	15.19

Note: The author chose the ships VLCC Warta and ULCC Blue Lady for this research, taking into account the fact that models of these ships are also available and used for research in the Foundation for Safety of Navigation and Environment Protection Ship Handling Research and Training Centre,  $\text{Hawa-Poland}$ .

Tab. 7. Sample values of the bordered safe speed  $V_{ZD}$  calculated for VLCC Warta manoeuvring in navigational channel approaching port with the following parameters: width  $b=350$  m, assumed depth of the basin  $h > T_{max}$  aligned to desired ship's domain depth  $h=SD_D$ , navigational risk  $R_{ND}=0$ , with limitation  $SD_D > n \cdot T_{max} + k \cdot h_f$ , measured at moderate sea with wave height  $h_f=1.5$  m. Source: Author's own research Apr. 2019

Accepted method for $V_{ZD}$ (Equation No.)		VLCC WARTA $D=176967$ t, $L=293$ m, $B=48.0$ m, $T=15.5$ m, $C_B=0.844$ , $V_{max}=15$ kn, $P=29000$ HP, 122 rpm, $H_{HP}=55$ m, $n=1.15$ , $m=1.0$ , $k=0.66$ , $l=1.25$				
Desirable $SD_D=h$		18.9 [m]	19.0 [m]	19.5 [m]	20.0 [m]	20.5 [m]
Bordered safe speed $V_{ZD}$ [knots]	(3)	3.30	4.80	9.10	11.95	14.28
	(5)	3.17	4.68	9.01	11.85	14.13
	(7)	2.24	3.31	6.37	8.38	9.99
	(9)	2.71	4.19	8.82	12.16	15.03
	(11)	3.38	4.99	9.66	12.79	15.34

Tab. 8. Sample values of the bordered safe speed  $V_{ZD}$  calculated for ULCC Blue Lady manoeuvring in navigational channel approaching port with the following parameters: width  $b=350$  m, assumed depth of the basin  $h > T_{max}$  aligned to desired ship's domain depth  $h=SD_D$ , navigational risk  $R_{ND}=0$ , with limitation  $SD_D > n \cdot T_{max} + k \cdot h_f$ , measured at moderate sea with wave height  $h_f=1.5$  m. Source: Author's own research Apr. 2019

Accepted method for $V_{ZD}$ (Equation No.)		ULCC BLUE LADY $D=323660$ t, $L=331$ m, $B=57.0$ m, $T=20.6$ m, $C_B=0.790$ ; $V_{max}=15$ kn, $P=27000$ HP, 85 rpm, $H_{HP}=75$ m, $n=1.15$ , $m=1.0$ , $k=0.66$ , $l=1.25$				
Desirable $SD_D=h$		24.7 [m]	25.0 [m]	25.5 [m]	26.0 [m]	26.5 [m]
Bordered safe speed $V_{ZD}$ [knots]	(3)	1.59	6.04	9.56	12.11	14.23
	(5)	1.59	6.36	10.19	12.93	15.18
	(7)	1.13	4.50	7.20	9.14	10.73
	(9)	1.26	5.92	10.11	13.34	16.14
	(11)	1.59	6.37	10.24	13.06	15.40

## NAVIGATIONAL RISK FACTOR

According to the author's own research (from 2000 to 2020) on definition of the ship's domain, every ship will be safe (in the navigational meaning) as long as it is the exclusive object that can generate danger within its domain. With reference to a vertical plane OZ of the three-dimensional co-ordinates XYZ established down from the central point of the local ship's reference system, one can state unambiguously that every ship will remain safe as long the value of the ship's domain depth  $SD_D$  is smaller than the real value of the sea depth  $h$ . Therefore, component  $R_{ND}$  of  $R_N$  can be referred to as the vertical component of the navigational risk, which

concerns keeping sufficient required under-keel clearance, or risk concerning the under-keel clearance.

$$R_{ND} = \begin{cases} 0 & \text{when } h > SD_D \\ \frac{SD_D - h}{SD_D - T_{max}} & \text{when } T_{max} < h \leq SD_D \\ 1 & \text{when } h \leq T_{max} \end{cases} \quad (12)$$

where:

$R_{ND}$  = Numeric factor defining vertical component of the navigational risk  $R_N$  that concerns keeping sufficient required under-keel clearance,

$SD_D$  = Ship's domain depth expressed in metres, [m],

$h$  = Actual water depth, [m],

$T_{max}$  = The maximum draft of the vessel, [m].

Formula (12) indicates that the value zero of the navigational risk, deriving from factors (objects), signifies total navigational safety with respect to these factors (objects). Consequently, according to formula (12), the assumption  $h > SD_D$  can be defined as the guarantee of safe shipping (navigation) with reference to all underwater objects or obstructions immersed at a depth less than  $h$ . If the sea depth  $h$  is less than or equal to the ship's maximum draft ( $T_{max}$ ), that is  $h \leq T_{max}$ , according to formula (12) sea passage can be unfeasible or highly risky.

Tab. 9. Relationship between ship speed  $V$ , domain depth  $SD_D$ , ship's squat and navigational risk factor  $R_{ND}$  calculated for VLCC Warta ( $B=48m$ ,  $L=293m$ ,  $T=15m$ ,  $CB=0.844$ ) manoeuvring in navigational channel with different speed inside port area with the following parameters: width  $b=150m$ , assumed depth of the basin  $h=1.1 \cdot T_{max}=16.5m$ , wave height  $h_w=1.0m$ , factors:  $m=1$ ,  $n=1.1$ ,  $k=0.75$ .  
Source: Author's own research Dec. 2019

V	0	2	4	6	8	10	12	14
Squat	0	0.07	0.28	0.65	1.17	1.87	2.73	3.76
$SD_D$	17.25	17.32	17.53	17.90	18.42	19.12	19.98	21.01
$R_{ND}$	0.33	0.35	0.41	0.48	0.56	0.64	0.70	0.75

Note: For estimating ship's squat the Barrass method [1, 11] has been used, with limitation  $0.5 \leq CB \leq 0.9$ ;  $0 \leq t/L \leq 0.005$ ;  $1.1 \leq h/T \leq 1.4$ . For calculating  $SD_D$  formula (2) has been used and for  $R_{ND}$  formula (12).

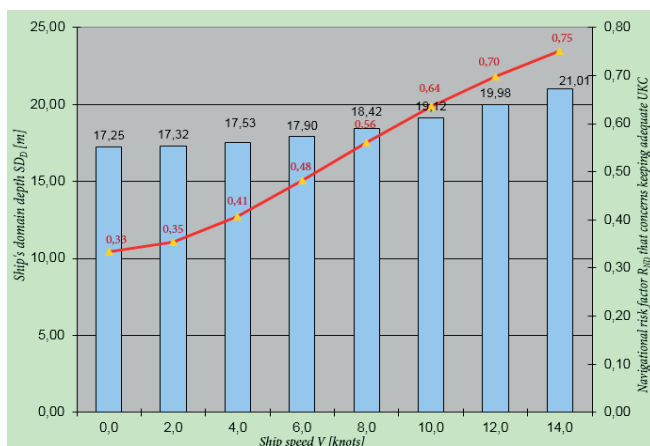


Fig. 1. Relationship between ship speed  $V$ , domain depth  $SD_D$  and navigational risk factor  $R_{ND}$  calculated for VLCC Warta based on data available in Tab. 9.  
Source: Author's own research Dec. 2019

In that situation the value of the navigational risk  $R_{ND}$  will equal one, and in all probability, it will signify an unquestionable (100%) risk of collision with some underwater object(s) immersed at a depth less than  $h$ . Furthermore, we can also say that the value of navigational risk  $R_{ND}$  for the sea depth  $h$  limited between  $T_{max}$  and  $SD_D$ : ( $T_{max} < h \leq SD_D$ ) will be limited between zero and one ( $R_{ND} \in [0,1]$ ).

The relationship between the vessel speed  $V$ , ship's squat, domain depth  $SD_D$  and navigational risk factor  $R_{ND}$  prepared for VLCC Warta is presented in Table 9 and Fig. 1.

## CONCLUSION

Summing up, it can be stated that, regardless of the voyage option adopted, according to COLREG regulations and the principles of good seamanship, the ship should always move at a safe speed. According to COLREG, what is a safe speed will depend on the vessel and circumstances, bearing in mind that every vessel shall at all times proceed at a safe speed so that it can take proper and effective action to avoid collision and be stopped within a distance appropriate to the prevailing circumstances and conditions. COLREG sets out some factors to be considered by all vessels and vessels with operational radar. However, the unambiguous definition of a safe speed, disregarding the ship's margin of safety determined by the outline of its three-dimensional domain, is too complex an issue, which at the present state of knowledge cannot give us an unambiguous answer as to the specific value of the ship's safe speed when navigating in restricted sea areas.

Practice prescribes that choosing the right ship speed in restricted sea areas on confined waters is a form of compromise between the optimal speed (due to time or fuel consumption) and the safe speed set for the current navigational situation [9,19].

The optimum speed (the right one) will therefore be the speed enabling travel to be made at the right time (fulfilling the contract), and at the same time guaranteeing a constant safety margin (so-called speed reserves) in the event of unpredictable, emergency situations and those resulting from the deployment (position) of navigational obstacles around the ship. As a result, the optimal speed setting will always be reduced to the comparative analysis of individual components of the safe speed:  $V_X$ ,  $V_Y$ ,  $V_Z$ , determined based on the outline of the ship's domain.

From a practical point of view, the initial element for the analysis of the navigational risk in restricted waters (areas restricted by the water depth, air vertical clearance under the bridges and/or width of navigable waters) is the estimation of the ship's domain parameters (her depth  $SD_D$ , height  $SD_H$ , width  $SD_W$  and length  $SD_L$ ).

The author's own research [16, 17, 18, 19] proves that these activities (calculations) can be performed on a ship in real time, and their results, if necessary (e.g. for controlling the movement of ships manoeuvring in restricted waters based on the value of their navigational risk indicators), can be

attached to standard reports e.g. via the ship's Automatic Identification System AIS.

In this way it is shown that, contrary to the accepted practice, modelling the domain of a ship when manoeuvring in restricted waters is also possible. In practice, this means that a thorough analysis of the navigational risk of ships sailing in restricted waters is also possible and may help us choose such conditions (internal and/or external) in which the sea passage will be effective, safe and in line with the needs of the global maritime transportation system, including selection of the optimal safe speed on shallow water.

## REFERENCES

1. Barrass C. B. (1994): *Further Discussion on Squat*. Seaways, March 1994.
2. Duda D., Norwicz K. (1976): *Definition of a ship's safe reserve and under keel clearance. Ship's squat*. In Polish: Określenie bezpiecznej rezerwy pod stępką. Osiedlenie statku., WSM, Gdynia, Poland.
3. Ferreiro L. D. (1992): *The effects of confined water operations on ship performance: A guide for the perplexed*. Naval Engineers Journal, November, 1992.
4. Fujii Y. and Tanaka K. (1971): Traffic capacity. *Journal of Navigation*, 24, 543–552.
5. Gucma S., Jagniszczak I. (1997): *Navigation for the master mariner*. In Polish: Nawigacja Morska dla Kapitanów, Foka Publisher, Szczecin, Poland.
6. Goodwin E. M. (1975): *A statistical study of ship domains*. *The Journal of Navigation*, 28, 328–344.
7. Hansen M. G., Jensen T. K., Lehn-Schiøler T., Melchild K., Rasmussen F. M., Ennemark F. (2013): *Empirical ship domain based on AIS data*. *The Journal of Navigation*, 66, 931–940.
8. Hooft J. P. (1969): *On the critical speed range of ship in restricted waterways*. *International Shipbuilding Progress*, No 177.
9. Jurdziński M. (1999): *Planning the speed of the ship in confined waters*. In Polish: Planowanie prędkości statku na wodach ograniczonych, Gdynia, Poland.
10. Millward A. (1990): *A preliminary design method for the prediction of squat in shallow water*. *Marine Technology*, Vol.27 (No 1).
11. Nowicki A. (1999): *Knowledge about manoeuvring with sea going vessels*. In Polish: Wiedza o manewrowaniu statkami morskimi, Trademar Publisher, Gdynia.
12. Pietrzykowski Z. (2008): Ship's fuzzy domain - A criterion for navigational safety in narrow fairways. *Journal of Navigation*, 61, 499–514.
13. Pietrzykowski Z., Uriasz J. (2003): *Methods of artificial intelligence in navigational safety assessment of ship encounters*. Proc. of Computer and Information Technology Applications in the Maritime Industries COMPIT 2003, Hamburg.
14. Pietrzykowski Z., Uriasz J. (2009): *The ship domain - A criterion of navigational safety assessment in an open sea area*. *The Journal of Navigation*, 62, 93–108.
15. Porada J. (1972): *Theoretical and practical reasons for determining the permissible speed of ships on fairway and navigational channels*. In Polish: Teoretyczne i praktyczne przesłanki ustalenia dopuszczalnej prędkości statków na torach i w kanałach morskich, TGM 3 Poland.
16. Rutkowski G. (2016): *Determining ship's safe speed and best possible speed for sea voyage legs*. DOI: 10.12716/1001.10.03.07, ISSN 2083-6473 EISSN: 2083-6481, *TransNav - The International Journal on Marine Navigation and Safety of Sea Transportation*, 10 (3), 425–430.
17. Rutkowski G. (2018): *ECDIS limitations, data reliability, alarm management and safety settings recommended for passage planning and route monitoring on VLCC tankers*. *TransNav - The International Journal on Marine Navigation and Safety of Sea Transportation*, 12, 483–490.
18. Rutkowski G. (2019): *Determining the optimal ship's safe speed*, 1st Ed., LAP Lambert Academic Publishing, ISBN 97862000074 21, Printed by Schaltungsdienst Lange o.H.G., Berlin 2019 by European Union OmniScriptum Publishing Group, 2019-04-26.
19. Rutkowski G. (2019): *Voyage planning, seafarers' competencies and watchkeeping procedures in the restricted sea areas, in the narrow channels and sharp bend fairways*, 1st Ed., LAP Lambert Academic Publishing, ISBN 9786200094148, Printed by Schaltungsdienst Lange o.H.G., Berlin 2019 by European Union OmniScriptum Publishing Group, 2019-05-13.
20. Schofield R. B. (1974): *Speed of ships in restricted navigation channels*. *Journal of the Waterways, Harbours and Coastal Engineering Division*, May 1974.
21. Vermeer H. (1977): *The behaviour of a ship in restricted waters*. *International Shipbuilding Progress*, No 280.
22. Wang Y. Y. (2016): *An empirically-calibrated ship domain as a safety criterion for navigation in confined waters*. *Journal of Navigation*, 69, 257–276.

23. Wielgosz M., Pietrzykowski Z. (2012): *Ship domain in the restricted area - Analysis of the influence of ship speed on the shape and size of the domain*. Scientific Journals of the Maritime University of Szczecin, 30(102), 138–142.
24. Zhu X., Xu H. and Lin J. (2001): *Domain and its model based on neural networks*. Journal of Navigation, 54, 97–103.
25. Zong Z. (2017): *An introduction to ship hydrodynamics*. Lecture notes based on Tupper E. C. (2004) *Introduction to Naval Architecture*, 4th Edition, Elsevier.

#### CONTACT WITH THE AUTHOR

**Grzegorz Rutkowski**

*e-mail: kptgrzegorzrutkowski@gmail.com*

Gdynia Maritime University,  
Morska 81-87, 81-225 Gdynia,

**POLAND**

Master Mariners Association,  
Al. Jana Pawła II 3, 81-963 Gdynia,

**POLAND**

## SAILING ROUTE PLANNING METHOD CONSIDERING VARIOUS USER CATEGORIES

Marcin Życzkowski  
Gdańsk University of Technology, Poland

### ABSTRACT

*The article describes the methodology related to determining the multi-criteria routes for sailing ships. Details of sea area discretisation and discretisation of the description of the sailing vessel properties and manoeuvring principles are shown. User requirements were specified (for five different categories of users) and on this basis the criteria for selecting the most suitable shipping route were formulated. The presented algorithm recommends a route for a given user category by means of defined restrictions and configuration parameters. The applied multi-criteria approach proves the universality and usability of the sailing ship route planning method.*

**Keywords:** sailing vessel, weather routing, multi-criteria, navigation, comfort

### INTRODUCTION

The planning of routes in maritime transport inspired scientists as early as the era when sailing vessels were still the only means of transport enabling ocean travel. The first attempts at sailing vessel route recommendations (least-time tracks based on statistical wind and current data) were made by Maury 7 in the 19th century. In the 20th century, power-driven ships became the main means of maritime transport. In turn, sailing vessels have changed their role in transport from cargo ships to vessels used in regattas and for tourism. Initially, after this change of role, sailing vessels lost their importance in transport. It should be emphasised, however, that cultural changes in the face of commercialisation have strongly influenced the development of urban tourism 16. This has also increased interest in cruise ships, and as a result also

influenced the specificity and role of sailing. What is more, regattas and extreme cruises have become very popular. In recent years, during large commercial regattas, the border between sport and passenger transport has been blurred, becoming understood as a paid transport service. The crew consists of both professional and amateur sailors, i.e. paying participants (partly with the rights of “passengers”). This allows regatta organisers to obtain additional financial benefits, and “passengers” seeking extreme sensations are provided with experiences that they would not experience on a typical tourist ship.

An important role in sailing is played by the speed of the sailing vessel, so it is important to know the speed characteristics of the ship. These are closely related to the technical parameters of the ship, and can be obtained using appropriate software (for example, the commercial Bentley

Systems package). The use of such characteristics is crucial during regattas. However, the role of speed characteristics in recreational and tourist shipping should also be emphasised. The possibility of setting a relatively fast route may have an impact on the safety of the often small ship, its crew and passengers. Effective planning of a route to the harbour of refuge in the event of deteriorating weather conditions is an important issue 3. Security issues are extremely important. This also applies to autonomous sailboats 15. This subject is discussed at the annual International Robotic Sailing Conference (IRSC), which also emphasises the importance of this issue. The purpose of this article is to present a multi-criteria method for determining the route of a sailing vessel from the starting point to the final point, taking into account hydrometeorological data and various travel criteria. The universality and usability of the method were shown through the categories of users under consideration with different preferences. They were defined by criteria and restrictions that take into account the requirements of both regatta and recreational ship users seeking extreme sensations, as well as as beginner sailors and unmanned sailing ships.

The article is a continuation of the author's research on determining routes for sailing vessels. In the previous stages of the author's work, the discrete research environment consisted of 3528 points (navigable and non-navigable) and discretely defined the area of the Gulf of Gdańsk 17–20. The current research environment has been increased to 14,523,121 available points, which makes it possible to cover the discrete research area of the Baltic Sea area to a latitude of 57 ° N.

## RELATED WORKS

Route planning methods in shipping can be divided into two groups depending on the approach used. The first group are deterministic methods that give the same solution for the same input data 2,6,8,13,4,1time and space complexity, search space auto-adaptation properties. This solution does not take into account the order and time factor in the introduction of preliminary assumptions. Tasks carried out on the same input data obtain repeatable calculations. Updating the input data or changing the initial assumptions can lead to a different solution.

The second group are non-deterministic methods that take into account issues that would be too time-consuming for deterministic methods 10–12,9,5,14. These concern oceanic routes, which take into account the many variants of weather forecasts, as well as the avoidance of tropical cyclones in ocean navigation or anti-collision manoeuvres. Non-deterministic methods consider more complex phenomena with more input data than deterministic methods. However, non-deterministic methods reduce the range of input data using random phenomena, which means that the final result is an approximate value.

The route calculation method presented in this article is for parts of the southern Baltic Sea. Due to the fact that the research area is not very large, the presented method uses a

deterministic approach. However, it is necessary to implement this method based on 64-bit architecture.

## SAILING ROUTE PLANNING METHODS

The task of the presented method is to recommend a route within the permissible sailing area for a specific user, taking into account his requirements and restrictions resulting from safety requirements. The task formulated in this way requires consideration of the most likely route selection options under the conditions prevailing in the given navigation area. Further, an adequate description of the ship's properties and user requirements is important. Fig. 1 shows the information flow needed to perform this analysis. In addition to the description of the navigation space, presentation of the conditions in this space, the ship properties and user requirements, appropriate route calculation algorithms as well as supporting procedures are necessary. Besides, due to the possible dynamics of changes in the navigable area in question, it is necessary to know current external data on hydrometeorological changes. Due to the nature of the phenomena described and the complexity of aerodynamic and hydrodynamic problems, an appropriate and effective modelling method is also required, which requires the use of various types of software, including appropriate IT services.

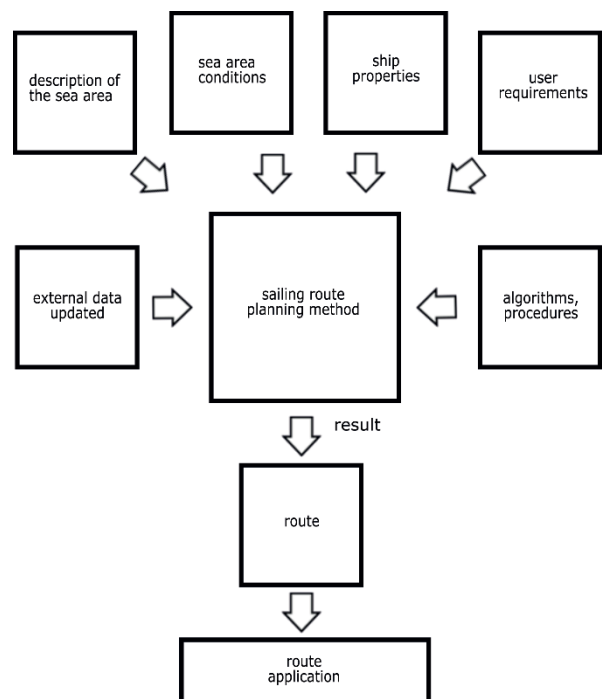


Fig. 1. Information flow in the sailing vessel route planning method

This means the need to map the real world through the digital environment, as well as to develop an appropriate work methodology. It consists of the following activities:

- Discretisation of the navigable area

- Discretisation of the description of the sailing vessel properties and manoeuvring rules
- Specifying user requirements and, on this basis, formulating criteria for selecting the most suitable shipping route.
- Development of an algorithm of multi-criteria selection of the most suitable route.

The above activities will be discussed in more detail in the following sections.

### NAVIGATION AREA DISCRETISATION

In the described method, the marine environment was limited to a finite discrete sea area. The variable parameters of the sailing vessel movement were: geographical position, ship course, ship speed, course change speed.

In turn, a limited area of the marine environment is designated on the globe by coastal parallels and meridians  $(\varphi_p, \varphi_m, \lambda_p, \lambda_n)$ . Fig. 2 shows a simplified section of the marine environment, where land is marked in grey and sea is marked in white. In practice, it can take various shapes resulting from a given geographical area.

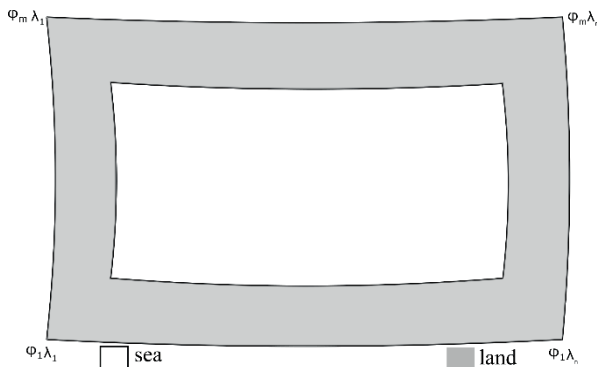


Fig. 2. A fragment of the real marine environment

For the given granularity, a grid of intersection points between horizontal and vertical curves was created as formula (1).

$$Z = \frac{(\varphi_{max} - \varphi_{min}) \times (\lambda_{max} - \lambda_{min})}{m \times n} \quad (1)$$

where:

$m$  – the number of horizontal curves, and  $n$  the number of vertical curves of the analysed grid

$\varphi_{max} (\lambda_{max}), \varphi_{min} (\lambda_{min})$  – the minimum and maximum latitude (longitude).

$\varphi_{min} = \min \{\varphi_i, i=1,2,..,m\}, \lambda_{min} = \min \{\lambda_i, i=1,2,..,n\}, \varphi_{max} = \max \{\varphi_i, i=1,2,..,m\}, \lambda_{max} = \max \{\lambda_i, i=1,2,..,n\}$ .

Fig. 2 shows a simplified representation of a section of the real area. With the help of the grid used, the sections of the real area are replaced by a set of points  $P_{ij}$ , set at regular intervals and determined by the appropriate geographical coordinates: latitude  $\varphi_i$  and longitude  $\lambda_i$ , i.e.

$$P_{ij} = P(\varphi_i, \lambda_j) \quad (2)$$

$$i = 1, 2, \dots, m ; j = 1, 2, \dots, n$$

where:

$\varphi_i$  – latitude value

$\lambda_j$  – longitude value

In the obtained discrete model, each geographical position from the real area is represented by an approximate, interpolated point from the set of points  $P_{ij} \in P$  (Fig. 3). The grid of points consists of both navigable and non-navigable points, and navigable and non-navigable areas retain the same granularity. The choice of granularity may depend on the dynamics of the marine environment conditions or the required accuracy of the route description. The author changes the granularity of the mesh in the context of the ship's approach to hazardous areas in another article 17. Each point  $P_k = P_{ij}$  has information on hydrometeorological data specifying the changing conditions of the marine environment at the moment  $t$ .

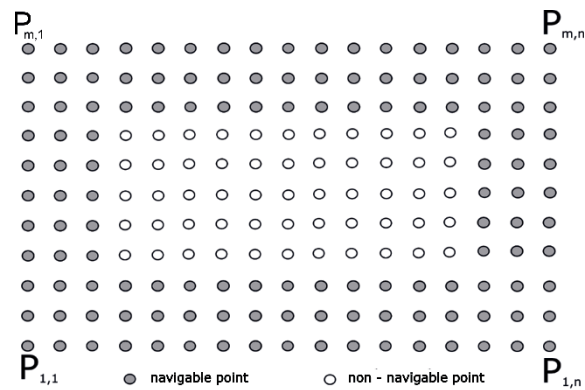


Fig. 3. Navigable and non-navigable points grid

### DESCRIPTION OF THE PROPERTIES OF A SAILING SHIP AND MANOEUVRING RULES

The course change in the real marine environment is continuous, which means that one can choose any course if it meets the safety requirements. In the presented discrete sailing model, the selection of a specific navigation route is possible only if it is possible to connect the current point with the next point of travel, where both belong to the navigable zone. In this discrete model, it is also assumed that the ship's movement takes place only according to the proposed sailing rules, i.e. in accordance with the accepted number of allowed sailing directions  $\in \{8,16,32\}$ .

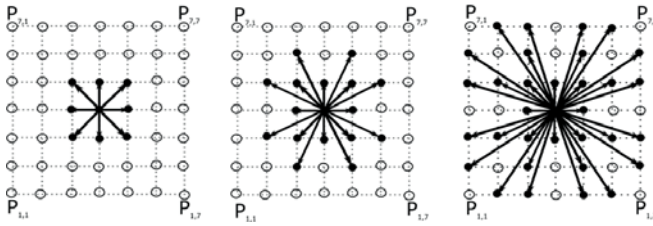


Fig. 4. Variants of permissible sailing directions {8,16,32}

The selection of the permissible number of sailing directions depends on the assumed accuracy of route planning. The higher the number, the higher the accuracy; however, this can result in longer tacks. Considering the current point  $P_k$  in the navigable area, we can consider all possibilities of choosing the next point  $P_l$ . The combination of points  $P_k$  and  $P_l$  is called the segment. The total route is a path that contains at least one segment. Thus, the entire route of a sailing vessel can be described by means of a set of consecutive sequences of points according to formula (3).

$$\text{Route} = \langle P_{k_1}, P_{k_2}, \dots, P_{k_9} \rangle \quad (3)$$

where:

$k_i$  – marks the next point belonging to this route,  $i=1,2, \dots, L$   
 $L$  – is the number of all route points

Each point  $P_k$ , where  $k \in (1,2, \dots, m \cdot n)$ , represents a specific geographical position and changing environmental conditions. On each segment of the route, additional parameters are also determined, which depend on the subsequent route points  $P_{k_i}$ , where  $i \in (1,2, \dots, L)$ . They are as follows: direction of movement from point  $P_{k_i}$  to point  $P_{k_{i+1}}$ ; length of segment from point  $P_{k_i}$  to point  $P_{k_{i+1}}$ ; time of the ship's passage after the section from  $P_{k_i}$  to point  $P_{k_{i+1}}$ .

Variants of permissible sailing directions are shown in Fig. 4. The length of the segment from point  $P_{k_i}$  to point  $P_{k_{i+1}}$  is determined as the actual distance between these points, described by the relevant geographical coordinates. The crossing time, in turn, depends on the speed of the sailing vessel moving along this section. The vector  $\vec{P_{k_i}P_{k_{i+1}}}$  between two points  $P_{k_i}$  and  $P_{k_{i+1}}$  has a certain direction, which is defined as the angle between this vector and the north direction. It is designated as  $\alpha_{i,i+1}$ , which is shown in Fig. 5.

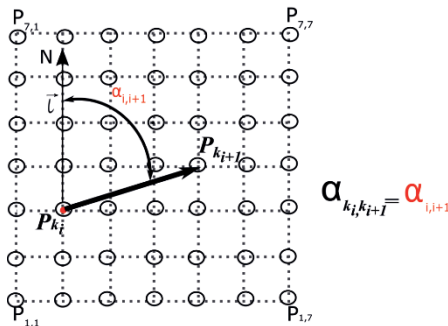


Fig. 5. Method of determining the direction of movement from point to point

As already mentioned, the length of the segment from point  $P_{k_i}$  to point  $P_{k_{i+1}}$  is denoted as  $d(P_{k_i}, P_{k_{i+1}})$  and we calculate it according to the following formula (4).

$$d(P_{k_i}, P_{k_{i+1}}) = \sqrt{(\varphi_{k_i} - \varphi_{k_{i+1}})^2 + ((\lambda_{k_i} - \lambda_{k_{i+1}}) \cdot \cos((\varphi_{k_i} + \varphi_{k_{i+1}})/2))^2} \quad (4)$$

Each point  $P_k$  has its geographical position  $\varphi_k$  and  $\lambda_k$ . The length of the section between two points is measured in nautical miles (Nm). It is assumed that 1 Nm is 1852 m. When determining the length of the section, the navigational deviation was taken into account. The passage time of the ship after the segment is denoted by  $t(P_{k_i}, P_{k_{i+1}})$  and using formula (5).

$$t(P_{k_i}, P_{k_{i+1}}) = \frac{d(P_{k_i}, P_{k_{i+1}})}{v(P_{k_i}, P_{k_{i+1}})} \quad (5)$$

where:

$v(P_{k_i}, P_{k_{i+1}})$  – segment passage speed from  $P_{k_i}$  to  $P_{k_{i+1}}$ , expressed in knots.

The ship speed is estimated using the ship's polar characteristics, which are different for each ship and developed experimentally by its designers or manufacturers. It shows the relationship between the speed of the ship and the angle of attack of the wind at a certain speed. As Fig. 6 (b) shows, not all directions of movement are acceptable due to the efficiency of the sail wing. Typically, estimates of the speed characteristics of a sailing vessel by VPP-type programs are presented for calm water.

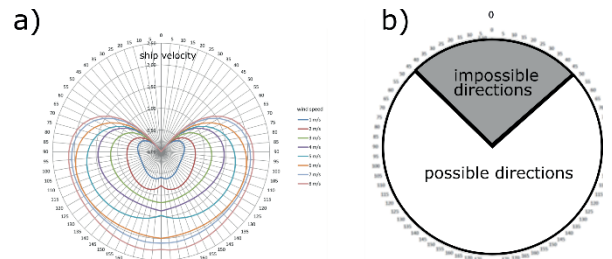


Fig. 6. a) Polar characteristics of the sailing vessel and b) illustration of permitted and prohibited directions

During the passage of the segment from point  $P_{k_i}$  to point  $P_{k_{i+1}}$ , the ship's heel determined by the function  $\text{heel}(P_{k_i}, P_{k_{i+1}})$  is included. The expected value of heel for specific parameters and a specific choice of direction of movement from point  $P_{k_i}$  to point  $P_{k_{i+1}}$  is determined by formula (6).

$$\text{heel}(P_{k_i}, P_{k_{i+1}}) = \vartheta(\vec{W}_{k_i}(t), \alpha_{i,i+1}) = \vartheta(w_{k_i}(t), \beta_{i,i+1}(t)) \quad (6)$$

where:

$\alpha_{i,i+1}$  – course of ship from point  $P_{k_i}$  to point  $P_{k_{i+1}}$

$\beta_{i,i+1}$  – angle of attack of wind on the vessel flowing from point  $P_{k_i}$  to point  $P_{k_{i+1}}$

Function  $\vartheta(w_{k_{i+1}}(t), \beta_{i,i+1}(t))$  predicts the ship's heel based on its polar characteristics, wind speed  $w_{k_{i+1}}(t)$  and angle of attack of wind on the vessel flowing  $\beta_{i,i+1}(t)$ .

## USER REQUIREMENTS AND CRITERIA

Depending on the nature of the trip and the requirements of the watercraft user, different initial assumptions and tasks to be performed may be specified. These differ in the case of the owner of a commercial unit, the captain of the sailing vessel, the team of the sailing yacht participating in an ocean regatta, or the person managing the unmanned vessel. For this reason, the route with the shortest lead time is not always the only desired result of using the optimisation method. Important route selection criteria can also include a feeling of comfort (for passenger ships, as well as recreational yachts), minimal consumption of inventory (for a commercial unit), a sense of security (for beginner sailors), or finding the longest route without repetitions (for monitoring an area). In view of the wide variety of expectations of the stakeholders of the navigation, the priority of navigation is to choose the optimal route for the vessel user. In the article, based on a review of the literature, the author's own experience and expert opinions, five categories of users (U1, U2, U3, U4, U5) were distinguished, presenting different scenarios of the preferences of potential users of sailing vessels. U1 are participants of recreational cruises, attached to comfort, determined by the conditions of travel and ensuring safety. U2 are people seeking extreme sensations, assuming reduced safety restrictions and deciding to choose extreme sailing conditions. U3 are beginner sailors who care about mastering the art of sailing with security. U4 are the controllers of unmanned sailing ships who seek to ensure that they reach their destination safely. U5 are the participants in the regatta, who want to complete the route in the shortest possible time in well-recognised sailing conditions while maintaining moderate safety.

User preferences translate into criteria and restrictions in mapping the route. The following five travel selection criteria were adopted (K1, K2, K3, K4, K5).

K1 means getting the shortest travel time from a given start point to the destination. K2 is a choice of favourable travel conditions (good weather, no waves). K3 is to ensure the safety of travel through the precision of manoeuvres performed (turns and tilts, not exceeding the set values). K4 is to achieve travel comfort, which means reaching the destination in a given time and ensuring insurance manoeuvres, described by values much lower than the limit ones. K5 is to take risky decisions resulting from certain premises, exceeding the permissible capacity of the ship or sailing conditions.

It is possible to formulate links between categories of users and the adopted criteria, as presented in Table 1.

Tab. 1. User categories and route selection criteria

Criteria \ User categories	Criteria				
	K1	K2	K3	K4	K5
U1		+	+	+	
U2	+				+
U3		+	+		
U4		+		+	
U5	+		+		+

When calculating the route in accordance with the assumed criteria, it is necessary to take into account certain restrictions for each user category. This approach brings the result of the route calculation method closer to the user's requirements. Five types of restrictions were adopted (O1, O2, O3, O4, O5). O1 is the permissible number of manoeuvres during a journey, where each manoeuvre is associated with time delay and discomfort. O2 is the permissible angle of change of the ship's course, ensuring its safe performance. O3 is the allowable number of tack changes (and heels resulting from this), related to comfort. O4 is the permissible roll value that indicates the presence of a hazard. O5 is the permissible angle of the ship's attack on the wind, also determining the safety of sailing.

By bringing the method results closer to the user's expectations, in addition to the limit, configuration parameters have been introduced. Configuration parameters include P1, P2 and P3. P1 is the choice of the number of traffic directions allowed, ensuring greater accuracy and affecting travel comfort. P2 is the number of currently considered weather forecasts affecting the reliability of the received route and maximising the instantaneous achievements. P3 is a change in the grain size of the sailing area to ensure the accuracy of the manoeuvre.

Tab. 2. Restrictions and configuration parameters

Restriction and configuration parameter \ User category	Restriction and configuration parameter								
	O1	O2	O3	O4	O5	P1	P2	P3	
U1	••	•	•••	••	••	•	•	•	
U2		•		•	•	••		••	
U3		•	•	•	••	•	••	•	
U4	•	•	•	••	••	•	•	•	
U5	•	•	•	•	••	•••	•••	••	

Of course, other parameters may affect the implementation of the route in accordance with the criteria of the trip, but their inclusion does not require changes in the proposed method for selecting the optimal route within the accepted categories of users. The restrictions and configuration parameters necessary for the implementation of the route in accordance with these categories of users are shown in Table 2.

The dots indicate the significance of a given restriction or configuration parameter for the implementation of a route consistent with a particular user category. Because the user category is related to the implementation of various goals, the number of dots determines the priority, taking into account

the relevant restrictions and configuration parameters. Table 2 shows that for users of category U1, the most important is the O3 limit, while O1, O4 and O5 are very important. For category U2, the parameters P1 and P3 are very important, while the restrictions O1, O3 and P2 are immaterial. For category U3, the O5 limitation and the P2 parameter are very important, while the O1 limitation is insignificant. For category U4, O4 and O5 are very important, while the others are less important. For category U5, the most important are parameters P1 and P2, P3 and O5 are very important, while the others are less important. Table 2 indicates the role that these restrictions and configuration parameters play in choosing a route that meets the expectations of users of a particular category.

### PROPOSED GOAL FUNCTION

It was assumed that the route depends on human decisions, taking into account existing or anticipated situations. Human decisions can be taken into account by using configuration parameters ( $P_1, P_2, P_3$ ) and restrictions introduced in advance ( $O_1, O_2, \dots, O_3$ ). The situations encountered in turn describe the discomfort coefficients ( $\gamma_1, \dots, \gamma_6$ ). The basic categories of travel discomfort for a sailing vessel include too abrupt manoeuvres of the vessel, too much rocking of the vessel, too strong heel of the vessel and too large and too small wind angles. Any discomfort encountered affects the end result of the goal function. The route will therefore be a function of these quantities (7).

$$\text{Route} = f_g(O_1, O_2, \dots, O_5, P_1, P_2, P_3, \gamma_1, \dots, \gamma_6) \quad (7)$$

Each  $i$ -th discomfort can last  $\tau(i)$  time, as a result of which it increases the value of the goal function. Taking into account the adopted restrictions and configuration parameters, it can be considered that the goal function is as shown below (8).

$$f_g = t(\text{Route}) + \sum_{p=1}^5 \tau_p \cdot \gamma_p \quad (8)$$

where:

$\tau_p$  – total cost associated with taking the  $p$ -th discomfort into account.

Restrictions and configuration parameters and travel discomfort are input arguments for the objective function that affect its result. It is worth noting that O1 and O3 are restrictions that increase the cost of passing between route points. For example, in Tab. 2 “O1 = •” marks the additional cost of the function during each course change (the greater the change in course, the greater the cost). What is more, “O1 = ••” and “O1 = •••” mean a greater cost for each degree of change in course. On the other hand, O2, O4 and O5 do not allow certain connections between points in this discrete model due to limitations: as to the maximum value of the

course change, as to the maximum roll, or the maximum wind attack. In these cases, the greater the number of dots, the greater the number of inaccessible connections between points in this discrete model. As another input argument of function, the configuration parameters P1, P2, P3 increase or decrease the number of points or connections in this discrete model. With these parameters, we can increase the accuracy of the route we are looking for, but this also increases the necessary computing power.

When searching for the optimal route, we may encounter travel discomfort (if it is included as a function input parameter), which causes additional costs for the destination function. The value of the objective function is also influenced by travel discomfort. During the search for the optimal route, we encounter one of the discomforts of travel, which causes additional costs for the objective function.

Simulation studies were limited to the following categories of discomfort: violent manoeuvres, strong roll, and excessive or small angles of wind attack during travel.

### SAILING ASSISTANCE APPLICATION AS A TEST ENVIRONMENT

Simulation tests are carried out in a specially prepared test environment, called the Sailing Assistance application. The application consists of three layers (Data, Routing Algorithm, Route Visualisation), which allows independent development of each layer.

Route Visualisation		
Routing Algorithm		
Optimisation criteria	User requirements	Restrictions
Data		
Ship characteristics	Shipping conditions	Sailing area

Fig. 7. Sailing assistance application

The user interface of the Sailing Assistance application enables the configuration of parameters such as: selection of the number of allowable directions of movement (8, 16, 32); selection of the starting point  $P_s$  and ending  $P_F$  in a defined rectangular area; determination of granularity, density of  $P_k$  points (low, high); selection of a sailing vessel from the list of available vessels (Conrad, Oceania); taking into account the comfort factor when calculating the route (yes / no); taking into account the additional time needed to change the course (0s / deg, 1s / deg, ..., 16s / deg); taking into account the limit of the value of a one-off exchange rate change (20, 30, 40, ..., 360); taking into account the minimum wind angle (20, 30, ..., 60).

## RESULTS

During the simulation, the preferences of 4 categories of users were taken into account: recreational cruises, seeking extreme sensations, beginner sailors, and steering unmanned sailing ships. For these users, the parameter settings in the Sailing Assistance application are given in Table 2. The simulation tests were carried out in three series.

Each series includes a different start and end position. During the simulation, constant wind conditions were assumed for the entire area covered by the algorithm analysis. Changing wind conditions are included in another article by the author [17]. The results of optimal routes according to the criteria of specific categories of users are shown in Table 3, while route visualisations are presented in Figs. 9-20.

Tab. 1. Results of the simulation study

Stable navigation conditions: wind direction N, wind strength 12m / s.						
User name	Time	Distance	Goal function value	Number of direction changes	Number of points $P_k$	Route number (figure number)
	[min]	[Nm]				
Series 1 $\varphi_p = 55.14^\circ \text{ N}, \lambda_p = 20.66^\circ \text{ E}$			$\varphi_k = 54.10 \text{ N}, \lambda_k = 14.36^\circ \text{ E}$			
Recreational cruises	1931	240	6510	3	475	1 (Fig. 9)
Beginner sailors	2928	264	5980	9	303	2 (Fig. 10)
Seeking extreme sensations	1851	234	1851	3	1522	3 (Fig. 11)
Unmanned ship	1920	240	1920	3	475	4 (Fig. 12)
Series 2 $\varphi_p = 54.49^\circ \text{ N}, \lambda_p = 20.66^\circ \text{ E}$			$\varphi_k = 55.94 \text{ N}, \lambda_k = 14.36^\circ \text{ E}$			
Recreational cruises	2130	189	8457	4	247	5 (Fig. 13)
Beginner sailors	2374	202	8259	7	221	6 (Fig. 14)
Seeking extreme sensations	1656	175	1656	3	551	7 (Fig. 15)
Unmanned ship	2014	183	2014	3	269	8 (Fig. 16)
Series 3 $\varphi_p = 55.13^\circ \text{ N}, \lambda_p = 14.17^\circ \text{ E}$			$\varphi_k = 54.55 \text{ N}, \lambda_k = 19.65^\circ \text{ E}$			
Recreational cruises	2105	229	6223	6	336	9 (Fig. 17)
Beginner sailors	2361	244	6002	4	262	10 (Fig. 18)
Seeking extreme sensations	1564	198	1564	23	1555	11 (Fig. 19)
Unmanned ship	1602	201	1602	8	442	12 (Fig. 20)

### Simulations for Series 1.

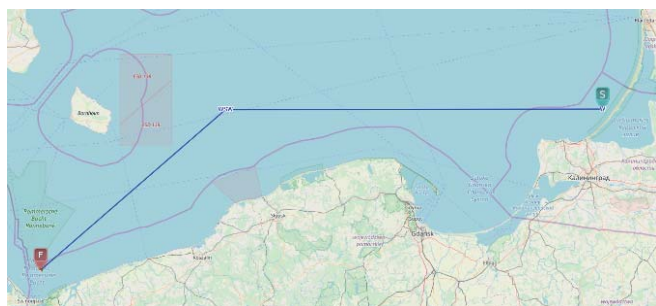


Fig. 8. Route number 1, recreational cruises

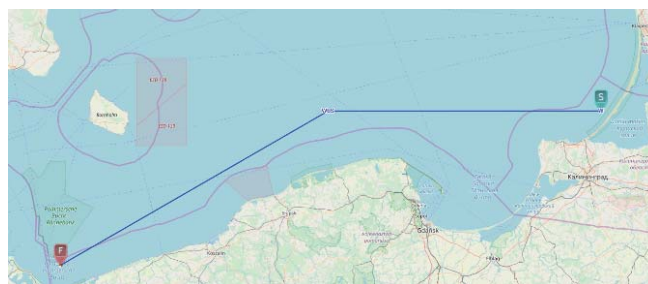


Fig. 10. Route number 3, seeking extreme sensations

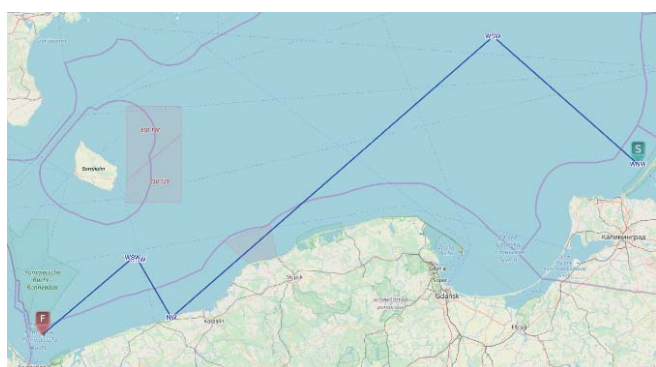


Fig. 9. Route number 2, beginner sailors



Fig. 11. Route number 4, steering unmanned sailing ships

### Simulations for Series 2.

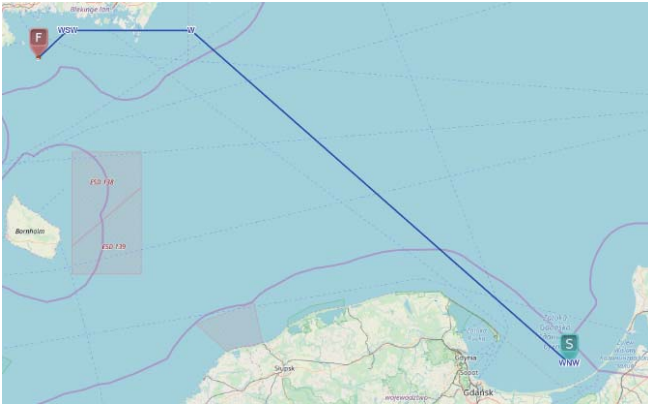


Fig. 12. Route number 5, recreational cruises

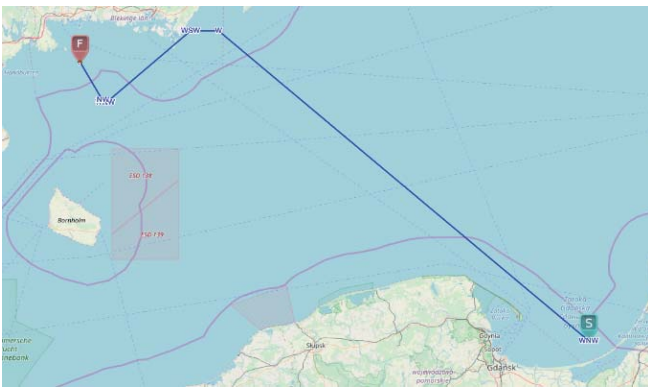


Fig. 13. Route number 6, beginner sailors

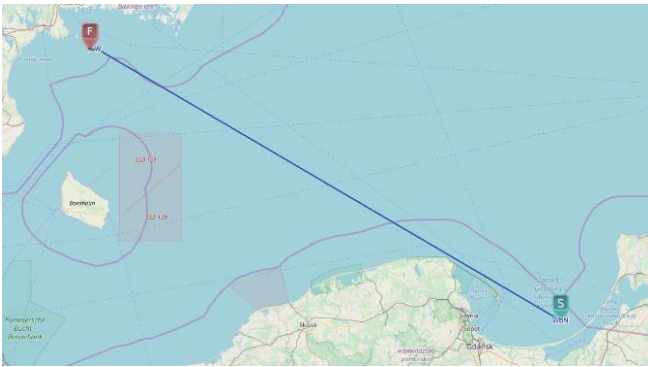


Fig. 14. Route number 7, seeking extreme sensations

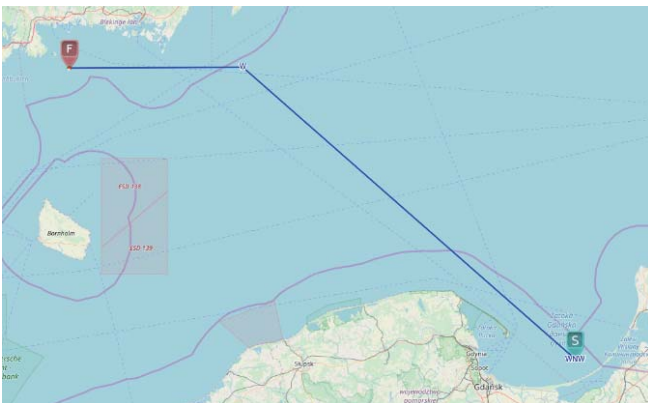


Fig. 15. Route number 8, steering unmanned sailing ships

### Simulations for Series 3.



Fig. 16. Route number 9, recreational cruises



Fig. 17. Route number 10, beginner sailors



Fig. 18. Route number 11, seeking extreme sensations



Fig. 19. Route number 12, steering unmanned sailing ships

## DISCUSSION

Table 3 presents the results of users as well as their restrictions and configuration parameters. The largest values in a given series are marked in red font. The lowest values in a given series are marked in bold. As Table 3 shows, in the research series carried out, seeking extreme sensations obtained the lowest values of travel time, distance and goal function values. For this user, the optimal route search

algorithm included the fewest restrictions (only 3 dots for O1, O4 and O5). This user needed the most  $P_k$  points to complete the route. This results from the fact that it uses the highest accuracy of route search (4 dots for parameters P1 and P3). The highest values of travel time, distance and goal function values were obtained by beginner sailors, and recreational cruises, because these users had the most restrictions.

possible. This user selects favourable travel conditions, and his route is devoid of turns and inclinations exceeding the set values.

Users seeking extreme sensations, in turn, count on the maximum speed of sailing, while accepting a lower level of safety. During the test, this user obtained the fastest time and the shortest route. It was not important for him to limit the number of manoeuvres, or the number of changes in

Tab. 3. User restrictions and configuration parameters and results

Restriction and configuration parameter User category	O1 number of manoeuvres	O2 permissible angle of change	O3 number of tack changes	O4 roll value	O5 attack on the wind	P1 traffic directions	P2 weather forecasts	P3 the grain size		time	distance	value	direction changes	points $P_k$
Recreational cruises	••	•	•••	••	••	•	•	•	Series1	1931	240	6510	3	475
									Series2	2130	189	8475	4	247
									Series3	2105	229	6223	6	336
Beginner sailors		•	•	•	••	•	••	•	Series1	2928	264	5980	9	303
									Series2	2374	202	8259	7	221
									Series3	2361	244	6002	4	262
Seeking extreme sensations		•		•	•	••		••	Series1	1851	234	1851	3	1522
									Series2	1656	175	1656	3	551
									Series3	1564	198	1564	23	1555
Unmanned ship	•	•	•	••	••	•	•	•	Series1	1920	240	1920	3	475
									Series2	2014	183	2014	3	269
									Series3	1602	201	1602	8	442

## CONCLUSIONS

The simulation study presented was based on the multi-criteria method of selecting the optimal route discussed for different categories of users. The simulation results allow one to observe visible differences in both the route and its time and length. It should be emphasised that travel time was not always the most important criterion. We observe the minimisation of travel time in the case of users seeking extreme experiences, and this is a factor much less important in the case of other categories of users. This is due to different user preferences.

For cruise users, travel comfort is as important as the minimum travel time, as it has a large effect on the overall satisfaction of passengers. In the study presented, this recreational cruiser made the fewest turns and avoided unnecessary roll when sailing, which extended its travel time.

The beginner sailor in all series obtained the longest travel time from all categories of users. He made the most course changes in order to avoid large course changes and run with a large roll. For this user, a route with a minimum travel time was therefore not the priority. In this case, the most important criterion for route planning was the safety resulting from favorable navigation conditions and as few manoeuvres as

inclination during travel, which significantly affects the comfort of travel.

As for the unmanned sailing ship, it is important to maintain its navigation capability from the beginning to the end of the route. Great emphasis is placed on safety. This means that the ship must reach its destination while maintaining a high level of security. During the study, this user made relatively few turns and did not choose the route with the shortest travel time. For this category of users, the route is determined by restrictions specifying the permissible amount of heel and the permissible angle of the ship's wind attack.

The presented study was to determine the optimal route for various categories of users by adopting a multi-criteria approach. Depending on different user requirements, the method allows different sequences of travel points to be obtained for identical input data. In each case, the proposed route is adapted to the user's navigation preferences, which is proof of both the usability and universality of the adopted method.

## REFERENCES

1. Dębski, R.: An adaptive multi-spline refinement algorithm in simulation based sailboat trajectory optimization using onboard multi-core computer systems, Int. J. Appl. Math. Comput. Sci. 26 (2016) 351–365.

2. Goldberg, A. V: Point-to-Point Shortest Path Algorithms with Preprocessing, in: LNCS 4362 - SOFSEM 2007 Theory Pract. Comput. Sci., 2007.
3. Krata, P., J. Szłapczyńska: Weather Hazard Avoidance in Modeling Safety of Motor-Driven Ship for Multicriteria Weather Routing, *TransNav*. 6 (2012) 71–78.
4. Ladany, S.P., O. Levi: Search for optimal sailing policy, *Eur. J. Oper. Res.* 260 (2017) 222–231.
5. Lisowski, J.: The Sensitivity of State Differential Game Vessel Traffic Model, *Polish Marit. Res.* 23 (2016) 14–18.
6. Mannarini, G., G. Coppini, P. Oddo, N. Pinardi: A Prototype of Ship Routing Decision Support System for an Operational Oceanographic Service, *TransNav, Int. J. Mar. Navig. Saf. Sea Transp.* 7 (2013) 53–59.
7. Maury, M.F.: *The Physical Geography of the Sea and Its Meteorology*, Harper Bros, New York, 1855.
8. Neumann, T.: The shortest path problem with uncertain information in transport networks, in: *Commun. Comput. Inf. Sci.*, Springer, Cham, 2016: pp. 475–486.
9. Szłapczyńska, J., R. Szłapczyński: Preference-based evolutionary multi-objective optimization in ship weather routing, *Appl. Soft Comput.* 84 (2019) 105742.
10. Szłapczyński, R.: Evolutionary Sets of Safe Ship Trajectories : Evaluation of Individuals, *Int. J. Mar. Navig. Saf. Sea Transp.* 6 (2012) 345–353.
11. Szłapczyński, R.: Evolutionary Planning of Safe Ship Tracks in Restricted Visibility, *J. Navig.* 68 (2015) 39–51.
12. Szłapczyński, R., J. Szłapczyńska: A method of determining and visualizing safe motion parameters of a ship navigating in restricted waters, *Ocean Eng.* 129 (2017) 363–373.
13. Tagliaferri, F., I.M. Viola: A real-time strategy-decision program for sailing yacht races, (2017).
14. Vettor, R., C.G. Soares: Development of a ship weather routing system, *Ocean Eng.* 123 (2016) 1–14.
15. Wrobel, K., P. Krata, J. Montewka, T. Hinz: Towards the Development of a Risk Model for Unmanned Vessels Design and Operations, *TransNav, Int. J. Mar. Navig. Saf. Sea Transp.* 10 (2016) 267–274.
16. Życzkowska, K.: Uniqueness or Uniformity - Studies of Media Architecture, *IOP Conf. Ser. Mater. Sci. Eng.* 471 (2019) 072040.
17. Życzkowski, M.: Sailing Vessel Routing Considering Safety Zone and Penalty Time for Altering Course, *TransNav, Int. J. Mar. Navig. Saf. Sea Transp.* 11 (2017) 49–54.
18. Życzkowski, M.: Method of routing ships sailing in dedicated environment, *Annu. Navig.* 24 (2017) 147–159.
19. Życzkowski, M., P. Krata, R. Szłapczyński: Multi-objective weather routing of sailboats considering wave resistance, *Polish Marit. Res.* 25 (2018) 4–12.
20. Życzkowski, M., R. Szłapczyński: Multi-objective weather routing of sailing vessels, *Polish Marit. Res.* 24 (2017) 10–17.

#### CONTACT WITH THE AUTHOR

**Marcin Życzkowski**  
*e-mail: marzyczk@pg.edu.pl*

Gdańsk University of Technology  
 11/12 Gabriela Narutowicza Street  
 80-233 Gdańsk  
**POLAND**

# HYDRODYNAMIC MODEL OF THE NEW WATERWAY THROUGH THE VISTULA SPIT

Michał Szydłowski  
Tomasz Kolerski  
Gdańsk University of Technology, Poland

## ABSTRACT

The decision to build a new waterway (strait) in the Polish part of the Vistula Spit was made in 2017. The new connection between the Gulf of Gdańsk and the Vistula Lagoon is planned as an artificial navigable channel with a lock and a small port. During storm surges and wind tides in the gulf or in the lagoon, sluicing will be required for vessels to tackle the Vistula Spit. This procedure does not require significant water flow through the channel in normal conditions. However, in the case of a lock failure or in the case of controlled opening of the gate to increase water exchange in the lagoon or to reduce flood risk in the Vistula Lagoon, high flow rates may occur in the navigable channel and in the neighboring port basin. In order to investigate the hydraulic conditions in such extraordinary situations, numerical modeling of the hydrodynamics during water damming in the gulf or in the lagoon is performed. To analyze the hydrodynamics of the artificial connection between the sea and the lagoon during periods of high water stages, mathematical modeling is required. This paper presents the shallow water equations (SWE) model adapted to simulate the flow through the port basin and the navigable channel. The calculations allowed the relation between the water head and the capacity of the navigable channel to be found, as well as to analyze circulations which may occur in the port basin.

**Keywords:** navigable canal, waterway, Vistula Spit, Vistula Lagoon, hydrodynamics, mathematical modeling

## INTRODUCTION

The Vistula Lagoon is located in the east part of the Gulf of Gdańsk (Baltic Sea) (Fig. 1). The lagoon represents a transboundary water body divided into two parts by the country border between Poland and Russia. The length of the lagoon is 90.7 km, and its width varies from almost 6 km up to 13 km. The lagoon is a shallow basin with a mean depth of about 2.75 m. It is separated from the Gulf of Gdańsk by the Vistula Spit. The length of the spit is 65 km. The only connection between the Vistula Lagoon and the Baltic Sea is through the Strait of Baltiysk (located in the Russian part of the lagoon), which is 2 km long, 440 m wide and approximately 8.8 m deep. The total area of the lagoon measures 838 km<sup>2</sup>, of which 472.5 km<sup>2</sup> belongs to Russia. The shoreline is 270 km long [1] [2].

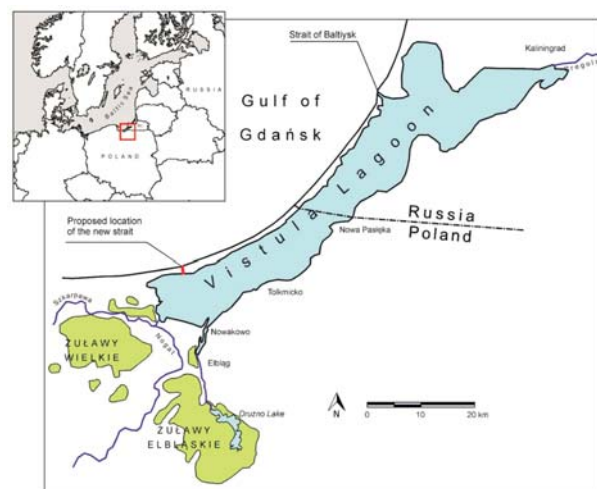


Fig. 1. Location of the Vistula Lagoon and the new strait

Hydraulic conditions in the Vistula Lagoon are usually the result of variations in the sea level in the Gulf of Gdańsk and the wind action on the water surface of the lagoon [1] [3] [4]. When the water stage of the Gulf of Gdańsk rises, a difference in sea level occurs in relation to the lagoon. This results in a strong water current through the Strait of Baltiysk directed into the lagoon. A decrease in the water table in the Baltic Sea causes the lagoon water to flow into the sea, creating a strong current in the strait in the opposite direction. The long-lasting damming of water in the southern part of the lagoon can be a cause of flood risk for the lowland areas of Żuławy Elbląskie [5] [6].

Currently, the project [7] of a new strait connecting the Baltic Sea with the Vistula Lagoon is in progress. Similar investments are known in the world [8], but each of them is different and requires individual political, economic and technical analysis. This work focuses solely on the hydraulic aspects of the issue. Over the years, the idea of a Polish strait was often revived [9] [10], and the final decision to build this hydro-engineering structure was made in 2017. Nowy Świat was chosen as the location (Fig. 1) for the new navigable channel. The aim of the project is to significantly shorten the waterway from the Polish port of Elbląg to the Baltic Sea. Moreover, due to the possibility of opening the channel for outflowing water in case of the accumulation and rise of water in the southern part of the Vistula Lagoon, the flood risk for the polders of the lowland areas of Żuławy Elbląskie can potentially be limited [11]. This problem was analyzed in detail in [5], but in this paper only the local impact of the investment on water flow dynamics around the new artificial strait is considered. Additionally, the opening of the channel can be used to force the flow from the gulf to the lagoon to exchange the water in the basin and to improve the quality of water in the Polish part of the lagoon.

The new strait project is currently being implemented. The basic elements of the waterway include the construction of a navigable channel through the Vistula Spit, the construction of a fairway from the mouth of the Elbląg Bay to the channel, an artificial island in the Vistula Lagoon, breakwaters at the entrances to the navigable channel, and a small port in the Gulf of Gdańsk. Under normal conditions, the water flow through the port and the navigable channel will be controlled and limited by the operation of a lock located in the navigable channel. In accordance with the project, the lock will only be open for navigational purposes, and thus the flow exchange will be limited to the amount filled in the lock chamber. However, in exceptional situations, such as a lock failure, damage to (breaking of) the gates, the emergency opening of the gates during flooding at Żuławy Elbląskie or controlled opening to exchange the water in the lagoon, high discharges of water flow can be expected in the navigable channel. The flow dynamics (flow rate, velocity, profile of the water table, direction of currents) will depend on the actual difference in water levels in the gulf and in the lagoon and on the geometry (shape) of the breakwaters, the navigable channel and the lock.

The main purpose of the work is to find the hydraulic characteristics of the new navigable channel together with

some hydro-engineering structures like the breakwaters and port basin. The basic characteristics should include elements such as possible flow rates and velocities in the navigable channel, the water surface profile along the channel and the structure of water circulations in the port basin. In order to investigate the dynamics of the water flow through the port, the navigable channel and at the areas near the breakwaters located in the Gulf of Gdańsk and in the Vistula Lagoon, numerical simulations are needed. This paper presents the mathematical modeling of the hydrodynamics of the artificial strait in the Vistula Spit, based on the solution of shallow water equations (SWE) by the finite volume method (FVM) [12] considering the different water levels in the Gulf of Gdańsk and the Vistula Lagoon.

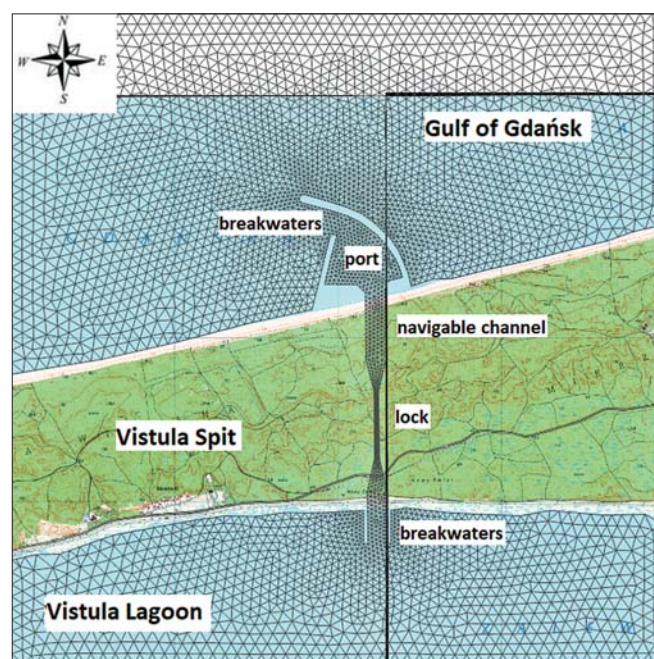


Fig. 2. Schematic geometry of the new waterway and numerical mesh of the flow area (image prepared by the authors on the basis of the <https://www.geoportal.gov.pl/map> and waterway project [7], area 4 km × 4 km without scale)

## MATERIALS AND METHODS

### DATA

The new waterway design was conceived in 2017 by two companies – Mosty Gdańsk Ltd. and Projmors Biuro Projektów Budownictwa Morski Ltd. [7]. Full information about the project is public and can be found on <https://www.umgdy.gov.pl/>. All data necessary to perform the calculations were taken from this project.

### STUDY AREA

Nowy Świat and its surroundings was the chosen location for the channel (Fig. 1 and Fig. 2). The course of the navigable channel is along a North–South direction. The approximate location of the axis of the channel, in the Poland CS92 system,

is at coordinate  $x = 520235$ . The length of the channel from the northern shoreline to the end of the southern breakwaters is 1,515 m. The channel has a basic width of 90 m, and it narrows to 25 m in the lock area (420 m long). The channel stretches from coordinate  $y = 720760$  (Vistula Lagoon) to  $y = 722275$  (Gulf of Gdańsk). The northern breakwater of the port on the Gulf of Gdańsk reaches the coordinate  $y = 722880$ . The flat bottom of the channel and the port is located at  $-5.0$  m above sea level.

## HYDRAULIC ASPECTS OF THE NEW STRAIT

The new strait (Fig. 2) in the land area is composed of an artificial open channel of rectangular cross-section and a constriction (local restriction of the channel cross-section) in the lock segment. The one-dimensional hydraulic theory of flow through such a non-prismatic channel was described by Chow [13]. The impact of the constriction on the water flow depends mainly on the channel geometry, the flow rate and the regime of flow, which can be sub- or supercritical. In channels with mild slopes, the flow is usually subcritical. If the narrowing is local (short), the obstruction induces a backwater effect that may extend over a long distance upstream, and the flow is subcritical along the constriction and the downstream channel. But if the constriction is sufficiently long, it forms a narrow channel. This can mean that the minimum of specific-energy rises in the constriction section corresponds to the critical water stage. Such a situation results in a supercritical flow occurring in the narrow part of the channel, which can be returned to normal conditions (subcritical flow) by the formation of a hydraulic jump.

Different effects can be observed in steep slope channels for supercritical flow conditions. When a flow is supercritical, the constriction disturbs only the water surface that is adjacent to the upstream side of the constriction. If the constriction is local, only the water surface close to the constriction is disturbed and the effect does not extend farther upstream. If the constriction is long, it can make the depth upstream of the constriction greater than the critical depth due to the need to increase the specific energy upstream of the obstruction. This makes the flow subcritical in this channel section and requires the formation of a hydraulic jump.

The theoretical one-dimensional description of the influence of the channel constriction provides only information about averaged flow parameters along the channel. In the current study, a more complex analysis of the flow structure in the navigable channel, lock, port basin and flow area around the breakwaters is proposed. Therefore, multidimensional hydrodynamics modeling must be implemented to solve the problem. In the case of the designed navigable channel, the bottom is horizontal, so the flow is determined only by the hydraulic conditions (water stages) in the Gulf of Gdańsk and in the Vistula Lagoon. The flow parameters along the waterway depend on the actual difference (water head) between the water surface elevation in the gulf and the lagoon. In this study, numerical simulations were performed for various water heads, which cover the possible hydrological

conditions observed in this region. In the vicinity of the new navigable channel, SW winds can cause a rise in the water level in the Gulf of Gdańsk and in the Vistula Lagoon of even 0.8 m asl. However, NE winds in particular cause a dangerous water level rise in the southern part of the Vistula Lagoon. For long periods of strong NE winds, a rise in the water level exceeding +1.0 m and in extremes reaching +1.5 m asl can be observed [1] [5].

## MATHEMATICAL MODEL AND SOLUTION METHOD

The problem of how complex a model is needed to mathematically describe the hydrodynamics depends on the aim of the numerical simulation. Simplified models [14] [15] can be applied in cases of horizontal water flow with limited water stage changes. If a strong variation in flow parameters is expected, fully hydrodynamic models should be used [16]. Many mathematical models of the Vistula Lagoon have been developed over the last decades, including two-dimensional (2D) hydrodynamic models [5] [4] [17], 2D models composed of hydrodynamics, water quality and eutrophication models [18] [19] [20], and recently developed three-dimensional models used for sediment transport and migration [21] [22]. However, the complex hydrodynamics inside the planned waterway through the Vistula Spit have not been simulated so far.

In the current study, the water flow is investigated by applying the SWE two-dimensional hydrodynamic model. The system of shallow water equations in conservation form [23] can be written as:

$$\frac{\partial \mathbf{U}}{\partial t} + \frac{\partial \mathbf{E}}{\partial x} + \frac{\partial \mathbf{G}}{\partial y} + \mathbf{S} = 0 \quad (1)$$

where

$$\mathbf{U} = \begin{bmatrix} h \\ uh \\ vh \end{bmatrix}, \quad \mathbf{S} = \begin{bmatrix} 0 \\ -gh(S_{ox} - S_{fx}) \\ -gh(S_{oy} - S_{fy}) \end{bmatrix} \quad (2A, B)$$

$$\mathbf{E} = \begin{bmatrix} uh \\ u^2h + 0.5gh^2 \\ uvh \end{bmatrix}, \quad \mathbf{G} = \begin{bmatrix} vh \\ uvh \\ v^2h + 0.5gh^2 \end{bmatrix} \quad (2C, D)$$

In this system of equations,  $h$  represents water depth,  $u$  and  $v$  are the depth-averaged components of velocity in  $x$  and  $y$  directions, respectively,  $S_{ox}$  and  $S_{oy}$  denote the bed slope terms,  $S_{fx}$  and  $S_{fy}$  are the bottom friction terms defined by the Manning formula [13], and  $g$  is the acceleration due to gravity. Equation (1) can be written in another form:

$$\frac{\partial \mathbf{U}}{\partial t} + \text{div} \mathbf{F} + \mathbf{S} = 0 \quad (3)$$

where, assuming unit vector  $\mathbf{n} = (n_x, n_y)^T$ , the vector  $\mathbf{F}$  is defined as  $\mathbf{F} = \mathbf{E}n_x + \mathbf{G}n_y$ .

In order to integrate the SWE in space using the finite volume method, the calculation domain is discretized into set of triangular cells (Fig. 3).

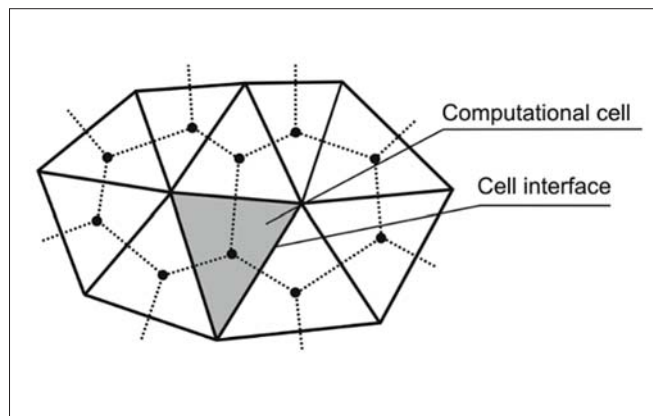


Fig. 3. Triangular computational cells for FVM

After the integration and substitution of integrals by corresponding sums, equation (3) can be rewritten as

$$\frac{\partial U}{\partial t} \Delta A_i + \sum_{r=1}^3 (\mathbf{F}_r \mathbf{n}_r) \Delta L_r + \sum_{r=1}^3 \mathbf{S}_r \Delta A_r = 0 \quad (4)$$

where  $\mathbf{F}_r$  is the numerical flux of mass or momentum, and  $\Delta L_r$  represents the cell-interface length.  $\mathbf{S}_r$  and  $\Delta A_r$  are the components of source terms and the area of cell  $i$  assigned to the  $r^{\text{th}}$  cell-interface. In order to calculate the fluxes  $\mathbf{F}_r$ , the solution of the approximated Riemann problem was used. A full description of the method was presented in [12]. The numerical algorithm was complemented by a two-stage explicit scheme of time integration. The model had already been verified for the rapidly varied free surface flow by a comparison of the computed results with measurements carried out in an experimental channel at the hydraulic lab [24] [25] [26]. The model was also applied to simulate some unique case studies, such as water flow in artificial channels like slides [24] and whitewater courses [27], as well as to investigate some field problems like urban and catastrophic floods [16] [28] and river flows influenced by hydro-engineering structures [29]. Reliable results of the performed simulations confirmed the possibility of using the developed model for a numerical simulation of flow through the designed elements of the waterway, i.e. the breakwaters, port basin, and navigable channel and lock.

## NUMERICAL SIMULATIONS AND DISCUSSION OF THE RESULTS

In order to simulate two-dimensional water flow in the area of the Gulf of Gdańsk, the Vistula Lagoon and the waterway through the Vistula Spit using FVM, the real geometry of the water area had to be transformed

into a numerical mesh. Because only the local problem of flow in the waterway is considered in this study, the computational domain is limited to a 16 km<sup>2</sup> square area. The 4 km × 4 km flow domain, containing parts of the Gulf of Gdańsk and the Vistula Lagoon, was covered by a mesh of triangles composed of 8,312 computational cells (Fig. 2). The lengths of the sides of the triangles were variable in a range from 5 m in the lock segment, 25 m in the navigable channel, and up to 75 m at the open boundaries of the gulf and the lagoon.

Boundary conditions were imposed in accordance with the geometry of the flow area. The vertical walls of the navigable channel and lock were treated as closed boundaries, and the free-slip condition was enforced there. In the same way (as the land boundaries), the breakwaters, the quays and the shoreline were represented in the numerical model of the waterway. As the model domain was extended into the Gulf of Gdańsk and the Vistula Lagoon, the open (water) boundaries were located there.

The goal of performing the numerical simulations was to determine the basic flow characteristics (current direction, flow rate and velocity, water surface profile) in a hypothetically open navigable channel for specified conditions in the Gulf of Gdańsk and the Vistula Lagoon. Steady conditions were assumed in both basins. They were forced by constant water stages at the open boundaries of the flow area. It was assumed that in each simulation the lower elevation of the water surface corresponds to the average sea state (0.0 m asl). The values of 0.05, 0.10, 0.25, 0.50, 0.75 and 1.0 m were selected as examples of the difference in the water stages in the gulf and the lagoon.

Each flow simulation was performed starting from the hydrostatic state, assuming that the closed lock gate separates two water bodies, each with a different (assumed) elevation of the water surface. Then the gate was fully opened, which allowed water to flow through the channel in a direction depending on the initial position of the water surface. The calculations were carried out for permanent boundary conditions, forcing the initial elevations of the water surface at the open boundaries (gulf and lagoon). At the same time, the free flow of water across these borders was ensured. The constant-in-time water surface elevations at the gulf and the lagoon allowed a steady state to be reached, which was the final solution.

The two-dimensional flow modeling allowed the velocity field in the area of the navigable channel to be mapped. Figures 4 and 5 show the distribution of velocity vector module for the largest assumed difference in water levels (1.0 m), respectively for the flow from the Gulf of Gdańsk to the Vistula Lagoon and in the opposite direction. The navigable channel hydraulics, created under such flow conditions, resemble the flow in a Venturi channel [13]. There is a strong increase in the flow velocity in the narrow part of the channel (lock), which, regardless of the flow direction, reaches almost 5 m/s.

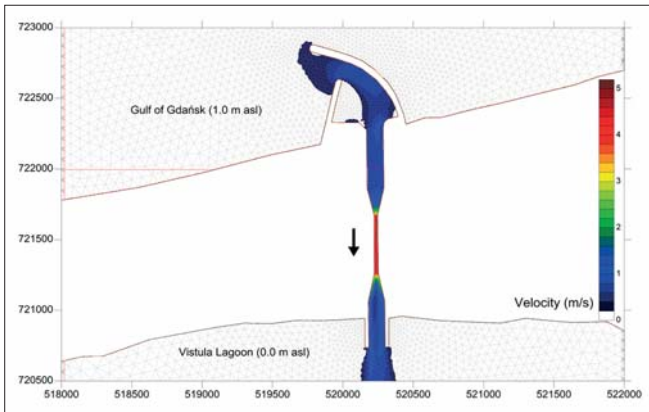


Fig. 4. Velocity vector module – flow direction from the Gulf of Gdańsk to the Vistula Lagoon

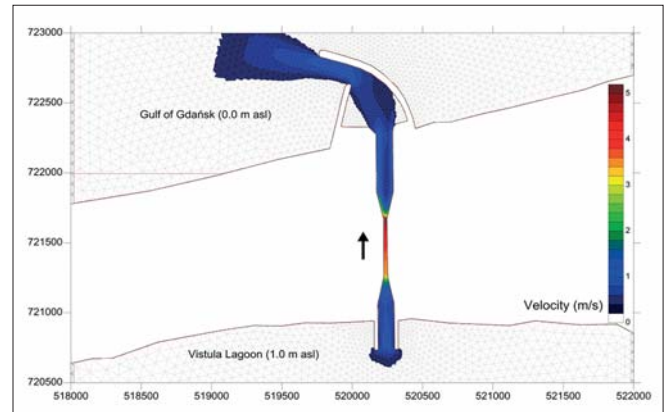


Fig. 5. Velocity vector module – flow direction from the Vistula Lagoon to the Gulf of Gdańsk

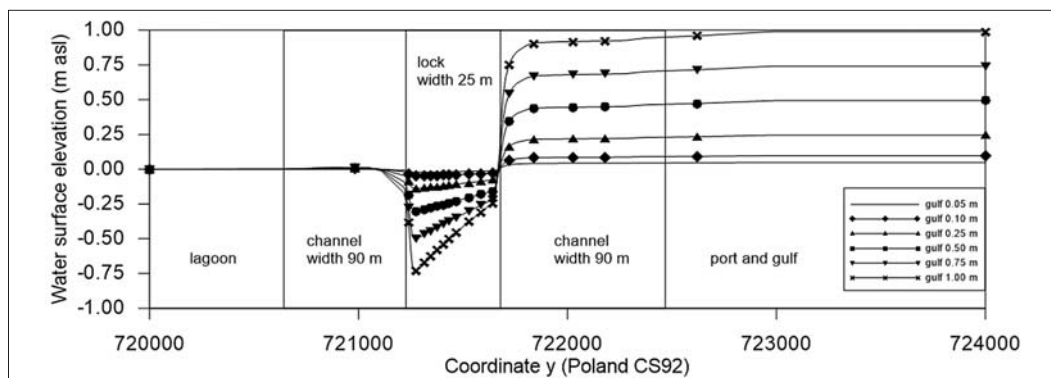


Fig. 6. Profiles of the water surface along the axis of the navigable channel (90 m wide) and lock (25 m wide) during the flow from the Gulf of Gdańsk to the Vistula Lagoon

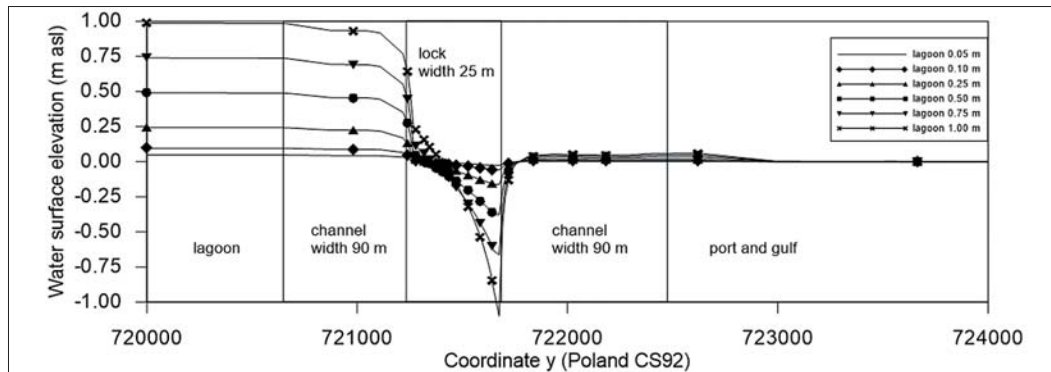


Fig. 7. Profiles of the water surface along the axis of the navigable channel (90 m wide) and lock (25 m wide) during the flow from the Vistula Lagoon to the Gulf of Gdańsk

There is a significant decrease in the water surface level at the same place in the lock. Figures 6 and 7 show the 4 km long water surface profiles along the coordinate  $x = 520235$  (navigable channel axis). The drawings show the basic section of the channel, where the channel is 90 m wide, and the channel constriction (lock), which is 25 m wide. The water table elevation in this region reaches a level below the initial position of the water surface. Such a hydraulic phenomenon is often observed for flows through channel constrictions [13].

As can be seen in the charts, the elevation of the water surface along the narrow part of the channel, in the case of the largest difference of water levels in the gulf and the lagoon, is

significantly reduced, by a maximum of about 0.75 m, when water flows from the gulf to the lagoon, and by over 1.0 m for the opposite flow direction. This is accompanied by a significant increase in the flow velocity, as seen in Figs. 4 and 5. If smaller differences in water levels exist in both basins, the water surface depression in the lock is also relatively smaller.

Despite the strong depression in the water surface and the considerable increase in velocity in the navigable channel and the lock, a supercritical flow was not observed there in the performed simulations and no hydraulic jump was formed in the channel. However, the flow was almost critical (with the Froude number [13] close to unity) when the largest difference in water surface levels was modeled.

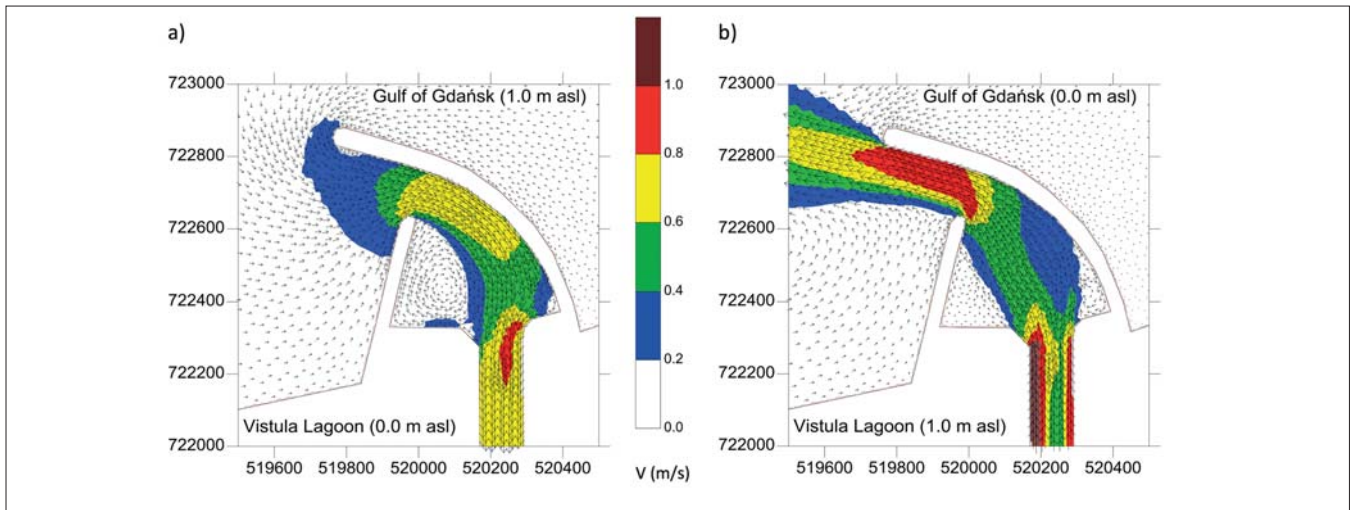


Fig. 8. The velocity vectors in the area of the port in the Gulf of Gdańsk forced by the flow from the Gulf of Gdańsk to the Vistula Lagoon (a) and in the opposite direction (b)

Details of the spatial distribution of the velocity field and the current directions can be investigated using the simulation results. Figure 8 shows the velocity vectors in the area of the port in the Gulf of Gdańsk for two flow directions. In the case of flow from the gulf to the lagoon (Fig. 8a), the velocities increase between the western and northern breakwaters. In the area of the western breakwater and the southern quay, a single circulation of low velocity is formed filling the entire area, while the mainstream runs along the northeastern breakwater.

In the case of flow from the lagoon to the gulf (Fig. 8b), just near the channel outlet to the port basin, two circulations are formed at both breakwaters, and the mainstream is located in the middle of the port basin. Due to local stream expansion, the velocity in the pool decreases slightly to increase again in the narrow area between the breakwater heads.

As can be seen from the results, for both flow directions, strong currents and large eddies may occur in the port basin. Such a situation may be dangerous and undesirable for all vessels in the waterway and ships anchoring at the quays.

Finally, the numerical simulations allowed the values of the flow rates in the navigable channel to be determined for the adopted range of water stages. The calculated results, obtained for the assumed water heads (differences in water surface elevation in the gulf and the lagoon), were collected in Tables 1 and 2. Figures 9a and 9b show the flow rate curves (relation between the water head and flow rate) respectively in the case of flow from the gulf to the lagoon and in the opposite direction.

Regardless of the direction of flow, the flow rate curves are similar to each other. Some small discrepancies in the

Tab. 1. Hydraulic parameters of the navigable channel for the flow from the Gulf of Gdańsk to the Vistula Lagoon (water level in the lagoon 0.0 m asl)

Water level in the gulf (m asl)	Maximum velocity (m/s)	Minimum depth (m)	Flow rate (m <sup>3</sup> /s)	Froude number Fr (-)
0.05	0.92	4.99	114.77	0.13
0.10	1.33	4.97	165.25	0.19
0.25	2.15	4.92	264.45	0.31
0.50	3.06	4.86	371.79	0.44
0.75	3.75	4.79	449.06	0.55
1.00	4.34	4.27	463.30	0.67

Tab. 2. Hydraulic parameters of the navigable channel for the flow from the Vistula Lagoon to the Gulf of Gdańsk (water level in the gulf 0.0 m asl)

Water level in the lagoon (m asl)	Maximum velocity (m/s)	Minimum depth (m)	Flow rate (m <sup>3</sup> /s)	Froude number Fr (-)
0.05	0.91	4.97	113.07	0.13
0.10	1.32	4.94	163.02	0.19
0.25	2.16	4.83	260.82	0.31
0.50	3.05	4.62	352.28	0.45
0.75	4.10	4.36	446.90	0.63
1.00	5.01	3.90	488.48	0.81

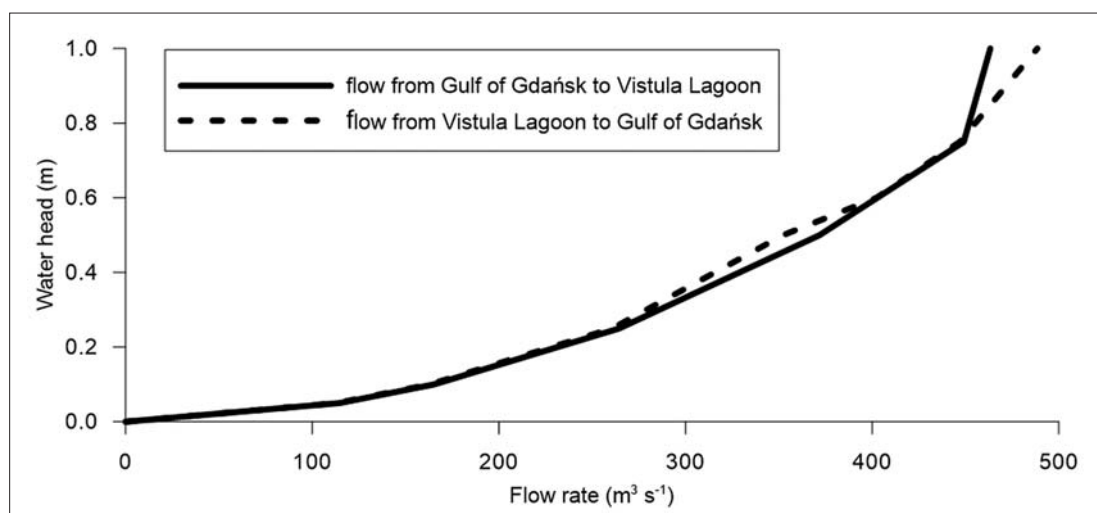


Fig. 9. Flow rate curves for the flow in the navigable channel from the Gulf of Gdańsk to the Vistula Lagoon and in the opposite direction

relations are the result of differences in the channel geometry in the northern and southern part of the waterway. The shape of the breakwaters at both channel ends causes hydraulic losses, depending on the flow direction, so different discharges are observed for the same water head.

It can be found that only a 5 cm water stage difference between the Gulf of Gdańsk and the Vistula Lagoon can cause a flow with the maximum velocity reaching 1 m/s in the narrow part of the channel with a rate exceeding 100 m<sup>3</sup>/s. During extreme hydrological conditions, for the highest damming in the gulf or in the lagoon (1.0 m assumed in this study), the maximum velocity in the lock segment can reach 5 m/s and the rate increases up to 500 m<sup>3</sup>/s.

## CONCLUSIONS

The results of the two-dimensional numerical simulations of the hydrodynamics of the new strait (waterway) through the Vistula Spit allow the following to be concluded.

- The mathematical model based on 2D SWE can be successfully applied to simulate the flow through the complex hydraulic system of a waterway composed of breakwaters, a port basin, a navigable channel and a lock.
- Assuming open lock gates, the difference in water levels in the Gulf of Gdańsk and the Vistula Lagoon (water head) will force a significant flow in the navigable channel. A significant decrease in the water level in the channel is observed, which is accompanied by an increase in the flow velocity. Such a situation can prevent the movement of vessels during extreme and exceptional situations.
- Even though a water head of 1 m between the gulf and the lagoon is assumed, no supercritical flow occurs in the lock, nor is a hydraulic jump formed in the navigable channel.
- For both flow directions, strong currents and circulations may occur in the port basin. Such a situation, during significant damming and the opening of the navigable

channel, may be dangerous and undesirable for all vessels in the port.

- The calculations allowed the relation between the water head and the capacity of the navigable channel to be found. This can be helpful to estimate the total water exchange between the sea and the lagoon during periods when the new artificial strait is open.

## REFERENCES

1. Szymkiewicz, R. *Hydrodynamics of Vistula Lagoon*; Warsaw, 1992.
2. Cieśliński, R. Hydrochemical variability of the ecosystem of the Gulf of Elbląg (north-eastern Poland). *Baltica* 2016, 29, 121–132.
3. Cieśliński, R.; Lewandowski, A. Hydrological regime of the Vistula Lagoon and the possible changes due to the construction of the waterway connecting the Vistula Bay with the Gulf of Gdansk. *Inżynieria Morska i Geotechnika* 2013, 69–78.
4. Chubarenko, I.P.; Chubarenko, B.V. General water dynamics of the Vistula Lagoon. *Environmental and Chemical Physics* 2002, 24, 213–217.
5. Szydłowski, M.; Kolarski, T.; Zima, P. Impact of the artificial strait in the Vistula Spit on the hydrodynamics of the Vistula Lagoon (Baltic Sea). *Water* 2019, 11, 990.
6. Szymkiewicz, R. A mathematical model of storm surge in the Vistula Lagoon, Poland. *Coastal Engineering* 1992, 16, 181–203.
7. Nadolny, A.; Samulak, M. Construction of a waterway connecting the Vistula Lagoon with the Bay of Gdańsk 2017.

8. García-Oliva, M.; Pérez-Ruzafa, Á.; Umgiesser, G.; McKiver, W.; Ghezzi, M.; De Pascalis, F.; Marcos, C. Assessing the hydrodynamic response of the Mar Menor Lagoon to dredging inlets interventions through numerical modelling. *Water* 2018, *10*, 959.
9. Dubrawski, R.; Zachowicz, J. Navigation channel in the Vistula Spit – Positives and negatives for the marine environment. *Inżynieria Morska i Geotechnika* 1997, 301–307.
10. Dembicki, E.; Jednorał, T.; Sedler, B.; Jaśkowski, J.; Zadroga, B. Navigation channel in Polish part of Vistula Sandbar. *Inżynieria Morska i Geotechnika* 2006, 275–286.
11. Szymkiewicz, R. Analysis of a concept of changing the hydrodynamic conditions of the Vistula Lagoon. *Inżynieria Morska* 1984, 258–260.
12. Toro, E.F. *Riemann Solvers and Numerical Methods for Fluid Dynamics: A Practical Introduction*; 3rd ed.; Springer-Verlag: Berlin Heidelberg, 2009; ISBN 978-3-540-25202-3.
13. Chow, V.T. *Open-channel hydraulics*; McGraw-Hill Book Company: New York, 1959;
14. Zima, P. Modeling of the two-dimensional flow caused by sea conditions and wind stresses on the example of Dead Vistula. *Polish Maritime Research* 2018, *25*, 166–171.
15. Gąsiorowski, D. Analysis of floodplain inundation using 2D nonlinear diffusive wave equation solved with splitting technique. *Acta Geophys.* 2013, *61*, 668–689.
16. Szydłowski, M. Mathematical modelling of flash floods in natural and urban areas. In *Proceedings of the Transboundary Floods: Reducing Risks Through Flood Management*; Marsalek, J., Stancalie, G., Balint, G., Eds.; Springer Netherlands, 2006; pp. 143–153.
17. Kolerski, T.; Zima, P.; Szydłowski, M. Mathematical modeling of ice thrusting on the shore of the Vistula Lagoon (Baltic Sea) and the proposed artificial island. *Water* 2019, *11*, 2297.
18. Kwiatkowski, J.; Rasmussen, E.K.; Ezhova, E.; Chubarenko, B.V. The eutrophication model of the Vistula Lagoon. *Oceanological Studies* 1997, *26*, 5–33.
19. Chubarenko, I.; Tchepikova, I. Modelling of man-made contribution to salinity increase into the Vistula Lagoon (Baltic Sea). *Ecological Modelling* 2001, *138*, 87–100.
20. Ołdakowski, B.; Kwiatkowski, J. Forecast model of water quality of Vistula Lagoon. *Inżynieria Morska i Geotechnika* 1995.
21. Bielecka, M.; Kazmierski, J. A 3d mathematical model of Vistula Lagoon hydrodynamics – General assumptions and results of preliminary calculations; ECSA 8, Dublin, 2003; pp. 140–145.
22. Kruk, M.; Kempa, M.; Tjomsland, T.; Durand, D. The use of mathematical models to predict changes in the environment of the Vistula Lagoon. In *Vistula Lagoon – Natural environment and modern methods of his research project on the example of Visla*; Publishing PWSZ: Elbląg, 2011; pp. 165–180.
23. LeVeque, R.J. *Finite Volume Methods for Hyperbolic Problems*; Cambridge University Press, 2002; ISBN 978-0-521-00924-9.
24. Burzyński, K.; Szydłowski, M. Numerical simulation of rapidly varied water flow in ‘Wild River’ type water slide. *Archives of Hydro-Engineering and Environmental Mechanics* 2003, *50*, 3–23.
25. Szydłowski, M. Numerical simulation of open channel flow between bridge piers. *TASK Quarterly* 2011, *15*, 271–282.
26. Szydłowski, M. Numerical modeling of hydrodynamics as a tool for design of the leisure and sport water structures. *Acta Scientiarum Polonorum – Formatio Circumiectus* 2016, *15*, 353–367.
27. Szydłowski, M.; Mikos-Studnicka, P. Shallow water equations as a mathematical model of whitewater course hydrodynamics. In *Recent Trends in Environmental Hydraulics*; Geoplanet: Earth and Planetary Sciences; Springer Berlin Heidelberg: Berlin Heidelberg, 2020; p. accepted to publish.
28. Szydłowski, M. Application of hydrodynamics model for a case study of the Kolbudy II Reservoir Embankment hypothetical failure. In *Experimental Methods in Hydraulic Research*; Rowinski, P., Ed.; Geoplanet: Earth and Planetary Sciences; Springer Berlin Heidelberg: Berlin, Heidelberg, 2011; pp. 299–306 ISBN 978-3-642-17475-9.
29. Szydłowski, M.; Kolerski, T. Numerical modeling of water and ice dynamics for analysis of flow around the Kiezmark Bridge piers. In *Free Surface Flows and Transport Processes*; Geoplanet: Earth and Planetary Sciences; Springer Berlin Heidelberg: Berlin, Heidelberg, 2018; pp. 465–476.

## CONTACT WITH THE AUTHORS

**Michał Szydłowski**

*e-mail: mszyd@pg.edu.pl*

Gdańsk University of Technology  
Faculty of Civil and Environmental Engineering  
11/12 Gabriela Narutowicza Street, 80-233 Gdańsk  
**POLAND**

**Tomasz Kolerski**

*e-mail: tomkoler@pg.gda.pl*

Gdańsk University of Technology  
Faculty of Civil and Environmental Engineering  
11/12 Gabriela Narutowicza Street, 80-233 Gdańsk  
**POLAND**

# APPLICATION OF THE CHIMNEY CAP AS A METHOD OF IMPROVING THE EFFECTIVENESS OF NATURAL VENTILATION IN BUILDINGS

Romana Antczak-Jarząbska

Maciej Niedostatkiewicz

Gdańsk University of Technology, Poland

## ABSTRACT

*Adequately designed natural ventilation is the cheapest and easiest way to effectively remove indoor pollutants and keep the air inside a building fresh. A prediction of the performance and effectiveness of ventilation in order to determine the design of a ventilation system can provide real and long-term cost savings. The worst time in terms of the efficiency of natural ventilation is the spring-autumn transition period [7]. In order to improve the efficiency of natural ventilation, chimney caps are used, among others. They are designed to improve the chimney effect described in colloquial language as a chimney draft. The chimney effect is a physical phenomenon of the formation of a spontaneous flow of a warmer gas, e.g. air, from the bottom up in stem channels [12]. The article analyses the influence of the chimney cowl on the improvement of the chimney effect in an apartment of a multi-family building with natural ventilation. Long-term tests of the chimney draft were carried out for the case without and with a chimney cap. The paper presents the results of the performance (air change rate, ACH) of natural ventilation for a building with an inlet gap measured for the transitional season (between the heating and the summer season). The measurements were performed during a windy period.*

**Keywords:** natural ventilation, chimney cap, ACH, wind effect, effectiveness

## INTRODUCTION

Natural ventilation (NV) is the cheapest strategy for distributing fresh air inside a building. It is still the most popular system found in Poland and other Central and Eastern European countries. Natural ventilation is driven by two physical phenomena, wind [9,11] and buoyancy (stack effect) caused by the difference between the indoor and outdoor air temperatures [9,11].

However, Gładyszewska et al. [8] showed that NV is mainly affected by the wind direction and velocity. Natural ventilation should work when all or one of the natural forces are available. Unfortunately, the two main drivers causing natural ventilation flows are stochastic, so natural ventilation

may be difficult to control and difficult also to predict, analyse and design. Other disadvantages of natural ventilation are the reduced control of air distribution within the building and its ineffectiveness in summer conditions with minimal wind. Despite the difficulty in control, natural ventilation is still relied upon to meet the need for fresh air in many buildings. The study [10] shows that natural ventilation has become a new trend in building design in the architectural community. Furthermore, natural ventilation has been used in many types of buildings, even in hospitals with highly controlled indoor climates [6].

The quality of natural ventilation is usually determined by the performance indicator of the ventilation system. Performance means the air change rate (ACH). The ACH

measures how quickly the air in the interior space is replaced by air coming from the outside. In turn, ventilation effectiveness is the indicator of the ability of a ventilation system to remove a contaminant. Ventilation performance indicators serve to provide information concerning indoor air parameters in a room or a building. Therefore, proper information about the actual climate data of the local climate conditions is important, but is usually not provided. Generally, we have two different approaches: the local climate condition (LCS) at the construction site and climate data in atypical meteorological year (TMY). In engineering practice, it is not common to take into account the local climate conditions. As we can see in [13], the most common practice is to use climate data from the TMY. However, [13] rightly observed that when based on climate data from the TMY, such values are usually slightly over estimated. Therefore, in-situ measurements were used in the tests.

In this paper, the performance (air change rate, ACH) of natural ventilation for a building with a measured inlet gap was performed. A typical residential detached house, located in northern Poland, in a cold climate region, was chosen for the measurement campaign. Field measurements were performed in a test apartment in a detached family house. The measurement campaign ran from 2 April to 9 June. For better knowledge of the behavior of natural ventilation in the experimental measurement, a windy period of time was chosen. However, April and May are months in which the primary mechanisms for the transfer of air into a building occur simultaneously. In this paper we focus on the effect of wind on the NV for a building without a chimney cap and for a building with a chimney cap. The major contribution of the paper is the experimental determination of the performance of natural (stack) ventilation in a residential apartment with a chimney configuration and a window with an inlet gap on the air exchange rate for buildings without and with a chimney cap.

## TEST HOUSE

Long-term investigations were carried out in a residential, multi-family house, located in Gdańsk, northern Poland. The test apartment was inhabited during the measurement campaign. The residents' activity was registered mainly in the morning and in the evening (after 5:00 pm). In the building, there are three stairways, four floors, a full basement with an unused attic and individual one-storey dwellings.

The test apartment was equipped with a natural ventilation system in a configuration with air inlets and chimneys ducts. Air inlets are small appliances mounted in the casement or window frame, which allow for control of the fresh air inflow to the room. They were invented and introduced in the 1960s in Scandinavian countries [4].

The building is made from prefabricated components, and the structural system is mixed. The height of the building from the entry level to the ridge is 14.60 m. A double-sided apartment (including exterior walls oriented in two opposite

geographical directions) located on the top floor in the middle of the building was selected. Over the test dwelling, there is an unused and unheated attic. As a thermal barrier for the top floor ceiling, the project adopted the thermal insulation layer separating the apartment from the unused attic, but not the roof surface. Consequently, almost the entire length of the outlet ducts of the ventilation system pass through a space that is not heated and has no contact with the outside air (Fig. 1).

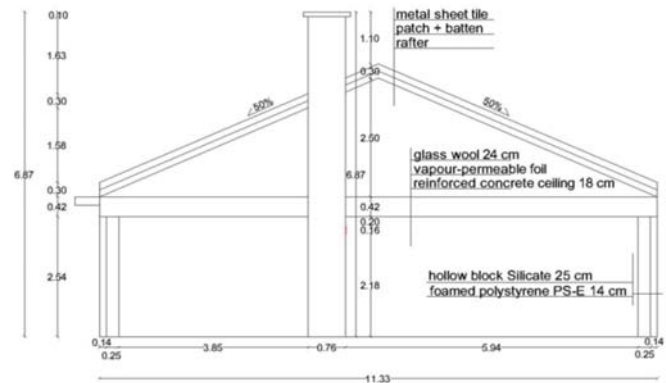


Fig. 1. Vertical cross-section through the attic above test apartment

The construction walls were made from 25 cm thick silicate blocks and 14 cm thick insulation, and the ceiling was made of 20 cm thick Filigran slabs. The roof structure was made from wood components, and the roof surfaces are symmetrical with a 26.5° slope. The ventilation chimney ducts were made from ceramic blocks 19/19 cm and a cross-section Ø15 cm extension on each floor. The transmission heat coefficient  $U$  was 0.25 W/(m<sup>2</sup> K) (external walls), 1.3 W/(m<sup>2</sup> K) (windows) and 0.22 W/(m<sup>2</sup> K) (roof).

## MEASUREMENT SETUP AND EQUIPMENT

The meaning of all symbols and denotations used in the formulae should be explained. To perform measurements, a number of sensors were used: LB-746 sensors to measure the wind velocity and direction, and an LB-801 anemometer with a thermometer function designed to measure the air flow velocity and temperature. All sensors had metrological properties confirmed. The sensors were connected to a data acquisition module. Data collected in the data acquisition module were automatically transferred to the SQL database, located on a PC, on which the measurement data management software LBX 2012 of LAB-EL [18] was installed. The schematic location of the sensors in the apartment is shown in Fig.2.

A description of the measured values and the location of the sensors is presented in Table 1. The sensors were positioned to determine the effect of the wind velocity and direction as well as the outside air temperature on the flow characteristics of the air in the rooms. The arrangements of the sensors were adapted to the expected flow profiles of air in the rooms. This made it possible to identify the velocity and temperature of the air flowing through the characteristic points of internal zones:

the air flow through the window inlets, a door opening in the inner wall of the living room and the ventilation duct outlet in the bathroom. The outside climate parameters were measured in close proximity to the air ventilation inlet. The location of the sensors made it possible to take into account the air inflow disturbances of the entering air mass on the facade of the building. The continuous measurement of physical values was performed from April till June. The sampling time was 60 seconds. Seven days were taken for analysis of the building without a chimney cap and 7 days for the building with a chimney cap.

## EXTERNAL CLIMATE CONDITIONS

The measurement campaign was from April till June, when the difference between the indoor and ambient air temperature is higher than 12 °C. Article shows how wind gusts can have a significant influence on the air flow patterns and characteristics. The magnitude of the wind velocity and its direction can rapidly increase the air exchange rate in the air inlet. The characteristics of the wind conditions at the test house location were included in the experiment data. The

meteorological station used was located in the middle of an urban area. For the test house, the wind direction profile is presented in Fig.3, which shows the percentage of wind direction at the measurement site according to the measured values. In both cases, similar wind velocity directions were used to compare the results. Due to the location in relation to the parts of world of the building, the biggest impact is that of the wind blowing from the south and west. During the measurement, data was taken when the dominant measured wind direction was the south-west direction SW (75%) followed by the west W (25%)

for the building without a chimney cap, while for the building with a chimney cap the dominant measured wind direction was again the south-west direction SW (70%) followed by the west W (30%).

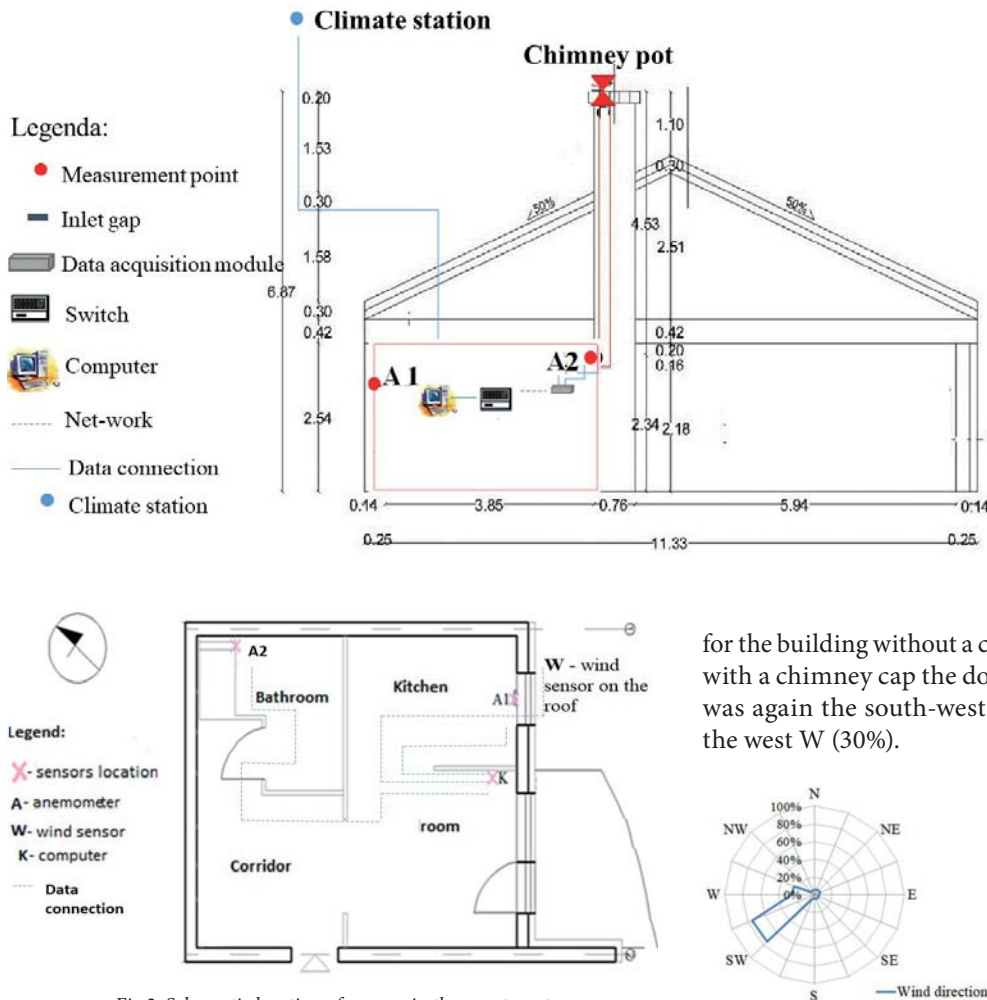


Fig.2. Schematic location of sensors in the apartment

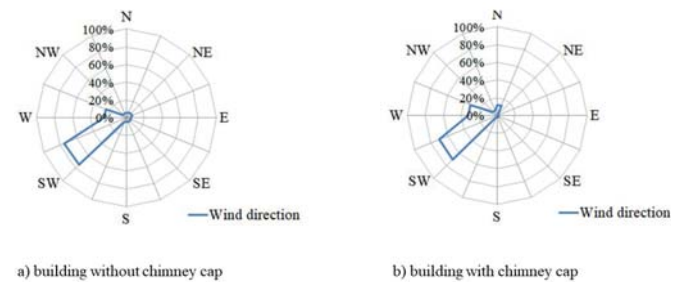


Fig. 3. The percentage of wind direction at the measurement site according to measured values

Tab. 1. A description of the measurement sensors

Symbol	Sensor name	Measured value	Sensor location
W	Wind sensor	Velocity [m/s]	On the railing of the balcony and parallel to the facade of the building.
	Wind sensor	Direction [°]	
A1	Anemometer	Velocity [m/s]	In the air distribution opening in the window in the kitchen.
	Anemometer	Temperature [°C]	
A2	Anemometer	Velocity [m/s]	In the ventilation duct outlet in the bathroom.
	Anemometer	Temperature [°C]	

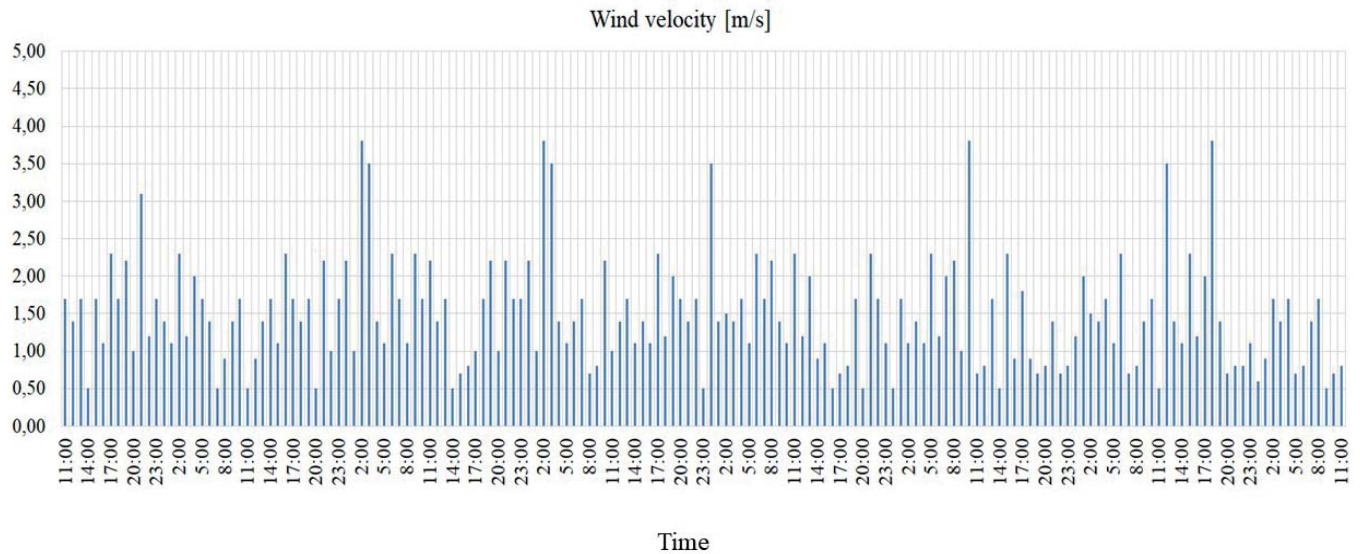
In both cases, similar wind velocities were used to compare the results. During the whole period of time, the air velocity in the inlet gap in the window was strongly dependent on the wind velocity. Fig.4 presents the wind velocity for the buildings without and with a chimney cap. During the experiment the wind velocity was not significant, as its maximum value was at most 4.5 m/s.

In order to better capture the influence of natural forces on the velocity of air exchange in the room, a wind velocity above 0.5 m/s was assumed for analysis. The average value of the air velocity during the measurements without the chimney cap was 1.49 m/s, while the average value with a chimney cap was 1.46 m/s.

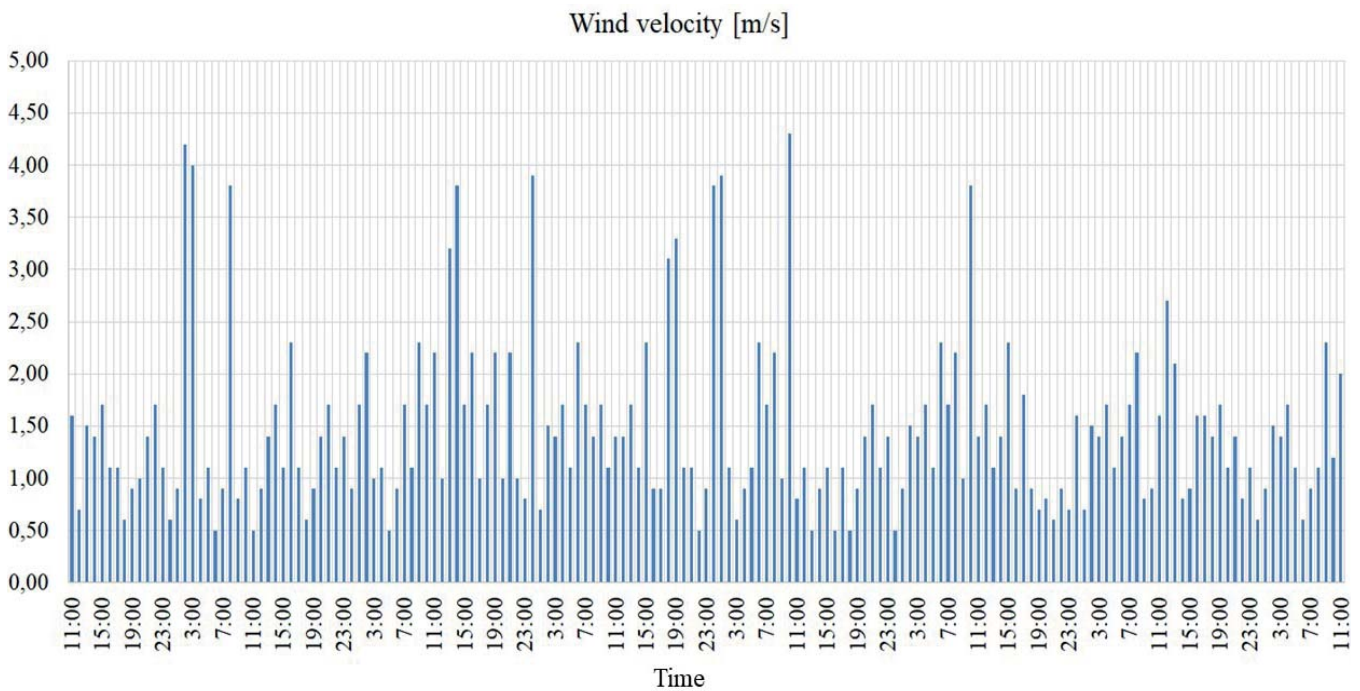
The most unpredictable conditions during the entire year for natural ventilation were caused by the wind effect. We already know how strong an impact the wind has on the air

change rate in buildings [1]. Besides, we also know that the stack effect is reduced significantly when the impact of wind gusts is significant. Therefore, the wind effect could not be ignored.

Thus, the major contribution of the paper is the experimental determination of the stack effect on the air exchange rate for natural ventilation with an inlet gap subject to the wind effect.



a) building without chimney cap



b) building with chimney cap

Fig. 4. The wind velocity for building without chimney cap and for building with chimney cap

## EFFICIENCY OF NATURAL VENTILATION (NV)

The performance means the air change rate (ACH) and it is the measure of how many times the air within a defined space is replaced [2,5]. Air change rates are often used as a principle with broad application that is not intended to be strictly accurate or reliable for every situation in ventilation design.

The air change rate per hour (ACH) is calculated based on the ratio of the total air supply ( $A_{\text{effinlet}} U_{\text{inlet}}$ ) (into a zone (i.e. a room or space) in relation to the volume of that zone's room volume ( $V_R$ ) [3,16]. The sum of the air supply measured at point A1 constitutes the total air supply into the apartment. The total air supply ( $A_{\text{effinlet}} U_{\text{inlet}}$ ) is named  $\dot{v}(t)$ . It is generally expressed as the air change per hour [ $\text{h}^{-1}$ ] or ACH. The ACH is defined by the ASHRAE as:

$$ACH(t) = (\dot{v}(t) * 3600 / V_R) \quad (1)$$

where:

ACH(t) – the ventilation rate or air change rate, h<sup>-1</sup>

$\dot{v}(t)$  – the total air supply into a room, m<sup>3</sup>/h

VR – the room's volume, m<sup>3</sup>

The exchange processes that take place during the measurement period are assumed to be temporally invariant. The air supply rate  $\dot{v}(t)$  and thus the air change rate ACH(t) are constant.  $\dot{v}(t)$  and ACH(t) can be replaced by  $\dot{v}$  and ACH [13,15]. For the air change rate, which is designed to calculate the performance of ventilation, the following simplifying assumptions have been made:

- the air is considered to be completely mixed throughout the measurements. Inside the room there are no concentration gradients, i.e. the concentration of air at a given time is the same for the whole room,
- the rooms presented in Fig.1 are considered a single zone system.

## DISCUSSION OF RESULTS

In the cold climate conditions of northern Poland, ventilation works in a winter regime from November to March, with January the coldest month. The average temperature is about -4°C but it can fall as low as -35°C. On the other hand, in the summer months of June, July and August, the average temperature is about 18°C and the maximum summer temperature is 40°C. All other time periods can be called transient climate conditions (TCC), which are characterized in this article by a day-time difference between the indoor and ambient temperature in the range of about (20°C, -2°C). These are the most unfavorable conditions during the entire year. This is due to the stack effect being reduced significantly, while the impact of wind gusts is very random and dependent upon the ventilation configuration. However, the time period

of transient climate conditions is very advantageous for field investigations of the quality of natural ventilation.

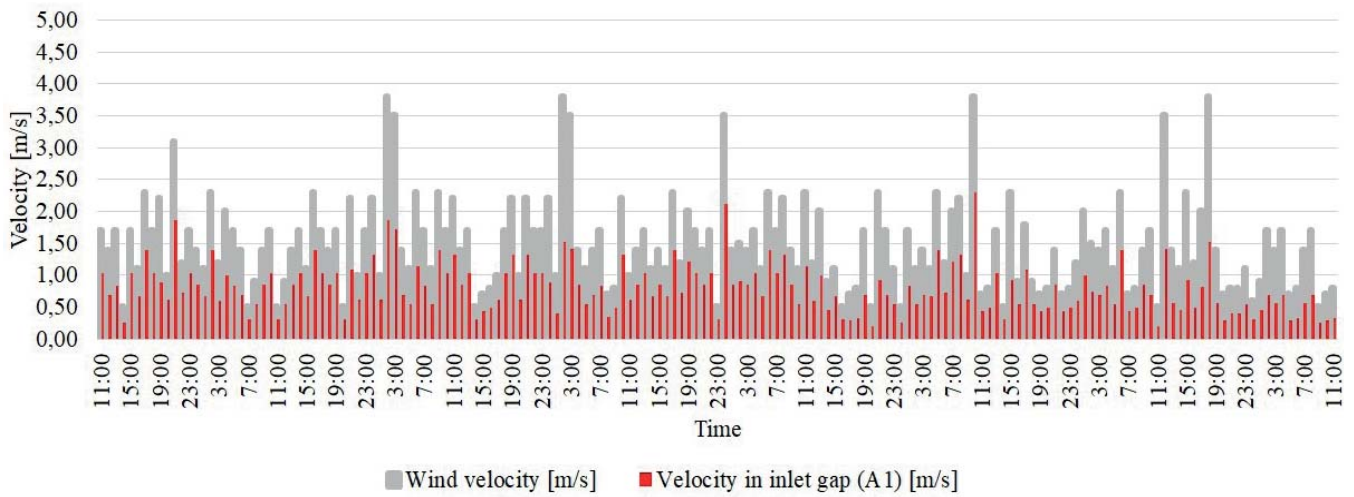
In this study, the test apartment was equipped with one air inlet gap located in the kitchen. According to the national regulations and standards [16], the active flow area of a fully open air-inlet should be designed to enable airflow in the range from 20 to 50 m<sup>3</sup>/h for a pressure difference of 10 Pa on both sides of the opening. In the test apartment, the inlet gap was located only in the kitchen and was in contact with the ambient air. When fully opened, it should ensure an air exchange rate of 0.8 1/h. The chimney duct of 14 x 14 cm<sup>2</sup> (min. 0.016 m<sup>2</sup>) was located in the bathroom. The active area of the air inlet to the chimney duct was 0.008 m<sup>2</sup>. During measurements the test apartment was occupied by two adults at the same times of the day: before work (6:00–7:00 am) and after work (6:00–10:00 pm).

For better knowledge of the influence of wind on the ACH in the building, the study includes a windy period with a wind velocity higher than 0.5 m/s. The ventilation performance was investigated as the air change rate per the apartment's total volume during 1h (ACH). The results were compared with the requirements of the industry standard [17] (natural ventilation in the test apartment should exchange 50 m<sup>3</sup>/h of air during the day-time).

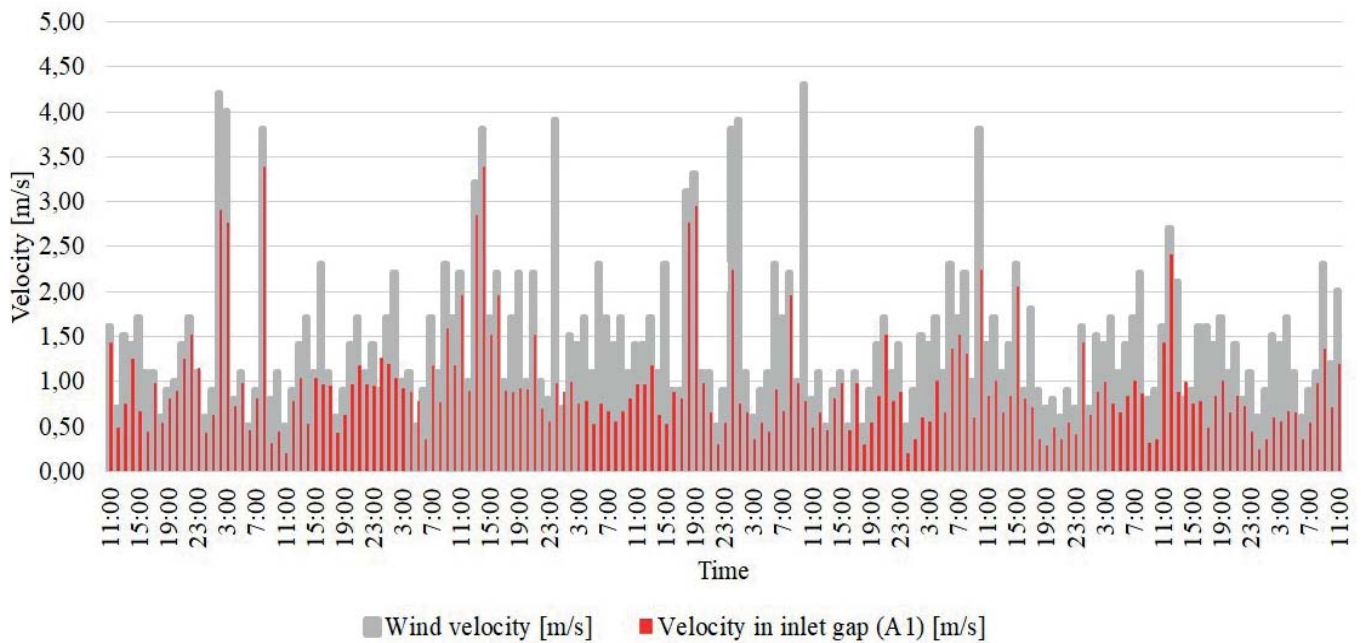
Fig.5 shows the wind effect for a velocity measurement at point A1. In order to better understand the influence of the chimney cap on the improvement of natural ventilation, the direction of the wind was selected from the side of the building in which the window gap was located. The results of measurements of velocity (Fig. 5) in the inlet in the window showed a distinct relation between the external wind velocity and the airflow direction in the air inlet. The air velocity at the inlet is directly proportional to the wind speed.

Fig.6 shows the wind effect on the flow rate in the apartment. For a wind velocity higher than 0.5 m/s, the day-time flow rate was fulfilled for 48% of the time without a chimney cap, while for the chimney with a cap the day-time flow rate was fulfilled for 60% of the time.

Fig.6 shows a large time-variation of the ACH during a windy period typical of the cold climate in Poland. Considering this time-variation, the air change rate in the experiment varied between a minimum of ACH  $\approx$  0.23 h<sup>-1</sup> and a maximum of ACH  $\approx$  2.59 h<sup>-1</sup> for the measurement without a chimney cap, and between a minimum of ACH  $\approx$  0.22 h<sup>-1</sup> and a maximum of ACH  $\approx$  3.84 h<sup>-1</sup> for the measurement with a chimney cap. The average value of the air change rate during the measurements without a chimney cap was 0.88 h<sup>-1</sup>, while the average value of the ACH during the measurements with a chimney cap was 1.04 h<sup>-1</sup>.

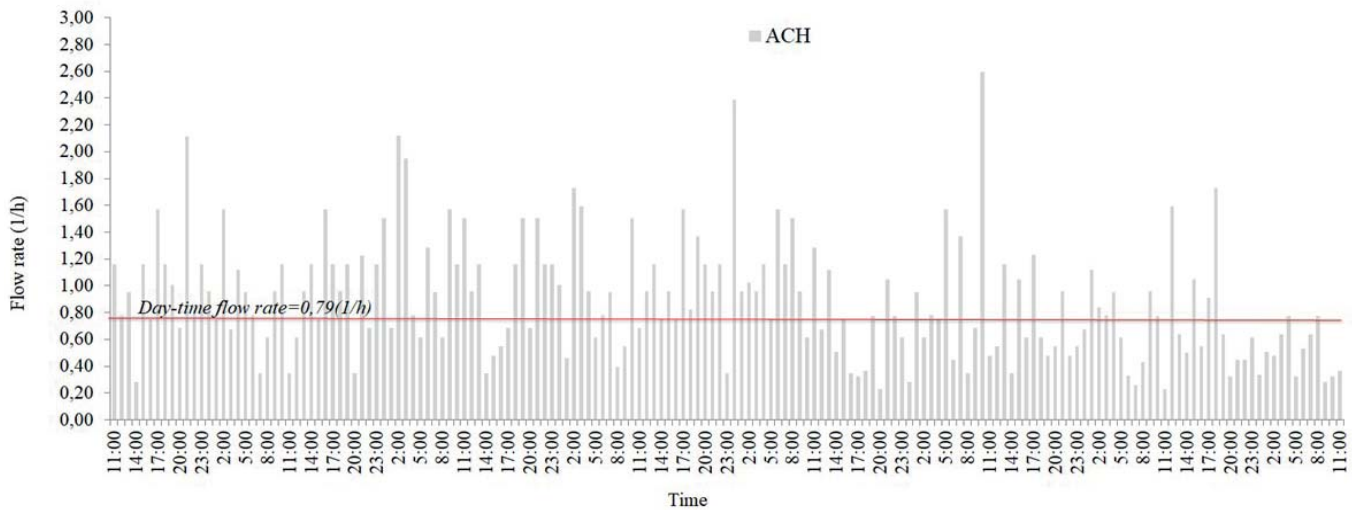


a) building without chimney cap

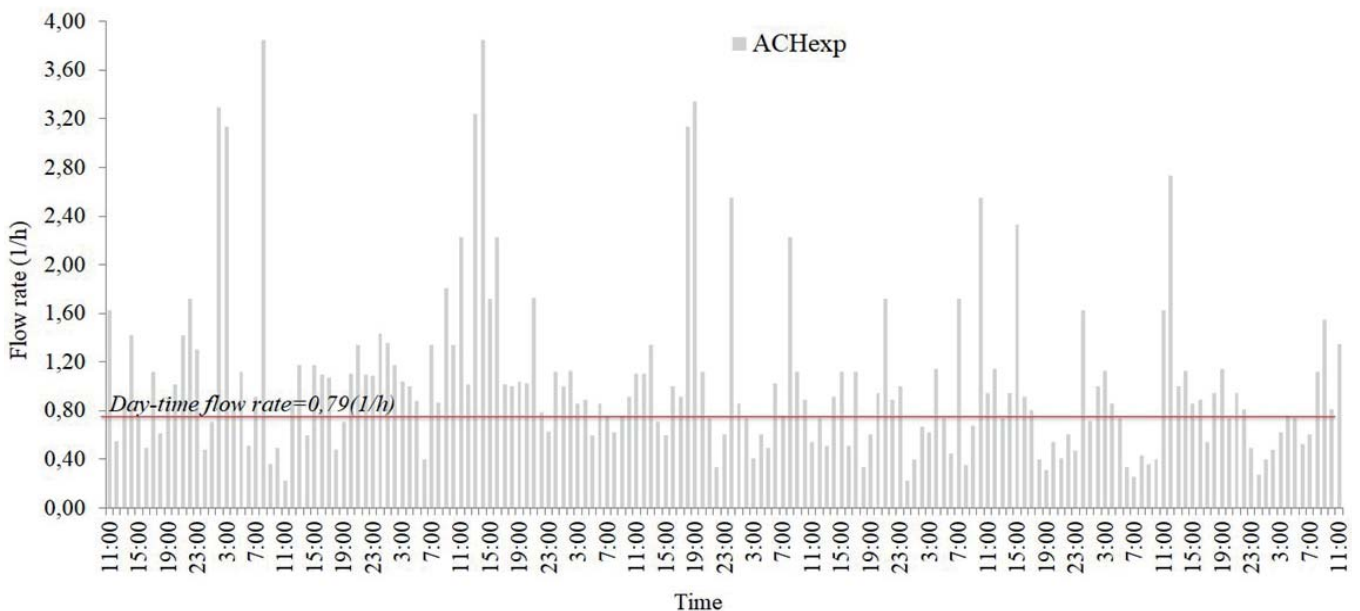


b) building with chimney cap

Fig.5. Wind effect for a velocity measurement in point A1



a) building without chimney cap



b) building with chimney cap

Fig.6. Ventilation performance in the test apartment with respect to air change rates (ACH) was selected

## CONCLUSIONS

Field investigations on the prediction of the air flow rate in an apartment with natural (stack) ventilation with an inlet gap in a window, with and without a chimney cap, were performed. The measurements were carried out in a test apartment within a detached family house located in a cold climate. The measurement campaign was conducted in transient climate conditions.

The ACH was investigated under steady climate conditions in a windy period. The main influence on the ACH in the apartment was the wind velocity normal to the inlet. The results of measurements of velocity at the inlet in the window showed a distinct relation between the external wind velocity and the airflow direction in the air inlet. The air velocity at the inlet is directly proportional to the wind speed. The minimum value which fulfilled the day-time flow rate requirement was a wind velocity in the inlet (A1) equal to 0.7 m/s.

The experiment shows the large time-variation of the ACH during a windy period typical of the cold climate in Poland.

The maximum value of the ACH with a chimney cap was 3.84 1/h, which was 48% higher than the maximum ACH for a standard chimney without a chimney cap.

The use of the chimney cap improves the efficiency of natural ventilation by 15.5%. It is surprising, however, that, despite the chimney cap, the windy period and the measurements at a time when the wind direction was directed towards the window with the inlet gap for as much as 40% of the time, the day-time standard flow rate was not met.

## REFERENCES

1. Awbi H. (1991): *Ventilation of buildings*, Chapman & Hall.
2. Awbi H., Gan G. (1992): *Simulation of solar induced ventilation*, Second World Renewable Energy Congress, vol. 4, Solar and Low Energy Architecture, September 1992, Pergamon Press, Oxford.
3. Axley J. (1998): *Introduction to the design of natural ventilation system loop equation*, Proc. 19th AIVC Conf. Ventilation Technologies Urban Areas, 47-56.
4. Bülow-Hübe H. (2001): *Energy-Efficient Window Systems*. Doctoral Dissertation. ISSN 1103-4467. Lund University, Lund Institute of Technology, Lund.
5. Cao G., Awbi H., Yan R., Fan Y., Siren K., Kosonen R., Zhang J. (2014): *A review of the performance of different ventilation and airflow distribution systems in buildings*. Buildings and Environment, 73, 171-186.
6. Clarke D. (2001): *A breath of fresh air*. Hospital Development, 32(11), 13-17.
7. Fitzgerald S.D., Woods A.W. (2008): *The influence of stacks on flow patterns and stratification associated with natural ventilation*. Energy and Buildings, 43, 1719-1733.
8. Gładyszewska-Fiedoruk K., Gajewski A. (2012): *Effect of wind on stack ventilation performance*. Energy and Buildings, 51, 242-247.
9. Jarząbska-Antczak R., Niedostatkiwicz M. (2017): *Design and diagnostics of gravitational ventilation. Selected problems*.
10. Polskie Centrum Budownictwa Difin i Muller sp. z o.o., 1-80, Warszawa.
11. Krishan A. (2001): *Climate responsive architecture: a design handbook for energy efficient buildings*, Tata McGraw-Hill, New York.
12. LBNL (2007): *Energy Plus Engineering Reference*, November 6, 2007, pp. 384 and 381.
13. Nazaroff W. W. (2008): *Inhalation intake fraction of pollutants from episodic indoor emissions*. Building and Environment, 43(3), 269-277.
14. Novoselac A., Srebric J. (2003): *Comparison of air exchange efficiency and contaminant removal effectiveness as IAQ indices*. ASHRAE Trans., 109, 339-349.
15. Okisalo J., Kurnitski J., Korpi M., Kalamees T., Vinha J. (2009): *Building leakage, infiltration, and energy performance analyses for Finnish detached houses*. Building and Environment, 44, 377-387.
16. Roos A. (1998): *The air exchange efficiency of the desk displacement ventilation concept-Theory, measurements and simulations*, Proc. Roomvent'98, vol.1, pp.249-256, Stockholm, Sweden.
17. Sandberg M. (1981): *What is ventilation efficiency?* Building and Environment, 16, 123-135.
18. PN-83/B-03430 (including revision A3:2000). *Ventilation in collective dwelling places and public buildings – requirements*, (in Polish).
19. LAB-EL Elektronika Laboratoryjna s.j. Available from [www.label.pl](http://www.label.pl).

## CONTACT WITH THE AUTHORS

**Romana Antczak-Jarząbska**

e-mail: [romana.antczak@pg.edu.pl](mailto:romana.antczak@pg.edu.pl)

**Maciej Niedostatkiwicz**

e-mail: [mniedost@pg.edu.pl](mailto:mniedost@pg.edu.pl)

Gdańsk University of Technology  
11/12 Gabriela Narutowicza Street  
80-233 Gdańsk  
**POLAND**

# ANALYSING THE IMPACT ON UNDERWATER NOISE OF CHANGES TO THE PARAMETERS OF A SHIP'S MACHINERY

Krystian Buszman

Polish Naval Academy, Poland

## ABSTRACT

*A ship moving over the surface of water generates disturbances that are perceived as noise, both in the air and under water. Due to its density, water is an excellent medium for transmitting acoustic waves over long distances.*

*This article describes the impact of the settings of a ship's machinery on the nature of the generated noise. Our analysis includes the frequency characteristics of the noise generated by the moving ship. Data were obtained using an underwater measurement system, and the measured objects were two ships moving on specific trajectories with certain machinery settings. The acquired data were analysed in the frequency domain to explore the possibilities of the acoustic classification of ships and diagnostics of source mechanisms.*

**Keywords:** shipping noise, hydroacoustic passive measurement, narrowband, 1/3-octave analysis, diagnosis, classification

## INTRODUCTION

The monitoring of underwater noise generated by ships has been a topic of interest to research scientists for several years [11, 14], and measurement standards have been developed for this type of noise [10]. One area of research is the impact of noise on the natural environment [2, 12], and in particular on underwater fauna, which researchers from many institutes and pro-ecological organisations have focused on [3, 15]. Another aspect is mechanical engineering methods of diagnostics for ship equipment [9, 13], using on-board and external measurement systems. A further area of underwater noise research is the safety of the ship in terms of the threat

from non-contact mines with hydroacoustic igniters [5, 6]. In addition, studies have been conducted for statistical purposes for different types of customers, for example physicists, biologists, logisticians and various services connected with maritime transport. In each of these areas, the parameters characterising the recorded underwater noise are very important. The noise emanating from ships is connected with the equipment necessary for their movement, which uses specific parameters. The main parameter is the speed, which determines the attributes of the ship's machinery of operation. A change in a ship's propulsion settings affects the speed of the ship, and causes noise with different characteristics to be generated.

## DISTINGUISHABILITY OF OBJECTS BASED ON THE PARAMETERS OF MECHANICAL OPERATION OF SHIPS

An underwater noise analysis was carried out based on measurements of a particular ship using a bottom measuring system [6, 7]. The measuring circuit included a hydrophone that received signals in the range 5–120 kHz. The complete measuring system consisted of a recorder unit with A/D converters with a maximum sampling frequency of 51.2 kHz, and a computer with data logging software. The recorder unit was located inside the bottom nod, which was connected with the computer at a land-based station via a hybrid cable. A block diagram of this system is shown in Fig. 1.

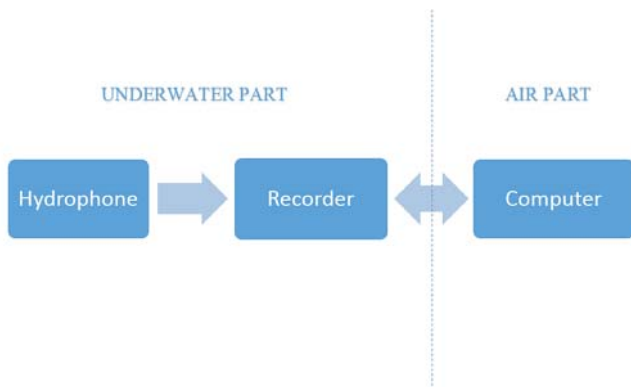


Fig. 1. Block diagram of the underwater noise measurement circuit.

The input parameters of the recorded signals determine the output parameters in the frequency domain, and in particular, the frequency resolution depends on the duration of the analysed signal. The width of the overlap was 50% of the number of samples. This operation allowed us to obtain a set of results as a series of amplitude values for each second of the analysed signal, assuming the determined time for a single analysis.

The results of the signal analysis over the time duration, corresponding to the noise generated by the ship when it passes the hydrophone at its closest point of approach (CPA), are in the form of a spectrum of pressure levels with reference to 1  $\mu\text{Pa}$ , with a resolution depending on the parameters of the FFT analysis. In case of 50% overlap, a spectrum was presented for 2 s of average SPL (102,400 samples). To increase the performance of the FFT analysis, the length of the signal was increased up to the next power of two of the number of samples used (131,072). The resulting frequency resolution was better than 0.5 Hz, as can be seen from the narrowband spectra results.

We also show that it is possible to identify sources of noise on the ship when the RPM of the machinery is known. This depends on the parameters of operation of the ship's machinery. Data were collected onboard during underwater noise measurements. The parameters must be unchanged throughout the signal analysis period. In the following, the spectra for two ships crossing over the hydrophone are shown.

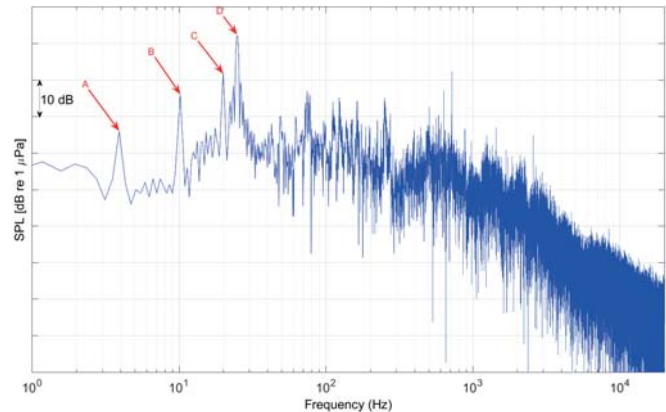


Fig. 2. Narrowband spectrum with specific frequencies corresponding to the working parameters of selected components of the first ship. The spectrum is the result of a 2 s signal when the ship was at its CPA to the bottom nod in shallow water.

In a document describing the measurement standards for noise generated by ships [10], it is advised to use a longer averaging time for deep water measurements.

Fig. 2 shows several characteristic frequencies related to the first vessel. These are related to the operational components of the ship, which was equipped with two 700 kW diesel engines and moved with the following parameters, as labelled in Fig. 2: A – drive shafts, rotational speed 234 RPM, B – main engines, rotational speed 600 RPM, C – propellers with five blades, rotational speed 234 RPM, D – generators, rotational speed 1500 RPM.

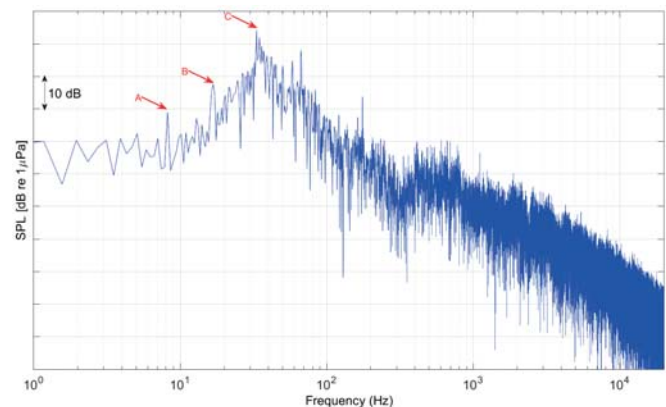


Fig. 3. Narrowband spectrum with the specific frequencies corresponding to the working parameters of selected components of the second ship. The spectrum is based on a 2 s signal when the ship was at its CPA to bottom nod in shallow water.

Fig. 3 shows a similar spectrum labelled with the specific characteristic frequencies of the second ship. This ship was equipped with two 9000 kW diesel engines and the following parameters of motion:

A – main engines, rotational speed 500 RPM,  
B – propellers with four blades, rotational speed 252 RPM,  
C – generators, rotational speed 1992 RPM.

By comparing these two figures, differences can be observed in the tonal frequencies and amplitudes, corresponding to differences in the RPM of the machinery. The tonal frequencies are characteristic of a specific vessel at a specific speed; when the speed of the vessel changes, the RPM of the shaft and propulsion engines also changes, while the RPM of the auxiliary engines usually remains constant.

In the frequency spectra presented here for these two ships, there are many other distinctive frequencies associated with other mechanisms of operation. The distinction of selected frequencies is only informative, and offers the possibility of identifying a given ship based on the characteristic frequency components of the recorded signal.

## EXPERIMENTAL EXAMINATION OF UNDERWATER NOISE GENERATED BY A MOVING SHIP

The aim of this research was to determine whether two configurations of a given ship could be distinguished by means of hydroacoustic passive measurements, using repeated passes of the ship over the measurement system.

The ship (length 60 m, width 10 m, draught 3 m) had a speed of up to 12 knots, and moved in both directions along a given course above a stationary measuring system. A hydrophone was placed at a depth of about 10 m. The experiment was divided into two stages, each of which required the ship to have different configuration of fixed machinery and speed.

Fig. 4 shows the first set of paths of the ship, in the form of GPS traces plotted on a map of the area used for research.

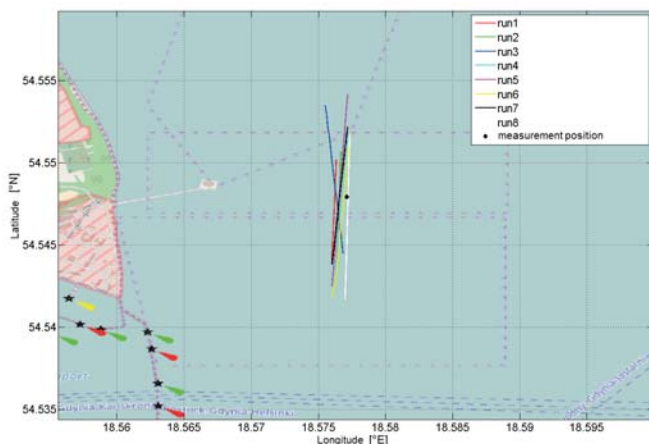


Fig. 4. Map of the area with the first set of trajectories and the position of the measuring system.

Fig. 5 shows the second set of transitions, in which the GPS traces of the ship are shown in the same way.

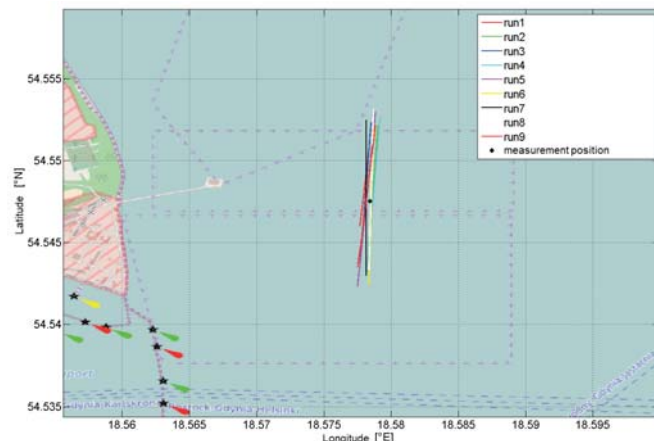


Fig. 5. Map of the area with the second set of trajectories and the position of the measuring system.

The data analysis process was divided into two stages. The first step was to determine the sound pressure level for each of the transitions. Figs. 6 and 7 show the results plotted as 3D charts, showing the distance of the ship from the measurement system.

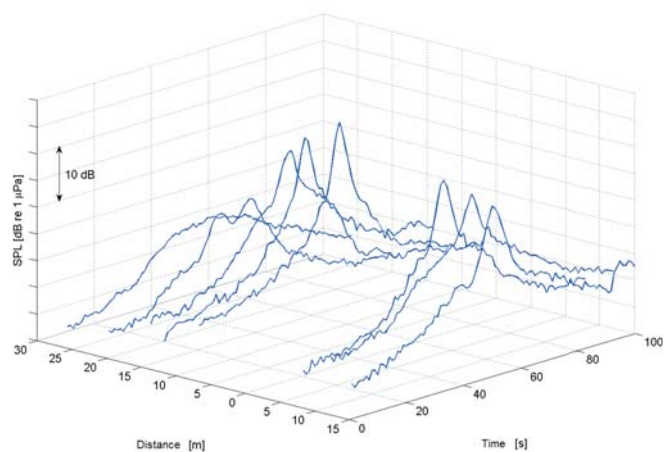


Fig. 6. Set of broadband SPL values for individual ship runs for the first configuration. Results corrected with absorption coefficient in bandwidth up to 25 kHz.

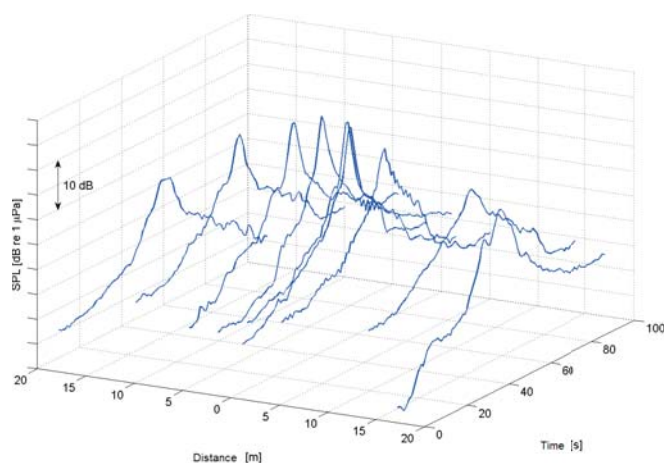


Fig. 7. Set of broadband SPL values for individual ship runs for the second configuration. Results corrected with absorption coefficient in bandwidth up to 25 kHz.

The graphs of SPL show changes (decreases) with increasing distance, both before and after the measuring point along the trajectory of the tested ship. The effect of the lateral distance at which the ship passes the position of the hydrophone can also be observed. The machinery parameters for each configuration were unchanged during each set of runs. CPA data were used at the frequency analysis stage, taking into account the dependence on absorption coefficient as a function of frequency [1, 4]. The results were corrected using a curve representing absorption in the frequency domain taken from [1], based on the Francois–Garrison equation. According to this equation, the absorption coefficient affects only higher frequencies of the broadband signal, above 1 kHz. It is caused by small distances (up to 30 m). The absorption loss below 1 kHz is negligible and does not affect the results of measurement. The absorption in different underwater environments is shown in Fig. 8 as a set of curves in the frequency domain up to  $10^3$  kHz [1].

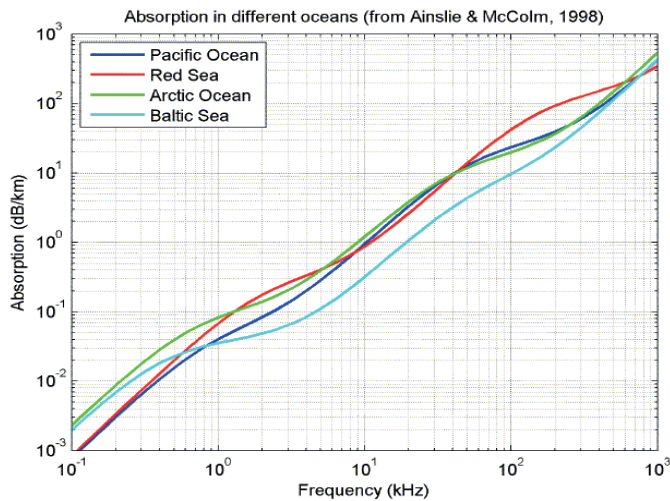


Fig. 8. Acoustic wave absorption versus frequency for different water environments [14].

The next step was to perform a frequency analysis at two bandwidths, 1/3-octave [8] and narrowband. The results of 1/3-octave analysis for each of the transitions are shown as a set of curves in Figs. 9 and 10 for both sets of measurements.

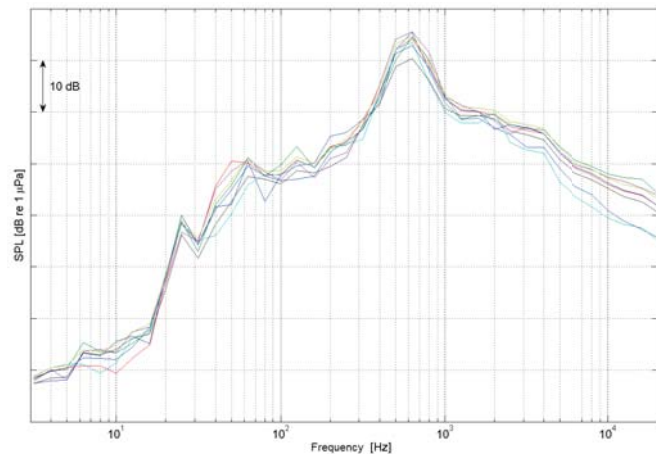


Fig. 9. Results of 1/3-octave spectral analysis for the first configuration with absorption loss correction.

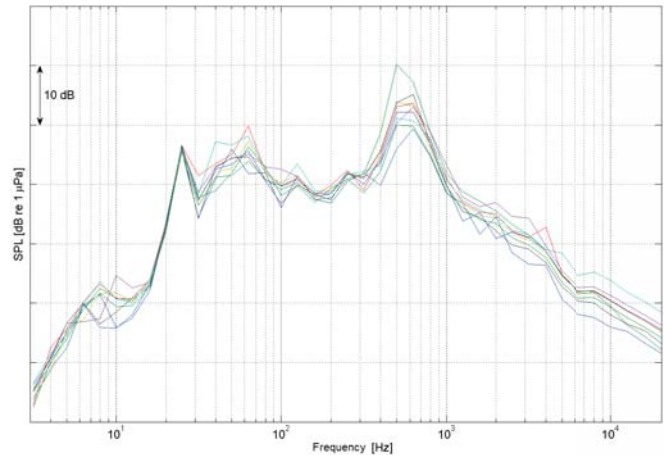


Fig. 10. Results of 1/3-octave spectral analysis for the second configuration with absorption loss correction.

The results of 1/3-octave analysis shown in Figs. 9 and 10 were obtained for two configurations of the ship's machinery, with repeated measurements. The narrowband spectrum was analysed in the same way.

To demonstrate the differences in the spectra for the two configurations of the ship's machinery, the result for all runs were averaged and presented in Fig. 11.

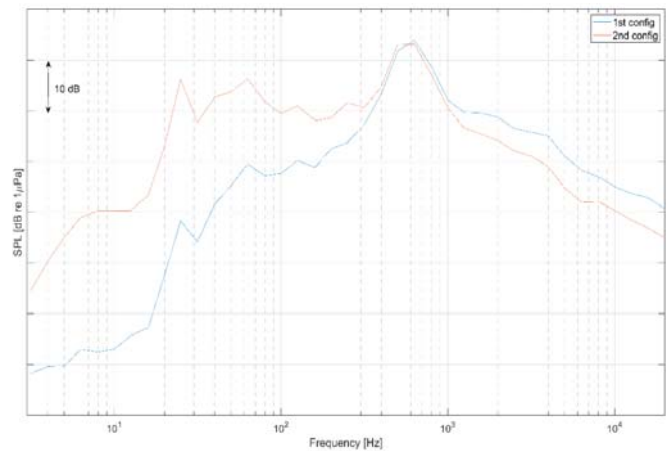


Fig. 11. Comparison between the average results of a 1/3-octave spectral analysis for two configurations of the operating mechanism of a ship.

A narrowband frequency analysis was performed in the range 5–2 kHz. The spectrum was calculated for the CPA, i.e. the highest SPL value of the signal. The maximum SPL value was located close to the centre of the ship, a few metres to the stern. This analysis also takes into account the absorption coefficient as a function of frequency, based on the Francois–Garrison equation. A set of curves was obtained representing the amplitude spectra for the same ship for the two configurations, and the results are shown in Figs. 12 and 13.

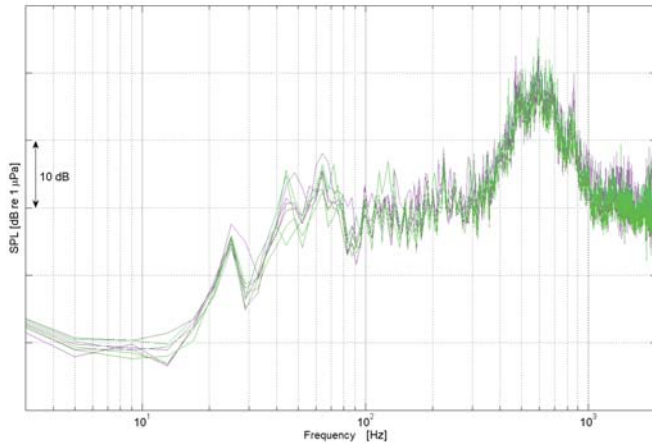


Fig. 12. Results of narrowband spectral analysis for the first configuration.

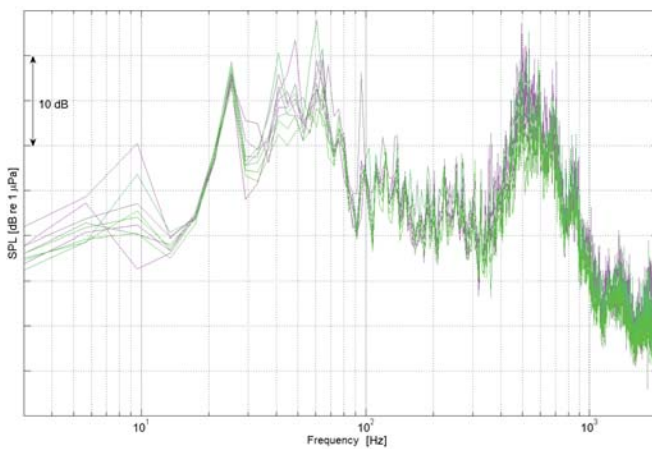


Fig. 13. Results of narrowband spectral analysis for the second configuration.

In a similar way to the 1/3-octave spectrum analysis, the narrowband spectrum results for all runs were averaged for each configuration, and are shown in Fig. 14. Both these results and those for the 1/3-octave spectrum show how the noise spectra generated by a given ship are connected with the configuration of the source parameters for the ship's machinery. This demonstrates the possibility of applying diagnostics to a particular configuration for a ship.

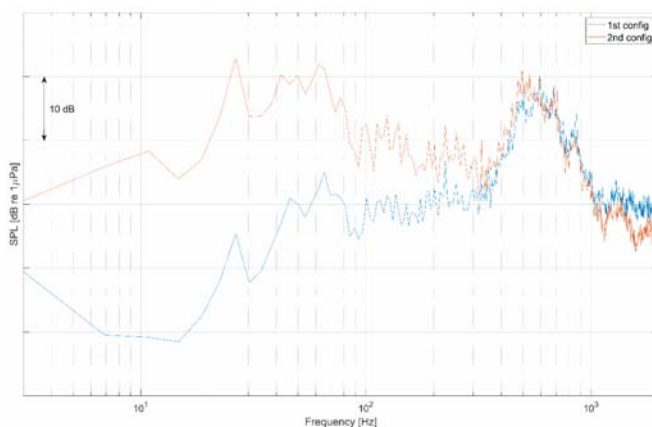


Fig. 14. Comparison between average narrowband spectral analysis results for two configurations of a ship's operating mechanism.

The sound pressure level of between 300 Hz and 1 kHz was similar for the first and second configurations, suggesting that the predominant source mechanism does not change when the configuration changes. A similarity between the amplitude spectra for both configurations can be observed; characteristic frequencies appear in both cases, although the amplitudes differ. This means that a given type of a ship could be identifiable based on the specific frequencies, while the differences in level indicate a change in the parameters of the ship's components.

All spectra shown in Figs. 9 to 14 were corrected for the absorption effect. The absorption calculations were made for the near field, and were based on the Francois–Garrison formula for the relevant bandwidth, for a water depth of up to 10 m with salinity 7 ppm. There were no significant differences in the results obtained for the different directions in which the ship passed, but the heading data were collected for each pass and added as metadata to the recorded signals.

## CONCLUSIONS

A frequency analysis of the hydroacoustic field of a moving ship can be used to support the process of object classification. These analyses can also be used in diagnostic testing of a ship's machinery in conjunction with the use of an on-board measurement system. To achieve this, it is necessary to create a database of the main settings and operating parameters of the ship's equipment. For ships of the same type, it is possible to determine the configuration of the operating equipment based on the narrowband and 1/3-octave spectra.

The use of an experiment involving multiple transitions of the ship with certain settings demonstrated similarities between the designated individual spectra for CPA.

## REFERENCES

1. Ainslie M. A., McCollm J. G. (1998): *A simplified formula for viscous and chemical absorption in sea water*. The Journal of the Acoustical Society of America, 103(3), 1671-1672. DOI: 10.1121/1.421258.
2. Arveson P. T., Vendittis D. J. (2000): *Radiated noise characteristics of a modern cargo ship*. The Journal of the Acoustical Society of America, 107(1), 118-129. DOI: 10.1121/1.428344.
3. Erbe C., Marley S. A., Schoeman R. P., Smith J. N., Trigg L. E., Embling C. B. (2019): *The effects of ship noise on marine mammals*. Review Frontiers in Marine Science, 6. DOI: 10.3389/fmars.2019.00606.
4. Francois R. E., Garrison G. R. (1982): *Sound absorption based on ocean measurements: Part II: Boric acid contribution and equation for total absorption*. Journal of the Acoustical Society of America, 72(6), 1879-1890. DOI: 10.1121/1.388673.

5. Freitag L., Grund M., Von Alt C., Stokey R. (2005): *A shallow water acoustic network for mine countermeasures operations with autonomous underwater vehicles*. Conference Proceedings of Underwater Defense.
6. Gloza I., Buszman K. (2011): *The multi-influence passive module for underwater environment monitoring*. Hydroacoustics, 14, 47-54.
7. Gloza I., Buszman K., Józwiak R. (2013): *Tracking underwater noise sources with the use of a passive method*. Acta Physica Polonica A, 123(5), 1090-1093. DOI: 10.12693/APhysPolA.123.1090.
8. Gloza I., Józwiak R., Buszman K. (2014): *The one-third octave spectrum as a method of vessel identification*. Hydroacoustics, 17, 63-68.
9. Grządziela A. (2006): *Analysis of vibration parameters of ship gas turbine engines*. Polish Maritime Research, 2, 22-26.
10. ISO 17208-1:2016 (2016): *Underwater acoustics—Quantities and procedures for description and measurement of underwater sound from ships*.
11. Kozaczka E., Grelowska, G. (2018): *Propagation of ship-generated noise in shallow sea*. Polish Maritime Research, 2(98), 37-46. DOI: 10.2478/pomr-2018-0052.
12. Kuşku H., Yiğit M., Ergün S., Yiğit Ü., Taylor N. (2018): *Acoustic noise pollution from marine industrial activities: Exposure and impacts*. Aquatic Research, 1(4), 148-161. DOI: 10.3153/AR18017.
13. Lus T. (2012): *Marine diesel engine diagnostics in operating conditions*. Diagnostyka, 2(62), 43-47.
14. McKenna M. F. (2012): *Underwater radiated noise from modern commercial ships*. Journal of the Acoustical Society of America, 131(1), 92-103. DOI: 10.1121/1.3664100.
15. Southall B. L. (2004): *Shipping noise and marine mammals: A forum for science, management, and technology*. Final Report of the National Oceanic and Atmospheric Administration (NOAA) International Symposium. U.S. NOAA Fisheries, Arlington, Virginia, May 18–19.

## CONTACT WITH THE AUTHOR

**Krystian Buszman**

e-mail: k.buszman@amw.gdynia.pl

Polish Naval Academy,  
Smidowicza 69  
81-127 Gdynia,  
**POLAND**

## EFFECT OF ROTATIONAL SPEED OF A SELF-ASPIRATING MIXER ON OXYGEN SATURATION IN WATER

Andrzej Wróblewski

Aldona Skotnicka-Siepsiak

University of Warmia and Mazury in Olsztyn, Poland

### ABSTRACT

*There are two categories of gas-liquid mixers: conventional and special-purpose. In theory, any conventional mixer can be applied to aerate a liquid, but fast-rotating devices are generally preferred. Special-purpose mixers (tubular, prismatic, cylindrical) have a hollow shaft, and operate by drawing gas from above the surface of the liquid and dispersing it inside the liquid. This process is referred to as aspirated aeration. In contrast, conventional mixers increase the pressure of the aspirated gas. Gas drawn from above the surface of the liquid flows through channels bored inside the shaft and the impeller, and is introduced to the liquid in this way. This article presents the results of an experiment investigating the aeration efficiency of a six-tube self-aspirating mixer at different rotational speeds. The experiment was conducted in a flow tank. The results indicate that self-aspirating mixers are effective devices for water aeration and mixing.*

**Keywords:** water aeration, self-aspirating mixer, tubular mixer

### INTRODUCTION

The oxygen content of water is a very important consideration in analyses of environmental processes, and this problem has been addressed by numerous researchers. According to Gamo [1], the concentration of oxygen at the bottom of the Sea of Japan has decreased by approximately 8–10% over the last 30 years, which can be attributed to global climate change and higher sea surface temperatures in winter. Seasonal changes in oxygen concentration in the North Sea have also been extensively researched [2]. An analysis of more than 19,000 sets of data covering the period 1980 to 2010 revealed that oxygen concentration ranged between 0.9 and 1.8 mg/l between July and October. Human activities

also induce changes in the surface aeration of bodies of water and rivers. Stigebrandt and Kalen [3] evaluated the effect of hypolimnetic oxygenation in five Danish lakes, and demonstrated that deep water aeration should be used only as a temporary strategy to promote the survival of aquatic organisms in anaerobic periods. To promote a sustainable increase in oxygen concentration, this method should be combined with a reduction in nutrient levels. Mostefa and Ahmed [4] analysed the effectiveness of hypolimnetic oxygenation with the use of the “Tanytarsus” diffuser system in Lake Hallwil in Switzerland. In a study by Stigebrandt et al. [5], the deep water of the anoxic By Fjord in Sweden was aerated with oxygen aspirated from the surface. A 10-year study of forced aeration and destratification was also carried out in Lake Długie in Olsztyn [5]. Aeration techniques have

been successfully used to remediate the Oeiras River in Portugal, the Emsche in Germany, the Thames in the UK, and the Homewood Canal in the USA [7].

Aeration is widely applied in the treatment of water and effluent to enhance the biological potential of wastewater and make it suitable for reuse. Water is aerated via the use of pressure aerators, air-stripping towers, bubble diffusers, surface aerators and cascade aerators with aeration nozzles [8], and new technologies for water and wastewater treatment are being constantly developed [9]. Advanced oxidation processes (AOPs) show considerable potential in view of the provisions of Directive 2013/39/EU on priority substances in the field of water policy [10], since these treatments can remove natural organic matter [11] and pharmaceuticals [12] from drinking water. AOPs are also applied in hybrid treatment processes, sulphate-radical oxidation, heterogeneous semiconductor photocatalysis and electrochemical advanced oxidation for water/wastewater treatment [13]. AOPs can also be combined with biological methods to reduce costs [14]. Recent years have also witnessed considerable interest in electrochemical oxidation, which is particularly effective in removing textile, olive oil, pulp, paper mill and tannery effluents [15]. Kumar, Nidheesh and Kumar [16] relied on the above method to remove colour and chemical oxygen demand (COD). Efforts are also being made to optimise and improve existing technologies. Aeration processes can be modelled to minimise the demand for energy during effluent and water treatment without compromising the quality of the water. Aeration is the most energy-intensive process in wastewater treatments that rely on the activated sludge method. During upgrading of a wastewater treatment plant in Tychy, energy consumption was decreased to 0.46 kWh/m<sup>3</sup> by modelling the demand for oxygen in the activated sludge process and introducing efficient aeration devices [17]. Asadi et al. [18] analysed industrial data obtained from the Detroit Water and Sewerage Department, which provides water and wastewater services to around 35% of Michigan's population. They relied on a multi-adaptive regression spline algorithm to demonstrate that the airflow rate could be decreased by around 31% while keeping the quality of the water within the acceptable range. Numerical simulation methods were also employed by Daskiran et al. [19], who developed a large eddy simulation model for a modular pump-turbine to analyse oxygen dissolution inside the draft tube. Kalenik et al. [20] analysed the effects of air and water flow rates on the oxygen content of water oxygenated in a pipe aerator. Filtering and aeration technologies are also being optimised, such as the use of biological aerated filters for the removal of iron and manganese ions in water treatment [21]. Future research is likely to focus on up-flow biological aeration filters (BAFs) and non-pathogenic microbes isolated from the resident environment. Bao et al. [22] investigated the applicability of autoclaved aerate concrete particles in BAFs. Kujawiak et al. [23] analysed the effectiveness of aeration in moving bed airlift bioreactors, and found that beds with a high specific surface area improved aeration and that the optimal position of the aeration nozzle in the airlift pump significantly

improved circulation and increased oxygen concentration in the reactor. Boog et al. [24] examined the application of two prototype systems, a saturated horizontal flow system (HA) and a saturated vertical down-flow system (VA), for aerated sub-surface flow treatment wetlands, to determine the resilience of organic carbon and nitrogen removal processes after an interruption in aeration. Freeman et al. [25] proposed a new aeration approach for sites such as airports, which was based on unplanted, artificially aerated, horizontal subsurface flow constructed wetlands. The described solution was significantly more effective in removing pollutants than alternative methods, and more than 90% of the influent load for COD, BOD<sub>5</sub> and TOC was removed. Shulka and Goel [26] analysed the performance of two sets of solid jet aerators with openings with areas of 594.96 mm<sup>2</sup> and 246.30 mm<sup>2</sup> and rectangular nozzles with rounded ends. In an article by Shukla et al. [27], the authors analysed the impact of changes to the shapes of the aerator holes on the efficiency of the oxygenation process. Of the different types of jet geometry considered (elliptical, circular, rectangular, and rectangular with rounded edge) they reported that the most beneficial shape for high oxygen transfer aerators was rectangular openings with rounded ends. Ghotli et al. [28] dealt with the influence of rotor design, mixing time and air entrainment point, and carried out a study of a single liquid phase under turbulent conditions using both conventional and new impeller designs. Experimental comparative studies of various aerator designs were presented in [29], involving various configurations of the aeration process and energy consumption, and curved blade impellers with three, six, nine, and 12 blades. The optimal configuration turned out to be a construction with nine blades. Work by Du et al. [30] focused on sewage collection and aeration in rectangular water tanks, which were compared with three layouts of fine-pore aeration tubes (a disc-type diffuser, a four-corner-type diffuser and a distribute-type diffuser) at three airflow rates. The issue of maintaining the critical level of oxygen concentration in fluids with high viscosity was studied in [31], and the authors examined how the aeration efficiency could be enhanced by operating a downward-pumping high-solidity ratio central impeller at a low critical speed with a slowly-rotating anchor impeller.

Special attention was paid to published studies aiming to optimise or develop new structural solutions for aeration mixers. Rzymiski and Stelmach [32] analysed aeration processes involving a helical screw and ribbon impellers. Stelmach [33] investigated the effectiveness of turbine-disc impellers with a stator, and Heim and Stelmach [34] examined several types of impellers for sparger aeration. Various solutions for modifying impellers with diagonally folded blades were also analysed [35]. It appears that a self-aspirating mixer with a tubular structure could pose an alternative solution; this device has a simple structure and does not require an external air supply source, which minimises operating costs without compromising aeration efficiency. A self-aspirating mixer with a tubular structure was designed, built and tested in this study (Fig. 1).

## MEASUREMENT METHODS

The air flow rate can be measured in water treatment plants and in wastewater treatment plants with the activated sludge system using models to simulate the activated sludge treatment process. In a water treatment plant, the aeration rate is determined by removing oxygen from the water and measuring the increase in the oxygen content of the water over time. The concept of oxygenation capacity was developed by Kessener and Ribbius, and was further elaborated by Pasveer [36], who proposed the following formula:

$$OC = 11.33 \cdot \frac{1}{\Delta t} \ln \frac{D_0}{D_t} \cdot \sqrt{\frac{k_{10}}{k_t}} \quad (1)$$

where OC is the oxygenation capacity in g/m<sup>3</sup>h, the value 11.33 is the oxygen saturation in water at a temperature of 10°C, where water comes into contact with air with 20.9% oxygen content under an atmospheric pressure of 1013 hPa, in g/m<sup>3</sup>,

$\Delta t = t_1 - t_0$  is the observation time, in h,

$D_0 = C_s - C_0$ , in g/m<sup>3</sup>,

$D_t = C_s - C_t$ , in g/m<sup>3</sup>,

$C_0$  is the initial oxygen concentration, in g/m<sup>3</sup>,

$C_s$  is the oxygen saturation, in g/m<sup>3</sup>,

$C_t$  is the oxygen concentration after time t, in g/m<sup>3</sup>,

$\sqrt{\frac{k_{10}}{k_t}}$  is the coefficient for temperature compensation, where  $k_t$  is the temperature of the experimental water, and  $k_{10}$  is the reference temperature (10°C) (Table 1).

Table 1. Ratio of oxygen diffusion constants  $\sqrt{\frac{k_{10}}{k_t}}$  for different temperatures (°C).

Temperature °C	$\sqrt{\frac{k_{10}}{k_t}}$	Temperature °C	$\sqrt{\frac{k_{10}}{k_t}}$
9	1.019	17	0.878
10	1.000	18	0.861
11	0.982	19	0.845
12	0.964	20	0.830
13	0.946	21	0.815
14	0.928	22	0.799
15	0.911	23	0.784
16	0.895	24	0.770

Oxygenation capacity (OC) describes the rate at which oxygen is introduced to deoxygenated water (0 mg O<sub>2</sub>/m<sup>3</sup>) at a temperature of 10°C under an atmospheric pressure of 1013 hPa. A formula describing the effect of temperature on OC values can be used to perform measurements under different conditions:

$$OC_{(t)} = OC_{10} \cdot \frac{C_{S(t)}}{C_{S(10)}} \cdot \sqrt{\frac{k_t}{k_{10}}} \quad (2)$$

OC can also be expressed in terms of the overall coefficient of oxygen transfer  $K_{La}$ . The relationship between OC and  $K_{La}$  can be described as follows:

$$OC = C_s K_{La} \quad (3)$$

where  $C_s$  is the oxygen saturation at a temperature of 10°C under an atmospheric pressure of 1013 hPa, in g/m<sup>3</sup>.

Since  $K_{La}$  is determined at a temperature of 20°C, the relevant adjustments have to be made to the calculations of  $K_{La}$  and OC.

In real-life conditions, the value of  $K_{La}$  is generally lower for sewage than for mains water. A coefficient  $\alpha$  was therefore introduced to express the correlation between the OC of sewage and the OC of mains water.

$$\alpha = \frac{K_{La}(\text{sewage})}{K_{La}(\text{water})} \quad (4)$$

Since  $\alpha$  is calculated for a specific sewage sample, and oxygen saturation in wastewater generally differs from that determined in mains water, a further coefficient  $\beta$  was introduced:

$$\beta = \frac{C_s'(\text{sewage})}{C_s(\text{water})} \quad (5)$$

For an atmospheric pressure other than 1013 hPa, the oxygen saturation in water is calculated using the following equation:

$$(C_s)_p = (C_s)_{1013} \left[ \frac{P-p}{1013-p} \right] \quad (6)$$

where P is the pressure under aeration conditions, in hPa, and p is the saturation pressure of water vapour, in hPa.

The influence of temperature on the value of the coefficient  $K_{La}$  is expressed by the following formula:

$$(K_{La})_t = (K_{La})_{20} \cdot 1.024^{(t-20)} \quad (7)$$

where t is the temperature under specific aeration conditions.

The total OC under the given conditions can be expressed by the following formula [31]:

$$OC = \alpha (K_{La})_{20} \left[ \frac{P-p}{1013-p} \beta C_s - C_L \right] \cdot 1.024^{(t-20)} \quad (8)$$

where  $C_L$  is the oxygen concentration in the aeration chamber in the activated sludge process, in g/m<sup>3</sup>.

## EXPERIMENTAL DESIGN

The experiment involved a self-aspirating mixer composed of six tubes. A design patent application for the mixer has been submitted to the patent office (Fig. 1). The self-aspirating mixer operates on a very simple principle: the tubes (Fig. 1) (2) are bevelled at an angle, and negative pressure is produced at the end of the impeller tubes at a given rotational speed in a given direction (Fig. 1) (2). As a result of the difference in pressure, air above the surface of the water is drawn in and diffused into the liquid.

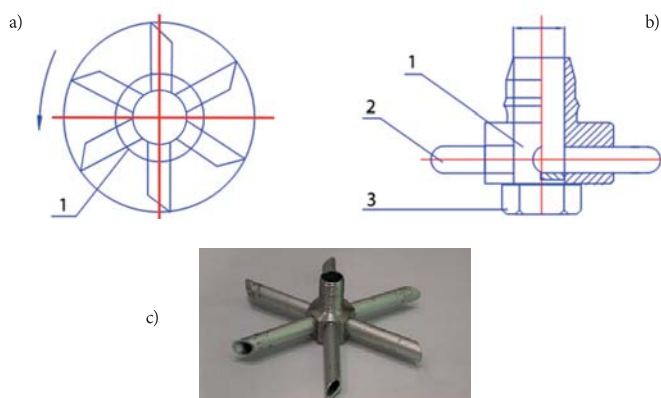


Fig. 1. Six-tube mixer: (a) top view of the mixer; (b) cross-sectional view of the mixer (1 – body, 2 – tube, 3 – screw); (c) photograph of the mixer.

The experiment was conducted in a flow tank measuring 1.2 x 0.8 x 0.4 m. Oxygen content was measured with two oxygen probes, one of which was placed inside aeration chamber 1, and the other in aeration chamber 2 (Fig. 2). The data supplied by the probes were analysed to determine the dissolution of oxygen from the air supplied by the aerator.

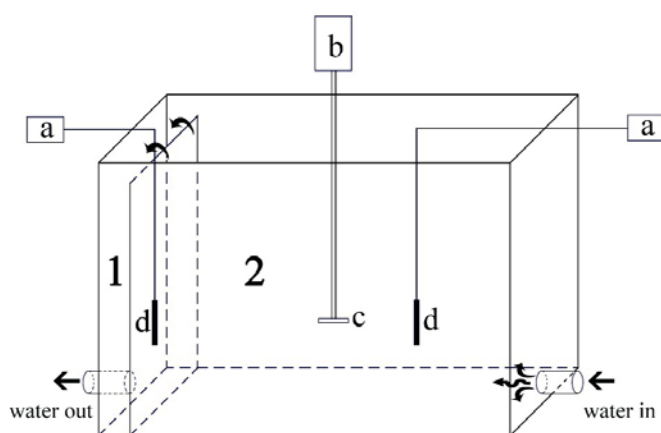


Figure 2. Diagram of the test stand: 1- chamber1, 2-chamber2; (a) oxygen meter, (b) engine, (c) six-tube mixer, (d) oxygen sensor

Measurements were performed using Elmetron laboratory oxygen sensors with a detection range of 0 to 60 mg/dm<sup>3</sup> and a resolution of 0.001 mg/dm<sup>3</sup>. These sensors automatically compensate for the effects of atmospheric pressure and temperature on the oxygen concentration of a liquid. The

dose of Na<sub>2</sub>HSO<sub>3</sub> required for oxygen removal was determined based on the results of previous experiments. Na<sub>2</sub>HSO<sub>3</sub> solution was added to water in a separate 1.2 m<sup>3</sup> tank and stirred for 3 min. The oxygen concentration of the water was checked every 3 min, and when this had stabilised, it was adopted as the initial value (C<sub>p</sub>). The rate at which oxygen was dissolved in the water was determined using a self-designed mixer composed of six tubes with a diameter of 50 mm (Fig. 1), at various rotational speeds in the range  $n = 1000$  to 4000 rpm and a flow rate of  $Q = 70$  dm<sup>3</sup>/min. The oxygen concentration of the water was measured every 5 s. The data were used to calculate the OC using Equation (1), and the results are shown in Figures 4 and 6. The period of measurement at a rotational speed of 4000 rpm was shortened for safety reasons.

## RESULTS

The results of the experiment indicate that the OC increased considerably in the first stage of aeration with the self-aspirating mixer. The first stage of aeration generally lasted 100 to 400 s, subject to rotational speed, and the OC decreased successively after that time.

Oxygen concentration C<sub>x</sub> increased with a rise in OC, within the first 50–400 s of aeration on average, and then stabilised. Oxygen levels increased proportionally with an increase in rotational speed, i.e. the higher the speed, the higher the value of C<sub>x</sub>. When the changes in the values of C<sub>x</sub> (Fig. 3) and OC (Fig. 4) in chamber 2 are compared with the changes in the values of C<sub>x</sub> (Fig. 5) and OC (Fig. 6) in chamber 1, certain variations can be observed in the maximum values obtained in both chambers. The values of C<sub>x</sub> and OC were higher in chamber 1 than in chamber 2. The values of OC were higher by 3 kg O<sub>2</sub>/m<sup>3</sup> h in chamber 1 (Fig. 6) than in chamber 2 (Fig. 4). In chamber 2, water was intensively aerated, while deaerated water was mixed. The aerated and mixed water then flowed into chamber 1, which can explain the differences in OC values (Fig. 2). The results can be analysed and interpreted in various ways [37]. In this work, empirical equations  $y = a \ln(x) + b$  were used, as shown in Table 2. Calculations were carried out in Microsoft Excel. The coefficient of determination  $R^2 = 1 - \varphi^2$  was adopted as the correlation measure. These equations describe the oxygen concentration only until oxygen saturation is reached; after this, the amount of oxygen does not change, and the graph takes the form of a horizontal line. Table 2 shows the time for which logarithmic behaviour is seen before reaching oxygen saturation.

Table 2. Coefficients of the equation  $y = a \ln(x) + b$

Mixer speed (RPM)	a	b	R <sup>2</sup>	Time (s)
1000	14.41	79.44	0.961	572
1500	24.97	128.08	0.939	470
2000	28.46	161.53	0.985	210
2500	35.14	168.9	0.922	270
3000	39.11	202.37	0.924	280
3500	39.92	219.09	0.927	280
4000	40.88	237.75	0.963	150

## SUMMARY

The results of the experiment indicate that our self-aspirating tubular mixer is an effective aeration device. The mixer has a simple structure, which does not require an external air supply source, and this reduces the operating costs. Aeration intensity was calculated using the ratio of the observed oxygen concentration to the potential oxygen concentration that can be achieved at a given temperature. The self-designed tubular mixer enabled the relatively rapid achievement of the target oxygen saturation: target saturation values were obtained within approximately 100 s at mixing speeds of 2500–4000 rpm (Figs. 3 and 5), although aeration was less effective at lower rotational speeds. Oxygen concentration became stabilised over successive stages of aeration, and significant changes in this parameter were not observed during continued mixer operation.

It should also be noted that the self-designed mixer has relatively low power requirements for rotational speeds of 500, 1000, 1500, 2000, 2500, 3000, 3500 and 4000 rpm. This can be largely attributed to the small size of the mixer, and the small tube diameters and short arms. Due to its small size and low energy requirements, the mixer is suitable for use in domestic wastewater treatment systems and in water treatment installations.

In summary, the proposed self-aspirating tubular mixer can achieve a high oxygenation intensity within a relatively short operating time. Its design is very simple, cheap and straightforward. However, questions remain about the possibility of cooperation of such mixers working in the technological line. The effect of the distance between the mixers may affect the oxygenation values obtained, and rotational speeds may be important. In future work, simulations could be carried out using hydraulic software and compared with experimental results.

## REFERENCES

1. Gamo, T. (2011): Dissolved oxygen in the bottom water of the Sea of Japan as a sensitive alarm for global climate change. *TrAC Trends in Analytical Chemistry*, 30(8), 1308-1319.
2. Topcu, H. D., Brockmann, U. H. (2015): Seasonal oxygen depletion in the North Sea, a review. *Marine Pollution Bulletin*, 99(1-2), 5-27.
3. Stigebrandt, A., Kalén, O. (2013): Improving oxygen conditions in the deeper parts of Bornholm Sea by pumped injection of winter water. *Ambio*, 42(5), 587-595.
4. Mostefa, G., Ahmed, K. (2012): Treatment of water supplies by the technique of dynamic aeration. *Procedia Engineering*, 33, 209-214.
5. Stigebrandt, A., Liljebladh, B., De Brabandere, L., Forth, M., Granmo, Å., Hall, P., ... Norén, F. (2015): An experiment

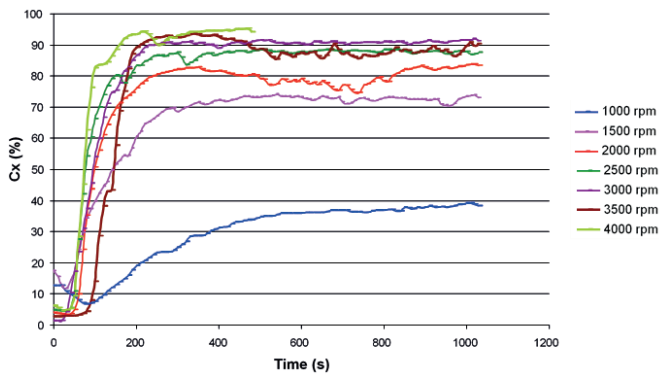


Fig. 3. Oxygen concentration in chamber 2 at different mixer speeds.

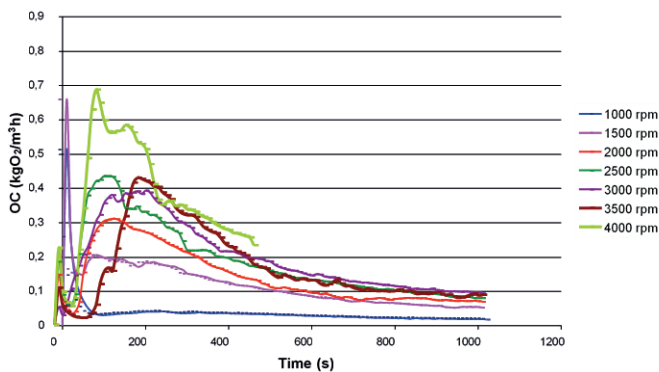


Fig. 4. Oxygenation capacity in chamber 2 at different mixer speeds.

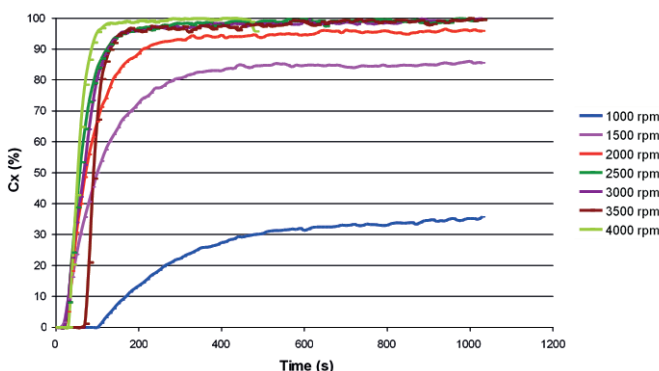


Fig. 5. Oxygen concentration in chamber 1 at different mixer speeds.

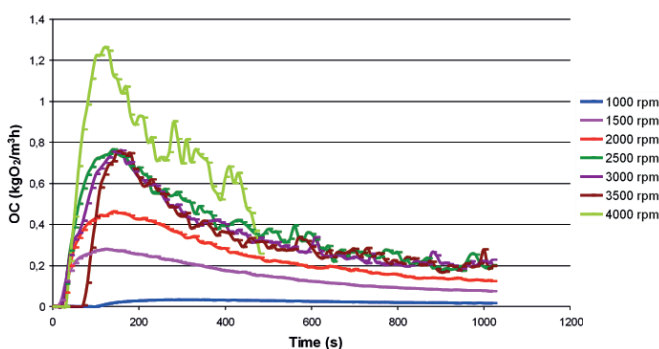


Fig. 6. Oxygenation capacity in chamber 1 at different mixer speeds.

- with forced oxygenation of the deepwater of the anoxic By Fjord, Western Sweden. *Ambio*, 44(1), 42-54.
6. Grochowska, J., Gawronska, H. (2004): Restoration effectiveness of a degraded lake using multi-year artificial aeration. *Polish Journal of Environmental Studies*, 13(6).
  7. Wang, J., Liu, X. D., Lu, J. (2012): Urban river pollution control and remediation. *Procedia Environmental Sciences*, 13, 1856-1862.
  8. Anielak, A. M. (2015): Wysokoefektywne metody oczyszczania wody.
  9. Salgot, M., Folch, M. (2018): Wastewater treatment and water reuse. *Current Opinion in Environmental Science Health*.
  10. Ribeiro, A. R., Nunes, O. C., Pereira, M. F., Silva, A. M. (2015): An overview on the advanced oxidation processes applied for the treatment of water pollutants defined in the recently launched Directive 2013/39/EU. *Environment International*, 75, 33-51.
  11. Matilainen, A., Sillanpää, M. (2010): Removal of natural organic matter from drinking water by advanced oxidation processes. *Chemosphere*, 80(4), 351-365.
  12. Kanakaraju, D., Glass, B. D., Oelgemöller, M. (2018): Advanced oxidation process-mediated removal of pharmaceuticals from water: A review. *Journal of Environmental Management*, 219, 189-207.
  13. Dewil, R., Mantzavinos, D., Poullos, I., Rodrigo, M. A. (2017): New perspectives for advanced oxidation processes. *Journal of Environmental Management*, 195, 93-99.
  14. Oller, I., Malato, S., Sánchez-Pérez, J. (2011): Combination of advanced oxidation processes and biological treatments for wastewater decontamination—A review. *Science of the Total Environment*, 409(20), 4141-4166.
  15. Särkkä, H., Bhatnagar, A., Sillanpää, M. (2015): Recent developments of electro-oxidation in water treatment—A review. *Journal of Electroanalytical Chemistry*, 754, 46-56.
  16. Kumar, A., Nidheesh, P. V., Kumar, M. S. (2018): Composite wastewater treatment by aerated electrocoagulation and modified peroxi-coagulation processes. *Chemosphere*, 205, 587-593.
  17. Roksel, M., Heidrich, Z. (2017): Energochłonność napowietrzania w procesie osadu czynnego. *Gaz, Woda i Technika Sanitarna*.
  18. Asadi, A., Verma, A., Yang, K., Mejabi, B. (2017): Wastewater treatment aeration process optimization: A data mining approach. *Journal of Environmental Management*, 203, 630-639.
  19. Daskiran, C., Riglin, J., Schleicher, W. C., Oztekin, A. (2018): Computational study of aeration for wastewater treatment via ventilated pump-turbine. *International Journal of Heat and Fluid Flow*, 69, 43-54.
  20. Kalenik, M., Wichowski, P., Morawski, D., Chalecki, M. (2017): Kinetics of water oxygenation in pipe aerator. *Infrastruktura i Ekologia Terenów Wiejskich*.
  21. Marsidi, N., Hasan, H. A., Abdullah, S. R. S. (2018): A review of biological aerated filters for iron and manganese ions removal in water treatment. *Journal of Water Process Engineering*, 23, 1-12.
  22. Bao, T., Chen, T., Wille, M. L., Chen, D., Bian, J., Qing, C., ... Frost, R. L. (2016): Advanced wastewater treatment with autoclaved aerated concrete particles in biological aerated filters. *Journal of Water Process Engineering*, 9, 188-194.
  23. Kujawiak, S., Gawrońska, A., Matz, R., Makowska, M. (2017): Efektywność procesu napowietrzania w reaktorach barbotażowych ze złożem ruchomym. *Czasopismo Techniczne*, 2017 (Volume 3).
  24. Boog, J., Nivala, J., Aubron, T., Mothes, S., van Afferden, M., Müller, R. A. (2017): Resilience of carbon and nitrogen removal due to aeration interruption in aerated treatment wetlands. *Science of The Total Environment*, 621, 960-969.
  25. Freeman, A. I., SurrIDGE, B. W., Matthews, M., Stewart, M., Haygarth, P. M. (2018): New approaches to enhance pollutant removal in artificially aerated wastewater treatment systems. *Science of the Total Environment*, 627, 1182-1194.
  26. Shukla, B. K., Goel, A. (2018): Study on oxygen transfer by solid jet aerator with multiple openings. *Engineering Science and Technology: An International Journal*, 21(2), 255-260.
  27. Shukla, B. K., Khan, A., Saikiran, G., Sriram, M. A. (2019): Comparative study on effect of variation in opening shape on oxygenation performance of surface jet aerators used in water and wastewater treatment. *Journal of Green Engineering*, 9(3), 427-440.
  28. Ghotli, R. A., Shafeeyan, M. S., Abbasi, M. R., Raman, A. A. A., Ibrahim, S. (2020): Macromixing study for various designs of impellers in a stirred vessel. *Chemical Engineering and Processing - Process Intensification*, 148, 107794.
  29. Adel, M., Shaalan, M. R., Kamal, R. M., El Monayeri, D. S. (2019): A comparative study of impeller aerators

configurations. *Alexandria Engineering Journal*, 58(4), 1431-1438.

30. Du, Y., Chen, F., Zhou, L., Qiu, T., Sun, J. (2020): Effects of different layouts of fine-pore aeration tubes on sewage collection and aeration in rectangular water tanks. *Aquacultural Engineering*, 102060.
31. Jegatheeswaran, S., Kazemzadeh, A., Ein-Mozaffari, F. (2019): Enhanced aeration efficiency in non-Newtonian fluids using coaxial mixers: High-solidity ratio central impeller with an anchor. *Chemical Engineering Journal*, 378, 122081.
32. Rzyski, E., Stelmach, J. (2005): Napowietrzanie z użyciem mieszadła ze zwiniętymi śrubowo łopatkami wstęgowymi. *Inżynieria i Aparatura Chemiczna*, (5s), 58-62.
33. Stelmach, J. (2006): Efektywność mieszadeł turbinowo-tarczowych z kierownicą. *Przemysł Chemiczny*, 85(8-9), 1150-1153.
34. Heim, A., Stelmach, J. (2009): Porównanie efektywności wnikania masy dla mieszadeł z napowietrzaniem bełkotkowym. *Rocznik Ochrona Środowiska*, 11, 207-219.
35. Rieger, F., Jirout, T., Stelmach, J. (2017): Wpływ modyfikacji mieszadła z łamanymi łopatkami na efektywność mieszania. *Przemysł Chemiczny*, 96.
36. Suschka J., Zieliński J. (1979): Grajcar E. Urządzenia do natleniania ścieków. *Warszawa, Wydawnictwo Arkady*.
37. Burgan, H.I., Aksoy, H. (2020): Monthly flow duration curve model for ungauged river basins. *Water*, 12, 338.

## CONTACT WITH THE AUTHORS

**Andrzej Wróblewski**

*e-mail: andrzej.wroblewski@uwm.edu.pl*

**Aldona Skotnicka-Siepsiak**

*e-mail: aldona.skotnicka-siepsiak@uwm.edu.pl*

University of Warmia and Mazury in Olsztyn,  
Michała Oczapowskiego 2  
10-719 Olsztyn,  
**POLAND**